Preface

The 2016 GFD Program theme was *Fluid-Structure Interaction in the Living Environment* with Professors Mike Shelley of New York University and Anette 'Peko' Hosoi of the Massachusetts Institute of Technology serving as principal lecturers. Together they introduced the audience in the cottage and on the porch to a fascinating mixture of topics ranging from swimming and swarming to cycling and sprinting, with Professor Jun Zhang of New York University interjecting some more traditional GFD (and art) part way through. The first ten chapters of this volume document these lectures, each prepared by pairs of the summer's GFD fellows. Following the principal lecture notes are the written reports of the fellows' own research projects. This summer's fellows were:

- Sahil Agarwal, Yale University
- Keaton Burns, Massachusetts Institute of Technology
- Christopher Miles, University of Michigan
- Paula Doubrawa, Cornell University
- Michael Gomez, University of Oxford
- Qi Li, Princeton University
- Colin Meyer, Harvard University
- Jason Olsthoorn, University of Cambridge
- Oceane Richet, École polytechnique
- Anna Skipper, Georgia Institute of Technology

In 2016, the Sears Public Lecture was delivered by Professor Mimi Koehl, of the University of California, Berkeley on the topic of "Swimming and crawling in a turbulent world". The topic was particularly suitable for the summer's theme: combining key biological fluid-structure interactions in the world's oceans, and brilliantly presented by Mimi to a large and enraptured audience, who then enjoyed refreshments in the evening afterwards outside Redfield Auditorium.

Neil Balmforth and Colm-cille Caulfield acted as directors, and a large number of long-term staff members ensured that the fellows never lacked for guidance. The seminar series was filled by a steady stream of visitors, talking about topics as diverse as how icebergs melt to the true function of the foot. Anders Jensen worked his usual magic in the Lab, dealing inventively with spinning wheels, funky fluids, and many, many particles. As ever, Janet Fields, Julie Hildebrandt and Michelle Slattery kept the program running smoothly behind the scenes, with their assistance (and patience) hugely appreciated by the directors.

Table of Contents

Principal Lectures

Fellows' Reports

2016 Geophysical Fluid Dynamics Participants

FELLOWS

Agarwal, Sahil	Yale University
Burns, Keaton	Massachusetts Institute of Technology
Doubrawa, Paula	Cornell University
Gomez, Michael	University of Oxford
Li, Qi	Princeton University
Meyer, Colin	Harvard University
Miles, Christopher	University of Michigan, Ann Arbor
Olsthoorn, Jason	University of Cambridge
Richet, Océane	École Polytechnique
Skipper, Anna	Georgia Institute of Technology

STAFF AND VISITORS

Adduce, Claudia	University Roma Tre
Akers, Benjamin	Air Force Institute of Technology
Anderson, James	Stevens Institute of Technology
Arratia, Cristobal	Nordic Institute for Theoretical Physics
Balmforth, Neil	University of British Columbia
Breuer, Kenneth	Brown University
Colm-cille Caulfield	University of Cambridge
Cenedese, Claudia	Woods Hole Oceanographic Institution
Chini, Gregory	University of New Hampshire
Constantinou, Navid	Scripps Institution of Oceanography
Cvitanovic, Predrag	Georgia Institute of Technology
Davies Wykes, Megan	University of Cambridge
Doering, Charles	University of Michigan
Dressaire, Emilie	New York University
Eaves, Thomas	University of British Columbia
Flierl, Glenn	Massachusetts Institute of Technology
Fowler, Andrew	University of Limerick
Gallet de St. Aurin, Basile	CEA Saclay
Gelderloos, Renske	Johns Hopkins University
Goluskin, David	University of Victoria
Helfrich, Karl	Woods Hole Oceanographic Institution
Hewitt, Ian	University of Oxford
Hewitt, Duncan	University of Cambridge
Hosoi, Anette	Massachusetts Institute of Technology
Ishimoto, Kenta	Kyoto University
Jensen, Oliver	University of Manchester
Kaminski, Alexis	Oregon State University
Keller, Joseph	Stanford University

Lee, Sungyon	Texas A&M University
Maas, Leo	Royal Netherlands Institute for Sea Research
Mahadevan, Amala	Woods Hole Oceanographic Institution
Malkus, Willem	Massachusetts Institute of Technology
Mandre, Shreyas	Brown University
Moore, Nicholas	Florida State University
Oza, Anand	New York University
Pedlosky, Joseph	Woods Hole Oceanographic Institution
Powers, Thomas	Brown University
Pramanik, Satyajit	Nordic Institute for Theoretical Physics
Sauret, Alban	Centre Nationale de la Recherche Scientifique
Shelley, Michael	New York University
Spagnolie, Saverio	University of Wisconsin, Madison
Spiegel, Edward	Columbia University
Sutherland, Bruce	University of Alberta
Thiffeault, Jean-Luc	University of Wisconsin, Madison
Vasil Geoffrey	University of Sydney
Veronis, George	Yale University
von Herzen, Brian	The Climate Foundation
Whitehead, John	Woods Hole Oceanographic Institution
Worster, Grae	University of Cambridge
Yecko, Philip	Cooper Union
Young, Yuan-Nan	New Jersey Institute of Technology
Zhang, Jun	New York University

2016 Principal Lecturers

Anette “Peko” Hosoi

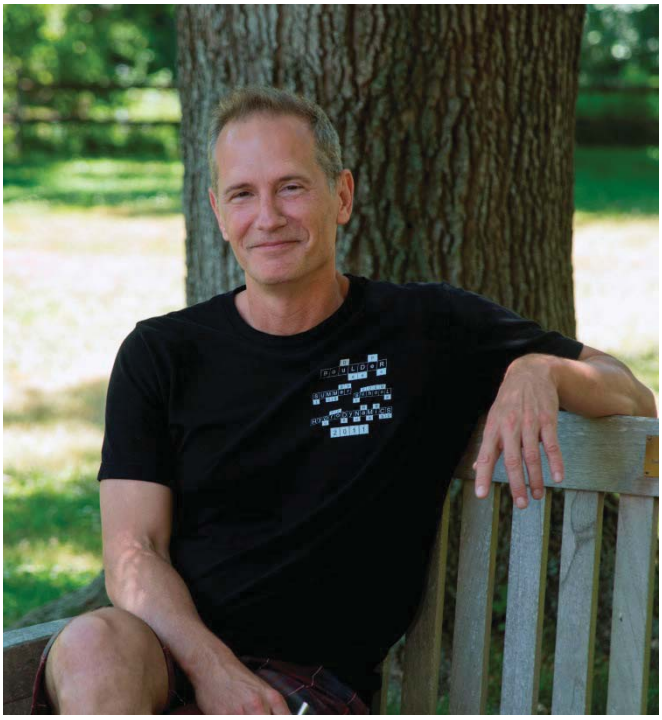

Michael Shelley

2016 Geophysical Fluid Dynamics Summer School Participants

First Row (L-R): (All seated) Peko Hosoi, Michael Gomez, Christopher Miles, Keaton Burns, Colin Meyer, Sahil Agarwal, Anna Skipper, Jason Olsthoorn, Oceane Richet, Qi Li, Paula Doubrawa, Michael Shelley, Shreyas Mandre

Second Row (L-R): Ed Spiegel (standing), Charlie Doering, David Goluskin, Ian Hewitt, Saverio Spagnolie, Greg Chini, Renske Gelderloos, George Veronis, Jean-Luc Thiffeault, Claudia Adduce, Basile Gallet, Alexis Kaminski, Neil Balmforth, Kenta Ishimoto, Brian von Herzen (standing)

Third Row (L-R): Satyajit Pramanik, Emilie Dressaire, Phil Yecko, Colm-cille Caulfield, Alban Sauret, Claudia Cenedese, Jack Whitehead, Glenn Flierl, Jim Anderson, Joe Pedlosky, Cristobal Arratia, Yuan-Nan Young, Karl Helfrich, Geoff Vasil

Missing from photo: Benjamin Akers, Navid Constantinou, Predrag Cvitanovic, Megan Davies Wykes, Andrew Fowler, Duncan Hewitt, Oliver Jensen, Sungyon Lee, Leo Maas, Amala Mahadevan, Nick Moore, Anand Oza, Thomas Powers, Bruce Sutherland, Grae Worster

Lecture Schedule

PRINCIPAL LECTURES

Monday, June 20

A Primer on Continuum and Fluid Mechanics
Michael Shelley

Tuesday, June 21

Canonical Fluid-structure Problems: Elastic Structures Interacting with High-speed Flows
Michael Shelley

Wednesday, June 22

Flapping Flight: Symmetry Breaking and the Transition to Flapping Flight
Michael Shelley

Thursday, June 23

High Re Fluid-structure Interactions in Sports
Anette Hosoi

Friday, June 24

High Re Fluid-structure Interactions in Sports (cont'd)
Anette Hosoi

Monday, June 27

Low Reynolds Number Swimming Introduction: RFT and a Slender-body Theory Teaser, Three-link Swimmer, Single Flagellum, Two Flagella, Optimization
Anette Hosoi

Some (Unexpected) Boundary Effects in Thermal Convection
Jun Zhang, New York University

Tuesday, June 28

Low Reynolds Number Phenomena
Michael Shelley

Wednesday, June 2

Collective Behavior at Low Reynolds Number
Michael Shelley

Thursday, June 20

Thin Films with Elastic Boundaries
Anette Hosoi

Friday, July 1

Hydrodynamics of Textured Surfaces (Hairy Hydrodynamics in Nature)
Anette Hosoi

SEMINARS

Tuesday, July 5

Applications of Optimization and Optimal Control to Some Fundamental Problems in Mathematical Fluid Dynamics
Charlie Doering, University of Michigan

Wednesday, July 6

Mechanics of Swimming Microorganisms in Complex Fluids
Tom Powers, Brown University

Thursday, July 7

Fluid-structure Interactions in Plant and Animal Physiology
Oliver Jensen, University of Manchester

Friday, July 8

Flows Induced by 1D, 2D and 3D Internal Wavepackets
Bruce Sutherland, University of Alberta

Monday, July 11

Warm-water Pathways towards Kangerdlugssuaq Fjord
Renske Gelderloos, Johns Hopkins University

Tuesday, July 12

Overturned Traveling Interfacial Waves
Benjamin Akers, Air Force Institute of Technology

Wednesday, July 13

Energy Dissipation in Rotating Turbulence
Basile Gallet, CEA Saclay

Thursday, July 14

Bounding Average Quantities: Typical Limitations and How to Surmount Them
David Goluskin, University of Michigan

Friday, July 15

Flow in Highly Deformable Porous Media: The Coffee Press and Other Problems
Duncan Hewitt, University of Cambridge

Monday, July 18

The Structure, Function, and Evolution of the Human Foot
Shreyas Mandre, Brown University

Tuesday, July 19

Topographic Beta-Plane Turbulence and Form Stress
Navid Constantinou, Scripps Institution of Oceanography

Wednesday, July 20

How Bodies Erode and Dissolve in Fluid Flows
Nick Moore, Florida State University

Thursday, July 21

Bio-inspired Flow Systems: From Wetting to Particle Dispersal
Emilie Dressaire, New York University

Friday, July 22

Is Swimming Obstructed by Dead Water?
Leo Mass, Royal Netherlands Institute for Sea Research

Monday, July 25

A Dynamical System for Interacting Flapping Swimmers
Anand Oza, New York University

Tuesday, July 26

A Multi-basin Residual-mean Model for the Global Overturning Circulation
Andy Thompson, California Institute of Technology

Wednesday, July 27

Flow-structure Interaction at the Micro-scale
Megan Davies Wykes, New York University

Thursday, July 28

Transient Growth and Transition to Turbulence in Strongly Stratified Shear Flows
Alexis Kaminski, University of Cambridge

Friday, July 29

Melting Icebergs and Glaciers
Claudia Cenedese, Woods Hole Oceanographic Institution

Monday, August 1

Sinking Labile Particles and the Flux of Organic Matter in the Ocean
Amala Mahadevan, Woods Hole Oceanographic Institution

Tuesday, August 2

Ice Sheets with Rapid Basal Sliding
Ian Hewitt, University of Oxford

Wednesday, August 3

Sniffing with Hairy Noses in the Turbulent Odor Plumes
Mimi Koehl, University of California, Berkeley

Thursday, August 4

Dimensions of Continents and Oceans–Water has Carved a Perfect Cistern
Jack Whitehead, Woods Hole Oceanographic Institution

Sears Public Lecture: *Swimming and Crawling in a Turbulent World*
Mimi Koehl, University of California, Berkeley

Friday, August 5

Magnetohydrodynamics and Elastic Buckling
Geoff Vasil, University of Sydney

Monday, August 8

Entrapment, Escape, and Diffusion of Swimming Bodies in Complex Environments
Saverio Spagnolie, University of Wisconsin, Madison

Tuesday, August 9

Shaping Interfaces
Alban Sauret, Centre National de la Recherche Scientifique

Wednesday, August 10

Vortices in Sinusoid Jets
Glenn Flierl, Massachusetts Institute of Technology

Thursday, August 11

The Dynamics of Marine Ice Sheets
Grae Worster, University of Cambridge

Friday, August 12
Cosmical Gas Dynamics
Ed Spiegel, Columbia University

FELLOWS' PRESENTATIONS

Tuesday, August 23:

Effects of Kelvin and Topographic Rossby Waves on the Denmark Strait Overflow
Océane Richet, Ecole Polytechnique

A Vortex Method for Modeling Multiple Wakes
Paula Doubrawa, Cornell University

Modeling Morphodynamics of a Tidally Forced Wetland
Qi Li, Princeton University

A Continuum Model for Flow of Meltwater through Snow
Colin Meyer, Harvard University

Wednesday, August 24

Rolling Resistance on Sand
Keaton Burns, Massachusetts Institute of Technology

Splash and Spray of a Partially Submerged Rotating Disk
Anna Skipper, Georgia Institute of Technology

Simple Models of Sea Ice Distribution and Mixed-layer Depths in Fram Strait
Sahil Agarwal, Yale University

Erosion in a Uniform Background Flow
Jason Olsthoorn, University of Cambridge

Thursday, August 25

Capillary Sorting: Thin-film Flows of Particles
Michael Gomez, University of Oxford

Clusters, Confinement, and Collisions in Active Matter
Christopher Miles, University of Michigan, Ann Arbor

Lecture 1: A Primer on Continuum and Fluid Mechanics

Michael Shelley (notes by Colin Meyer & Keaton Burns)
June 20, 2016

1.1 Eulerian frame

Consider a fixed subvolume $V_0 \in V$, the mass of the fluid in this subvolume is

$$M[V_0, t] = \int_{V_0} dV_x \rho(\underline{x}, t),$$

where $\rho(\underline{x}, t)$ is the density of the fluid and the subscript x on dV_x indicates that the integral is taken in the Eulerian frame. Mass conservation dictates that

$$\frac{d}{dt}\int_{V_0} dV_x \rho(\underline{x}, t) = -\int_{\partial V_0} dS_x \rho \underline{u} \cdot \hat{n},$$

where $\underline{u}$ is the velocity and $\hat{n}$ is the normal vector pointing out of the subvolume. By the divergence theorem and the arbitrariness of the subvolume, we have

$$\frac{\partial \rho}{\partial t} + \nabla_x \cdot (\rho \underline{u}) = 0.$$

1.2 Lagrangian frame

A passive particle moves along a Lagrangian or material path starting from $\underline{X}_0 = \underline{X}(t = 0)$ and moves along to $\underline{X}(t)$. The velocity of the particle is

$$\frac{d\underline{X}}{dt} = \underline{u}(\underline{X}(t), t).$$

The rate of change of a passive tracer, e.g. the density, with time in the Lagrangian frame is

$$\frac{d\rho(\underline{X}(t), t)}{dt} = \frac{\partial \rho}{\partial t}\bigg|_{\underline{X}(t)} + \frac{d\underline{X}}{dt} \cdot \nabla_x \rho \bigg|_{\underline{X}(t)} = \frac{\partial \rho}{\partial t} + \underline{u} \cdot \nabla_x \rho|_{\underline{X}(t)} = \frac{D\rho}{Dt},$$

where we define the material (substantial) derivative as

$$\frac{D}{Dt} = \frac{\partial}{\partial t} + \underline{u} \cdot \nabla.$$

Thus, we can write mass conservation as

$$\frac{D\rho}{Dt} = -\rho \left(\nabla \cdot \underline{u}\right).$$

Now if

$$\frac{Df}{Dt} = 0,$$

for some field f, this means that f is conserved along material paths.

1.3 Lagrangian volumes

We start with some initial volume of fluid $\Omega_0 = \Omega(t=0)$ and it moves along a Lagrangian path to a volume at time t given by $\Omega(t)$. In other words, $\Omega(t)$ is the set of all points that begin in Ω_0.

1.3.1 Lagrangian flow map

The Lagrangian flow map (LFM) is the mapping $\Omega_0 \longrightarrow \Omega(t)$. This is equivalent to

$$\underline{\alpha} \in \Omega_0 \longrightarrow \underline{X}(\underline{\alpha}, t) \in \Omega(t),$$

where $\underline{\alpha}$ is Lagrangian variable and constant along the Lagrangian path. The Lagrangian flow map is defined by

$$\frac{\partial \underline{X}(\underline{\alpha}, t)}{\partial t} = \underline{u}(\underline{X}(\underline{\alpha}, t), t) \quad \text{subject to} \quad \underline{X}(\underline{\alpha}, t=0) = \underline{\alpha}.$$

Some properties of the Lagrangian flow map are

1. Time derivatives in the Lagrangian frame are given by the material derivative in the Eulerian frame:

$$\frac{\partial f(\underline{\alpha}, t)}{\partial t} = \frac{\partial f(\underline{X}(\underline{\alpha}, t), t)}{\partial t} = \left.\frac{\partial f}{\partial t}\right|_{\underline{X}(\underline{\alpha}, t)} + \left.\frac{\partial \underline{X}(\underline{\alpha}, t)}{\partial t} \cdot \nabla_x f\right|_{\underline{X}(\underline{\alpha}, t)} = \left.\frac{Df}{Dt}\right|_{\underline{X}(\underline{\alpha}, t)}$$

2. The deformation tensor is given as

$$\underline{\underline{F}} = \frac{\partial \underline{X}}{\partial \underline{\alpha}} \quad \text{or} \quad F_{ij} = \frac{\partial X_i}{\partial \alpha_j},$$

which encodes information about shear, stretch, and rotation.

3. The time derivative of the deformation tensor is

$$\frac{\partial F_{ij}}{\partial t} = \frac{\partial}{\partial t}\frac{\partial X_i}{\partial \alpha_j} = \frac{\partial}{\partial \alpha_j}\frac{\partial X_i}{\partial t}.$$

Now the Lagrangian velocity $\underline{V}(\underline{\alpha}, t)$ is given by

$$\frac{\partial \underline{X}(\underline{\alpha}, t)}{\partial t} = \underline{V}(\underline{\alpha}, t) = \underline{u}(\underline{X}(\underline{\alpha}, t), t).$$

Thus, we can insert this into the time derivative of the deformation tensor and find that

$$\frac{\partial F_{ij}}{\partial t} = \frac{\partial V_i}{\partial \alpha_j}.$$

4. The derivative of the velocity V_i along α_j can be written in the Eulerian form as

$$\frac{\partial}{\partial x_j} u_i(\underline{X}(\underline{\alpha}, t), t) = \frac{\partial u_i}{\partial x_k}\frac{\partial X_k}{\partial \alpha_j} = \frac{\partial u_i}{\partial x_k} F_{kj}.$$

Thus, in the Eulerian frame

$$\frac{DF_{ij}}{Dt} = \frac{\partial u_i}{\partial x_k} F_{kj}.$$

5. The Finger tensor (after Josef Finger) or the First (Left) Cauchy-Green tensor is given as

$$b_{ij} = F_{ik} F_{jk},$$

which evolves according to

$$\frac{Db_{ij}}{Dt} = \frac{DF_{ik}}{Dt} F_{jk} + F_{ik} \frac{DF_{jk}}{Dt}.$$

Now using the fact that

$$\frac{DF_{ij}}{Dt} = \frac{\partial u_i}{\partial x_k} F_{kj},$$

we find

$$\frac{Db_{ij}}{Dt} = \frac{\partial u_i}{\partial x_\ell} F_{\ell k} F_{jk} + F_{ik} \frac{\partial u_j}{\partial x_\ell} F_{\ell k}.$$

In vector notation this is written as

$$\frac{D\underline{\underline{b}}}{Dt} = (\nabla_x \underline{u})^T \cdot \underline{\underline{b}} + \underline{\underline{b}} \cdot \nabla_x \underline{u}.$$

This is a closed expression for b_{ij} in the sense that no knowledge of F_{ij} is required.

6. Based on the result for the evolution of the Finger tensor, we define the Upper-convected Derivative as

$$\overset{\triangledown}{b}_{ij} = \frac{Db_{ij}}{Dt} - \frac{\partial u_i}{\partial x_k} b_{kj} - b_{ik} \frac{\partial u_j}{\partial x_k}$$

7. The Second (Right) Cauchy-Green tensor is given as

$$B_{ij} = F_{ki} F_{kj},$$

which evolves according to

$$\frac{DB_{ij}}{Dt} = \frac{DF_{ki}}{Dt} F_{kj} + F_{ki} \frac{DF_{kj}}{Dt}.$$

Now using the fact that

$$\frac{DF_{ij}}{Dt} = \frac{\partial u_i}{\partial x_k} F_{kj},$$

we find

$$\frac{DB_{ij}}{Dt} = \frac{\partial u_k}{\partial x_\ell} F_{\ell i} F_{kj} + F_{ki} \frac{\partial u_k}{\partial x_\ell} F_{\ell j},$$

which doesn't close like the Finger tensor evolution equation.

1.4 Liouville's formula

The determinant of the deformation tensor is given as

$$J(\underline{\alpha}, t) = \det\left(\underline{\underline{F}}\right),$$

which is the Jacobian. The mapping is such that

$$J(\underline{\alpha}, t = 0) = 1.$$

The evolution equation for $J(\underline{\alpha}, t)$ is given as

$$\frac{\partial J}{\partial t} = \frac{\partial u_k}{\partial x_k} J.$$

1.5 Mass conservation in the Lagrangian frame

Recall that $\Omega(t)$ is the Lagrangian volume, which moves with the flow. The mass contained in the volume $\Omega(t)$ is

$$M[\Omega(t)] = \int_{\Omega(t)} dV_x \rho(\underline{x}, t) = \int_{\Omega_0} dV_\alpha \rho(\underline{X}(\underline{\alpha}, t), t) J(\underline{\alpha}, t),$$

where the second equality comes from a change of coordinates. By mass conservation, we have that

$$M[\Omega(t)] = M[\Omega_0].$$

Using this fact we find that

$$\rho(\underline{X}(\underline{\alpha}, t), t) J(\underline{\alpha}, t) = \rho(\underline{\alpha}, t = 0).$$

1.5.1 Incompressibility

In an incompressible fluid, mass conservation in the Lagrangian frame implies that

$$J(\underline{\alpha}, t) = 1,$$

which further implies that

$$\nabla_x \cdot \underline{u} = 0 \quad \text{and} \quad \frac{D\rho}{Dt} = 0.$$

Thus, that density is conserved along particles paths.

1.5.2 Transport theorem

The transport theorem in the Lagrangian frame is given as

$$\frac{d}{dt} \int_{\Omega(t)} dV_x \rho f = \int_{\Omega(t)} dV_x \rho \frac{Df}{Dt},$$

which is due to the fact that $\rho(\underline{\alpha}, t) J(\underline{\alpha}, t)$ is independent of time (mass conservation).

1.6 Momentum Balance

The acceleration of fluid parcels in the Eulerian frame are given as

$$a_i(t) = \frac{d^2 X_i(t)}{dt^2} = \frac{d}{dt} u_i(\underline{X}(t), t) = \frac{\partial u_i}{\partial t} + u_k \frac{\partial u_i}{\partial x_k} = \frac{Du_i}{Dt}.$$

Now the momentum in a Lagrangian volume is given as

$$\underline{m}(t) = \int_{\Omega(t)} dV_x \rho \underline{u}.$$

The momentum evolves due to two main forces

1. Body forces,
$$\underline{f}_{body} = \int_{\Omega(t)} dV_x \rho \underline{g}(\underline{x}, t).$$

2. Tractions and forces of stress
$$\underline{s}(\underline{x}, t) = \underline{\underline{\sigma}}(\underline{x}, t) \cdot \hat{n},$$
where $\hat{n}$ is the normal vector and $\underline{\underline{\sigma}}(\underline{X}, t)$ is the Cauchy stress tensor. The stress force is given as
$$\underline{f}_{stress} = \int_{\Omega(t)} dV_x \underline{\underline{\sigma}}(\underline{x}, t) \cdot \hat{n}.$$

Thus, we can write
$$\frac{d\underline{m}(t)}{dt} = \underline{f}_{body} + \underline{f}_{stress}.$$
Using the transport theorem, we have that
$$\frac{d\underline{m}(t)}{dt} = \int_{\Omega(t)} dV_x \rho \frac{D\underline{u}}{Dt}.$$
Thus, we find that
$$\int_{\Omega(t)} dV_x \rho \frac{D\underline{u}}{Dt} = \int_{\Omega(t)} dV_x \rho \underline{g} + \int_{\Omega(t)} dV_x \nabla_x \cdot \underline{\underline{\sigma}}.$$
By the arbitrariness of $\Omega(t)$, we have that
$$\rho \frac{D\underline{u}}{Dt} = \rho \underline{g} + \nabla_x \cdot \underline{\underline{\sigma}},$$
which is the governing equation for all of continuum mechanics.

1.7 Stress tensor

The name of the game in much of continuum mechanics is specifying the constitutive relations, which relates the stress to the strain or strain rate. As an aside, for fluids that contain particles, Kirkwood and Batchelor did a significant amount of work on describing the rheology through an averaging procedure using separation of scales arguments. Typically, this requires one to assume that the particle density is low (dilute) and that the shear flow around the particles is nearly linear. These arguments are contained within the Einstein suspension viscosity.

Often, the stress tensor is broken up into normal and deviatoric components as
$$\sigma_{ij} = -p\delta_{ij} + d_{ij} \quad \text{and} \quad d_{kk} = 0,$$
where p is the isotropic pressure. Three examples are:

1. In the incompressible Euler equations, $\underline{\underline{d}} = 0$ and we have
$$\rho \frac{D\underline{u}}{Dt} = -\nabla p, \quad \frac{D\rho}{Dt} = 0, \quad \text{and} \quad \nabla_x \cdot \underline{u} = 0.$$

A special case of these equations are when $\rho = \rho_0$ is a constant, which gives

$$\rho_0 \frac{D\underline{u}}{Dt} = -\nabla p, \quad \text{and} \quad \nabla_x \cdot \underline{u} = 0.$$

It is important to note that neither of these equations is an evolution equation for the pressure p. Continuity (mass conservation) serves as a constraint for the velocity field that the pressure is a Laplace multiplier to enforce. Taking the divergence of the incompressible Euler equations (with constant density) we find that

$$\nabla^2 p = -\rho_0 \nabla \cdot (\underline{u} \cdot \nabla \underline{u}) .$$

The left side is an elliptic operator and, therefore, the solution is nonlocal.

2. In the isotropic, incompressible Navier-Stokes equations

$$\sigma_{ij} = -p\delta_{ij} + 2\mu E_{ij},$$

where E_{ij} is the symmetric rate of strain given by

$$E_{ij} = \frac{1}{2}\left(\frac{\partial u_i}{\partial x_j} + \frac{\partial u_j}{\partial x_i}\right)$$

and E_{ij} is trace free. Assuming a constant density this constitutive relation gives

$$\rho_0 \frac{D\underline{u}}{Dt} = -\nabla p + \mu \nabla^2 \underline{u} \quad \text{and} \quad \nabla \cdot \underline{u} = 0.$$

3. A Neo-Hookean solid (which can be derived from microscale bead/spring models) is given by

$$\sigma_{ij} = -p\delta_{ij} + GJ^{-1} b_{ij}, \quad \nabla_x \cdot \underline{u} = 0 \quad \text{and} \quad \overset{\triangledown}{b}_{ij} = 0,$$

where G is Young's modulus and J is the determinant of the deformation tensor.

In the Lagrangian frame, the Neo-Hookean solid is given as

$$\rho_0 \frac{\partial \underline{V}}{\partial t} = G \nabla_\alpha \cdot \underline{\underline{F}} \quad \text{and} \quad \frac{\partial \underline{\underline{F}}}{\partial t} = \nabla_\alpha \underline{V},$$

where we have dropped the pressure.

Lecture 2: Canonical Fluid-structure Problems: Elastic Structures Interacting with High-speed Flows

Michael Shelley (notes by Sahil Agarwal & Jason Olsthoorn)

June 21, 2016

1 Vorticity

Recall the Navier-Stokes equations:

$$\rho_0 \frac{D\vec{u}}{Dt} = -\nabla P + \mu \nabla^2 \vec{u}, \qquad \nabla \cdot \vec{u} = 0.$$

One of the central quantities of interest when considering fluid flow is vorticity $\vec{\omega} = \nabla \times \vec{u}$. Taking the curl of the Navier-Stokes equations produces the vorticity equation

$$\rho_0 \frac{D}{Dt}\vec{\omega} = \nabla \vec{u} \cdot \vec{\omega} + \mu \nabla^2 \vec{\omega}. \tag{1}$$

The first section of this lecture will be discussing an analysis of this equation.

1.1 2D

In two-dimensions, the vorticity vector is direct entirely out-of-plane (in the $\hat{z}$ direction)

$$\vec{\omega} = \omega \hat{z} = (v_x - u_y)\, \hat{z}. \tag{2}$$

If we define the molecular viscosity $\nu = \frac{\mu}{\rho_0}$, then in two dimensions the vorticity equation reduces to

$$\frac{D}{Dt}\omega = \nu \nabla^2 \omega.$$

Now, from vector calculus we know that any vector can be decomposed into the gradient of a potential function and a divergence free field, written as

$$\vec{u} = \nabla \phi + \nabla \times \vec{\psi}.$$

In this problem, the velocity field $\vec{u}$ is divergence free which implies that

$$\begin{aligned} \vec{u} &= \nabla \times \vec{\psi} \\ &= \hat{z} \nabla^{\perp} \psi = -\partial_y \psi \hat{x} + \partial_x \psi \hat{y}, \qquad (2D) \qquad (3) \\ \nabla^2 \psi &= \omega, \qquad (4) \end{aligned}$$

where $\hat{}x$, $y\hat{}$ define some right-handed, cartesian coordinate system. Thus, the velocity field can be entirely determined according to a Biot-Savart law, which is written (assuming an infinite domain in both directions),

$$\begin{aligned}\psi(\vec{x}) &= \frac{1}{2\pi}\int_{\mathbf{R}^2} dA\ \omega(\vec{x}')\ln|\vec{x}-\vec{x}'| \\ \vec{u}(\vec{x}) &= \frac{1}{2\pi}\int_{\mathbf{R}^2} dA\ \omega(\vec{x}')\frac{(\vec{x}-\vec{x}')^{\perp}}{|\vec{x}-\vec{x}'|^2}.\end{aligned} \tag{5}$$

1.1.1 Inviscid 2D

For an inviscid fluid ($\nu = 0$) , the vorticity equation reduces further to

$$\frac{D}{Dt}\omega = 0. \tag{6}$$

As we have seen in Lecture 1, this implies that ω is conserved along material lines. That is to say

$$\omega(\vec{\alpha};t) = \omega(\vec{\alpha};t=0).$$

Thus, any Lagrangian particle at point $\vec{x}$ defined such that $\frac{\partial}{\partial t}\vec{x}(\vec{\alpha};t) = \vec{u}(\vec{x}(\vec{\alpha};t),t)$, evolves according to the relation:

$$\frac{\partial}{\partial t}\vec{x} = \frac{1}{2\pi}\int_{\mathbf{R}^2} dA_{\alpha'}\ \omega_0(\vec{\alpha}')\frac{(\vec{x}-\vec{x}')^{\perp}}{|\vec{x}-\vec{x}'|^2}. \tag{7}$$

This implies a self-contained evolution of the Lagrangian flow map.

1.1.2 Inviscid 3D

We can simplify the three-dimensional vorticity equation using the rank-2 distortion tensor $\overline{\overline{F}}$.

$$\begin{aligned}\frac{D\vec{\omega}}{Dt} &= \nabla\vec{u}\cdot\vec{\omega} \\ &= \nabla\vec{u}\cdot\overline{\overline{F}}\,\overline{\overline{F}}^{-1}\cdot\vec{\omega} && \text{(Multiply by Identity)} \\ &= \left(\frac{D}{Dt}\overline{\overline{F}}\right)\overline{\overline{F}}^{-1}\cdot\vec{\omega} && \text{(Derived Identity)} \\ &= -\overline{\overline{F}}\left(\frac{D}{Dt}\overline{\overline{F}}^{-1}\right)\cdot\vec{\omega}. && \left(\text{ as } \frac{D}{Dt}\left(\overline{\overline{F}}\,\overline{\overline{F}}^{-1}\right)=0\right)\end{aligned} \tag{8}$$

By the product rule, we can then compact this into

$$\frac{D}{Dt}\left(\overline{\overline{F}}^{-1}\cdot\vec{\omega}\right) = \vec{0}.$$

As we have just seen, this implies that (as $\overline{\overline{F}}(t=0)=1$),

$$\overline{\overline{F}}^{-1}\vec{\omega} = \vec{\omega}_0 \implies \vec{\omega}(\vec{\alpha};t) = \overline{\overline{F}}\cdot\vec{\omega}_0(\vec{\alpha}). \tag{9}$$

Hence, the evolution of the vorticity field is entirely determined by the deformation tensor.

As an aside, we can construct the Enstrophy tensor

$$\overline{\overline{W}} = \vec{\omega}\vec{\omega}^T.$$

We can then use the inviscid vorticity equation to show that

$$\begin{aligned}\frac{D}{Dt}\overline{\overline{W}} &= \nabla\vec{u}\cdot\vec{\omega}\vec{\omega}^T + \vec{\omega}\vec{\omega}^T\left(\nabla\vec{u}\right)^T \\ &= \nabla\vec{u}\cdot\overline{\overline{W}} + \overline{\overline{W}}\left(\nabla\vec{u}\right)^T.\end{aligned}$$

Thus, using the convective derivative defined in the previous lecture,

$$\overline{\overline{W}}^{\triangle} = 0. \tag{10}$$

2 The Reynolds Number

We again write down the Navier-Stokes (N-S) equations as

$$\rho_0\frac{D\vec{u}}{Dt} = -\nabla P + \mu\nabla^2\vec{u}, \qquad \nabla\cdot\vec{u} = 0.$$

If we consider a problem with a single length scale L and a single velocity scale U, we can then non-dimensionalize the N-S equations in the following manner:

$$x \to Lx, \qquad t \to \frac{L}{U}t, \qquad \text{and } P \to \mathbf{P}P.$$

Using these transformations,

$$\mathrm{Re}\frac{D\vec{u}}{Dt} = -\mathbf{P}\frac{L}{\mu U}\nabla P + \nabla^2\vec{u}, \qquad \nabla\cdot\vec{u} = 0.$$

Here, we have defined the Reynolds Number as

$$\begin{aligned}\mathrm{Re} &= \frac{\rho_0 U^2 L^2}{\mu U L} \\ &\equiv \frac{\text{Inertial Force}}{\text{Viscous Force}} \\ &\equiv \frac{\text{Form Drag } (\sim L^2)}{\text{Viscous Drag } (\sim L)}.\end{aligned} \tag{11}$$

2.1 High Reynolds Number

For large Reynolds numbers ($\mathrm{Re} \gg 1$), the N-S equations reduce to a non-local initial-value problem. This regime is typical of macroscale motion such as swimming fish, flying birds, etc.

If we scale the pressure as $\mathbf{P} = \mathrm{Re}\frac{\mu U}{L}$, we can simplify the N-S equations as

$$\frac{D\vec{u}}{Dt} = -\nabla P + \frac{1}{\mathrm{Re}}\nabla^2\vec{u}, \qquad \nabla\cdot\vec{u} = 0.$$

The formal limit $\mathrm{Re}\to\infty$ reduces the N-S equations to the Euler equations.

2.2 Low-Reynolds Number

For low Reynolds numbers (Re$\ll 1$), the advective terms in the N-S equations are significantly less important. In the limit Re$\to 0$, the N-S equations reduce to the Stokes equations. If we scale pressure as $\mathbf{P} = \frac{\mu U}{L}$, the Stokes equations are written

$$-\nabla P + \nabla^2 \vec{u} = 0, \qquad \nabla \cdot \vec{u} = 0. \tag{12}$$

This is a boundary value problem. Note that for certain non-equilibrium initial conditions, inertial may be important over a very short time scale. This is not captured by the Stokes equations.

Now, consider the stress tensor $\overline{\overline{\Sigma}}$ which is given

$$\overline{\overline{\Sigma}} = -P\overline{\overline{I}} + 2\mu\overline{\overline{E}}.$$

The total force acting on an arbitrary fluid volume is given

$$m\ddot{x} = \int_{\partial B} dS_x \overline{\overline{\Sigma}} \cdot \hat{n}.$$

In the Re$\to 0$ limit, inertial is null which states

$$\int_{\partial B} dS_x \overline{\overline{\Sigma}} \cdot \hat{n} = 0. \tag{13}$$

Bodies move under the condition of zero force and zero torque.

3 Some Moving/Deforming Bodies Interacting with Fluids

In 1878, Lord Rayleigh identified a weak instability of a flat surface in inviscid fluids. This instability is associated with the flapping of a flag in the wing. To model this problem, We consider a hydrodynamical model which presents the flag as a surface of discontinuity moving under stress (vortex sheet).

Consider an inextensible elastic sheet of length L, mass per unit length ρ_s, and rigidity E, moving under a pressure load.

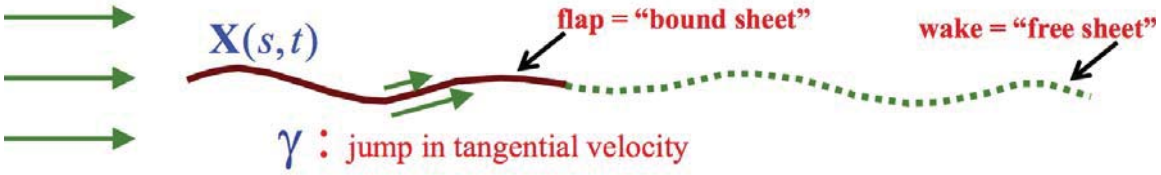

Figure 1: A schematic of the flag model, depicting the regions of bound flag and the free sheet. (From Lecture notes by Michael Shelley, GFD '16)

Let the arc length, s, be a material parametrization of the flag and $\overline{U} \to U\hat{x}$ is the background flow. Let S_1 and S_2 be two dimensionless parameters.

Computing the force balance on the flag gives:

$$S_1\overline{X}_{tt} = \partial_s(T\overline{X}_s) - S_2\overline{X}_{ssss} + [p]X_s^{\perp} \tag{14}$$

(i.e. Inertial = Tensile + Bending + Pressure forces). Here, $S_1 = \frac{\rho_s L}{\rho_f L^2}$, $S_2 = \frac{E/L}{\rho_f U^2 L^2}$, and ρ_f is mass per unit area of the fluid. The parameter S_1 is the ratio of the mass of flag to the mass of fluid and S_2 is the ratio of the potential elastic energy to the fluid kinetic energy of the flag.

Now,

$$\begin{aligned} X_s.X_s &= 1 \\ ,\Rightarrow X_s.X_{st} &= 0, \\ \Rightarrow X_s.(X_t)_s &= 0, \\ \Rightarrow X_s.V_s &= 0. \end{aligned} \tag{15}$$

Let $C = C_B \cup C_f$, the union of the bound flag C_B and the free sheet C_f. Because the flag is also a free surface moving in the fluid, its normal velocity is equal to the fluid's continuous normal velocity at C_B. That is,

$$\overline{X}_t = \nu\overline{X}_s^{\perp} + \tau\overline{X}_s \tag{16}$$

We can define ν such that

$$\nu = U^+.\overline{X}_s^{\perp}, \qquad\qquad = U^-.\overline{X}_s^{\perp}.$$

Requiring that s is independent of time,

$$\begin{aligned} X_s.X_{ts} &= \tau_s - \nu\kappa \\ \tau &= \int_o^s \nu\kappa ds' \end{aligned} \tag{17}$$

From Biot-Savart law, integrating across the flag, and using $\gamma = -X_s(U^+ - U^-)$ as the jump in tangential velocity across the flag surface, we get

$$\overline{U}(\overline{X}) = \hat{X} + \frac{1}{2\pi}\int_{C(t)} ds'\gamma(s')\frac{(\overline{X}(s,t) - \overline{X}(s',t))^{\perp}}{|\overline{X}(s,t) - \overline{X}(s',t)|^2} \tag{18}$$

Separating the principal value and the residue for the integral,
$\Rightarrow$

$$\overline{U}^{\pm}(\overline{X}(s,t),t) = \mp\frac{\gamma(s)X_s}{2} + \overline{W} \tag{19}$$

$$\overline{W} = \hat{X} + \frac{1}{2pi}\mathbb{P}\int ds'\gamma(s')\frac{(\overline{X} - \overline{X}(s',t))^{\perp}}{|\overline{X} - \overline{X}(s',t)|^2} \tag{20}$$

Here, $\mathbb{P}\int$ is the principal value integral.
And so,

$$\gamma_t = -\partial_s(\gamma(\overline{W}.\overline{X_s} - \tau)) + [p]_s \tag{21}$$

Lecture 3a: Flapping Flight: Symmetry Breaking and the Transition to Flapping Flight

Michael Shelley (notes by Christopher Miles)

June 22, 2016

1 Hydrodynamic model of a flapping flag: revisited

Recall from last time, we were discussing the hydrodynamic model of a flag as outlined in Ref. [1]. We had the following model for the elastic sheet.

$$(\text{inertial} = \text{tensile} + \text{bending} + \text{pressure})\text{forces}$$

$$S_1 \mathbf{X}_{tt} = (T\mathbf{X}_s)_s + S_2 \mathbf{X}_{ssss} + [p]\mathbf{X}_s^{\perp}$$

where

$$S_1 = \frac{\text{mass of flag}}{\text{mass of the fluid}} = \frac{mL}{\rho f L^2},$$

$$S_2 = \frac{\text{potential elastic energy}}{\text{fluid kinetic energy}} = \frac{E/L}{\rho f L^2 U^2},$$

s parameterizes the curve, t is time, $\mathbf{X}$ is the position of the flag, and $[p]$ is the jump in pressure, m is the mass of the flag, L is the length of the flag, ρ is the fluid density, f is the film thickness, U is the incident fluid velocity, and E is the rigidity of the flag. Figure 1 shows the setup of the model.

Furthermore, we have the following kinematic boundary conditions,

$$\begin{aligned} \mathbf{X}_t &= \nu \mathbf{X}_s^{\perp} + \tau \mathbf{X}_s \\ \gamma_t &= -(\gamma(\mathbf{W} \cdot \mathbf{X}_s - \tau))_s + [p]_s = 0, \end{aligned}$$

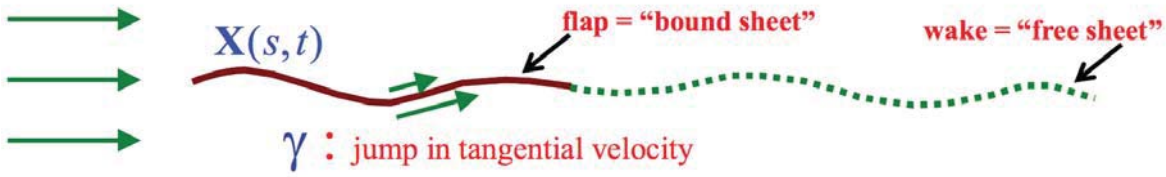

Figure 1: Flag model.

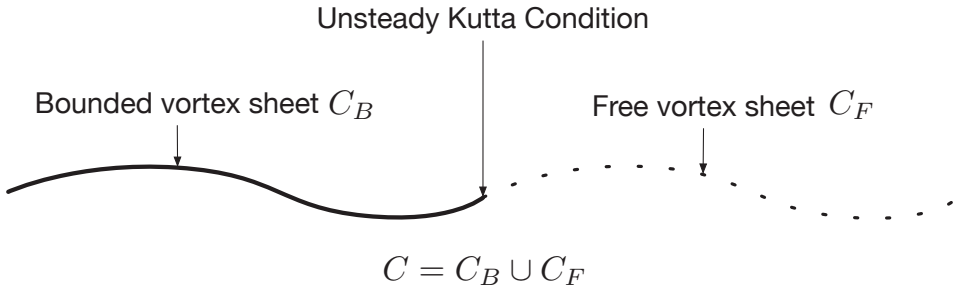

Figure 2: Vortex sheet in flag model. The point vortices shedding off the flag's end point obey the unsteady Kutta condition (Eq. 1).

where $\nu = \mathbf{W} \cdot \mathbf{X}_s^{\perp}$, $\tau = \int_0^s U(s')\kappa(s')ds'$, and γ is the jump in tangential velocity. The average velocity on the sheet is given by

$$\mathbf{W}[s] = \frac{1}{2\pi} P \int_C \gamma(s') \frac{(\mathbf{X}(s) - \mathbf{X}(s'))^{\perp}}{|X(s) - X(s')|^2} ds$$

where $(x, y)^{\perp} = (-y, x)$. Figure 2 shows the entire vortex sheet C used in the flag model. C is the union of bound vertex sheet C_B representing the flag and the free vortex sheet C_F representing the wake. We have already shown how to deal with C_B. As for C_F, the sheet is discretized into point vortices which are free to move with the flow. There is an unsteady Kutta condition [2] at the junction which tells you the rate at which you should shed vortices tangentially at the end of C_B (equivalently at $s = 1$). The rate of change of the circulation, Γ, that you are 'shooting off' into vortices is given by

$$\frac{d\Gamma}{dt} = \gamma\nu|_{s=1}. \tag{1}$$

The free vortex sheet suffers from the Kevin-Helmholtz instability. The growth rate σ behaves like $\sigma^2 \sim \Gamma k^2$ where k is the wavenumber. To avoid instability at small length scales, one uses the Krasny regularization

$$\mathbf{W}(s) = \frac{1}{2\pi} P \int_C \gamma(s') \frac{(\mathbf{X}(s) - \mathbf{X}(s'))^{\perp}}{|X(s) - X(s')|^2 + \delta^2} ds$$

where δ is on the order of the smallest length scales that can be resolved.

One can decrease the dimensionless rigidity S_2. Its effect is illustrated in Figures 4(a) and 4(b). For high rigidity (top plot), you can see that the wake exhibits a clean vortex street. The wake develops more complex small scale structure as the rigidity is decreased. Figure 4(b) shows how the temporal power spectra of flag bending energy changes with S_2 while keeping $S_1 = 0.3$. S_2 is equal to (a) 0.01445, (b) 0.01436, (c) 0.0138, and (d) 0.0025 for the corresponding subplots.

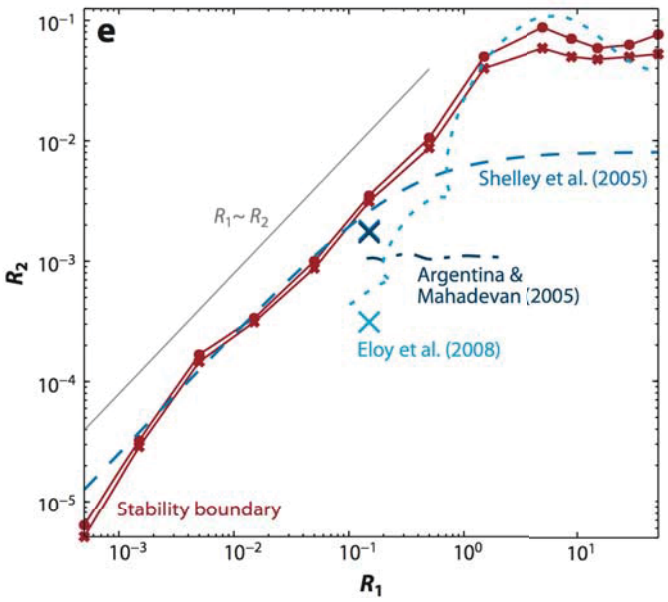

Figure 3: Stability plot (Image from Ref. [5]).

2 Simple model of a nearly flat flag

Let us consider a simple model of a nearly flat flag. We will drop the inextensibility (T) in this model. Now, let $\underline{X}$ be the displacement of the flag given by

$$\underline{X} \quad = \quad (X, \epsilon\eta(X,t)).$$

We will perturb the flag about the unperturbed flat flag state described by

$$\begin{aligned} X_0 &= (X, 0) \\ [p_0] &= 0 \\ \gamma_0 &= 0. \end{aligned}$$

The elastic mechanics are governed by

$$S_1\eta_{tt} = -S_2\eta_{xxxx} + [p] \tag{2}$$

while the fluid surface is governed by

$$\eta_t + \eta_x = \frac{1}{2}H[\gamma] \tag{3}$$

$$\gamma_t + \gamma_x = -[p]_x \tag{4}$$

where $H[\cdot]$ is the Hilbert transform (Carrier et al 1966),

$$H[f] = \frac{1}{\pi}P\int dy \frac{f(y)}{x-y}.$$

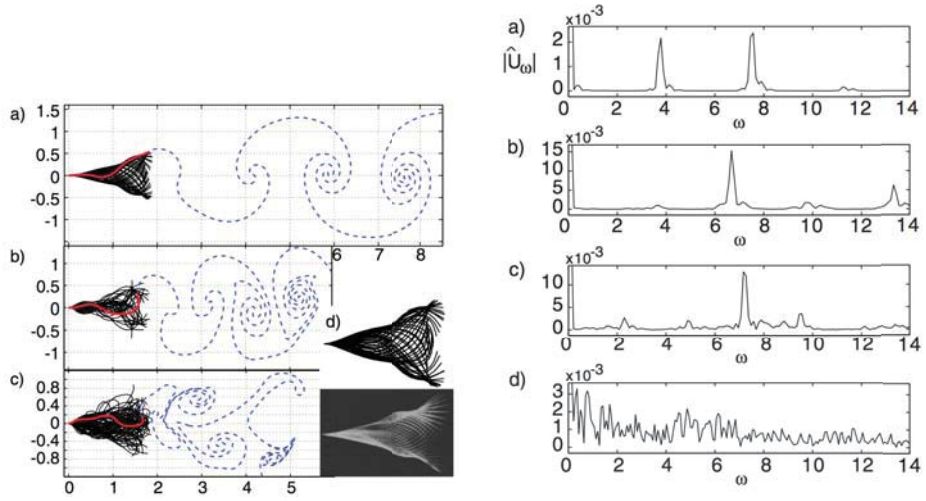

(a) (b)

Figure 4: The effect of decreasing nondimensional rigidity S_2. The top plot within each subfigure represents high rigidity. The subsequent plots are ordered by decreasing rigidity. You can see that wake pattern (left subfigure) looks more turbulent for low values of rigidity and develops a broader frequency spectrum.

The Hilbert transform has the nice property that

$$H[e^{ikx}] = -i\,\mathrm{sign}(k)e^{ikx}.$$

By using equations 2-4, one can derive

$$(\partial_t + \partial_x)^2\eta = -\frac{1}{2}H[[p]_x] = -\frac{1}{2}H[S_1\eta_{xtt} + S_2\eta_{xxxxx}].$$

Let $\eta = \eta_0 e^{i(\omega t+kx)}$. Then,

$$(\omega + k)^2 = \frac{1}{2}(-S_1|k|\omega^2 + S_2|k|^5)$$

$$\omega = -k\frac{1 \pm |k|^{1/2}d^{1/2}}{1 + S_1|k|}$$

where d is the discriminant given by

$$d(k) = S_1S_2|k|^3 + 2S_2|k|^2 - 2S_1.$$

Now, let's consider various cases.

1. No convective terms: (Set η_x and γ_x terms set to zero.)

$$\omega^2 = \frac{1}{2}(-S_1|k|\omega^2 + S_2|k|^5)$$

Thus, this gives dispersion.

2. $k \gg 1$:

$$\omega \simeq \pm \left(\frac{S_2}{S_1}\right)^{1/2} k^2$$

Again, this gives dispersion.

3. No mass: $(S_1 = 0)$

$$\omega = -k[1 \pm S_2^{1/2}|k|^{3/2}]$$

We see dispersion.

4. No elasticity: $(S_2 = 0)$

$$\omega = -k\frac{1 \pm i\left(\frac{S_1}{2}\right)^{1/2}|k|^{1/2}}{1 + \frac{1}{2}S_1|k|}$$

This shows that it is always unstable.

From this linear analysis, you can determine a stability criterion. We ask for the conditions on S_1 and S_2 that cause the fundamental mode of $k = 2\pi$ which has a corresponding wavelength that spans the entire length of the flag to become unstable. This transition happens when the discriminant changes from positive to negative. Hence, the transition criterion is

$$d(2\pi) = 8\pi^3 S_1 S_2 + 4\pi^2 S_2 - 2S_1 = 0$$

The solid red line in Figure 3 is simulation data generating the stability boundary. The long-dash line is the stability condition above for comparison. The remaining curves represent predictions from alternative theories.

The criterion from linear stability has reasonable agreement with experimental results. In the soap film experiment, it was observed that instability occurs at a critical length of 4 cm at 50 Hz while theory predicts 1 cm at 90 Hz. In an alternative experiment by Shelly, *et al* [4], long copper plates were attached to a Mylar sheet as shown in Figure 5(a). In this experiment, bistability was observed as illustrated in Figure 5(b).

3 Dynamics due to multiple flags

There have been extensions made of the flag experiments presented thus far. For example, work has been done on body-body coupling (see Figure 6(a)) and drafting of flexible bodies (see Figure 6(b)). The main question for the studies on drafting is "what happens to the drag on the body following behind another?" An obvious analogy is bike racing where a bicyclist takes advantage of the reduction in drag due to following another cyclist. However, the situation is different for flexible bodies. It turns out that followers have a *greater* drag than the leader.

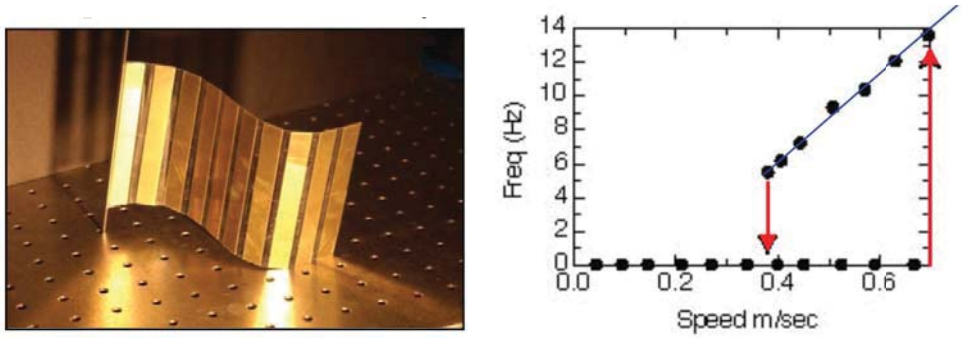

(a) Copper-plated flag

(b) The relationship between frequency of the copper-plated flag and fluid speed exhibits bistability.

Figure 5: Copper-plated flag experiment. [4]

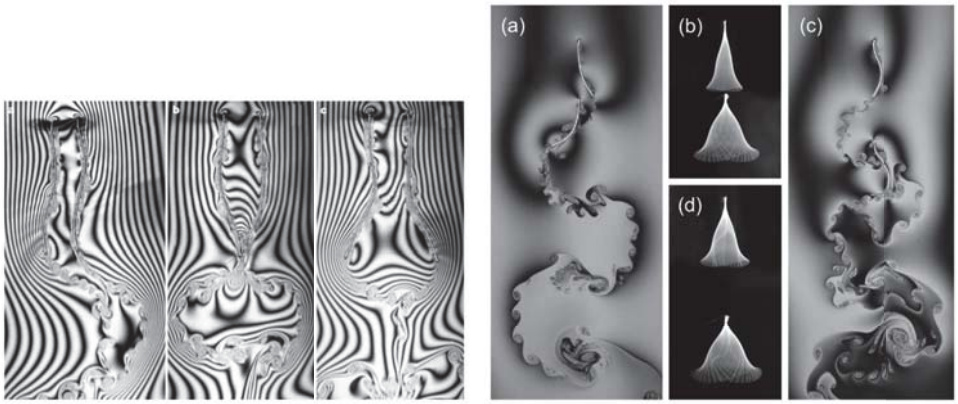

(a) Body-body coupling.

(b) Drafting of flexible bodies [3].

Figure 6: Extensions of flag models and experiments.

References

[1] S. Alben and M. J. Shelley, *Flapping states of a flag in an inviscid fluid: bistability and the transition to chaos*, Physical Review Letters, 100 (2008), p. 074301.

[2] M. A. Jones, *The separated flow of an inviscid fluid around a moving flat plate*, Journal of Fluid Mechanics, 496 (2003), pp. 405–441.

[3] L. Ristroph and J. Zhang, *Anomalous hydrodynamic drafting of interacting flapping flags*, Physical Review Letters, 101 (2008), p. 194502.

[4] M. Shelley, N. Vandenberghe, and J. Zhang, *Heavy flags undergo spontaneous oscillations in flowing water*, Physical Review Letters, 94 (2005), p. 094302.

[5] M. J. Shelley and J. Zhang, *Flapping and bending bodies interacting with fluid flows*, Annual Review of Fluid Mechanics, 43 (2011), pp. 449–465.

Lecture 3b: Flapping Flight: Symmetry Breaking and the Transition to Flapping Flight (continued)

Michael Shelley (notes by Michael Gomez)
June 22, 2016

1 Drag reduction in flows around flexible bodies

Consider fluid moving at high speed past a rigid body. The basic scaling behavior of the Euler equations predicts that the drag force D experienced by the body is

$$D = \frac{1}{2} C_{\mathrm{D}} \rho U^2 A, \tag{1}$$

where U is the velocity of the fluid, ρ is the fluid density, and A is the surface area that the body presents to the flow (the reference area); the pre-factor C_{D} is the drag coefficient, a dimensionless number that depends on how streamlined the object is. The drag coefficient also varies with the Reynolds number, but in many practical flows of interest at high Reynolds number (tree leaves in a wind, flow past a cyclist, the trajectory of a baseball) the variation is small and C_{D} can be regarded as constant (for a given shape). Equation (1) then implies that the drag force is proportional to the square of the velocity, which is known as the classic "U^2–law" for the drag.

What if instead of a rigid object, we have a flexible body that obstructs a high-speed flow? If the body is sufficiently flexible, its shape and reference area A can change significantly as the flow rate is increased; generally we expect the body to become more streamlined as it deforms. This results in a drag force that grows slower with the velocity than the classic U^2-law. In other words, the flexibility of the body leads to a 'self-streamlining' mechanism where its deformation lowers the drag force it experiences.

Self-streamlining of bodies in high speed flows is commonly found in biology. For example, tree leaves deform into streamlined shapes when exposed to winds typical of their everyday conditions. Wind tunnel observations made by Steve Vogel show how at low speeds leaves fold at their upstream edge, before rolling up into increasingly tight cone shapes at higher speeds (figure 1). This suggests a universal mechanism by which plants and other organisms living in windy/wavy conditions can lower drag forces to reduce damage.

1.1 Self-streamlining of flexible fibres

To further understand the mechanism of self-streamlining, let's study a simple model system: a flexible fiber arranged in a two-dimensional flow. The fiber is clamped at its midpoint initially perpendicular to an oncoming stream, while its ends are free to deflect. Qualitatively speaking, this system is a rotated version of the flapping flag problem (studied in lecture 2) so that the edge of the fiber now obstructs the flow. In this way we can regard the fiber as a "1D leaf in a 2D wind".

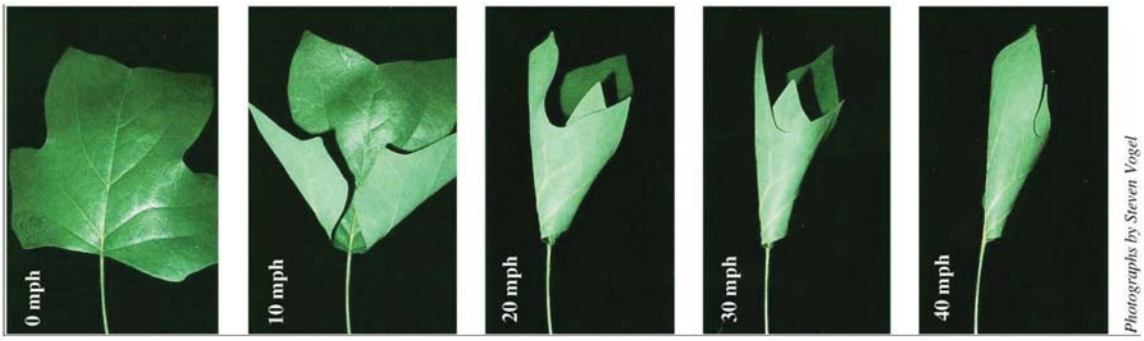

Figure 1: Self-streamlining of a tree leaf in a wind [photographs courtesy of Steve Vogel].

1.1.1 Experiments

Experiments have been performed by Alben et al. [2002], who mounted fiber optic glass fibers into a soap film that falls freely under gravity; see figure 2. Soap films are easily visualized and are well described as two-dimensional Navier-Stokes fluids, which explains their wide usage in studying flow phenomena (soap films were used in the flapping flag experiments discussed in lecture 2). (While thickness variations in the film can lead to compressibility effects, these do not play a large role in this system which we will regard as incompressible). The midpoint of the fiber is clamped to a stiff cantilever beam passing through the film. The slight deflection of the cantilever can be used to measure the drag force exerted on the fiber (via a suitable calibration). This is recorded as the flow speed is increased, as well as the shape of the fiber and the flow field (using interferometry). The Reynolds number of the flow is $\sim 10^4$.

Alben et al. [2002] observe that the fiber remains nearly straight at low flow speeds U, but a sharp transition to bending occurs at higher speeds; see figure 3a,b. This is associated with large displacements of the ends of the fiber, so that the overall shape is bent downstream and more aligned to the flow. Figure 4a shows the drag force exerted on a flexible fiber compared to a very stiff fiber, and confirms that this self-streamlining reduces the drag by as much as a factor of three. The drag also grows much slower than the classic U^2-law, being closer to linear growth in U.

The flow pattern past the fiber is typical of high Reynolds number flow past a bluff body. At each free end of the fiber, a boundary layer separates and divides the surrounding flow from a downstream wake (figure 3a,b). The wake itself is characterized by turbulent flow featuring two large, rotating eddies. The speeds in the wake are around two orders of magnitude slower that the surrounding flow, which remains roughly laminar.

1.1.2 Model

The structure of the wake can be exploited in a simple model of the fluid flow. Due to the large size of the wake and the very slow velocities inside, we can approximate the wake as a semi-infinite region of stagnant fluid where the pressure is constant and equal to the far-field pressure (its value known as the wake under-pressure). This is separated from the surrounding flow by 'free-streamlines' — particle paths that originate from the free ends

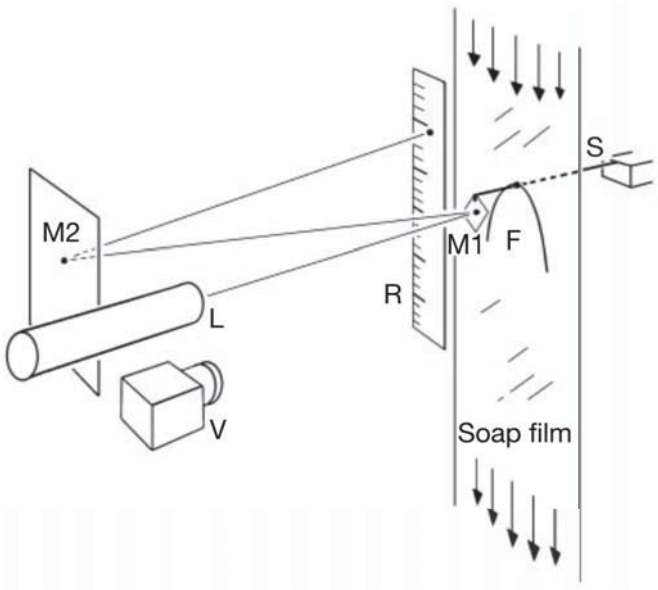

Figure 2: The setup considered by [Alben et al., 2002]. F denotes the flexible glass fiber (length 1–5 cm, diameter 34 μm, bending rigidity $E = 2.8 \times 10^{-7}$ Pa m^4), clamped to a steel cantilever S and arranged transverse to the falling soap film (thickness 1–3 μm, width 9.0 cm, density $\rho = 1000$ kgm^{-3}). The other equipment shown is used to measure the deflection of S to calculate the drag force [reprinted from Alben et al., 2002].

of the fiber — across which the pressure is continuous. By coupling the fluid pressure to the elasticity of the fiber, this model becomes an extension of free-streamline theory (FST) for inviscid flow, originally formulated by Helmholtz to describe the wake structure for flow past flat plates [Helmholtz, 1868].

The surrounding flow is assumed to be inviscid and irrotational. We consider a steady state, i.e. we ignore any time-dependent effects such as possible Kelvin-Helmholtz instability of the free-streamlines. The fluid pressure p and velocity $\mathbf{u}$ are then related by Bernoulli's equation (setting the far-field pressure to zero)

$$p + \frac{1}{2}\rho|\mathbf{u}|^2 = \frac{1}{2}\rho U^2.$$

Together with a no-flux condition on the fiber surface, this allows the velocity (and so pressure) to be determined for a given fiber shape (see Alben et al. [2004] for details).

The fiber itself is modeled as an inextensible elastica, i.e. a linearly elastic beam undergoing large global displacements in the limit of small strains. Its deformation is driven by a difference between the fluid pressure evaluated on its upstream side, p_{fiber}, and the constant pressure in the downstream wake (set to be zero). Balancing tensile and bending forces in the fiber with this pressure jump then yields (subscripts denoting differentiation)

$$(-T\hat{\mathbf{s}})_s + (E\kappa_s\hat{\mathbf{n}})_s = f p_{\text{fiber}}\hat{\mathbf{n}}, \tag{2}$$

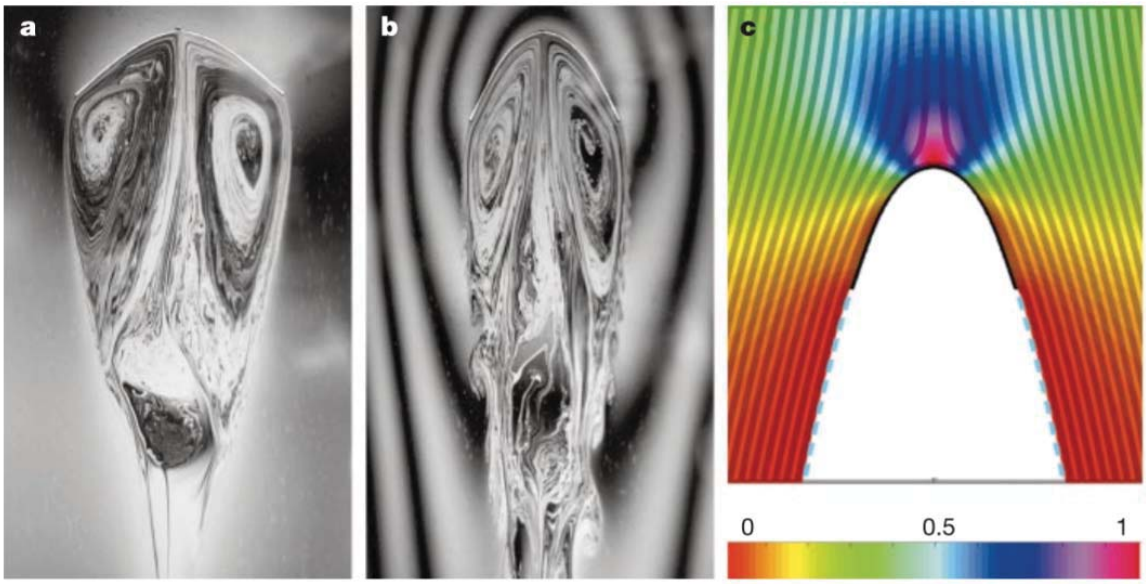

Figure 3: The observed fiber shape and flow pattern when the flow speed is (a) $U = 69$ cms^{-1}, and (b) $U = 144$ cms^{-1}. (c) Dimensionless pressure field and fluid streamlines obtained by solving the beam/FST system numerically; here $\eta = 27$ [reprinted from Alben et al., 2002].

where s is arclength along the centreline, $\hat{\mathbf{s}}$ is the unit tangent vector, $\hat{\mathbf{n}}$ is the unit normal, κ is the curvature, E is the bending stiffness, T is the (unknown) tension in the fiber (in general this is non-zero to enforce inextensibility), and f is the thickness of the soap film. At the free ends of the fiber we specify $T = \kappa = \kappa_s = 0$, i.e. the tension, transverse shear force and bending moment must vanish there. The horizontal clamping condition at the midpoint of the fiber then closes the problem.

At this stage we can guess the qualitative behavior of the fiber. Note that arclength naturally scales as $s \sim L$ where L is the length of the fiber, while Bernoulli's equation implies that the fluid pressure scales as $p_{\text{fiber}} \sim \rho U^2/2$. From (2), the ratio of hydrodynamic forces to bending forces is then

$$\eta^2 = \frac{\rho f U^2/2}{E/L^3} = \left(\frac{L}{L_0}\right)^3, \tag{3}$$

where we have introduced

$$L_0 = \left(\frac{2E}{\rho f U^2}\right)^{1/3}.$$

The parameter L_0 is an intrinsic length scale in the problem and gives the characteristic length over which the fiber deflects due to fluid loading. If all other parameters apart from the fluid speed U are fixed, notice that L_0 scales as $L_0 \sim U^{-2/3}$ and hence decreases with U. This is the essence of the self-streamlining effect: for $L \gg L_0$, i.e. very flexible fibers/high-speed flows, the bending will be confined to a small region around the midpoint of the fiber of size $\sim L_0$ (this is where the fluid pressure is highest due to a stagnation point). The material outside this region will be roughly aligned with the flow and experience little drag.

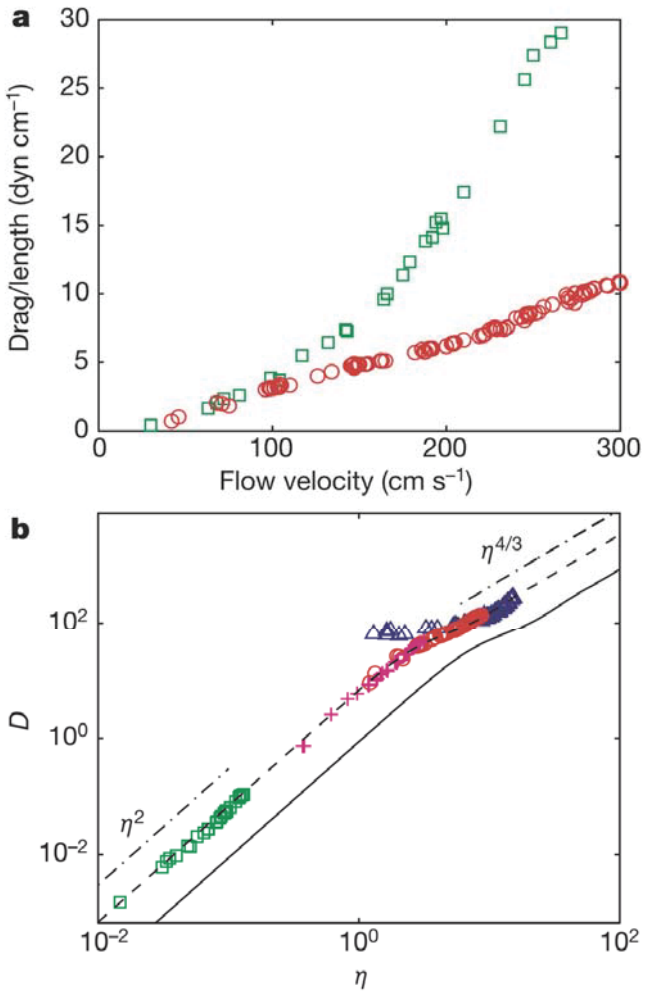

Figure 4: (a) Drag force (normalized by fiber length) as a function of the flow speed U for a flexible fiber (red circles) and a very stiff fiber (green squares, rigidity $E = 2.0\times10^{-6}$ Pam^4). (b) The same data in dimensionless form, together with additional data obtained for flexible fibers of different lengths (pink crosses, blue plus signs). The theoretical value predicted by free-streamline theory is also shown (solid line) [reprinted from Alben et al., 2002].

The relevant length scale that determines the drag is therefore L_0, yielding a drag force

$$D \sim \frac{1}{2}\rho U^2 L_0 f \sim U^{4/3},$$

which grows much slower than the classic U^2-law for a rigid body. We expect to recover the U^2-law in the rigid limit $L \ll L_0$.

Using the above scalings to make the full beam/FST system dimensionless, it turns out that η is the only control parameter in the problem (which enters as a normalised fluid velocity). This is solved numerically by Alben et al. [2002] using conformal mapping techniques to determine the drag force and fiber shape as η is varied (for more details

see Alben et al. [2004]). As anticipated, the fiber is nearly flat for $\eta \ll 1$ but undergoes significant bending for $\eta \gg 1$, in good agreement with what is observed experimentally (figure 5a). These bent shapes can be made to collapse onto a universal curve when rescaled by the intrinsic length L_0; see figure 5c,d. This curve is roughly parabolic and can be deduced by asymptotic analysis in the limit $\eta \gg 1$.

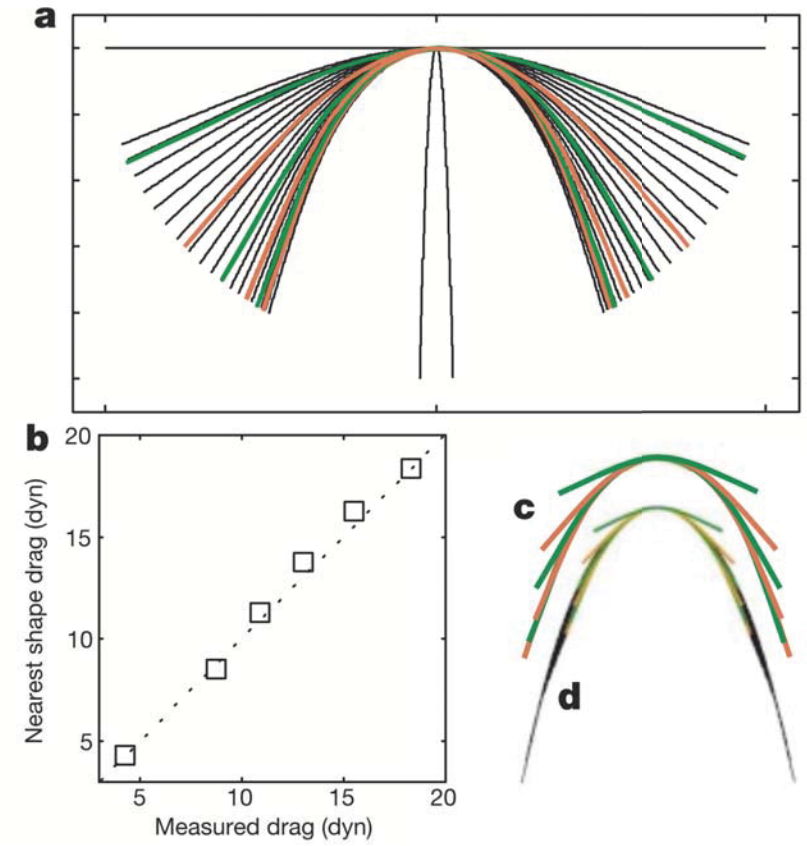

Figure 5: (a) The shape of the fiber predicted by the beam/FST model as η is varied (black curves). Also shown for comparison are the experimentally observed shapes (orange, green curves). (b) Matching the shapes of experimental and theoretical fiber shapes gives like drags. Rescaling by the intrinsic length L_0 collapses both (c) the experimental, and (d) the numerically determined shapes [reprinted from Alben et al., 2002].

The behavior of the dimensionless drag force is shown in figure 4b. The experimental data is also shown for comparison, which disagrees with the theoretical prediction by a uniform factor of around 2.8. Alben et al. [2002] interpret this as due to finite-size effects, which results in excess 'back-pressure' in the wake near the fiber. Shifting the theoretical curve with this correction factor (dashed curve), both model and experiments then collapse onto the expected scaling laws for the drag. (The limited experimental data for values $\eta \gg 1$ is due to breakage of the soap film at higher speeds). Despite its simplicity, the beam/FST model is therefore able to capture the interplay between elasticity and fluid flow essential for the self-streamlining effect.

2 Locomotion by destabilizing symmetries

We now turn to another fluid-structure interaction that occurs in the living environment: how organisms propel themselves using flapping movements. Inviscid aerofoil theory tells us that a wing, flapping perpendicularly to the direction of travel, can generate forward thrust through the downstream shedding of vortices; this flapping is seen in the wings of birds or the fins of swimming fish. A very different picture is seen on the scale of microorganisms, such as bacteria, where viscous dissipation dominates inertia. Here reciprocal flapping no longer generates a net thrust (this is known as the Scallop Theorem, and is essentially a consequence of time-reversibility when inertia is negligible). Microorganisms must therefore use non-reciprocal motions, e.g. the beating of cilia or rotation of a flagella, to propel themselves.

Of course, not all organisms lie at one of these two extremes. A remarkable exception is *Clione antartica*, a type of shell-less mollusc that lives in the waters beneath the Antarctic sea ice (figure 6). The typical Reynolds number for flow past these organisms is ~ 10, so that they reside at the transition between a viscous-dominated and inertia-dominated world. As juveniles, when the molluscs are at their smallest, they swim by beating bands of cilia that encircle their bodies. However, larger adults switch strategies and instead use the flapping of wings to move around [Childress and Dudley, 2004].

Figure 6: *Clione antarctica*

The switch in behavior shown by *Clione antartica* suggests there a decisive change in the way a fluid and a freely moving body interact as the Reynolds number increases. To fix ideas, consider a rigid, two-dimensional 'wing' of characteristic size c, immersed in a fluid of density ρ and dynamic viscosity μ. At its simplest, we can regard flapping as consisting of vertical oscillations of the wing; crucially, its horizontal motion is not prescribed, so that any motion in this direction must arise due to forces exerted by the fluid. If the oscillations have frequency f and amplitude a, then the importance of inertia to viscosity is measured by the driving Reynolds number

$$\mathrm{Re}_f = \frac{\rho f a c}{\mu}, \tag{4}$$

As the Reynolds number is increased, we might expect that the reciprocal flapping eventually give rise to horizontal motion, i.e. the wing has 'taken flight'. If so, what is the nature

of this transition? Is it pressure or viscous forces in the fluid that is responsible for initiating the forward motion? Moreover, what is the role of the mass of the wing and its shape?

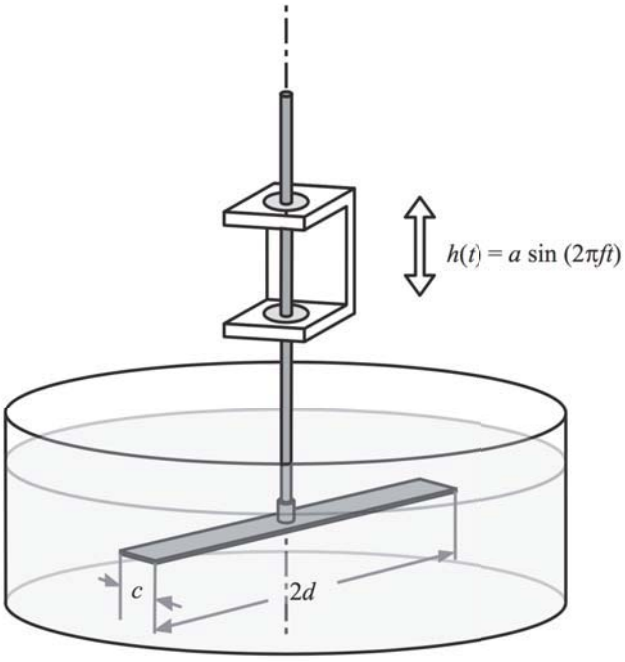

Figure 7: The rotary reciprocal flapping experiment of Vandenberghe et al. [2004], featuring a flat wing (length 15.2 cm, width $c = 1.9$ cm, thickness 0.16 cm) driven periodically in the vertical direction (amplitide $a = 1.4$ cm) at a frequency f varied up to 6 Hz [reprinted from Vandenberghe et al., 2004].

2.1 Rotary reciprocal flapping experiment

Experiments on this simple system have been performed by Vandenberghe et al. [2004], who immersed a flat rectangular wing into a cylindrical tank of water; see figure 7. The wing is composed of stainless steel and is effectively rigid. The center of the wing is attached to a vertical plunger, which oscillates the wing vertically while it is free to rotate about the vertical axis. Because of the cylindrical geometry, the system is able to settle to a steady state without obstruction. The speed of this rotation is measured as the driving Reynolds number is varied (by varying the frequency f at a fixed amplitude a).

For values $\mathrm{Re}_f < 390$, no horizontal motion of the wing is observed. Due to the dominant role of viscosity, the non-rotating state remains stable and any disturbance quickly decays away. Visualizing the structure of the flow in this regime shows that the wing sheds two counter-rotating vortices at each half cycle (figure 8a). These remain left-right symmetric so that no net sideways thrust is produced. (The flow structure remains roughly two-dimensional except in isolated regions near the tips of the wing and the center of the tank).

For higher driving Reynolds numbers, $\mathrm{Re}_f \gtrsim 500$, symmetry breaking occurs in the flow structure, reminiscent of the classic von-Kármán instability of a symmetric wake behind a

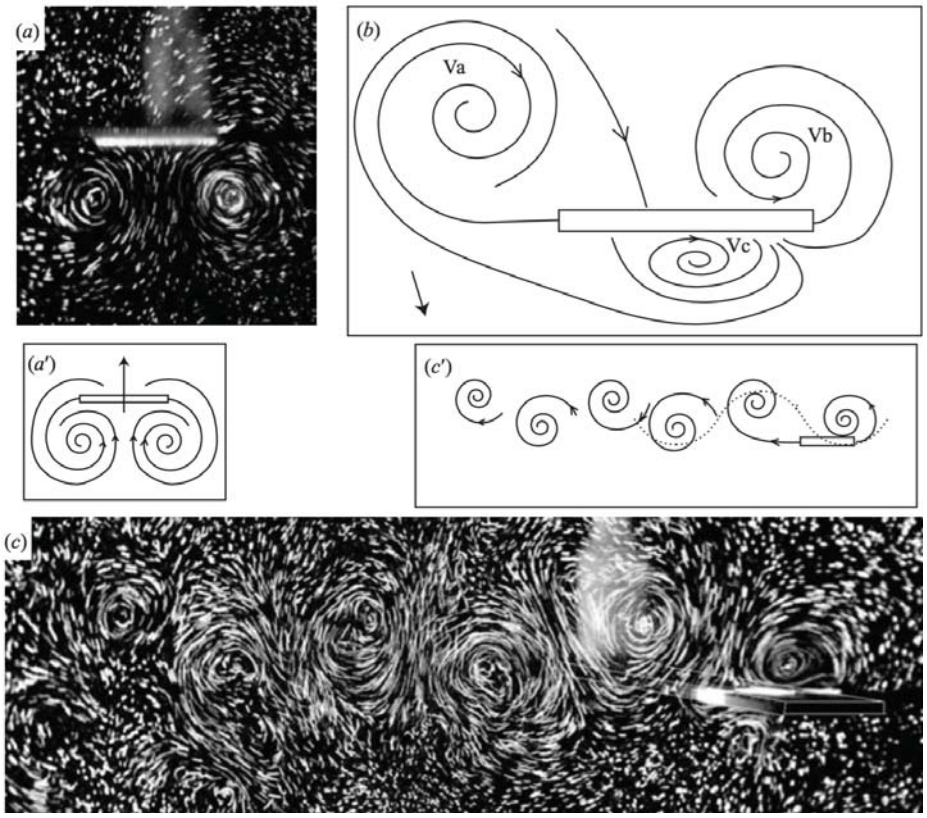

Figure 8: The flow pattern observed (a) for a wing in a non-rotating state, (b) as the wing is accelerating, and (c) after the wing has settled down to a steady rotating state at higher driving frequency (the tracer particles illuminated here are small bubbles of hydrogen produced by applying a voltage between the wing and fluid) [reprinted from Vandenberghe et al., 2004].

bluff object. Leading and trailing-edge vortices can be distinguished from each-other (figure 8b), which appear to exert both pressure suction forces and viscous shear stresses in the direction in which the wing is accelerated. Eventually, the wing settles down to a steady rotating state with a well-defined wake, featuring a characteristic inverted von-Kármán vortex street (figure 8c) (The wake diffuses sufficiently fast so that self-interactions between the two half-wings are negligible).

Figure 9 plots the dimensionless rotating frequency, Re_Ω, as a function of the driving Reynolds number. This reveals the structure of the symmetry-breaking bifurcation from a non-rotating state ($\mathrm{Re}_\Omega = 0$) to a steady rotating state ($\mathrm{Re}_\Omega \neq 0$). In certain regimes, the system is bistable and exhibits hysteresis, suggesting that a subcritical bifurcation occurs. At higher Reynolds numbers the rotating frequency grows linearly with the driving frequency. The Strouhal number $\mathrm{St} = \mathrm{Re}_f/\mathrm{Re}_\Omega$ — a common way to measure the efficiency of thrust generation — approaches a constant value of around 0.26. This is within the range $(0.2, 0.4)$ considered to be 'efficient' for animal swimming/flight.

The forward flight observed by Vandenberghe et al. [2004] is quite remarkable in that

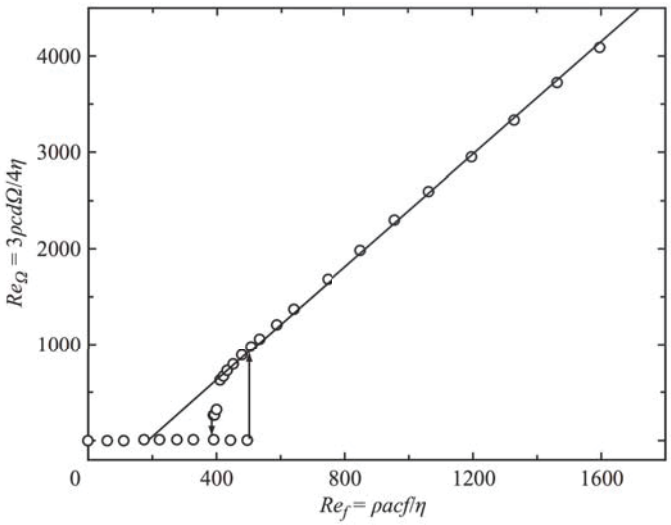

Figure 9: Dimensionless rotating frequency of a reciprocal flapper as a function of the driving Reynolds number [reprinted from Vandenberghe et al., 2004].

it arises due to a very simple interaction between ambient fluid and an oscillating wing. Interestingly, this is a possible route by which the wings of flying organisms could have evolved from small appendages present in early organisms, which were initially developed for some other use such as feeding. As these grew in size and their driving Reynolds number increased, the appendages would have been able to generate forward thrust and develop into wings.

2.1.1 Model

To further examine how symmetry breaking leads to forward flight, Alben and Shelley [2005] study the dynamics of a rigid ellipse (density ρ_b, major axis length L, area A_0) driven vertically in a two-dimensional fluid (pressure p, density ρ). The horizontal velocity of the ellipse is not specified but is determined by a force balance along its boundary. In dimensionless variables this gives the equation of motion

$$M\mathrm{Re}_f \frac{\mathrm{d}u_b}{\mathrm{d}t} = \hat{\mathbf{x}} \cdot \mathbf{F}_{\text{fluid}}, \tag{5}$$

where the net force exerted by the fluid on the ellipse is

$$F_{\text{fluid}} = \int_{\text{body}} (-p\mathbf{I} + 2\mathbf{E})\, \mathrm{d}s. \tag{6}$$

Here Re_f is the driving Reynolds number (defined as in (4), with the major axis L now acting as a characteristic size), $M = (\rho_b/\rho)(A_0/L^2)$ is the mass of the ellipse normalized by the mass of the displaced fluid, $\mathbf{E}$ is the rate of strain tensor, $\mathbf{n}$ is the outward normal and s is arclength along the boundary. Equation (5) is solved together with the incompressible Navier-Stokes equations in the fluid. The system is closed by a no-flux boundary condition

on the body surface, so that the aspect ratio of the ellipse also enters as a dimensionless parameter. The full system is solved numerically using a vorticity-stream-function formulation on a conformal grid.

In line with the experiments of Vandenberghe et al. [2004], the flow structure remains left-right symmetric at small driving Reynolds numbers Re_f (figure 10a) with the state of zero horizontal motion remaining stable, while symmetry breaking and acceleration of the wing occurs at higher Re_f. The vorticity structure of the flow during the acceleration stage is shown in figure 10b,c and reveals the mechanism by which the body "takes flight". At some stage one of the symmetric counter rotating vortices shed by the ellipse runs into a vortex of opposite sign that was shed during the previous half cycle. These vortices combine to form a dipole that propagates away from the body. This advects momentum and so generates an opposing thrust on the body, which accelerates and quickly settles down to steady locomotion (figure 10f).

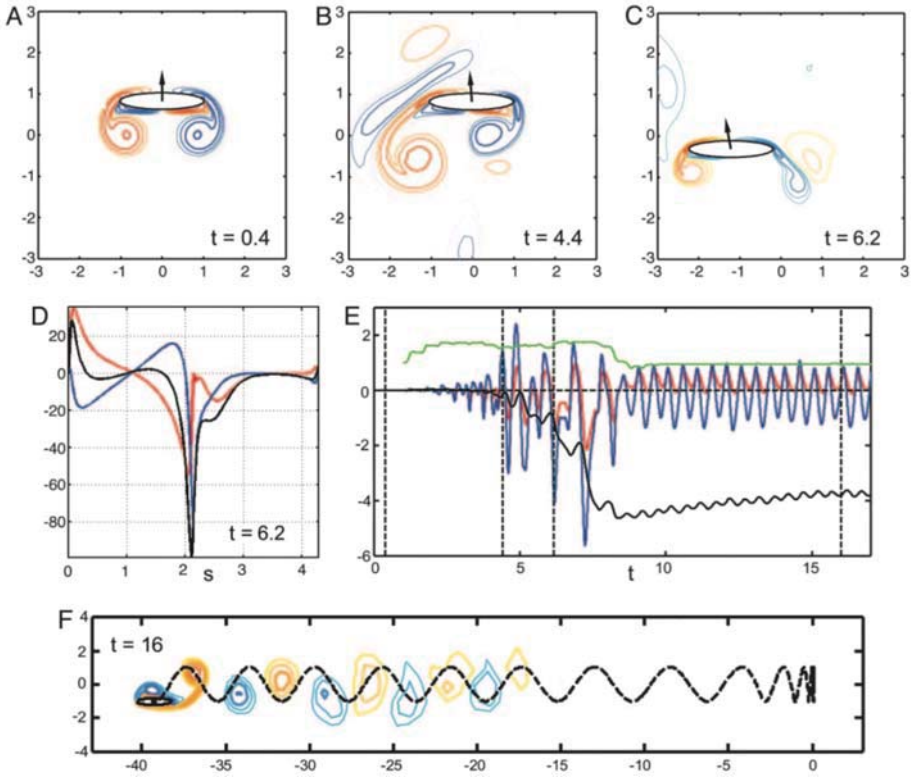

Figure 10: (a)–(c) The flow pattern around a flapping ellipse during the early stages of "taking flight" (here $\mathrm{Re}_f = 35$, $\rho_b/\rho = 35$, aspect ratio 5 : 1). The curves correspond to contours of the vorticity field. (e) Evolution of the net horizontal pressure force (blue line), viscous force (red line), horizontal body velocity (black line) and input power (green line).(e) The trajectory of the ellipse and vorticity field during steady flight [reprinted from Alben and Shelley, 2005].

Figure 10e shows how the net horizontal pressure and viscous forces that act on the body evolve in time, as well as the horizontal velocity u_b and the input power required to

drive the body through the fluid. As the body is accelerated, the horizontal velocity grows exponentially in time and both pressure and viscous forces contribute. At later times, however, as the body settles to steady locomotion, these act in opposing directions. This locomoting state is highly efficient: the input power drops by almost a factor of two.

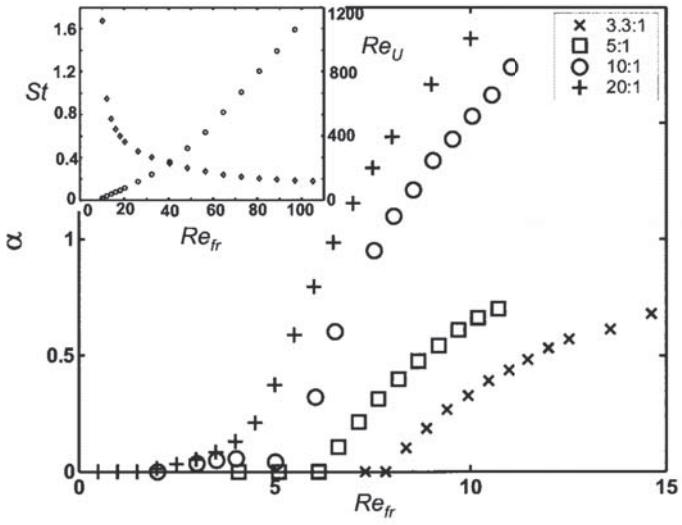

Figure 11: Main plot: The dependence of the growth rate of instability on the driving Reynolds number Re_f for various aspect ratios. Inset: Average horizontal speed and Strouhal number during locomotion ($\rho_b/\rho = 32$, aspect ratio $10:1$) [reprinted from Alben and Shelley, 2005].

The exponential growth rate of the horizontal velocity depends strongly on the driving Reynolds number and the aspect ratio of the ellipse; see figure 11. Generally, thinner bodies undergo symmetry breaking at lower driving frequencies. In contrast, relatively little dependence on the mass ratio is found. This is evidence that the instability is driven by the fluid, as with the classic von-K´arm´an instability of a symmetric wake. Focusing on a very slender ellipse (aspect ratio $10:1$), the inset of figure 11 shows the dependence of the average horizontal velocity and corresponding Strouhal number. Unlike the experiments of Vandenberghe et al. [2004], there is no evidence of a subcritical bifurcation or any bistablity/ hysteresis in the system. These are likely the result of bearing friction in the rotating plunger used by Vandenberghe et al. [2004].

Finally, we note that the mass ratio M and body shape are crucial parameters in determining the response once symmetry breaking has occurred. Thinner bodies tend to move more smoothly into a state of steady locomotion (figure 12a), which is most likely due to viscous forces being more important in this case (figure 12b). Decreasing the body mass M, the locomotion instead becomes highly irregular and chaotic in appearance (figure 12c). If the body is too light, it is unable to sustain horizontal motion as it interacts with the vortices it sheds over each cycle. These conclusions are summed up in the phase diagram shown in figure 13.

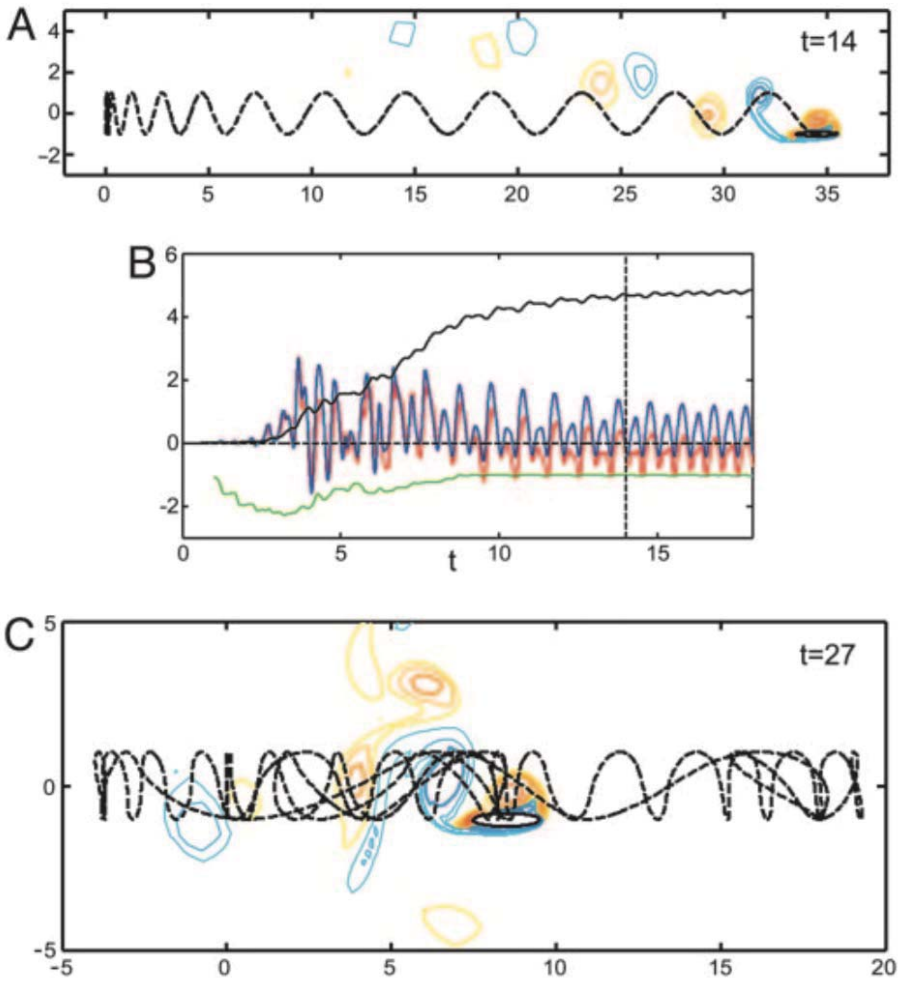

Figure 12: (a)–(b) The same plots in figure 10 though now with the aspect ratio decreased to 10 : 1. (c) Decreasing the density ratio to $\rho_b/\rho = 1$ (while keeping aspect ratio, Re_f fixed) results in a chaotic trajectory [reprinted from Alben and Shelley, 2005].

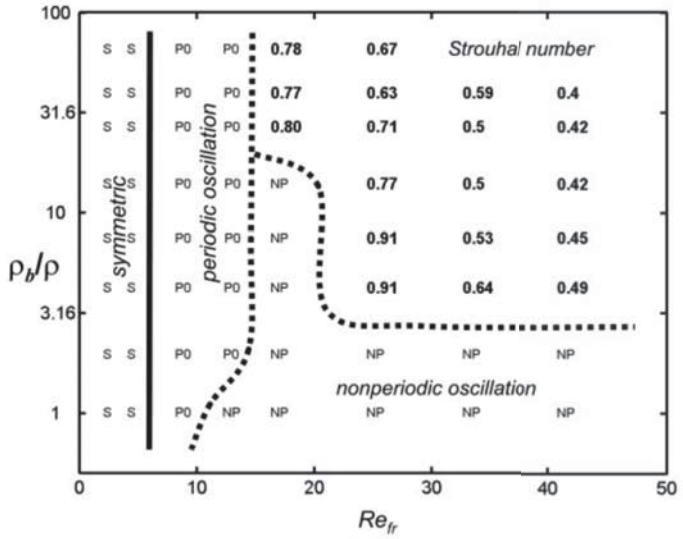

Figure 13: Classifying the locomoting state in the phase plane of Re_f and ρ_b/ρ (aspect ratio fixed at $10:1$). [reprinted from Alben and Shelley, 2005].

References

S. Alben and M. Shelley. Coherent locomotion as an attracting state for a free flapping body. *Proceedings of the National Academy of Sciences*, 102(32):11163–11166, 2005.

S. Alben, M. Shelley, and J. Zhang. Drag reduction through self-similar bending of a flexible body. *Nature*, 420(6915):479–481, 2002.

S. Alben, M. Shelley, and J. Zhang. How flexibility induces streamlining in a two-dimensional flow. *Physics of Fluids*, 16(5):1694–1713, 2004.

Stephen Childress and Robert Dudley. Transition from ciliary to flapping mode in a swimming mollusc: flapping flight as a bifurcation in Re_ω. *Journal of Fluid Mechanics*, 498: 257–288, 2004.

H. Helmholtz. Uber discontinuierlich flussigkeitsbewegungen, monatsberichte konigl, 1868.

N. Vandenberghe, J. Zhang, and S. Childress. Symmetry breaking leads to forward flapping flight. *Journal of Fluid Mechanics*, 506:147–155, 2004.

Lecture 4: High Re Fluid-structure Interactions in Sports

Anette Hosoi (notes by Colin Meyer & Qi Li)

June 23, 2016

4.1 The sports lecture (part I)

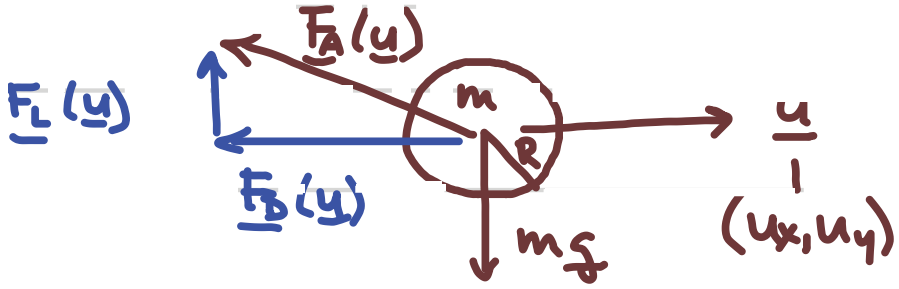

Figure 1: Forces acting on a sports ball

All sports take place in a fluid and in many cases, the fluid plays an important role. This is, of course, neglecting Al Shepard's golfing on the moon. We start by considering a spherical sports particle. A force diagram for the ball is shown in figure 1. The aerodynamic force $\underline{F}_A$ can be decomposed into components of drag $\underline{F}_D$ and lift $\underline{F}_L$. Principally, the drag opposes forward motion and the lift counteracts gravity. The differential equation that describes the force balance show in in figure 1 is given as

$$m\frac{d\underline{u}}{dt} = mg\hat{z} + \underline{F}_D + \underline{F}_L. \tag{1}$$

We label these terms as (1), (2), (3), and (4) from left to right. The steady state balance between gravity and the drag term, i.e. a balance between terms (2) and (3), gives the terminal velocity, V_T. For sports where the maximum ball velocity v_{max} is much less than the terminal velocity, aerodynamics does not play a significant role. Thus, we can classify sports by the maximum speed of the ball relative to the terminal velocity, as shown in figure 2.

Another way to classify sports, is to consider the plot aerodynamic force components, which are shown in figure 3. Along the x-axis, sports where the maximum ball velocity is less than the terminal velocity are to the left and sports with faster ball speed are to the right. Rotation is important in sports where normalized lift is greater than unity, such as soccer balls bending into goals and infield pop flies in baseball.

4.1.1 Quadrant I: low lift and drag

Here we consider the first quadrant, which is the canonical first-year physics problem of a drag and lift free projectile. In other words, we consider a dominant balance of equation (1) between terms (1) and (2) as

$$\frac{d\underline{u}}{dt} = \underline{g}.$$

Thus, we have the two equations

$$\ddot{x} = \dot{u} = 0 \quad \text{and} \quad \ddot{y} = \dot{v} = -g,$$

where the dots are total derivatives and $\underline{u} = (u, v)$ in Cartesian directions. Integrating each of these equations once gives

$$\dot{x} = u_0\cos(\theta_0) \quad \text{and} \quad \dot{y} = u_0\sin(\theta_0) - gt,$$

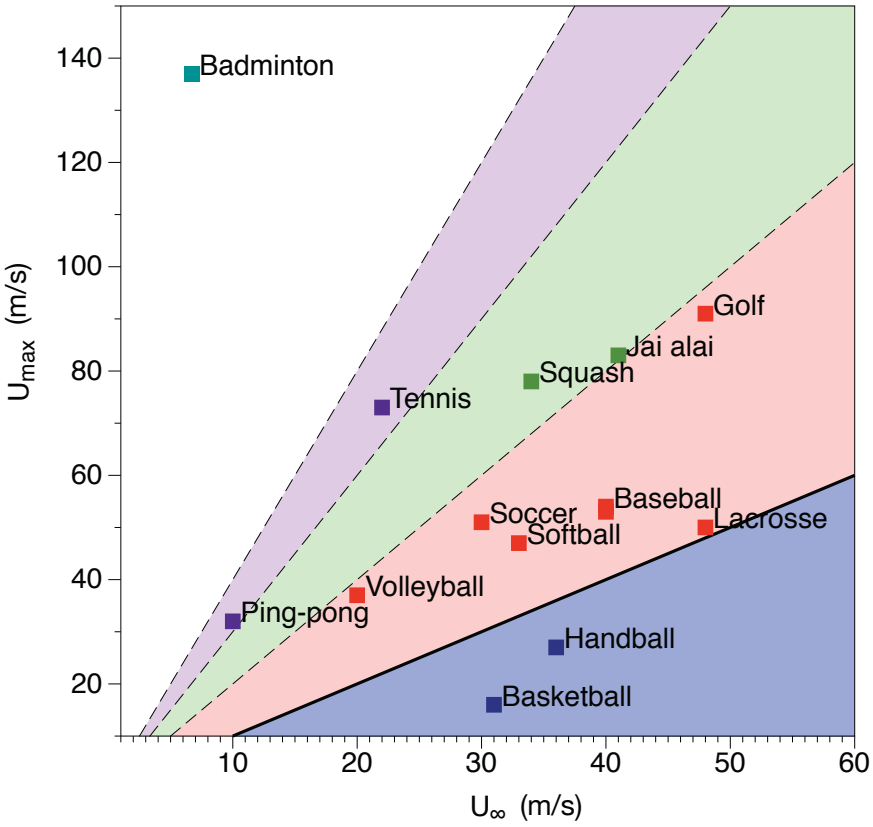

Figure 2: Comparison between the maximum speed of balls in each sport and their terminal velocity. Notice that badminton is very much an outlier.

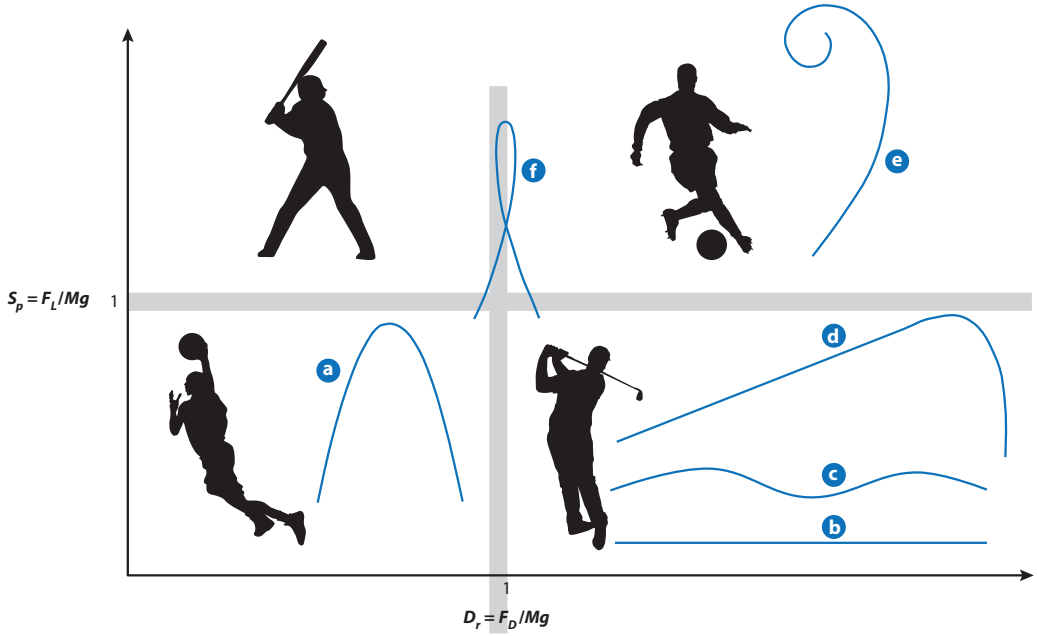

Figure 3: The four quadrants of sports based on the importance of terms in equation (1). The typical sport and quadrant label are: basketball (quadrant I), golf/badminton (quadrant II), soccer (quadrant III), and baseball (quadrant IV).

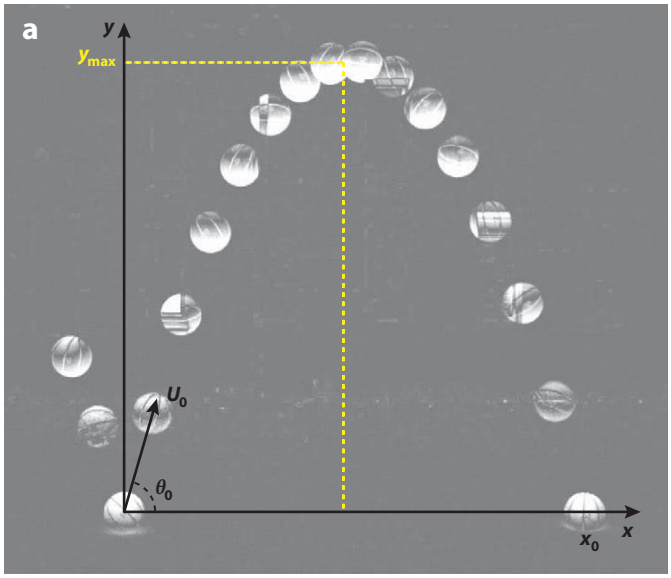

Figure 4: Bouncing basketball tracing a perfect parabolic trajectory (Darbois-Texier, 2013).

with the initial velocity given by $\underline{u}(t=0) = u_0(\cos(\theta_0), \sin(\theta_0))$. Integrating these equations again gives

$$x = u_0 \cos(\theta_0)t \quad \text{and} \quad y = u_0 \sin(\theta_0)t - \frac{g}{2}t^2.$$

We can combine these two expressions to give

$$y = \tan(\theta_0)x - \frac{gx^2}{2u_0^2 \cos^2(\theta_0)}.$$

This is a parabola and is in excellent agreement with the motion of a bouncing basketball (figure 4). We can compute the range, or total horizontal distance traveled, of this projectile by setting $y = 0$ (the other root occurs at $x = 0$) as

$$x = \frac{u_0^2}{g} \sin(2\theta_0).$$

The maximum range, therefore, occurs for $\theta_0 = \pi/4$ or 45°.

4.1.2 Quadrant II: high drag and low lift

We now consider the trajectory of badminton shuttlecock. In this quadrant, there are three important effects: acceleration, gravity, and drag, i.e. terms (1), (2), and (3) in equation (1). Thus, we can expect that two terms balance at a time: initially acceleration is inhibited by drag balance and gravity can be neglected (a balance of the first and third terms in equation (1)). This leads to a nearly linear trajectory, as shown in figure 5. Then, the shuttlecock reaches its apex - a region of its trajectory where all three terms balance—and then falls back down in a terminal velocity balance between gravity and drag. At no point along its flight is the trajectory parabolic, and this trajectory is called a Tartaglia after the Italian scientist.

In the initial portion of the trajectory, where acceleration and gravity balance, we have

$$m\frac{\partial \underline{u}}{\partial t} = -\frac{1}{2}\rho_f u \underline{u} A C_D,$$

where ρ_f is the density of the fluid, A is the cross sectional area, C_D is the drag coefficient, and m is the mass of the shuttlecock. We can parameterize the curve by the arc length s and angle $\theta(s)$,

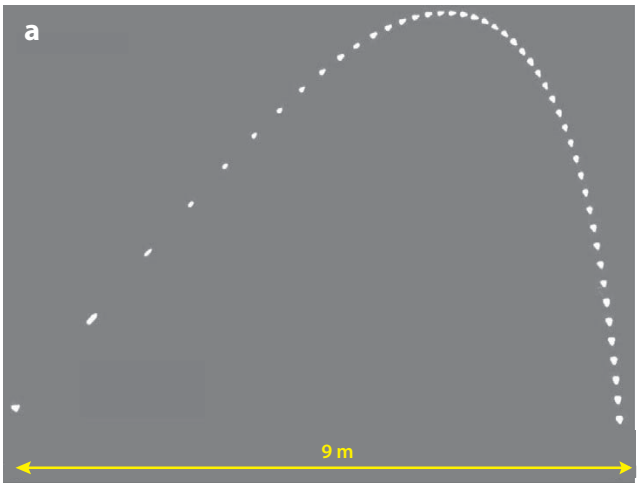

Figure 5: The Tartaglia of a badminton shuttlecock (Darbois-Texier, 2014).

so that

$$u = \frac{ds}{dt},$$

and

$$\frac{d\underline{u}}{ds} = -\frac{\rho_f A C_D}{2m}\underline{u}.$$

Integrating this expression once gives

$$\underline{u} = \underline{u}_0 e^{-s/\delta},$$

where δ is given by

$$\delta = \frac{\rho_f A C_D}{2m}.$$

Implicit in this analysis is the assumption that the drag coefficient is constant with velocity. Figure 6 shows that for large Reynolds numbers, i.e. $10^4 - 10^6$, this is a good approximation. At around $Re \sim 10^7$, however, there is a strong drop in the drag, which is known as the "drag crisis" and it is the critical Reynolds number at which the boundary layer around the ball becomes turbulent. Wind tunnel observations show that a turbulent boundary remains attached to the surface for a greater portion of the surface of the ball than for a laminar boundary layer and, therefore, the drag is reduced with a turbulent boundary layer. This is shown in the insert of Figure 6. Cricketers smooth one side of a roughened cricket ball to trigger the drag crisis on one side of the ball leading it to hook the ball the opposite way from normal (an anecdote joyfully recalled by Colm Caulfield).

We can solve the problem when all three terms balance by writing the equation in tangential and normal components as

$$mu\frac{du}{ds}\hat{t} + mu^2\frac{d\theta}{ds}\hat{n} = -mg\cos(\theta)\hat{n} - mg\sin(\theta)\hat{t} - \frac{1}{2}\rho C_D u^2 A\hat{t}.$$

Equating the normal components gives

$$u^2\frac{d\theta}{ds} = -g\cos(\theta).$$

We now need to determine u. To do this, we examine the x-momentum equation as

$$mu\frac{du_x}{ds} = -\frac{1}{2}\rho C_D u u_x A,$$

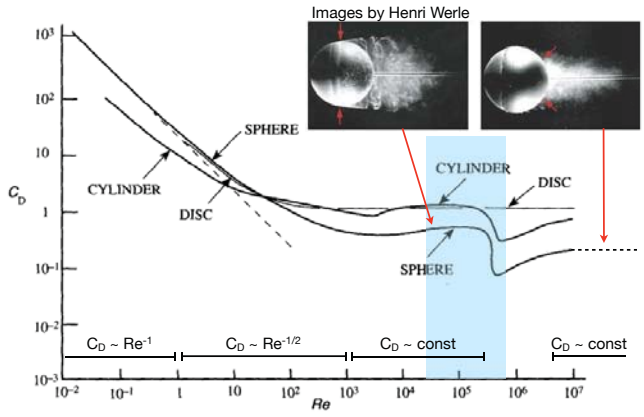

Figure 7.13 Log–log plot of drag coefficient C_D as a function of Reynolds Number Re for spheres, transverse cylinders, and face-on discs. The broken straight line represents Stokes's law.

Figure 6: The "drag crisis" .

which gives that

$$u_x(s) = u_{0x}e^{-s/\delta},$$

where δ is the same as before. We also know that

$$u_x(s) = u(s)\cos(\theta(s)).$$

Thus,

$$u_0^2\cos^2(\theta_0)e^{-2s/\delta}\frac{d\theta}{ds} = -g\cos^3(\theta).$$

We can separate and integrate as

$$\int_{\theta_0}^{\theta(s)}\frac{d\theta'}{\cos^3(\theta')} = -\frac{g}{u_0^2\cos^2(\theta_0)}\int_0^s e^{2s'/\delta}ds'.$$

We call the left side $f(\theta)$—it is easy to evaluate in Mathematica, yet the output is lengthy, which gives

$$f(\theta) = -\frac{g\delta}{2u_0^2\cos^2(\theta_0)}\left(e^{2s/\delta}-1\right).$$

Thus, we could solve for s implicitly as a function of θ.

An easy method to estimate the range of the shuttlecock is to determine the point along the trajectory s where the angle θ is equivalent to $-\theta_0$, which is the minus of the initial angle. Converting it into the horizontal distance gives

$$x \approx s(\theta = -\theta_0)\cos(\theta_0),$$

and we could compute the maximum by taking the derivative with respect to θ_0.

4.1.3 Sports fields

Imagine that the size of a sports field is given by L_{field} and that the maximum range for the ball is x_{max}, then it takes a long time to move th e ball down the field in sports where $L_{field} \gg x_{max}$ and it is hard to keep the ball in bounds in sports where $L_{field} \ll x_{max}$. We can also think of two timescales in the sport characterizing the speed of the balls and the speed of the players as

$$t_{sport} = \frac{L_{field}}{U_{max}} \quad \text{and} \quad t_{player} = \frac{L_{player}}{U_{max}^{player}}.$$

$$\frac{\tau_{sport}}{\tau} = \frac{L_{field}}{U_{max}.\tau}$$

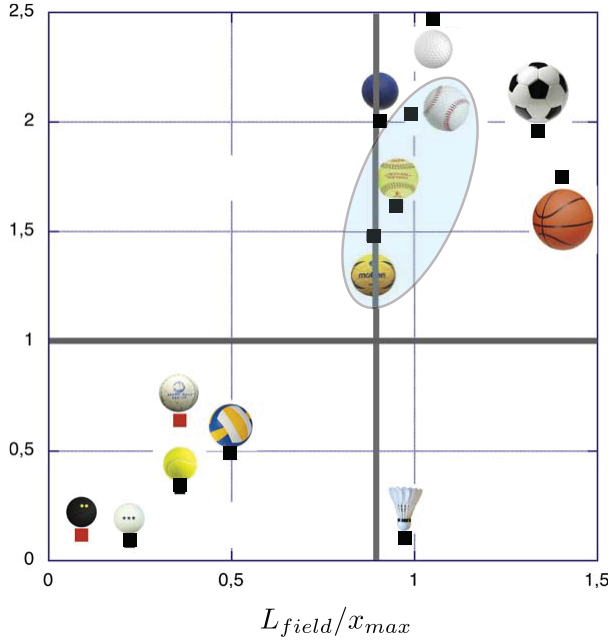

Figure 7: The travel for a ball across a field of length L_{field} normalized by the player timescale as a function of the ratio of field size to maxmimum projectile range.

Thus, we can again make a four quadrant plot of sports with t_{sport}/t_{player} as a function of L_{field}/x_{max}, see figure 7. In sports where $(t_{sport}/t_{player}) < 1$ and $(L_{field}/x_{max}) < 1$ are fast and require precision, players are rewarded for quick reflexes and keeping the ball in bounds such as in ping pong or squash. In other sports $(t_{sport}/t_{player}) < 1$ yet $(L_{field}/x_{max}) > 1$, so a little sloppiness is tolerable, for instance badminton. The upper quadrants have slower game play and larger fields, which is often made more challenging by having targets (such as goals) or they require collaboration as team sports.

4.1.4 Quadrant III: high drag and high lift

We now move to the part of parameter space where lift on sports particles is important. In order to get lift, asymmetry is required to move the stagnation points. This can easily be done by spinning the ball (i.e. a curve ball) or by adding roughness (such as baseball stitches). Figure 8 shows a spinning golf ball with a downward induced lift due to a rotation of the stagnation points. A classic example of lift in sports is the curving soccer kick such as "Bend it like Beckham" or Roberto Carlos. For a soccer ball (i.e. sphere) of radius R, the force of lift scales as

$$\underline{F}_L \sim \rho \cdot 2\pi R^2 \underline{\Omega} \times \underline{u} \cdot 2R,$$

We can also write the lift as

$$\underline{F}_L = \rho R^3 C_\Omega \underline{\Omega} \times \underline{u}.$$

Returning to equation (1), we can neglect gravity (second term) and write

$$m\frac{d\underline{u}}{dt} = -\frac{1}{2}\rho C_D u \underline{u} A + \rho R^3 C_\Omega \underline{\Omega} \times \underline{u}.$$

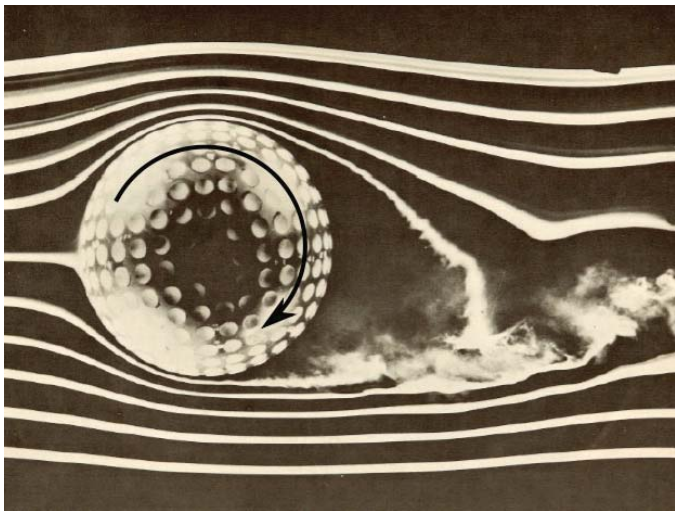

Figure 8: Downward induced lift due to spin on a golf ball.

If we assume that the soccer ball rotates completely around the vertical axis, i.e. $\underline{\Omega} = \Omega_0 \hat{z}$, then we can break the simplified force balance into normal and tangential components as

$$mu\frac{du}{ds}\hat{t} + mu^2\frac{d\theta}{ds}\hat{n} = -\frac{1}{2}\rho C_D u^2 A\hat{t} + \rho R^3 C_\Omega \Omega_0 u\hat{n}.$$

Equating the normal and tangential components gives

$$\frac{du}{ds} = -\frac{C_D \rho A}{2m}u \quad \text{and} \quad u\frac{d\theta}{ds} = \frac{\rho R^3 C_\Omega}{m}\Omega_0.$$

Integrating the left expression first we have that

$$u = u_0 e^{-s/\delta},$$

where δ is the same as before. We can now insert this into the normal balance to find the ode

$$u_0 e^{-s/\delta} \frac{d\theta}{ds} = \frac{\rho R^3 C_\Omega}{m} \Omega_0,$$

which integrates to

$$\theta(s) = \frac{2}{\pi} S^* \frac{C_\Omega}{C_D} \left(e^{s/\delta} - 1 \right), \tag{2}$$

where we define S^* as the spin number, defined as

$$S^* = \frac{\Omega R}{u_0},$$

and use the fact that the cross sectional area is $A = \pi R^2$. The result for $\theta(s)$ given in equation (2) is a spiral and shows how Roberto Carlos' ball can curve so drastically!

Lecture 5: High Re Fluid-structure Interactions in Sports (continued)

Anette Hosoi (notes by Anna Skipper & Oceane Richet)

June 24, 2016

1 Sports Ballistics (continued)

How do you make a pop-up in softball? The trajectory of a pop-up is almost vertical - the ball goes straight up in the air.

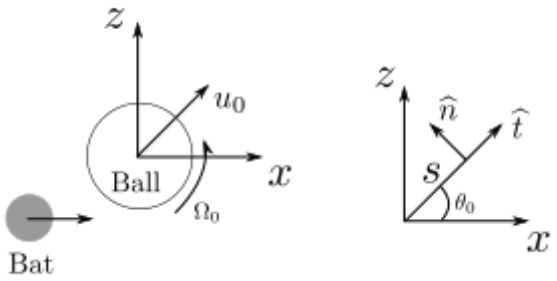

Figure 1: Schematic drawing of the experimental set up.

- Lift force: $F_L \sim mg$
- Drag force: $F_D << mg \implies$ negligible compared to mg and F_L.
- Spin: $\underline{\Omega} = -\Omega_0 \widehat{y}$

Definition of the tangent and the normal:

$$\widehat{t} = (\frac{dx}{ds}, 0, \frac{dz}{ds}) = (\cos\theta, 0, \sin\theta), \tag{1}$$

$$\widehat{n} = (-\frac{dz}{ds}, 0, \frac{dx}{ds}) = (-\sin\theta, 0, \cos\theta). \tag{2}$$

In the case of a pop-up with a nearly vertical trajectory:

$$\widehat{t} = (0, 0, \frac{dz}{ds}) = (0, 0, \sin\theta), \tag{3}$$

$$\widehat{n} = (-\frac{dz}{ds}, 0, 0) = (-\sin\theta, 0, 0). \tag{4}$$

A simple force balance of the ball yields:

$$m\frac{d\underline{u}}{dt} = -m\underline{g} + \cancel{\underline{F_D}} + \underline{F_L}. \tag{5}$$

We can then plug in the expression for $\underline{F_L}$:

$$m\frac{d\underline{u}}{dt} = -mg\widehat{z} + \rho R^3 C_\Omega \underline{\Omega} \times \underline{u} = -mg\widehat{z} + \rho R^3 C_\Omega \Omega_0 u_0 \widehat{x}. \tag{6}$$

To solve, we can balance the $\widehat{z}$ and $\widehat{x}$ terms separately.

$$\widehat{z}: \ \cancel{m}\frac{dw}{dt} = -\cancel{m}g \implies \boxed{z(t) = -\frac{1}{2}gt^2 + u_{z_0}t} \tag{7}$$

$$\widehat{x}: \ m\frac{du}{dt} = -\rho R^3 \Omega_0 C_\Omega u_0 \frac{dz}{ds}. \tag{8}$$

$$\begin{aligned}
m\frac{ds}{dt}\frac{du}{ds} &= -\rho R^3 \Omega_0 C_\Omega u_0 \frac{dz}{ds}, \\
mu_0\frac{du}{ds} &= -\rho R^3 \Omega_0 C_\Omega u_0 \frac{dz}{ds}, \\
m\cancel{u_0}\frac{du}{\cancel{ds}} &= -\rho R^3 \Omega_0 C_\Omega \frac{dz}{\cancel{ds}}\cancel{u_0}, \\
\Rightarrow u_x(z) &= -\frac{\rho R^3 \Omega_0 C_\Omega}{m} z(t) + u_{x_0}, \\
\implies \boxed{u_x(t) = -\frac{\rho R^3 \Omega_0 C_\Omega}{m}\left(-\frac{1}{2}gt^2 + u_{z_0}t\right) + u_{x_0}}&.
\end{aligned} \tag{9}$$

We can now rescale our equations in the following way:

$$\overline{X} = \frac{g}{u_0^2}x, \tag{10}$$

$$\overline{Z} = \frac{g}{u_0^2}z, \tag{11}$$

$$\bar{t} = \frac{g}{u_0}t. \tag{12}$$

Integrating Equation 9 with respect to time yields

$$x(t) = -\frac{\rho R^3 \Omega_0 C_\Omega}{m}\left(-\frac{1}{6}gt^3 + \frac{u_{z_0}}{2}t^2\right) + u_{x0}t. \tag{13}$$

After rescaling, remembering that the spin number, $Sp = \frac{R\Omega_0}{u_0}$, we will obtain the following expressions for the trajectory:

$$\overline{X}(\bar{t}) = \cos\theta_0\bar{t} - \frac{1}{2}S_p\sin\theta_0\bar{t}^2 + \frac{1}{6}S_p\bar{t}^3, \tag{14}$$

$$\overline{Z}(\bar{t}) = \sin\theta_0\bar{t} - \frac{1}{2}\bar{t}^2. \tag{15}$$

How does this equation change as a function of Sp? Looking at Figure 2, we see that as we increase the Sp, the parabola becomes a cusp. If we continue to increase Sp, the ball can actually loop! This is why even the pros sometimes look silly catching pop-ups.

Figure 2: Evolution of the trajectory of the ball when S_p increases

So what is the critical value of Sp that will yield a cusp? For the cusp, $u_x = u_z = 0$. From Equation 9,

$$\begin{aligned} u_x = 0 = u_{x_0} - \frac{\rho R^3\Omega_0 C_\Omega}{m}(u_{z_0}t - \frac{1}{2}gt^2), \\ u_0 cos(\theta_0) = \underbrace{\frac{\rho R^3\Omega_0 C_\Omega u_0}{mg}}_{\text{Sp}} \frac{g}{u_0}(u_{z_0}t - \frac{1}{2}gt^2). \end{aligned} \tag{16}$$

If we take the derivative with respect to time of Equation 7, we will obtain a similar expression for u_z

$$\begin{aligned} u_z = 0 = u_{z_0} - gt, \\ u_0 sin(\theta_0) = gt, \\ \Rightarrow t = \frac{u_0 sin(\theta_0)}{g}. \end{aligned} \tag{17}$$

We can substitute both u_{z_0} and the expression from Equation 17 back into Equation 16 to finally obtain the critical Sp as a function of θ_0 only.

$$\begin{aligned} u_0 cos(\theta_0) = Sp\frac{g}{u_0}\left(u_0 sin(\theta_0)\frac{u_0 sin(\theta_0)}{g} - \frac{g}{2}\frac{u_0^2 sin^2(\theta_0)}{g^2}\right) \\ \Rightarrow cos(\theta_0) = \frac{Sp}{2}sin^2(\theta_0) \\ \boxed{\Longrightarrow Sp = \frac{2cos(\theta_0)}{sin^2(\theta_0)}} \end{aligned} \tag{18}$$

If $\theta_0 = 85\,\text{deg}$, then $Sp = 0.183$ to get a cusp.

2 Athletes

The goals of an athlete are to:

- maximize power/strength $\longrightarrow$ training+technique
- maximize efficiency, manage energy budget $\longrightarrow$ training+technique+strategy.

The relatively recent invention of power meters on bicycles have revolutionized sports. Now athletes can actually measure the power they are getting out of their legs. This data allows them to construct a critical power curve such as the one shown below. These critical power curves aid the athletes when training.

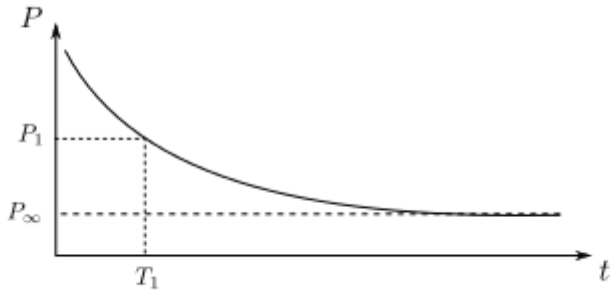

Figure 3: Critical power curve. P_1 is the power which can be maintained during a time T_1. P_∞ corresponds to the power if the absorption of oxygen equals its consumption by muscles.

We can use a differential equation to relate this quantity, power, to the velocity of an athlete in order to get kinematics equations. For example, the kinematics for a runner are given by the following equation:

$$\frac{dv}{dt} + \frac{v}{\tau} = f(t), \tag{19}$$

where v/τ is the dissipation or the resistance and $f(t)$ is the propulsion power divided by the mass. A cyclist will have get a another equation governing his or her kinematics, which is given below: a cyclist

$$\frac{dv}{dt} = f(t) - f_D(t) - f_R(t) - g\sin\theta, \tag{20}$$

where f_D is the drag per unit of mass and f_R the rolling resistance per unit of mass.

This problem was first thought about with a conceptual model of three tanks, shown below. The tank on the far left represents oxygen intake, which is always full. The oxygen goes to an energy source, which outputs whatever representative kinematics are appropriate. When the energy source tank (the middle tank) reaches a certain level, the glycolysis tank begins to drain into the energy source tank. Once the glycolysis and energy source tanks are empty, there is no more energy in the system.

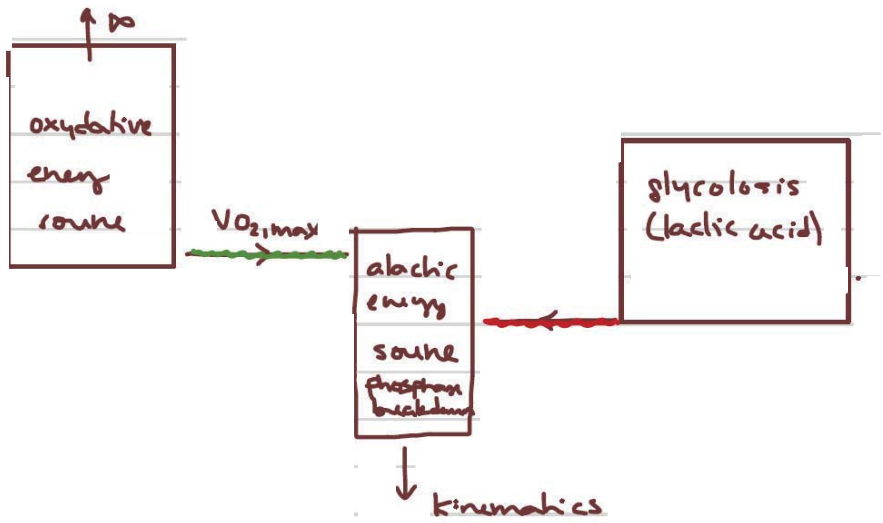

Figure 4: Qualitative picture of exercise using "tanks" which represent different physical processes: oxygen intake, energy production, and glycolysis.

2.1 The Optimal Velocity in Race (Keller 1974)

Keller (1974) took a less qualitative approach and calculated the velocity, $v(t)$, that would minimize the total time T to run a given distance D:

$$D = \int_0^{\boldsymbol{T}} v(t)dt. \tag{21}$$

The acceleration is given by Equation 19 above. The acceleration of the runner must balance both the resistive force from the track and the propulsive force from the runner. This equation is subject to the following constraints:

$$v(0) = 0, \tag{22}$$

$$f(t) \leq F, \tag{23}$$

where F is the maximum force the runner can produce.

The change in the energy of this system is given by

$$\frac{dE}{dt} = \sigma - fv, \tag{24}$$

where *sigma* is the rate of oxygen supplied by breathing and circulation and fv is the power output (or oxygen consumption) of the runner.

This equation is also constrained:

$$E(0) = E_0, \tag{25}$$

$$E(t) \geq 0, \tag{26}$$

where E_0 is some finite energy. The second constrain is a physical one: the energy can never be negative, which would represent the runner taking energy out of the system.

We want to find $v(t)$, $f(t)$, and $E(t)$ such that the total T is minimized for a given distance, D. We will assume that the four physiological constants (τ, F, σ, and E_0) are given.

We can eliminate f and E by expressing them in terms of $v(t)$ only, combining Equations 19 and 23 for $f(t)$

$$f(t) = \frac{dv}{dt} + \frac{v}{\tau} \leq F, \tag{27}$$

and then substituting this expression into Equation 24. We will then integrate both sides to get the following expression for E:

$$\begin{aligned} \int_0^{E_0} dE &= \int_0^t \left[\sigma - v\left(\frac{dv}{ds} + \frac{v}{\tau}\right)\right] ds, \\ E(t) - E_0 &= \sigma t - \frac{v^2(t)}{2} - \frac{1}{\tau}\int_0^t v^2 ds, \\ \boxed{E(t) &= E_0 + \sigma t - \frac{v^2(t)}{2} - \frac{1}{\tau}\int_0^t v^2 ds \geq 0}. \end{aligned} \tag{28}$$

2.2 Case I: Short Races

For a short race, the strategy that makes sense is to use the maximum force available ($f(t) = F$), effectively making these races strength limited. The resulting velocity is given below.

$$\begin{aligned} \frac{dv}{dt} + \frac{v}{\tau} &= F, \\ \Rightarrow v(t) &= F\tau(1 - e^{-t/\tau}). \end{aligned} \tag{29}$$

Now we can substitute this expression for $v(t)$ into Equation 28 to obtain

$$E_0 + \sigma t - F^2\tau^2\left(\frac{t}{\tau} + e^{-}t/\tau - 1\right) \geq 0. \tag{30}$$

This equation is fine as long as $t \leq T_c$, where T_c is the time it takes E to reach zero. If, however, $t > T_c$, we will need to consider another solution.

2.3 Case II: Longer Races

If $t > T_c$, the race is energy limited, tests of endurance rather than pure speed. There will still be a segment ($0 \leq t \leq t_1$) of the race in which the runner uses his or her maximum force to propel him or herself. At some later time, $t_2 \leq T$, the runner's energy will go to zero. But how should the athlete run in the middle part of the race?

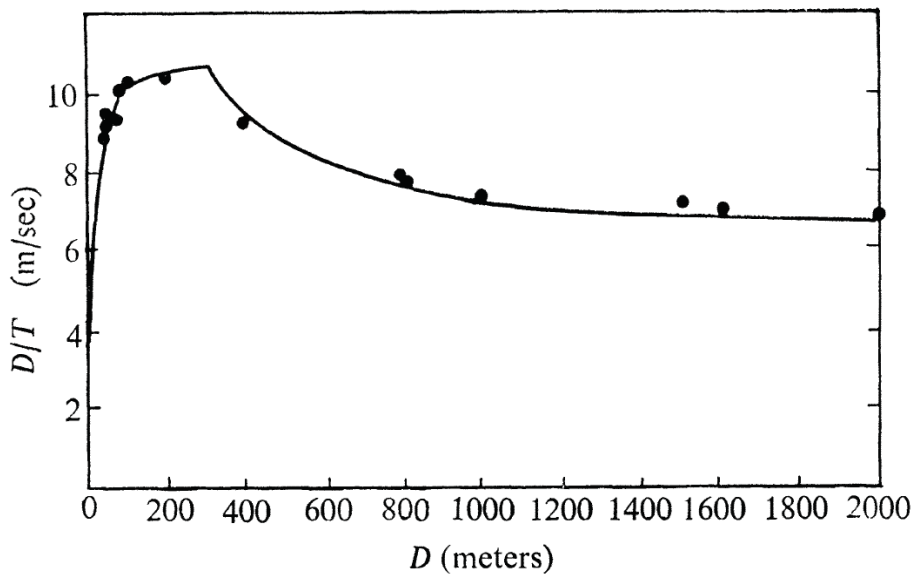

Figure 5: The average speed (D/T) plotted against race distances, D.

First we will need to compute $v_2(t)$, the speed during the last segment of the race. We will set Equation 24 equal to zero to get an expression for $v(t_2)$.

$$v_2^2(t) = \sigma\tau + [v^2(t_2) - \sigma\tau]e^{2(t_2-t)/\tau}, \qquad t_2 \leq t \leq T. \tag{31}$$

If we plug in these expressions into Equation 21, we will obtain

$$D = \int_0^{t_1} \underbrace{v_1(t')}_{\text{Known}}\, dt' + \int_{t_1}^{t_2} \underbrace{v(t')}_{?}\, dt' + \int_{t_2}^{T} \underbrace{v_2(t')}_{\text{Known}}\, dt'. \tag{32}$$

We want to maximize D, which is subject to $E(t_2) = 0$. We will use calculus of variations to maximize

$$D + \lambda E(t_2)/2. \tag{33}$$

After a lot of math, we will finally obtain that the speed $v(t)$ which maximizes D is equal to a constant. (See Keller for more details).

The calculation was compared to actual world record holders, shown below. The four physiological parameters are fitted using the first portion of the curve $(D < 291m)$ using least squares. These same constants are used to plot the rest of the curve.

2.4 Point Particle Model for Soccer Players

We can reframe the kinematics of short races in the following way:

$$\tau\frac{dv}{dt} + v = v_{max}. \tag{34}$$

We can use these kinematics to consider one-on-one interactions in soccer between attackers (A) and defenders (D). There are several types of interactions in soccer we be observe and categorize:

- juke: the attacker oscillates back and forth until he "fakes out" the defender
- loop: the attackers loops around the defender
- run: the attacker runs past the defender
- catch: the defender catches the attacker and takes the ball.

The kinematics equations for both players are shown below.

$$\tau_A \frac{dv_A}{dt} + v_A = v_{A,max}(\underline{x}_G - k_D \underline{x}_D + k_N \underline{\eta})), \tag{35}$$

$$\tau_D \frac{dv_D}{dt} + v_D = v_{D,max}(\underline{x}_G + k_A \underline{x}_D). \tag{36}$$

where k_D and k_A are constants representing interaction strength; k_N is another coefficient; $\underline{x}_D$ is the defenders position; η is a measure of randomness to approximate "skill"; and $\underline{x}_A$ is the position of the attacker.

Both players are attracted to the goal - otherwise the observations look like "six-year-old soccer," where the defender just follows the attacker around. The defender is attracted to the attacker, but the attacker is repelled by the defender.

$$\uparrow k_N \rightarrow juke$$
$$\uparrow k_A \rightarrow loop$$
$$\downarrow k_N \rightarrow run$$
$$\uparrow v_{D,max}, \tau_D \rightarrow catch$$

We can see these relationships in the figure below. The randomness coefficient is plotted on the x-axis and $\frac{v_{A,max}/\tau_A}{v_{D,max}/\tau_D}$. The higher up the y-axis, the faster and more agile the attacker is. Lower values indicate that the defender is very fast and agile.

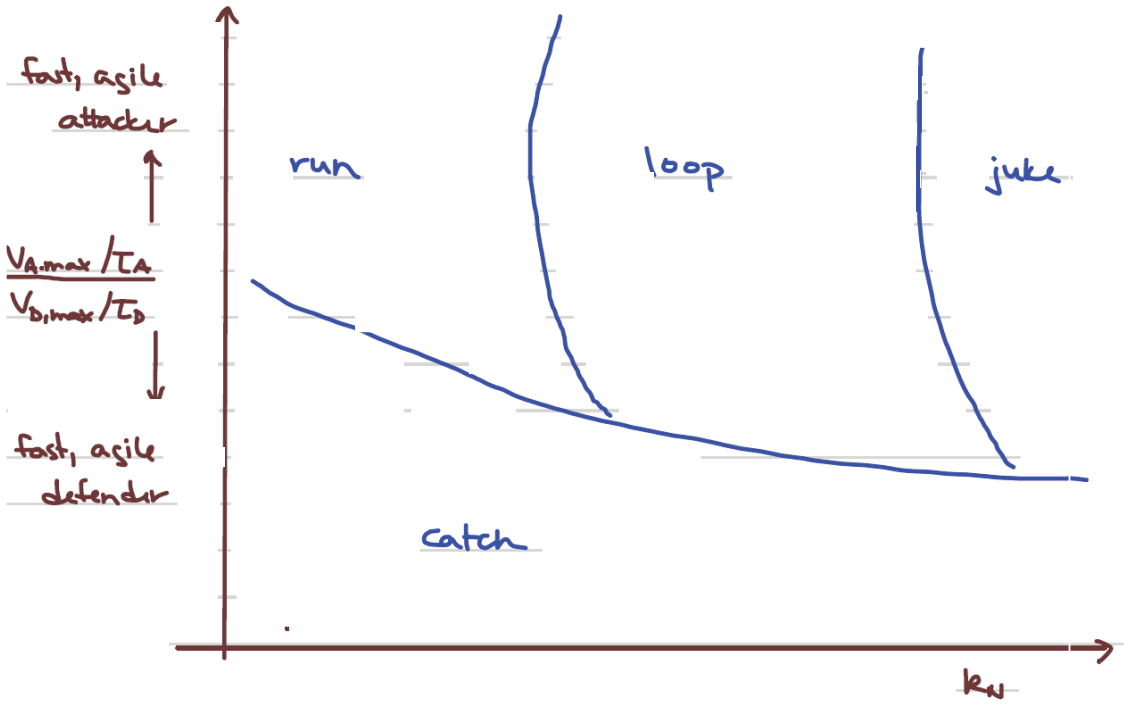

Figure 6: The randomness coeffcient, k_N plotted against the relative strength of the attacker vs. the defender ($\frac{v_{A,max}/\tau_A}{v_{D,max}/\tau_D}$). For a sufficiently skillful, but not very agile attacker (or a very agile defender), the defender can catch the ball. However, if the attacker is very agile, or the defender very poor, the attacking interactions can be seen (run, loop, and juke). The juke is only observable when the attacker is skillful and agile.

Lecture 6: Swimming at Low Reynolds Number

Anette Hosoi (notes by Jason Olsthoorn & Anna Skipper)
June 27, 2016

1 Introduction

Recall from Lecture 2 (Tuesday, Week 1) that for low Reynolds numbers (Re$\ll$ 1), the advective terms in the N-S equations become negligible. That is, in the limit Re$\to$ 0, the N-S equations reduce to the Stokes equations. For a body with characteristic length L, velocity U and dynamic viscosity μ, if we scale pressure as $\mathbf{P} = \frac{\mu U}{L}$ (viscosity scales as a shear stress), the stokes equations are written

$$-\nabla P + \nabla^2 \vec{u} = 0, \qquad \nabla \cdot \vec{u} = 0. \tag{1}$$

We similarly recall that in a Stokes flow, where inertia is negligible, the sum of the Forces $\vec{F_i}$ and moments $\vec{M_i}$ is zero. That is,

$$\sum \vec{F_i} = 0, \qquad \sum \vec{M_i} = 0.$$

In the context of biology, typically the fluid of interest has similar properties to that of water. That is, the molecular viscosity ν is estimated

$$\nu = \frac{\mu}{\rho_0} \sim 10^{-6} \mathrm{m}^2/\mathrm{s}.$$

Here, ρ_0 is the characteristic density of the fluid.

As another general rule, the velocity of a biological creature is typically on the order of $U \sim L$/second. Table 1 lists a few typical examples of a creature with an associated characteristic Reynolds number.

In the discussion below, we are interested in the swimming of biological organisms. We define swimming as

Table 1: Table of typical Reynolds numbers associated with different creatures.

Creature	Length (L)	Reynolds Number $\left(\mathrm{Re}=\frac{UL}{\nu}\right)$
Swimming Human	1m	$\sim 10^{-5}$
Ant	$\sim$ 1mm	$\sim$1
Bacteria	$\sim 1\mu$m	$\sim 10^{-4}$

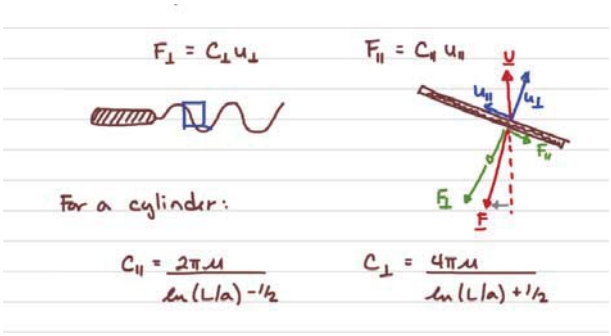

Figure 1: Diagram of the anisotropy leading to a net translation.

Definition 1 *Swimming: To undergo cyclic deformations that result in a net translation/rotation with no externally applied forces/torques.*

This leads us to two interesting phenomenological properties of low Reynolds number flows.

1.1 Propulsion comes from anisotrophy in drag

As the sum of the forces action of a fluid body must sum to zero, the only mechanism to drive propulsion come from an asymetry in the drag applied to the body.

In Stokes flow, the drag acting on a body ($\vec{F}$) is proportional to its velocity ($\vec{U}$). If we investigate the forces acting on a thin plate, we can decompose the drag forces into its parallel ($\vec{F}_{\|}$) and perpendicular ($\vec{F}_{\perp}$) components, written

$$F_{\|} = C_{\|} u_{\|}, \qquad F_{\perp} = C_{\perp} u_{\perp}.$$

For a cylindrical rod of length L and radia a, these proportionality components can be explicitly computed as

$$C_{\|} = \frac{2\pi\mu}{\log\left(\frac{L}{a}\right) - \frac{1}{2}}, \qquad C_{\perp} = \frac{4\pi\mu}{\log\left(\frac{L}{a}\right) + \frac{1}{2}}.$$

In the limit where $L \gg a$, the ratio of these components tends to $\frac{C_{\|}}{C_{\perp}} = 2$.

In the case of propulsion, the anisotropy in drag can result in in a net translation. If we consider a coordinate system such that $\hat{t}$ is the unit vector parallel to the plate, and $\hat{n}$ is the unit vector normal to the plate, then

$$\begin{aligned} \vec{F} &= F_{\|}\hat{t} + F_{\perp}\hat{n} && (2)\\ &= C_{\|} u_{\|}\hat{t} + C_{\perp} u_{\perp}\hat{n} && (3)\\ &= \frac{C_{\|}}{C_{\perp}}\vec{u} + \left(1 - \frac{C_{\|}}{C_{\perp}}\right)\vec{u}_{\text{propulsion}}. && (4) \end{aligned}$$

That is, if $\frac{C_{\|}}{C_{\perp}} = 1$, there can be no net propulsion. Alternatively, with a given anisotrophy, this admits the possibility of a propulsive velocity $\vec{u}_{\text{propulsion}}$. Figure 1 presents a diagram of this anisotropy in tangential and normal forces.

This leads into the formulation of Resistive Force theory (RFT). See Gary and Hancock (1955). In the limit where the radius of curvature $\frac{1}{\kappa} \gg 2a$, one can approximate the segment of a deformed body as straight cylinders. This leads to the approximation that the force acting on a body is given as

$$F = \int_0^L C_{\parallel} u_{\parallel}(s) + C_{\perp} u_{\perp}(s) ds.$$

This is often the first approach used to solve for the forces acting on a geometrically complex swimmer.

1.2 Scallop Theorem

As there is no inertial in a Stokes flow, there is also no time dependence for the flow field. As a result, the velocity of a fluid body is given solely as a functon of its shape (paramaterized by Γ) and its current deformation rate $\dot{\Gamma}$. That is

$$\vec{u}(t) = f(\Gamma)\dot{\Gamma},$$

for some function f. This leads intuitively to the Scallop theorem.

Theorem 1 (Scallop Theorem) *No reciprical motion will result in a net translation.*

2 G.I. Taylor Swimming Sheet

Taylor (1951) proposed to model the spermatozoon tail as a two-dimensional sheet along which waves propagate in the lateral direction. The reference frame is moving with the sheet. A schematic of the wave sheet is provided in figure 2 below. The asterisk (*) refers to dimensional quantities.

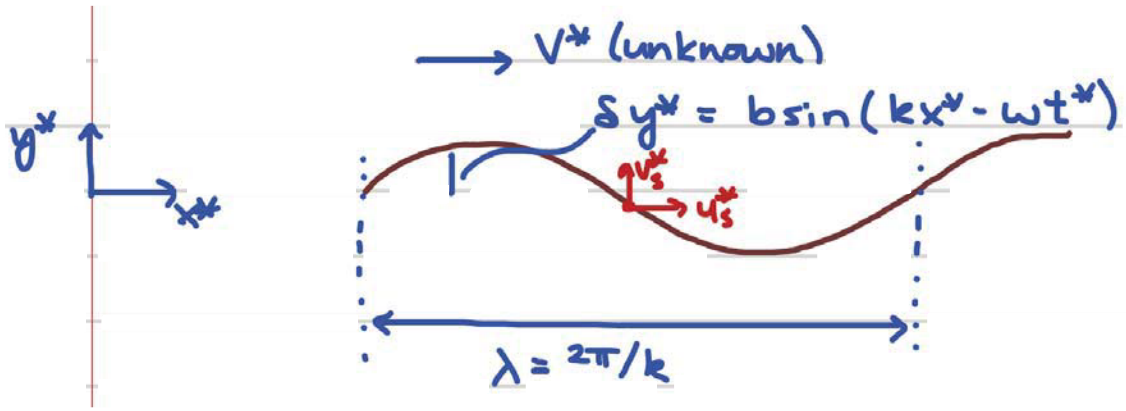

Figure 2: Schematic of the Taylor sheet.

V^* is the unknown fluid velocity off of the sheet, u_s^* is the velocity of the sheet, $\lambda = \frac{2\pi}{k}$ is the wavelength of the sheet, x^* and y^* are the dimensional coordinate directions.

The shape of the sheet, δy^*, is given by

$$\delta y^* = bsin(kx^* - \omega t^*), \tag{5}$$

where b is the amplitude of the wave form, k is the wave number, and ω is the wave frequency.

To solve, we begin with the Stokes equations

$$\nabla \underline{p}^* = \mu \nabla^2 \underline{u}^*, \tag{6}$$

$$\nabla \cdot \underline{u}^* = 0. \tag{7}$$

If we take the curl of equation 6, the pressure term goes away. We can then replace $\underline{u}^*$ with the streamfunction, which is defined as

$$\psi^*{}_{,y} = u^*, \qquad -\psi^*{}_{,x} = v^*. \tag{8}$$

We then replace $\underline{u}^* = (u^*, v^*)$ by the relations in equation 8 to obtain

$$\begin{aligned} 0 &= -\psi^*_{,x,x,x,x} - \psi^*_{,x,x,y,y} - \psi^*_{,y,y,x,x} - \psi^*_{,y,y,y,y} \\ &= \nabla^4 \psi^*. \end{aligned} \tag{9}$$

The equation will be subject to the following boundary conditions:

$$y^* \to \infty : \;\; u^* \to V^*, \;\; v^* \to 0, \tag{10}$$

$$y^* = \delta y^* : \;\; u^* = u^*_s \hat{x}, \;\; v^* = v^*_s \hat{y}. \tag{11}$$

We then make the small amplitude assumption that $b << \lambda$, meaning that $bk << 1$. The assumption effectively means that all the motion is perpendicular to the sheet with very small tangential velocities which can be ignored. This assumption leads to the simplification of 11, which becomes

$$y^* = \delta y^* : \;\; u^* = u^*_s \hat{x} \approx 0, \;\; v^* = v^*_s \hat{y} \approx -\omega b cos(kx^* - \omega t^*). \tag{12}$$

We can now nondimensionalize our equations in the following way:

$$\underline{x}^* = (x^*, y^*) = \underline{x}/k, \tag{13}$$

$$\underline{u}^* = (u^*, v^*) = b\omega \underline{u}, \tag{14}$$

$$\psi^* = b\omega k \psi, \tag{15}$$

$$t^* = t/\omega. \tag{16}$$

Finally, our system of equations to solve is

$$0 = \nabla^4 \psi, \tag{17}$$

$$u(x, y = \delta y; t) = 0, \tag{18}$$

$$v(x, y = \delta y; t) = -cos(x - t), \tag{19}$$

$$u \to V, \;\; v \to 0 \;\; as \;\; y \to \infty. \tag{20}$$

It is important to note that the previous equations have the prescribed kinematics already baked in - we're not allowing for arbitrary phases. In addition, time does not appear in any of the equations of motion, which means that we need to solve instantaneously at each t.

We also need to rescale δy^* by k, yielding

$$\begin{aligned} \delta y &= k\delta y^* \\ &= bksin(kx^* - \omega t^*) \\ &= \varepsilon sin(x - t). \end{aligned} \tag{21}$$

Now we perform an asymptotic expansion in ε for both the streamfunction and the far field velocity V and solve them order by order.

$$\begin{aligned} &= \psi_0 + \varepsilon\psi_1 + \varepsilon^2\psi_2 + \dots \\ V &= V_0 + \varepsilon V_1 + \varepsilon^2 V_2 + \dots \end{aligned} \tag{22}$$

The boundary conditions then become

$$\begin{aligned} u(x, \delta y(x; t); t) &= u(x, 0; t) + \delta y \frac{\partial u}{\partial y}\bigg|_{y=0} + \dots = 0 \\ &= u(x, 0; t) + \varepsilon sin(x - t)\frac{\partial u}{\partial y} + \dots = 0. \end{aligned} \tag{23}$$

$$v(x, \delta y(x; t); t) = v(x, 0; t) + \epsilon sin(x - t)\frac{\partial v}{\partial y} + \dots = -cos(x - t). \tag{24}$$

First we'll find the zero-order solution, ψ_0 and V_0. Let ϕ_0 represent $\nabla^2\psi_0$.

$$\begin{aligned} \nabla^4\psi_0 &= \nabla^2(\nabla^2\psi_0) \\ &= \nabla^2(\phi_0) = 0. \end{aligned} \tag{25}$$

Using separation of variables, as well as considering the form of the solution that we want (oscillatory in x and a decaying in y), we can solve for ϕ_0,

$$\nabla^2\psi_0 = \phi_0 = C_1 sin(x - t)e^{-y}. \tag{26}$$

Now we can solve $\nabla^2\psi_0 = \phi_0$ by solving for the homogeneous and particular solutions. The homogeneous solution is similar to the solution for ϕ_0 and is shown below.

$$\psi_H = C_1 sin(x-t)e^{-y} + C_2 y + C_3 x + C_4. \tag{27}$$

The coefficient C_4 can be ignored since it is an arbitrary constant. C_3 must be zero because we need x to be periodic only. To find the particular solution, we could make this an eigenvalue problem. The easier thing to do is to make an educated guess as to the form of the solution, shown in Equation 28 below.

$$\psi_P = e^{-y} sin(x-t) f(x,y). \tag{28}$$

Take the second derivatives with respect to x and y to obtain

$$\psi_{P,y,y} = e^{-y} sin(x-t) f - 2e^{-y} sin(x-t) f_{,y} + e^{-y} sin(x-t) f_{,y,y}, \tag{29}$$

$$\psi_{P,x,x} = -e^{-y} sin(x-t) f + 2e^{-y} cos(x-t) f, x + e^{-} y sin(x-t) f_{,x,x}. \tag{30}$$

Adding Equations 29 and 30 and setting expression equal to ϕ_0 yields

$$\begin{aligned} C_1 e^{-y} sin(x-t) = {} & e^{-y} sin(x-t) f - 2e^{-y} sin(x-t) f_{,y} + e^{-y} sin(x-t) f_{,y,y} \\ & + -e^{-y} sin(x-t) f + 2e^{-y} cos(x-t) f, x + e^{-} y sin(x-t) f_{,x,x}. \end{aligned} \tag{31}$$

By setting the coefficients on the sine and cosine terms on the right hands side equal to those on the right, we can show that f is a function of y only. The equation for f becomes

$$f(y) = f_H + f_P = C_4 e^{2y} + C_5 y. \tag{32}$$

However, the e^{2y} term will grow too quickly at zero order, so this term goes away and leaves only the linear term. We now let $C_1 = B_0$ and $C_5 = A_0$. In order to satisfy the boundary conditions, C_2 must equal V_0. Finally, the solution for psi_0 is given as

$$\psi_0 = (A_0 y + B_0) e^{-y} sin(x-t) + V_0 y. \tag{33}$$

The horizontal velocity u is found as shown in Equation 8.

$$u = \psi_{0,y} = sin(x-t)[-(A_0 + B_0)e^{-y} + A_0 e^{-y}] + V_0. \tag{34}$$

If we plug in the boundary condition for u at $y = 0$, we will find that $V_0 = 0$ at zero order. This means there is no swimming in the zero order solution!

For the meantime, we will continue to solve for ψ_0 by plugging in the boundary conditions for v at $y = 0$ to find that $A_0 = B_0 = 1$. This yields the solution for psi_0 shown below.

$$\psi_0 = (1+y)e^{-y} sin(x-t). \tag{35}$$

Now we will find the first order solution, ψ_1.

$$\nabla^2 \psi_1 = 0. \tag{36}$$

At $y = 0$,

$$\psi_{1,y} + sin(x-t)\psi_{0,y,y} = 0,$$
$$-\psi_(1,x) - sin(x-t)\psi_{0,x,y} = 0. \tag{37}$$

As $y \to \infty$,

$$\psi_{1,y} \to V_1, \quad \psi_{1,x} \to 0. \tag{38}$$

If we plug in the expression for Equation 35 into Equations 37 and 38 and evaluate them at $y = 0$ we will obtain the following expressions for $\psi_{1,y}$ and $\psi_{1,x}$:

$$\psi_{1,y}(y=0) = sin^2(x) = \frac{1}{2} - \frac{1}{2}cos(2x),$$
$$\psi_{1,x}(y=0) = 0.$$

We then follow the same procedure outlined above for the zero order solution to find the first order solution ψ_1,

$$\psi_{\ 1} = (A_1 + B_1)e^{2y}cos(2x) + V_1 y. \tag{39}$$

If we take the derivative of Equation 39 with respect to x, evaluated at $y = 0$, which is subject to the x boundary condition in 37, we will find that $A_1 = 0$. We can then use the y boundary condition at $y = 0$ to find B_1 and V_1 simultaneously.

$$\psi_{1,y}(y=0) = V_1 + B_1 cos(2x) = \frac{1}{2} - \frac{1}{2}cos(2x). \tag{40}$$

It is obvious from Equation 40 that $B_1 = -\frac{1}{2}$ and $V_1 = \frac{1}{2}$. Finally, our swimmer swims! If we think back to the asymptotic expansion for V shown in Equation 22, we can show that the fluid velocity, $V$is (to first order)

$$V = V_0 + \varepsilon V_1 + \cdots = 0 + bk\frac{1}{2}. \tag{41}$$

If we go back to the dimensional form of V, V^*, we have the final form of the fluid velocity shown below.

$$V^* = bwV = bk\frac{1}{2}bV_w k = \frac{(bk)^2 V_w}{2}. \tag{42}$$

where V_w is the velocity of the wave (in this case, the swimmer).

Taylor (1951) continues to take the problem to fourth order, but the first order approximation is good enough in most cases. At higher orders, the constants decay nicely as one would expect. However, it should be noted that if the amplitude of the swimmer (b) is finite, the velocity given here will be an overestimate.

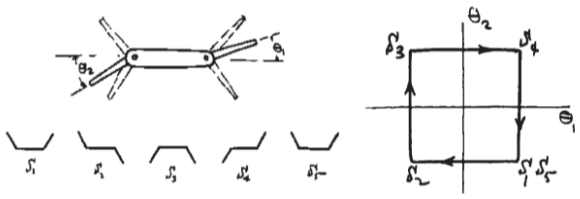

Figure 3: Diagram of a three-link swimmer.

3 Optimizing a Fluid Swimmer

We now know from the Scallop theorem that no reciprical motion of a body in a Stokes flow will result in a net translation. As such, in order to swim at low Reynolds numbers, an anisitropy must be introduced in the swimmer's movement in order to propagate in a desired direction. Purcel (1977) proposed a three-link swimmer design which can introduce isotropy by way of the order of oscillations of its tails. See figure 3 for the basic propagating motion of this three-link swimmer. Notice how anisotropy is introduced by a directional closed contour in phase-space. A reciprocal motion would result in a reverse path along the same trajectory. The obvious question to ask then is this: for the fixed geometry of the three-link swimmer, which closed-contour in the phase-space of paddle motion will result in its optimal propagation (speed/efficiency)?

Slender-body theory is used to model the forces acting on the swimmer, which incorporates the effects of the interactions between links. As slender-body theory will be discussed in the next lecture, we do not present the equations here. We note that the derivations of the corresponding equations can be found in [1]. These equations are then used in a looped iteration scheme, under the constraint that the links are attached to the body, in order to optimize either the swimming speed or the efficiency (useful work/ energy dissipated) of the corresponding motion.

The optimal curves are then presented in figure 4, where red is the efficiency optimal and blue is the speed optimal trajectory.

3.1 Biological Swimmers

The analysis presented above demonstrates that for a given constraint, there does exist a closed contour in phase space which optimizes the motion of a three-link swimmer. This is now extended to investigate the optimal motion of a biological swimmer. Here, we investigate the optimal swimmer for a sperm cell. A diagram of a model cell is found in figure 5, which is again discussed in [1].

It turns out that nearly all eukaryotic cells share a similar structure for their flagella and cilia. They have a 9+2 structure for their internal microtubule structure with a diameter of approximately 250-400 nm. Thus, the radius of the tail is nearly constant and, as such, the only optimization parameters for this model are the length of the sperm tail. Thus, for a given tail length, the phase-space contour was computed to optimize the swimmer efficiency (ϵ). Plotting this efficiency for many tail lengths results in the curve presented in figure 6. Here, the computed optimal efficiences for a

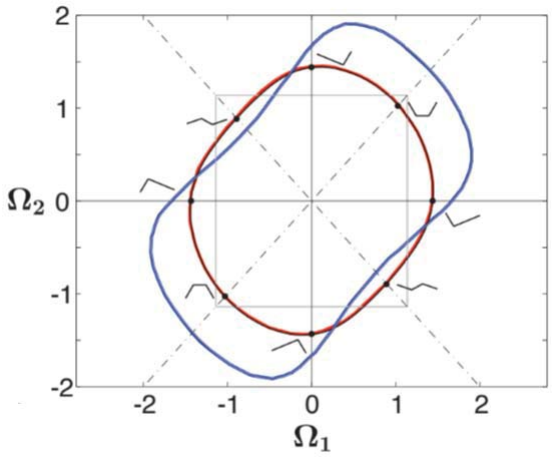

Figure 4: Optimal curves in phase-space for the three-link swimmer, where red is optimized for efficiency and blue is optimized for speed.

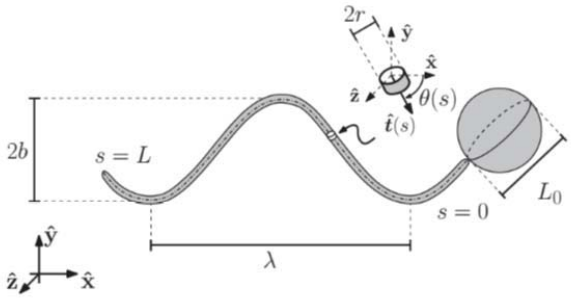

Figure 5: Model diagram of a biological swimmer.

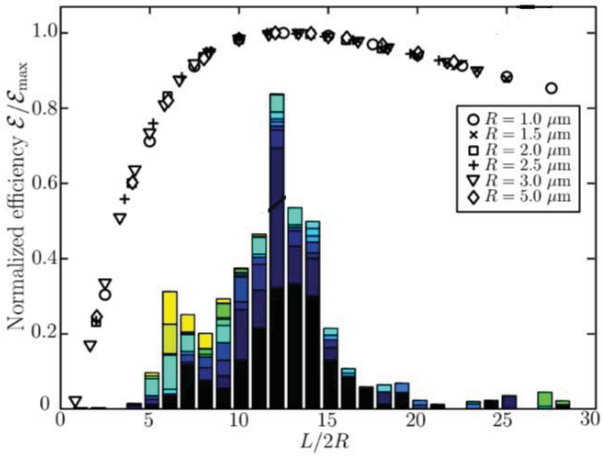

Figure 6: Optimal efficiencies found for a given tail length (dots). A histogram of the tail lengths for a set of real sperm cells is provided (coloured histogram).

given tail length are plotted as dots. A histogram of the tail lengths for a set of real sperm cells is also provided. We see that nature appears to have optimised the sperm tails many animals whose flagella are modelled as above.

References

[1] R. G. Cox. The motion of long slender bodies in a viscous fluid part 1. general theory. *Journal of Fluid Mechanics*, 44:791–810, 12 1970.

[2] E. M. Purcell. Life at low reynolds number. *American Journal of Physics*, 45(1):3–11, 1977.

[3] G.I. Taylor. Analysis of the swimming of microscopic organisms. *Proceedings of the Royal Society of London. Series A. Mathematical and Physical Sciences*, 209(1099):447–461, 1951.

Lecture 7: Low Reynolds Number Phenomena

Michael Shelley (notes by Sahil Agarwal & Océane Richet)

June 28, 2016

1 Stokes Flows

Recall the Stokes equations:

$$-\nabla P + \mu \Delta \vec{u} = 0, \qquad \nabla \cdot \vec{u} = 0. \tag{1}$$

These are time-independent flows and form a Boundary Value Problem.

1.1 Classical Results

- *Stokes solution for a rigid sphere of radius a*

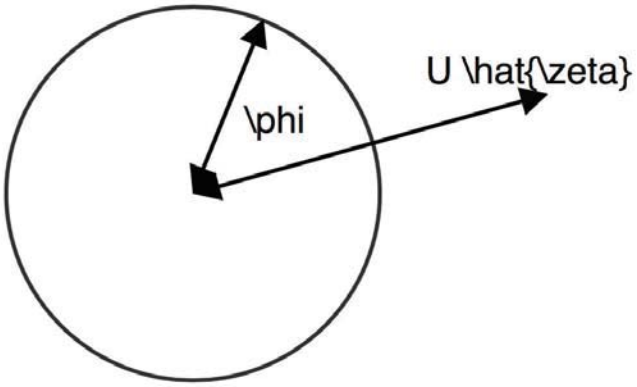

Figure 1: A schematic of a rigid sphere of radius a, angle with flow ϕ and flow velocity $U\hat{\zeta}$, and $P = P_\infty$

$$\overline{S} = \left[-P_\infty cos\phi + \mu \frac{3U}{2a} \right] \tag{2}$$

and,

$$\overline{F} = \int_{Sphere} ds\overline{S} = 6\pi\mu a U \tag{3}$$

- *Jeffery's equation for ellipsoidal particles*

  Let $\overline{U}(\overline{x}) = \overline{U} + \overline{\overline{A}}\overline{x}$, with $tr(A) = 0$. Separating the symmetric and the asymmetric parts, we can write:

$$\begin{aligned} A &= \frac{1}{2}(A + A^T) + \frac{1}{2}(A - A^T) \\ &= \overline{\overline{E}} + \overline{\overline{W}} \end{aligned} \tag{4}$$

  $\overline{\overline{E}}$ is the strain tensor and $\overline{\overline{W}}$ is the rotation tensor.

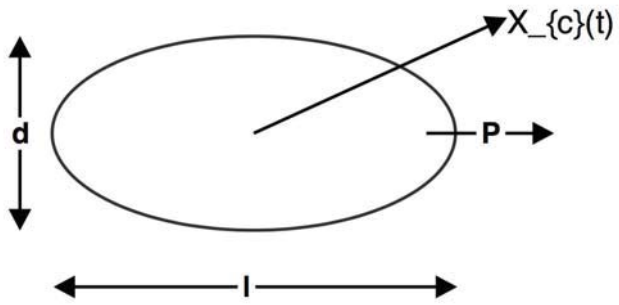

Figure 2: A schematic of an ellipsoid, with orientation vector $\hat{P}$, and center of mass $X_c(t)$ in a shear flow.

We can then write the velocity of the ellipsoid as:

$$\dot{\overline{X_c}} = \overline{U} + \overline{\overline{A}X_c} \tag{5}$$

and

$$\dot{\hat{P}} = |\overline{\overline{I}} - \hat{P}\hat{P}^T| \left[\overline{\overline{W}} + \frac{\lambda^2 - 1}{\lambda^2 + 1}\overline{\overline{E}}\right] \hat{P} \tag{6}$$

Here, $\overline{\overline{I}}$ is the identity matrix, and $\lambda = l/d$.

- For a thin rod ($\lambda = \infty$)

$$\dot{\hat{P}} = |\overline{\overline{I}} - \hat{P}\hat{P}^T|\overline{\overline{A}}\hat{P} \tag{7}$$

$$= |\overline{\overline{I}} - \hat{P}\hat{P}^T|\nabla U\hat{P} \tag{8}$$

  which is similar to vortex stretching ($\frac{D\omega}{Dt} = \nabla U\omega$).

– For a sphere ($\lambda = 1$)

$$\dot{\hat{P}} = |\overline{\overline{I}} - \hat{P}\hat{P}^T|\overline{\overline{W}}\hat{P} \tag{9}$$

1.2 Fundamental Solution to Stokes Equations

- *'Formal' Derivation* Find a solution $(\overline{\overline{\sigma}}, v, q)$ to the Stokes equations:

$$-\nabla q + \mu\Delta\vec{v} = \hat{e}\delta(x), \qquad \nabla\cdot\vec{v} = 0, \qquad |\hat{e}| = 1. \tag{10}$$

$$q = P_k\hat{e}_k, \qquad \overline{P} = \frac{-1\hat{x}}{4\pi|x|^2} \tag{11}$$

$$\overline{v} = \overline{\overline{S}}\hat{e}, \qquad \overline{\overline{S}} = \frac{1}{8\pi\mu}\frac{I + \hat{x}\hat{x}^T}{|x|} \tag{12}$$

Here, $\overline{\overline{S}}$ is also called the *Stokeslet/Oseen* tensor.

$$\tilde{\sigma} = -pI + 2\mu\overline{\overline{E}}_v, \qquad \sigma_{ij} = T_{ijk}e_k, \qquad T_{ijk} = \frac{3}{4\pi}\frac{\hat{x}_i\hat{x}_j\hat{x}_k}{|x|^2} \tag{13}$$

From $\overline{\overline{S}}$ and $\overline{\overline{T}}$, one can construct a boundary integral representation of solution to the Stokes equations.

2 Goal: write an integral equation to relate the surface stress to the surface velocity

$(\underline{\underline{\sigma}}, \underline{u}, p)$ is a solution to the Stokes equations and $(\underline{\underline{\sigma}}\tilde{}, \underline{v}, q)$ is the Green's theorem solution and it is singular in y (solution shifted $x \to x - y$).
If it exists 2 solutions to the Stokes equations with the same viscosity, so they satisfied the Lorentz identity

$$\nabla.(\underline{\underline{\sigma}}\ \underline{v} - \underline{\underline{\tilde{\sigma}}}\ \underline{u}) = \underline{0} \tag{14}$$

Now, we integrate this equation on the fluid domain Γ. We use the divergence theorem to integrate the divergence of a vector.

$$\int_V (14)\ \mathrm{d}V = \int_S (\underline{\underline{\sigma}}\ \underline{v} - \underline{\underline{\tilde{\sigma}}}\ \underline{u})\ \mathrm{d}s_X = \int_{\Gamma/B_\epsilon(y)} (\underline{\underline{\sigma}}\ \underline{v})\ \mathrm{d}s_X - \int_{\Gamma/B_\epsilon(y)} (\underline{\underline{\tilde{\sigma}}}\ \underline{u})\ \mathrm{d}s_X = \underline{0} \tag{15}$$

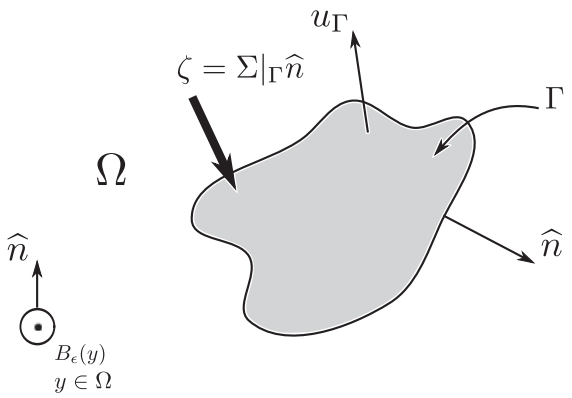

Figure 3: Schematic drawing of the experimental set up. ζ is the surface stress, u_Γ the surface velocity, Γ the surface, Ω the fluid domain and y a point inside the fluid.

(1) $\epsilon \longrightarrow 0$
Equation (15) becomes

$$\underline{u}(\underline{y}) = -\int_\Gamma \left[\underline{\underline{S}}(X'-y)\underline{\zeta}(X') + \underline{u}_\Gamma(X')\underline{\underline{T}}(X'-y)\widehat{n}(X')\right] \mathrm{d}s_X \tag{16}$$

This equation gives an expression of the velocity of the fluid in terms of surface quantities where ζ is the surface stress and u_Γ is the surface velocity.

(2) $y \longrightarrow X \in \Gamma$
Now, we are on the surface so $\underline{u} = \underline{u}_\Gamma$. Equation (16) becomes

$$\frac{1}{2}\underline{u}_{\Gamma,j} +_\Gamma \underline{u}_{\Gamma,i}(X')\underline{\underline{T}}_{jk}(X'-X)\widehat{n}_k(X')\mathrm{d}s_{X'} = -\int_\Gamma \underline{\underline{S}}_{jk}(X'-X)\underline{\zeta}_k(X')\mathrm{d}s_{X'} \tag{17}$$

where Γ is a principal value integral.
If the surface stress is known we can obtain an expression for the surface velocity.

3 Applications

Singularity representation simplifies for slender filament - Dynamics for filament centerline

$$8\pi\mu(\partial_t \underline{X}(s,t) - U(X,t)) = \overline{K}[f;X] = c(I + \widehat{s}\widehat{s}(s))f(s) + G[f;X](s) \tag{18}$$

where $\underline{U}$ is the background flow, $c(I + \widehat{s}\widehat{s}(s))f(s)$ is the "local drag" model, $\overline{G}$ is the nonlocal self interactions and $c = ln(\epsilon^2 e) < 0$ with $\epsilon = L/r \ll 1$ is an asymptotic parameter. The integral of the surface stress around the body gives the velocity of the centerline.
If $\eta = \frac{8\pi\nu}{|c|}$ the normalized viscosity and $X_s = \widehat{s}$ then

$$\eta(X_t(s,t) - U(X(s,t),t)) = (I + X_s X_s^T)\underline{f}(s) \tag{19}$$

where f is the force of the fiber on the fluid. This is the drag anisotropy seen with Peko previously.

The correction

$$\overline{G} = -\int_0^L \frac{I + \widehat{R}(s,s')\widehat{R}^T(s,s')}{|R(s,s')|} f(s') - \frac{I + \widehat{s}(s)\widehat{s}^T(s)}{|s-s')|} f(s) \;\; \mathrm{d}s' \tag{20}$$

The first part corresponds to the distribution of Stokeslet over the centerline. This part diverges so we need the second part. $\overline{G}$ is the finite part integral.

3.1 One flexible fiber

Now, look at the nonlocal hydrodynamics of a single flexible filament in a linear shear flow. There is a bending force with E and a tensile force with T.

[*Becker & Shelley, PRL, 2001*]

$$\underline{f} = -E\underline{x}_{ssss} + (T\underline{x}_s)_s \tag{21}$$

In the case of a linear flow, the equation (19) becomes

$$\eta(X_t(s,t) - \dot{\gamma}AX) = (I + X_s X_s^T)(E\underline{x}_{ssss} - (T\underline{x}_s)_s) \tag{22}$$

The boundary conditions are zero force and zero torque.

In nondimension

$$x \;\rightarrow\; Lx \tag{23}$$

$$t \;\rightarrow\; \dot{\gamma}^{-1}t \tag{24}$$

$$\eta(X_t(s,t) - \dot{\gamma}AX) \rightarrow\; \eta L\dot{\gamma} \tag{25}$$

$$E\underline{x}_{ssss} \rightarrow\; \frac{E}{L^3} \tag{26}$$

We obtain for the nondimension η

$$\tilde{\eta} = \frac{\eta\dot{\gamma}L^4}{|c|E} \tag{27}$$

If the rigidity E is sufficiently high $\tilde{\eta}$ is small and it is stable. There is a bifurcation when E is not sufficient and the fiber becomes unstable to a buckling instability (compressible tension on the fiber due to the surface shear stress).

3.2 Dynamics for interacting fibers

[*Tornberg & Shelley, JCP, 2004*]

$$8\pi\mu \quad \frac{\partial \underline{X}_i}{\partial t} - \underline{U}(\underline{X}_i, t)\Big) = \overline{K}[\underline{f}_i; \underline{X}_i] + \sum_{k \neq i} \underline{K}[\underline{f}_k; \underline{X}_i - \underline{X}_k] \tag{28}$$

where $\sum_{k \neq i} \underline{K}[\underline{f}_k; \underline{X}_i - \underline{X}_k]$ is the induced velocity by the other fibers (stokeslets+doublets).

4 Biological swimming at low Reynolds number

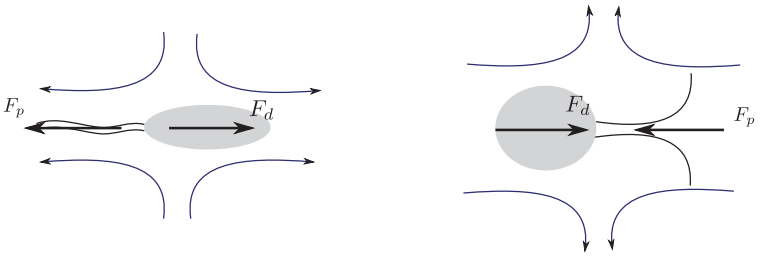

Pusher particle Puller particle

Figure 4: Schematic of a pusher and a puller particles and the induced flow.

Lecture 8a: Collective Behavior at Low Reynolds Number

Michael Shelley (notes by Keaton Burns & Colin Meyer)

June 29, 2016

1 Flexible fiber in a linear flow

Consider a flow that is locally linear near a flexible fiber, and given by:

$$\underline{u}(\underline{x}) = \underline{U} + \underline{\underline{A}} \cdot \underline{x} \tag{1}$$

where $\underline{\underline{A}}$ is traceless. The fiber's motion is given by

$$\eta(\underline{X}_t - \underline{U} - \underline{\underline{A}} \cdot \underline{X}) = (\underline{\underline{I}} + \underline{X}_s \underline{X}_s) \cdot \underbrace{((T\underline{X}_s)_s - E\underline{X}_{ssss})}_{\underline{f}} \tag{2}$$

where $\eta = -8\pi\mu/C$. Additionally, the evolution of the fiber must satisfy the no-extension constraint

$$\underline{X}_s \cdot \underline{X}_{st} = 0 \tag{3}$$

which determines the tension T in the fiber. If $T < 0$, i.e. the fiber is under compressive stress, the tension term looks like an antidiffusion that amplifies all lengthscales, but is regularized at small scales by the higher-order bending term.

Free-end boundary conditions on the fiber entail the constraints

$$T = \underline{X}_{ss} = \underline{X}_{sss} = 0 \qquad \text{at ends} \tag{4}$$

With these boundary conditions and the given forcing, the fiber is force and torque free, as required for a free particle in a Stokes flow.

Let's examine the special case of a straight fiber, whose position is described by

$$\underline{X}(s,t) = \underline{X}_0(t) + s\underline{p} \tag{5}$$

$$\underline{X}_s = \underline{p} \tag{6}$$

$$\underline{X}_t = \dot{\underline{X}}_0 + s\dot{\underline{p}} \tag{7}$$

where $-L/2 \leq s \leq L/2$ and $\underline{p}$ is a unit vector. Inserting this prescription into the equation of motion yields

$$\eta(\dot{\underline{X}}_0 + s\dot{\underline{p}} - \underline{U} - \underline{\underline{A}} \cdot \underline{X}_0 - s\underline{\underline{A}} \cdot \underline{p}) = (\underline{\underline{I}} + \underline{pp}) \cdot (T_s \underline{p}) \tag{8}$$

$$= 2T_s \underline{p} \tag{9}$$

Integrating the equation of motion over the length of the fiber yields

$$L\eta(\dot{\underline{X}}_0 - \underline{U} - \underline{\underline{A}} \cdot \underline{X}_0) = \int_{-L/2}^{L/2} 2T_s \underline{p} \, \mathrm{d}s \tag{10}$$

$$= 2\underline{p}[T]_{\text{ends}} \tag{11}$$

$$= 0 \tag{12}$$

We see that indeed the fiber is force free, and the center-point is advected with the background flow:

$$\dot{\underline{X}}_0 = \underline{U} + \underline{\underline{A}} \cdot \underline{X}_0 \tag{13}$$

We can also verify the torque balance on the fiber:

$$\int_{-L/2}^{L/2} (\underline{X} - \underline{X}_0) \times \underline{f} \, \mathrm{d}s = \int_{-L/2}^{L/2} (s\underline{p}) \times (2T_s \underline{p}) \, \mathrm{d}s \tag{14}$$

$$= \int_{-L/2}^{L/2} 2sT_s \underline{p} \times \underline{p} \, \mathrm{d}s \tag{15}$$

$$= 0 \tag{16}$$

Subtracting the center-point evolution from the equation of motion gives

$$\eta s(\dot{\underline{p}} - \underline{\underline{A}} \cdot \underline{p}) = 2T_s \underline{p} \tag{17}$$

We can solve for the tension by projecting this equation against $\underline{p}$ and utilizing the inextensibility constraint:

$$\eta s(\underbrace{\underline{p}\cdot\dot{\underline{p}}}_{0}-\underline{p}\cdot\underline{\underline{A}}\cdot\underline{p})=2T_s\underline{p}\cdot\underline{p} \tag{18}$$

$$-\eta s\underline{p}\cdot\underline{\underline{A}}\cdot\underline{p}=2T_s \tag{19}$$

$$T=\frac{\eta}{4}(\underline{p}\cdot\underline{\underline{A}}\cdot\underline{p})(L^2/4-s^2) \tag{20}$$

We note that the tension has the same sign as $\underline{p}\cdot\underline{\underline{A}}\cdot\underline{p}$. We can now write the force on the fiber as

$$\underline{f}=-\frac{s\eta}{2}(\underline{p}\cdot\underline{\underline{A}}\cdot\underline{p})\underline{p} \tag{21}$$

Putting the known tension into the equation of motion gives us the evolution of $\underline{p}$:

$$\eta s(\dot{\underline{p}}-\underline{\underline{A}}\cdot\underline{p})=-s\eta(\underline{p}\cdot\underline{\underline{A}}\cdot\underline{p})\underline{p} \tag{22}$$

$$\dot{\underline{p}}=\underline{\underline{A}}\cdot\underline{p}-\underline{p}(\underline{p}\cdot\underline{\underline{A}}\cdot\underline{p}) \tag{23}$$

$$=(\underline{\underline{I}}-\underline{pp})\cdot(\underline{\underline{A}}\cdot\underline{p}) \tag{24}$$

The orientation vector thus obeys Jeffery's equation, and we see that the fiber experiences the same forces and dynamics as would a rigid rod in the flow. This solution therefore forms a valid base-state for examining the stability of flexible rods in linear flows.

For example, let's consider a pure shear flow:

$$\underline{u}=\underline{U}+\dot{\gamma}\,(y,0,0) \tag{25}$$

$$\underline{\underline{A}}=\begin{bmatrix}0&\dot{\gamma}&0\\0&0&0\\0&0&0\end{bmatrix} \tag{26}$$

Taking $\underline{p}=(\cos(\theta),\sin(\theta),0)$, we see

$$\underline{p}\cdot\underline{\underline{A}}\cdot\underline{p}=\dot{\gamma}\cos(\theta)\sin(\theta) \tag{27}$$

$$=\frac{1}{2}\dot{\gamma}\sin(2\theta) \tag{28}$$

We see that when the fiber is tilted into the shear ($\pi \leq 2\theta \leq 2\pi$), $\underline{p} \cdot \underline{\underline{A}} \cdot \underline{p}$ and the tension will be negative, and so the fiber may be prone to buckling instabilities. Conversely, when the fiber is tilted away from the shear, the flow exerts an extensile force and the tension is positive, and no buckling instabilities take place.

1.2 Subcellular microtubule and motor-protein assemblies

Figure 1a is an image of a fertilized *C. elegans* egg. The red material is dyed DNA, contained in male and female pronuclei. Green fluorescent proteins mark out the centrosomal array of microtubules, which are stiff biopolymers nucleating from the centrosome. The growth of the microtubules enables the translation and rotation of the pronuclear complex into "proper position" at the center of the cell, oriented parallel to the long-axis of the cell. A mitotic spindle (Figure 1b) is then self-assembled from microtubules and motor proteins, and segregates proteins leading to the first cell division.

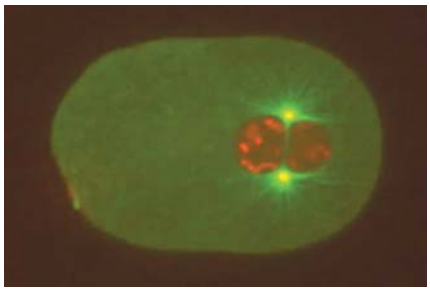

(a) Pronuclei (red) and centrosomal microtubule array (green) in fertilized *C. elegens* egg. Source: Sugimoto Lab, Tohoku

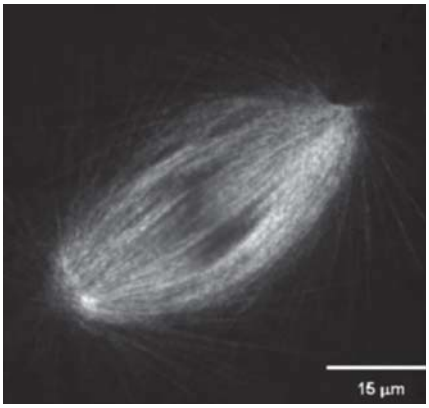

(b) Mitotic spindle performing chromosome segregation. Source: Needleman Lab, Harvard

This is all possible due to the growth and interaction of the roughly 10,000 microtubules with motor proteins and other cell components. The microtubules are flexible rods that behave essentially like Euler-Bernoulli elastica. They can be roughly 1-20 microns in length, but have a diameter of just 24 nanometers. Nonlocal slender body theory is thus a useful tool to study their dynamics.

An individual microtubule has an average lifetime of roughly 30 seconds, when they tend to catastrophically disassemble. Nonetheless, the structures they form, like the mitotic spindle, are robust and can last for hours. Good models need to incorporate both the biochemistry of microtubule nucleation, as well as the fluid mechanics affecting their dynamics.

Microtubules polymerize in a helical pattern, and hence have a handedness. Different types of motor proteins can preferentially walk towards either the "plus" or "minus" ends of the microtubules. Kinesin motor proteins are plus-end directed and can polarity-sort microtubules. Dynein motor proteins are minus-end directed, and are thought to cluster and carry payloads to minus-ends.

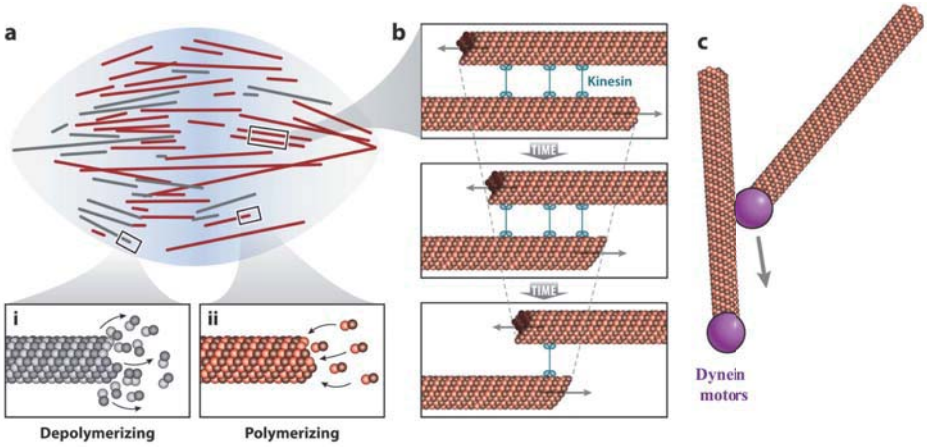

Figure 2: a) Microtubules continually polymerize and depolymerize on short timescales, but jointly form robust structures that last for much longer timescales. b) Kinesin motor proteins (plus-directed) sliding apart oppositely oriented microtubules. c) Dynein motor proteins clustering minus-ends.

Single microtubules can be modeled as Euler-Bernouli beams using local or nonlocal slender body theory. Boundary integral methods can be used to determine the local flow around a single microtubule due to the other microtubules and cell surfaces, typically including a rigid sphere as a pronuclear complex, and an ellipsoidal cell boundary. A fast parallel solver for the problem can be constructed that gives $\mathcal{O}(N)$ computational cost per timestep, using implicit integration and spectral spatial discretizations for the microtubules. Such a model can be used to test different mechanisms for achieving proper position, and examine the corresponding cytoplasmic flows and microtubule conformation.

One model is motility due to payload-carrying Dynein motor proteins. In this model, as the Dynein move towards the centrosome, they produce a pulling force on the fluid along the microtubules. Centering and proper position are achieved since longer microtubules gather more motor proteins and pull more strongly on their side of the pronuclear complex. The microtubules in this case remain nearly straight since they are always under extensile stress due to the pulling motor proteins.

A second model entails motility due to pushing on the cell boundary by the growing microtubules. In this case, the microtubules are under compressive stress and

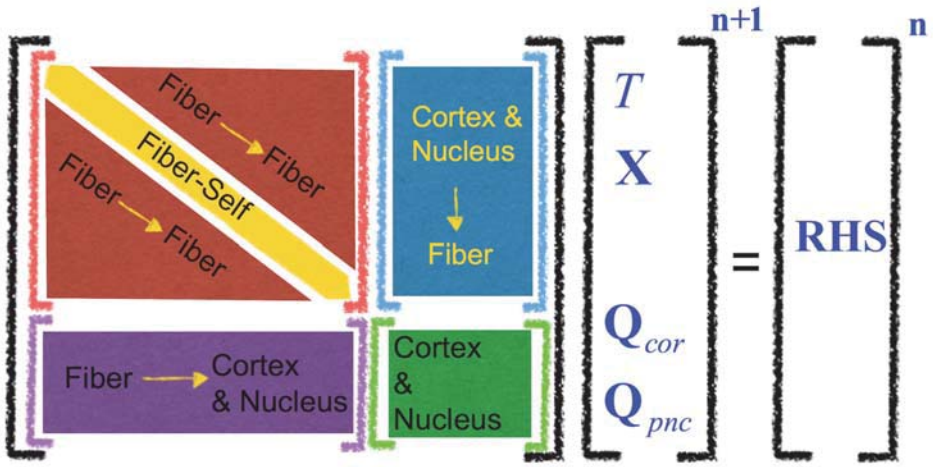

Figure 3: Matrix system for fiber and cell structure interactions. Source: Nazockdast et al. 2016

subject to buckling instabilities. Figure 4 shows the cytoplasmic flows computed for these two models. Both of these mechanisms, as well as others such as cell-surface-mounted Dyneins pulling on the microtubules, are likely at play in the physical system.

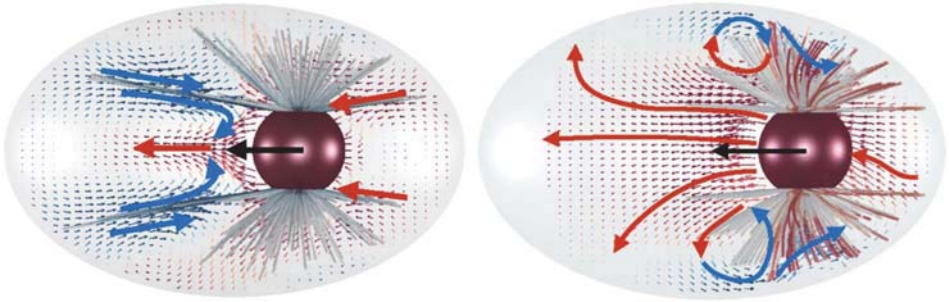

Figure 4: Left: Dipole-like flow for model of pronuclear migration due to pulling by Dynein motor proteins. Right: Stokeslet-like flow for model of pronuclear migration due to pushing by growing microtubules. Source: Nazockdast et al. 2016

References

Nazockdast, E., A. Rahimian, D. Zorin, M. Shelley, *A fast platform for stimulating semi-flexible fiber suspensions applied to cell mechanics,* Journal of Computational Physics, 329 (2016), pp. 173-209.

Lecture 8b: Collective Behavior at Low Reynolds Number (continued)

Michael Shelley (notes by Keaton Burns & Colin Meyer)

June 29, 2016

3 Soft active systems

Active suspensions are suspensions of self-propelled particles (e.g. bacteria, microalgae, artificial microswimmers) within a fluid. Figure 1 shows some examples of active suspensions. It is common for active suspensions to exhibit the following properties:

1. correlated motion over length scales that greatly exceed the particle dimensions
2. diffusive behavior
3. apparent large-scale density fluctuations suggesting self-organization within the suspensions.

Using the rule of the thumb that an organism travels at the speed of 1 body length per second, a single bacterium roughly moves at a speed of 10μm/s in isolation. However, when a collection of *Bacillus subtilis* bacteria are placed in a suspension at high concentration, the speed of a single bacterium can significantly amplify up to about 50 μm/s as demonstrated by C. Dombrowski *et al* [3] (see Figure 2).

3.1 Single particle dynamics

Before we discuss the dynamics of collectives. Let's first review work done on modeling single particles. The simulation of single particle dynamics (to a fair level of complexity) has been well-developed.

For example, Keaveny *et al* [5] studied the optimal 3-dimensional helical shape of a microswimmer driven by an applied magnetic field (see Figure 3). The key component that made these simulations possible is a boundary integral formulation that evolves the system to an optimal velocity given an input power.

Another example of single particle dynamics is demonstrated by the study of swimming nematodes. Figure 4(a) shows a snapshot of a simulation of a swimming nematode through an array of obstacles in grey. The nematode is free to swim in the negative space between the obstacles. The nematode is modeled such that it naturally relaxes to its preferred state of curvature. The internal forces trying to enforce this relaxation are competing with the external forces imposed by the Stokes flow in the surroundings. Interestingly, the dynamics of the simulation look remarkably similar to a real swimming nematode. At particular instances in the simulation, the nematode has the appearance of contemplating over which way to go when encountering a 'fork' in the lattice. In fact, the model does not endow the

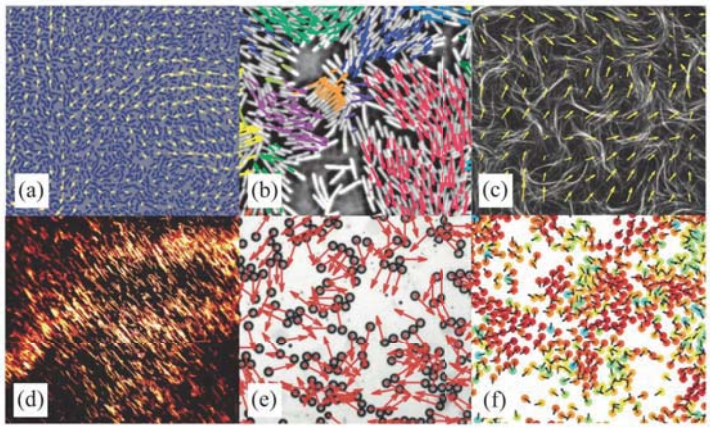

Figure 1: (Image from Ref. [11]) Examples of soft active systems. (a) Arrows show the velocity field over a suspension of swimming bacteria; (b) This is a collection of swimming bacteria sitting on top of a layer of agar; (c) a suspension of microtubules and kinesin motors; (d) active polymer sitting on a layer of myosin molecular motors; (e) a suspension of self-propelling liquid droplets in a Hele-Shaw cell (f) vibrated polar disks on a substrate

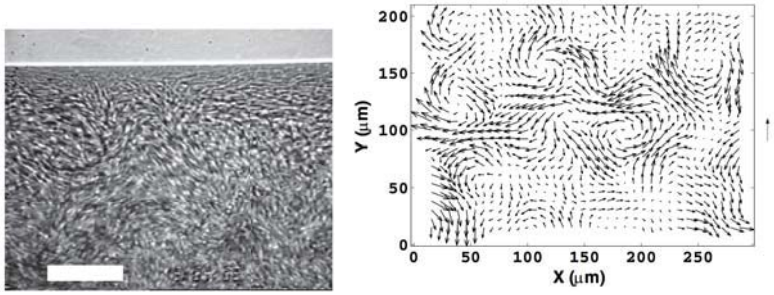

(a) Image of bacterial suspension. The scale bar is 35 μm.

(b) Instantaneous velocity field of bacterial suspension determined through PIV. For reference, the arrow on the right indicates a speed of 35μm/s

Figure 2: Bacterial suspension (Images from Ref. [3]).

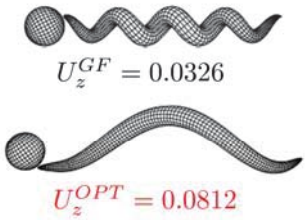

Figure 3: Shape-optimized rotating driven 'swimmers' (see Ref. [5]).

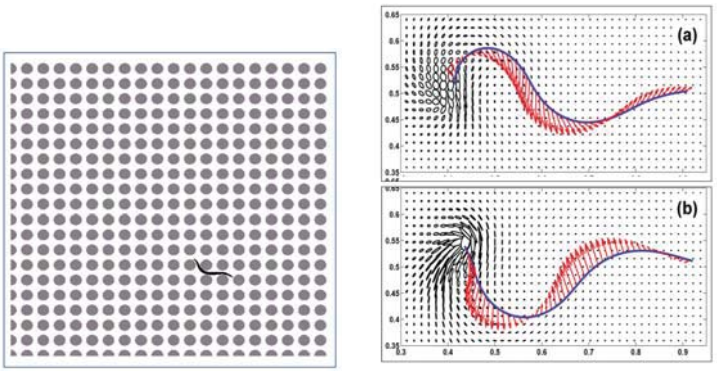

(a) Swimming in complex environments using the Force Coupling Method (see Ref. [6]).

(b) Swimming through a complex media (see Ref. [12]).

Figure 4: Modeling of swimming.

nematode with any cognition and the appearance of decision-making is purely the result of *deterministic* mechanical motion. The appearance of random choice is attributed to the chaotic nature of the high-dimensional system.

J. Teran *et al* [12] investigated a variation of this model by considering a swimming sheet through a non-Newtonian viscoelastic fluid (see Figure 4(b)). It can be shown that one can achieve greater speeds than those possible in a Newtonian fluid.

3.2 Collective dynamics

Let's return to collective motion of many swimmers. To be able to simulate many swimmers, you must simplify the model for an individual swimmer. For example, one can use slender body theory to model 'pullers' and 'pushers' as done by Saintillan *et al* [9]. A pusher has a shear stress imposed on the bottom half of a rod-like particle and a no-slip condition on the top half. This causes the flow shown in Figure 5(a). A puller particle has a shear stress imposed on the top portion while having a no-slip condition on bottom half. In this situation, the particle will be propelled in the same direction as the pusher particle but will exhibit the flow pattern shown in Figure 5(b).

We now consider a suspension of either pusher or pullers with an initial distribution of random orientations and positions. It is useful to allow a passive dye field to be advected with the resulting flow to visualize the dynamics more easily. At low density (for both pullers and pushers), the dye field is slowly diffused. At 10 times the density of pullers, the dye field diffuses again but more rapidly. However, if one looks at a system with a high density of pushers rather than pullers, then the system develops turbulent flows.

It is useful to look at the particle occupancy statistics of the number of particles falling inside a cubic interrogation cell placed at an arbitrary location inside the simulation box. For a purely random distribution of particles, Poisson statistics predicts:

$$P = \frac{\langle N \rangle^N e^{-\langle N \rangle}}{N!}$$

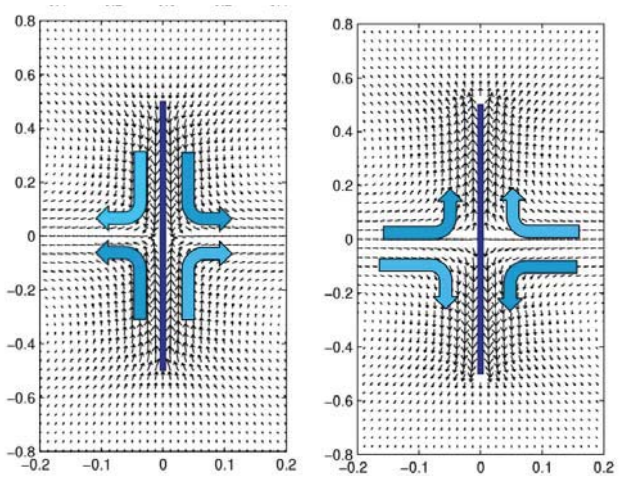

(a) Puller (b) Pusher

Figure 5: Slender body swimmers

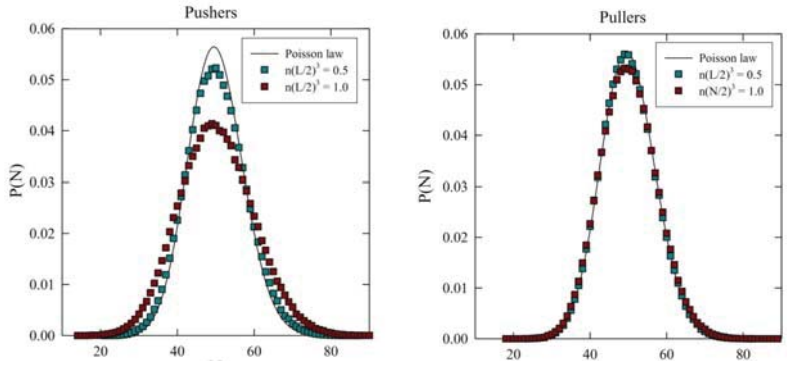

Figure 6: Statistics of the number of particles falling inside a cubic interrogation cell placed at an arbitrary location inside the simulation box.

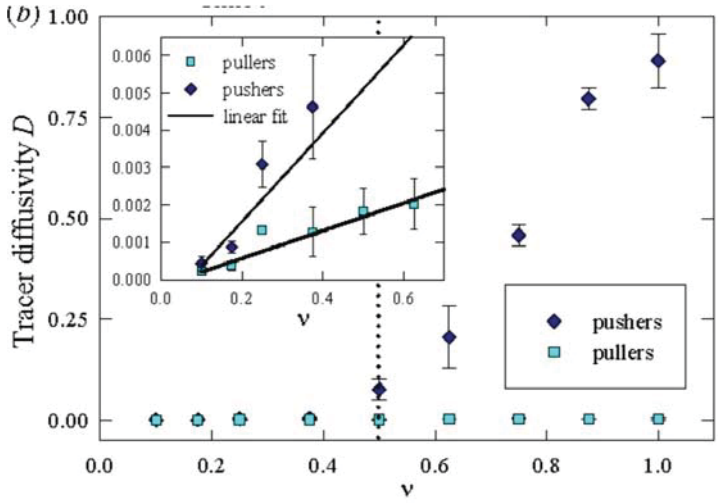

Figure 7: Effective diffusivity dependence on volume concentration.

The pusher's distribution in Figure 6 develops fat tails as you increase the volume concentration. Contrast this with the distribution for puller particles; the volume concentration does not seem to affect the distribution. If you increase the volume concentration of pullers, this causes an increase in the average suspension speed. While for pushers, an increase in volume concentration has the opposite effect and causes a decrease in average suspension speed. Another useful metric is the effective tracer diffusivity (see Figure 7). This diffusivity increases linearly with volume concentration for pullers. As for pushers, the diffusivity remains low for low values of volume concentration. However, the system passes a bifurcation point when the volume concentration passes 0.5 and the diffusivity drastically increases as the flow becomes turbulent. If you start with an oriented suspension, it will quickly lose directionality regardless of type, hence showing that this state is unstable.

In summary, there are three main observations.

1. There is a critical concentration above which isotropic pusher suspensions become unstable.

2. Isotropic puller suspensions do not become unstable.

3. Initially aligned suspensions – pusher or puller – are unstable.

3.3 Kinetic model

So what you need is a theoretical model which you can query and ask about stability and length scales. We are going to take a page from the now classic book Doi and Edwards's The theory of polymer dynamics [2]. Doi has modeled for the dynamics of molecules undergoing thermal fluctuations and interactions. You can go from microscopic dynamics to macroscopic dynamics. In the microscopic model is what we have already outlined before. Recall this was done by having a propulsive stress on half of the swimmer. We used slender body theory to determine the flow generated by such as swimmer. For a swimmer moving in a linear background flow, this yields

$$\begin{aligned}
\dot{\mathbf{X}}_c &= U_0\mathbf{p} + \mathbf{u}(\mathbf{X}_c) \\
\dot{\mathbf{p}} &= (\mathbf{I} - \mathbf{pp})\nabla\mathbf{u}(\mathbf{X}_c)\mathbf{p} \quad \text{(Jeffrey's equation)} \\
\mathbf{f} &= a(s)\mathbf{p}
\end{aligned}$$

where U_0 is the propulsion speed.

Then, you coarse-grain. You pick one among many swimmers. You assume that the particle is small relative to the flow scale. Keep in mind that the only interaction that occurs among swimmers is that which is mediated through the flow created by the ensemble. The task is to solve the single particle problem using slender body theory. Once this is known, you evolve the distribution function $\Psi(\mathbf{x}, \mathbf{p}, t)$. An important and necessary piece is determining the stress induced by the active suspention. One can derive a volume-averaged 'extra'-stress tensor given the function 1. This is calculated by [1]

$$\Sigma^e = -\frac{1}{V}\sum_{m=1}^{M}\int ds \mathbf{X}_m(s)\mathbf{f}_m(s)^T$$

The *active* part of the volume-averaged stress on a single rod to leading order becomes

$$\Sigma^a = \frac{\sigma_0}{V}\sum_{m=1}^{M}\mathbf{p}_m\mathbf{p}_m^T$$

where σ_0 is the stresslet coefficient. σ_0 is negative for pushers and positive for pullers. We then construct the distributional average version of this result by converting the summation to an integral to arrive at

$$\Sigma^a(\mathbf{x}, t) = \pm\sigma_0\mathbf{D}(\mathbf{x}, t)$$

where

$$\mathbf{D}(\mathbf{x}, t) = \int dS_p \Psi(\mathbf{x}, \mathbf{p}, t)\mathbf{pp}^T. \tag{1}$$

We then couple this into a Fokker-Planck equation,

$$\Psi_t + \nabla_x \cdot (\dot{\mathbf{x}}\Psi) + \nabla_p \cdot (\dot{\mathbf{p}}\Psi) = 0, \tag{2}$$

which dictates how the distribution evolves over time. From the microscopic picture seen earlier, the time evolution of the variables $\mathbf{x}$ and $\mathbf{p}$ are determined by the equations,

$$\begin{aligned}
\dot{\mathbf{x}} &= \mathbf{p} + \mathbf{u}(\mathbf{x}, t) - \nabla_x(D\ln\Psi) &(3)\\
\dot{\mathbf{p}} &= (\mathbf{I} - \mathbf{pp}^T)\nabla\mathbf{u}\,\mathbf{p} - \nabla_p(d\ln\Psi), &(4)
\end{aligned}$$

where we have added diffusion in translation and in orientation. The flow is determined by Stokes equations driven by active stress,

$$\begin{aligned}
\nabla q - \Delta\mathbf{u} &= \nabla\cdot\boldsymbol{\Sigma}^{active} &(5)\\
\nabla\cdot\mathbf{u} &= 0 &(6)
\end{aligned}$$

where

$$\Sigma^{active}(\mathbf{x},t) = \alpha \mathbf{D}(\mathbf{x},t).$$

α is the dimensionless stokeslet coefficient given by $\alpha = \sigma_0/\mu U_0 l^2$ where μ is viscosity and l is the length of a single rod. α is negative for pushers and positive for pullers. To numerically solve this system of equations (1-6), you perform the following procedure. Given Ψ at a particular time step, you can calculate D by using equation 1 which allows you to determine $\mathbf{u}$ via equations 5 - 6. Once you have $\mathbf{u}$, you can evolve Ψ forward in time with equations 2-4. Given the new Ψ, we can now repeat these steps again and march forward in time. Numerical simulations using this formulation were performed by Saintillan *et al* [7, 8, 10], and Ezhilan *et al* [4].

To characterize the amount of 'structure' in Ψ, we consider the configurational entropy [8] given by

$$S = \int dV_x \int dS_p \left(\frac{\Psi}{\Psi_0}\right) \ln\left(\frac{\Psi}{\Psi_0}\right)$$

where $S = 0$ only for $\Psi = \Psi_0$ (uniform, isotropic equilibrium state). One can show that

$$\frac{dS}{dt} = -\frac{6}{\alpha \Psi_0} \int dV_x |\mathbf{E}|^2 - \frac{1}{\Psi_0} \int dV_x \int dS_p \Psi \left[D |\nabla_x \ln \Psi|^2 + d |\nabla_p \ln \Psi|^2 \right]$$

where $\mathbf{E}$ is the symmetric rate of strain tensor.

Now, we can consider different suspensions to see what this equation above tells us. If we consider a suspension of pullers ($\alpha > 0$), then fluctuations, as measured by S, will dissipate. If we consider a suspension of *pushers*, we see that the input power increases fluctuations until limited by diffusion processes. This is consistent with the previous observations from simulation. This theory also explains why the aligned suspension state is unstable (see Ref. [7]). Furthermore, it can also explain the bifurcation seen from the homogeneous isotropic state to large-scale turbulent flow pattern that occurs past a critical volume fraction density of pusher particles (see Ref. [7]).

References

[1] G. Batchelor, *The stress system in a suspension of force-free particles*, Journal of Fluid Mechanics, 41 (1970), pp. 545–570.

[2] M. Doi and S. F. Edwards, *The theory of polymer dynamics*, vol. 73, Oxford University Press, 1988.

[3] C. Dombrowski, L. Cisneros, S. Chatkaew, R. E. Goldstein, and J. O. Kessler, *Self-concentration and large-scale coherence in bacterial dynamics*, Physical Review Letters, 93 (2004), p. 098103.

[4] B. Ezhilan, M. J. Shelley, and D. Saintillan, *Instabilities and nonlinear dynamics of concentrated active suspensions*, PhysicsofFluids(1994-present),25 (2013), p. 070607

[5] E. E. Keaveny, S. W. Walker, and M. J. Shelley, *Optimization of chiral structures for microscale propulsion*, Nano letters, 13 (2013), pp. 531–537.

[6] T. Majmudar, E. E. Keaveny, J. Zhang, and M. J. Shelley, *Experiments and theory of undulatory locomotion in a simple structured medium*, Journal of The Royal Society Interface, 9 (2012), pp. 1809–1823.

[7] D. Saintillan and M. J. Shelley, *Instabilities and pattern formation in active particle suspensions: kinetic theory and continuum simulations*, Physical Review Letters, 100 (2008), p. 178103.

[8] ——, *Instabilities, pattern formation, and mixing in active suspensions*, Physics of Fluids, 20 (2008), p. 123304.

[9] ——, *Emergence of coherent structures and large-scale flows in motile suspensions*, Journal of the Royal Society Interface, (2011), p. rsif20110355.

[10] ——, *Active suspensions and their nonlinear models*, Comptes Rendus Physique, 14 (2013), pp. 497–517.

[11] ——, *Theory of active suspensions*, in Complex Fluids in Biological Systems, Springer, 2015, pp. 319–355.

[12] J. Teran, L. Fauci, and M. Shelley, *Viscoelastic fluid response can increase the speed and efficiency of a free swimmer*, Physical Review Letters, 104 (2010), p.038101.

Lecture 9a: Thin Films with Elastic Boundaries
Part 1: Snails

Anette Hosoi (notes by Paula Doubrawa and Michael Gomez)

June 20, 2016

1 Introduction

Snails' motion does not involve direct contact between the snail and the ground. Instead, the mollusk produces mucus (i.e. a viscous non-Newtonian fluid) in which it generates stresses (Fig. 1). The forces resulting from these stresses result in the crawling motion of the snail. Depending on the species, these stresses can be generated either by out-of-plane (direct) or in-plane (retrograde) waves. Both mechanisms are explained in detail in the following sections.

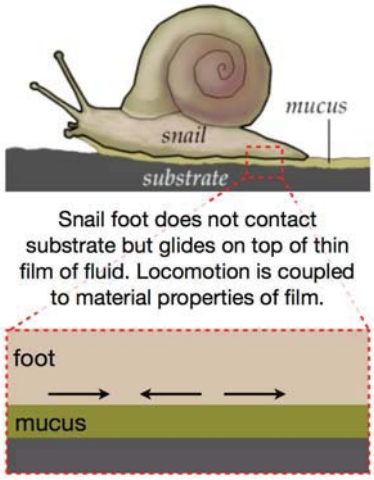

Figure 1: Schematic of snail, mucus and substrate.

2 Retrograde waves

In this section we find the wave profile that maximizes the snail crawling speed when using retrograde waves. Consider a frame of reference moving with the wave (Fig. 2B) so that

the wave shape is stationary. The variables involved in the two-dimensional problem are rescaled such that

$$y = \widehat{y}/H \qquad x = \widehat{x}/L \qquad t = \widehat{t}\frac{U}{L}$$
$$u = \widehat{u}/U = \frac{\widehat{u}}{\widehat{V}_w} \qquad v = \widehat{v}/V = \frac{\widehat{v}L}{\widehat{V}_w H}$$
$$p = \widehat{p}\left(\frac{H^2}{\mu U L}\right)$$

where y is the vertical direction, x the horizontal direction along the snail, and t time. Hats denote dimensional quantities. H is the wave amplitude, L the wavelength, and (u,v) the snail velocity in the horizontal and vertical directions. $U = \widehat{V}_w$ is the velocity of the wave in the horizontal direction. In order to write $\widehat{V}$ in terms of $\widehat{V}_w$, we use the continuity equation

$$\widehat{\nabla} \cdot \underline{\widehat{u}} = \frac{\partial \widehat{u}}{\partial \widehat{x}} + \frac{\partial \widehat{v}}{\partial \widehat{y}} = 0 \tag{1}$$

to deduce

$$\frac{\widehat{V}_w}{L} + \frac{V}{H} = 0 \;\; \therefore \;\; V \sim \frac{\widehat{V}_w H}{L}. \tag{2}$$

Conservation of momentum is given by Navier-Stokes

$$\rho\left[\frac{\partial \underline{\widehat{u}}}{\partial \widehat{t}} + \left(\underline{\widehat{u}} \cdot \widehat{\nabla}\right)\underline{\widehat{u}}\right] = -\widehat{\nabla}\widehat{p} + \mu\widehat{\nabla}^2\underline{\widehat{u}} \tag{3}$$

where the scaling for $\widehat{\nabla}\widehat{p}$ should be chosen so that it balances the viscous forces $\mu\widehat{\nabla}^2\underline{\widehat{u}}$ since the Reynolds number is small. Moreover, a separation of length scales is made possible since $H \sim \mathcal{O}(\mu\text{m})$ and $L \sim \mathcal{O}(\text{mm})$. Neglecting higher order terms in H/L, we end up with the (dimensionless) lubrication equations,

$$\begin{aligned} \frac{\partial p}{\partial y} &= 0 \\ \frac{\partial p}{\partial x} &= \frac{1}{\mu}\frac{\partial^2 u}{\partial y^2}. \end{aligned} \tag{4}$$

Integrating once with respect to y:

$$\begin{aligned} \int \frac{\partial^2 u}{\partial y^2} dy = \int \frac{\partial}{\partial y}\frac{\partial u}{\partial y} dy &= \int \frac{1}{\mu}\left(\frac{\partial p}{\partial x}\right) dy \\ \frac{\partial u}{\partial y} &= \frac{1}{\mu}\left(\frac{\partial p}{\partial x}\right) y + c_1, \end{aligned} \tag{5}$$

and then integrating a second time with respect to y,

$$\int \frac{\partial u}{\partial y} dy = \int \left[\frac{1}{\mu}\left(\frac{\partial p}{\partial x}\right) y + c_1\right] dy \tag{6a}$$

$$u(x,y) = \frac{1}{2\mu}\left(\frac{\partial p}{\partial x}\right) y^2 + c_1 y + c_2 \tag{6b}$$

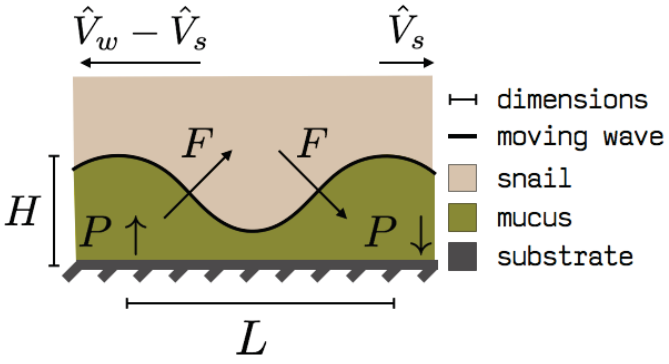

t

(a) Lab frame of reference.

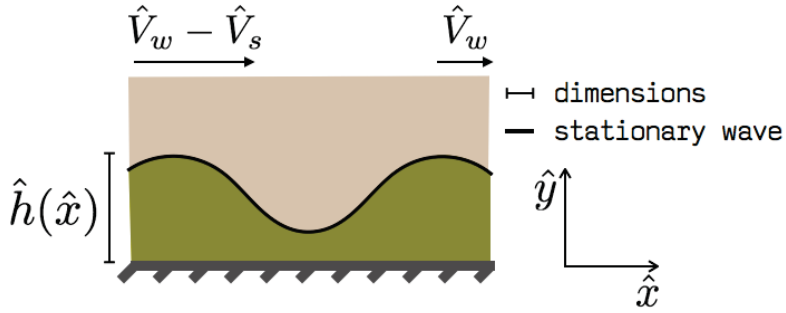

(b) Wave frame of reference.

Figure 2: Schematic of variables involved in the snail crawling problem.

In order to determine the integration constants c_1 and c_2, we apply the boundary conditions

$$u|_{y=0} = 1 - V_s = 1 - \frac{\widehat{V}_s}{\widehat{V}_w}$$
$$u|_{y=h} = 1.$$

When $y = 0$ in Eq. (6b),

$$u(y=0) = c_2 \;\; \therefore \;\; c_2 = 1 - V_s \tag{7}$$

and when $y = h$ in Eq. (6b),

$$\begin{aligned} 1 &= \frac{1}{2}\frac{\partial p}{\partial x}h^2 + c_1 h + 1 - V_s \\ c_1 h &= -\frac{1}{2}\frac{\partial p}{\partial x}h^2 + V_s \\ c_1 &= -\frac{h}{2}\frac{\partial p}{\partial x} + \frac{V_s}{h}. \end{aligned} \tag{8}$$

And finally, replacing c_1 and c_2 in Eq. (6b),

$$u(x,y) = \frac{1}{2}\left(\frac{\partial p}{\partial x}\right) y(y-h) + V_s\left(\frac{y}{h} - 1\right) + 1 \tag{9}$$

where h is a known function (prescribed by the snail). Since V_s and $\partial p/\partial x$ are unknown, another equation is needed. The depth-averaged conservation of mass can be expressed as

$$Q = \int_0^h u(x,y)dy \tag{10}$$

where Q is a constant volume flow rate. Therefore

$$\begin{aligned} Q &= \int_0^h \frac{1}{2}\frac{\partial p}{\partial x}y^2 dy - \int_0^h \frac{1}{2}\frac{\partial p}{\partial x}hy dy + \int_0^h V_s\frac{y}{h}dy - \int_0^h V_s dy + \int_0^h dy \\ &= \frac{1}{6}\frac{\partial p}{\partial x}h^3 - \frac{1}{4}\frac{\partial p}{\partial x}h^3 + \frac{V_s h}{2} - V_s h + h \\ &= \frac{1}{12}\frac{\partial p}{\partial x}\left(2h^3 - 3h^3\right) + h\left(\frac{V_s}{2} - 2\frac{V_s}{2} + 1\right) \\ &= -\frac{h^3}{12}\frac{\partial p}{\partial x} + h\left(1 - \frac{V_s}{2}\right) \end{aligned} \tag{11}$$

and an expression can be found for $\partial p/\partial x$, namely

$$\frac{\partial p}{\partial x} = \frac{12}{h^3}\left[h\left(1 - \frac{V_s}{2}\right) - Q\right]. \tag{12}$$

Given a periodic pressure where $p(0) = p(1)$,

$$\int_0^1 \frac{\partial p}{\partial x}dx = p(1) - p(0) = 0. \tag{13}$$

Eqs. (11) and (13) can be used to solve for Q,

$$\begin{aligned}
\int_0^1 \frac{\partial p}{\partial x} dx &= \int_0^1 \frac{12}{h^3}\left[h\left(1-\frac{V_s}{2}\right)-Q\right]dx \\
0 &= \int_0^1 \frac{1}{h^2}\left(1-\frac{V_s}{2}\right)dx - Q\int_0^1 \frac{1}{h^3}dx \\
QI_3 &= I_2\left(1-\frac{V_s}{2}\right) \\
Q &= \frac{I_2}{I_3}\left(1-\frac{V_s}{2}\right)
\end{aligned} \tag{14}$$

where $I_j = \int_0^1 \frac{dx}{h^j(x)}$.

All of the expressions so far are given in terms of the snail velocity V_s, which is still unknown. To find the crawling velocity, consider the balance of forces ($\sum \underline{F} = 0$) on the snail. The only forces acting are pressure and traction. The force on the snail foot can be written as

$$\underline{F} = \underline{\underline{\sigma}} \cdot \widehat{n}. \tag{15}$$

In two dimensions and in the lubrication limit,

$$\underline{\underline{\sigma}} \approx \begin{bmatrix} -p & \frac{\partial u}{\partial y} \\ \frac{\partial u}{\partial y} & -p \end{bmatrix}. \tag{16}$$

The tangential and normal unit vectors can be defined as

$$\begin{aligned}
\widehat{t} &= \left(1, \frac{dh}{dx}\right) \\
\widehat{n} &= \left(-\frac{dh}{dx}, 1\right)
\end{aligned} \tag{17}$$

(so that $\widehat{n} \cdot \widehat{t} = 0$) and using this normal vector and the expression for $\underline{\underline{\sigma}}$, Eq. (15) can be written as

$$\underline{F} = \begin{bmatrix} -p & \frac{\partial u}{\partial y} \\ \frac{\partial u}{\partial y} & -p \end{bmatrix} \begin{bmatrix} -\frac{\partial h}{\partial x} \\ 1 \end{bmatrix} = \begin{bmatrix} p\frac{\partial h}{\partial x} + \frac{\partial u}{\partial y} \\ -\frac{\partial u}{\partial y}\frac{dh}{dx} - p \end{bmatrix}. \tag{18}$$

Consider the forces acting along the x-axis ($-\frac{\partial u}{\partial y}\frac{dh}{dx} - p$); since the snail is not accelerating, the net force in the x direction must be zero. Integrating over the snail foot, and using

Eq. (9) for u and Eq. (12) for $\frac{\partial p}{\partial x}$,

$$\begin{aligned}
\underline{F} &= 0 \\
&= \int_0^1 \left[p\frac{dh}{dx} + \left.\frac{\partial u}{\partial y}\right|_{y=h} \right] dx \\
&= \int_0^1 \left[\frac{d}{dx}(ph) - h\frac{\partial p}{\partial x} + \left(\frac{h}{2}\frac{\partial p}{\partial x} + \frac{V_s}{h} \right) dx \right] \\
&= \int_0^1 \left[\frac{\partial p}{\partial x}\left(-h + \frac{h}{2} \right) + \frac{V_s}{h} \right] dx \\
&= \int_0^1 \left[\left(\frac{12}{h^3} \right) \left(h - \frac{V_s h}{2} - Q \right) \left(-h + \frac{h}{2} \right) + \frac{V_s}{h} \right] dx \\
&= \int_0^1 \left[-\frac{12}{h} + \frac{6V_s}{h} + \frac{12Q}{h^2} + \frac{6}{h} - \frac{3V_s}{h} - \frac{6Q}{h^2} + \frac{V_s}{h} \right] dx \\
&= I_1(-3 + 2V_s) + I_2(3Q)
\end{aligned} \tag{19}$$

which, by combining this with the expressions for Q, gives

$$V_s = \frac{6(A-1)}{3A-4} \tag{20}$$

where $A = \frac{I_2^2}{I_1 I_3}$ and I_j was previously defined.

Using the Cauchy-Schwartz inequality, a bound can be put on A. In order for the snail to move fast, the wave shape $h(x)$ should maximize V_s. As seen in Fig. 3, V_s is maximized as $A \to 0$ and $V_s \to \frac{3}{2}$. However, this value indicates that $\widehat{V}_s = \frac{3}{2}\widehat{V}_w$ or that the snail moves faster than the wave. Indeed, this indicates "forward slipping" which can be achieved if the wave takes, for example, a pointed shape (shown in Fig. 5) which is the $h(x)$ profile that

- maximizes the useful pressure difference by minimizing the distance "a" in Fig. 4 and by making the wave boundary perpendicular to the direction of motion, symbolized by the arrow "b" in Fig. 4
- minimizes the viscous dissipation by maximizing "d" and minimizing "c" in Fig. 4

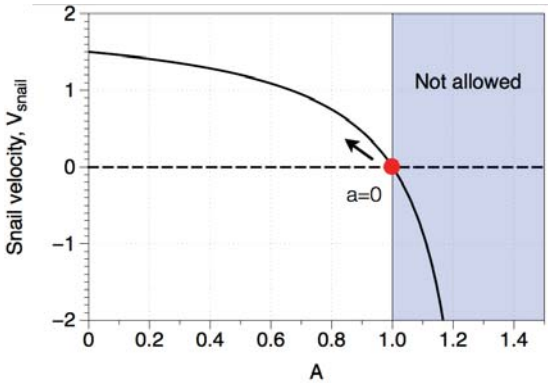

Figure 3: Snail velocity as a function of A.

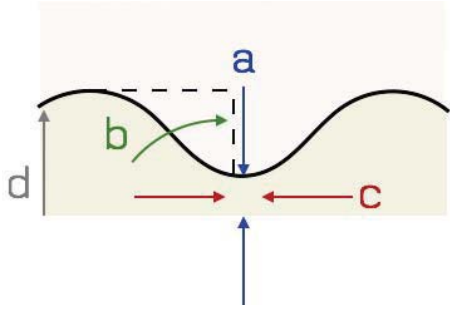

Figure 4: Snail velocity as a function of amplitude for different wave profiles $h(x)$.

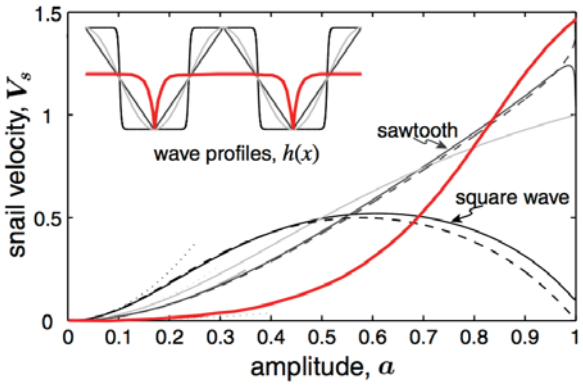

Figure 5: Snail velocity as a function of amplitude for different wave profiles $h(x)$.

Table 1: Wave profiles $h(x)$ for snail retrograde motion.

Profile	A	V_s
$h(x) = 1 + a\delta(x)$	$\sim 1 - a^2\overline{\delta^2}$	$\sim 6a^2\overline{\delta^2}$
$(x)h \sim h_* + \frac{h''_*(x-x_*)^2}{2}$	$\to \frac{2}{3}$	$\to 1$
$h(x) = 1 - a\cos(2\pi x)$	$\frac{2}{2+a^2}$	$\frac{3a^2}{1+2a^2}$
Square wave	$\frac{(1+a^2)^2}{1+3a^2}$	$\frac{6a^2(1-a^2)}{1+6a^2-3a^4}$
Sawtooth wave	$\frac{2a}{M}$	$\frac{3(M-a)}{2M-3a}$

References

Chan, Brian, AE. Hosoi, and N. Balmforth. Building a better snail: Lubrication and adhesive locomotion. *Physics of Fluids* **17**(11) 2005.

Hosoi, AE., and Eric Lauga. Tuning gastropod locomotion: Modeling the influence of mucus rheology on the cost of crawling. *Physics of Fluids* **18**(11) 2006.

Lecture 9b: Thin Films with Elastic Boundaries (cont'd)

Anette Hosoi (notes by Michael Gomez)

June 20, 2018

1 Direct waves

Unlike marine species, which make use of retrograde waves, terrestrial snails propel themselves forward using direct waves. The foot of the snail consists of a continuous band of muscle that contracts, sending a wave of compression forward from the tail. As this wave reaches the head, the snail extends to its full length and shifts forward. Note that, unlike retrograde crawling, this mechanism does not require any of out-of-plane motion of the foot to change the thickness of the fluid layer; the propulsion comes entirely from the adhesive forces generated in the fluid. Indeed, the muscles in the snail are probably not strong enough to overcome its own weight to lift the foot [Denny, 1980].

To test this type of crawling action, consider the mechanical crawler RoboSnail II. Rather than a continuous foot of muscle, RoboSnail II consists of discrete foot pads that move relative to the main body along rails. The rails run parallel with the foot so that no out-of-plane motion is permitted; see figure 1a. The idea is to activate the foot-pads in a sequence starting from the 'tail' in a way that mimics the muscle action of a real snail (figure 1b). When the wave passes the front foot-pad, the robot slides forward along the rails. This resets the position of each foot-pad and the whole process repeats.

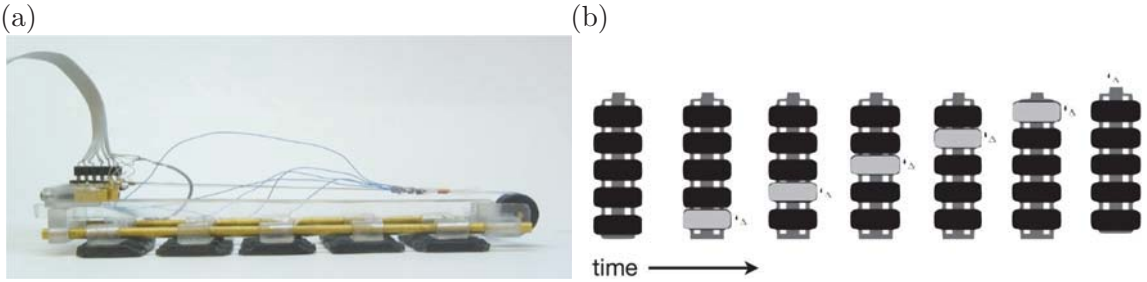

Figure 1: (a) The mechanical crawler Robosnail II, which makes use of direct waves to move forward. Discrete pads make up a flat 'foot' which activate to form a direct compression wave. (b) The sequence in which the foot-pads are activated; the 'head' of the snail is facing upwards [reprinted from Chan et al., 2005].

1.1 Crawling on a Newtonian fluid

When placed on a thin layer of Newtonian fluid, can Robosnail II move itself forward? To answer this question, we perform a force balance on a single foot-pad as it is activated in the sequence. Let $\hat{V}_1$ be the steady velocity of the foot-pad. The footbad is made to slide

forward by a force F that is generated by mechanical contraction in the neighboring gap (in real snails this contraction is achieved by muscles). Because the foot-pad is flat, we approximate the flow generated in the fluid layer as simply Couette-type, i.e. we ignore any $\hat{x}$-dependence due to interactions with other foot-pads that are shearing the fluid with different velocities. This is valid provided the fluid layer is long and thin. Balancing the contractile force with the resistive shear stress exerted by the fluid, we obtain

$$F = \mu \frac{\hat{V}_1}{H} A, \tag{1}$$

where $\hat{H}$ is the (constant) thickness of the fluid layer and A is the area of each foot-pad.

The remaining foot-pads, i.e. those that are not activated, can be lumped together into a second control volume on which the contractile force F acts in the opposite direction. If this volume moves backwards with speed $\hat{V}_2$, a balance of forces requires that

$$F = \mu \frac{\hat{V}_2}{\hat{H}} A(N-1), \tag{2}$$

where N is the total number of foot-pads. The center of mass of the snail moves at the average velocity over all the foot-pads, i.e.

$$V_{\text{snail}} = \frac{\hat{V}_1 - (N-1)\hat{V}_2}{N}. \tag{3}$$

(The negative sign arises because of the different directions of motion between activated and non-activated foot-pads.) Solving (1)–(2) for $\hat{V}_1$ and $\hat{V}_2$ and substituting into (3) gives the crawling speed

$$\hat{V}_{\text{snail}} = \frac{F\hat{H}}{AN}\left(\frac{1}{\mu} - \frac{1}{\mu}\right) = 0, \tag{4}$$

so that Robosnail II does not move at all!

Remembering that the fluid in the lubricating layer flows at low Reynolds number (because it is long and thin), this result should come as no surprise: essentially we are seeing a consequence of the Scallop Theorem (discussed in lecture 6). To see what is going wrong, let's focus on a single foot-pad as the compression wave passes: as the previous foot-pad in the sequence is activated, the contractile force pushes the foot-pad backwards, and this motion is entirely reversed when the foot-pad itself is activated. Thus, each foot-pad moves in an entirely reciprocal way, and the Scallop Theorem guarantees no net thrust can be produced.

1.2 Crawling on a yield-stress fluid

If Robosnail II is recreating the crawling action of real snails, this then begs the question: how do direct crawlers in Nature break this reversibility? The answer lies at the micro scale: real snails propel themselves on a thin layer of secreted mucus, which contains a mixture of water and mucins, complex long-chain proteins. The effect of mucins is to alter the rheology of the mucus, so that it is highly non-Newtonian with a finite yield stress τ_0. In the compression wave, the foot of the snail exerts a large amount of shear on the mucus

layer, overcoming this yield stress and driving a flow. Away from the wave region where the foot is stationary (known as the interwave region), the fluid does not yield and is effectively rigid; see figure 2a. This sets up a strong adhesive force which is able to overcome the shear force generated in the wave regions, allowing the snail to propel itself forward.

To explore this mechanism further, we model the mucus secreted by the snail using the Bingham model for a yield-stress fluid. This assumes that the strain rate grows linearly with the stress once the yield stress is exceeded. While we could use a more general power-law model such as a Herschel–Bulkley fluid to capture shear-thinning/thickenings effects, we restrict to a Bingham model for the sake of simplicity here.

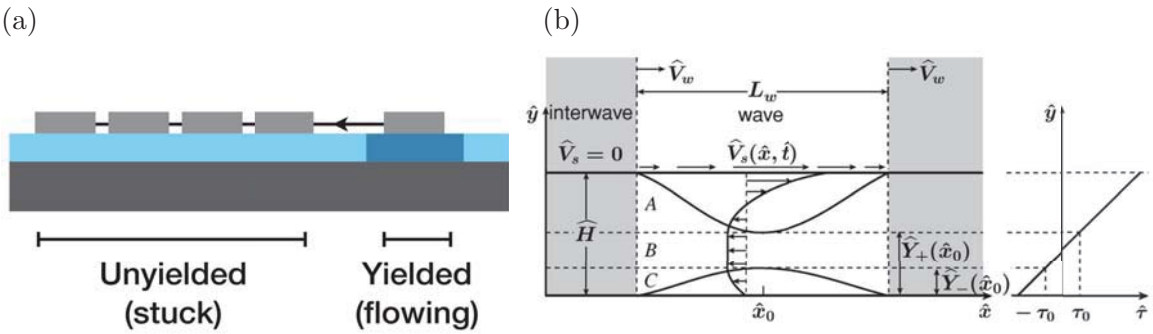

Figure 2: (a) Due to a finite yield stress, only the mucus below the compression wave (dark blue) is flowing. This is the source of differential friction that allows the snail to move. (b) Velocity profile in the fluid layer underneath the foot in the laboratory frame (left). In the wave region the upper boundary moves with speed $\hat{V}_s$ due to muscle contraction, but remains at rest in the interwave region (shaded). The lower substrate remains stationary. Also shown is the profile of the shear stress throughout the fluid layer (right), which remains linear in $\hat{y}$ in the lubrication limit [reprinted from Chan et al., 2005]

As with our earlier analysis for the retrograde crawler, we consider a two-dimensional domain in the $\hat{x}$–$\hat{y}$ plane that is periodic in the $\hat{x}$–direction. We now assume that the foot remains flat at all times $\hat{t}$ (ignoring any elastic deformations due to the lubrication pressures) so that the fluid layer has a constant thickness $\hat{H}$. In the laboratory frame, we zoom in on the region of the foot that contains a moving compression wave of length $L_w \gg \hat{H}$ (figure 2b). The compression of the muscles in the wave imposes a surface velocity $\hat{V}_s(\hat{x}, \hat{t})$ on the upper boundary of the fluid layer. The wave is surrounded by the interwave region where the fluid is stationary. The wave/interwave boundary moves with the wave velocity $\hat{V}_w$, which needn't be equal to $\hat{V}_s$ (the size of $\hat{V}_s$ is related to how strong the muscles contract, while $\hat{V}_w$ measures how fast the snail sends the compression wave along the foot).

For the snail to crawl forward, the shear force applied by the foot in the wave region must be sufficient to overcome the yield stress τ_0 in the fluid. Note that, unlike the case of Newtonian fluid considered above, the flow beneath the wave is not simply Coutette-type: because the fluid is stationary in the interwave region, the flux fluid in this region is zero, and by conservation of mass the flux through any vertical line drawn through the wave region must also be zero. This sets up an adverse pressure gradient $\partial\hat{p}/\partial\hat{x}$ which acts to push flow backwards while fluid is still pulled forward near the foot. The result is a backward plug flow in the region $\hat{Y}_- < \hat{y} < \hat{Y}_+$ (where the fluid is unyielded), with

two parabolic profiles outside where the flow adjusts to the no-slip boundary conditions on the substrate and foot. This is drawn in figure 2b. Note that we are implicitly making a lubrication approximation here (valid for $L_w \gg \hat{H}$) by neglecting any $\hat{x}$-dependence in the flow field.

Using conservation of momentum in the fluid (expanded in the lubrication limit), together with the Bingham constitutive law, we can solve for the velocity in each of these three parts. After imposing continuity of velocity and shear stress at all points, these solutions can be expressed in terms of the positions $\hat{Y}_\pm$ of the yield surfaces and the velocity in the plug region, $\hat{u}_p$; for details on the calculation (using a Herschel–Bulkley fluid) see Chan et al. [2005]. Together with the pressure gradient $\partial\hat{p}/\partial\hat{x}$, there are therefore four unknowns in the problem. The system is closed by applying conservation of mass, no-slip boundary conditions on the foot and substrate, and the yield condition that the shear stress $\hat{\tau}$ varies from $-\tau_0$ to $+\tau_0$ across the width of the plug.

Unlike our analysis for the retrograde crawler, we no longer specify that the net force exerted on the snail is zero. Instead, for forward motion to be possible, we impose that the adhesive force in the interwave regions must exceed the shear force exerted in the wave region, as well as any horizontal component of gravity; otherwise the snail will slide backwards. This requires that

$$\tau_0 L_I \geq \hat{\tau}_w L_w + mg\sin\alpha, \tag{5}$$

where L_I is the length of the interwave region, $\hat{\tau}_w$ is the total shear force exerted by the foot in the wave region, m is the mass of the snail (per unit width in the $\hat{z}$-direction) and α is the angle made by the snail to the horizontal.

Having solved for the fluid pressure and velocity, subject to the force constraint (5), it is not obvious what speed the snail will crawl at: on the foot we have both moving bands of wave regions and stationary interwave regions. We visualise these using the space-time plot shown in figure 3. Consider the motion of a single material point on the foot (dotted line). As each interwave region passes, the point remains stationary (since there is no compression of the foot) for some time $\hat{t}_I$. If $|\hat{X}_w|$ is the displacement of the point in each wave region, and $\hat{t}_w$ is the time spent there, the speed of the snail is

$$\hat{V}_{\text{snail}} = \frac{|\hat{X}_w|}{\hat{t}_w + \hat{t}_I}.$$

By simple geometric arguments based on figure 3, we can relate $|\hat{X}_w|$, $\hat{t}_w$ and $\hat{t}_I$ to the wave speed $\hat{V}_w$, surface speed $\hat{V}_s$ and the lengths L_w and L_I. We find that

$$\hat{V}_{\text{snail}} = \frac{\hat{V}_w\hat{V}_f}{\hat{V}_w + R(\hat{V}_w - \hat{V}_f)},$$

where we have introduced the length ratio

$$R = \frac{L_I}{L_w}.$$

The wave speed $\hat{V}_w$, compression speed $\hat{V}_s$ and length ratio R are all design parameters that are free to be chosen by a snail or roboticist alike (subject to the force constraint

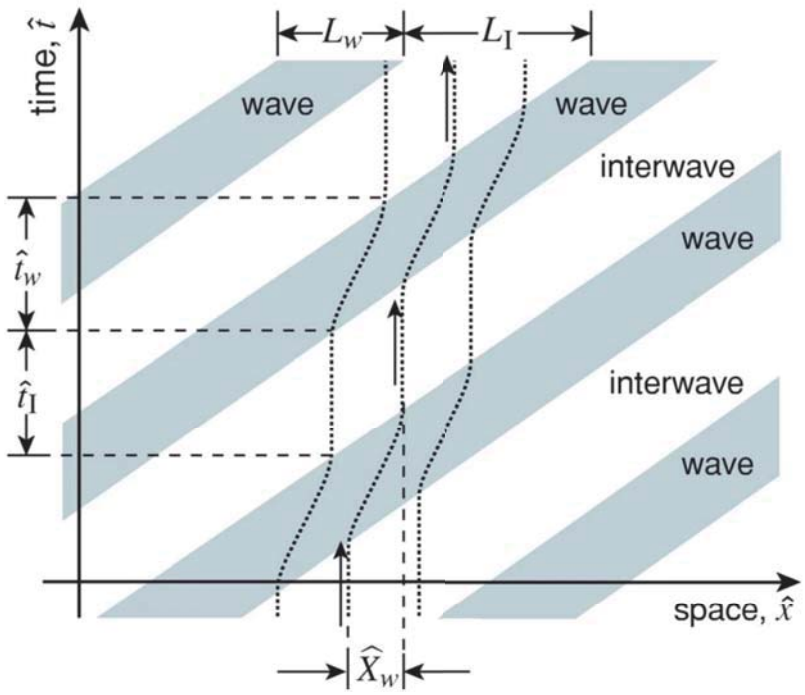

Figure 3: Space-time diagram illustrating how compression waves propagate along the foot of the snail into stationary interwave regions. The trajectories (world lines) of material points on the foot are given by the dotted lines [reprinted from Chan et al., 2005]

(5)). For an optimal design of a direct crawler, we can imagine maximizing $\hat{V}_{\text{snail}}$ or minimizing the energy consumption for a given value of $\hat{V}_{\text{snail}}$. Another interesting question is whether it is more energy efficient for snails to have evolved either shear-thickening or shear-thinning mucus. Considering a primitive type of snail whose mucus rheology is only slightly non-Newtonian, Lauga and Hosoi [2006] have performed a lubrication analysis of a direct crawler along the lines described above. They find that a shear-thickening mucus lowers the dissipation of energy due to viscous resistance, while a shear-thinning mucus lowers the cost of producing mucin molecules. So which effect wins in practice? It turns out that the chemical cost is the deciding factor, due to the very high cost of snail crawling compared to other types of animal locomotion; see figure 4 (notice the y-axis is a log scale!) A shear-thinning mucus should therefore be more favorable, and this is indeed what is found for the mucus of most species.

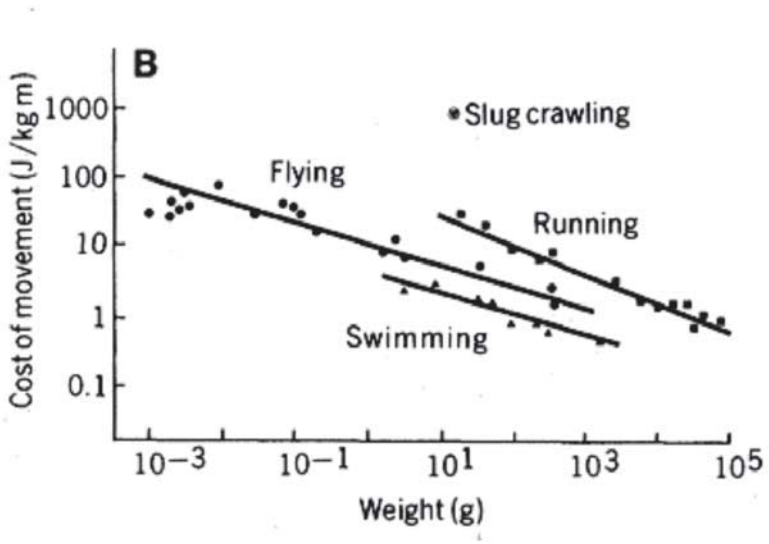

Figure 4: The energetic cost of different types of animal locomotion [reprinted from Denny, 1980].

References

B. Chan, N. J. Balmforth, and A. E. Hosoi. Building a better snail: Lubrication and adhesive locomotion. *Physics of Fluids*, 17(11):113101, 2005.

M. Denny. Locomotion: the cost of gastropod crawling. *Science*, 208(4449):1288–1290, 1980.

E. Lauga and A. E. Hosoi. Tuning gastropod locomotion: modeling the influence of mucus rheology on the cost of crawling. *Physics of Fluids*, 18(11):113102, 2006.

Lecture 10: Hairy Hydrodynamics in Nature

Anette Hosoi (notes by Paula Doubrawa and Qi Li)

July 1, 2016

1 Part 1

For a hairy diode (See Fig.1), the flow in the hairy region can be modeled as Darcy flow as:

$$\underline{u_o}(z) = \frac{k(\theta(z))}{\mu}\frac{\Delta p}{L}, \tag{1}$$

where k is the permeability and k is a function of θ, the angle that the hair makes with the vertical z axis. In the core region, the flow is a Poisseuille flow.

$$-\frac{\Delta p}{L}\widehat{x} = \nabla p = \mu\nabla^2\underline{u} \tag{2}$$

$$u_i = \frac{-\Delta p}{2\mu L}z^2 + C_1 z + C_2$$

is the solution to Eq.2, and by symmetry, $C_1 = 0$. Matching the velocity on the interface between the inner core and the edge of the hairy region:

$$u_i(z = h - R) = u_o(z = h - R)$$

$$-\frac{\Delta p}{2\mu L}(R-h)^2 + C_2 = \frac{k_{tip}}{\mu}\frac{\Delta p}{L}$$

$$u_i = \frac{\Delta p}{2\mu L}\left(2k_{tip} + (R-h)^2 - z^2\right). \tag{3}$$

The hair on the outer region is not rigid. It can be modeled as a rigid fiber with torsional

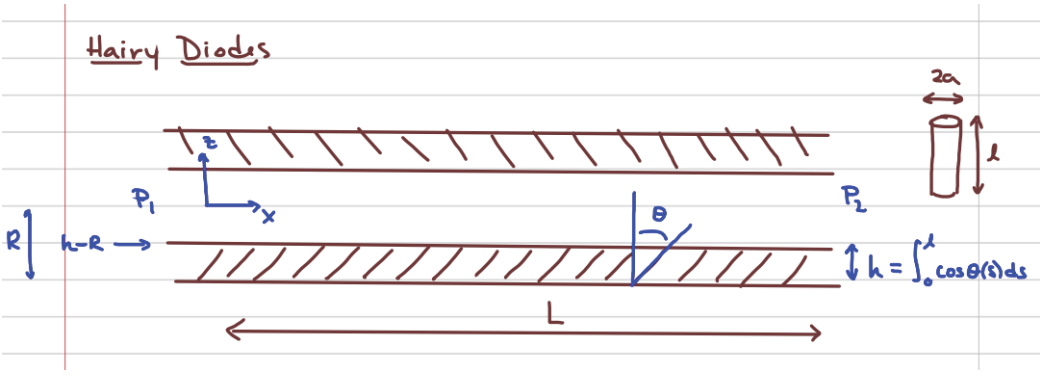

Figure 1: Sketch of the hairy channel.

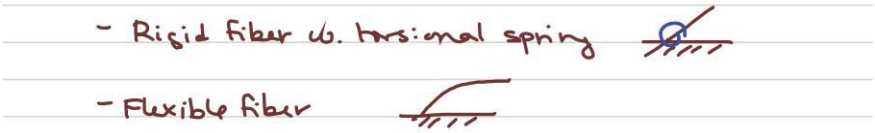

Figure 2: Sketch of the fiber. left: a rigid fiber with torsional spring on the base; right: a completely flexible fiber.

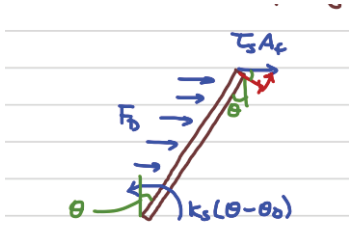

Figure 3: Sketch of the fiber with the torsional spring on the base.

spring on the base or flexible fiber (See Fig.2). Now consider the fiber with torsional spring (See Fig.3) (flexible fiber is similar but the algebra is more involved).

$$\tau_s = \mu \frac{\partial u_i}{\partial z} = \mu \frac{\Delta p}{2\mu L}(-2z), \tag{4}$$

for $z = h - R$. Thus

$$\tau_s = \frac{\Delta p}{L}(R - h), \tag{5}$$

is the viscous drag. ϕ_s (See Fig.4) is the volume fraction of fibers, which is given by

$$\phi_s = \frac{\pi a^2]}{A_f}. \tag{6}$$

Force on the tip of the hair F_{tip} is

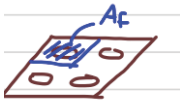

Figure 4: Illustration of the cross-section of fiber.

$$F_{tip} = \frac{\pi a^2}{\phi_s} \frac{\Delta p}{L}(R - h) \tag{7}$$

The moment on the tip M_{tip} is given by

$$M_{tip} = F_{tip} l \cos\theta = \frac{h\pi a^2}{\phi_s} \frac{\Delta p}{L}(R - h). \tag{8}$$

The pressure drop is balanced by the drag on the fiber as illustrated in Fig. 5.

$$F = dph = \frac{\Delta p}{L} wh = \frac{\Delta p}{L} \frac{\pi a^2}{\phi_s}$$

The moment due to drag force M_{drag} is given by

$$M_{drag} = \frac{\Delta p}{L} \frac{\pi a^2}{\phi_s} l \sin\theta \frac{1}{2} l \sin\theta = \frac{\Delta p}{L} \frac{\pi a^2}{\phi_s} \frac{h^2}{2} \tag{9}$$

From balancing the torque:

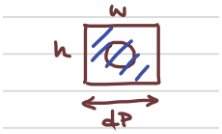

Figure 5: Illustration of the patch of outer hairy region where drag force acts on.

$$\frac{h\pi a^2}{\phi_s} \frac{\Delta p}{L} (R-h) + \frac{\Delta p}{L} \frac{\pi a^2}{\phi_s} \frac{h^2}{2} = k_s(\theta - \theta_0) \tag{10}$$

$$\frac{\pi a^2}{\phi_s} \frac{\Delta p}{L} h(R - h/2) = k_s(\theta - \theta_0) \tag{11}$$

Thus,

$$\cos\theta \left(1 - \alpha/2 \cos\theta\right) = \frac{k_s \phi_s L}{\pi a^2 \Delta p l R} (\theta - \theta_0), \tag{12}$$

where $T_e = \frac{k_s \phi_s L}{\pi a^2 \Delta p l R}$ (called the "Tesla number") and $\alpha = l/R$, which is the aspect ratio of the hairy fiber. The flow anisotropy $\frac{Q^+}{Q^-}$,

$$\begin{aligned} Q &= 2\int_0^{R-h} u_i dz + 2\int_{R-h}^{R} u_o dz \\ &= 2\int_0^{R-h} \frac{\Delta p}{2\mu L} \left[2k_{tip} + \frac{(R-h)^2}{2} - \frac{z^2}{2}\right] dz + 2\int_{R-h}^{R} \frac{k(\theta)}{\mu} \frac{\Delta p}{L} dz \\ &= \frac{2\Delta p}{\mu L} \left\{ \left[k(\theta)R + \frac{(R-h)^2}{2}\right] z - 1/6 z^3 \right\} \Bigg|_0^{R-h} \\ &= \frac{2\Delta p}{\mu L} \left(k(\theta)R + 1/3(R - l\cos\theta)^3\right) \end{aligned} \tag{13}$$

The flow anisotropy is:

$$\frac{Q^+}{Q^-} = \frac{3k(\theta^+) + R^2(1 - \alpha\cos\theta^+)^3}{3k(\theta^-) + R^2(1 - \alpha\cos\theta^-)^3} \tag{14}$$

2 Part 2

The term "Landau-Levich" refers to a classical problem in which a submerged plate is withdrawn from a reservoir of fluid, by which process the plate ends up coated in a thin film. The same experiment can be done for plunging as opposed to withdrawing of the plate. Experiments have been conducted for plates with smooth and micro textures. Here we discuss an analogous problem with hairy surfaces of mesoscale structure.

2.0.1 Plunging a Surface with Mesotexture

Some marine mammals (e.g. fur seal, sea otter) use primarily fur for thermal insulation, and entrain layers of air in their fur. Others, which use a combination of fur and blubber, do not entrain air. The question is to determine under which conditions these air-entraining mammals entrain air when they dive. An experiment was conducted and air entrainment was observed. A model was subsequently developed. Starting with

$$P_0 + \rho g y + \frac{1}{2}\rho \dot{x}^2 - \gamma k - \frac{\mu}{k}\frac{\dot{x}x}{r^2} = P_0 \tag{15}$$

where P_0 is gauge pressure; $\rho g y$ is the hydrostatic pressure pushing air into the mammal's hair as it dives; $\frac{1}{2}\rho\dot{x}^2$ represents inertia which is high in the initial period (upon entering the water) but goes to $\mathcal{O}(10^{-3})$ after that so this term can be neglected for most of the dive; γk is the capillary term which is also negligible, and $\frac{\mu}{k}\frac{x\dot{x}}{r^2}$ is the viscous term. The viscous scaling comes from

$$\begin{aligned} \mu\frac{\dot{x}}{r}(rx)(\frac{1}{r^2}) =& (\text{shear stress})(\text{interface})(\text{area over which force acts}) \\ =& \mu\frac{\dot{x}x}{r^2} \end{aligned} \tag{16}$$

and k is an "effective permeability", added to the expression to describe the arrangement of hairs on the surface. The expression to be solved then becomes

$$\rho g y = \mu\frac{\dot{x}x}{r^2} \tag{17}$$

With the plunging velocity $v = \frac{dy}{dt}$,

$$\rho g y = \frac{\mu}{k}\frac{x}{r^2}\frac{dx}{dy}\frac{dy}{dt} \tag{18}$$

which results in

$$\begin{aligned} \int_y^{y_m} \rho g y dy &= \int_0^x \frac{\mu v}{k r^2} x dx \\ x^2 &= \frac{v_*}{v}(y^2 - y_m^2) \end{aligned} \tag{19}$$

where $v_* = \frac{k\rho g r^2}{\mu v}$ is the characteristic velocity with which the liquid is moving into the hair.

The dry depth quantifies how far the animal can dive to maintain the layer of air in its fur. Assuming that y_m is small,

$$h_{\text{dry}} = \sqrt{\frac{v}{v_*} L} \tag{20}$$

An analogous experiment can be performed for withdrawing of meso-textured surfaces, in which the context is that of bat tongues.

Effects of Kelvin and Topographic Rossby Waves on the Denmark Strait Overflow

Océane Richet

(advised by Renske Gelderloos, Larry Pratt and Jiayan Yang)

October 4, 2016

1 Introduction

The Atlantic Ocean is separated from the Nordic and Arctic Seas by the Greenland-Iceland-Scotland Ridge (GISR, Fig. 1). The surface waters from the Atlantic flow into the Nordic Seas where they lose buoyancy and form a dense water mass through deep convection [6]. The dense water spills over the shallow sills in the various channels that cut through the GISR, and mix with lighter water masses downstream to form North Atlantic Deep Water (NADW), which feeds the lower limb of the Atlantic Meridional Overturning Circulation (AMOC) [1][3]. The overflow volume of dense water, Denmark Strait Overflow Water (DSOW, potential density larger than 27.8 $kg.m^{-3}$ [1]) over the GISR is equal to 6 Sv (1 Sv = 10^6 $m^3.s^{-1}$) and distributed between the Denmark Strait (sill depth 620 m, 3 Sv), the Faroe Bank Channel (sill depth 840 m, 2 Sv) and the Iceland Faroe Ridge (sill depth 420 m,1 Sv) [4].

From the Nordic Seas side of the ridge, three currents approach the Denmark Strait: the East Greenland Current (EGC), which follows the East Greenland coastline and is the main conduit for Arctic-origin fresh water flowing into the subpolar gyre on the East side of Greenland [10]; the North Icelandic Jet (NIJ), which approaches Denmark Strait along the Iceland shelf break [14] [5]; and the separated-EGC (sEGC), which branches off the EGC upstream of Denmark Strait and joins the NIJ close to the Denmark Strait [14] [5]. The Denmark Strait Overflow Water (DSOW) is found underneath these surface currents. Its volume transport varies on short timescales of a few days [9] [15] but does not display seasonal variability or a long-term trend [1] [8] [7]. The overflow in the Denmark Strait is hydraulically controlled [16] [11] [2], which means that a perturbation in the supply of dense water in the upstream (Nordic Seas) basin will communicate via a long ocean waves reflected at the sill and modify the transport of the DSOW [12].

Given the typical time scale of variability in the overflow (2-4 days) [9] [15], we propose to study the effect of long waves on a hydraulically controlled overflow in a 1.5-layer reduced gravity model. The model set up is described in section 2, followed by the description of a simulation with a dam break. In section 3, we present simulation results from a case with a dam break and an inflow/outflow as initial conditions and the impact of a perturbation in the inflow and its response.

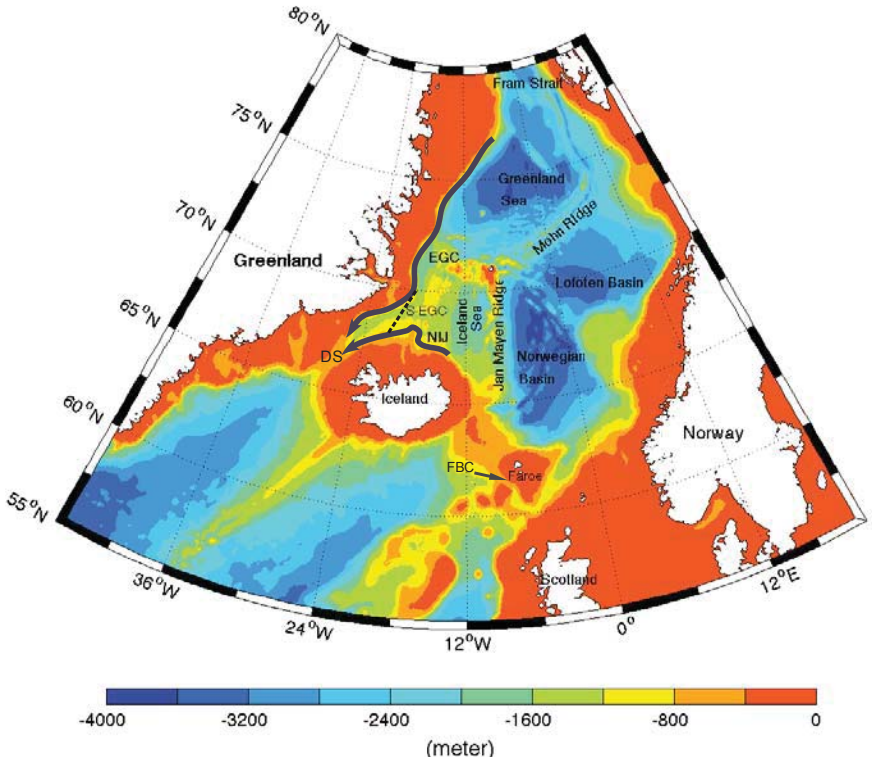

Figure 1: Bathymetry of the Nordic Seas from [17]. Abbreviations correspond to, **DS**: Denmark Strait, **EGC**: East Greenland Current, **NIJ**: North Icelandic Jet, **s-EGC**: separated EGC and **FBC**: Faroe Bank Channel.

2 Methods

2.1 Model

The model used in this study is a 1.5 layer reduced gravity model. It is assumed that the overlying fluid layer is very thick compared to the bottom layer and is motionless. The horizontal velocity (u, v) and the layer thickness H of the thin, dynamically active bottom layer are governed by the shallow water equations:

$$\partial_t u + \underline{u} \cdot \underline{\nabla} u - fv = -g' \partial_x h + \nu \nabla^4 u, \tag{1}$$

$$\partial_t v + \underline{u} \cdot \underline{\nabla} v + fu = -g' \partial_y h + \nu \nabla^4 v, \tag{2}$$

$$\partial_t H + \underline{u} \cdot \underline{\nabla} H + H(\partial_x u + \partial_y v) = 0, \tag{3}$$

where f is the Coriolis frequency, h the interface displacement, $g' = \Delta\rho g/\rho_0$ is the reduced gravity and $\nu = 10^{10}$ m^4.s^{-2} is the horizontal biharmonic viscosity. The control simulation's latitude is 60°N. At the initial state, the fluid in the bottom layer is at rest and the interface is flat. The initial layer thickness is equal to $H_0(x, y)$, which is larger in the upstream basin and varies according to the bathymetry. The lateral boundary conditions are

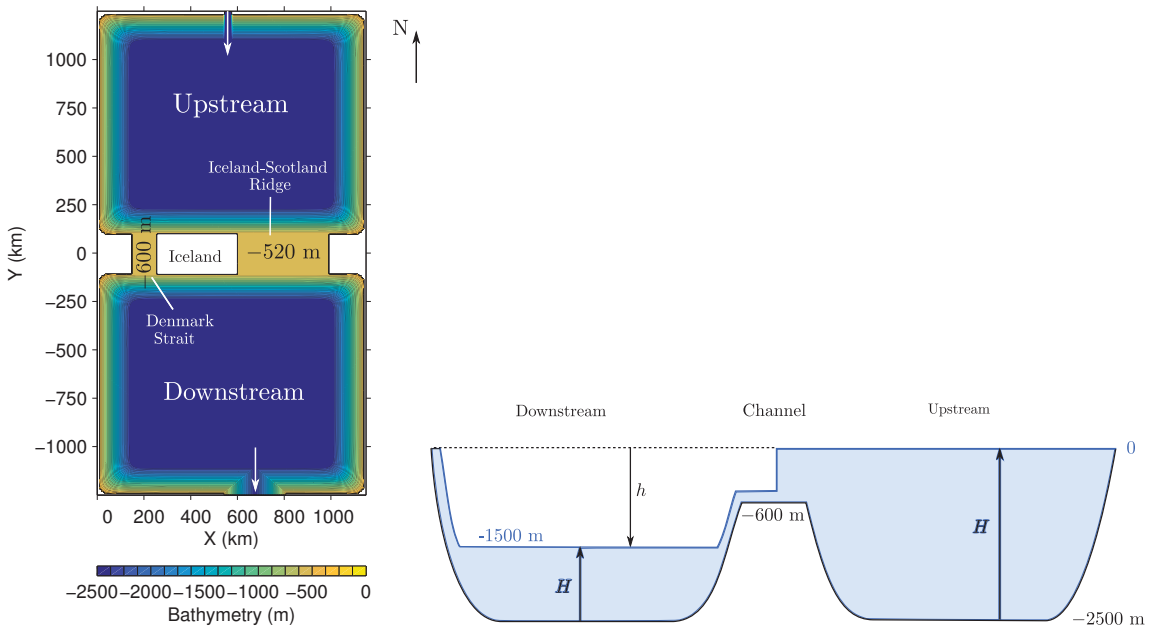

Figure 2: (a) Bathymetry of the model (left) and (b) initial condition for the interface depth (right).

no-slip and no-normal flow through solid boundaries. In the absence of sources and sinks, a steady state is reached, and a perturbation corresponding to an inflow/outflow through a lateral opening is added. The horizontal resolution is the same in the $x-$ (zonal) and $y-$ (meridional) directions and equals to 5 km. The discretization of the model is based on the Arakawa C-grid and the model domain spans 1155 km zonally and 2505 km meridionally.

The upstream and downstream basins have a flat bottom, except along the boundaries where there is a slope. The depth of the Denmark Strait is equal to 600 m and the depth of the Iceland-Scotland Ridge is a bit shallower with a depth of 520 m. The initial state corresponds to a situation where the lower layer depth is more than twice as large in the upstream basin, and separated from the downstream basin by virtual dams in the middle of the Denmark Strait and the Iceland-Scotland Ridge. The maximum thickness in the upstream basin is equal to 2500 m and 1000 m in the downstream basin. The interface is set to be zero in the upstream basin. To prevent grounding with the 1.5 layer reduced gravity model, a minimum layer thickness equal to 80 m is imposed on the lower layer.

2.2 Simulations

2.2.1 Dam break simulation

The first simulation is initialized with a step in the interface depth between the upstream and downstream basin, as shown on Fig. 2b. The upstream basin has a maximum lower layer thickness of 2500 m and the downstream basin a maximum of 1000 m. The step is located in the middle of the Denmark Strait and the Iceland-Scotland Ridge. It thus works

as a virtual dam, which breaks when the simulation starts.

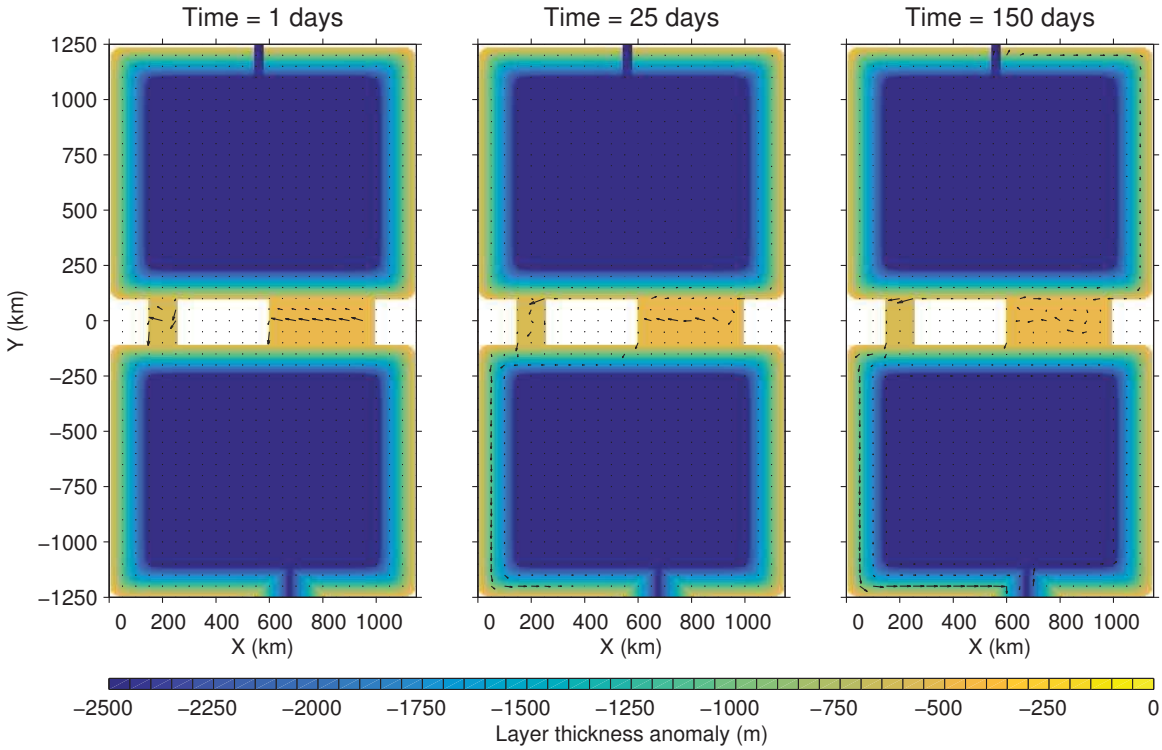

Figure 3: Snapshots of the velocity field (arrows) at different times (from left to right: (a) 1 day, (b) 25 days and (c) 150 days) after the dam breaks. Colours represents the bathymetry. The latitude is 60° and $\Delta\rho = 0.3$ kg.m^{-3}.

A snapshot of the circulation induced by the dam break is shown in Fig. 3 (black arrows) at 1 day, 25 days and 150 days. The dam break generates a current from the Denmark Strait and the Iceland-Scotland Ridge which propagates along the eastern boundary in the upstream basin and the western boundary in the downstream basin. The generated circulation in the upstream basin is thus anti-cyclonic, while in the downstream basin the circulation is cyclonic. The flow in both basins is maximum over the slope. The strongest current is located in the Denmark Strait.

In the Denmark Strait, the initial state corresponds to a layer thickness step between the upstream basin and the downstream basin. The layer thickness anomaly is equal to 0 m in the northern part of the channel and to -520 m in the southern part (Fig. 4a). Two hundred days after the dam break, the surplus of dense water in the channel has flown into the downstream basin and the effect of the rotation constrains the lower-layer flow to the western flank of the channel (Fig. 4b).

Fig. 5 shows the interface displacement for 3 snapshots in the simulation. The dam break generates a wave in both channels which propagates in the cyclonic direction in both basins.

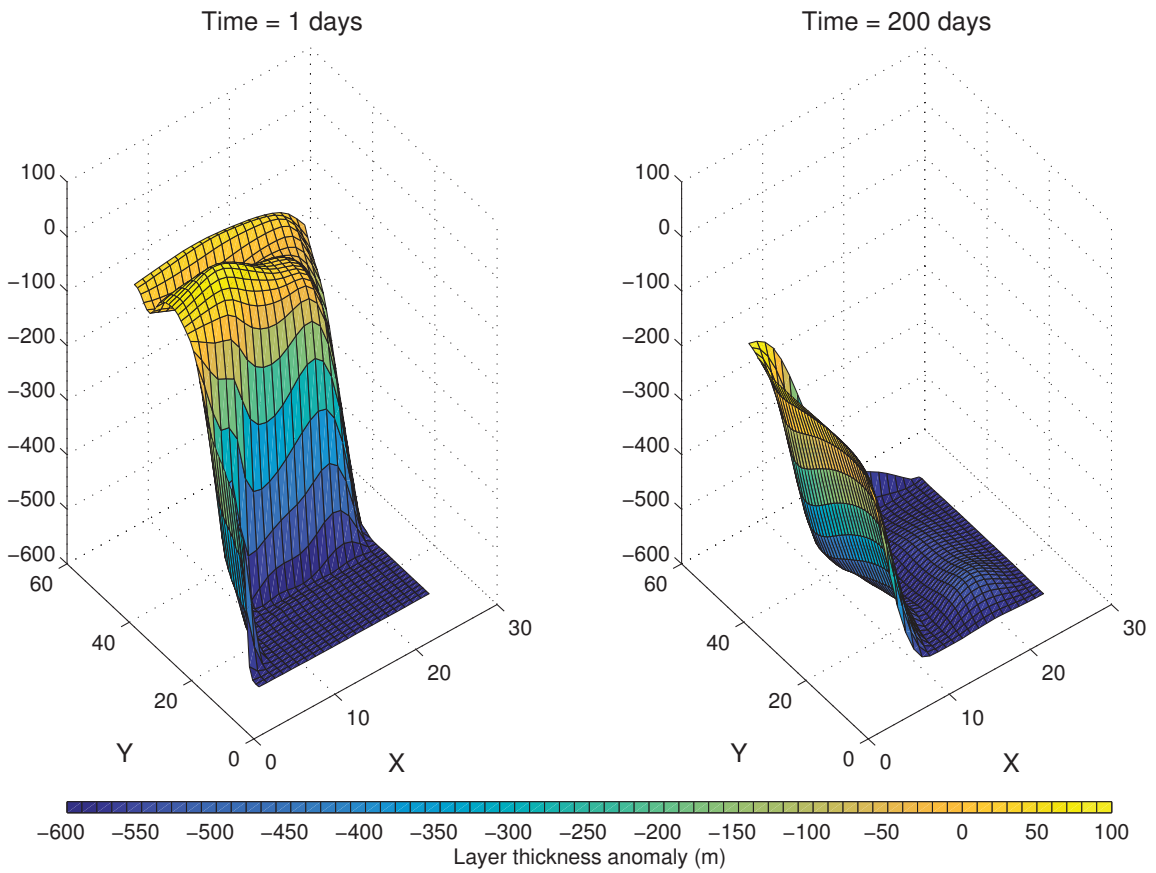

Figure 4: Snapshots of the layer thickness anomaly in the Denmark Strait at different time (from left to right: (a) 1 day, (b) 200 days) after the dam breaks. The latitude is 60° and $\Delta\rho = 0.3$ kg.m^{-3}.

The wave shows up as a decrease in the layer thickness along the upstream boundary and an increase along the downstream boundary.

The wave can be tracked in the interface displacement signal (see Fig. 6). The figure shows the temporal evolution of the interface displacement at different locations in the upstream basin and around the island. The first point reached by the wave is point 3, where the layer thickness decreases rapidly just after the Denmark Strait dam break. The wave propagates along the eastern and northern boundaries before reaching point 1 and then point 2, which show a fairly constant interface displacement followed by a rapid decrease. Point 4 corresponds to the dam break in the Iceland-Scotland Ridge. The decrease seems to be less abrupt than in the point 3 because point 4 is located on the western flank of the channel where the water banks due to rotation.

At point 5, the interface displacement at the beginning of the simulation is equal to 80 m. After the Iceland-Scotland dam breaks a small amount of water from the upstream part of the channel flows to this point and then down the slope. The model imposes a minimum

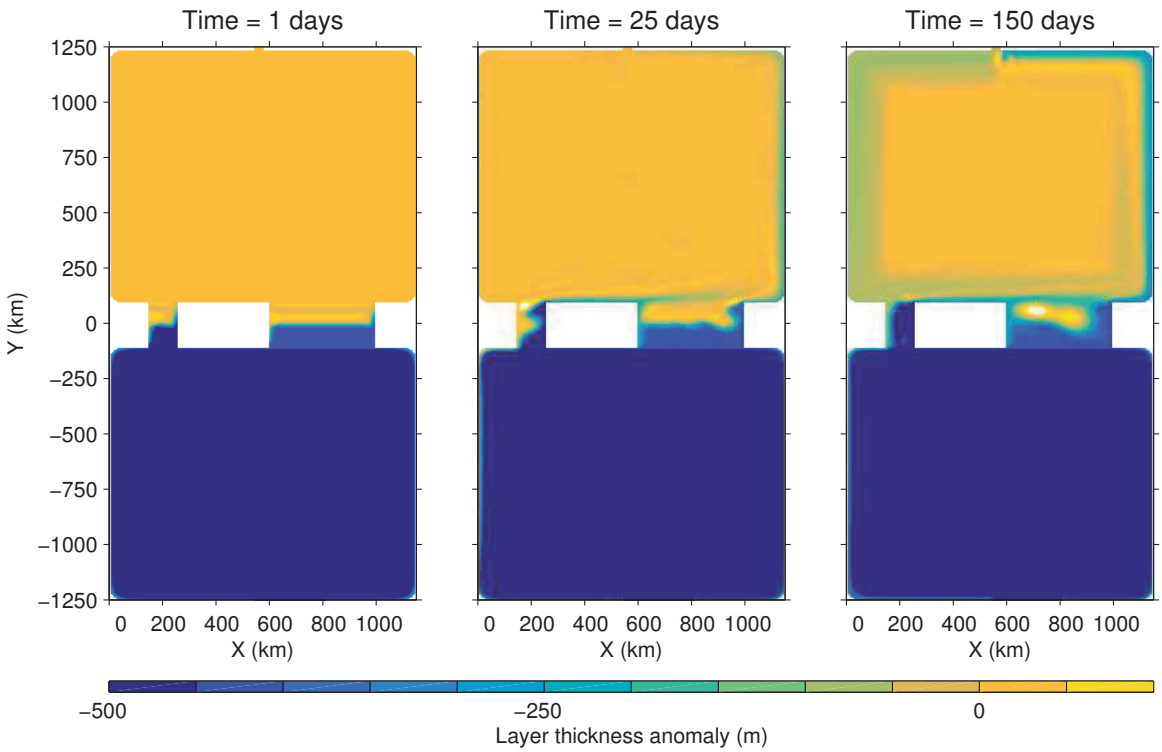

Figure 5: Snapshots of the layer thickness anomaly at different times (from left to right: (a) 1 day, (b) 25 days and (c) 150 days) after the dam breaks. The latitude is 60° and $\Delta\rho = 0.3$ kg.m^{-3}.

thin layer thickness of 80 m if there is no more water. At point 6, the water in the Denmark Strait oscillates after the dam break before to being constrained to the western side of the channel, causing a decrease in the layer thickness at the eastern side. The signal observed at the different points corresponds to the transitory phase of the system. After 200 days, the interface displacement induced by the dam break can be considered a permanent interface displacement in the upstream basin.

2.2.2 Dam break simulation with an inflow/outflow

The next simulations have the same initial condition as the dam break simulation plus an inflow/outflow forcing. The inflow is imposed at the northern boundary of the upstream basin with a constant transport of 3 Sv. To ensure volume conservation, an outflow of the same magnitude is added on the southern boundary of the downstream basin.
The simulation is run to a steady state. Once the steady state is reached (after 150 days), the inflow is perturbed for a period of 5 days increasing the transport from 3 Sv to 5, 7 or 9 Sv.

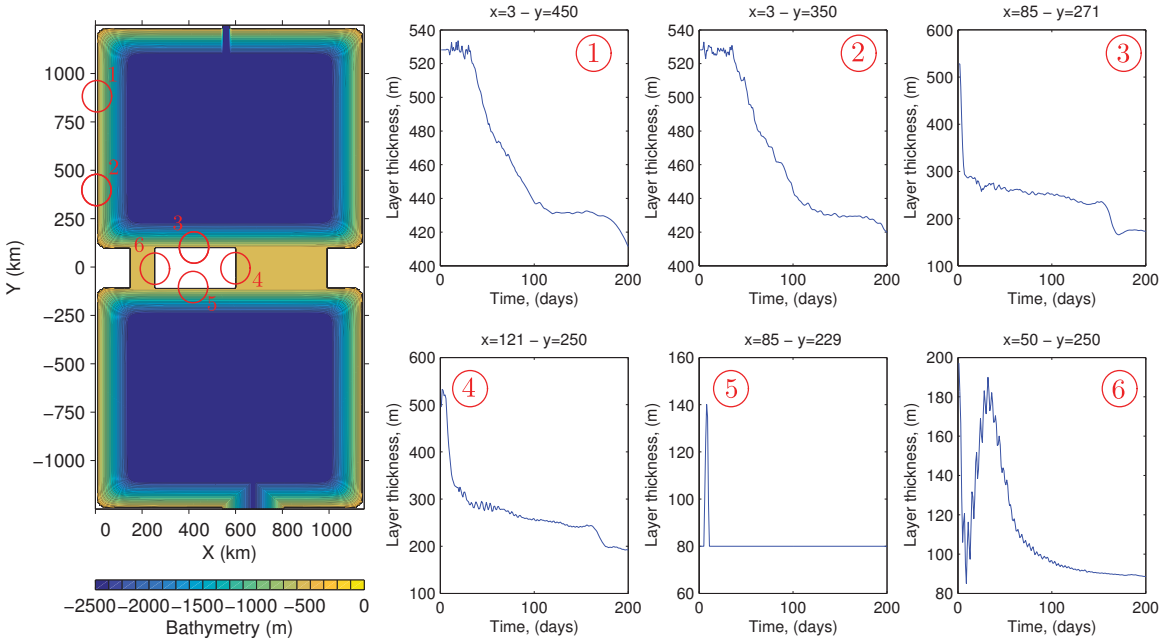

Figure 6: Temporal evolution of the layer thickness in different locations in the control simulation 1 (right) and location of the different points (left). The latitude is 60° and $\Delta\rho = 0.3$ kg.m^{-3}.

3 Results

3.1 Hydraulic control in Denmark Strait

The dam break in the Denmark Strait and at the Iceland-Scotland Ridge induces an anticyclonic circulation in the upstream basin, and an interfacial wave that moves cyclonically around the basin. Now, we add a constant inflow of 3 Sv through the northern boundary of the upstream basin to obtain a steady state circulation.

It is important to have a hydraulically controlled flow if we want to see the information transmission in the upstream basin when inflow transport varies. Normally, the setup of simulations ensures a hydraulically controlled flow in both channels. To confirm this assumption, we calculate the maximum local Froude number, $Fr = U/\sqrt{g'H}$, in the Denmark Strait for different density differences $\Delta\rho$, latitudes f and inflow/outflow Q (Fig. 7). The maximum local Froude number increases with density difference and inflow/outflow transport and decreases with latitude. The maximum local Froude number can be larger than 1 (supercritical flow) which implies a hydraulically controlled flow in the Denmark Strait. Unfortunately, this criteria does not work well (only one simulation with a Froude number greater than 1) presumably caused by our no-slip condition.

Another way to show hydraulic control is to look at the interface displacement in the upstream basin. Figure 8 shows snapshots of the layer thickness anomaly at day 1, 25 and

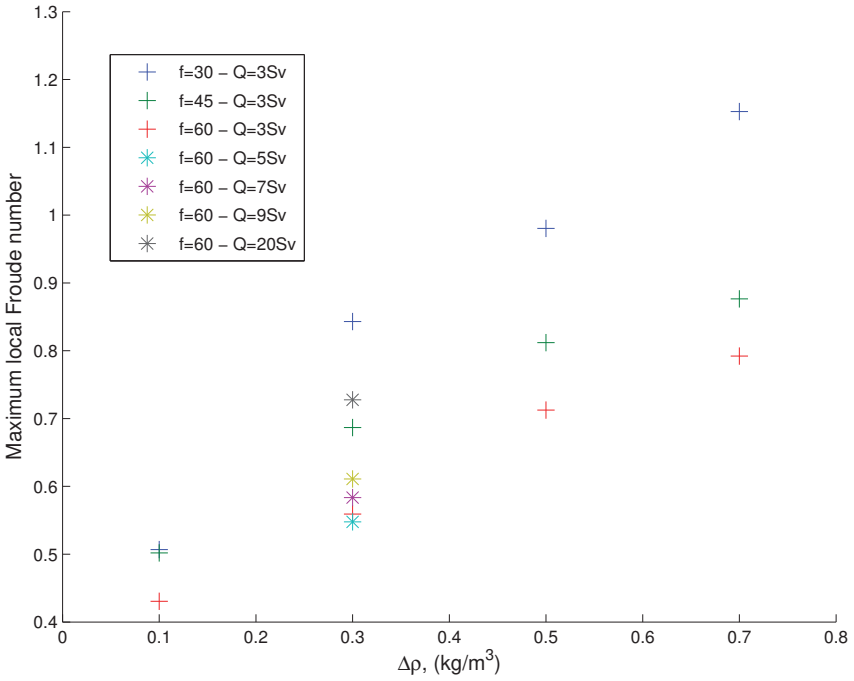

Figure 7: Maximum local Froude number as a function of density difference, inflow/outflow transport and latitude.

150 for a simulation with a dam break and inflow/outflow. In steady state, at 150 days (Fig. 8c), the interface displacement in the upstream basin is permanent, which means that the simulation is hydraulically controlled.

3.2 Circulation in the upstream basin

Figure 9 shows snapshots of the velocity field at day 1, 25 and 150. The circulation in the upstream basin is anti-cyclonic and cyclonic in the downstream basin. The dam break generates waves that propagate with the coast on their right-hand side in both basins. The inflow is directed southward through the channel in the bathymetry. The outflow channel prevents propagation of the signal from Denmark Strait around the downstream basin and back into the upstream basin.

The anti-cyclonic circulation in the upstream basin follows from the potential vorticity budget. Following [13], [18] and [19], and considering $w = w(z)$, $f = f_0 + \beta y$ and after derivation of the model equations ($\zeta = \partial_x(2) - \partial_y(1)$)

$$\mathrm{d}_t(\zeta) + (\zeta + f)\nabla.\underline{u} + \beta v = \nabla \times (\nu \nabla^4 \underline{u}), \tag{4}$$

where ζ is the relative vorticity and d is the Lagrangian derivative. Considering $\mathrm{d}_t = \beta v$

$$\mathrm{d}_t(\zeta + f) + (\zeta + f)\nabla.\underline{u} = \nabla \times (\nu \nabla^4 \underline{u}). \tag{5}$$

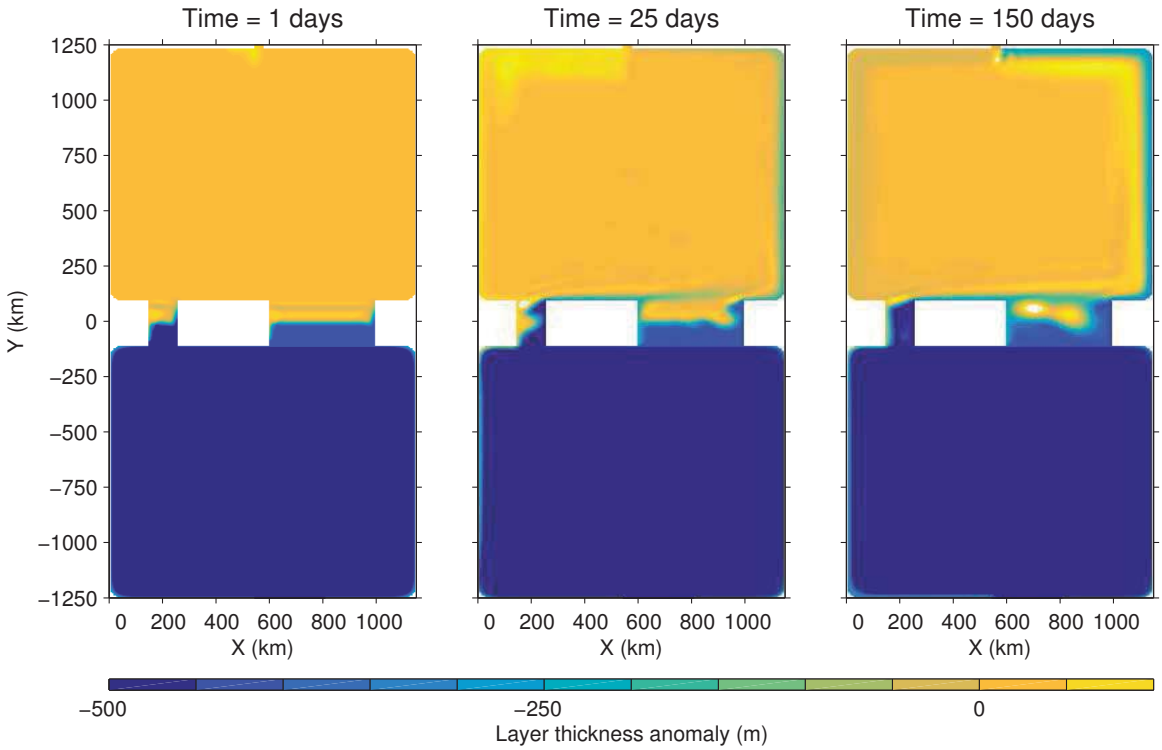

Figure 8: Snapshots of the layer thickness anomaly at different time (from left to right: (a) 1 day, (b) 25 days and (c) 150 days) after the dam breaks and with an inflow/outflow. The latitude is 60° and $\Delta\rho = 0.3$ kg.m^{-3}.

Using the continuity equation and multiplying by $1/H$

$$\mathrm{d}_t\left(\frac{\zeta+f}{H}\right) + \frac{(\zeta+f)}{H}\partial_z w = \frac{1}{H}\nabla\times(\nu\nabla^4\underline{u}). \tag{6}$$

Now in steady state and considering only the vertical component

$$\underline{u}.\nabla\left(\frac{\zeta+f}{H}\right) - \left(\frac{\zeta+f}{H}\right)\partial_z w = \frac{1}{H}\nabla\times(\nu\nabla^4\underline{u}), \tag{7}$$

where the first term is the vorticity advection, the second term is vortex stretching and last term is the friction. $q = \frac{\zeta+f}{H}$ is the potential vorticity. In that case, the vertical component in the potential vorticity budget is small compare to the relative vorticity ζ

$$\nabla.\left(U_h\left(\frac{\zeta+f}{H}\right)\right) = \nabla\times(\nu\nabla^4\underline{u}). \tag{8}$$

After integration over the whole domain and using the Stokes theorem

$$\oint_C(\underline{U}_h.\widehat{n})\left(\frac{\zeta+f}{H}\right)\mathrm{d}S = \int\int_A D_p\mathrm{d}x\mathrm{d}y, \tag{9}$$

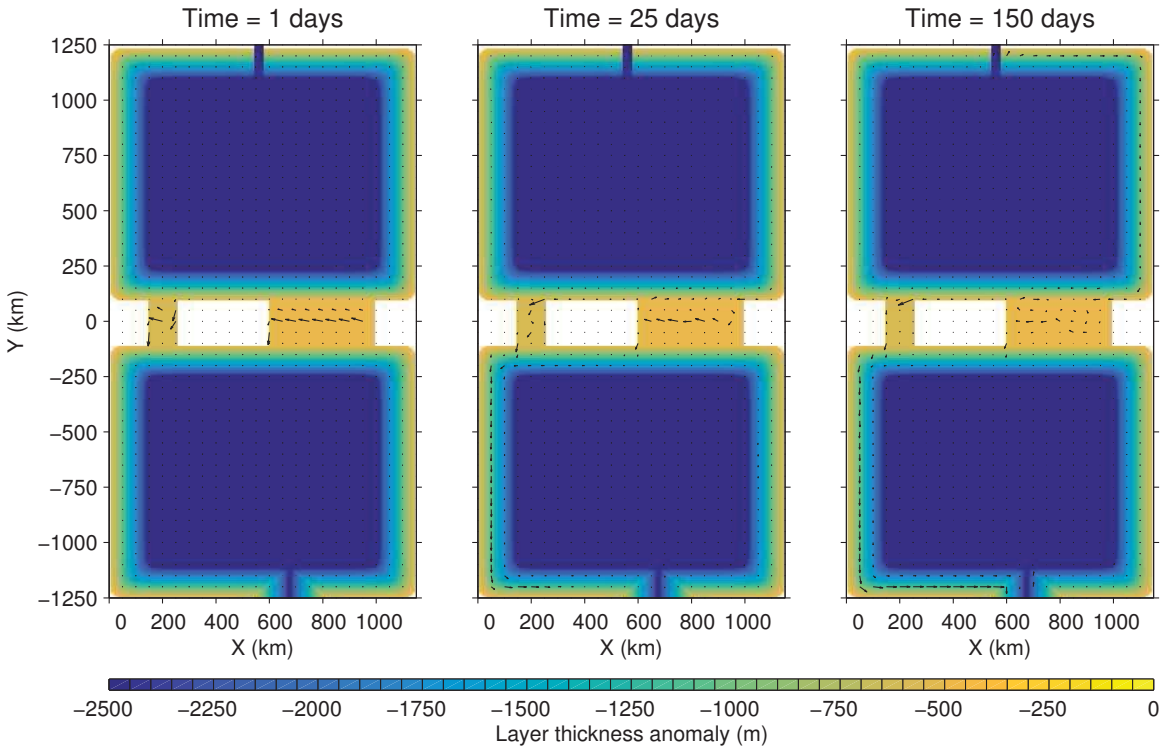

Figure 9: Snapshots of the velocity field (arrows) at different time (from left to right: (a) 1 day, (b) 25 days and (c) 150 days) after the dam breaks and with an inflow/outflow of 3 Sv. Colours represents the bathymetry. The latitude is 60° and $\Delta\rho = 0.3$ kg.m^{-3}.

where $\underline{U}_h = H(u, v)$ and D_p is the curl of the friction. The left hand side in the equation corresponds to the lateral potential vorticity advection and the right hand side to the frictional torque. Considering the relative vorticity ζ is smaller than the planetary vorticity f, the deviation of the layer thickness from the initial value is small, and the friction is approximated as a Rayleigh friction

$$\sum_{i=1}^{N} \frac{Q_i f_i}{H_{0i}} \approx -\lambda \oint_C (\underline{u}.\underline{l}) dS, \tag{10}$$

where u is the tangential velocity along the boundary, Q_i is the volume transport out of the basin across the sill, λ the Rayleigh friction coefficient and l the unit tangential vector.

In our simulations, the inflow channel in the upstream basin is deeper than the Denmark Strait, which induces a positive potential vorticity anomaly and thus an anti-cyclonic circulation. We also find from figure 9 that the current is stronger in the Denmark Strait (depth 600 m) than in the Iceland-Scotland Ridge (depth 520 m). This difference can be explained by lower layer thickness being larger in the case of the Denmark Strait, which induces a smaller potential vorticity frictional torque. The flow chooses preferentially the channel with the smallest potential vorticity frictional torque, or the least resistance.

3.3 Wave response

3.3.1 Kelvin and topographic Rossby waves

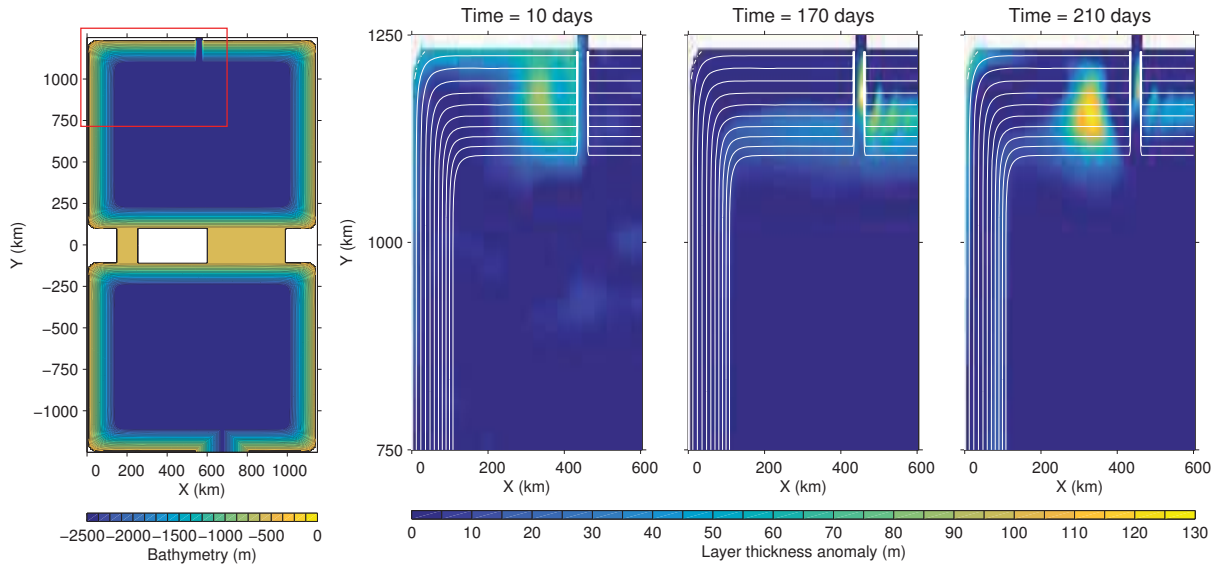

Figure 10: Snapshots of the interface displacement at different times (from left to right: (b) 10 day, (c) 170 days and (d) 210 days) after the dam breaks and with an inflow/outflow. White lines represent the bathymetry in the northwest corner of the upstream basin. The left figure (a) shows the bathymetry of the domain and the location of the zoom (red square). The latitude is 60° and $\Delta\rho = 0.3$ kg.m^{-3}. At 200 days the inflow is temporarily increased to 9 Sv for a period of 5 days.

A close up of the northwest corner of the upstream basin (Fig. 10b) reveals the presence of a fast and narrow wave along the boundary and a second wider and slower-propagating wave on the slope. Both waves propagate around the upstream basin and return to the same location with a smaller intensity (170 days, 10c).

The phase speed of the two waves is shown as a function of density difference $\Delta\rho$ and latitude f (Fig. 11). The Kelvin wave (narrow wave along the boundary) propagates faster than the topographic Rossby wave (wide wave on the slope), around 2 to 4 times faster (Figs. 10 and 11). Kelvin wave phase speed is independent of latitude ($c = \sqrt{g'H}$) but is a function of the stratification through the reduced gravity term ($g' = \Delta\rho/\rho_0$). The numerical results follow the theoretical value of Kelvin qualitatively (Fig. 11a, blue curve - $H = 1131$ m). However the numerics seem to depend on a shallower water depth (black curve - $H = 700$ m). Topographic baroclinic Rossby wave phase speed depends on both latitude and stratification ($c = \beta_{topog} \times R_{bc}^2$ where β_{topog} is the topographic beta and R_{bc} is the baroclinic Rossby radius of deformation). Numerical results follow the theoretical phase speed curves qualitatively (Fig. 11b, dashed curves), but more factors seem to be

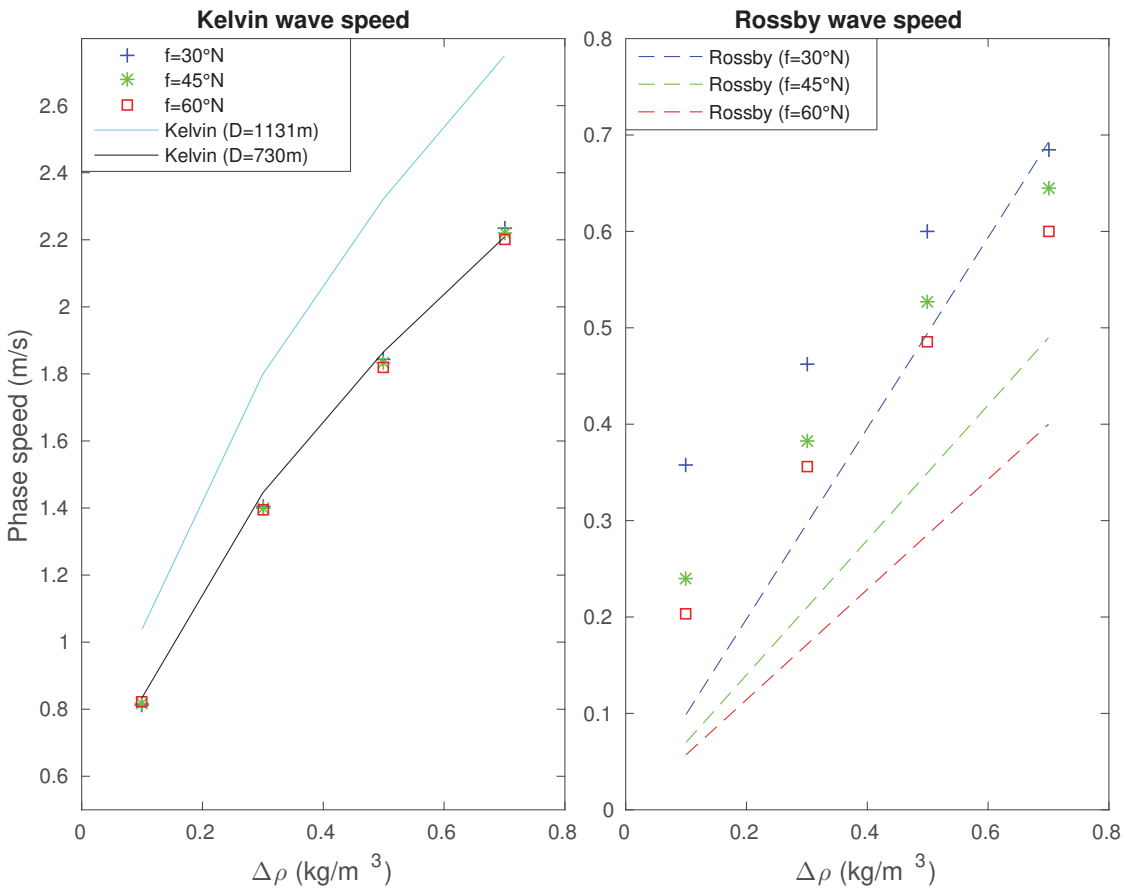

Figure 11: (a) Phase speed of the narrow wave along the boundary as a function of the density difference $\Delta\rho$. The solid blue curve corresponds to the theoretical phase speed of the Kelvin wave for $H = 1131$ m (layer thickness in the model). The solid black curve is the theoretical phase speed of the Kelvin wave for $H = 700$ m. (b) Phase speed of the wide wave on the slope as a function of the density difference $\Delta\rho$. Dashed lines corresponds to the theoretical phase speed of the topographic Rossby wave at different latitudes.

important (amongst the possible candidates are the non-uniform bathymetric slope and the beta plane approximation). The strong dependence on these parameters and their variations in time and in the domain make it difficult to predict the passage of waves at a certain point.

The dam break thus generates an interfacial wave which propagates in the cyclonic direction and it corresponds to a decrease of the interface in the upstream basin. Conversely, the inflow generates 2 waves, a Kelvin wave along the boundary and a topographic Rossby wave on the slope. Both propagate in the cyclonic direction but they correspond to a temporary increase of the interface level.

3.3.2 Response of the DSOW to a 5-day inflow perturbation

After reaching a steady state at 200 days, the inflow is perturbed for a period of 5 days from an initial inflow of 3 Sv to 9 Sv. The density difference $\Delta\rho$ is equal to 0.3 kg.m^{-3} and the latitude is 60°.

Fig. 10d shows the generated Kelvin and topographic Rossby waves at 210 days, so 10 days after the initiation of the perturbation. The 2 new waves have the same phase speed as the ones generated by the initial inflow, as this is a function only of the density difference and the Coriolis frequency, not of the magnitude of the perturbation.

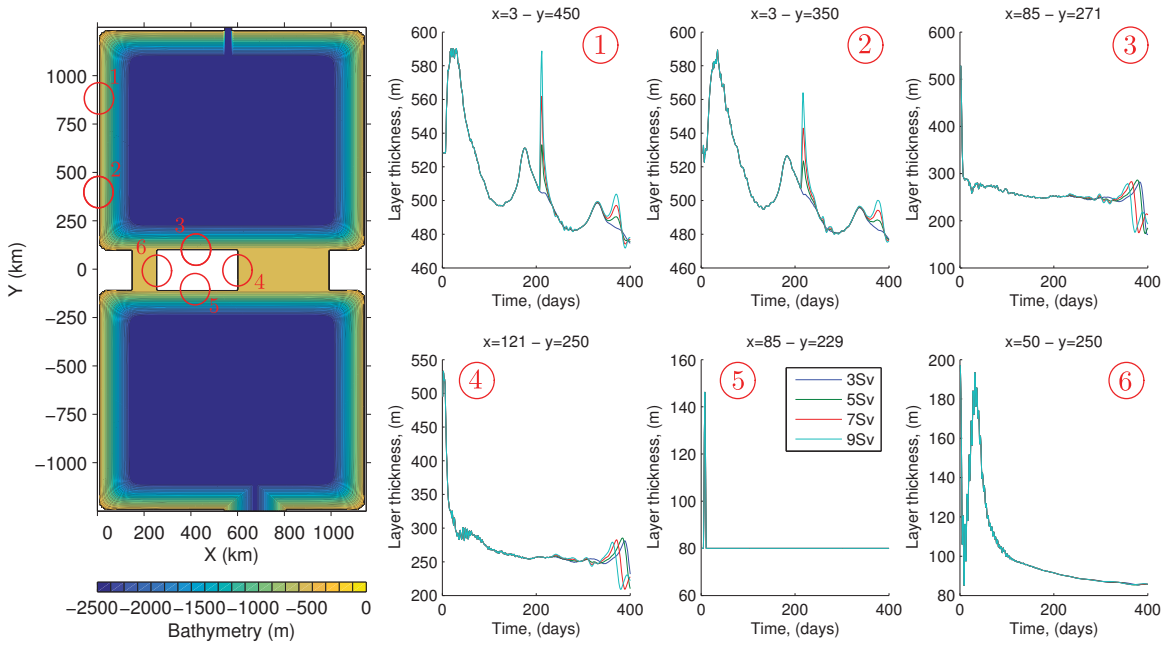

Figure 12: Temporal evolution of the layer thickness in different locations in the control simulation 2 (right) before and after the perturbation and location of the different points in the upstream basin (left).The different color lines correspond at different magnitude of the inflow perturbation transport. The dark blue curve is the control simulation with a constant inflow of 3 Sv during the whole simulation.

The Kelvin wave can be tracked in the upstream basin as a time variation of the layer thickness. In Fig. 12, one can see the time evolution of the layer thickness close to the boundary in several locations as indicated in Figures 12a. At points 3, 4 and 5, the rapid decrease in lower-layer thickness as a result of the Denmark Strait dam break is again clearly visible at the start of the simulation. At points 1 and 2, the signal of the wave generated by the dam breaks is modified by the one generated by the initial inflow. The initial Kelvin wave travels around the upstream basin in about 170 days and we can see its effect on the layer thickness, which increases at each passage. 170 days is larger than the time necessary with the initial phase speed (around 1.4 m/s). This can be due to the variation of the layer

thickness around the upstream basin. In the eastern part, the layer thickness is thinner in response to the dam break, which decreases the phase speed ($c = \sqrt{g'H}$). Furthermore, the magnitude of the Kelvin wave decreases at each passage (for example at point 1, 1st passage: 590 m, 2nd passage: 530 m and 3rd passage: 500 m).
At 200 days, the inflow perturbation imposed induces a signal in the layer thickness. This signal is proportional to the amplitude of the inflow transport perturbation (indicated by the different color lines in Fig. 12) and decreases rapidly (difference of magnitude between point 1 and 2). It also propagates around the upstream basin and modifies the layer thickness temporarily. At point 3, after 300 days, the passage of the waves modifies the circulation (not shown) at the entrance of the Denmark Strait, which permits the Kelvin wave to propagate along the northern coast of Iceland and to interact with the circulation at this location. The signal is also visible at point 4. That could be the propagation of the Kelvin wave around Iceland.

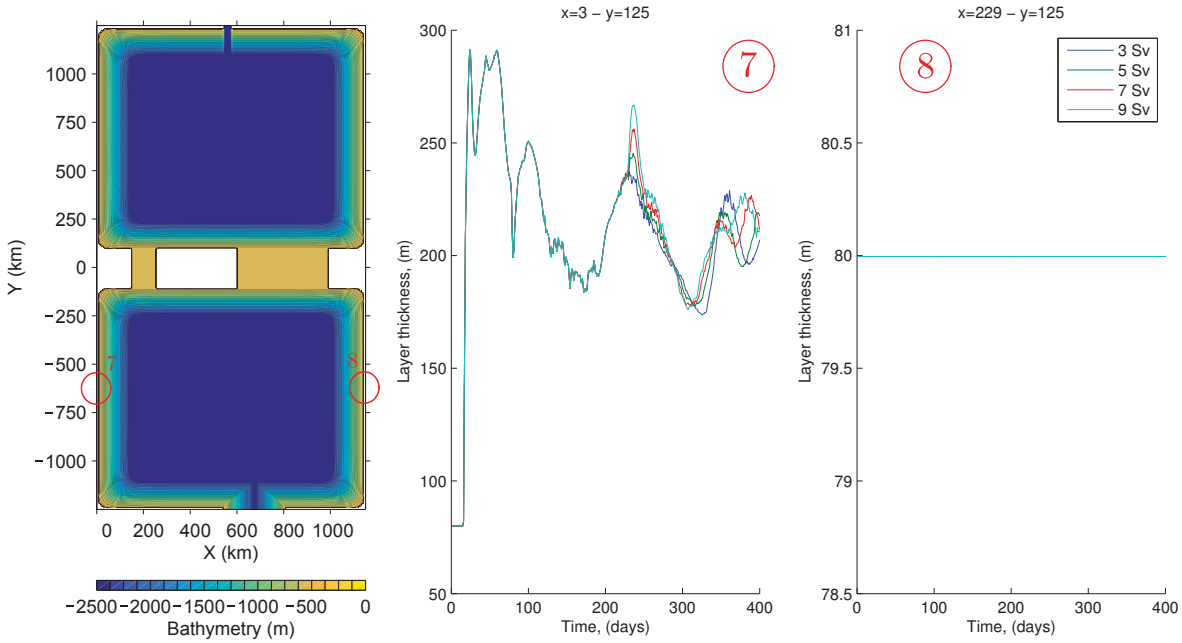

Figure 13: Temporal evolution of the layer thickness in different locations in the control simulation 2 (right) before and after the perturbation and location of the different points in the upstream basin (left). The different color lines correspond to different magnitude of the inflow perturbation transport. The dark blue curve is the control simulation with a constant inflow of 3 Sv during the whole simulation.

The Kelvin wave signal can be also tracked in the downstream basin (Fig. 13). At point 7, downstream of Denmark Strait, the interface is first perturbed at around 20 days as a results of both Denmark Strait dam break and the upstream basin inflow. After the steady state is reached (after 200 days), we can identify the presence of the Kelvin wave induced by the inflow perturbation. Just after 200 days, the signal of the initial inflow Kelvin wave and the one from the perturbation seem to coincide in the downstream basin and after the

second round of the initial and of the perturbation Kelvin waves seems to be dissociated. The Kelvin waves seem to be reflected at the sill and thus propagate all around the upstream basin but a part seems to cross the sill and propagate in the downstream basin. At point 8, there is no signal of the Kelvin waves perhaps as a result of the presence of the outflow channel. It is difficult to predict when the Kelvin wave will arrive at a certain point because the phase speed of the Kelvin wave depends on the layer thickness and this layer thickness varies in time around the upstream basin but also in the downstream basin.

4 Discussion and conclusions

The 1.5-layer reduced gravity model with or without an inflow induced an anti-cyclonic circulation in the upstream basin due to the potential vorticity balance. Unfortunately this model cannot reproduce the deep circulation of the Nordic Seas (cyclonic circulation). A way to obtain the proper cyclonic circulation like the Nordic Seas circulation, is to use a 2-layer reduced gravity model forced by a wind stress. The wind-stress term will appear in the potential vorticity budget, which will modify the potential vorticity balance and induce a cyclonic circulation in the upstream basin. This kind of model has already been used by [17]. In this study, they have a realistic bathymetry of the Nordic Seas and they force the 2-layer reduced gravity model with a positive wind stress curl and they add a uniform wind stress forcing between the 2 layers. With this setup, they obtain the main components of the Nordic Seas circulation (southward and eastward current along Iceland-Faroe ridge, eastward extension of NIJ, strong western boundary current, EGC and sEGC).
The simulations are hydraulically controlled (based on the interface displacement argument) but, in our case, the local Froude number criterium does not work very well because the model uses the no-slip condition. If we want to use the local Froude number as a criterium to confirm the hydraulic control, a free-slip boundary condition would be a better choice. In the case of a free-slip condition, a bottom drag needs to be added for dissipation. New simulations with a free-slip boundary condition and a bottom drag would be a cleaner way to study the effect of an inflow perturbation at the Denmark Strait.
Mastropole et al. [9] and Von Appen et al. [15] show the presence of boluses (cold and salty anomalies with a cyclonic vorticity and a periodicity of 3.4 days) and pulses (lighter overflow water with an anticyclonic vorticity and a periodicity of 5.6 days) at the Denmark Strait. These phenomena could be a manifestation of the propagation of the Kelvin and topographic Rossby waves around Iceland. So, with a free-slip condition it is possible to study the circulation around Iceland and to see if the Kelvin and topographic Rossby modify the circulation.

The 1.5-layer reduced gravity model is a good first step (it runs much faster than the 2-layer model) to study the effect of the Kelvin and topographic Rossby waves on the transport through the Denmark Strait. The presence of virtual dams permits obtaining a hydraulically controlled flow and thus transmitting the wave information in the upstream basin. The dam beak should generate a wave in both the upstream and the downstream basins but we focus our study on the upstream basin where the waves can modify the amount of

dense overflow water at the Denmark Strait. The constant inflow/outflow plus the dam break generates a strong and steady circulation. This circulation is modified when the inflow transport is perturbed for a short period. The inflow perturbation generates a Kelvin and a topographic Rossby wave, which propagate cyclonically along the boundary in both the upstream and the downstream basins. Those two waves can interact with the sill and by reflection continue to propagate in the upstream basin or to cross the sill and propagate in the downstream basin. They modify temporarily the layer thickness and thus the transport through the Denmark Strait.

The next step is to run simulations with the 1.5-layer reduced gravity model and the free-slip condition for a longer period to achieve a clean steady state. After obtaining a steady circulation, we will impose a short perturbation and study in more details the effect of the waves on the circulation and the transport through the Denmark Strait. Once we understand this problem, we will use a 2-layer reduced gravity model with the realistic bathymetry and perturb the steady state to see if it is possible to obtain boluses and pulses and how these perturbations can change the circulation and the transport of DSOW through the Denmark Strait.

References

[1] R. R. Dickson and J. Brown, *The production of north atlantic deep water: sources, rates, and pathways*, Journal of Geophysical Research: Oceans, 99 (1994), pp. 12319–12341.

[2] J. B. Girton, L. J. Pratt, D. A. Sutherland, and J. F. Price, *Is the Faroe Bank Channel overflow hydraulically controlled?* Journal of Physical Oceanography, 36 (2006), pp. 2340–2349.

[3] B. Hansen and S. Østerhus, *Faroe Bank Channel overflow 1995–2005*, Progress in Oceanography, 75 (2007), pp. 817–856.

[4] B. Hansen, S. Østerhus, W. R. Turrell, S. Jónsson, H. Valdimarsson, H. H´at´un, and S. M. Olsen, *The inflow of Atlantic water, heat, and salt to the Nordic Seas across the Greenland–Scotland Ridge*, in Arctic–Subarctic Ocean Fluxes, (2008), pp. 15–43.

[5] B. E. Harden, R. S. Pickart, H. Valdimarsson, K. V ° age, L. de Steur, C. Richards, F. Bahr, D. Torres, E. Børve, S. J´onsson, et al., *Upstream sources of the Denmark Strait Overflow: Observations from a high-resolution mooring array*, Deep Sea Research Part I: Oceanographic Research Papers, 112 (2016), 94-112.

[6] T. Hattermann, P. E. Isachsen, W.-J. von Appen, J. Albretsen, and A. Sundfjord, *Eddy-driven recirculation of Atlantic water in Fram Strait*, G e o p h y s i c a l Research Letters, 43 (2016), pp. 3406–3414.

[7] K. Jochumsen, D. Quadfasel, H. Valdimarsson, and S. Jonsson, *Variability of the Denmark Strait Overflow: Moored time series from 1996–2011*, Journal of Geophysical Research: Oceans, 117 (2012), C12003.

[8] S. Jonsson, *The circulation in the northern part of the Denmark Strait and its variability,* ICES CM L:06, ICES Journal of Marine Science (1999).

[9] D. Mastropole, R. S. Pickart, H. Valdimarsson, K. Vage, K. Jochumsen, and J. B. Girton, *Hydrographic structure of overflow water passing through Denmark Strait,* Journal of Geophysical Research, 122, (2017), pp. 306-321.

[10] C. Mauritzen, *Production of dense overflow waters feeding the North Atlantic across the Greenland-Scotland Ridge. Part 1: Evidence for a revised circulation scheme*, Deep Sea Research Part I: Oceanographic Research Papers, 43 (1996), pp. 769–806.

[11] A. Nikolopoulos, K. Borenäs, R. Hietala, and P. Lundberg, *Hydraulic estimates of Denmark Strait Overflow*, Journal of Geophysical Research: Oceans, 108 (2003).

[12] L. Pratt and J. A. Whitehead, *Rotating hydraulics*, Rotating Hydraulics, by LLJ Pratt and JA Whitehead. Berlin: Springer, 2008. ISBN 978-0-387-36639-5, 1 (2008).

[13] L. J. Pratt and S. G. Llewellyn Smith, *Hydraulically drained flows in rotating basins. Part* I*: Method*, Journal of Physical Oceanography, 27 (1997), pp. 2509–2521.

[14] K. Våge, R. S. Pickart, M. A. Spall, G. Moore, H. Valdimarsson, D. J. Torres, S. Y. Erofeeva, and J. E. Ø. Nilsen, *Revised circulation scheme north of the Denmark Strait*, Deep Sea Research Part I: Oceanographic Research Papers, 79 (2013), pp. 20–39.

[15] W.-J. Von Appen, D. Mastropole, R. S. Pickart, and J. B. Girton, *On the nature of the mesoscale variability in Denmark Strait*, Journal of Physical Oceanography, 47, (2016), pp. 567-582..

[16] J. Whitehead, A. Leetmaa, and R. Knox, *Rotating hydraulics of strait and sill flows*, Geophysical and Astrophysical Fluid Dynamics, 6 (1974), pp. 101–125.

[17] J. Yang and L. J. Pratt, *Some dynamical constraints on upstream pathways of the Denmark Strait Overflow*, Journal of Physical Oceanography, 44 (2014), pp. 3033–3053.

[18] J. Yang and J. F. Price, *Water-mass formation and potential vorticity balance in an abyssal ocean circulation*, Journal of Marine Research, 58 (2000), pp. 789–808.

[19] J. Yang and J. F. Price, *Potential vorticity constraint on the flow between two basins*, Journal of Physical Oceanography, 37 (2007), pp. 2251–2266.

A Vortex Method for Modeling Multiple Wakes

Paula Doubrawa

October 16, 2016

1 Introduction

The concept of vortex sheets has been widely used to model free shear layers resulting from the interactions of fluid flow and solid bodies [10, 11]. Vorticity is a particularly appealing quantity because it fully describes the flow if incompressibility can be assumed. Additionally to incompressibility, the flow is often assumed to be irrotational for mathematical and computational tractability. Potential flow theory can therefore be used, and the continuous vortex sheet is modeled as a finite number of discrete point vortices [7]. The number of point vortices used governs the resolution obtained with the model, and should be determined based on the available computational resources and the level of detail required for the problem. Two distinct approaches can be found in literature for two-dimensional modeling of vortex shedding in the wake of a solid body in potential flow. The more expensive alternative sheds a new steady vortex at every time step [4, 9] resulting in a high fidelity description of a continuous vortex sheet. In [9], the strength of the shed vortex is such that it bounds the velocity everywhere in the flow, thus satisfying the unsteady Kutta condition. The high resolution discretization of the bound and free vortex sheets in this method is shown in Fig. 1. Alternatively, fewer vortices can be shed if their circulation is allowed to be unsteady as shown in Fig. 2. In this case, continuous vortex shedding is not necessary to satisfy flow regularity conditions. The unsteady vortex evolves until its intensity reaches a maximum, which signals rolling up of the vortex sheet, triggers new shedding [12], and freezes the circulation of the previously shed vortices.

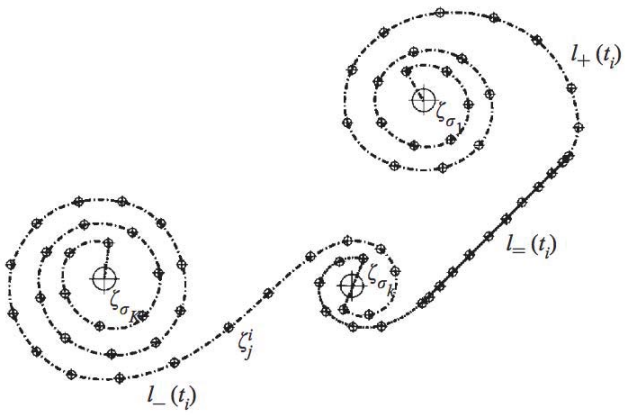

Figure 1: Discretization of bound vortex sheet ($l_=$) and free vortex sheets (l_+ and l_-) from [9], where a flat plate moves through a flow generating trailing vortices.

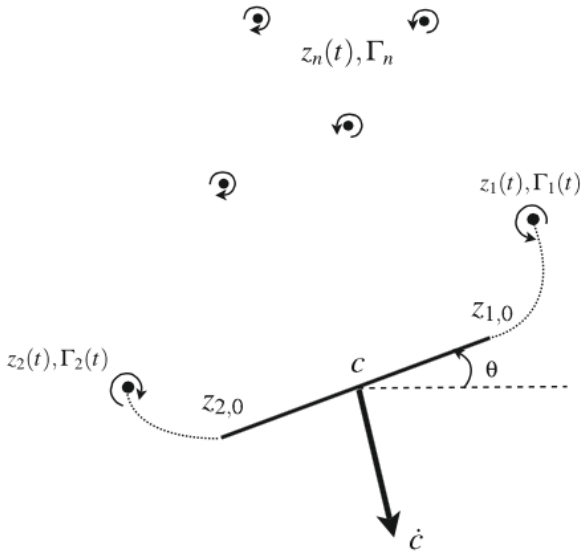

Figure 2: Schematic of vortex shedding around a falling card in the work of [12] where c indicates the center of gravity, subscripts 1 and 2 are the currently shed vortices location z and strength Γ, and subscript n the previously shed vortices.

In this work, the main objective is to model the vorticity field in the wake of multiple oscillating foils. The continuous shedding framework of [9] allows for inclusion of multiple plates if the added computational cost can be tackled. Conversely, the less expensive methodology of [12] does not allow for it because it uses conformal mapping to solve for the potential flow, which becomes difficult when multiple propulsive surfaces are considered. Our approach addresses these difficulties and produces a method where individual ellipses can move independently, and the number of variables to represent the ellipse are minimal. This benefit comes at the cost of using the Brown and Michael formulation [3], which yields a system of differential algebraic equations. We provide a detailed methodology to solve this system of equations for the vorticity field.

The novel approach proposed in this report also allows to solve for the distribution of vorticity at a manageable computational cost. This is needed because of the motion of the foils, which may lead to interaction between vorticity shed by the trailing and leading edges of the foils (resulting in resonance or annihilation of the lift on the surfaces [6]) or to interaction between the leading foil vorticity field with the trailing foil [1]. Therefore, describing the shed vorticity by a single vortex and neglecting the remainder of the vorticity in the free vortex sheet is not a good approach for this application. Likewise, shedding a vortex at each time step is likely to result in an extremely high computational cost once multiple foils are considered. The presented model builds on previously proposed techniques and reaches a compromise between the two previously described methods. The unsteady vortex shedding approach of [12] is used but unsteady vortices are shed

from the separation point at a higher frequency. New shedding is triggered based on the distance of the unsteady vortices from the plate tip, and the threshold maximum distance for a vortex to remain unsteady is a model parameter provided by the user. This results in a more detailed representation of the vorticity distribution close to and away from the shedding body, without the need to shed a vortex at each time step. This report describes the model development (Section 2), numerical implementation (Section 3), and results for a test simulation (Section 4).

2 Model Development

2.1 Potential Flow

Although the algorithms were developed in a modular and flexible manner and can be easily extended to a variety of problems, the original motivation for the model development is high Reynolds number flow past oscillating hydrofoils where the wake has forced (i.e., due to the foil motion) and unforced components. In the limit of infinite Reynolds number, the effect of viscosity is limited to a very shallow boundary layer and the outer fluid can be assumed inviscid. For the wake flows considered, the effects of viscosity are limited to the shedding of vorticity [11, 9] and can be treated separately from the outer flow which can be assumed to be irrotational and modeled with potential flow theory. The complex potential

$$w(z) \equiv \phi + i\psi \tag{1}$$

is defined in terms of the velocity potential ϕ (recall $\vec{u} = \nabla\phi$) and the streamfunction ψ (recall $\nabla \times \psi = \vec{u}$) for points on the complex plane $z = x + iy$. For flow past an oscillating flat ellipse, the total instantaneous potential at any point is described in the model as

$$\begin{aligned} w(z) = & \underbrace{\overline{V} z}_{\text{I}} + \underbrace{\sum_{v=1}^{N_v} \left[\frac{i\Gamma_v}{2\pi} \log\left(z - z_v\right) \right]}_{\text{II}} \\ & + \underbrace{\sum_{v=1}^{N_v} \left\{ \frac{i\Gamma_v}{2\pi} \sum_{\varepsilon=1}^{N_\varepsilon} \left[-\log\left(\frac{a_\varepsilon}{2}\right) + \log\zeta_\varepsilon - \log\left(\frac{1}{\zeta_\varepsilon} - \overline{\zeta}^{+}_{v,\varepsilon}\right) - \log\left(\zeta_\varepsilon - \zeta^{-}_{v,\varepsilon}\right) \right] \right\}}_{\text{III}} \\ & + \underbrace{\sum_{\varepsilon=1}^{N_\varepsilon} \left[\frac{i\Gamma_{0,\varepsilon}}{2\pi} \log\zeta_\varepsilon \right]}_{\text{IV}} + \underbrace{\sum_{\varepsilon=1}^{N_\varepsilon} \sum_{p=1}^{N_p} \frac{c_{p,\varepsilon}}{\zeta_\varepsilon^p}}_{\text{V}} \end{aligned} \tag{2}$$

where a linear superposition of different contributions ensures regularity in the flow. The flow velocity in the physical plane can be easily obtained from the complex potential as

$$u = \overline{\frac{dw}{dz}} \tag{3}$$

Throughout this report, the overbar represents the complex conjugate. The terms in Eq. (2) represent contributions from (I) the free stream, (II) the vortices in the flow, (III) the image vortices that model the presence of the ellipses in the domain, (IV) the bound vortex at the center of each ellipse, and (V) the residual necessary to fully enforce the no-penetration condition at each ellipse. Equation (2) is derived for N_v vortices and N_ε ellipses, and a detailed description of terms III-V is given in Sections 2.1.1 to 2.1.3.

2.1.1 Conformal Map

The solid bodies in the model are flat plates approximated as thin ellipses. In order to include their effect on the flow and to enforce regularity conditions it is convenient to use conformal mapping. The function

$$z = \frac{1}{2}\left[a_\varepsilon \zeta_\varepsilon e^{-i\alpha_\varepsilon} + \frac{b_\varepsilon}{\zeta_\varepsilon e^{-i\alpha_\varepsilon}}\right] e^{i\alpha_\varepsilon} + h_\varepsilon \tag{4}$$

maps spatial points between the physical plane (z-plane) and the circle plane of a specific ellipse (ζ_ε-plane). The ellipses are defined by a major ($a_\varepsilon + b_\varepsilon$) and a minor ($a_\varepsilon - b_\varepsilon$) axis, and the minor axis is taken to zero for the flat plate limit. The ellipse center h_ε and angle of attack α_ε are defined in the physical plane and can be a function of time for oscillating plates.

By defining

$$\tilde{z} = (z - h_\varepsilon)\, e^{-i\alpha_\varepsilon}$$
$$\tilde{\zeta_\varepsilon} = \zeta_\varepsilon e^{-i\alpha_\varepsilon}$$

and solving the quadratic equation $a_\varepsilon \tilde{\zeta_\varepsilon}^2 - 2\tilde{z}\tilde{\zeta_\varepsilon} + b_\varepsilon = 0$ the inverse map

$$\tilde{\zeta_\varepsilon} = \frac{\tilde{z} \pm \sqrt{\tilde{z}^2 - a_\varepsilon b_\varepsilon}}{a_\varepsilon} \tag{5}$$

can be obtained, with the square root sign matching the sign of the real part of z.

2.1.2 Image Potential

The effect of the solid body on the flow is modeled in two parts. First, its response to the presence of vortices is included. For each vortex in the flow, an image vortex is added inside the ellipse using the Milne-Thomson circle theorem

$$w_{i,\varepsilon} = \overline{w_v\left(\frac{1}{\overline{\zeta_\varepsilon}}\right)} \tag{6}$$

where w_v and w_i are the potential due to the vortex and its image respectively, both defined in the circle plane of ellipse ε and evaluated at point ζ_ε.

The potential in the physical plane due to a vortex is given by

$$w_v(z) = \frac{i\Gamma_v}{2\pi} \log(z - z_v) \tag{7}$$

and an expression equation can be derived using circle-plane coordinates by combining this expression and the conformal map (Eq. (4))

$$w_v = \frac{i\Gamma_v}{2\pi} \log \left[\frac{1}{2} \left(a\zeta + \frac{b}{\zeta} \right) - z_v \right]$$

multiplying the log argument by 2ζ

$$w_v \propto \frac{i\Gamma_v}{2\pi} \log \left[a\zeta^2 - z_v\zeta + b \right]$$

and factorizing it

$$w_v \propto \frac{i\Gamma_v}{2\pi} \log \left[\frac{a}{2\zeta} \underbrace{(\zeta - \zeta_v^+)}_{\text{I}} \underbrace{(\zeta - \zeta_v^-)}_{\text{II}} \right]$$

where term (I) represents a vortex outside the circle, and term (II) a vortex inside the circle. Employing the Milne Thomson circle theorem to the vortex outside the circle, the total contribution of image vortices to the potential at a point ζ_ε is given by

$$w_i(\zeta_\varepsilon) = \sum_{v=1}^{N_v} \sum_{\varepsilon=1}^{N_\varepsilon} \frac{i\Gamma_v}{2\pi} \left[-\log\left(\frac{a_\varepsilon}{2}\right) + \log \zeta_\varepsilon - \log\left(\frac{1}{\zeta_\varepsilon} - \overline{\zeta}_{v,\varepsilon}^+\right) - \log\left(\zeta_\varepsilon - \zeta_{v,\varepsilon}^-\right) \right] \tag{8}$$

2.1.3 Series Potential

If more than one ellipses are present in the domain, the addition of an image vortex in any ellipse requires adding an image of the image to all of the other ellipses, *ad infinitum*. To circumvent this, a series of monomials is used to account for the effect of the solid body on the flow in response to the addition of the image vortices, and in response to the free stream. Potential flow around a smooth body can be defined by a linear superposition of singularities, expressed as a partial sum of the Laurent Series

$$f(\zeta) = \sum_{p=-\infty}^{\infty} c_p \left(\zeta - \zeta_0\right)^p$$

For $p < 0$ (i.e. the principal part of the series) monomials are poles of order p with a singularity at ζ_0. For the conformal map used (Eq. (4)) the expansion point is the origin $\zeta_0 = 0$. The residual of the potential that violates the no-penetration condition

$$u(z_\varepsilon) \cdot \hat{n}_\varepsilon = 0 \tag{9}$$

can therefore be described by the linear superposition of a point source and N_p poles

$$w_s(\zeta_\varepsilon) = \sum_{\varepsilon=1}^{N_\varepsilon} \left[\frac{i\Gamma_{0,\varepsilon}}{2\pi} \log \zeta_\varepsilon \right] + \sum_{\varepsilon=1}^{N_\varepsilon} \sum_{p=1}^{N_p} \frac{c_{p,\varepsilon}}{\zeta_\varepsilon^p} \tag{10}$$

where $\Gamma_{0,\varepsilon}$ is the circulation of the bound vortex located in the center of the ellipse. It is determined by enforcing Kelvin's circulation theorem, which states that the total circulation must be zero around a closed contour for a system that is impulsively started from rest.

The coefficients $c_{p,\varepsilon}$ are determined by enforcing a no-penetration condition on the ellipse and for simplicity is done outside of the system of equations. For a domain with a single ellipse, the only contribution to the series is the ellipse response to the free stream and there are N_p coefficients, where N_p is the number of points chosen by the user to describe the ellipse geometry. For a domain with N_ε ellipses, $N_p N_\varepsilon$ coefficients must be determined.

The velocity in the physical plane u is related to the velocity in the circle plane U by

$$u(z) = \frac{dw}{d\zeta_\varepsilon}\frac{d\zeta_\varepsilon}{dz} = U_\varepsilon \frac{d\zeta_\varepsilon}{dz} = \frac{U}{g'} \tag{11}$$

where g is the conformal map (Eq. (4)), $g' = \frac{dz}{d\zeta_\varepsilon}$, and capital U_ε is used to describe velocities in circle plane ε. To enforce the no penetration condition the series velocity must cancel the normal component of the velocity U_ε. Consider a point in the circle plane $e^{i\theta}$ where θ is the local azimuth angle. The unit tangent $\hat{t}$ to the circle is therefore

$$\hat{t} = \frac{g'(e^{i\theta})}{|g'(e^{i\theta})|} = ie^{i\theta} g'(e^{i\theta})$$

and the unit normal is $\hat{n} = -i\hat{t}$

$$\hat{n} = \Re\left\{ e^{i\theta} \frac{g'(e^{i\theta})}{|g'(e^{i\theta})|} \right\}$$

The velocity we seek to describe by the series is aligned with the inward normal direction and is therefore

$$\begin{aligned} u_s &= \Re\left\{ \frac{U}{g'} \frac{e^{-i\theta}\overline{g'}}{|g'|} \right\} \\ &= \Re\left\{ e^{-i\theta} \frac{U}{|g'|} \right\} \end{aligned} \tag{12}$$

The values of U_ε are known and represent the contribution to the normal velocity from the free stream, the vortices, and the images. Since we are seeking only the real part of U_ε,

$$u_s \left|g'\right| = e^{-i\theta} \Re\left\{ \sum_{p=1}^{N_p} c_p e^{-ip\theta_p} \right\} \tag{13}$$

and a Fast Fourier Transform (FFT) can be used to determine the series coefficients a_p that cancel the velocities penetrating the solid body.

2.2 System of Equations

At each time step there are $4N_\varepsilon + N_v$ equations and unknowns in the system, which account for the evolution of the unsteady ($\dot{z}_v$ and $\dot{\Gamma}_v$, 2 per ellipse therefore $4N_\varepsilon$ unknowns) and steady ($\dot{z_v}$) vortices. The evolution of the unsteady vortices

$$\Gamma_v \dot{z}_v = \underbrace{\Gamma_v u_{ds}(z_v)}_{\text{I}} - \underbrace{(z_v - z_t)\,\dot{\Gamma}_v}_{\text{II}} \tag{14}$$

is determined by (I) its self-advection and (II) the Brown and Michael correction [3]. The self-advection of the vortex is given by the desingularized velocity at its location

$$u_{ds}(z_v) = \lim_{z \to z_v} \left\{ \frac{d}{dz} \left[w - \frac{i\Gamma_v}{2\pi} \log\left(z - z_v\right) \right] \right\} \tag{15}$$

and the correction term in Eq. (14) is added to ensure zero net force on the vortex system, which are disturbed by the inclusion of a feeding vortex sheet [3]. The correction is scaled by the distance between the vortex (z_v) and the ellipse tip (z_t) from which it was shed. The strength of the unsteady vortices is determined by enforcing the unsteady Kutta condition

$$U(\zeta_t) = 0 \tag{16}$$

in the circle plane of each ellipse. After the locations and strenghts of the unsteady vortices are computed, the Kelvin Circulation Theorem is enforced by adjusting the circulation of the bound vortex in the center of the ellipse

$$\dot{a}_0 + \dot{\Gamma}_1 + \dot{\Gamma}_2 = 0 \tag{17}$$

to cancel the circulation of both vortices being shed by that ellipse. Note that the subscripts 1 and 2 differentiate between quantities related to either of the plate tips, and the subscript v refers to any vortex location. Once a shed vortex reaches a maximum user-defined distance from the plate tip (Δz_{max}), it is turned to a steady vortex that moves with the flow maintaining a constant circulation. Its motion is determined by the desingularized potential

$$\dot{z}_v = u_{ds}(z_v) \tag{18}$$

and therefore there is one equation per steady vortex in the system. The system of equations for a domain with a single ellipse, two unsteady vortices, and a single steady vortex therefore is

$$\Gamma_1 \dot{z}_1 - \Gamma_1 u_{ds}(z_1) + (z_1 - z_{t,1})\,\dot{\Gamma}_1 = 0 \tag{19a}$$
$$\Gamma_2 \dot{z}_2 - \Gamma_2 u_{ds}(z_2) + (z_2 - z_{t,2})\,\dot{\Gamma}_2 = 0 \tag{19b}$$
$$U(\zeta_{t,1}) = 0 \tag{19c}$$
$$U(\zeta_{t,2}) = 0 \tag{19d}$$
$$\dot{z}_v - u_{ds}(z_v) = 0 \tag{19e}$$

3 Numerical Implementation

3.1 Time Discretization

The evolution of the steady vortices is given by an analytical equation (Eq. (19e)) and can therefore be easily determined at any instant. The equations for the shed vortices (Eqs. (19a) to (19d)) need to be solved together to ensure that the unsteady Kutta condition is satisfied. Using forward differencing,

$$\Gamma_v^{n+1} = \Gamma_v^n + \Delta\Gamma_v$$
$$z_v^{n+1} = z_v^n + \Delta z_v$$

Eqs. (19a) to (19d) become

$$\Gamma_v \Delta z_v + (z_v - z_t)\Delta\Gamma_v = \Gamma_v u_{ds}(z_v)\Delta t$$
$$\Gamma_2 \Delta z_2 + (z_2 - z_{t,2})\Delta\Gamma_2 = \Gamma_2 u_{ds}(z_2)\Delta t$$
$$\frac{dU}{d\Gamma_1}(\zeta_{t,1})\Delta\Gamma_1 + \frac{dU}{d\Gamma_2}(\zeta_{t,1})\Delta\Gamma_2 + \frac{dU}{dz_1}(\zeta_{t,1})\Delta z_1 + \frac{dU}{dz_1}(\zeta_{t,1})\Delta z_2$$
$$\frac{dU}{d\Gamma_1}(\zeta_{t,2})\Delta\Gamma_1 + \frac{dU}{d\Gamma_2}(\zeta_{t,2})\Delta\Gamma_2 + \frac{dU}{dz_1}(\zeta_{t,2})\Delta z_1 + \frac{dU}{dz_1}(\zeta_{t,2})\Delta z_2$$

and can be further simplified by letting

$$\widetilde{\Delta z}_v = \Gamma_v \frac{\Delta z_v}{\Delta t}$$
$$\widetilde{\Delta\Gamma}_v = (z_v - z_t)\frac{\Delta\Gamma_v}{\Delta t}$$

where v is a place holder for indices 1 or 2. The final system to be solved is therefore

$$\widetilde{\Delta z}_1 + \widetilde{\Delta\Gamma}_1 = \Gamma_1 u_{ds}(z_1) \tag{20a}$$
$$\widetilde{\Delta z}_2 + \widetilde{\Delta\Gamma}_2 = \Gamma_2 u_{ds}(z_2) \tag{20b}$$
$$\frac{dU}{dz_1}(\zeta_{t,1})\frac{\widetilde{\Delta z}_1}{\Gamma_1} + \frac{dU}{dz_2}(\zeta_{t,1})\frac{\widetilde{\Delta z}_2}{\Gamma_2} + \frac{dU}{d\Gamma_1}(\zeta_{t,1})\frac{\widetilde{\Delta\Gamma}_1}{z_1 - z_{t,1}} + \frac{dU}{d\Gamma_2}(\zeta_{t,1})\frac{\widetilde{\Delta\Gamma}_2}{z_2 - z_{t,2}} = 0 \tag{20c}$$
$$\frac{dU}{dz_1}(\zeta_{t,2})\frac{\widetilde{\Delta z}_1}{\Gamma_1} + \frac{dU}{dz_2}(\zeta_{t,2})\frac{\widetilde{\Delta z}_2}{\Gamma_2} + \frac{dU}{d\Gamma_1}(\zeta_{t,2})\frac{\widetilde{\Delta\Gamma}_1}{z_1 - z_{t,1}} + \frac{dU}{d\Gamma_2}(\zeta_{t,2})\frac{\widetilde{\Delta\Gamma}_2}{z_2 - z_{t,2}} = 0 \tag{20d}$$

The coefficients are used to generate a matrix which is inverted to solve for the unknowns. The time discretization uses forward differencing for z and central differencing for Γ.

3.2 Time Integration

Time integration is done using fractional time stepping and the system dynamics is decomposed

$$\frac{dy}{dt} = L_1(y) + L_2(y)$$

where L_1 and L_2 are differential operators for a linear dynamical system, and the solution is obtained by using Strang splitting [13]

$$y = e^{\frac{1}{2}\Delta t L_1} e^{\Delta t L_2} e^{\frac{1}{2}\Delta t L_1} y_0$$

where each time integration consists in (i) taking a half time step for dynamics L_1, (ii) a full time step for dynamics L_2, and (iii) a half time step for dynamics L_1. For the model being presented, L_1 and L_2 correspond to the evolution of the unsteady and steady vortices, respectively.

3.3 Time Stepping

The initial time step is prescribed by the user and adaptive time stepping is used within the model to speed up calculations while ensuring stability (if no value is provided, the model defaults to $\Delta t_0 = 1.5 \times 10^{-7}$). The decision to increase or decrease the time step Δt is given by the ℓ^2 norm

$$\|\epsilon\|^2 = \sum_{j=1}^{N} \left| \mathbf{x}_j^{n+\frac{1}{2}\Delta t} - \mathbf{x}_j^{n+\Delta t} \right|^2$$

of the difference ϵ between the unknowns $\mathbf{x}$ after a half time step $\mathbf{x}^{n+\frac{1}{2}\Delta t}$ and a full time step $\mathbf{x}^{n+\Delta t}$ for a system of N unknowns. The tolerance defaults to $\xi = 1 \times 10^{-4}$ but may be prescribed by the user upon initialization. The model keeps track of the running time step Δt and of a suggested time step Δt^*

$$\Delta t^* = 0.9 \Delta t \left(\frac{\xi}{\|\epsilon\|} \right)$$

which is iteratively adjusted and replaces Δt based on the values of the norm.

3.4 Initial Conditions

The solver needs initial conditions for the initially shed vortices, which are determined at each tip following analytical solutions previously proposed [5] for vortices shed past a semi-infinite thin plate. The initial distance from the plate edge ($z_t = 0$) for each shed vortex is

$$\begin{aligned} z_v &= \left[\frac{1}{2^{5/2}U}\int_0^t U^2(t')dt'\right]^{2/3} \\ &= \frac{(Ut)^{2/3}}{2^{5/3}} \end{aligned} \tag{21}$$

If needed, the initial condition for the vortex velocity is therefore given by

$$\dot{z}_v = \frac{2}{3}\frac{z}{t} \tag{22}$$

The initial circulation is given by

$$\begin{aligned} \Gamma_v &= \pi U\left[\frac{1}{2U}\int_0^t U^2(t')dt'\right]^{1/3} \\ &= \pi\left(\frac{Ut}{2}\right)^{1/3} U \end{aligned} \tag{23}$$

and its time derivative

$$\dot{\Gamma}_v = \frac{1}{3}\frac{\Gamma_v}{t} \tag{24}$$

These expressions are derived for a constant U. The initial time is pre-determined by the user and should be on the order of the integration time steps.

Once an attached vortex reaches a threshold distance Δz_{max} from the ellipse tip from which it was shed, its circulation stops evolving and new vortices are shed from the ellipse. The location of a vortex shed at time n is set to a fixed distance away from the shedding tip z_t^n

$$z_v^n = z_t^n - ie^{i\alpha_\varepsilon^n} \times 10^{-7}$$

and its circulation Γ_v^n is initialized based on the sign of the vortex that is being replaced Γ_v^{n-1}

$$\Gamma_v^n = \left[\text{sign}\left(\Gamma_v^{n-1}\right)\right]\left[1 \times 10^{-14}\right]$$

If the Δz_{max} determined by the user is too large and an unsteady vortex evolves to a point that its circulation changes sign, the method of [12] is used and the vortices are forced to become steady.

4 Benchmarking

This section presents results for a simulation with a single, stationary flat plate at a 90° angle to a free stream $V = 1 + 0i$. The plate was discretized with 8 equally spaced points, the tolerance was set to $\xi = 1 \times 10^{-2}$ and the initial time step to $\Delta t_0 = 1 \times 10^{-5}$. The maximum distance to the plate tip for a vortex to remain unsteady was kept as the default value Δz_{max} $= 0.05\,[a_\varepsilon + b_\varepsilon]$ (i.e. 5% of the ellipse major axis).

4.1 Model Caller

A sample caller routine is given in Fig. 3. The model is implemented as a Python (version 2.7) class, and can be easily instantiated (line 8) after loading the required packages (lines 1-4) and generating ellipse and vortices objects (lines 6-7). Initialization is done by calculating the initial coefficients of the series (line 10) that enforces no-penetration on the ellipses (see Section 2.1.3) using Eqs. (21) and (23) to initialize the unsteady vortices (line 11). After initializing the coefficients and the tip vortices, the model can be integrated (lines 12-15) including the free vortices calls until a user-specified maximum time `tmax` is reached. The caller routine should periodically check the distance between the attached vortices and the ellipse tips in order to trigger new shedding. In the sample code this is done at every time step (line 14) but this frequency can be modified by the user depending on the value of Δz_{max} specified. The boolean variable `flags` returned in lines 14-15 indicate whether vortices were set free from each ellipse tip.

```
1  import numpy
2  from ellipse import Ellipse
3  from vortices import Vortices
4  from VortexModel import VortexModel
5
6  e = Ellipse(alpha=numpy.pi/2)
7  v = Vortices()
8  m = VortexModel([e],v,tol=1e-2,dt0=1e-5)
9
10 m.initialize_series_coefficients()
11 m.initialize_vortices()
12 tmax = 1.01
13 while (m.t <= tmax):
14     flags = m.free_vortices()
15     dt_sugg, forced_flags = m.adaptive_step(dt_sugg)
```

Figure 3: Sample model caller routine.

4.2 Results

The movement of the initial shed vortices follows the analytical predictions by [5] as given by Eq. (21) and shown in Fig. 4. The simulation was run to $t = 6$, shedding 36 symmetrical vortices from each tip and taking $\sim$ 130 seconds to run on a personal computer. The initialized state and final solution are given in Fig. 6. Before integration (Fig. 6a), the strength of the vortices is small and the flow goes around the plate tips. Once the vortices grow in strength (Fig. 6b), the tips become separation points satisfying the Kutta condition, and a symmetrical wake develops. The dynamics of the system is singular upon initialization with the shed vortices moving and growing very quickly as given by Eqs. (22) and (24) and shown in Fig. 5.

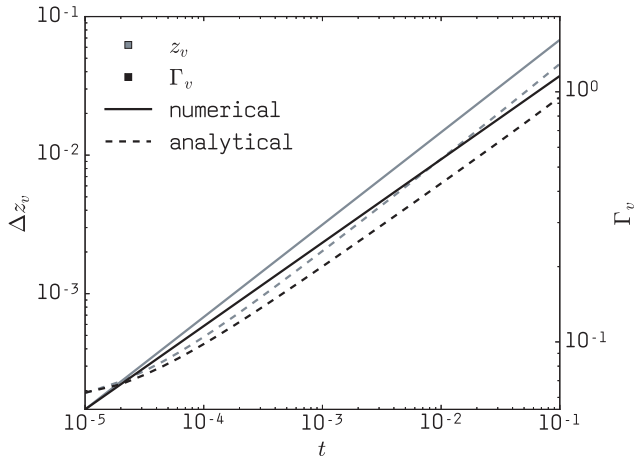

Figure 4: Evolution of first shed vortex position (z_v, grey) and circulation (Γ_v, black) as predicted by the model (dashed) and by the analytical solution (solid).

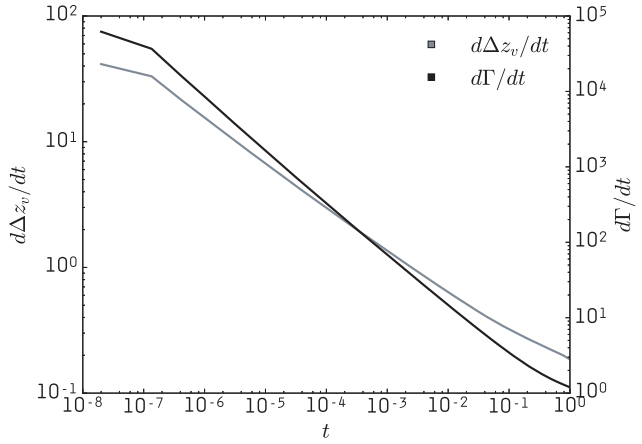

Figure 5: Evolution of first shed vortex velocity distance from the tip (grey) and circulation (black) as predicted by the model.

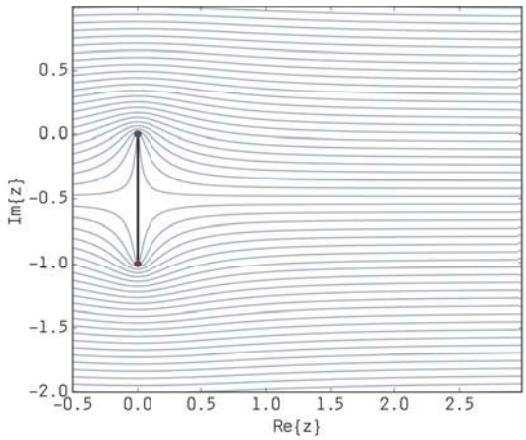

(a) $t = 0$

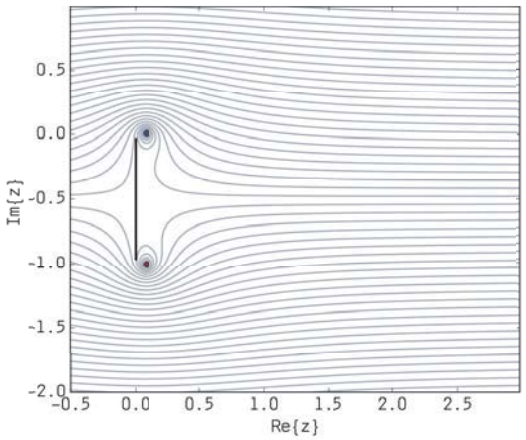

(b) $t \sim 0.2$

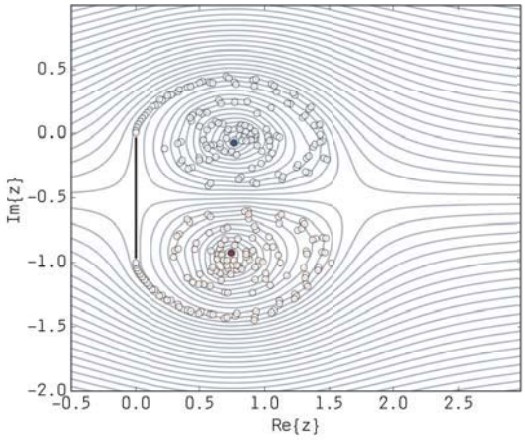

(c) $t = 6$

Figure 6: Streamlines upon initialization (a), at t $\sim$ 0.2 (b) and at t = 6 (c). Markers represent vortices in the field, color-coded by sign (blue for $\Gamma < 0$ and red for $\Gamma > 0$) and intensity (darker shades for stronger vortices).

4.3 Vortex Sheet Resolution

The number of vortices shed from the plate separation points is governed by the user-defined parameter Δz_{max} which is the distance between the last shed vortex z_v and the separation point z_t. Therefore, the resolution of the vortex sheet can be easily modified. In the continuous sheet limit ($\Delta z_{max} \to 0$) a vortex is shed at every time step and the model resembles the method proposed by [9]. Alternatively, in the point vortex limit ($\Delta z_{max} \gg 0$) the vortices are allowed to evolve until they reach maximum strength at which point they are forced to become steady, triggering renewed shedding as in the method proposed by [12].

Experiments were conducted to test the sensitivity of the currently presented model to Δz_{max} (Fig. 7) values in between these two limits. The number of vortices shed across experiments varies logarithmically (Fig. 7a). In terms of circulation, all experiments produced the same behavior (Fig. 7b) with the continuous sheet limit presenting slightly higher total circulation than the point vortex limit. Values of $\Delta z_{max} < 1\%$ are indistinguishable, and likewise values of $\Delta z_{max} > 25\%$ also appear to collapse to a limit curve for the benchmark case being presented. These results indicate that the model is robust, and users can take advantage of its vortex sheet resolution flexibility when limited by computational resources.

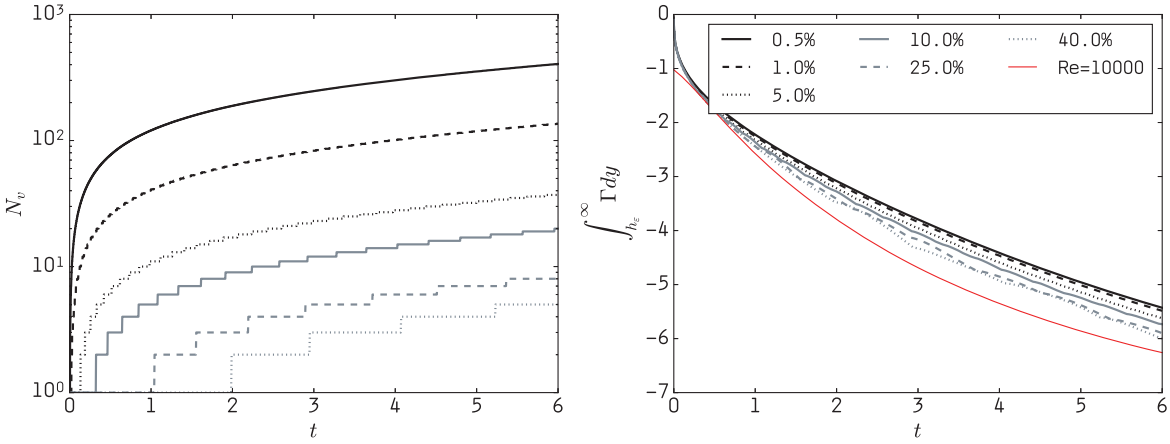

(a) (b)

Figure 7: Time evolution of the number of vortices shed off the plate top tip (a) and the total circulation above the plate centerline h_ε (b) for experiments with different Δz_{max} values, as given in percent of the ellipse major axis. Red line in (b) shows CFD results obtained with COMSOL for Re=10^4.

5 Summary and Outlook

In this work a new vortex method is proposed to model wakes behind thin ellipses. The model is developed using potential flow theory and vortex shedding. An expression for the complex potential was derived as a linear combination of different contributions: (i) point vortices, (ii) their image vortices, (iii) a bound vortex inside each ellipse, and (iv) a series of

monomials to ensure no flow normal to the solid bodies. The flows are two dimensional and incompressible, and conformal mapping is used to allow for simplified calculations in the circle planes of the ellipses. The shed vortices are unsteady and their evolution is dictated by their self-advection, the Brown and Michael correction, and by satisfying the unsteady Kutta condition. The Kelvin Theorem is also satisfied by a dynamic bound vortex at the center of each ellipse, whose circulation is equal and opposite to the vortices being currently shed by the ellipse. The evolution of the steady vortices which are no longer attached to their generating ellipses is dictated solely by the surrounding flow.

The method was implemented in Python 2.7 and the modular framework is extremely flexible. A minimal working example is provided in this report for the benchmark case of a flat stationary plate perpendicular to a constant free stream. While examples are not shown for multiple ellipses, the main innovation of the method is its scalability and low computational cost. The equations have been implemented for simulations with multiple solid bodies which can be stationary or move independently, and the resolution of the vortex sheet being shed at the separation points of each ellipse is easily changed by setting the maximum distance an unsteady point vortex is allowed to move before becoming steady thus triggering new shedding. Ongoing work focuses on benchmarking a multiple-ellipse simulation, and simulations for independently moving ellipses. The model can also be extended to include the forces of the fluid on the bodies and could possibly be applied for studies in flapping propulsion.

References

[1] J. M. Anderson, K. Streitlien, D. S. Barrett, and M. S. Triantafyllou, *Oscillating foils of high propulsive efficiency*, Journal of Fluid Mechanics, 360 (1998), pp. 41–72.

[2] G. K. Batchelor, *An introduction to fluid dynamics*, Cambridge University Press, 2000.

[3] C. E. Brown and W. H. Michael, *Effect of leading-edge separation on the lift of a delta wing*, Journal of the Aeronautical Sciences, 21 (1954), pp. 690–694.

[4] R. R. Clements, *An inviscid model of two-dimensional vortex shedding*, Journal of Fluid Mechanics, 57 (1973), pp. 321–336.

[5] L. Cortelezzi, *On the unsteady separated flow past a semi-infinite plate: Exact solution of the Brown and Michael model, scaling, and universality*, Physics of Fluids, 7 (1995), pp. 526–529.

[6] S. Deniz and T. Staubli, *Oscillating rectangular and octogonal profiles: interaction of leading- and trailing-edge vortex formation*, Journal of Fluids and Structures, 11 (1997), pp. 3–31.

[7] H. W. M. Hoeijmakers and W. Vaatstra, *A higher order panel method applied to vortex sheet roll-up*, AIAA Journal, 21 (1983), pp. 516–523.

[8] K. Horiuti, *A classification method for vortex sheet and tube structures in turbulent flows*, Physics of Fluids, 13 (2001), p. 3756.

[9] M. A. Jones, *The separated flow of an inviscid fluid around a moving flat plate*, Journal of Fluid Mechanics, 496 (2003), pp. 405–441.

[10] M. A. Jones and M. J. Shelley, *Falling cards*, Journal of Fluid Mechanics, 540 (2005), pp. 393–425. Copyright - 2005 Cambridge University Press; Last updated - 2015-08-15.

[11] S. Michelin and S. G. L. Smith, *Falling cards and flapping flags: understanding fluidsolid interactions using an unsteady point vortex model*, Theoretical and Computational Fluid Dynamics, 24 (2009), pp. 195–200.

[12] ——, *An unsteady point vortex method for coupled fluidsolid problems*, Theoretical and Computational Fluid Dynamics, 23 (2009), pp. 127–153.

[13] G. Strang, *On the construction and comparison of difference Schemes*, SIAM Journal on Numerical Analysis, 5 (1968), p. 12.

Modeling Morphodynamics of a Tidally Forced Wetland

Qi Li
(advised by Amala Mahadevan and Ian Hewitt)

November 5, 2016

1 Background and Introduction

Coastal salt marshes are landforms at the boundary between the sea and land. They serve critical functions valuable to both ecology and human economic activities. The long-term evolution of coastal salt marshes under external environmental changes such as the global sea-level rise is still an open question [Hughes et al., 2009]. One question pertinent to geomorphology of the salt marsh is the tidal channels extending head-ward (i.e. towards the land) in the salt marsh platform continuously, forming self-similar patterns over the years [Hughes et al., 2009]. A better understanding of salt marsh dynamics is required before explaining such continuously head-ward extension of the channels. Despite the complexity of a salt marsh, which can involve multiples disciplines such as eco-hydrology, geo-chemistry and eco-biology, various numerical modeling approaches make assumptions and simplifications in order to understand a few aspects of these processes. For example, Moffett et al. [2012, Table 1] summarizes some numerical models in the literature.

In this report, we introduce a numerical model for a salt marsh, which assumes the marsh platform as an unconfined, multi-phase porous medium. This starting point of this model is based on the laboratory experiment and numerical model previously developed in Mahadevan et al. [2012]. As a preliminary step, three questions below will be addressed to understand the dynamics of a tidally-driven salt marsh.

1. How do tidal cycles affect erosion and depostion?
2. What is the impact of initial heterogeneity in porosity?
3. What factors can affect the morphodynamics?

2 Models for erosion in a saturated, granular, porous medium

2.1 Previous model in Mahadevan et al. [2012]

Laboratory experiments [Lobkovsky et al., 2008, Mahadevan et al., 2012] have been conducted to study the internal erosion and preferential flow enhancement in a saturated, granular, porous medium. In particular, the experiment performed by Mahadevan et al. [2012] has considered a uni-directional flow through a bed of mixtures of particles with two grain diameters shown in figure 1. The grain with smaller diameter can be dislodged by the fluid with a prescribed inflow rate and the one with bigger diameter is immobile. A numerical model is also proposed in this paper, which qualitatively compares well with formation of channels in the experiment. The details of the numerical model are presented

by Mahadevan et al. [2012] and will only be outlined briefly as follows. For a multi-phase flow in a confined, saturated porous medium, three different states, namely solid (ϕ_s), granular (ϕ_g) and liquid (ϕ_l), coexist.

$$\phi_s + \phi_l + \phi_g = 1, \tag{1}$$

where ϕ_s is the volume fraction of the *immobile* solid phase, ϕ_g is the volume fraction of the granular mobile phase, and ϕ_l is the volume fraction of the liquid phase. Assuming that each phase is incompressible and from volume conservation for the individual phase

$$\frac{\partial \phi_s}{\partial t} = -e + d, \tag{2}$$

$$\frac{\partial \phi_g}{\partial t} = e - d - \nabla \cdot (\vec{u_g} \phi_g), \tag{3}$$

$$\frac{\partial (\phi_l)}{\partial t} = -\nabla \cdot (\vec{u_l} \phi_l), \tag{4}$$

where e is the erosion rate; d is the rate of deposition; $\vec{u_g}$ and $\vec{u_l}$ are the velocity of the granular and liquid phases, respectively. $\vec{u_g}$ and $\vec{u_l}$ are assumed to be equal. The global continuity equation from adding the conservation equation for each phase gives

$$\nabla \cdot (\phi_g + \phi_l). \tag{5}$$

Assuming Darcy's flow, the specific discharge q is given by

$$q \equiv= \vec{u} (\phi_g + \phi_l) = -D \nabla p, \tag{6}$$

where p is pressure and D is the hydraulic conductivity, which is a function of the porosity of the material.

Figure 1 highlights a crucial difference in the boundary conditions between the laboratory experiments on erosion and the scenario in a natural salt marsh. In the experiment, the erodible multi-phase material is confined between the solid plates and a constant flow rate is prescribed at one end whereas the other end is at atmospheric pressure. However, in the case of salt marsh, the tidal level on one end varies with time and thus the interface of the saturated medium also varies spatially and temporally, unlike the confined case in the experiment. Therefore, the appropriate model for the salt marsh should take into account the free-moving interface of the saturated medium. Figure 2 shows the schematic of the model and details of the model for the salt marsh are presented in the next section.

2.2 Model for a salt marsh

Assuming that the salt marsh has a depth $h_f(x, y)$, any control volume of depth $h_f(x, y)$ contains three different phases, namely the solid, granular and the liquid, denoted by ϕ_s, ϕ_g and ϕ_l respectively. The ϕ_s can be regarded as the material property of the salt marsh, which is the volume fraction (given any control volume) of the immobile parts (i.e. grass and other solids). ϕ_s can only be changed by erosion and deposition processes. ϕ_g is the volume fraction of the sediments that can be converted to or from ϕ_s and can be moved around. The volume fractions of the saturated medium follow.

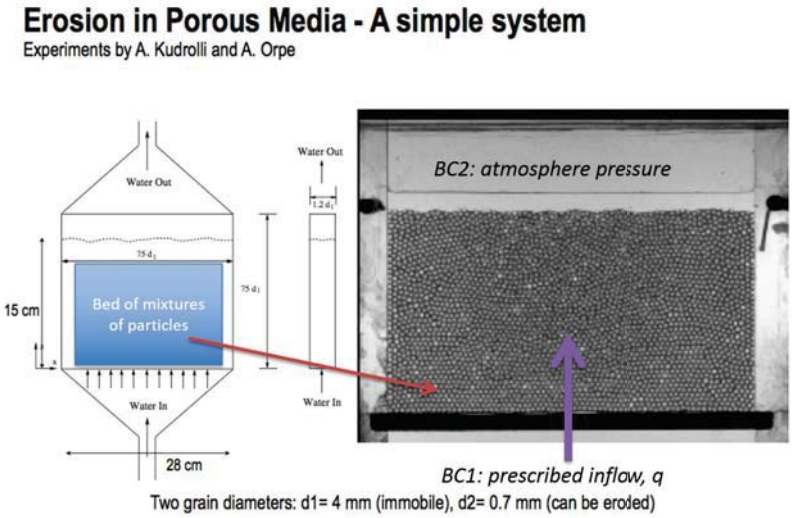

Figure 1: Schematic of the experimental setup (Fig. 1 in Mahadevan et al. [2012]).

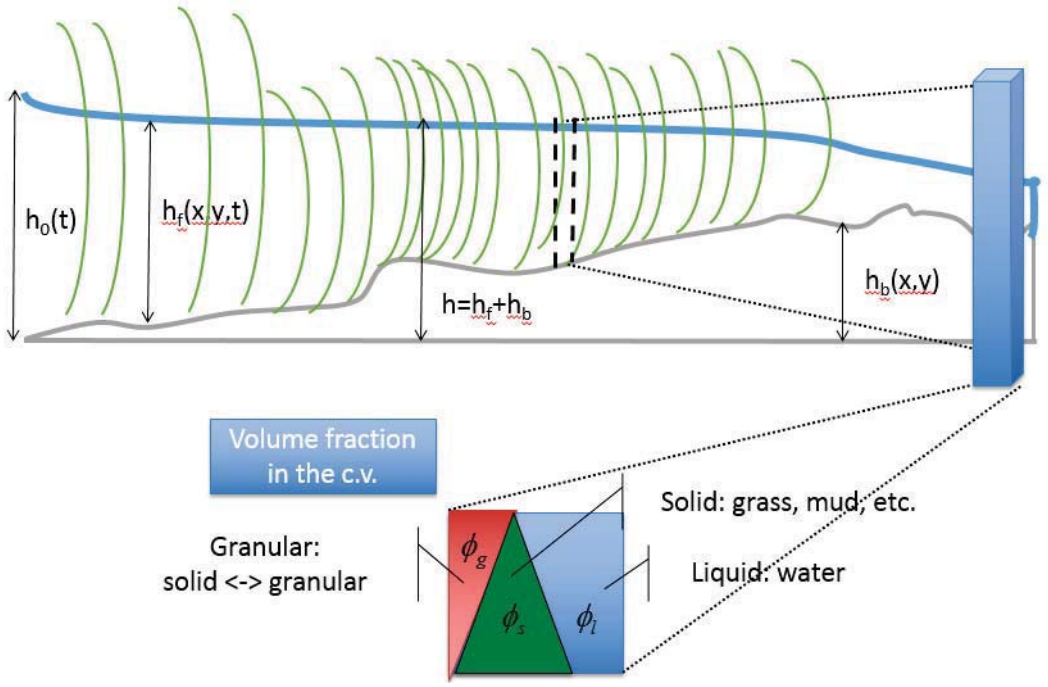

Figure 2: Sketch of the model for salt marsh. $h_0(t)$ varies with time. The thick blue line represents the level of the saturated medium; the bed topography level h_b can also vary spatially.

$$\phi_s + \phi_l + \phi_g = 1. \tag{7}$$

The volume fractions represent the vertically averaged quantities as shown in the cross-section in figure 2. Erosion and deposition processes will change the material property of the salt marsh. Thus, the solid fraction ϕ_s changes over time,

$$\frac{\partial \phi_s}{\partial t} = (-e + d)\,. \tag{8}$$

In the saturated column of height h_f, the granular fraction ϕ_g follow the mass conservation given by

$$\frac{\partial\,(h_f \phi_g)}{\partial t} = h_f\,(e - d) - \nabla \cdot (\vec{u_g} \phi_g h_f)\,. \tag{9}$$

For the liquid phase, mass conservation gives:

$$\frac{\partial\,(h_f \phi_l)}{\partial t} = -\nabla \cdot (\vec{u_l} \phi_l h_f)\,. \tag{10}$$

Similar to the model by Mahadevan et al. [2012], e is the rate of erosion (i.e. solid phase becomes granular phase); d is the rate of deposition (i.e. granular phase becomes solid phase); $\vec{u_g}$ and $\vec{u_l}$ are the velocities of granular materials and water, respectively. Summing Eq. 8-10 leads to

$$(1 - \phi_s)\,\frac{\partial h}{\partial t} = -\nabla \cdot (h_f \vec{u_g} \phi_g + h_f \vec{u_l} \phi_l)\,, \tag{11}$$

We can further assume the $\vec{u_g} = \vec{u_l} = \vec{u}$ [Mahadevan et al., 2012], which signifies the granular materials are passively carried by the liquid and move at the same speed. Then equation 11 becomes

$$(1 - \phi_s)\,\frac{\partial h}{\partial t} = -\nabla \cdot (h_f \vec{u}\,(1 - \phi_s)) \tag{12}$$

The flow in the salt marsh can be assumed to be laminar; thus, Darcy's law applies, where ϕ_s is $1 - \phi$ for ϕ being the porosity. With the assumption of hydrostatic equilibrium, the pressure p can be related to h as $p = \rho g h$. Thus, equation 12 gives

$$(1 - \phi_s)\,\frac{\partial h}{\partial t} = -\rho g \nabla \cdot (h_f D(\phi) \nabla h)\,. \tag{13}$$

With appropriate boundary conditions and models for rate of erosion e and rate of deposition d, Eqs. 8-10 and 13 can be solved numerically with finite volume method.

The threshold shear stress condition is applied for erosion, which is a common approach in the literature pertaining to cohesive sediments [Fagherazzi et al., 2012]. The erosion rate is proportional to the solid volume fraction and is determined by how much the shear stress (given by the term $\rho|\vec{u}|^2$) exceeds the erosion threshold σ. Thus, the erosion rate is modeled as

$$e = k_e \left(\rho|\vec{u}|^2) - \sigma\right) \phi_s, \tag{14}$$

where k_e is the erosion constant with dimension of s^{-1}. The rate of deposition is modeled the same as in Mahadevan et al. [2012] based on a binary collision picture, given by

$$d = k_d \phi_s \phi_g, \tag{15}$$

where k_d is the deposition constant with unit s^{-1}.

3 Linear approximation of the model

With appropriate choice of scales, the non-dimensionalized equations are as follows, where details are given in A.

$$\frac{\partial \phi_s}{\partial \hat{t}} = -\epsilon \hat{t} + \delta \hat{d} \tag{16}$$

$$\frac{\partial \left(\hat{h}\phi_g\right)}{\partial \hat{t}} = \left(\epsilon \hat{e} - \delta \hat{d}\right)\hat{h} - l_r^2 \nabla \cdot \left(\phi_g \hat{u} \hat{h}\right) \tag{17}$$

$$\frac{\partial \left(\hat{h}\phi_l\right)}{\partial \hat{t}} = -l_r^2 \nabla \cdot \left(\phi_l \hat{u} \hat{h}\right). \tag{18}$$

The flux balance equation is

$$(1-\phi_s)\frac{\partial \hat{h}}{\partial \hat{t}} = l_r^2 \nabla \cdot \left(\hat{D}\hat{t}\nabla \hat{h}\right). \tag{19}$$

The non-dimensionalized Darcy's law is

$$\hat{q} \equiv \phi \hat{u} = -l_r^2 \hat{D} \nabla \hat{h}. \tag{20}$$

The erosion and deposition in dimensionless forms are

$$\hat{e} = \left(|\hat{u}|^2 - \hat{\sigma}\right) \tag{21}$$

and

$$\hat{d} = \phi_g \phi_s. \tag{22}$$

The boundary condition on the southern end is given by the temporally varying tidal levels as

$$\hat{h}(\hat{y}=0,\hat{t}) = 1 + A\cos\left(2\pi \hat{t}\right). \tag{23}$$

On the northern end, a no flux boundary condition, in which $\hat{q}=0$ is applied to signify the impermeable surface on the landward side of the salt marsh.

Some insight can be gained from the linearized approximation of the non-linear equation 19. Especially in the fields of ground water hydrology and agricultural drainage [Bear], assuming that $\hat{h} = \hat{h_0} + \hat{h}'$, where $\hat{h}' \ll \hat{h_0}$. This gives

$$(1-\phi_s)\frac{\partial \hat{h}}{\partial \hat{t}} = \nabla \cdot \left(\hat{D}\hat{h_0}\nabla^2 \hat{h}\right). \tag{24}$$

Thus, we consider the one-dimensional version of equation 24 with the boundary conditions of $\hat{h}(\hat{x}=0,t) = 1+\cos(\hat{t})$ and $\frac{\partial \hat{h}}{\partial \hat{x}} = 0$ at $\hat{x}=1$. With constant porosity (i.e. zero rate of erosion and deposition), analytical solution for the steady state can be found from standard text such as [Carlaw and Jaeger, 1959]. The analytical solution is given as

$$\hat{h}(\hat{x},\hat{t}) = 1 + A\cos\left(\hat{t} - \hat{x}\hat{k}\right)\exp(-\hat{k}\hat{x}). \tag{25}$$

where $\hat{k} = \sqrt{\frac{(1-\phi_s)}{2\hat{D}\hat{h_0}}}$; The analytical solution and the numerical solution obtained by solving the full non-linear equation assuming $\hat{h}' = 0.01\hat{h_0}$. Figure 3 shows good comparison between analytical and numerical solutions.

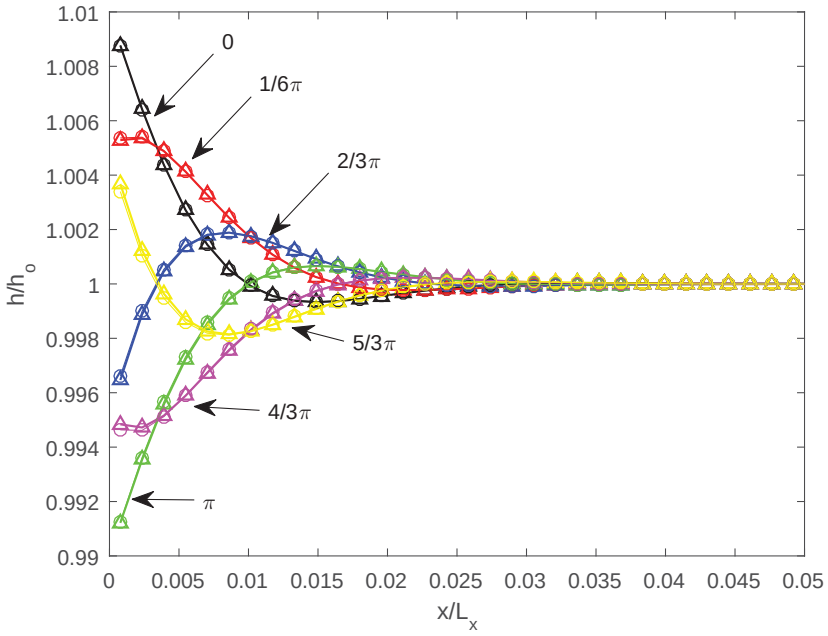

Figure 3: Comparison between analytical (Eq. 25) and numerical solution. △ markers are the numerical results and lines of different colors represent analytical solutions for different phases within one period of forcing at the boundary.

4 Results and discussion

In this section, the three questions raised in the beginning are addressed here. Table 1 shows the parameters that the model depends on. By varying some of the parameters, we explore how the model predicts the evolution of porosity and the morphodynamics. One parameter to highlight here is the length scale $L_D = (D_0 \rho g h_0 T_0)^{1/2}$, which arises from the non-dimensionalization. In the linearized analysis, the exponentially decaying sinusoidal solution largely depends on the value of $\hat{k}$, which modulates the phase difference and the rate at which $\hat{h}$ decays. With deposition and erosion that significantly alter the material property in the long run, a quasi-steady state can be assumed during one tidal cycle. Thus, the solution is expected to exhibit qualitatively some similarity to the linearized analysis. Figure 4 shows the decrease in magnitude in the space-time diagram of v/u_0; the slanting feature is also constant with the expected phase-lag in y. However, within one tidal cycle T_0, the erosion and deposition rates can vary during different phases of one cycle.

4.1 Effect of tidal cycles

To investigate the spatial and temporal variation of the deposition and erosion rates and hence the net change in ϕ_s, the first case is studied using the set of parameters in table 1, case C1. The initial conditions for the volume fractions are: $\phi_s = 0.7$, $\phi_l = 0.3$ and $\phi_g = 0$ for all x and y. As shown in figures 5a-5c, at different phases within one tidal cycle, ap-

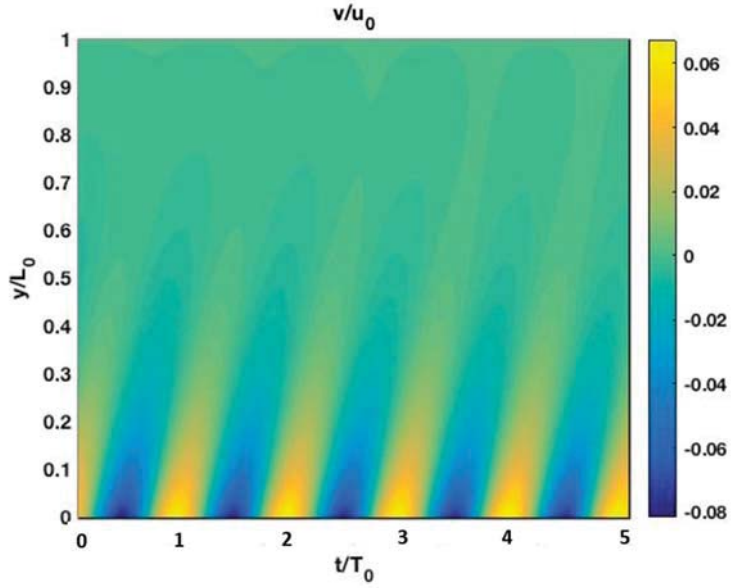

Figure 4: Space-time plot of velocity component v.

Case	Erosion Cst.ϵ	Deposit. Cst. δ	Threshold	$\phi_g(x, y = 0)$	$l_r = L_D/L_0$	Tidal Range A
C1	1	1	2×10^{-5}	0	1	0.1
C2	1	1	2×10^{-5}	0	10	0.1
C3	1	1	2×10^{-5}	0.005	1	0.1
C4	1	1	2×10^{-5}	0.01	1	0.1
C5	1	1	2×10^{-5}	0.05	1	0.1
C6	1	1	2×10^{-5}	0.05	1	0.067
C7	1	1	2×10^{-5}	0.05	1	0.05

Table 1: Model parameters for different cases analyzed in this study.

proximately 10% of the domain significantly change in the rates of erosion and deposition. During the lowest tidal water level (i.e. figure 5b), significant net erosion occurs; whereas when the tidal level increases (i.e. figure 5c) rate of deposition greatly exceeds erosion rate.

In the model, ϕ_s and hence porosity of the salt marsh is quasi-steady during one tidal cycle. However, is it often of interest to study the eveolution of the salt marsh in the long run, especially the speed and the spatial extent at which net erosion occurs. Figures 6a-6b show the long-term change in erosion, deposition and the variations in each phase for 200 tidal cycles. Spatial average is performed in x direction because there is no initial horizontal heterogeneity in x. The rate of deposition for a given y/L_0 remains approximately constant over the number of tidal cycles analyzed here but the erosion rate decreases with time. Thus, there is a decrease in the magnitude of the net erosion. For $y/L_0 > 0.1$ and after about 100 tidal cycles, there is a net deposition, where more sediment is transformed back into solid phase. This process further decreases porosity and hydraulic conductivity, which reduces the velocity hence the rate of erosion. This example with initially uniform porosity suggests that the "front" of erosion (i.e. position at where ϕ_s decreases) may will decrease in its speed of propagation inward. The tidal creeks observed in the fields, which consistently exceed towards the land at a speed of about 2 m/s, are likely to be caused by factors other than the tidal forcing.

4.2 Impact of initial heterogeneity in porosity

In order to understand how two-dimensional perturbations in the initial state grow with time, we run the model with the same set of parameters as in case1 in table 1 but different initial condition by adding white noise with standard deviation of 0.01 to the intiail ϕ_s and ϕ_l. The initial ϕ_s is shown in figure 7a. After 200 tidal cycles, the result is shown in figure 7b. Compared to the case considered previous with a uniform initial porosity, this case also shows that ϕ_s for approxiamtely 10% of the domain decreases, preferentially forming some regions of low ϕ_s. Nevertheless, regions of higher ϕ_s (than initial ϕ_s) are also formed, signifying a net deposition. Nevertheless, initial variations in porosity will not lead to continuously extending tidal channels.

Comparing with the previous case, we calculated $(\langle \Delta\phi_s^2 \rangle)^{1/2}$, where $\Delta\phi_s$ is the difference between $\phi_s(x, y, t)$ in this case and that in the case with uniform initial porosity. Initially, figure 8 shows that $(\langle \Delta\phi_s^2 \rangle)^{1/2}$ is 0.01 because of the initial white noise perturbation has standard deviation of 0.01. However, across all x/L_0, $(\langle \Delta\phi_s^2 \rangle)^{1/2}$ increases with time although the rate of increase varies in x/L_0.

Thus, spatially averaged $(\langle \Delta\phi_s^2 \rangle_{xy})^{1/2}$ increases faster with time (figure 10). This shows that magnitude of the difference in ϕ_s for this case compared to the case of uniform initial porosity in porosity becomes increasing divergent.

4.3 Factors that affect morphodynamics

Unlike the uni-directional flow that is modeled in Mahadevan et al. [2012], a length scale ($L_D = (\ D_0\rho g h_0 T_0)^{1/2}$) is important in determining the dynamics. Varying the ratio L_r is equivalent to changing the hydraulic conductivity. Therefore, we performed case2 with parameters in table 1, where L_r is 10 times that in case1. After a total of 20 tidal cycles, the change in ϕ_s from initial values is shown in figure 11. Approximately 20% of the domain shows significant decrease in ϕ_s. Therefore, by increasing L_r and thus the hydraulic conductivity, the tidal channels can extend further. A closer look at the change in x-averaged individual phase shows that a larger fraction of the domain shows a decreasing ϕ_s. ϕ_g is a small fraction during 20 tidal cycles and ϕ_l increases steadily over time. Dependence on L_r is expected because the linearized approximation shows that the magnitude of velocity (which controls the rate of erosion) is an exponentially decaying function with y. Since L_r $1/\hat{k}$, L_r largely controls the spatial pattern of erosion.

Another practical problem that people are interested in is how external environmental factors impact the evolution of salt marsh. For instance, by conducting runs using parameters listed in table 1 from Case 3, Case 4 and Case 5, figure 13 illustrates that starting from uniform ϕ_s=0.8, higher ϕ_g as flow enters the domain will likely to bring more sediment into the salt marsh, thus ϕ_s can increase to some steady state (case5, $\phi_g(y = 0 \quad , x\ ) = 0\ .05$). The variations in net erosion/deposition rate in one cycle (on the right of figure 13) can be drastically changed in Case 5. Thus, the model is sensitive to this parameter, especially in the long-term behavior of the material property of the salt marsh.

The impact of relative sea level rise on the salt marsh is an important question. Here, by varying the initial water level and keeping the constant tidal range, we are increasing the relative tidal range, A. The control run with solid line (figure 14) uses parameters of Case 1 and the other two correspond to Case 6 and Case 7 in table 1. As the initial water level increases (i.e. relative tidal range decreases), ϕ_s decreases more slowly with time. Physically, the relative tidal range over the entire length of the domain gives a measure of the pressure gradient. Stronger pressure gradient leads to higher flow rate and stronger erosion, with all other factors constant. One thing to note is that figure 13 and figure 14 have different initial ϕ_s for the control runs (i.e. the solid line), changes of ϕ_s depend on initial conditions. However, more analyses are required to address the impact of different initial conditions, which is beyond the scope of the current parameter sensitivity studies.

5 Conclusion

In this report, we developed a numerical model for a tidally driven salt marsh. The tidal forcing is found to modify the erosion and deposition balance in a tidal cycle. In the long run, the imbalance in erosion and deposition can create regions where more erosion versus deposition has occured, vice versa. The initial heterogeneity in porosity can lead to some regions being preferentially eroded but the extension of the tidal channels is not enhanced by the initial horizontal heterogeneity in porosity. The length scale in the model $L_D = (D_0\rho g h_0 T_0)^{1/2}$, which is analogous to a diffusion length scale, controls the spatial extension of the eroded region. Unlike the uni-directional flow in the previous laboratory

experiment Mahadevan et al. [2012], dynamics of a tidally driven salt marsh depends on this length scale according to our model. In addition, the external environmental factors like sediment supply and relative tidal range can also impact the long-term behavior of the salt marsh.

The observed head-ward erosion of salt marsh channels can be due to bioturbation and vegetative feedbacks [Hughes, 2012]. It has long been recognized that the fiddler crabs that live in the head of the tidal channels for oxygen and nutrients can changes in the sedimentation processes [Gardner et al., 1987, Gardner and Wilson, 2006]. Future work includes modeling the bioturbation effect and adds into the current framework of the model. Based on the current results, the tidal forcing without any bioturbation, can initiate channel formations and the extension of the channels depend on the material property (i.e. the length scale L_D). Adding the bioturbation effect will enable us to quantitatively study the impact of fiddler crabs on channel formation and extension, which have been observed in the fields [Hughes et al., 2009].

The current model is also limited by treating the liquid phase as water, whereas the viscosity can change (i.e. dependent on ϕ_g). Another limitation is that the marsh platform is completely wet but in reality as the tidal level rises, the marsh platform slowly becomes wet. Future work will aim to address these limitations.

A Nondimensionalization of the equation

To facilitate studying the parameters, Eqs. 8-10 and 13 can be nondimensionalized by choosing appropriate scales. The boundary condition on the southern boundary (see figure 15) normalized by the vertical length scale h_0 is

$$h(y=0,t)/h_0 = 1 + A\cos(\omega t), \tag{26}$$

where ω is the angular frequency of the tidal cycle given by $\omega = 2\pi/T_0$, for T_0 being the time scale, which is equivalent to the tidal cycle of 12 hours. The hydraulic conductivity D is chosen as the canonical Kozeny-Camen relation, which is

$$D = \frac{l_g^2}{A_m \mu}\frac{\phi^3}{(1-\phi)^2} = D_0 \frac{\phi^3}{(1-\phi)^2}, \tag{27}$$

where l_g is the nominal pore size (which scales with the diameter of the solid part in the salt marsh such as size of the stems of the vegetation) of the porous medium and the constant A_m is 180.The velocity scale u_0 is given by $\frac{D_0 \rho g h_0}{L_0}$, where L_0 is the horizontal length scale. The erosion rate can also be nondimensionalized with $e_0 = k_e \rho u_0^2$ and the nondimensional erosion constant becomes $\epsilon = e_0 T_0$. The deposition rate constant is also nondimensionalized as $\delta = d_0 T_0 = k_d T_0$. Thus, with some manipulations the following equations can be obtained, where $\hat{}$ represents the dimensionless quantities:

$$\frac{\partial \phi_s}{\partial \hat{t}} = -\epsilon \hat{t} + \delta \hat{d} \tag{28}$$

$$\frac{\partial\left(\hat{h}\phi_g\right)}{\partial \hat{t}} = \left(\epsilon \hat{e} - \delta \hat{d}\right)\hat{h} - l_r^2 \nabla \cdot \left(\phi_g \hat{u} \hat{h}\right) \tag{29}$$

$$\frac{\partial\left(\hat{h}\phi_l\right)}{\partial\hat{t}} = -l_r^2\nabla\cdot\left(\phi_l\hat{u}\hat{h}\right). \tag{30}$$

The flux balance equation is

$$(1-\phi_s)\frac{\partial\hat{h}}{\partial\hat{t}} = l_r^2\nabla\cdot\left(\nabla\hat{h}\hat{h}\right). \tag{31}$$

The nondimensionalized Darcy's law is

$$\hat{q} \equiv \phi\hat{u} = -l_r^2\hat{D}\nabla\hat{h}. \tag{32}$$

The erosion and deposition in dimensionless forms are

$$\hat{e} = \left(|\hat{u}|^2 - \hat{\sigma}\right) \tag{33}$$

and

$$\hat{d} = \phi_g\phi_s. \tag{34}$$

References

J. Bear. *Dynamics of fluids in porous media*. Elsevier, New York, 1972.

HS Carlaw and JC Jaeger. Conduction of heat in solids. *Oxford University Press, Oxford*, 1959.

Sergio Fagherazzi, Matthew L Kirwan, Simon M Mudd, Glenn R Guntenspergen, Stijn Temmerman, Andrea D'Alpaos, Johan Koppel, John M Rybczyk, Enrique Reyes, Chris Craft, et al. Numerical models of salt marsh evolution: Ecological, geomorphic, and climatic factors. *Reviews of Geophysics*, 50(1), 2012.

Leonard Robert Gardner and Alicia M Wilson. Comparison of four numerical models for simulating seepage from salt marsh sediments. *Estuarine, Coastal and Shelf Science*, 69 (3):427–437, 2006.

LR Gardner, P Sharma, and WS Moore. A regeneration model for the effect of bioturbation by fiddler crabs on 210 pb profiles in salt marsh sediments. *Journal of Environmental Radioactivity*, 5(1):25–36, 1987.

Zoe J Hughes. Tidal channels on tidal flats and marshes. In *Principles of Tidal Sedimentology*, pages 269–300. Springer, 2012.

Zoe J Hughes, Duncan M FitzGerald, Carol A Wilson, Steve C Pennings, Kazimierz Wieski, and Amala Mahadevan. Rapid headward erosion of marsh creeks in response to relative sea level rise. *Geophysical Research Letters*, 36(3), 2009.

Alexander E Lobkovsky, Ashish V Orpe, Ryan Molloy, Arshad Kudrolli, and Daniel H Rothman. Erosion of a granular bed driven by laminar fluid flow. *Journal of Fluid Mechanics*, 605:47–58, 2008.

Amala Mahadevan, AV Orpe, A Kudrolli, and L Mahadevan. Flow-induced channelization in a porous medium. *EPL (Europhysics Letters)*, 98(5):58003, 2012.

Kevan B Moffett, Steven M Gorelick, Robert G McLaren, and Edward A Sudicky. Salt marsh ecohydrological zonation due to heterogeneous vegetation–groundwater–surface water interactions. *Water Resources Research*, 48(2), 2012.

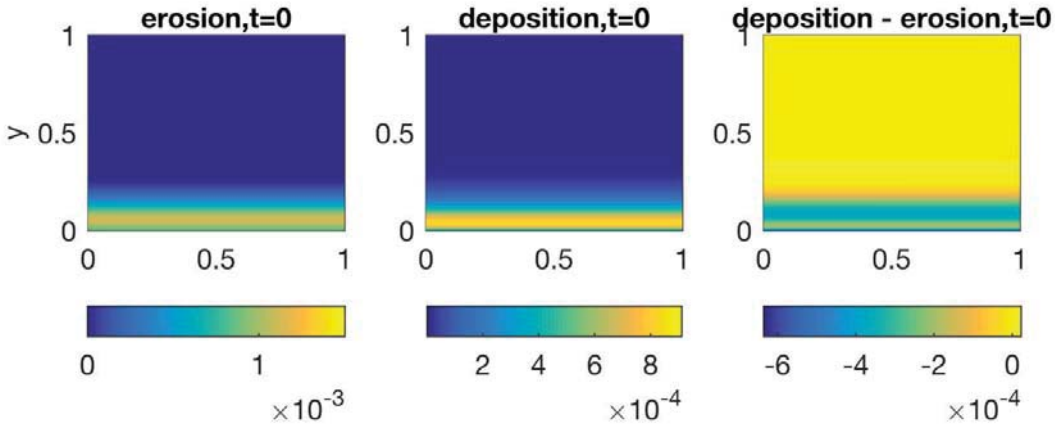

(a) Erosion, deposition and the difference during at the highest tidal level.

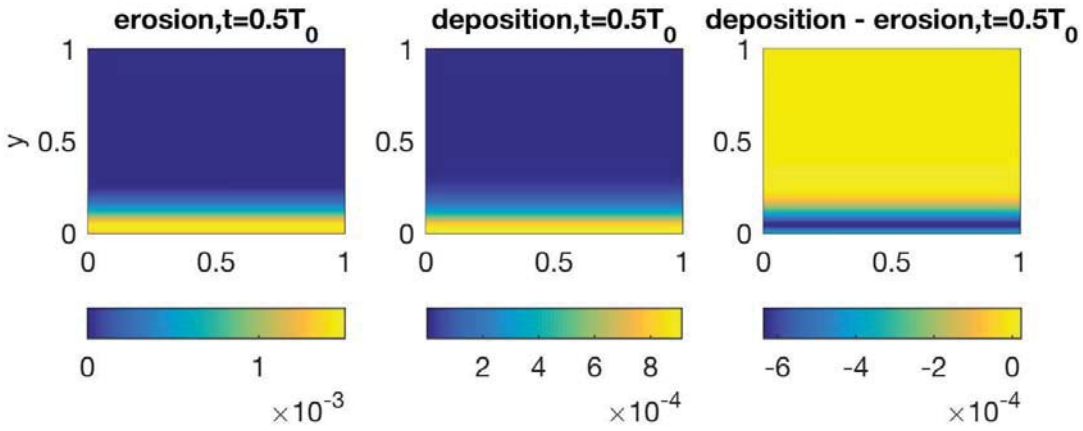

(b) Erosion, deposition and the difference during at the lowest tidal level.

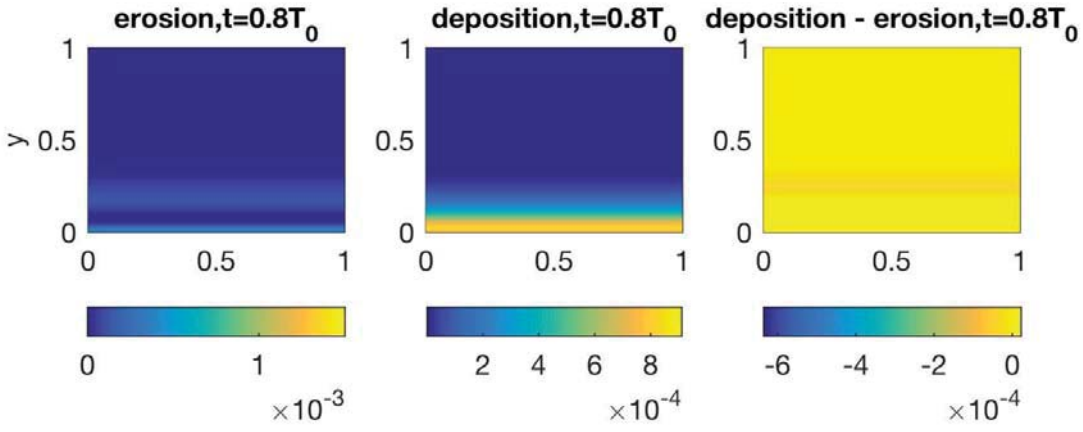

(c) Erosion, deposition and difference when tidal water level increases from low to high

Figure 5

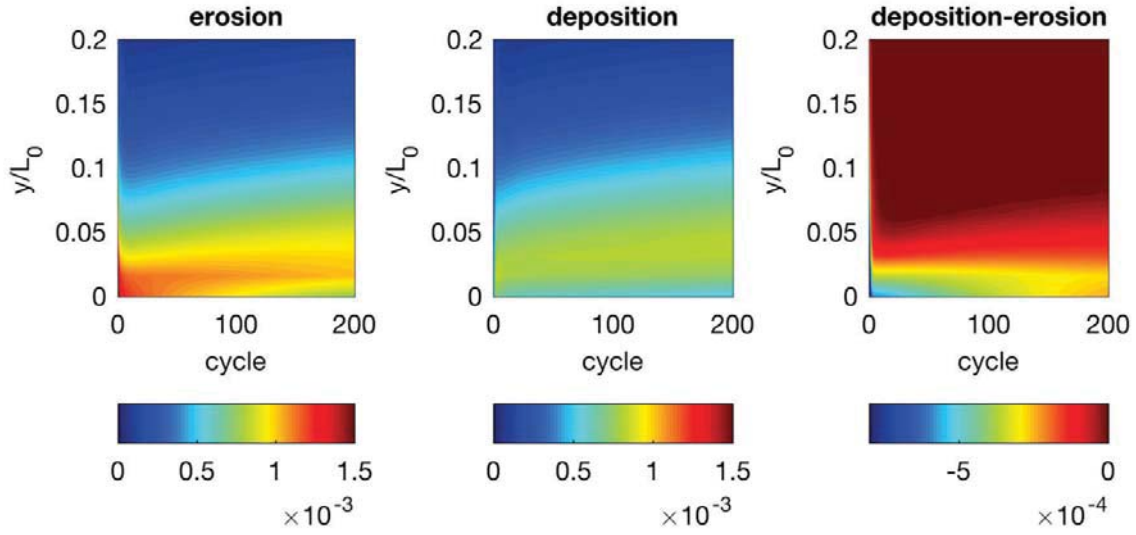

(a) Erosion, deposition and the difference averaged across x for 200 tidal cycles.

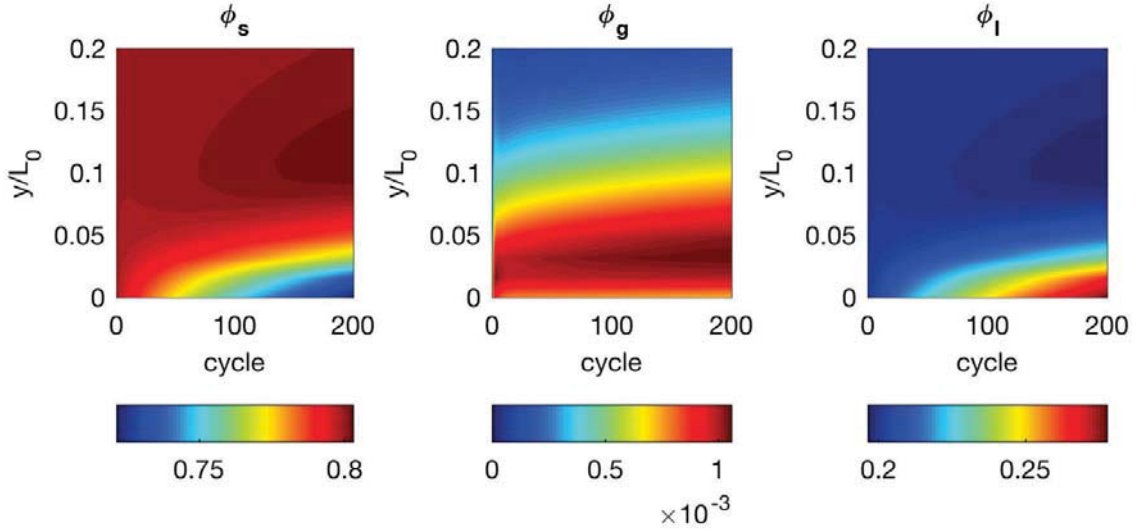

(b) ϕ_s, ϕ_g and ϕ_l averaged across x for 200 tidal cycles.

Figure 6: Long-term change in erosion rate, deposition rate and the volumetric amount of the three states.

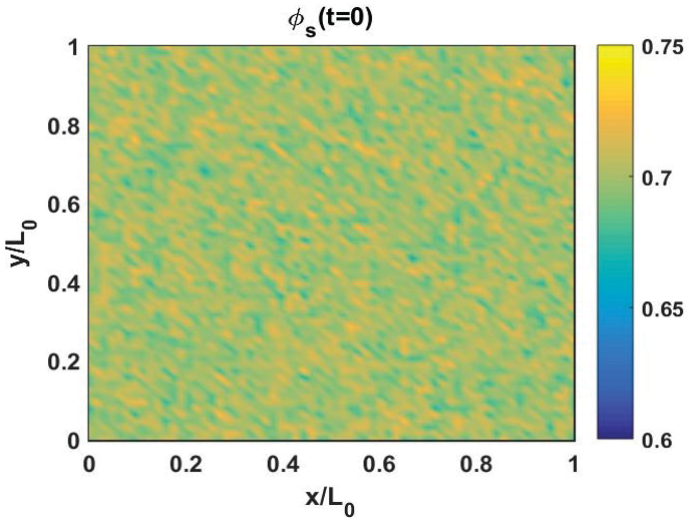

(a) Initial $\phi_s(x, y)$, where the area average of ϕ_s is 0.7 and the standard deviation of the white noise 0.01.

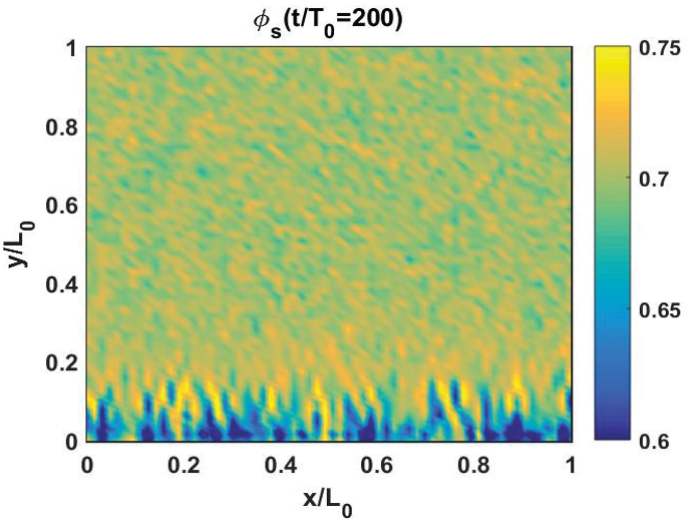

(b) Spatial distribution of $\phi_s(x, y)$ after 200 tidal cycles.

Figure 7

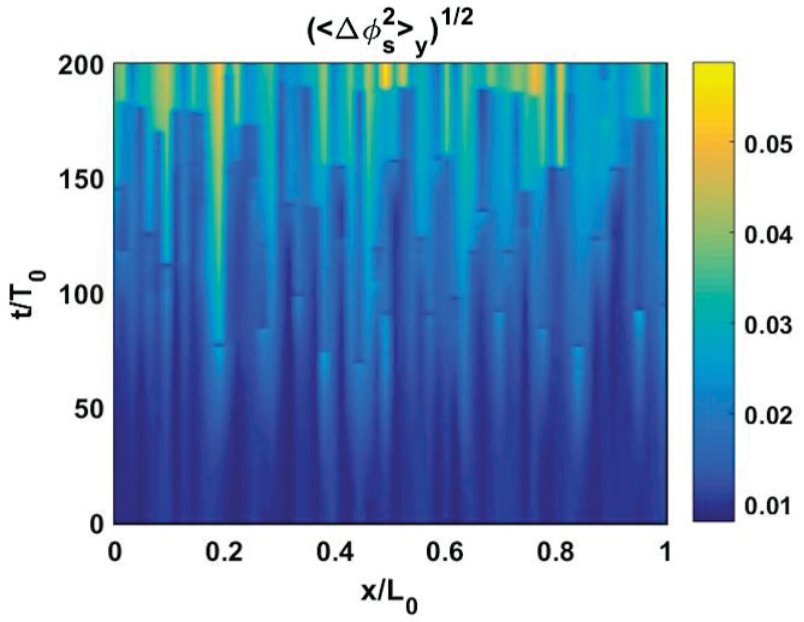

Figure 9: The space-time plot of $(\langle \Delta\phi_s^2 \rangle)^{1/2}$ for 200 tidal cycles

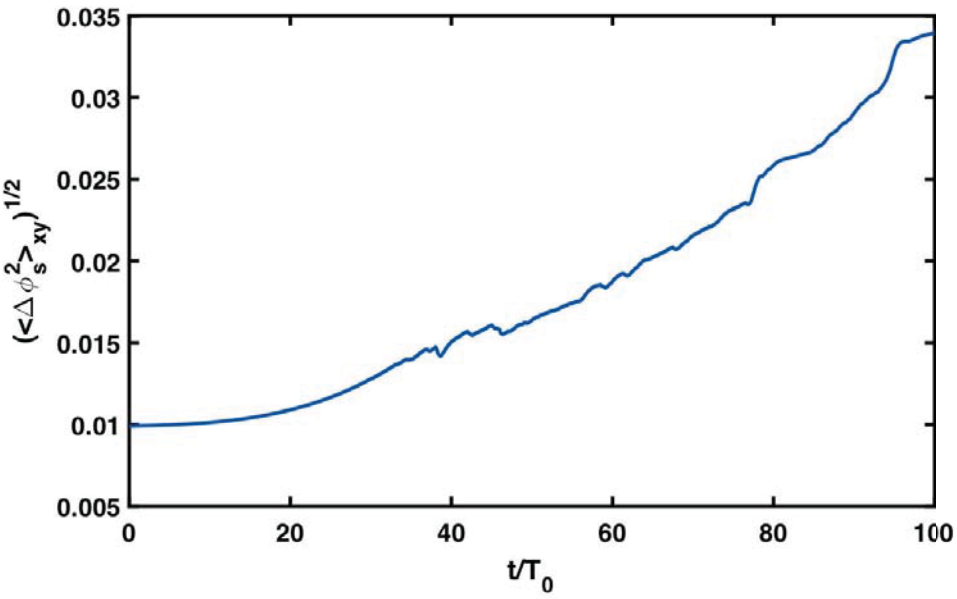

Figure 10: Average of $(\langle \Delta\phi_s^2 \rangle)^{1/2}$ in both x and y for 200 tidal cycles.

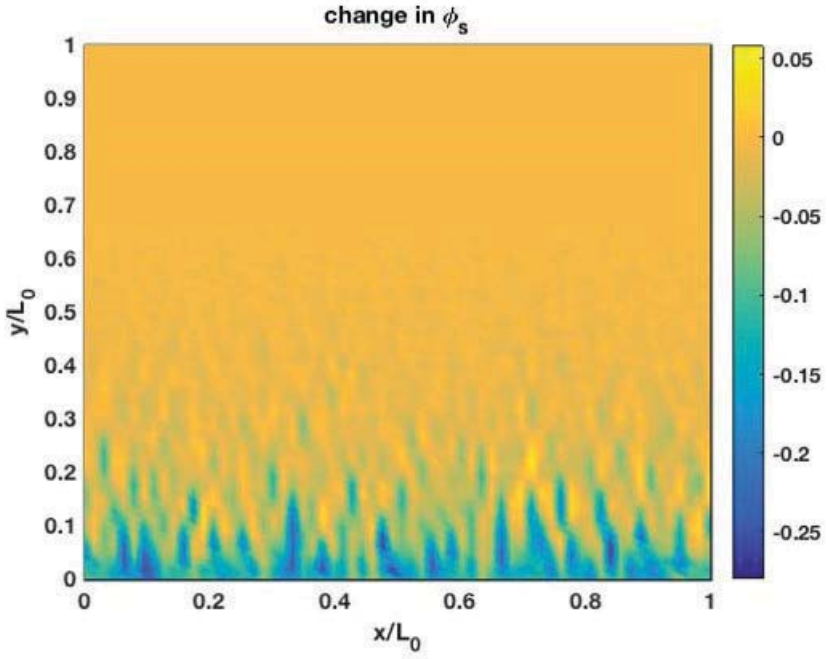

Figure 11: Change in ϕ_s after 20 tidal cycles using parameters in case2 and initial $\phi_s = 0.7 \pm 0.01$.

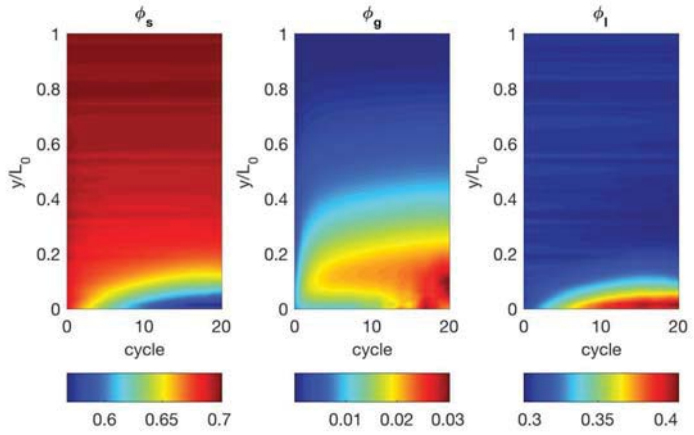

Figure 12: Spatially averaged ϕ_s, ϕ_g and ϕ_l in x direction after 20 tidal cycles.

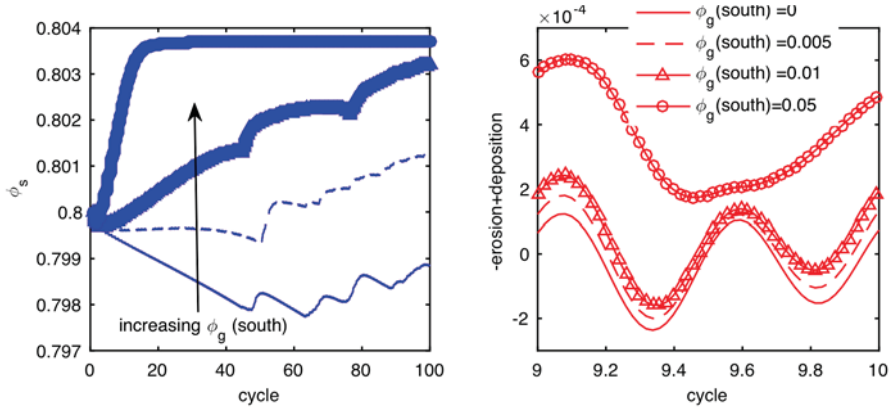

Figure 13: Varying ϕ_g at the southern boundary. left: ϕ_s after 100 tidal cycles; right: difference between erosion and deposition in one cycle.

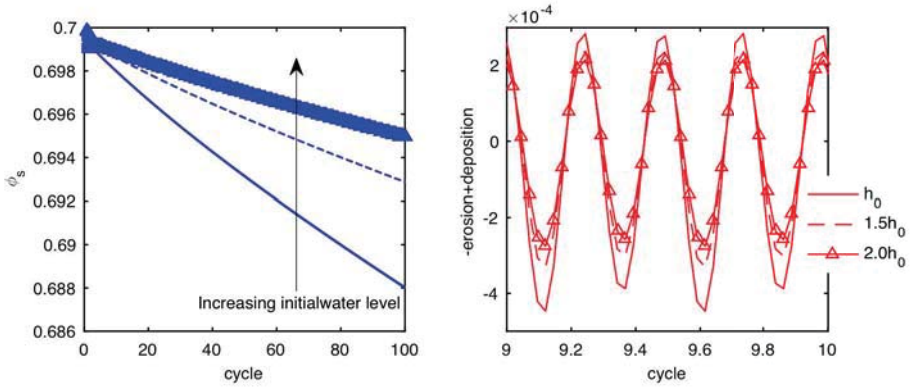

Figure 14: Varying the initial water level, thus equivalently decreases the relative tidal range. left: ϕ_s after 100 tidal cycles; right: difference between erosion and deposition in one cycle.

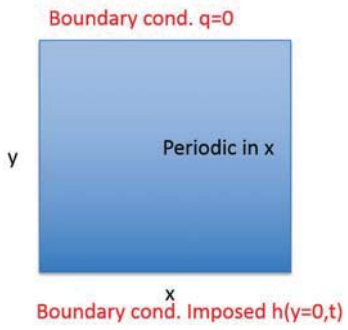

Figure 15: Set up of the two dimensional numerical model.

A Continuum Model for Flow of Meltwater through Snow

Colin R. Meyer

November 7, 2016

1 Introduction

Glaciers and ice sheets are large masses of ice that form due to the accumulation of snow over long periods of time. The snow lands on the ice surface and builds up at the highest elevations in what is known as the accumulation area. The temperature at the surface of glaciers and ice sheets varies with altitude and throughout the year due to seasonal solar forcing. In the summer, some but not all of the snow that accumulates on the surface melts or sublimates away. The surviving snow is called firn and its weight mechanically compacts the firn below, thereby transforming the snow into glacial ice [6]. Over long periods of time, ice slowly creeps as a shear-thinning viscous fluid and flows down to lower elevations and latitudes where there is net ablation [13, 28]. In the lower part of a glacier, where melting and sublimation dominate the accumulation of snow, the surface is exposed glacial ice and this region is called the ablation area. The elevation that separates the ablation and accumulation areas on average is called the equilibrium line altitude (ELA). This is an important elevation as changes in the location of the ELA are indicative of whether the glacier is shrinking or growing. The lower portion of the accumulation area that reaches the ELA is called the percolation zone because of the meltwater that percolates through the snow and refreezes [6, 17, 21].

The percolation zone may play an important role in buffering changes to climate by storing meltwater in the porous firn and modulating the glacier surface temperature. Meltwater stored in the firn (a) does not run off the surface of the ice sheet and contribute to sea level rise and (b) is not immediately routed to the bed, thereby delaying the influence of meltwater on ice dynamics [35]. Therefore, the capacity of firn to store water is an important metric in assessing the health of glaciers and ice sheets in a warming world [10, 11, 26]. The percolation of meltwater through firn also changes the thermal structure at the surface of a glacier or ice sheet. As the snow at the surface is melted, the liquid water carries a substantial quantity of latent heat. If the water runs off at the surface through supraglacial streams or drains to the bed through moulins, then the latent heat is carried away from the surface ice, leaving relatively cold ice. Thus, instead of warming the ice through the addition of sensible heat, the surface energy is converted into latent heat, which drains away as run off. On the other hand, the meltwater can percolate into the porous snow and refreeze, which releases the latent heat and warms the snow. Humphrey et al. [21] observe that the snow at 10 m depth in Greenland is often $>10^{\circ}$C warmer than the mean annual air temperature because of the refreezing of meltwater. Thus, the contribution of surface run off to sea level rise and the near-surface temperature structure is tied to the fate of

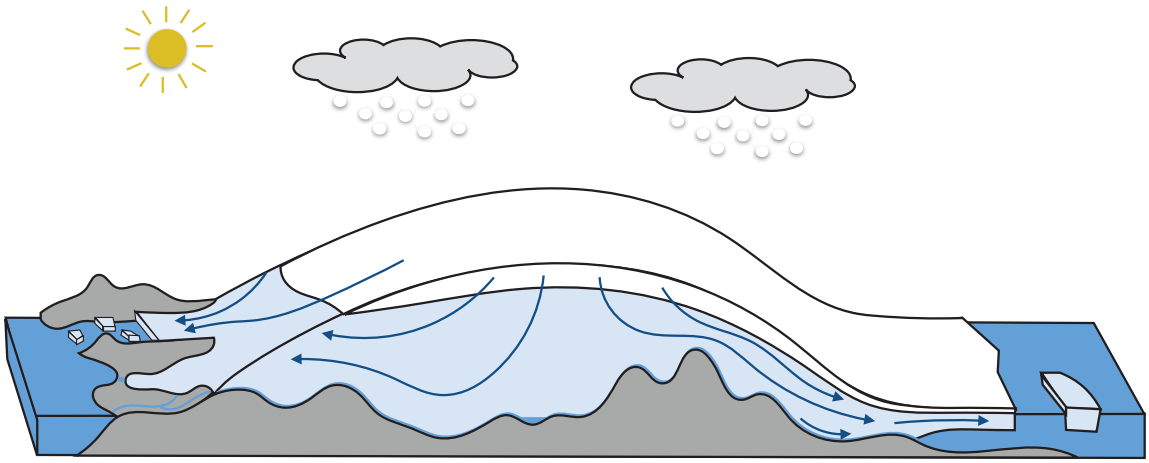

Figure 1: Schematic for mass balance of a glacier or ice sheet. Snow falls on the surface and some portion is melted away. The remaining snow (i.e. firn) compacts over time and turns into glacial ice, which then flows to the margin, where is melted or calves off into the ocean.

the meltwater. In this paper, we focus on the dynamics of meltwater percolating through porous snow.

Several models have been developed for the percolation of meltwater through porous snow. Colbeck [3, 4, 5] studies the problem of a propagating front of refreezing meltwater, analytically deriving the rate of melting and the speed of the front. Gray and Morland [14, 15, 16] clarify the previous analysis in the context of mixture theory and include the compaction snow. This work connects firn hydrology to the literature on dry compaction, such as the empirical models Herron and Langway [19] derive for the change of snow density with depth. In a more recent suite of models, Ligtenberg, Kuipers Munike and colleagues [23, 24, 25] take a different approach to the previous models by including an empirical 'tipping bucket' hydrology model. In this description of the hydrology, the firn is divided into distinct layers and water fills each layer up to the irreducible water content and then trickles down into the lower layers. Cummings et al. [7] describe a coupled hydrology, compaction, and thermal model implemented in FEniCS. For the hydrology, they use the enthalpy-gradient method as described by Aschwanden et al. [2], where the meltwater fully saturates the firn and percolates at a rate which is proportional to the gradient of porosity.

In this manuscript, we construct a continuum model for the surface of a glacier or ice sheet. We include a model for the temperature structure with depth. The surface heat flux varies throughout the year, oscillating between the warm summer maximum and cold winter minimum. This surface flux is advected and diffused through the snow and in the simplest case leads to the well-known "thermal wave" [6], which we analyze in §2. We include the effects of dry compaction of firn in §3, where ice density changes with depth due to the rearrangement of snow crystals, growth of snow crystals, and closure of air voids by overburden pressure. These physical processes are captured in several empirical models [1, 19, 27] and we compare these compaction models to data from Antarctica [18]. We then describe the physics of meltwater percolation and the interplay between refreezing of meltwater and the release of latent heat warming the ice. We unify the temperature, compaction, and melt-

water percolation physics into an enthalpy method. We write conservation equations for enthalpy and total water that are valid in both cold and temperate regions, which we solve numerically using a finite volume code implemented in MATLAB. In the temperate areas, the mixture temperature stays at the melting point allowing liquid water and ice crystals coexist. In these regions, we model the percolation of the liquid meltwater using Darcy's law, which allows for physically motivated connections between compaction, snow porosity, and the rate of meltwater flow.

Within the enthalpy framework, we analyze three problems. First, we look at a front of meltwater propagating through stationary, cold snow with constant porosity. The refreezing of the meltwater warms the snow and the front propagates at a constant velocity, which we determine analytically. We then compare the results to our numerical simulations and data from Humphrey et al. [21]. In the next problem, we subject the snow to an oscillatory surface energy forcing, where melting occurs for part of the year. The meltwater then propagates through the snow as a front and warms the snow as it refreezes. With a large enough surface energy input, sufficient meltwater is produced for water to exist year-round in the near-surface porous snow. In effect, the year-round presence of liquid water, i.e. a perennial firn aquifer [11], keeps the bottom of the firn warm as compared to the surface of the ice sheet, where the temperature drops below zero in the winter. Finally, we examine the dynamics of meltwater percolation when the snow becomes fully saturated with water, i.e. where all of the void space between snow crystals is taken up by liquid water. In this case, the amount of water that can enter the snow pack is limited and we must solve for the water pressure. To illustrate the dynamics, we reanalyze the propagation of a meltwater front in stationary, cold snow but with a porosity structure that decreases with depth. As the front propagates down, the saturation increases until the snow fully saturates, at which point the amount of meltwater that can enter the pore space decreases. Thus, a new upward-propagating front initiates and the speed of the upward and downward fronts is codependent.

2 Englacial temperature fluctuations

We start by analyzing the near-surface temperature structure of a glacier or ice sheet. In the ice interior, the internal energy equation is

$$\rho_i c_i \left(\frac{\partial T}{\partial t} + w_i \frac{\partial T}{\partial z} \right) = \frac{\partial}{\partial z} \left(K \frac{\partial T}{\partial z} \right) - \mathscr{L} M, \tag{1}$$

in which we only consider a single vertical dimension and ignore shear heating. The terms on the left side describe the advection of heat with the ice density ρ_i, ice heat capacity c_i, and vertical ice velocity w_i. The first term on the right side describes the conduction of heat with ice conductivity K and the next term is the latent heat of fusion, where $\mathscr{L}$ is the latent heat (per unit mass) and M is the internal mass melt rate per volume ($\mathrm{kg\ s^{-1}\,m^{-3}}$).

At the lower boundary condition we either consider zero heat flux (Neumann) or a prescribed far-field temperature (Dirichlet), i.e.

$$K \frac{\partial T}{\partial z} = 0 \quad \text{or} \quad T = T_\infty \quad \text{as} \quad z \to -\infty, \tag{2}$$

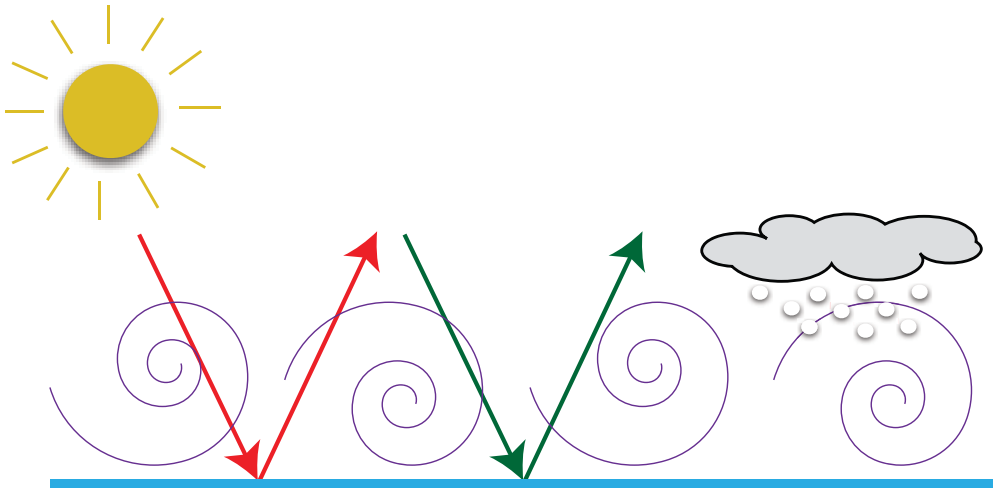

Figure 2: Schematic for the surface energy balance including the shortwave (red arrows) and longwave (green arrows) radiation from the sun, the heat transfer due to turbulence (purple eddies), and the addition of heat due to snow accumultion.

where we use the Neumann condition when ice is advected out of the domain and the Dirichlet condition when ice flows into the domain.

The upper boundary condition for equation (1) is applied at the ice surface $z_s(t)$, which is a free boundary. Using the kinematic condition, we can relate the velocity of the ice surface to the rate of accumulation $a(t)$ and surface melt rate per area m (kg s^{-1} m^{-2}), i.e.

$$\dot{z}_s = a + w_i - \frac{m}{\rho_i}, \tag{3}$$

where w_i is the vertical velocity of the ice.

While the kinematic condition gives the location of the ice surface, the surface energy balance provides the boundary condition for the internal energy equation. Here we write the surface energy balance as

$$K\frac{\partial T}{\partial z} + \mathscr{L}m = (1-\alpha)S_w + L_w - \epsilon\sigma T^4 + h(T_a - T) + \rho_i c_i a(T_s - T), \tag{4}$$

and a schematic is shown in figure 2. The terms in 4 are

$$\begin{aligned}
K\frac{\partial T}{\partial z} &\equiv \text{Thermal conduction} \\
\mathscr{L}m &\equiv \text{Latent heat of fusion} \\
\alpha &\equiv \text{Ice albedo (reflection fraction)} \\
S_w &\equiv \text{Incident short wave radiation} \\
L_w &\equiv \text{Incident long wave radiation} \\
\epsilon\sigma T^4 &\equiv \text{Outgoing longwave radiation} \\
h(T_a - T) &\equiv \text{Turbulent heat transfer} \\
\rho_i c_i a(T_s - T) &\equiv \text{Accumulation added heat}
\end{aligned}$$

K	2.1 W m^{-1} K^{-1}	Thermal conductivity
S_w	161 W m^{-2}	Net shortwave radiation
ϵ	0.97	Emissivity
σ	5.7×10^{-8} W m^{-2} K^{-4}	Stefan-Boltzmann constant
$L_w - \epsilon\sigma T_s^4$	-28 W m^{-2}	Net longwave radiation
ρ_i	917 kg m^{-3}	Ice density
c_i	2050 J kg^{-1} K^{-1}	Specific heat capacity
h	10.3 W m^{-2} K^{-1}	Turbulent heat flux
a_0	9.5×10^{-9} m s^{-1}	Accumulation
T_a	267 K	Average air temperature
T_m	273.15 K	Melting temperature

Table 1: Parameters for the surface energy balance [6, 34].

We define the constants and give representative values in table 2. The source heat of heat from accumulation arises from the fact that as a layer of snow lands on the surface of the ice it carries a certain amount of heat. This heat is advected through the ice and only results in a net heat transfer if the accumulation and advection are not balanced. The temperature of the snow need not be the air temperature T_a and may be another temperature T_s, however here we consider $T_a = T_s$.

2.1 Nondimensionalized equations

We now nondimensionalize the internal energy equation and boundary conditions. We start by writing the temperature as

$$T = T_m + \Delta T\theta, \tag{5}$$

where ΔT is a to-be-determined temperature difference, which we assume to be small compared to the melting temperature, T_m. We assume that the melting temperature is a constant and ignore all effects of premelting [8].

2.1.1 Surface conditions

We now linearize the surface energy balance, equation (4), around the melting temperature T_m. We scale lengths with the to-be-determined lengthscale ℓ as $z = \ell\hat{z}$ and scale the surface melt rate as $m = \mathscr{M}\hat{m}$. We drop the hats on nondimensional variables and linearize the nonlinear outgoing longwave radiation to find

$$\frac{K\Delta T}{\ell}\frac{\partial\theta}{\partial z} + \mathscr{L}\mathscr{M}m + \left(h + 4\epsilon\sigma T_m^3\right)\Delta T\theta + \rho c_i a\Delta T\theta = (1-\alpha)S_w + L_w - \epsilon\sigma T_m^4 + h(T_a - T_m) + \rho c_i a(T_a - T_m). \tag{6}$$

We call the right hand side $Q(t)$ and express it using the following

$$(1-\alpha)S_w = \overline{S}_w\left(1 - \cos\{2\pi t\}\right) \quad \text{where} \quad \overline{S}_w = 96 \text{ W m}, \tag{7}$$

$$L_w - \epsilon\sigma T_m^4 = \overline{L}_w \quad \text{where} \quad \overline{L}_w = -28 \text{ W m}^{-2}, \tag{8}$$

$$T_a = \overline{T}_a\left(1 - \Delta T_a\cos(2\pi t)\right) \quad \text{where} \quad \overline{T}_a = 267 \text{ K} \quad \text{and} \quad \Delta T_a = 10 \text{ K}, \tag{9}$$

where ΔT_a is a representative annual surface temperature variation (van den Broeke et al. [34]). Using these expressions the surface flux is given as

$$Q(t) = \left[\overline{S}_w + \overline{L}_w + h\left(\overline{T}_a - T_m\right) + \rho c_i a\left(\overline{T}_a - T_m\right)\right] + \left[\overline{S}_w + h\Delta T_a + \rho c_i \Delta T_a\right]\cos(2\pi t), \tag{10}$$

which can be estimated as

$$Q(t) \approx 5 - 200\cos(2\pi t)\ \text{W m}^{-2}. \tag{11}$$

Since the constant offset is about 3% of the fluctuation, we approximate this as

$$Q(t) = Q_0 F(t) \quad \text{where} \quad Q_0 = 200\ \text{W m}^{-2} \quad \text{and} \quad F(t) = -\cos(2\pi t). \tag{12}$$

We write the radiative and turbulent heat flux terms as H, i.e.

$$H = h + 4\epsilon\sigma T_m^3 \approx 14.8\ \text{W m}^{-2}\ \text{K}^{-1}, \tag{13}$$

so that

$$\frac{K\Delta T}{\ell}\frac{\partial\theta}{\partial z} + \mathscr{L}\mathscr{M}m + H\Delta T\theta + \rho c_i a\Delta T\theta = Q_0 F(t). \tag{14}$$

Examining the relative sizes of the terms in equation (14) shows that the dominant balance is

$$H\Delta T\theta \sim Q_0 F(t) \tag{15}$$

and from this we can determine the temperature difference as

$$\Delta T = \frac{Q_0}{H} \approx 13.5\ \text{K}. \tag{16}$$

At the same time, we choose the scale for the melt rate $\mathscr{M}$ to balance the surface flux scale Q_0 as

$$\mathscr{M} = \frac{Q_0}{\mathscr{L}} = 6\times 10^{-4}\ \text{kg s}^{-1}\ \text{m}^{-2}. \tag{17}$$

Thus, we can write the full nondimensional surface energy balance as

$$\frac{K\Delta T}{\ell Q_0}\frac{\partial\theta}{\partial z} + m + \theta + \frac{\rho_i c_i \omega\ell}{H}a\theta = F(t). \tag{18}$$

where we scale the accumulation rate with the velocity scale $\omega\ell$ as a natural timescale is the frequency of the seasonal oscillation $\omega = 1/\text{year}$.

Thus, the kinematic condition, i.e. equation (3), at the surface of the ice is given by

$$\dot{z}_s = a + w_i - \frac{Q_0}{\rho_i\mathscr{L}\omega\ell}m. \tag{19}$$

Based on this scaling, we define the lengthscale ℓ so that

$$\ell = \frac{Q_0}{\rho_i\mathscr{L}\omega} \approx 20.6\ \text{m} \tag{20}$$

and using this definition we find that

$$\frac{K\Delta T}{\ell Q_0} = \frac{1}{Pe\mathcal{S}} \approx 0.008 \quad \text{and} \quad \frac{\rho_i c_i\omega\ell}{H} = \frac{1}{\mathcal{S}} \approx 0.08, \tag{21}$$

where we define the Péclet and Stefan numbers as

$$Pe = \frac{\rho_i c_i \omega\ell^2}{K} \approx 11 \quad \text{and} \quad \mathcal{S} = \frac{\mathscr{L}}{c_p\Delta T} \approx 12. \tag{22}$$

2.1.2 Nondimensional internal energy

Inserting the nondimensional variables into equation (1) and dropping the hats gives

$$Pe\left(\frac{\partial\theta}{\partial t}+w_i\frac{\partial\theta}{\partial z}\right)=\frac{\partial}{\partial z}\left(K\frac{\partial\theta}{\partial z}\right), \tag{23}$$

subject to the surface energy balance and kinematic condition

$$\frac{1}{Pe\mathcal{S}}\frac{\partial\theta}{\partial z}+m+\theta+\frac{a}{\mathcal{S}}\theta=F(t) \quad \text{and} \quad \dot{z}_s=a+w_i-m \quad \text{on} \quad z=z_s, \tag{24}$$

and at depth, we either have the boundary condition

$$\theta=\frac{T_\infty-T_m}{\Delta T}=\theta_\infty \quad \text{or} \quad \frac{\partial\theta}{\partial y}=0 \quad \text{as} \quad z\to-\infty, \tag{25}$$

where, in the first case, $\theta_\infty\approx-O(1)$ and is a parameter of the system.

We can move into a frame relative to the ice surface as

$$y=z_s(t)-z, \tag{26}$$

where the space and time coordinates are transformed as

$$\frac{\partial}{\partial t}=\dot{z}_s\frac{\partial}{\partial y}+\frac{\partial}{\partial t} \quad \text{and} \quad \frac{\partial}{\partial z}=-\frac{\partial}{\partial y}. \tag{27}$$

Thus, nondimensional internal energy changes to

$$Pe\left[\frac{\partial\theta}{\partial t}+(a-m)\frac{\partial\theta}{\partial y}\right]=\frac{\partial}{\partial y}\left(K\frac{\partial\theta}{\partial y}\right), \tag{28}$$

subject to

$$\theta+\frac{1}{\mathcal{S}}\left(a\theta-\frac{1}{Pe}\frac{\partial\theta}{\partial y}\right)=F(t) \quad \text{on} \quad y=0 \quad \text{and} \quad \frac{\partial\theta}{\partial y}=0 \quad \text{as} \quad y\to\infty \quad (\theta<0). \tag{29}$$

When the surface reaches the melting the temperature, the boundary condition switches to the Dirichlet condition $\theta=0$ at $y=0$ and the surface energy flux determines the rate of melting m. Without an internal source of heat or meltwater percolation, melting can only occur at the surface and, therefore, the new boundary conditions are

$$\frac{1}{Pe\mathcal{S}}\left[-\frac{\partial\theta}{\partial y}\right]_{y=0}+m=F(t), \quad \theta=0 \ \text{ on } \ y=0 \ \text{ and } \ \theta=\theta_\infty \ \text{ as } \ y\to\infty \ \ (m>0). \tag{30}$$

2.2 Analytical benchmarks

2.2.1 Simple seasonal fluctuations

Here we show the classical problem of the seasonal oscillation of englacial temperature [6]. We prescribe the temperature at the surface as a function of time and enforce zero heat flux at depth. We take $Pe\mathcal{S}=\infty$, $F=-\cos(2\pi t)$, $a=m=0$, and K independent of depth

and temperature. Thus, our problem is to determine the diffusion of heat away from a wall with an oscillating temperature, i.e.

$$\frac{\partial \theta}{\partial t} = \frac{1}{Pe}\frac{\partial^2 \theta}{\partial y^2} \quad \text{subject to} \quad \theta(y=0) = -1 - \cos(2\pi t) \quad \text{and} \quad \left[\frac{\partial \theta}{\partial y}\right]_{y\to\infty} = 0. \tag{31}$$

We look for solutions of the form

$$\theta(y,t) = -1 - \Re\left\{f(y)e^{2\pi i t}\right\}. \tag{32}$$

Inserting this into the internal energy equation, we find

$$f'' = 2\pi i Pe f. \tag{33}$$

We look for exponential solutions of the form

$$f = Ce^{-\alpha y}, \tag{34}$$

and find that

$$\alpha = \pm\sqrt{\pi Pe}(1+i). \tag{35}$$

We choose the positive branch so that α is positive and

$$\left[\frac{\partial \theta}{\partial y}\right]_{y\to\infty} = 0. \tag{36}$$

Now at $y = 0$, we have that

$$\Re\left\{Ce^{2\pi i t}\right\} = \Re\left\{e^{2\pi i t}\right\}. \tag{37}$$

This gives that

$$\theta(y,t) = -1 - e^{-\sqrt{\pi Pe}y}\cos(2\pi t - \sqrt{\pi Pe}y), \tag{38}$$

which is plotted in figure 3.

2.2.2 Robin seasonal model with advection

We now consider the full heat flux boundary condition (i.e. a Robin condition) and include advection with $a = 1$ and $m = 0$. We still apply $F = -\cos(2\pi t)$ and enforce zero heat flux as $y \to \infty$. Thus, we solve the problem

$$Pe\left(\frac{\partial \theta}{\partial t} + \frac{\partial \theta}{\partial y}\right) = \frac{\partial^2 \theta}{\partial y^2}, \tag{39}$$

subject to

$$\left[\theta + \frac{1}{\mathcal{S}}\theta - \frac{1}{Pe\mathcal{S}}\frac{\partial \theta}{\partial y}\right]_{y=0} = -1 - \cos(2\pi t) \quad \text{and} \quad \left[\frac{\partial \theta}{\partial y}\right]_{y\to\infty} = 0. \tag{40}$$

Again we try for a solution of the form

$$\theta(y,t) = -1 - \Re\left\{f(y)e^{2\pi i t}\right\}, \tag{41}$$

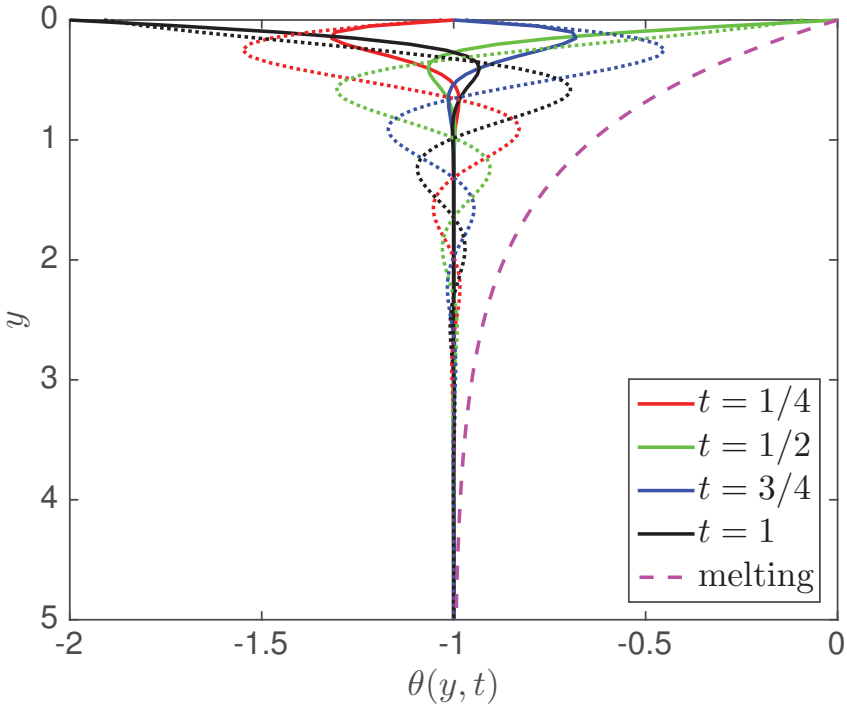

Figure 3: The oscillation of englacial temperature due to the seasonal variation of the surface heat flux and air temperature: solid lines are the simple temperature wave, equation (38) and dotted lines are the Robin waves, equation (47). The dashed magenta line is the solution for a continuously melting surface, equation (51). The penetration length is governed by the Péclet number, which is chosen to be $Pe = 11$ in all cases. We also choose the Stefan number to be $\mathcal{S} = 12$ in equations (47) and (51) as well as choose the constant forcing in equation (51) to be $F = 0.1$.

and find that

$$f'' - Pef' - 2\pi iPef = 0. \tag{42}$$

Inserting negative exponential solutions of the form $f = Ce^{-\alpha y}$ gives

$$\alpha^2 + Pe\alpha - 2\pi iPe = 0. \tag{43}$$

The quadratic formula gives

$$\alpha = \frac{Pe}{2}\left(-1 + \sqrt{1 + \frac{8\pi i}{Pe}}\right). \tag{44}$$

where we choose the positive sign so that the flux decays at infinity. Thus, we have that

$$f = Ce^{-\alpha y} = C\exp\left\{-\frac{Pe}{2}\left(-1 + \sqrt{1 + \frac{8\pi i}{Pe}}\right)y\right\}. \tag{45}$$

Inserting this into the Robin condition at the surface gives

$$C = \frac{\mathcal{S}Pe}{\mathcal{S}Pe + Pe + \alpha}. \tag{46}$$

Thus, we find that

$$\theta(y,t) = -1 - \Re\left\{\frac{\mathcal{S}Pe}{\mathcal{S}Pe + Pe + \alpha}e^{2\pi it - \alpha y}\right\}, \tag{47}$$

which is also shown in figure 3. The advection due to accumulation leads to oscillations deeper in the ice. Also, the Robin boundary condition is well approximated by a Dirichlet condition as both solutions agree quite well at the surface.

2.2.3 Continuous melting

Here we study the problem of continuous melting driven by a constant surface forcing. Thus, we have that

$$\frac{\partial\theta}{\partial t} - m\frac{\partial\theta}{\partial y} = \frac{1}{Pe}\frac{\partial^2\theta}{\partial y^2} \quad (m \neq 0) \quad \text{subject to} \quad \theta(y=0) = 0 \quad \text{and} \quad \theta(y\to\infty) = \theta_\infty, \tag{48}$$

with the additional constraint

$$\frac{1}{Pe\mathcal{S}}\left[-\frac{\partial\theta}{\partial y}\right]_{y=0} + m = F \quad \text{at} \quad y = 0. \tag{49}$$

We choose F as a constant and, therefore in the steady state problem, m is also a constant. The internal energy equation in steady state is

$$\frac{\partial^2\theta}{\partial y^2} + PeM\frac{\partial\theta}{\partial y} = 0, \tag{50}$$

which integrates to

$$\theta = \theta_\infty\left(1 - e^{-PeMy}\right). \tag{51}$$

We can insert this into the surface energy balance to solve for m to find

$$m = \frac{F\mathcal{S}}{\mathcal{S}+1}, \tag{52}$$

which states that the forcing must add sensible heat to warm the ice up from T_∞ to T_m and then add the latent heat required to melt. This solution for the steady-state temperature profile below a continuously melting surface is also shown on figure 3.

3 Compaction of porous ice

The snow that falls on the surface of a glacier is porous, i.e. a mixture of solid and air. The parameter that characterizes the amount of void space is the porosity ϕ. Thus, the total density ρ_T of the mixture becomes

$$\rho_T = \rho_i(1-\phi) + \rho_a\phi \tag{53}$$

However, the density of air ρ_a is so small by comparison that we neglect it. Since the volume fraction will change with depth, the conservation of ice is given by

$$\frac{\partial}{\partial t}\left[\rho_i(1-\phi)\right] + \nabla\cdot\left[\rho_i(1-\phi)\underline{u}_i\right] = 0. \tag{54}$$

In addition, we need an evolution equation for ϕ, which we write in the form

$$\frac{\partial\phi}{\partial t} + \underline{u}_i\cdot\nabla\phi = -\mathscr{C}, \tag{55}$$

where $\mathscr{C}$ is a compaction function that describes how porosity changes with depth. The standard empirical firn densification model is given by Herron and Langway [19] and is of the form

$$\mathscr{C} = -c\phi, \tag{56}$$

where the constant c (yr^{-1}) is potentially dependent on both the accumulation rate and temperature, i.e.

$$c = \begin{cases} \frac{11a}{\rho_w}\exp\left\{-\frac{10160}{RT}\right\} & \text{if } \phi > 0.4 \\ 575\sqrt{\frac{a}{\rho_w}}\exp\left\{-\frac{21400}{RT}\right\} & \text{if } \phi \le 0.4 \end{cases}, \tag{57}$$

where a is the accumulation rate, R is the ideal gas constant, T is the absolute temperature, and ρ_w is the density of water. Other forms for the prefactor are discussed by Morris and Wingham [27], Reeh [29], and Zwally and Li [36].

Another empirical compaction function relates the closure of voids to the difference in ice and air pressures, i.e.

$$\mathscr{C} = -\frac{(p_i - p_a)}{\eta}\phi, \tag{58}$$

where p_i is the hydrostatic ice pressure, i.e.

$$\frac{\partial p_i}{\partial z} = -(1-\phi)\rho_i g. \tag{59}$$

The other terms in equation (58) are the air pressure p_a (which we neglect) and η is the ice viscosity, which is potentially a nonlinear function of the strain rates [6]. In this model, the decrease of porosity occurs by the creep closure of air voids, which is in many ways similar to the creep closure of subglacial conduits [12, 31].

Near the surface of glaciers and ice sheets, the growth of ice crystals is important densification process and neglected in equation (58). Arthern et al. [1] incorporate the growth of ice crystals into an empirical model of the form

$$\mathscr{C} = -\frac{\varkappa^2 \phi p_i}{r^2 \eta}, \tag{60}$$

where r^2 is the surface area of snow grains, $\varkappa^2$ is a baseline crystal size. In this model, an increase in the ice crystal size leads to an increase in ice viscosity and the crystals grow according to

$$\frac{\partial r^2}{\partial t} + \underline{u}_i \cdot \nabla r^2 = K_r, \tag{61}$$

where K_r is a temperature-dependent growth rate.

3.1 Steady-state solutions

In this section, we derive the one-dimensional vertical, steady-state solutions for each of the three compaction laws described above. All three models rely on mass conservation, which in steady state is

$$\frac{\partial}{\partial z}\left[(1-\phi) w_i\right] = 0. \tag{62}$$

The boundary conditions are

$$\phi = \phi_0, \quad w_i = -a, \quad r^2 = 0 \quad \text{and} \quad p_i = 0 \quad \text{on} \quad z = z_s, \tag{63}$$

which state that the snow falls with a fixed porosity ϕ_0, the velocity of the snow at the surface is balanced by the accumulation rate, the snow crystals are negligibly small when they land on on the surface, and there is no hydrostatic pressure of the ice at the surface. Integrating mass conservation once, we find that

$$w_i = -\frac{a_0}{(1-\phi)}, \tag{64}$$

where we choose $a_0 = (1-\phi_0)a$.

3.2 Herron and Langway model

In the empirical model of Herron and Langway, the steady-state compaction is given by equation (56) as

$$\mathscr{C} = -w_i \frac{d\phi}{dy} = -c\phi, \tag{65}$$

where we use depth coordinates $y = z_s - z$. Inserting the velocity from equation (64) gives a single equation for ϕ as

$$\frac{d\phi}{dy} = -\frac{c}{a_0}\phi(1-\phi) \quad \text{subject to} \quad \phi = \phi_0 \quad \text{on} \quad y = 0. \tag{66}$$

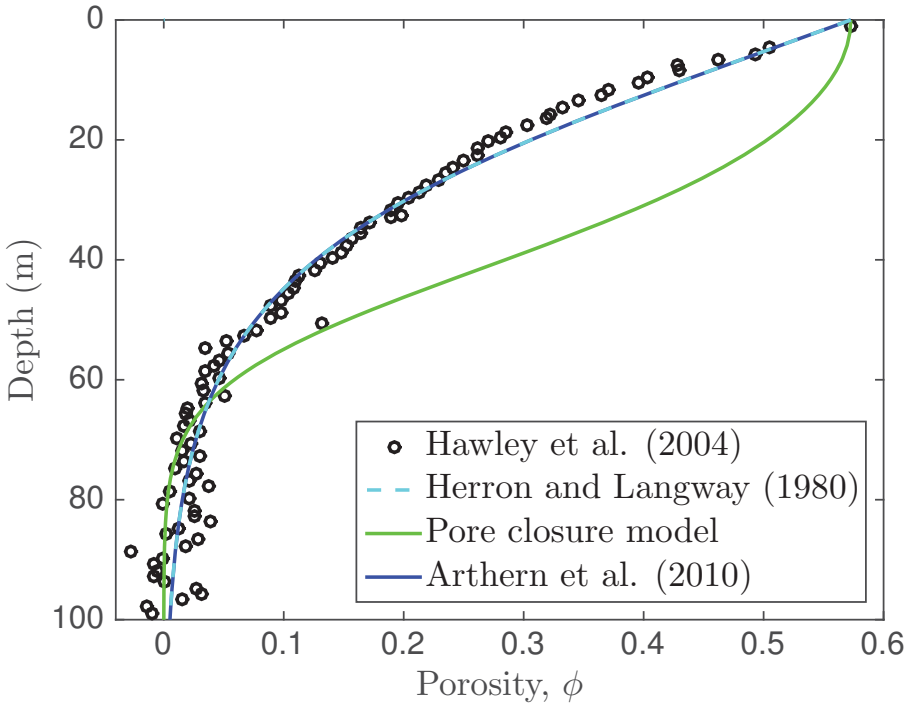

Figure 4: Comparison between dry compaction models and Simple Dome snow density data from Hawley et al. [18]. The Arthern et al. [1] and Herron and Langway [19] models reduce to the same equation and therefore yield the same fit, yet with different interpretations for the constants that set the compaction lengthscale.

Integrating, we find that

$$\phi = \frac{\phi_0 \exp\left\{-\frac{c}{a_0} y\right\}}{1 - \phi_0 + \phi_0 \exp\left\{-\frac{c}{a_0} y\right\}}, \tag{67}$$

where the compaction lengthscale is given by the ratio between the porosity-weighted accumulation and the compaction prefactor, $\delta_c = a_0/c$.

We compare this model to the Hawley et al. [18] data in figure 4. The two fitting parameters are the initial density, which we just take as the first data point, and the compaction length. Here we find that $\delta_c \approx 18$ m fits the data well. Using the inferred value of $a_0 \approx 0.12$ m yr^{-1} from Ref. [18] we find that $c \approx 7 \times 10^{-3}$ yr^{-1}, which is close to the empirical value for c when $\phi \leq 0.4$.

3.3 Pore closure model

The compaction function in steady state for the pore closure model is given by

$$\mathscr{C} = -w_i \frac{d\phi}{dy} = -\frac{p_i}{\eta}\phi, \quad \text{with} \quad \frac{dp_i}{dy} = (1-\phi)\rho_i g, \tag{68}$$

Inserting the velocity into the second equation and taking a derivative, we find a single equation for ϕ as

$$\frac{1}{(1-\phi)}\frac{d}{dy}\left(\frac{1}{\phi(1-\phi)}\frac{d\phi}{dy}\right) = -\frac{\rho_i g}{a_0 \eta}, \tag{69}$$

subject to

$$\phi = \phi_0 \quad \text{and} \quad \frac{d\phi}{dy} = 0 \quad \text{on} \quad y = 0. \tag{70}$$

We now use the change of variables

$$\frac{1}{(1-\phi)}\frac{d}{dy} = \frac{d}{d\zeta} \quad \text{or equivalently} \quad \frac{dy}{d\zeta} = \frac{1}{1-\phi} \quad \text{and} \quad y = \int_0^\zeta \frac{d\xi}{1-\phi(\xi)}. \tag{71}$$

to write this as

$$\frac{\partial^2}{\partial \zeta^2}\ln(\phi) = -\frac{\rho_i g}{a_0 \eta}. \tag{72}$$

Integrating twice gives

$$\phi(\zeta) = C\exp\left\{-\frac{\rho_i g}{2a_0\eta}\zeta^2 + D\zeta\right\}, \tag{73}$$

for arbitrary constants C and D. The surface $y = 0$ is collocated with $\zeta = 0$, therefore, $C = \phi_0$. The derivative condition on the surface gives that

$$\left[\frac{d\phi}{d\zeta}\right]_{\zeta=0} = 0 \longrightarrow D = 0. \tag{74}$$

Thus, we have that

$$\phi(\zeta) = \phi_0\exp\left\{-\frac{\rho_i g}{2a_0\eta}\zeta^2\right\} \quad \text{and} \quad y = \int_0^\zeta \frac{d\xi}{1-\phi_0\exp\left\{-\frac{\rho_i g}{2a_0\eta}\xi^2\right\}}. \tag{75}$$

In this model, the compaction lengthscale is given by

$$\delta_c = \sqrt{\frac{a_0\eta}{\rho_i g}}. \tag{76}$$

This model is shown in figure 4 using $\delta_c = 25$. Using the inferred accumulation rate from Ref. [18] and the viscosity of glacial ice, it appears that $\delta_c = 20$ might be a better choice but in either case, this model does not fit the data well. The two primary problems are that the zero pressure condition at the surface leads to a zero derivative on porosity, which is clearly not reflected in the data. Second, the decay of porosity is not fast enough near the surface and too fast at depth [6].

3.4 Arthern et al. model

The model employed by Arthern and colleagues builds on the pore closure model by adding the growth of ice crystals, which changes the rate of decay of porosity and physically motivates the Herron and Langway compaction model. The compaction function in this case is

$$\mathscr{C} = -w_i\frac{d\phi}{dy} = -\frac{\varkappa^2\phi p_i}{r^2\eta} \quad \text{with} \quad \frac{dp_i}{dy} = (1-\phi)\rho_i g \quad \text{and} \quad w_i\frac{dr^2}{dy} = K_r. \tag{77}$$

Inserting the velocity, these equations become

$$\frac{d\phi}{dy} = \frac{\varkappa^2 \phi(1-\phi)p_i}{a_0 r^2 \eta} \quad \text{with} \quad \frac{dp_i}{dy} = (1-\phi)\rho_i g \quad \text{and} \quad \frac{dr^2}{dy} = \frac{K_r}{a_0}(1-\phi). \tag{78}$$

The structure of the equations for pressure and crystal size are such that we can divide one by the other, i.e.

$$\frac{dp_i}{dr^2} = \frac{\rho_i g a_0}{K_r} \quad \text{which implies that} \quad p_i = \frac{\rho_i g a_0 r^2}{K_r}, \tag{79}$$

where we have used the fact that both ice pressure and crystal size are zero at the surface. Inserting this into the evolution equation for porosity, we find that

$$\frac{d\phi}{dy} = \frac{\rho_i g \varkappa^2}{\eta K_r}\phi(1-\phi) \quad \text{subject to} \quad \phi = \phi_0 \quad \text{on} \quad y = 0. \tag{80}$$

This is exactly the Herron and Langway model with the empirical constant given by $c = \rho_i g \varkappa^2 a_0/(\eta K_r)$. The compaction length in this case is $\delta_c = \rho_i g \varkappa^2/(\eta K_r)$. This model is overlain in figure 4 using the same compaction length, $\delta_c = 18$ m, which shows that the ratio $\varkappa^2/K_r$ is a very large number.

4 Percolation through porous ice

Here we examine the flow of meltwater through porous, compacting ice. We keep track of the porosity, the saturation, the flow of water, the compaction, and the melt/refreezing of water into ice. The void fraction is ϕ, the solid fraction is $1-\phi$, and the portion of the voids filled by water is given by the saturation S, which varies between 0 and 1. A schematic of each component is shown in figure 5. Conservation of mass for ice, water, and air are

$$\frac{\partial(S\phi\rho_w)}{\partial t} + \nabla\cdot(S\phi\rho_w \underline{u}_w) = M, \tag{81}$$

$$\frac{\partial}{\partial t}\left[(1-\phi)\rho_i\right] + \nabla\cdot((1-\phi)\rho_i \underline{u}_i) = -M, \tag{82}$$

$$\frac{\partial}{\partial t}[(1-S)\phi\rho_a] + \nabla\cdot[(1-S)\phi\rho_a \underline{u}_a] = 0, \tag{83}$$

where the subscripts w, i, and a indicate water, ice, and air, respectively. The rate at which meltwater refreezes and turns into ice internally is given by M. We again assume that the air flow and air density are negligible in order to neglect equation (83). Here there are four unknowns ϕ, S, $\underline{u}_i$, and $\underline{u}_w$, thus, we supplement equations (81) and (82) with two other equations: Darcy's law and a compaction function.

For the flow of water through the porous snow we use Darcy's law for a partially saturated medium, i.e.

$$\phi S\left(\underline{u}_w - \underline{u}_i\right) = -\frac{k(\phi)}{\mu} k_r(S)\left(\nabla p_w + \rho_w g\hat{z}\right), \tag{84}$$

where p_w is the water pressure, $k(\phi)$ is the permeability, $k_r(S)$ is the relatively permeability, and μ is the viscosity of the water. As long as the snow is partially saturated, i.e. $S < 1$,

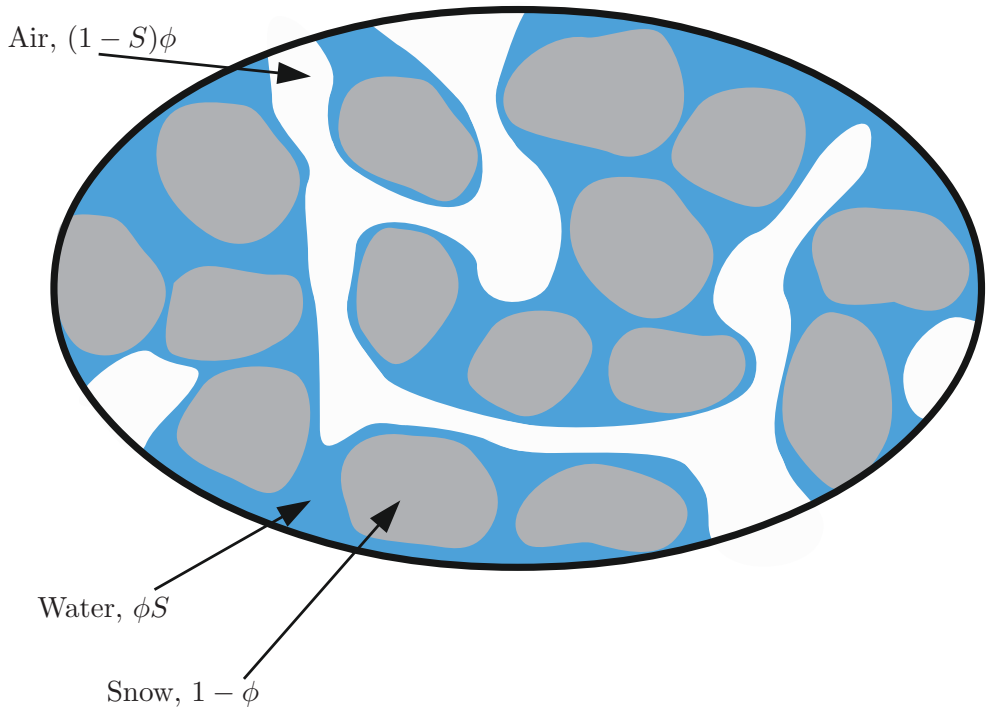

Figure 5: The three components of meltwater-infiltrated snow: air, water, and snow (adapted from [32]).

the flow is driven by capillary forces along liquid bridges connecting snow crystals. Thus, we relate the water pressure to the capillary pressure p_c as $p_w = p_a - p_c$, where p_a is the air pressure and the capillary pressure is a prescribed function of the saturation S. If the snow is fully saturated, i.e. $S = 1$, the flow is no longer driven by capillary forces and the water pressure must be solved for, which we describe in §4.2. We close the problem by empirically relating permeability, relative permeability, and capillary pressure to the porosity and saturation. For the permeability as a function of the porosity, we use the Carman-Kozeny relationship, given by

$$k(\phi) = \frac{\phi^3 r^2}{180(1-\phi)^2}, \tag{85}$$

where r is a measure of the snow particle grain size. For the relative permeability and capillary pressure, we choose

$$k_r(S) = S^\beta \quad \text{and} \quad p_c = -p_w = \frac{\gamma}{r} S^{-\alpha}, \tag{86}$$

with the surface tension given by γ.

We take the compaction physics to be unchanged with the addition of meltwater and continue to use the dry compaction law of the form

$$\frac{\partial \phi}{\partial t} + \underline{u}_i \cdot \nabla \phi = \frac{M}{\rho_i} - \mathscr{C}\left(\phi, p_i, r^2\right), \tag{87}$$

where $\mathscr{C}\left(\phi, p_i, r^2\right)$ is the compaction law that is potentially a function of the porosity ϕ, the hydrostatic ice pressure p_i, and the ice crystal size r^2.

In the region where the meltwater flows, we take the ice/water mixture to be fixed at the constant melting temperature T_m. In the adjacent cold regions, we solve the temperature evolution equation as described in §2, except that we consider the ice to be a porous media. In this case, the internal energy equation is given by

$$[\rho_i c_i(1-\phi) + \rho_w c_w \phi S] \frac{\partial T}{\partial t} + [\rho_i c_i (1-\phi)\underline{u}_i + \rho_w c_w \phi S \underline{u}_w] \cdot \nabla T = -\mathscr{L} M + \frac{\partial}{\partial z}\left(\overline{K}\frac{\partial T}{\partial z}\right), \quad (88)$$

where $\overline{K}$ could be a constant or $\overline{K} = (1-\phi)K_i + \phi S K_w$. The temperature is constant in the temperate regions where $S > 0$ and, therefore, in the cold regions the terms multiplying S are identically zero. Writing the equation in this fashion facilitates the construction of the enthalpy formulation.

4.1 Enthalpy methods

In this section, we combine the englacial temperature analysis with snow compaction and percolation of meltwater and derive conservation equations for the enthalpy and total water content of the system. The full equations are

$$\frac{\partial(\rho_w \phi S)}{\partial t} + \nabla \cdot [\rho_w \phi S \underline{u}_w] = M, \quad (89a)$$

$$\frac{\partial}{\partial t}[\rho_i(1-\phi)] + \nabla \cdot [\rho_i(1-\phi)\underline{u}_i] = -M, \quad (89b)$$

$$\phi S\left(\underline{u}_w - \underline{u}_i\right) = -\frac{k(\phi)}{\mu} k_r(S)\left(\nabla p_w + \rho_w g \hat{z}\right), \quad (89c)$$

$$\frac{\partial \phi}{\partial t} + \underline{u}_i \cdot \nabla \phi = \frac{M}{\rho_i} - \mathscr{C}\left(\phi, p_i, r^2\right), \quad (89d)$$

$$[\rho_i c_i(1-\phi) + \rho_w c_w \phi S] \frac{\partial T}{\partial t} + [\rho_i c_i (1-\phi)\underline{u}_i + \rho_w c_w \phi S \underline{u}_w] \cdot \nabla T = -\mathscr{L} M + \frac{\partial}{\partial z}\left(\overline{K}\frac{\partial T}{\partial z}\right). \quad (89e)$$

Here we include the rate of internal melting or refreezing M, which is a source of mass that only operates on interfaces and we include it here to ensure that mass is conserved. We combine equations (89a)-(89e) in order to conserve total water (ice plus liquid water) and enthalpy (sensible and latent heat) across melting or refreezing interfaces. Using this approach, commonly referred to as the enthalpy method, we can avoid tracking the phase change interfaces and solve for their location using inequalities.

4.1.1 Total water

We now assume that the density of water and ice are the same, unless multiplied by gravity, which is the Boussinesq approximation. Thus, for the majority of the time we will write

$\rho_i = \rho_w = \rho$, which is a constant. Thus, equations (89a) and (89b) simplify to

$$\frac{\partial(S\phi)}{\partial t} + \nabla \cdot (S\phi \underline{u}_w) = \frac{M}{\rho}, \tag{90}$$

$$\frac{\partial}{\partial t}(1-\phi) + \nabla \cdot [(1-\phi)\underline{u}_i] = -\frac{M}{\rho}. \tag{91}$$

We refer to the total water as $\mathcal{W}$, which is the sum of liquid and solid fractions, i.e.

$$\mathcal{W} = 1 - \phi + S\phi, \tag{92}$$

which we can write an equation for by summing the ice and water conservation equations as

$$\frac{\partial \mathcal{W}}{\partial t} + \frac{\partial}{\partial z}\left[(1-\phi)w_i + S\phi w_w\right] = 0. \tag{93}$$

By adding and subtracting $S\phi w_i$ within the derivative, we have that

$$\frac{\partial \mathcal{W}}{\partial t} + \frac{\partial}{\partial z}\left(\mathcal{W} w_i\right) + \frac{\partial}{\partial z}\left[\phi S\left(w_w - w_i\right)\right] = 0. \tag{94}$$

We can simplify the second term using Darcy's law, which gives

$$\frac{\partial \mathcal{W}}{\partial t} + \frac{\partial}{\partial z}\left(\mathcal{W} w_i\right) = -\frac{1}{\mu}\frac{\partial}{\partial z}\left[k(\phi)k_r(S)\left(p_c'(S)\frac{\partial S}{\partial z} - \rho g\right)\right]. \tag{95}$$

4.1.2 Enthalpy

We define the enthalpy as the sum of sensible and latent heat, which gives

$$\mathcal{H} = \rho c_p\left(1 - \phi + S\phi\right)(T - T_m) + \rho \mathscr{L} S\phi = \rho c_p \mathcal{W}(T - T_m) + \rho \mathscr{L} S\phi, \tag{96}$$

where we also assume that the specific heat capacity is the same for both phases, i.e. $c_i = c_w = c_p$. By mass conservation we can write the internal energy equation as

$$\begin{aligned}
&\rho c_p \frac{\partial}{\partial t}[\mathcal{W}(T - T_m)] + \rho c_p \frac{\partial}{\partial z}\left[w_i \mathcal{W}(T - T_m)\right] \\
&\quad + \frac{1}{\mu}\frac{\partial}{\partial z}\left\{\left[k(\phi)k_r(S)\left(p_c'(S)\frac{\partial S}{\partial z} - \rho g\right)\right](T - T_m)\right\} + \mathscr{L} M = K\frac{\partial}{\partial z}\left(\mathcal{W}\frac{\partial T}{\partial z}\right).
\end{aligned} \tag{97}$$

where we take $\overline{K} = K\mathcal{W}$. We can now insert the definition of M from water mass conservation as well as add and subtract $\rho \mathscr{L} S\phi w_i$ from inside the M term, which gives

$$\begin{aligned}
&\frac{\partial}{\partial t}[\rho c_p W(T - T_m) + \rho \mathscr{L} S\phi] + \frac{\partial}{\partial z}\left[\rho c_p w_i \mathcal{W}(T - T_m) + w_i \rho \mathscr{L} S\phi\right] \\
&\quad + \frac{1}{\mu}\frac{\partial}{\partial z}\left\{\left[k(\phi)k_r(S)\left(p_c'(S)\frac{\partial S}{\partial z} - \rho g\right)\right]\left[\rho c_p(T - T_m) + \rho \mathscr{L}\right]\right\} = K\frac{\partial}{\partial z}\left(\mathcal{W}\frac{\partial T}{\partial z}\right).
\end{aligned} \tag{98}$$

Using the definition of $\mathcal{H}$, we find that

$$\begin{aligned}
&\frac{\partial \mathcal{H}}{\partial t} + \frac{\partial}{\partial z}\left(w_i \mathcal{H}\right) = \\
&\quad -\frac{1}{\mu}\frac{\partial}{\partial z}\left\{\left[\frac{k(\phi)k_r(S)}{\mu}\left(p_c'(S)\frac{\partial S}{\partial z} - \rho g\right)\right]\left[\rho c_p(T - T_m) + \rho \mathscr{L}\right]\right\} + K\frac{\partial}{\partial z}\left(\mathcal{W}\frac{\partial T}{\partial z}\right).
\end{aligned} \tag{99}$$

Thus, we have an evolution equation for $\mathcal{H}$, an equation for $\mathcal{W}$, and we can determine θ, S, and ϕ from $\mathcal{H}$ and $\mathcal{W}$ as

$$T = T_m + \min\left\{0, \frac{\mathcal{H}}{\mathcal{W}}\right\}, \quad \phi = 1 - \mathcal{W} + \max\left\{0, \frac{\mathcal{H}}{\rho\mathscr{L}}\right\}, \quad \text{and} \quad S = \max\left\{0, \frac{\mathcal{H}}{\rho\mathscr{L}\phi}\right\}. \tag{100}$$

The final equation required to close the system comes from compaction as

$$(1-\phi)\frac{\partial w_i}{\partial z} = -\mathscr{C}\left(\phi, p_i, r^2\right), \tag{101}$$

where we use the dry compaction models from §3. Thus, the equations are

$$\frac{\partial \mathcal{H}}{\partial t} + \frac{\partial}{\partial z}\left(w_i \mathcal{H}\right) = -\frac{1}{\mu}\frac{\partial}{\partial z}\left\{\left[k(\phi)k_r(S)\left(p_c'(S)\frac{\partial S}{\partial z} - \rho g\right)\right]\left(\rho c_p(T - T_m) + \rho\mathscr{L}\right)\right\} + K\frac{\partial}{\partial z}\left(\mathcal{W}\frac{\partial T}{\partial z}\right), \tag{102}$$

$$\frac{\partial \mathcal{W}}{\partial t} + \frac{\partial}{\partial z}\left(w_i \mathcal{W}\right) = -\frac{1}{\mu}\frac{\partial}{\partial z}\left[k(\phi)k_r(S)\left(p_c'(S)\frac{\partial S}{\partial z} - \rho g\right)\right]. \tag{103}$$

$$(1-\phi)\frac{\partial w_i}{\partial z} = -\mathscr{C}\left(\phi, p_i, r^2\right) \tag{104}$$

4.1.3 Boundary conditions for total water and enthalpy

The boundary conditions for w_i and w_w are

$$w_i = \dot{z}_s + \frac{m}{\rho} - a, \quad \phi S\left(w_w - \dot{z}_s\right) = -(1-\phi)\frac{m}{\rho} - r \quad \text{on} \quad z = z_s, \tag{105}$$

where r is the rain. We can combine these boundary conditions to give a flux boundary condition on $\mathcal{W}$ as

$$\mathcal{W}\left(w_i - \dot{z}_s\right) + \phi S\left(w_w - w_i\right) = -(1-\phi)a - r. \tag{106}$$

This boundary condition nicely shows that the total flux of water at the surface is given by the portion that falls as snow and the portion that falls as rain.

To derive the enthalpy boundary condition we start with the dimensional heat flux equation given by

$$\rho c_p\left[(1-\phi)\left(w_i - \dot{z}_s\right) + \phi S\left(w_w - \dot{z}_s\right)\right](T - T_m) - K\left[(1-\phi) + \phi S\right]\frac{\partial T}{\partial z} = -Q_0 F(t) + H(T - T_m) + \mathscr{L}(1-\phi)m, \tag{107}$$

where H includes contributions from turbulent heat transfer and long wave radiation. We can add and subtract $\rho c_p \phi S\left(w_i - \dot{z}_s\right)$ from the left term and use the definition $\mathcal{W} = 1 - \phi + \phi S$, which gives

$$\rho c_p\left[\mathcal{W}\left(w_i - \dot{z}_s\right) + \phi S\left(w_w - w_i\right)\right](T - T_m) - K\mathcal{W}\frac{\partial T}{\partial z} = -Q_0 F(t) + H(T - T_m) + \mathscr{L}(1-\phi)m. \tag{108}$$

Now we have the kinematic relationships for the ice and water speeds, given by

$$w_i - \dot{z}_s = \frac{m}{\rho} - a \quad \text{and} \quad \mathcal{W}\left(w_i - \dot{z}_s\right) + \phi S\left(w_w - w_i\right) = -(1-\phi)a - r. \tag{109}$$

We can add $\rho\mathscr{L}$ times the water flux, which gives

$$\rho c_p \mathcal{W}\left(w_i - \dot{z}_s\right)\left[\rho c_p(T - T_m) + \rho\mathscr{L}\right] + \phi S\left(w_w - w_i\right)\left[\rho c_p(T - T_m) + \rho\mathscr{L}\right] - K\mathcal{W}\frac{\partial T}{\partial z} = \\ -Q_0 F(t) + H(T - T_m) + \rho\mathscr{L}(1-\phi)\frac{m}{\rho} - \rho\mathscr{L}\left[(1-\phi)a + r\right] \tag{110}$$

Grouping terms, we have that

$$\left(w_i - \dot{z}_s\right) H + \phi S\left(w_w - w_i\right)\left[\rho c_p(T - T_m) + \rho\mathscr{L}\right] - K\mathcal{W}\frac{\partial T}{\partial z} = \\ -Q_0 F(t) + H(T - T_m) - \rho\mathscr{L} r. \tag{111}$$

4.1.4 Nondimensionalize

We scale the variables as

$$z = \ell\hat{z}, \quad t = \hat{t}/\omega, \quad T = T_m + \Delta T\theta, \quad w_i = \omega\ell\hat{w}_i, \quad k = k_0\hat{k}, \quad m = \mathcal{M}\hat{m}. \tag{112}$$

$$\mathcal{H} = \rho c_p \Delta T\hat{\mathcal{H}}, \quad p_c = \frac{\gamma}{r}\hat{p}_c, \quad w_w = \frac{\rho g k_0}{\mu}\hat{w}_w, \quad r = \omega\ell\hat{r}, \tag{113}$$

where we immediately drop the hats. Again, we choose ΔT and the scale for the surface melt velocity $\mathcal{M}$ to balance the heat flux Q_0. Thus, we have that

$$\Delta T = \frac{Q_0}{H} \sim 13.5 \text{ K} \quad \text{and} \quad \mathcal{M} = \frac{Q_0}{\mathscr{L}} \sim 6 \times 10^{-4} \text{ kg s}^{-1} \text{ m}^{-2}. \tag{114}$$

Thus, we can write equation (111) as

$$\frac{\rho c_p \omega\ell\Delta T}{Q_0}\left[\mathcal{W}\left(w_i - \dot{z}_s\right) + \phi S\left(\mathcal{U}w_w - w_i\right)\right]\theta - \frac{K\Delta T}{Q_0\ell}\mathcal{W}\frac{\partial\theta}{\partial z} = -F(t) + \theta + (1-\phi)m, \tag{115}$$

where we define

$$\mathcal{U} = \frac{\rho g k_0}{\omega\ell\mu} \sim 100 \quad \text{and} \quad \ell = \frac{Q_0}{\omega\rho\mathscr{L}} \sim 20.6 \text{ m}. \tag{116}$$

Thus,

$$\theta + (1-\phi)m - \frac{1}{\mathcal{S}}\left[\mathcal{W}\left(w_i - \dot{z}_s\right) + \phi S\left(\mathcal{U}w_w - w_i\right)\right]\theta + \frac{K\Delta T}{Q_0\ell}\mathcal{W}\frac{\partial\theta}{\partial z} = F(t), \tag{117}$$

where

$$S = \frac{\mathscr{L}}{c_p\Delta T} \sim 12 \quad \text{and} \quad \frac{K\Delta T}{Q_0\ell} = \frac{1}{Pe\mathcal{S}} = 0.008. \tag{118}$$

We can write equations (102)-(104), i.e. the full, nondimensional enthalpy, total water, and compaction equations as

$$\frac{\partial \mathcal{H}}{\partial t} + \frac{\partial}{\partial z}\left(w_i \mathcal{H}\right) = -\mathcal{U}\frac{\partial}{\partial z}\left\{\left[k(\phi)k_r(S)\left(\frac{p_c'(S)}{B}\frac{\partial S}{\partial z} - 1\right)\right](\theta + \mathcal{S})\right\} + \frac{1}{Pe}\frac{\partial}{\partial z}\left(\mathcal{W}\frac{\partial \theta}{\partial z}\right), \tag{119}$$

$$\frac{\partial \mathcal{W}}{\partial t} + \frac{\partial}{\partial z}\left(w_i \mathcal{W}\right) = -\mathcal{U}\frac{\partial}{\partial z}\left[k(\phi)k_r(S)\left(\frac{1}{B}p_c'(S)\frac{\partial S}{\partial z} - 1\right)\right], \tag{120}$$

$$(1-\phi)\frac{\partial w_i}{\partial z} = -\mathscr{C}\left(\phi, p_i, r^2\right). \tag{121}$$

where we have defined

$$Pe = \frac{\rho c_p \omega \ell^2}{K} \sim 11, \quad \mathcal{U} = \frac{\rho g k_0}{\omega \ell \mu} \sim 100, \quad \mathcal{S} = \frac{\mathscr{L}}{c_p \Delta T} \sim 12, \quad B = \frac{\gamma}{\rho g r \ell} \sim 260. \tag{122}$$

We summarize the boundary conditions on the surface of the ice as

$$w_i = \dot{z}_s + m - a \quad \text{on} \quad z = z_s, \tag{123}$$

$$\mathcal{W}\left(w_i - \dot{z}_s\right) + \phi S\left(\mathcal{U}w_w - w_i\right) = -(1-\phi)a - r \quad \text{on} \quad z = z_s, \tag{124}$$

$$-\left(w_i - \dot{z}_s\right)\mathcal{H} - \phi S\left(\mathcal{U}w_w - w_i\right)\left[\mathcal{S} + \theta\right] + \frac{1}{Pe}\mathcal{W}\frac{\partial T}{\partial z} = \mathcal{S}\left[F(t) - \theta + r\right] \quad \text{on} \quad z = z_s. \tag{125}$$

4.1.5 Numerical solution

We now write equations (119)-(121) in conservative form as

$$\frac{\partial \mathcal{H}}{\partial t} + \frac{\partial}{\partial z}\left\{w_i \mathcal{H} + \mathcal{U}\left[k(\phi)k_r(S)\left(\frac{p_c'(S)}{B}\frac{\partial S}{\partial z} - 1\right)\right](\theta + \mathcal{S}) - \frac{\mathcal{W}}{Pe}\frac{\partial \theta}{\partial z}\right\} = 0, \tag{126}$$

$$\frac{\partial \mathcal{W}}{\partial t} + \frac{\partial}{\partial z}\left[w_i \mathcal{W} + \mathcal{U}k(\phi)k_r(S)\left(\frac{p_c'(S)}{B}\frac{\partial S}{\partial z} - 1\right)\right] = 0, \tag{127}$$

$$w_i(z) - \dot{z}_s - m + a - \int_z^{z_s} \frac{\mathscr{C}\left(\phi, p_i, r^2\right)}{1-\phi} dz = 0. \tag{128}$$

We use the change variables $y = z_s(t) - z$, i.e.

$$\frac{\partial}{\partial t} = \dot{z}_s \frac{\partial}{\partial y} + \frac{\partial}{\partial t} \quad \text{and} \quad \frac{\partial}{\partial z} = -\frac{\partial}{\partial y}, \tag{129}$$

and find that

$$\frac{\partial \mathcal{H}}{\partial t} + \frac{\partial}{\partial y}\left\{\widetilde{w}_i \mathcal{H} + \mathcal{U}\left[k(\phi)k_r(S)\left(\frac{p_c'(S)}{B}\frac{\partial S}{\partial y} + 1\right)\right](\theta + \mathcal{S}) - \frac{\mathcal{W}}{Pe}\frac{\partial \theta}{\partial y}\right\} = 0, \tag{130}$$

$$\frac{\partial \mathcal{W}}{\partial t} + \frac{\partial}{\partial y}\left[\widetilde{w}_i \mathcal{W} + \mathcal{U}k(\phi)k_r(S)\left(\frac{p_c'(S)}{B}\frac{\partial S}{\partial y} + 1\right)\right] = 0, \tag{131}$$

$$\widetilde{w}_i(y) = \dot{z}_s - w_i(y) = -m + a - \int_0^{y} \frac{\mathscr{C}\left(\phi, p_i, r^2\right)}{1-\phi} dy. \tag{132}$$

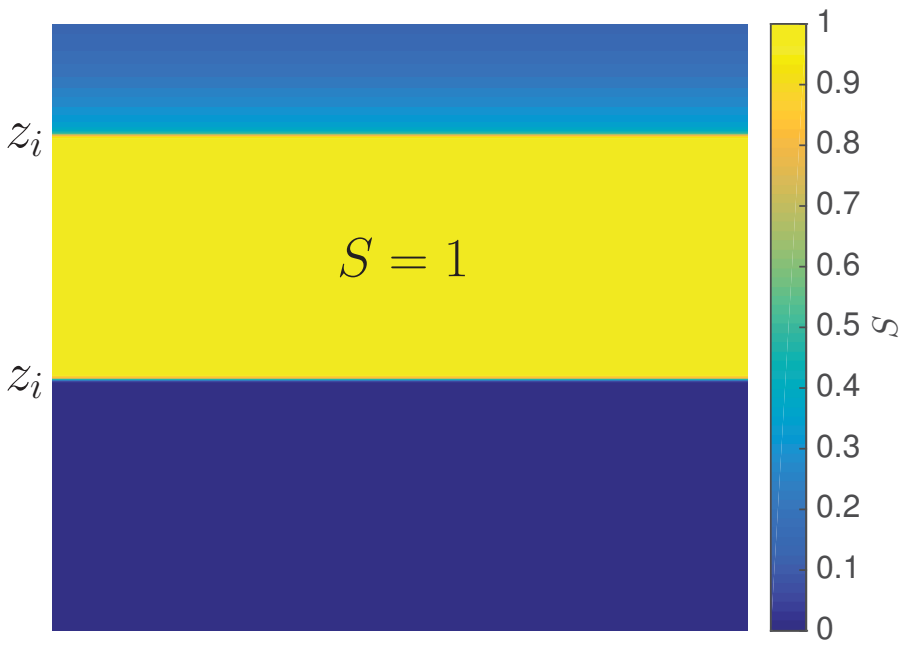

Figure 6: Schematic of a fully-saturated region in the middle of a porous snowpack. The interfaces between the partially and fully saturated are denoted as z_i.

We discretize the conserved fluxes in space using a finite volume method implemented in MATLAB. In this construction, the value of each variable is constant in each cell center and the velocities and fluxes are evaluated at cell edges, thereby transferring fluxes of each variable from one cell to another. For advection, we use an upwinding scheme where the value of the variable advected is a function of the velocity direction. We evolve equation (130)-(132) in time using explicit forward Euler timestepping. Thus, we evaluate the nonlinear quantities at the previous timestep and march forward in time.

4.2 Full saturation

When the water fills up all of the pore space between the snow crystals, the saturation S approaches unity, which is referred to as full saturation, see schematic in figure 6. In this case, all of the air is squeezed out and $\mathcal{W} = 1$ identically. This presents a problem for the enthalpy formulation because saturation is no longer a variable as it is known to be $S = 1$. The new variable is the water pressure in Darcy's law and the new equations are

$$\frac{\partial \phi}{\partial t} + \frac{\partial}{\partial z}\left(\phi w_w\right) = 0, \tag{133}$$

$$\frac{\partial}{\partial t}\left(1-\phi\right) + \frac{\partial}{\partial z}\left[(1-\phi) w_i\right] = 0, \tag{134}$$

$$\phi\left(w_w - w_i\right) = -\frac{k(\phi)}{\mu}\left(\frac{\partial p_w}{\partial z} + \rho g\right). \tag{135}$$

Adding equations (133) and (134) and then inserting equation (135) gives

$$\frac{\partial}{\partial z}\left[w_i - \frac{k(\phi)}{\mu}\left(\rho g + \frac{\partial p_w}{\partial z}\right)\right] = 0, \tag{136}$$

which is an elliptic problem for p_w. The boundary conditions are $p_w = -p_c(S=1)$ on the interfaces between partially- and fully-saturated layers z_i, see figure 6. We nondimensionalize this problem as before, except that $p_w = \rho g \ell \hat{p}_w$, which gives

$$\frac{\partial}{\partial z}\left[\mathcal{U}k(\phi)\left(1 + \frac{\partial p_w}{\partial z}\right)\right] = \frac{\partial w_i}{\partial z} \quad \text{subject to} \quad p_w = -\frac{p_c(S=1)}{B} \quad \text{on} \quad z = z_i. \tag{137}$$

The ice velocity is given through the compaction equation as

$$(1-\phi)\frac{\partial w_i}{\partial z} = -\mathscr{C}\left(\phi, p_i - p_w, r^2\right), \tag{138}$$

where the compaction is now a function of the effective pressure $p_i - p_w$. Moving into the $y = z_s - z$ coordinate system, we have that

$$\frac{\partial}{\partial y}\left[\mathcal{U}k(\phi)\left(1 - \frac{\partial p_w}{\partial y}\right)\right] = -\frac{\mathscr{C}\left(\phi, p_i, r^2\right)}{1-\phi} \tag{139}$$

subject to

$$p_w = -\frac{p_c(S=1)}{B} \quad \text{on} \quad y = y_i. \tag{140}$$

The enthalpy formulation can accommodate regions of full saturation by solving equation (139) for the water pressure p_w whenever $S = 1$. From p_w, we can compute the flux in the fully saturated region, i.e.

$$q_f = w_i - \frac{k(\phi)}{\mu}\left(\rho g + \frac{\partial p_w}{\partial z}\right), \tag{141}$$

and insert it into the flux of total water $\mathcal{W}$ and enthalpy $\mathcal{H}$, i.e. second terms in equations 130 and 131 in the regions of full saturation. At the interfaces y_i where the saturation transitions from partial to full, we take the normal to point out of the saturated region. With this convention, we choose the smaller (larger) value between the fully-saturated flux and the enthalpy flux when the interface advances in the direction of the positive (negative) normal.

5 Results

In this section we describe several results based on the enthalpy formulation. We start by describing the propagation of a meltwater front into dry snow. This is similar to the problem studied by Colbeck [3], Durey [9], and Gray [14]. We describe the model here to (a) clarify some of the assumptions in the previous analyses and (b) to benchmark our numerical computations. We also compare the results of the analytical solution for the propagation of the meltwater front to data from Humphrey et al. [21]. We then examine the solutions to the full model with periodic forcing. We model the seasonal forcing as a

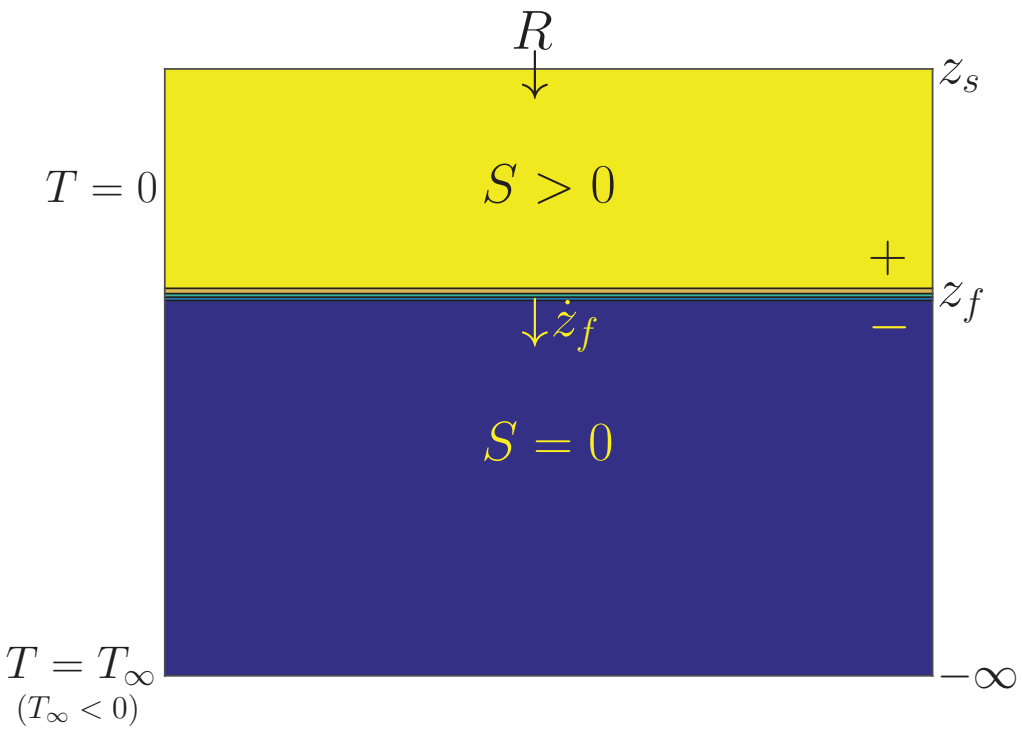

Figure 7: Rain falls at a rate R on the surface of an initially cold ($T = T_\infty < 0$), dry ($S = 0$) snowpack with porosity ϕ_0. The rainwater percolates through the snow, refreezes, releases latent heat which warms the snow, and this refreezing front propagates down.

sinusoid with the annual mean surface forcing as a control parameter. We find that when melting occurs at the surface and the firn is not fully saturated, the meltwater percolates down and significantly warms the lower firn. Finally, we extend the enthalpy model to accommodate scenarios where the snow becomes fully saturated with meltwater. In these cases, gradients in capillary pressure no longer drive the flow and we must compute the water pressure. We reanalyze the front propagation problem in an isothermal system where porosity decreases with depth. As the front propagates down the saturation increases and at a certain point there is insufficient space to accommodate the additional water. The porous firn fully saturates and a new front begins to propagate toward the surface.

5.1 Dry snow front with rain

We now consider the infiltration of rain into dry snow as a test problem. We start with a patch of dry snow ($S = 0$) with constant porosity, i.e. $\phi = \phi_0$, and temperature $\theta = \theta_\infty < 0$. There is no accumulation, surface forcing, or compaction and therefore the ice is stationary. At time $t = 0$ a fixed flux of rain R with a temperature $\theta = 0$ is applied at the surface and a wetting front at point $z = z_f$ moves down at velocity $\dot{z}_f$, see the schematic in figure 7.

As the rain water percolates into the snow, a smoothed shock forms and the water at the shock front refreezes. To start, we treat the smearing through the diffusive term in Darcy's law as negligible (i.e. infinite Bond number), which relegates the combination of

equations (89a) and (89c) to a hyperbolic partial differential equation for the saturation S. Integrating across the front at z_f gives the nondimensional jump conditions

$$\begin{aligned}
\left[\phi\left(w_i - \dot{z}_f\right)\right]_-^+ &= -m_I, && (142)\\
\left[\phi S\left(\mathcal{U} w_w - \dot{z}_f\right)\right]_-^+ &= m_I, && (143)\\
\frac{1}{Pe}\left[(1-\phi+S\phi)\frac{\partial\theta}{\partial z}\right]_-^+ &= -\mathcal{S} m_I, && (144)
\end{aligned}$$

which states that the mass m_I that melts from the solid ice enters the liquid phase and that the latent heat from refreezing warms the dry ice below. Note that here we scale the ice velocity w_i and the internal melt rate m_I with $\omega\ell$. We can simplify these equations using the fact that $\theta = 0$ in the upper portion $(+)$, $S = 0$ in the lower portion $(-)$, and zero ice velocity, which gives

$$\begin{aligned}
\left[\phi\right]_-^+ \dot{z}_f &= -m_I, && (145)\\
-R - \phi^+ S^+ \dot{z}_f &= m_I, && (146)\\
\frac{1}{Pe}(1-\phi^-)\left[\frac{\partial\theta}{\partial z}\right]^- &= \mathcal{S} m_I, && (147)
\end{aligned}$$

The equations to solve are

$$\begin{aligned}
\phi\frac{\partial S}{\partial t} &= \mathcal{U} k(\phi) k_r'(S)\frac{\partial S}{\partial z}, \quad (-\infty < z < z_f) \quad \text{and} \quad (z_f < z < z_s) && (148)\\
\frac{\partial \phi}{\partial t} &= 0, \quad (-\infty < z < z_f) \quad \text{and} \quad (z_f < z < z_s) && (149)\\
(1-\phi)\frac{\partial\theta}{\partial t} &= \frac{1}{Pe}\frac{\partial}{\partial z}\left((1-\phi)\frac{\partial\theta}{\partial z}\right), \quad (z < z_f) && (150)
\end{aligned}$$

where we have canceled the gradient of ϕ because ϕ is piecewise constant in space. The initial and boundary conditions for equations (148) to (150) are

$$\begin{aligned}
S = 0, \quad \phi = \phi_0, \quad \theta = 0 \qquad &\text{at} \qquad t = 0, && (151)\\
\phi = \phi_0, \quad \theta = \theta_\infty \qquad &\text{as} \qquad z \to -\infty, && (152)\\
\mathcal{U} k(\phi) k_r(S) = R \qquad &\text{on} \qquad z = z_s, && (153)\\
\theta = 0 \qquad &\text{on} \qquad z = z_f. && (154)
\end{aligned}$$

Now, in the lower, dry portion, the temperature evolves according to

$$\frac{\partial\theta}{\partial t} = \frac{1}{Pe}\frac{\partial^2\theta}{\partial z^2} \tag{155}$$

We can move into a translating frame $y = z_f(t) - z$, such that

$$\frac{\partial}{\partial t} = \dot{z}_f\frac{\partial}{\partial y} + \frac{\partial}{\partial t} \quad \text{and} \quad \frac{\partial}{\partial z} = -\frac{\partial}{\partial y}. \tag{156}$$

This gives

$$\frac{\partial\theta}{\partial t} + \dot{z}_f\frac{\partial\theta}{\partial y} = \frac{1}{Pe}\frac{\partial^2\theta}{\partial y^2}, \tag{157}$$

subject to the boundary conditions

$$\theta = 0 \quad \text{on} \quad y = 0 \quad \text{and} \quad \theta = \theta_\infty \quad \text{as} \quad y \to \infty. \tag{158}$$

If the wetting front moves very quickly, i.e. $|\dot{z}_f| \gg 1$, i.e. much faster than diffusion, but with $\dot{z}_f < 0$, then we have a singular perturbation problem. The outer problem is

$$\frac{\partial \theta}{\partial y} = 0, \tag{159}$$

which gives that $\theta = \theta_\infty$. The steady, inner coordinate comes from

$$\frac{\dot{z}_f}{y} \sim \frac{1}{Pey^2} \quad \text{which implies that} \quad y \sim \frac{1}{Pe\dot{z}_f}. \tag{160}$$

Thus, we define $\eta = Pe\dot{z}_f y$ as our inner variable, so that the equation reduces to

$$\frac{\partial \theta}{\partial \eta} = \frac{\partial^2 \theta}{\partial \eta^2}, \tag{161}$$

which gives that

$$\theta = \theta_\infty \left(1 - e^{Pe\dot{z}_f y}\right), \tag{162}$$

which is the same as the solution derived for continuous melting in §2.2.3. Taking the derivative of this expression on the dry side gives

$$\frac{1}{Pe}(1-\phi^-)\left[\frac{\partial \theta}{\partial y}\right]^- = \mathcal{S}m_I \longrightarrow m_I = -(1-\phi^-)\frac{\dot{z}_f \theta_\infty}{\mathcal{S}}. \tag{163}$$

The ice jump equation gives that

$$\phi^+ - \phi^- = -\frac{m_I}{\dot{z}_f} = (1-\phi^-)\frac{\theta_\infty}{\mathcal{S}} \longrightarrow \phi^+ = \phi^- + (1-\phi^-)\frac{\theta_\infty}{\mathcal{S}}, \tag{164}$$

which again shows that the porosity is smaller than $\phi^- = \phi_0$ on the upper side. The water conservation equation gives

$$-R - \phi^+ S^+ \dot{z}_f = m_I, \tag{165}$$

where the amount of rain R is equal to

$$R = \mathcal{U}k(\phi^+)k_r(S^+). \tag{166}$$

Using the form $k_r(S) = S^\beta$, we find that

$$S^+ = \left(\frac{R}{\mathcal{U}k(\phi^+)}\right)^{1/\beta} \tag{167}$$

and the velocity of the front is given as

$$\dot{z}_f = \frac{-R\mathcal{S}}{\phi^+ S^+ \mathcal{S} - (1-\phi^-)\theta_\infty}, \tag{168}$$

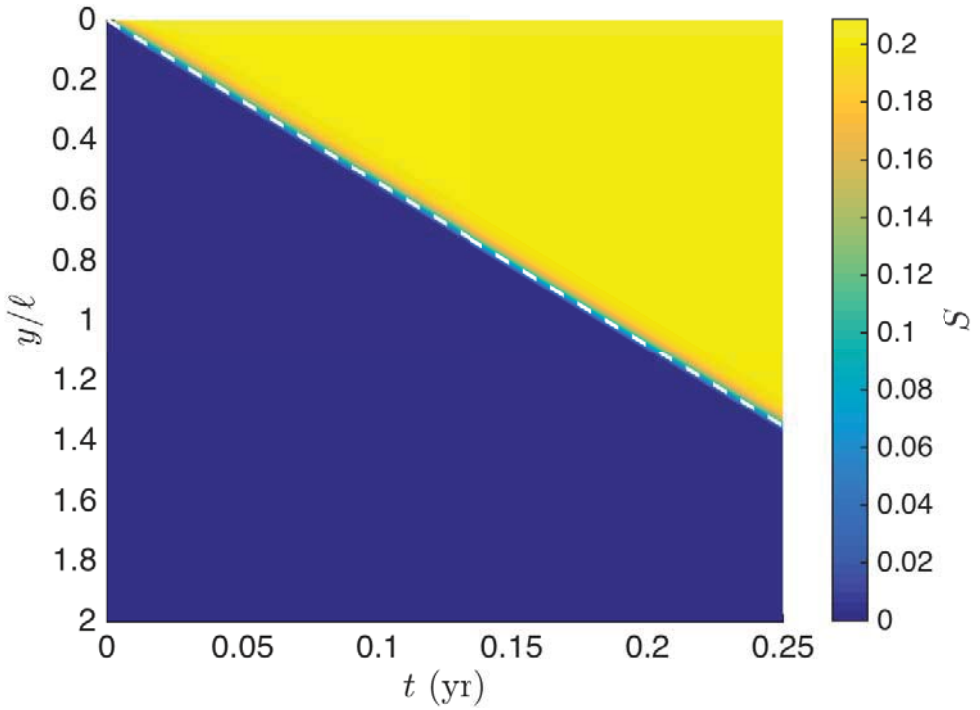

Figure 8: Space-time diagram for the propagation of a the refreezing front through saturation (color). The dashed white line shows the analytical prediction for the location of the freezing front. Here we choose $\theta_\infty = -0.5$, $\phi_0 = 0.4$, $R = 0.54$, and $\beta = 2$.

which is indeed much greater than unity for most parameter choices. This result corroborates the front velocity derived by [3, 9, 14]. In figure 8, we show a space-time diagram for the evolution of saturation. In a white dashed line we plot the location of the front as calculated from the jump analysis. The agreement is quite good considering diffusion is neglected across the front.

To capture the smoothing of the front, we can relax the assumption that the Bond number is infinite and derive the saturation boundary layer at the shock front. The full saturation equation is given as

$$\phi\frac{\partial S}{\partial t}+\mathcal{U}\frac{\partial}{\partial z}\left[k(\phi)k_r(S)\left(\frac{p_c'(S)}{B}\frac{\partial S}{\partial z}-1\right)\right]=0, \tag{169}$$

In the small region near the front, we must have that $z-z_f\sim(1/B)$, which motivates the change of variables $\eta=B(z_f-z)$. Thus, we have that

$$\phi\frac{\partial S}{\partial t}+B\frac{\partial}{\partial \eta}\left[\mathcal{U}k(\phi)k_r(S)\left(1+p_c'(S)\frac{\partial S}{\partial \eta}\right)+\phi S\dot{z}_f\right]=0. \tag{170}$$

Since B is very large, we have approximately that

$$B\frac{\partial}{\partial \eta}\left[\mathcal{U}k(\phi)k_r(S)\left(1+p_c'(S)\frac{\partial S}{\partial \eta}\right)+\phi S\dot{z}_f\right]=0. \tag{171}$$

with conditions

$$S=S^+ \quad \text{as} \quad \eta\to\infty \quad \text{and} \quad S=0 \quad \text{on} \quad \eta=0. \tag{172}$$

We can integrate this once and find

$$\mathcal{U}k(\phi)k_r(S)+\phi S\dot{z}_f+\mathcal{U}k(\phi)k_r(S)p_c'(S)\frac{\partial S}{\partial \eta}=q, \tag{173}$$

where q is a constant of integration. When evaluated in the far-field, we find that

$$q=\mathcal{U}k(\phi^+)k_r(S^+)+\phi^+S^+\dot{z}_f=-m_I. \tag{174}$$

We can also use the fact that $p_c=S^\alpha$, $k_r=S^\beta$ and $\alpha+1=-\beta$, to write the equation as

$$\alpha\frac{\partial S}{\partial \eta}=S^2-S^{+2}+\frac{\phi\dot{z}_f}{\mathcal{U}k(\phi)}\left(S-S^+\right), \tag{175}$$

where we have inserted $\beta=2$ and $\alpha=1$. Dividing through and integrating gives

$$\int_0^S\frac{1}{\varsigma^2-S^{+2}+\psi(\varsigma-S^+)}d\varsigma=\eta, \tag{176}$$

where we use ψ as

$$\psi=\frac{\phi\dot{z}_f}{\mathcal{U}k(\phi)}, \tag{177}$$

and it is important to note that $\dot{z}_f<0$. This integral can be solved to give

$$S=-\frac{\psi}{2}+\frac{\psi+2S^+}{2}\tanh\left\{\operatorname{arctanh}\left(\frac{\psi}{\psi+2S^+}\right)-\frac{\psi+2S^+}{2}\eta\right\}, \tag{178}$$

which was also derived by Gray [14].

5.2 Data comparison

The refreezing and release of latent heat as a front of meltwater moves through a firn layer allows the percolation of meltwater to be observed in englacial temperature data. Humphrey, Harper, Pfeffer, and colleagues [17, 21] collected temperature data in the percolation zone on the western flank of the Greenland ice sheet and inferred the movement of meltwater by the release of latent heat. They set up a vertical string of thermistors to determine the temperature profile in the upper 10 m of the ice sheet. Data from one vertical string between the dates of 5 July 2007 and 25 July 2007 (days 185-203) is shown in figure 9. From these data it is clear that the ice at depth progressively warmed, likely due to the refreezing of liquid meltwater. Over the twelve days between day 185 and day 197, the warming front propagated about a meter, while over the course of the next six days from day 197 to day 203, the meltwater penetrated two additional meters, showing a four-fold increase in front velocity. Humphrey et al. [21] infer that the warming spike on day 199 is due to an influx of meltwater from lateral sources. A minimum temperature is observed at around 5 m depth and the temperature recorded on the lower thermistors is warmer, which could be due to prior warming by meltwater pulses or a manifestation of the thermal wave, as described in §2.

We now compare these data to the boundary layer analytical solution for the temperature field ahead of a refreezing front. In dimensional variables, the temperature profile is given as

$$T = T_\infty \left(1 - \exp\left\{ \frac{\dot{z}_f (z_f - z)}{\kappa} \right\} \right). \tag{179}$$

We fit two different front speeds $\dot{z}_f$ for the days 185-197 and days 197-203, respectively. We fit a constant far-field temperature T_∞ and use the heat diffusivity for ice $\kappa = K/(\rho_i c_p) = 1.1 \times 10^{-6}$ m^2 s^{-1}. In light of the simplified analysis, the fit between equation (179) and the Humphrey et al. [21] data is quite good.

5.3 Periodic solutions

In §2 we derived the thermal wave for how surface energy forcing determines the englacial temperature structure as a function of time. This solution breaks down when the surface energy raises the surface temperature to the melting point. Any additional incident energy forms meltwater, which can percolate through the snow and refreeze, thereby warming the snow through the release of latent heat. To determine the effect of refreezing on the englacial temperature structure, we applied an oscillating surface forcing of the form

$$F(t) = \overline{F} - \cos(2\pi t), \tag{180}$$

where $\overline{F}$ is the annual mean surface forcing, which is the annual average temperature plus the heat added by accumulation. We now run a suite of numerical simulations, each time allowing the dynamics to reach a periodic state. A space-time diagram of these simulations is shown in figure 10. In this case, we set the annual mean surface forcing to $\overline{F} = -0.44$, so melting occurs in the summer months. The porosity of the falling snow is fixed at $\phi_0 = 0.3$ and the accumulation is held constant throughout the year at $a = 10$ m yr^{-1}, which is large enough such that the meltwater never fully saturates the snow. We ignore compaction

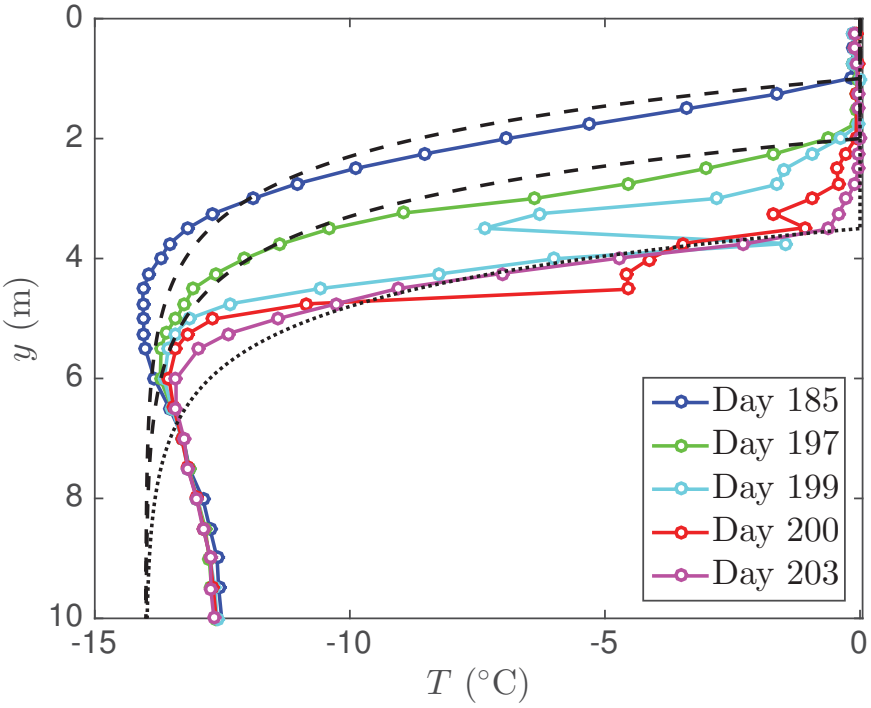

Figure 9: Data from Humphrey et al. [21] show the propagation of refreezing fronts in Greenland firn. We overlay the boundary layer solution (black lines) for the temperature ahead of a refreezing front. The speed of the front varies over the 18-day record: the dashed lines use the initial speed and the dotted line uses the final speed. The far-field temperature is assumed to be constant in the model whereas the data show a local minimum in temperature at around 5 m, which could be due to prior freezing fronts or the seasonal wave.

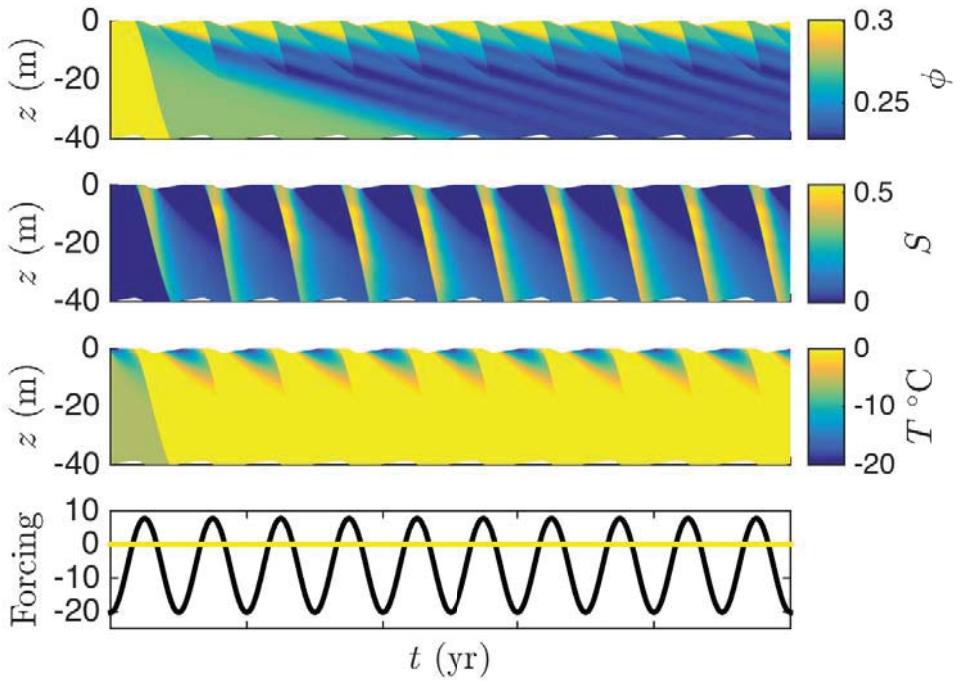

Figure 10: Space-time diagram showing the evolution of porosity (top), saturation (upper middle), temperature (lower middle), and the forcing (bottom) as a function of time. The annual mean surface forcing is $\overline{F} = -0.44$, the accumulation is $a = 10$ m yr^{-1}, and the porosity of the falling snow is $\phi_0 = 0.3$.

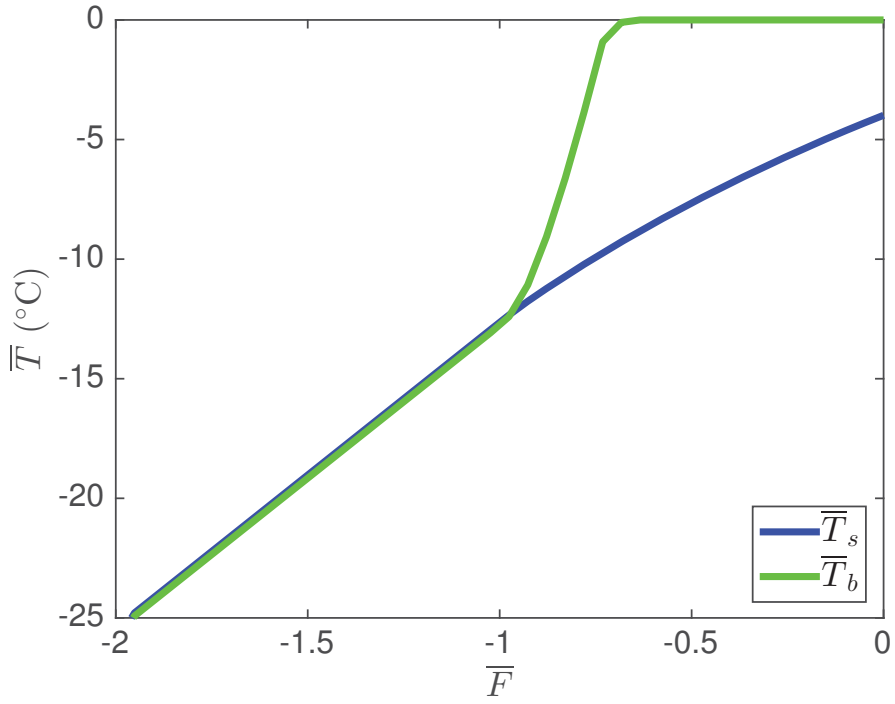

Figure 11: Annual mean temperature at the ice surface $\overline{T}_s$ and bottom of the domain $\overline{T}_b$ as a function of the annual mean surface forcing. For $\overline{F} > -1$ melting occurs at the surface and the meltwater percolates through the domain and warms the bottom.

and determine the far-field velocity required to keep the surface flat on average as the annual average accumulation less the melting. Thus, the structures visible in the porosity diagram show three signals: propagation of the leading meltwater front, the advection due to accumulation less melting, and the propagation of the trailing meltwater front. The propagation of the leading and trailing meltwater fronts can also be seen in the space-time diagram for the saturation, where the leading edge propagates the faster and with higher saturation than the trailing edge. The whole region of ice with meltwater stays at the melting temperature, which is also visible in temperature space as the wedge around the summer matches the saturation wedge. In the winter, the cold temperatures only reach part of the way into the snowpack, thus, the meltwater from the previous summer is able to persist and keep the lower firn warm. This effect was observed in the field by Humphrey et al. [21], where they found that the snow at 10 m depth in Greenland is often >10°C warmer than the annual mean air temperature because of the refreezing of meltwater and release of latent heat.

To quantify the lower firn warming in our model as a function of the imposed annual mean surface forcing, we compare the annual mean temperature at the top and bottom of the domain, see figure 11. For low annual mean surface forcing, where no melting occurs, the domain top and bottom temperatures are nearly identical. However, as soon as the annual mean surface forcing increases above $\overline{F} > -1$, the domain top and bottom temperatures

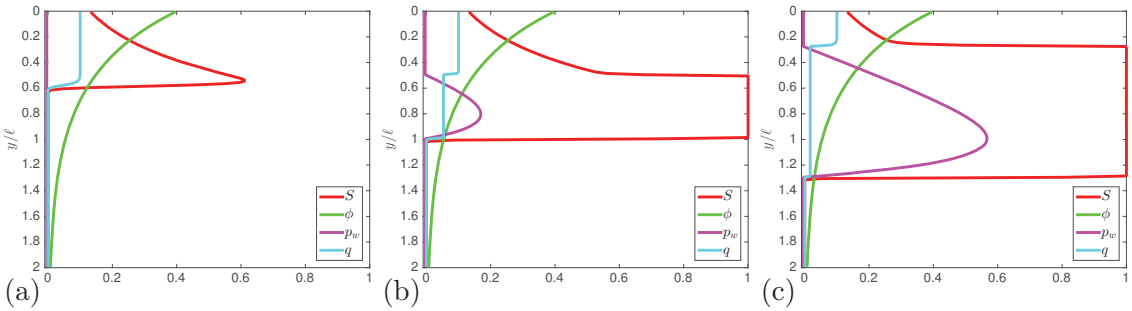

Figure 12: Fully-saturated fronts: evolution of water saturation (red), flux (cyan), and pressure (magenta) in stationary firn with porosity (green) that decreases exponentially with depth. Panel (a) shows the position of the front before the firn fully saturates. Panels (b) and (c) show the bidirectional motion of the fully-saturated fronts.

begin to diverge, due to the slow drainage of the liquid water in the porous snow. As the annual mean surface forcing increases, the surface temperature also increases yet the cold winters bring down the yearly average. The domain bottom temperature, on the other hand, is strongly influenced by the presence of meltwater. At around $\overline{F} > -0.7$, meltwater stays at the bottom of the domain throughout the year and the annual average temperature is exactly zero. In this way our simulations predict the formation of an perennial firn aquifer as observed by Forester et al. [11].

Thus, the thermal structure and water content of the lower firn are strongly tied to the amount of meltwater present, which in this model is tied directly to the annual mean surface forcing. In a warming world, the storage of meltwater in the firn will likely warm the lower firn and be crucial in buffering sea level rise by slowing surface run off. If, however, the firn fully saturates with meltwater, any additional melt will run off the glacier, entering the ocean directly contributing to sea level rise. Alternatively, the meltwater will be routed to the glacier bed and modulate ice dynamics. The influx of meltwater from the surface into the subglacial systems can develop channels that will slow the glacier advance or enter a distributed system, which would lead to rapid sliding [12, 20, 22]. The timing and quantity of meltwater routed to the bed will determine the style of subglacial system that develops and the subsequent ice dynamics [30, 33, 35].

5.4 Isothermal saturation fronts

We now consider the propagation of a full-saturated front. We rain on the surface of porous, unsaturated snow at a rate R. The porosity decreases exponentially with depth as

$$\phi(y) = \phi_0 e^{-y/\delta}, \tag{181}$$

where we choose $\delta = 1$. We ignore compaction and accumulation, i.e. the ice is stationary. We also consider the snow to be isothermal and temperate, so the porosity structure does not change due to advection or melting/refreezing. Initially, the rain partially saturates the snow and the front moves down with the maximum saturation at the edge of the front, see figure 5.3(a). Then, at a certain depth, the maximum saturation reaches unity and two fronts develop, one that propagates up and the other down, see figures 5.3(b) and 5.3(c).

5.4.1 Semi-analytical front locations

Here we calculate the motion of the fronts by describing the jump conditions across the fronts. Conservation of water at the nose of the front is given by

$$-R + \phi_f S^+ \dot{y}_f = 0, \tag{182}$$

where S^+ is the saturation in the region above as there is no saturation below the front. We can calculate the S^+ induced by the rain as

$$R = \mathcal{U}k(\phi_f)k_r(S^+) \longrightarrow S^+ = \left(\frac{R}{\mathcal{U}k(\phi_f)}\right)^{1/2}, \tag{183}$$

where the relative permeability is $k_r = S^\beta$ and we choose $\beta = 2$. We also use the simplified permeability expression

$$k(\phi) = \phi^3 = \phi_0^3 e^{-3y/\delta}. \tag{184}$$

Thus, the evolution equation for the front before full saturation is

$$\dot{y}_f = \sqrt{\mathcal{U}R\phi_0}\exp\left\{-\frac{y_f}{2\delta}\right\}. \tag{185}$$

Integrating gives that

$$y_f = 2\delta \ln\left\{1 + \frac{\sqrt{\mathcal{U}R\phi_0}}{2\delta}t\right\}. \tag{186}$$

We can calculate the position of the front where this solution will no longer be valid by noting that this will occur when $S^+ = 1$. Therefore, we have that

$$y_1 = \frac{\delta}{3}\ln\left\{\frac{\phi_0^3\mathcal{U}}{R}\right\} \quad \text{and} \quad t_1 = \frac{2\delta}{\sqrt{\mathcal{U}R\phi_0}}\left[\left(\frac{\phi_0^3\mathcal{U}}{R}\right)^{1/6} - 1\right]. \tag{187}$$

Now in the fully saturated region, we have that

$$\mathcal{U}k(\phi)\left(1 - \frac{\partial p_w}{\partial y}\right) = q_s, \tag{188}$$

where q_s is the constant flux of fluid in the fully saturated region, since there is no compaction. Rearranging and integrating again gives

$$p_w(y_s) - p_w(y_f) = 0 = y_s - y_f - \frac{q_s}{\mathcal{U}}\int_{y_f}^{y_s}\frac{dy}{k(\phi)}, \tag{189}$$

where y_s is the height of the upper front and y_f is the height of the lower front, i.e. the interfaces z_i in figure 6. We have applied the boundary conditions that the pressure is equal to zero on the edges. We can do this integral and find that

$$q_s = \frac{3\phi_0^3\mathcal{U}(y_s - y_f)}{\delta\left[e^{3y_s/\delta} - e^{3y_f/\delta}\right]}. \tag{190}$$

Since there is no melting/refreezing, water conservation across the lower front states that

$$\phi_f \dot{y}_f = q_s. \tag{191}$$

The jump condition on the upper front is

$$q_s - \phi_s \dot{y}_s = R - \phi_s S^+ \dot{y}_s, \tag{192}$$

which can be rewritten as

$$\phi_s \left[1 - \left(\frac{R}{\mathcal{U} \phi_s^3} \right)^{1/2} \right] \dot{y}_s = q_s - R, \tag{193}$$

where we have used the definition of S^+ from above. Thus, we have the ODEs

$$\dot{y}_f = \frac{q_s}{\phi_f} \quad \text{and} \quad \dot{y}_s = \frac{q_s - R}{\phi_s \left[1 - \left(\frac{R}{\mathcal{U} \phi_s^3} \right)^{1/2} \right]} \quad \text{with} \quad q_s = \frac{3 \phi_0^3 \mathcal{U} (y_s - y_f)}{\delta \left[e^{3 y_s / \delta} - e^{3 y_f / \delta} \right]}, \tag{194}$$

subject to the initial conditions

$$y_s = y_f = y_1 \quad \text{at time} \quad t = t_1. \tag{195}$$

We solve these coupled, nonlinear ODEs using a numerical integrator in MATLAB. A space-time diagram illustrating the upward and downward propagating fronts is shown in figure 13. Dashed white lines show the evolution of the semi-analytical solutions for the propagation of the fully-saturated fronts.

6 Conclusion

Meltwater is produced on the surface of glaciers and ice sheets when the seasonal surface energy forcing warms the ice above its melting temperature. This meltwater can percolate through the porous snow matrix and potentially refreeze, thereby warming the surrounding ice through the release of latent heat. In this paper, we describe a continuum model for the evolution of firn hydrology, compaction, and thermodynamics. We determine the internal ice temperature and glacier surface height based on the surface forcing and the accumulation of snow. When the surface temperature exceeds the melting temperature, we compute the amount of meltwater produced and lower the glacier surface accordingly. As the meltwater is produced, we solve for its percolation through the snow. Our model results in traveling regions of meltwater with fronts where refreezing occurs. We also allow the snow to compact mechanically and we analyze the interplay of compaction with meltwater percolation. We combine all of these physical processes into an enthalpy formulation, which is conserved across phase change interfaces. We compare the model for the temperature ahead of a refreezing meltwater front to temperature with depth data taken by Humphrey et al. [21] and show that the simple boundary layer solution works quite well. We also adapt the enthalpy formulation to accommodate regions of full saturation by solving for the water pressure and judiciously choosing the correct flux at interfaces between partial and full

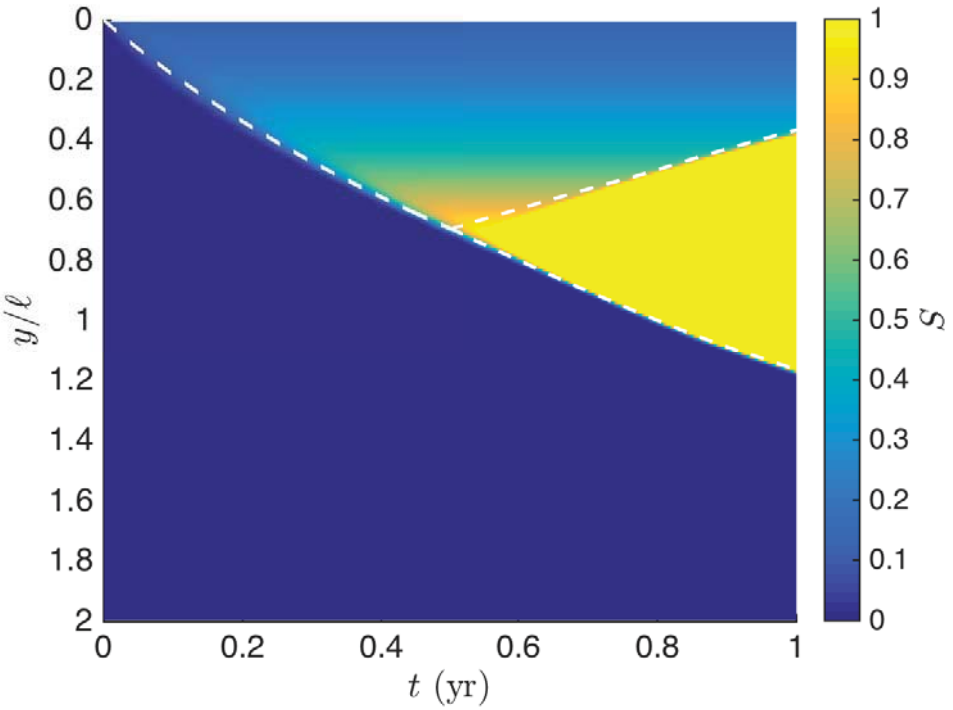

Figure 13: Propagation of a refreezing front into snow with a porosity distribution that decays exponentially with depth. Color shows the saturation of the snowpack and the white dashed lines are the analytical solutions. Initially, the snow is partially saturated and propagates as before. At a certain depth the water fully saturates the snow and two fronts emerge.

saturation. Our models help constrain the role that meltwater percolation and refreezing will have on ice-sheet mass balance and hence sea level.

There are several limitations to the models presented here that offer good opportunities for further research. First and foremost, this model is one dimensional. The data from Humphrey et al. [21] suggest the occurrence of 'piping events' where meltwater forms a vertical channel and breaks through to depths where the snow is much colder. These events could be captured in a two-dimensional mathematical framework, where the solid ice and liquid water have different temperatures. The physics of compaction are also a weak point of this analysis as it is not clear whether dry compaction models should be used when meltwater is present. More laboratory experiments and a detailed materials physics analysis of the processes that occur on the ice crystal scale are required. Additional field measurements of refreezing in the percolation zone will provide important physical constraints on these models and likely expose new limitations to our modeling. Furthermore, placing many vertical strings of thermistors located in close proximity on the surface of a glacier or ice sheet may elucidate the role of horizontal motion of meltwater. These measurements might constrain the transition between firn percolation and surface run off, which may be important for determining the effect of meltwater on sea level rise.

References

[1] R. J. Arthern, D. G. Vaughan, A. M. Rankin, R. Mulvaney, and E. R. Thomas, *In situ measurements of Antarctic snow compaction compared with predictions of models*, J. Geophys. Res., 115 (2010).

[2] A. Aschwanden, E. Bueler, C. Khroulev, and H. Blatter, *An enthalpy formulation for glaciers and ice sheets*, J. Glaciol., 58 (2012), pp. 441–457.

[3] S. C. Colbeck, *A theory of water percolation in snow*, J. Glaciol., 11 (1972), pp. 369–385.

[4] ——, *The capillary effects on water percolation in homogeneous snow*, J. Glaciol., 13 (1974), pp. 85–97.

[5] S. C. Colbeck, *An analysis of water flow in dry snow*, Water Resour. Res., 12 (1976), pp. 523–527.

[6] K. M. Cuffey and W. S. B. Paterson, *The Physics of Glaciers (Fourth Edition)*, ISBN 9780123694614, Elsevier, 2010.

[7] E. Cummings, J. Johnson, and D. Brinkerhoff, *Development of a finite element firn densification model for converting volume changes to mass changes*, arXiv preprint:1308.6616, (2013).

[8] J. G. Dash, A. W. Rempel, and J. S. Wettlaufer, *The physics of premelted ice and its geophysical consequences*, Rev. Mod. Phys., 78 (2006), p. 695.

[9] M. Durey, *Modelling snow and ice melt*, Master's thesis, University of Oxford, 2014.

[10] E. M. Enderlin, I. M. Howat, S. Jeong, M.-J. Noh, J. H. Angelen, and M. R. Broeke, *An improved mass budget for the Greenland ice sheet*, Geophys. Res. Lett., 41 (2014), pp. 866–872.

[11] R. R. Forster, M. R. van den Broeke, C. Miège, E. W. Burgess, J. H. van Angelen, J. T. M. Lenaerts, L. S. Koenig, J. Paden, C. Lewis, S. P. Gogineni, et al., *Extensive liquid meltwater storage in firn within the Greenland ice sheet*, Nat. Geosci., 7 (2014), pp. 95–98.

[12] A. G. Fountain and J. S. Walder, *Water flow through temperate glaciers*, Rev. Geophys., 36 (1998), pp. 299–328.

[13] J. W. Glen, *The creep of polycrystalline ice*, Proc. R. Soc. Lond. Ser. A, 228 (1955), pp. 519–538.

[14] J. M. N. T. Gray, *Water movement in wet snow*, Philos. Trans. R. Soc. London, Ser. A, 354 (1996), pp. 465–500.

[15] J. M. N. T. Gray and L. W. Morland, *A dry snow pack model*, Cold Reg. Sci. Technol., 22 (1994), pp. 135–148.

[16] ——, *The compaction of polar snow packs*, Cold Reg. Sci. Technol., 23 (1995), pp. 109–119.

[17] J. Harper, N. Humphrey, W. T. Pfeffer, J. Brown, and X. Fettweis, *Greenland ice-sheet contribution to sea-level rise buffered by meltwater storage in firn*, Nature, 491 (2012), pp. 240–243.

[18] R. L. Hawley, E. D. Waddington, G. W. Lamorey, and K. C. Taylor, *Vertical-strain measurements in firn at Siple Dome, Antarctica*, J. Glaciol., 50 (2004), pp. 447–452.

[19] M. M. Herron and C. C. Langway, *Firn densification: an empirical model*, J. Glaciol., 25 (1980), pp. 373–385.

[20] I. J. Hewitt, *Seasonal changes in ice sheet motion due to melt water lubrication*, Earth Planet. Sci. Lett., 371 (2013), pp. 16–25.

[21] N. F. Humphrey, J. T. Harper, and W. T. Pfeffer, *Thermal tracking of meltwater retention in Greenland's accumulation area*, J. Geophys. Res., 117 (2012).

[22] B. Kamb, C. F. Raymond, W. D. Harrison, H. Engelhardt, K. A. Echelmeyer, N. Humphrey, M. M. Brugman, and T. Pfeffer, *Glacier surge mechanism: 1982-1983 surge of Variegated Glacier, Alaska*, Science, 227 (1985), pp. 469–479.

[23] P. Kuipers Munneke, S. R. M. Ligtenberg, M. R. Broeke, J. H. Angelen, and R. R. Forster, *Explaining the presence of perennial liquid water bodies in the firn of the Greenland ice sheet*, Geophys. Res. Lett., 41 (2014), pp. 476–483.

[24] P. Kuipers Munneke, S. R. M. Ligtenberg, E. A. Suder, and M. R. van den Broeke, *A model study of the response of dry and wet firn to climate change*, Ann. Glaciol., 56 (2015), pp. 1–8.

[25] S. R. M. Ligtenberg, M. M. Heilsen, and M. R. van de Broeke, *An improved semi-empirical model for the densification of Antarctic firn*, Cryosphere, 5 (2011), pp. 809–819.

[26] H. Machguth, M. MacFerrin, D. van As, C. Charalampidis, W. Colgan, R. S. Fausto, H. A. J. Meijer, E. Mosley-Thompson, and R. S. W. van de Wal, *Greenland meltwater storage in firn limited by near-surface ice formation*, Nat. Clim. Change, 6 (2016), pp. 390–393.

[27] E. M. Morris and D. J. Wingham, *Densification of polar snow: Measurements, modeling, and implications for altimetry*, J. Geophys. Res., 119 (2014), pp. 349–365.

[28] J. F. Nye, *The mechanics of glacier flow*, J. Glaciol., 2 (1952), pp. 82–93.

[29] N. Reeh, *A nonsteady-state firn-densification model for the percolation zone of a glacier*, J. Geophys. Res., 113 (2008).

[30] C. Schoof, *Ice sheet acceleration driven by melt supply variability*, Nature, 468 (2010), pp. 803–806.

[31] C. Schoof and I. J. Hewitt, *A model for polythermal ice incorporating gravity-driven moisture transport*, J. Fluid Mech., 797 (2016), pp. 504–535.

[32] A. Szymkiewicz, *Modelling water flow in unsaturated porous media: accounting for nonlinear permeability and material heterogeneity*, Springer Science & Business Media, Germany, 2012.

[33] A. J. Tedstone, P. W. Nienow, N. Gourmelen, A. Dehecq, D. Goldberg, and E. Hanna, *Decadal slowdown of a land-terminating sector of the Greenland ice sheet despite warming*, Nature, 526 (2015), pp. 692–695.

[34] M. R. van den Broeke, C. J. P. P. Smeets, and R. S. W. van de Wal, *The seasonal cycle and interannual variability of surface energy balance and melt in the ablation zone of the west Greenland ice sheet*, Cryosphere, 5 (2011), pp. 377–390.

[35] H. J. Zwally, W. Abdalati, T. Herring, K. Larson, J. Saba, and K. Steffen, *Surface melt-induced acceleration of Greenland ice-sheet flow*, Science, 297 (2002), pp. 218–222.

[36] H. J. Zwally and J. Li, *Seasonal and interannual variations of firn densification and ice-sheet surface elevation at the Greenland summit*, J. Glaciol., 48 (2002), pp. 199–207.

Rolling Resistance on Sand

Keaton J. Burns
(advised by Neil Balmforth and Ian Hewitt)

November 28, 2016

1 Introduction

It is commonly experienced that motion over loose sand is greatly hindered by the reaction of the sand to applied loads. A canonical scenario for examining the resistance to motion over various materials is that of a rigid cylinder rolling without slipping. In the case of granular media, the behavior of rolling cylinders is practically applicable to the design of tires for vehicles traveling over sand, and may be applicable to geophysical processes such as the behavior of taluses. Understanding the basic form and dependencies of the rolling resistance force may also reveal interesting details about the system's dynamics, such as the possibility of steady rolling states on granular slopes.

While precise constitutive laws for various states of granular flow are the subject of a great deal of ongoing research, simplified models may be useful in some limits of the general rolling problem. In this work, we consider the rolling motion of a light cylinder, having a small mean density relative to the density of the granular material, over initially static granular beds. In this limit, the contact area between the cylinder and the bed will be small relative to the surface area of the cylinder, providing a small dimensionless number and allowing for the construction of an asymptotic model. For an initially static bed, simplified models based on plasticity theory may be useful in approximating the behavior of the granular medium. Earlier work has investigated the rolling resistance of rigid cylinders and spheres over model plastics, often with an eye towards industrial applications with metal rollers. Marshall [5] performed a perturbation calculation using slip-line theory for the deformation and rolling resistance of a smooth rigid cylinder on an ideal plastic with a fixed yield strength and neglecting gravity. Collins [3] extended this analysis to include rough cylinders, and examined the different solution regimes depending on the applied torque. Petryk [6] subsequently demonstrated that such solutions are non-unique as various geometries for the yielded region of the plastic are possible. Tordesillas & Shi [8] began applying this approach to granular media by considering a cohesive Mohr-Coulomb plastic, again neglecting gravity. De Blasio & Saeter [4] experimentally examined the rolling resistance experienced by heavy spheres on a sloped sand bed, finding resistances that were roughly independent of velocity, decreased with sphere radius, and increased with sphere density.

In this work, we describe a series of experiments measuring the rolling resistance of light cylinders on a flat granular bed. The experimental apparatus, procedures, and dataset are described in § 2. In § 3, we calculate the expected rolling resistance for a cohesionless Mohr-Coulomb plastic including gravity, which may be a more accurate model than those studied before for dry granular media as they begin to deform from a static state. We compare the predictions of this model to our experimental results in § 4. We summarize the work and discuss potential extensions in § 5.

Material	d (mm)	ρ_s (g/cm^3)	ϕ (deg)
Aquarium sand	0.9 ±0.15	1.59 ±0.09	37.9 ±1.3
Ballotini	1.0 ±0.2	1.55 ±0.7	24.9 ±0.7

Table 1: Mean particle diameter d, apparent density ρ_s, and friction angle ϕ for the granular media used in the experiments. Taken from Sauret et al. [7], who utilized the same materials.

2 Experiments

2.1 Apparatus

We constructed a channel to contain a bed of granular material, over which we rolled a variety of cylinders. The channel consisted of a high-density polyethylene board base, with lumber beams mounted along the edges of the base to form the sidewalls. The channel was approximately 244 cm in length, 31 cm in width, and 9 cm in depth. The tops of the side-rails were marked every 10 cm, for use in tracking the cylinder positions, as we describe in § 2.3. We took the tops of the side-rails to define our laboratory coordinate system, with x the along-track dimension, y the cross-track dimension, and z upwards normal to the track.

Two granular materials were used in our experiments: PetCo aquarium sand and Potters Industries A-100 glass beads (ballotini). Both materials had mean grain sizes near 1 m m , but the aquarium sand grains were much coarser than the nearly spherical ballotini, resulting in substantially different friction angles between the materials. The material parameters are provided in Table 1, and were taken from Sauret et al. [7], who utilized the same materials. Our test rollers consisted of various sections of cylindrical tubing, primarily PVC and other plastic pipes. The cylinders spanned from approximately 1 to 11 cm in radius, and 10 to 650 g in mass. Detailed measurements of the cylinders are listed in Table 2. The cylinders were sanded, cleaned, painted with high-visibility orange spray paint, and sanded again to give them consistent surface textures and appearances.

We mounted a video camera to the ceiling above the bed to record the cylinders' trajectories as we rolled them across the bed. We used an iPhone 6s to record the trajectories in color with 1080p resolution at 60 frames per second. From its stationary mount on the ceiling, the camera was positioned roughly 2 m above the bed, allowing the horizontal field of view to cover nearly the entire length of the bed.

2.2 Data acquisition

To prepare the granular bed, we filled the channel to an approximate level with a granular material. The top of the material was then scraped to a set depth, which was referenced from the top of the channel side-rails, and any additional granules were removed from the channel. To reset the bed after a large disturbance to the surface, we manually stirred the material throughout its depth, and repeated the leveling procedure. On the ballotini, the cylinders typically left large (several millimeter deep) tracks as they rolled, so the surface was reset between each run. On the aquarium sand, the cylinders typically left negligible tracks which were not apparent to the naked eye, but visible in shadows when illuminated

Cylinder	M (g)	D (cm)	δ (cm)	L (cm)	α	ρ_c (g/cm^3)
20	48.13	2.687	0.315	15.0	0.793	0.5658
21	72.06	3.343	0.360	15.0	0.807	0.5473
22	94.27	4.237	0.370	15.0	0.840	0.4457
23	113.56	4.857	0.385	15.0	0.854	0.4086
24	153.25	6.042	0.425	15.0	0.869	0.3563
25	246	7.288	0.560	15.0	0.858	0.3931
26	312	8.896	0.560	15.0	0.882	0.3346
27	754	21.94	0.500	16.2	0.955	0.1231
28	43.45	5.103	0.160	15.0	0.939	0.1416
29	34.84	5.094	0.145	15.0	0.944	0.1139
30	204	11.412	0.330	15.0	0.943	0.1329
31	656	11.445	0.950	15.0	0.847	0.4251
32	55.27	4.217	0.290	15.0	0.871	0.2638
33	25.95	1.873	0.150	15.0	0.852	0.6278
34	44.18	1.727	0.270	15.0	0.736	1.2573
36	79.50	9.559	0.155	15.0	0.968	0.0738
42	12.89	4.245	0.055	15.0	0.974	0.0607

Table 2: Reference number, mass M, outer diameter D, wall thickness δ, length L, dimensionless moment of inertia α, and mean density ρ_c for the cylinders used in the experiments.

from the side. To speed up the data taking process, we therefore only reset the aquarium sand surface when a large disturbance occurred (e.g. a stray or dropped cylinder).

The cylinders were placed on a rigid inclined ramp at the top of the runway and rolled onto the surface of the granular bed. The initial velocity of the cylinders as they entered the bed was controlled by adjusting the starting position of the cylinders along the ramp. Trials were deemed unsuccessful if they made contact or came within a few centimeters of the channel sidewalls, which tended to occur more frequently for lighter cylinders and at higher initial velocities. We repeated trials until we recorded three to five successful trials with the same experimental parameters.

Batches of trajectories were captured by continuously recording with the camera, and using a hotkey to record a timestamp during each trial on a laptop. This procedure allowed us to rapidly conduct and record trials, and to remove the timestamps of failed runs as they occurred.

2.3 Data processing

The post-processing consisted of three stages. First, "image trajectories" indicating the image coordinates of the cylinders for each video frame were calculated. Second, the position markers were used to infer the camera's projection for the scene. Third, the "object trajectories" indicating the real-space positions of the cylinders over time were extracted by inverting the camera projection for the calculated image trajectories.

2.3.1 Image trajectories

To extract cylinder trajectories from the videos, we first needed to determine the positions in image coordinates (u, v) of the cylinders as they rolled across the granular bed.

We initially attempted to isolate the cylinders from the rest of the scene by differencing the frames from nearby reference frames containing no cylinders. This technique can robustly detect the cylinders, but is easily confused by changing lighting conditions, the shadows cast by a cylinder on the granular bed, and slow changes in the surface grain pattern of the bed. To increase the specificity of the cylinder localization, we switched to using a color-based detection. Each cylinder was painted bright orange, and with no other orange objects in the scene, pixel color can precisely differentiate between the cylinder and the rest of the bed. We used the OpenCV 3.0 library [1] to extract individual frames from the video files and convert them to hue-saturation-value (HSV) color space. We then applied a slight (11 pixel) Gaussian blur to the frames, and computed the HSV color distance d of each pixel from a reference orange value of (4, 205, 255). We constructed a match value m for each pixel as $m = (1 - \tanh((d - 100)/5))/2)$, zeroed the match value for regions of the image outside of the granular bed, and took the centroid of match field to define the "image position" of the cylinder for that frame. The combination of the Gaussian blur and the smoothed match statistic (as opposed to a binary threshold) effectively dithers the edges of the cylinder, allowing for sub-pixel precision in the determination of the cylinder's image centroid. Figure 1 shows these processing stages for an example frame.

For each successful trial, the recorded timestamp was used to pick an "anchor" frame in the batch video. Starting with the anchor frame and iterating backwards, the image-positions of the cylinder were computed for each frame until the cylinder passed a position threshold near the edge of the image. Starting again from the anchor frame and iterating forwards, the image-positions were computed until the cylinder passed a position threshold near the other side of the image, for trials where the cylinder rolled across the entire bed, or until the cylinder passed below a speed threshold, for trials where the cylinder stopped rolling before the end of the bed. These positions were combined to form the image trajectory for each trial, indicating the pixel position as a function of frame index (or equivalently, time, given the camera's fixed frame rate). Figure 2 shows an example image trajectory.

2.3.2 Camera calibration

To accurately determine the cylinder's position in the lab frame from its image coordinates, the camera projection must be precisely characterized. We performed a standard camera calibration using routines from the OpenCV 3.0 library, which are based on a pinhole camera model (depicted in Figure 3) with corrections for common modes of lens distortion.

We first imaged a chessboard pattern from multiple angles and extracted and refined the image coordinates of the corners using the OpenCV `findChessboardCorners` and `cornerSubPix` routines. These coordinates were then used to infer the camera's intrinsic projection parameters, including the camera's principal point, focal lengths, and distortion coefficients using the OpenCV `calibrateCamera` routine. For each scene, we roughly determined the image positions of the distance markers on the channel side rails, which defined our object coordinate system, using color matching with manual refinement. The marker positions were used to infer each scene's pose, i.e. the combined rotation and translation

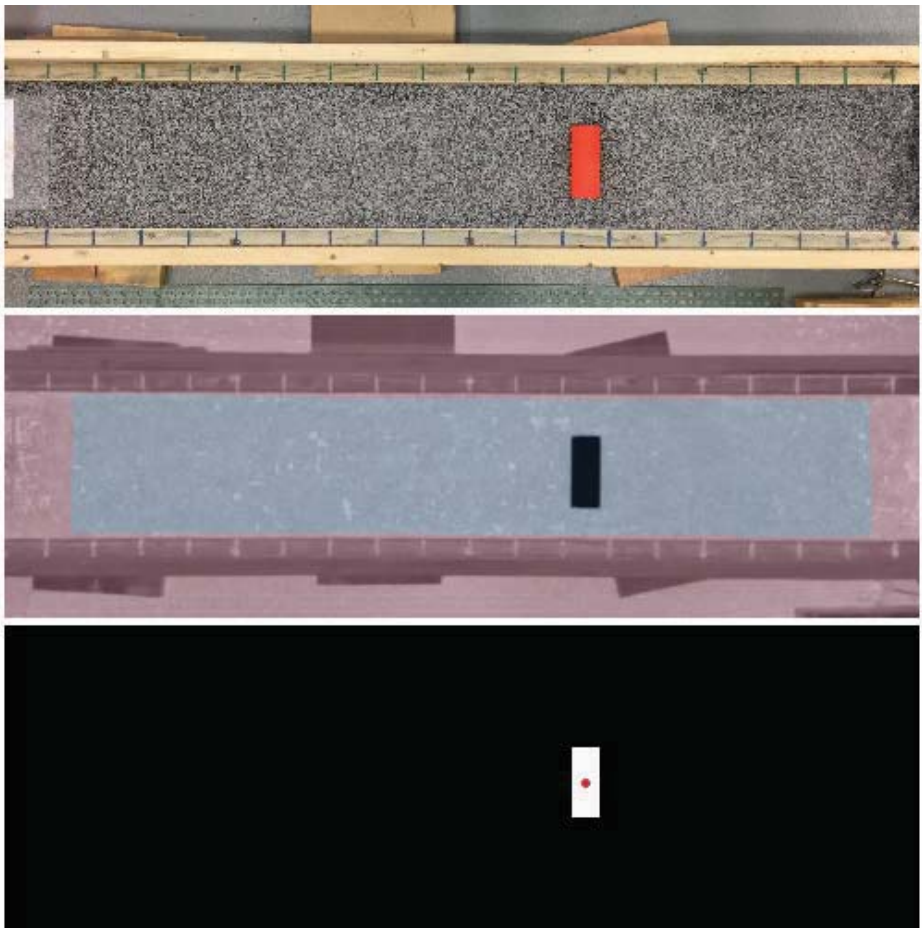

Figure 1: Stages of image-position extraction. Top: A raw frame from a video recording. Middle: The color distance from reference orange, indicated in greyscale with darker pixels being closer in HSV space. The shaded red region is excluded from further processing to isolate objects on the bed. Bottom: Match field derived from the color distance, with lighter pixels indicating a better match. The red dot indicates the centroid of the match field, and defines image position of the cylinder.

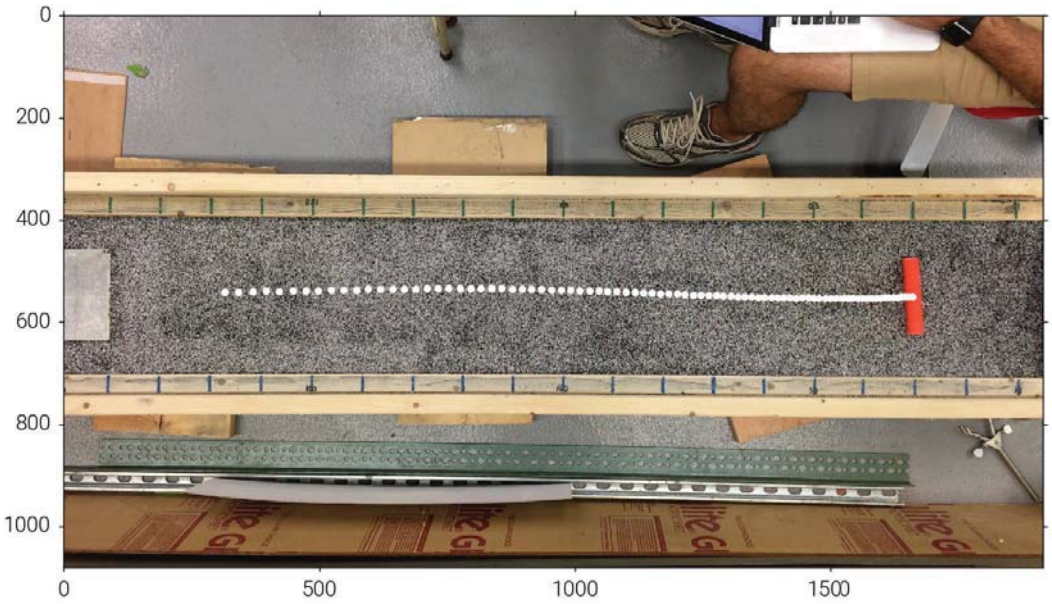

Figure 2: Final frame of one trial, with the corresponding image trajectory indicated in white.

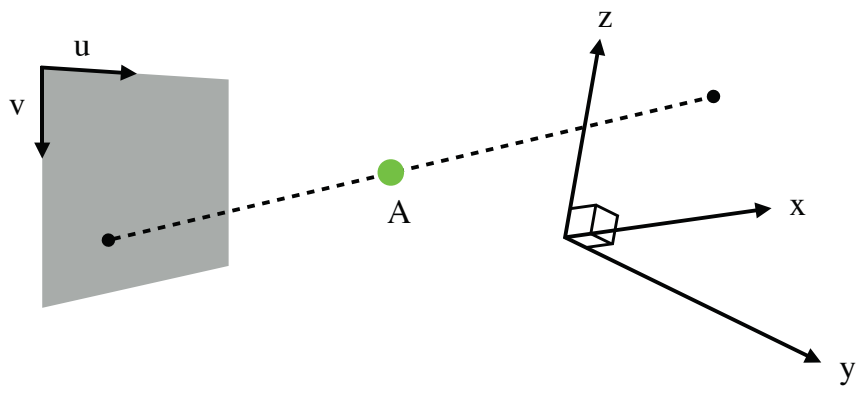

Figure 3: Pinhole model of camera projection: the image coordinates (u, v) of any point with object coordinates (x, y, z) are given by that point's projection onto the image plane through a fixed aperture point A.

mapping between the object coordinates and the camera-centered coordinates, using the OpenCV `solvePnP` routine.

The image coordinates of any point in the 3D laboratory frame can then be estimated by composing the pose transformation for that scene with the intrinsic camera projection using the OpenCV `projectPoints` routine. The difference between these estimated image coordinates and the measured image coordinates for the distance markers constitutes the reprojection error. Our calibration procedure typically yielded reprojection errors of $2.7 - 3.0\,\mathrm{px}$.

2.3.3 Object trajectories

The camera and scene calibrations were used to convert the image trajectories of the cylinders into "object trajectories" estimating the (x, y) position of the cylinder centers over time for each trial.

In a given scene, each image coordinate is the projection of an entire ray in the object coordinate space. If one of the object coordinates of a point is known, however, this is typically sufficient information to break the degeneracy and invert the projection to determine the two remaining unknown object coordinates from the image coordinates of the point. Since the distortion corrections render the camera projection nonlinear, we performed this inversion numerically. Given a z coordinate, we projected a grid covering the corresponding $x-y$ plane into image coordinates using the camera calibration parameters and scene pose. By interpolating between the projected points, we could therefore compute the x and y coordinates (for the given z) that would project to any image coordinate.

For each trial, we used the vertical offset of the material surface from the side rails, plus the radius of the cylinder, to estimate the height z of the plane containing the cylinder center. Assuming that the ray corresponding to the cylinder's image position passes through the center of the cylinder, the inversion of the image position at this z yields an estimate of the (x, y) coordinates of the center of the cylinder. We computed this inversion for each frame to convert each image trajectory into an object trajectory, describing the lab-frame coordinates of the center of each cylinder over time. Plots of one example trajectory on the aquarium sand are shown in Figure 4.

Typical gradients in our projection inversion are approximately $1\,\mathrm{mm}$ of x or y displacement per pixel in u or v, respectively. The characteristic $\sim 3\,\mathrm{px}$ reprojection error in the camera calibration therefore corresponds to a $\sim 3\,\mathrm{mm}$ systematic uncertainty in the absolute positions in our object trajectories.

2.4 Results

The above procedure was completed for over 1200 trials. We initially tilted the channel by supporting it at different heights under the two ends, and varied the angle to look for steady rolling states. We found, however, that the channel was insufficiently stiff and would flex under its own weight. When fully loaded with $9\,\mathrm{cm}$ of aquarium sand, we measured a bending amplitude (the displacement of the side-beam center below the line connecting the ends) of $4 - 5\,\mathrm{mm}$ using a laser level. This bending results in further errors in the calibration procedure, as well as a spatially varying effective (downslope) gravity. To avoid these issues, we decided to focus our analysis on runs taken with the bed lying flat on the

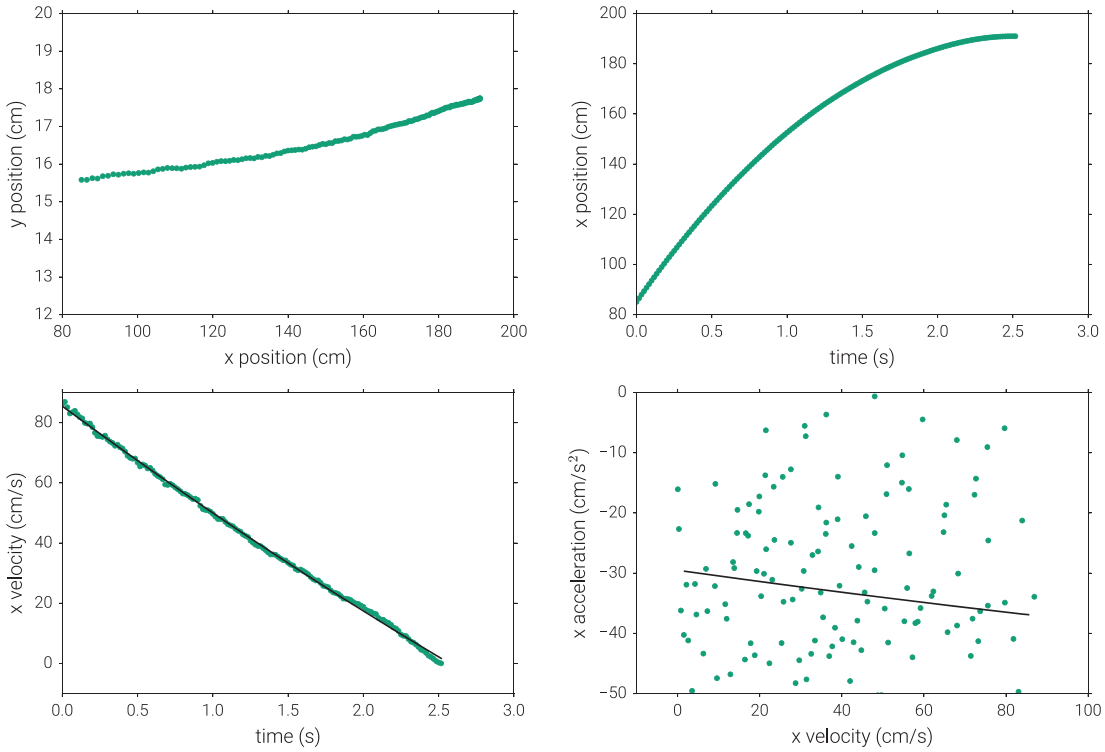

Figure 4: Example trajectory data for cylinder 23 on aquarium sand. Upper left: two-dimensional trajectory across bed. Upper right: downslope position over time. Lower left: downslope velocity over time, with the black line shows the least-squares quadratic fit to the data. Lower right: downslope acceleration versus velocity, with the black line showing the fit from the velocity data.

ground, with distributed support such that the side-rails were straight to within our $\sim 1\,\mathrm{mm}$ measurement precision.

To determine the influence of cylinder length on the trajectories, we performed a range of trials using several different lengths of the same PVC piping. We found no significant differences between the trajectories of these cylinders on the aquarium sand. We therefore decided to fix the cylinder lengths to 15 cm, to reduce the number of parameters being varied. This length was chosen because narrower cylinders tended to turn to the sides more strongly as they rolled, and wider cylinders had to be more precisely launched to avoid veering close to the sidewalls. We note that we did not systematically examine the effect of cylinder length on the ballotini, where the cylinders tended to dig in deeper than on the aquarium sand.

To determine the influence of material depth on the trajectories, we performed a range of trials using 1, 3, 5, 7, and 9 cm deep beds of aquarium sand. We again found no significant differences between the resulting trajectories. We therefore decided to fix the aquarium sand depth to 7 cm for the remaining trials. All of the ballotini trials were conducted with a depth of 2 cm, since we did not have enough material for larger depths.

With these considerations, we built a dataset consisting of trajectories for a range of 15 cm long cylinders, with a range of initial velocities, over a flat bed with 7 cm of aquarium sand, and a flat bed with 2 cm of ballotini. Plots of all trajectories for one cylinder on the aquarium sand are shown in Figure 5. Plots of all trajectories for several cylinders on the ballotini are shown in Figure 6. The precise trajectories contain a great deal of information, reflecting the complicated dynamics of the system.

For trials on the aquarium sand, where the surface was not reset between each run, we observed a systematic change in the stopping distances of the cylinders as they were alternated. Typically, after switching cylinders, the stopping distances of the first several trials would systematically increase or decrease until saturating, typically $\sim 10\,\mathrm{cm}$ away from the initial roll, as demonstrated in Figure 7. After 3-5 trials, the stopping distance was typically reproducible to within $\sim 2\,\mathrm{cm}$ centimeters. We term this behavior the "bedding-in" of the cylinders, as it seems that in some manner each cylinder affects the surface of the track slightly differently.

Two dimensional $x - y$ plots of the trajectory are useful for identifying trials where the cylinder rolled close to the side-rails, where they tended to substantially slow down. Some trials also changed direction upon closely approaching the side-rails, at times turning further towards the side, and at other times veering back towards the center of the channel, as can be seen in Figures 5 and 6. This may have been related to the bedding-in of the cylinders, which would have resulted in lateral variations of the surface of the bed based on the specific paths of prior trajectories. It may have also been due to modifications in the granular flow/stress field due to the proximity of side-rails. Whatever the cause, after the initial bedding-in, lateral variations in the trajectories typically resulted in substantial changes in their downslope motion.

Since most trajectories remained close to the center of the bed, we used the x components of the trajectories to study the one-dimensional kinematics of the cylinders. The millimeter-scale accuracy of the position determination allowed us to directly differentiate the trajectories in time using finite differences to produce accurate measurements of the downslope velocities. Further differentiation to determine the acceleration, however, was

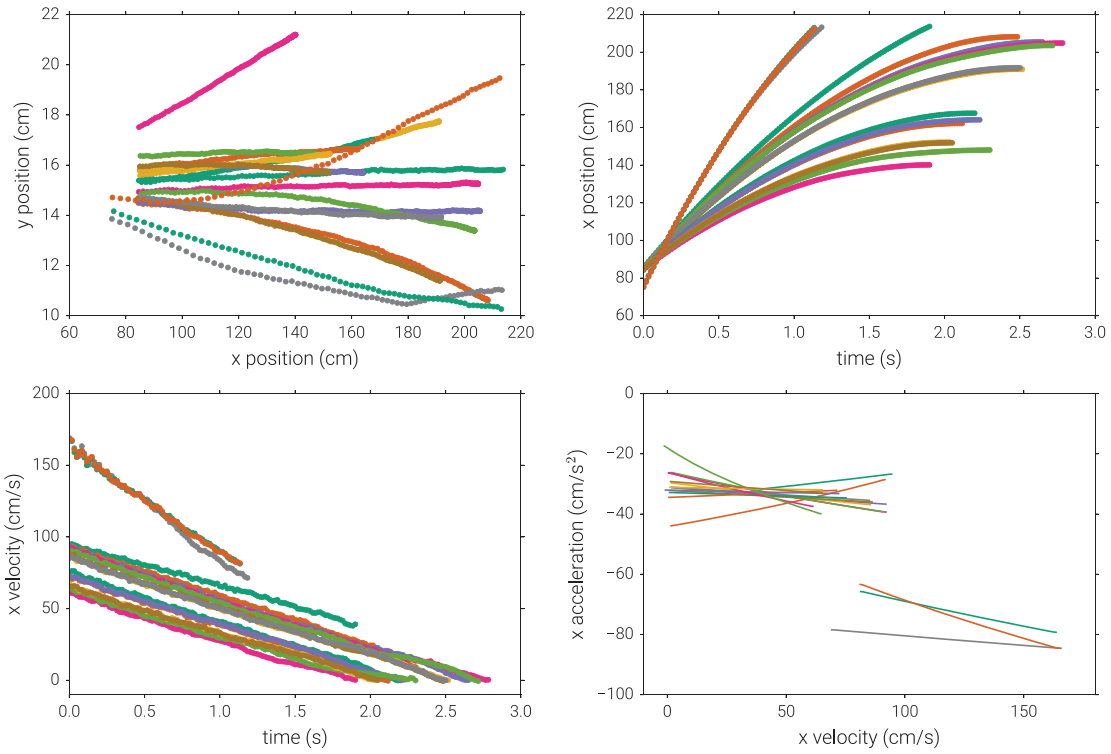

Figure 5: All trajectories for cylinder 23 on aquarium sand. Upper left: two-dimensional trajectories across the bed. Upper right: downslope positions over time. Lower left: downslope velocities over time. Lower right: downslope accelerations versus velocity, from least-squares quadratic fits to the velocity data.

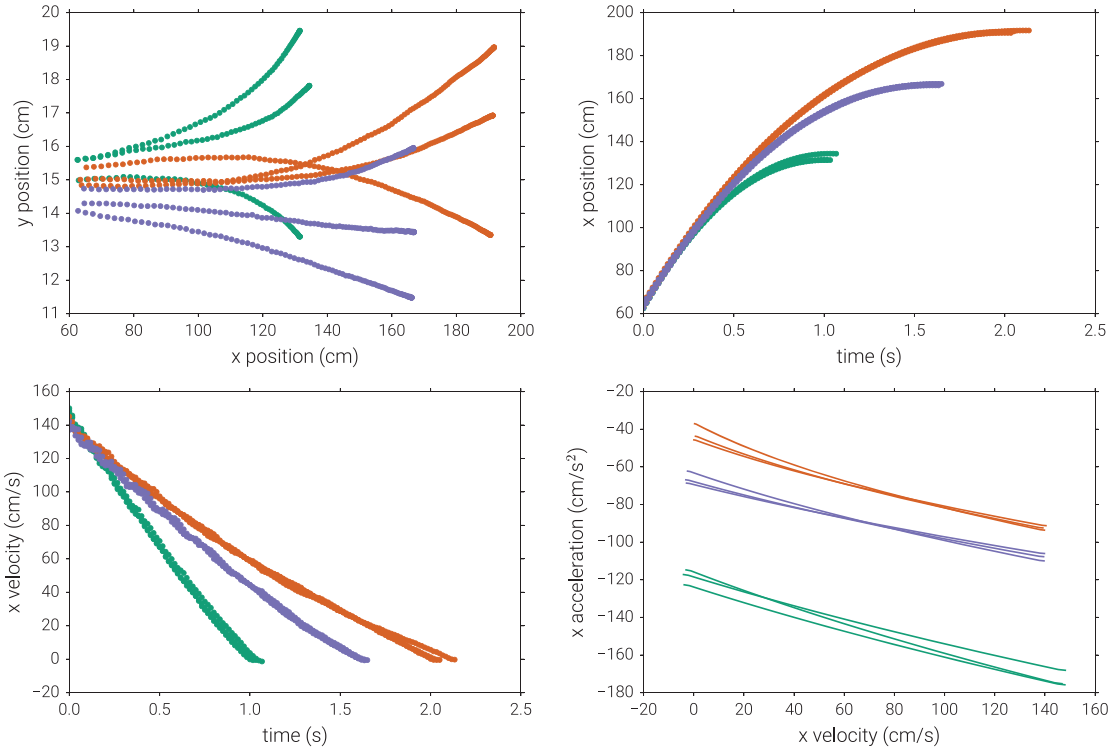

Figure 6: All trajectories for cylinder 24 (green), 29 (blue), and 36 (orange) on ballotini. Upper left: two-dimensional trajectories across the bed. Upper right: downslope positions over time. Lower left: downslope velocities over time. Lower right: downslope accelerations versus velocity, from least-squares quadratic fits to the velocity data.

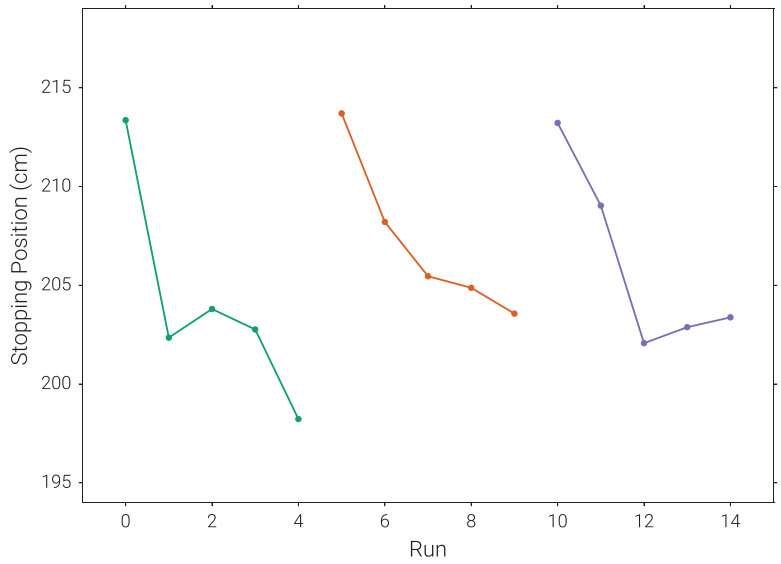

Figure 7: Bedding-in process, whereby the stopping distance of a cylinder would systematically increase (not shown) or decrease before saturating after several trials. The depicted runs correspond to, from left to right, cylinders 24, 23, and 25, on the aquarium sand.

precluded by noise. Instead, to roughly estimate the cylinder accelerations, we performed linear least squares fits of quadratic polynomials in time to the velocity data. These fits could then be differentiated to produce estimates of the trajectories in the (x component) velocity-acceleration phase space. We note that such a fit, however, severely restricts the allowed curves in phase space. In this case, since the velocity is fit to a quadratic function of time, the acceleration must be a linear function of time, implying the trajectory in phase space must be a parabola where the acceleration goes like the square root of the velocity. If such a trajectory is not expected on dynamical grounds, we should be cautious in our interpretation of the fit. We tried a number of other fitting procedures, including spline fits, various polynomial fits, and applying moving filters to both the position and velocity data, with the goal of better approximating the phase space trajectories of our trials. Ultimately, we favored a forward-modeling approach for studying the dynamics, as will be described in § 4.

Another interesting feature can be found at the end of the trajectories where the cylinders came to a stop on the bed. As shown in Figure 8, as they come to rest, the cylinders tend to roll backwards (upslope) several millimeters before coming to a complete stop. This feature may be useful in discriminating between more advanced dynamical models incorporating e.g. the history dependence of the granular disturbance induced by the cylinder, in the traveling frame.

Taking 50 cm/s as a characteristic velocity, 6 cm as a characteristic cylinder diameter, and $\nu \approx 1.5 \times 10^{-5}\,\mathrm{m}^2/\mathrm{s}$ for the kinematic viscosity of air, we expect the Reynolds number

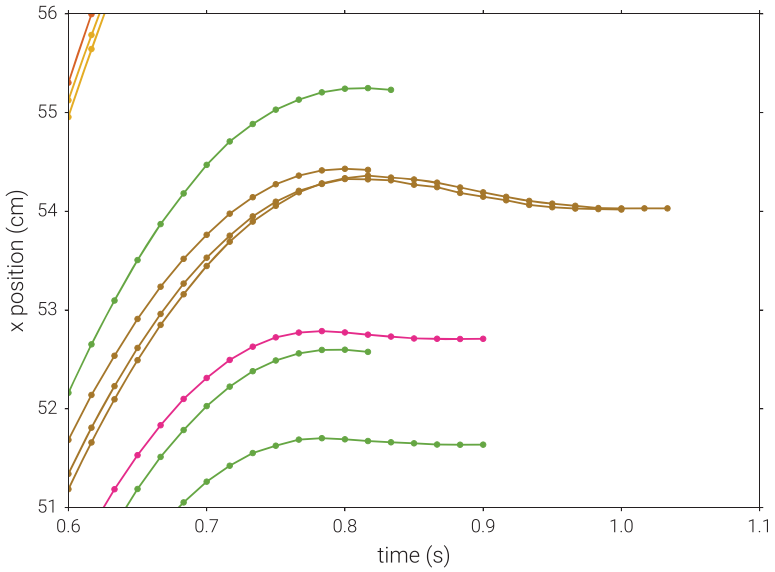

Figure 8: Rollback at the end of several trajectories on ballotini. The pink, green, and brown trajectories correspond to cylinders 20, 21, and 31, respectively.

of the airflow around the cylinders as they roll down the bed to be of order $\mathrm{Re} \sim 2000$. We therefore expect the air drag on the cylinders to depend quadratically on velocity with an order-one drag coefficient. To measure the effect of air resistance on the cylinders in the absence of large surface drag, we recorded additional trials of the cylinders rolling over a glass sheet which had been placed over the granular bed. In § 4, we perform a forward-modeling analysis of the dynamics of these runs, and the runs on the aquarium sand and ballotini.

3 Modeling

3.1 Cylinder dynamics

To model the dynamics of the cylinders, we consider the motion of a rigid cylinder rolling over a deformable surface. To simplify the analysis, we consider the two-dimensional case, neglecting span-wise variations and edge effects. We again note that tests on the aquarium sand displayed no substantial dependence on the length of the cylinder, but edge effects may be more important on softer materials, such as the ballotini.

The geometry of the problem is depicted in Figure 9. The cylinder is taken to have radius R, velocity $\dot{\vec{x}}$, and rotational velocity Ω. The upward force F_n, horizontal force opposing the motion F_r, and torque τ due to the surface stress over the contact area S with

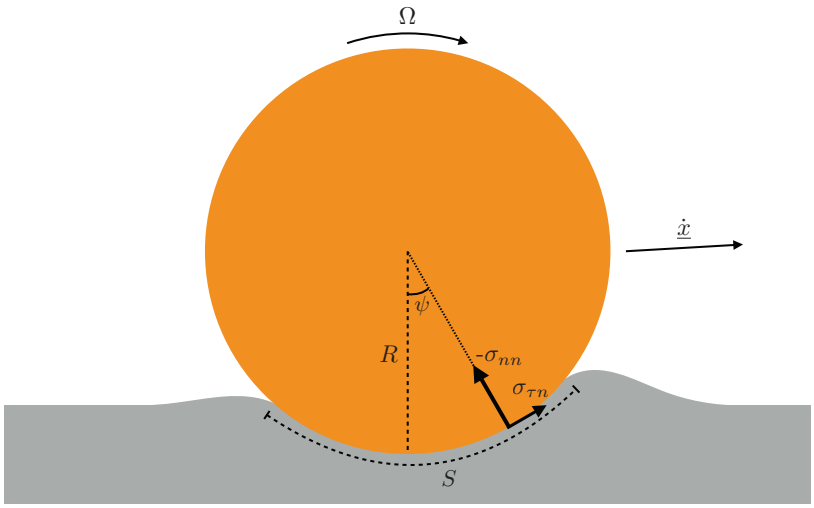

Figure 9: Model geometry of a rigid cylinder rolling on a deformable surface.

the underlying medium are given by:

$$F_n = \int_S \sigma_{\tau n} \sin(\psi) - \sigma_{nn} \cos(\psi) \, \mathrm{d}S \tag{1}$$

$$F_r = -\int_S \sigma_{nn} \sin(\psi) + \sigma_{\tau n} \cos(\psi) \, \mathrm{d}S \tag{2}$$

$$\tau = -R \int_S \sigma_{\tau n} \, \mathrm{d}S \tag{3}$$

With gravity of strength g as the only other force acting on the cylinder, the translational and rotational dynamics of the cylinder are given by:

$$m\ddot{x} = -F_r \tag{4}$$

$$m\ddot{z} = F_n - mg \tag{5}$$

$$I\dot{\Omega} = \tau \tag{6}$$

where m is the mass (per unit length) of the cylinder, and I is the moment of inertia (per unit length) of the cylinder. For an axisymmetric body with mass density $\rho(r)$, the moment of inertia is given by

$$I = \int_0^R r^2 \rho(r) 2\pi r \, \mathrm{d}r \equiv \alpha m R^2 \tag{7}$$

and α is a dimensionless description of the mass distribution, with e.g. $\alpha = 1/2$ for a uniform solid cylinder, and $\alpha \to 1$ for a cylindrical shell.

In the limit of a small deformation of a horizontal surface, the forces are given to first

order as

$$F_n = -\int_S \frac{x}{R}\sigma_{xz} + \sigma_{zz}\,\mathrm{d}x \tag{8}$$

$$F_r = -\int_S \frac{x}{R}\sigma_{zz} - \sigma_{xz}\,\mathrm{d}x \equiv F_r' + \frac{\tau}{R} \tag{9}$$

$$\tau = R\int_S \sigma_{xz}\,\mathrm{d}x \tag{10}$$

If we assume the cylinder to be rolling without slipping, we also have the constraint, to first order, that $\dot{x} = R\Omega$, and we can then rewrite the angular momentum equation as $I\ddot{x} = R\tau$. Using this expression and the first-order forms of the torque and horizontal force, we can rewrite the horizontal momentum equation as

$$(1+\alpha)m\ddot{x} = -F_r' = \int_S \frac{x}{R}\sigma_{zz}\,\mathrm{d}x \tag{11}$$

We see that when rolling without slipping, the tangential stress contribution to the horizontal force effectively acts as an added mass. The horizontal dynamics are then only driven by the horizontal projection of the normal stress, F_r'. This is the rolling resistance.

3.2 Plastic model for granular medium

Modeling the granular material as a continuum and neglecting inertia, the dynamics in the medium are governed by a balance between the material stresses and gravity, given by

$$\nabla \cdot \underline{\underline{\bar{\sigma}}} = \rho_s \underline{g} \tag{12}$$

where ρ_s is the density of the granular medium, and $\underline{\underline{\bar{\sigma}}} = -\underline{\underline{\sigma}}$ is the conventional representation of the stress used in soil mechanics.

To close the model, we use a Mohr-Coulomb plastic rheology, which may be suitable for studying static granular materials as they begin to deform. In Mohr-Coulomb theory, the maximum shear stress that a material can support before deforming is linearly related to the applied normal stress as

$$|\bar{\sigma}_{\tau n}| = c + \tan(\phi)\bar{\sigma}_{nn} \tag{13}$$

The friction angle ϕ and cohesion c are material parameters. To model the yielded regions of our dry granular materials, we'll consider such a rheology with zero cohesion, and a friction angle given by the material's angle of repose. In this case, the rheology can also be written in terms of the mean compressive stress $\bar{\sigma}$ and deviatoric stress $\bar{R}$ as

$$\bar{R} = \sin(\phi)\bar{\sigma} \equiv \mu\bar{\sigma} \tag{14}$$

We again consider the limit of small deformation, and assume the cylinder contacts the surface over a length a starting from its bottom edge. We assume the yielded region comprises a section of the medium beginning at this back contact, and extending out in front of the cylinder, as indicated in Figure 10. We'll continue in a polar coordinate system centered at the leading contact, with $r^2 = x^2 + z^2$ and $\tan(\theta) = z/x$.

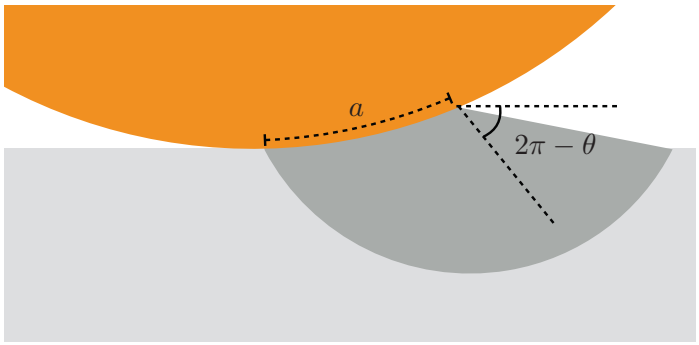

Figure 10: Assumed geometry of the yielded region (dark gray) under the cylinder. We consider the small-deformation limit, where we take the surface to be flat, and the cylinder to contact along a patch of length a, starting from its bottom-most point and going forward.

From Mohr's circle, the stress components in polar coordinates can then be written as

$$\bar{\sigma}_{rr} = \bar{\sigma}(1 + \mu\cos(2\theta - 2\theta_p)) \tag{15}$$

$$\bar{\sigma}_{\theta\theta} = \bar{\sigma}(1 - \mu\cos(2\theta - 2\theta_p)) \tag{16}$$

$$\bar{\sigma}_{\theta r} = -\mu\bar{\sigma}\sin(2\theta - 2\theta_p) \tag{17}$$

where θ_p is the angle of principal stress. The components of the force balance in polar coordinates are

$$r\partial_r\bar{\sigma}_{rr} + \partial_\theta\bar{\sigma}_{\theta r} + \bar{\sigma}_{rr} - \bar{\sigma}_{\theta\theta} = r\rho_s g_r \tag{18}$$

$$r\partial_r\bar{\sigma}_{\theta r} + \partial_\theta\bar{\sigma}_{\theta\theta} + 2\bar{\sigma}_{\theta r} = r\rho_s g_\theta \tag{19}$$

The boundary condition on the free surface ahead of the cylinder is that the mean stress is zero:

$$\bar{\sigma} = 0 \qquad (\theta = 0) \tag{20}$$

The boundary condition at the contact surface between the cylinder and the medium is that for a fully rough footing, i.e. that a plastic slip-line is parallel to the footing. The slip-lines are the two families of curves defined by tangent angles of $\theta_p \pm \epsilon$, where $\epsilon = \pi/4 - \phi/2$. These are the surfaces along which the normal and tangential stresses meet the yield criterion, and form the characteristic curves of the PDE. The resulting condition on the angle of principal stress under the footing is

$$\theta_p = -\pi + \epsilon \qquad (\theta = -\pi) \tag{21}$$

With this geometry and these boundary conditions, the equations possess a radial scaling symmetry and self-similar, separable solutions. Taking $\bar{\sigma} = r\rho_s g p(\theta)$ and $\theta_p = \theta_p(\theta)$, the force balances reduce to a pair of ordinary differential equations in θ, which can be recombined to give

$$(\mu - \cos(2\theta - 2\theta_p))\partial_\theta p = \cos(\theta - 2\theta_p) + \sin(2\theta - 2\theta_p)p \tag{22}$$

$$(\mu - \cos(2\theta - 2\theta_p))2\mu p\partial_\theta\theta_p = \sin(\theta) + \mu\sin(\theta - 2\theta_p) + (1 - \mu^2)p \tag{23}$$

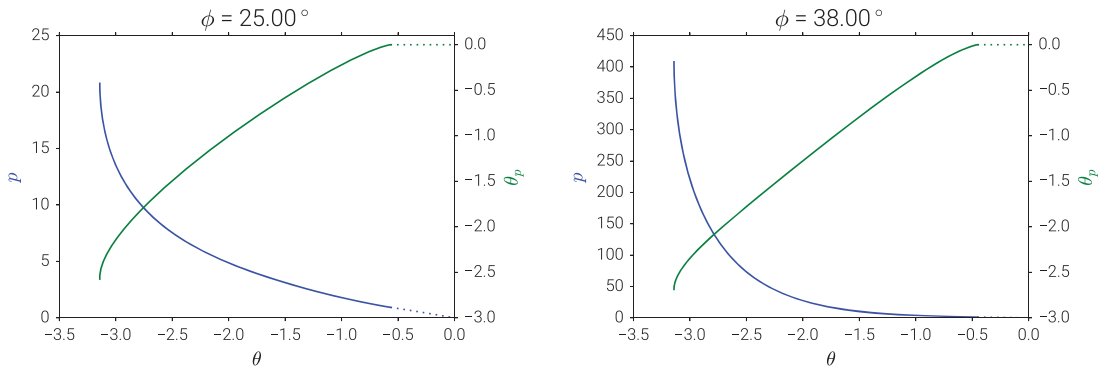

Figure 11: Similarity solutions for the dimensionless pressure p and angle of principal stress θ_p for a cohesionless plastic model with friction angles $\phi = 25°$ and $\phi = 38°$, near the values for the ballotini and aquarium sand, respectively.

The triangular region underlying the free surface, spanning $-\epsilon < \theta < 0$, is termed the "Rankine zone," with a solution given by $\theta = 0$ and $p = -\sin(\theta)/(1-\mu)$. The equations are singular when $\cos(2\theta - 2\theta_p) = \mu$, which occurs when $\theta - \theta_p = \pm\epsilon$. One such singularity defines the end of the Rankine zone, and another occurs at the boundary under the footing due to the rough boundary condition. We enforce regularity at the interior singularity by requiring the stress to match the Rankine solution. Under the rough footing, scaling analysis shows that the derivatives diverge as

$$p - p(\theta = -\pi) \sim \theta_p - (-\pi + \epsilon) \sim \sqrt{\theta - (-\pi)} \tag{24}$$

After reposing the equations in terms of the rescaled coordinate $\alpha = \sqrt{\theta + \pi}$, the equations can then be solved with standard numerical techniques for nonlinear boundary value problems. We used the Dedalus package [2] to solve the equations via Newton's method for Chebyshev polynomial discretizations of $p(\alpha)$ and $\theta_p(\alpha)$. The similarity solutions for a friction angles near those of the ballotini and aquarium sand are shown in Figure 11, and the corresponding slip-lines for the aquarium sand are depicted in Figure 12. The pressure under the footing $p_f = p(\theta = -\pi)$, as a function of the friction angle, is shown in the left half of Figure 13. This pressure is well-approximated as exponential in the tangent of the friction angle over the depicted range of solutions.

Along the footing, the stress components can be written from the similarity solution as

$$\bar{\sigma}_{xx} = -x\rho_s g p_f (1 + \mu^2) \tag{25}$$

$$\bar{\sigma}_{zz} = -x\rho_s g p_f (1 - \mu^2) \tag{26}$$

$$\bar{\sigma}_{xz} = -x\rho_s g p_f \mu \sqrt{1 - \mu^2} \tag{27}$$

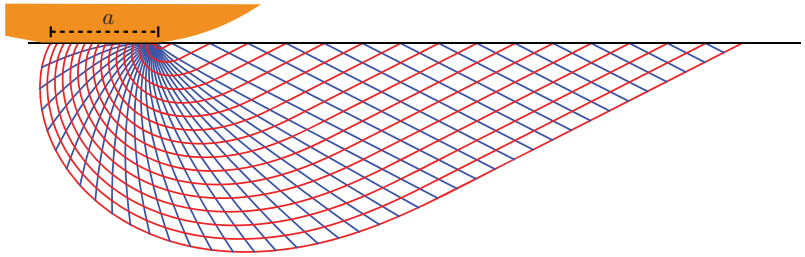

Figure 12: Slip-line solution for a cohesionless plastic model with friction angle $\phi = 38^\circ$.

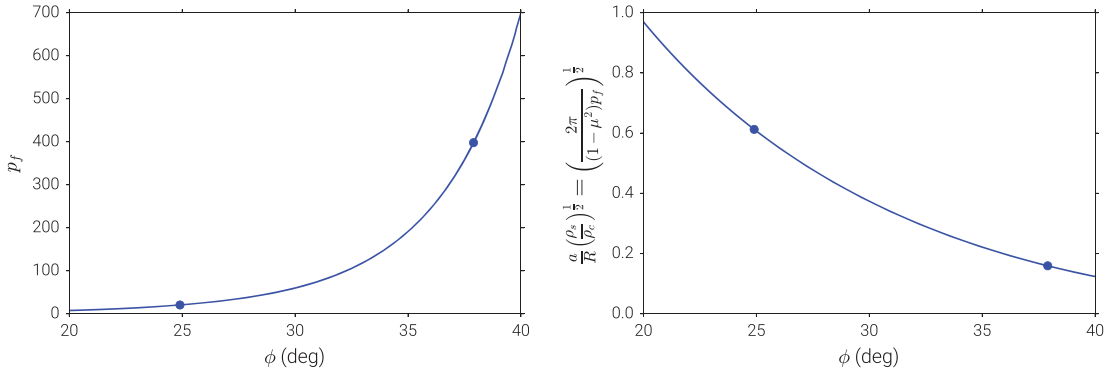

Figure 13: Left: Dimensionless pressure under the footing p_f for a cohesionless plastic model as a function of the friction angle. Right: Leading order contact area for a cylinder in vertical equilibrium in the cohesionless plastic model as a function of friction angle. The dots emphasize the expected values for the ballotini and aquarium sand.

The forces on the cylinder can then be calculated using Eq. 8-10 to be

$$F_n = -\frac{\rho_s g p_f \mu\sqrt{1-\mu^2}}{R}\int_{-a}^{0} x(x+a)\,\mathrm{d}x - \rho_s g p_f (1-\mu^2)\int_{-a}^{0} x\,\mathrm{d}x \tag{28}$$

$$= \frac{\rho_s g p_f \mu\sqrt{1-\mu^2}a^3}{6R} + \frac{\rho_s g p_f (1-\mu^2)a^2}{2} \tag{29}$$

$$F_r' = -\frac{\rho_s g p_f (1-\mu^2)}{R}\int_{-a}^{0} x(x+a)\,\mathrm{d}x = \frac{\rho_s g p_f (1-\mu^2)a^3}{6R} \tag{30}$$

$$\tau = R\rho_s g p_f \mu\sqrt{1-\mu^2}\int_{-a}^{0} x\,\mathrm{d}x = -\frac{R\rho_s g p_f \mu\sqrt{1-\mu^2}a^2}{2} \tag{31}$$

Taking the leading-order term in the normal force, we see that the ratio between the rolling resistance and normal force is simply related to the contact area by

$$\frac{F_r'}{F_n} = \frac{1}{3}\frac{a}{R} \tag{32}$$

If we then assume that the vertical acceleration of the cylinder is small, we can use the vertical force balance $F_n \approx mg = \pi R^2 \rho_c g$, where ρ_c is the mean density of the cylinder, to determine the contact area:

$$\frac{a}{R} = \left(\frac{\rho_c}{\rho_s}\frac{2\pi}{(1-\mu^2)p_f}\right)^{1/2} \tag{33}$$

Moving the density ratio to the left of this expression, the remaining terms on the right only depend on the friction angle, and are plotted on the right side of Figure 13. For a given density ratio, we see that we expect the contact area and hence rolling resistance to decrease with increasing friction angle.

We note that this solution is not generally consistent with rolling without slipping. This can be seen from the ratio of the torque to the rolling resistance:

$$\frac{\tau}{RF_r{}'} = -\frac{3\mu}{\sqrt{1-\mu^2}}\frac{R}{a} \tag{34}$$

which will generally not be equal to, and is of an asymptotically different order than, the rolling-without-slipping ratio of

$$\frac{\tau}{RF_r'} = -\frac{\alpha}{1+\alpha} \tag{35}$$

A more sophisticated model with another internal parameter would be needed to produce a general prediction for the rolling resistance with a self-consistent torque on the cylinder. Nevertheless, this simple model still offers a prediction for the scaling of the rolling resistance with the cylinder and material parameters.

4 Analysis

To test the dynamics predicted by the plasticity model, we performed a forward-modeling analysis to fit our experimental data with model trajectories governed by force laws with

constant and quadratic velocity terms:

$$\ddot{x} = C_0 + C_2\dot{x}^2 \tag{36}$$

First, we removed any trajectories on the sand that strayed more than 4 cm from the center of the track to reduce the biases introduced by lateral variations in the bed. Runs showing obvious bedding behavior, typically the first two runs after switching cylinders on the sand, were also removed. We then truncated the remaining trajectories once their velocity dropped below approximately 5 cm/s. This truncation prevents the final halting dynamics of the cylinder, which aren't captured by this simple model, from affecting our inferred parameters for the rolling resistance during motion.

We then performed a joint fit over all of the trials for a given cylinder and granular material to estimate the corresponding force coefficients. For each trial, a model trajectory was simply integrated from the assumed force law as

$$x_i(t) = x_i(0) + \int_0^t v_i(t')\,\mathrm{d}t' \tag{37}$$

$$v_i(t) = v_i(0) + \int_0^t C_0 + C_2 v_i(t')^2\,\mathrm{d}t' \tag{38}$$

A nonlinear least-squares fit was then performed to determine the optimal initial position and velocity for each trial, and the force-law coefficients C_0 and C_2 for that cylinder/material combination. Uncertainties in the fit parameters were determined using the covariances from the nonlinear fit, scaled by the square-root of the 95th percentile of the corresponding χ^2 distribution, with the uncertainties in the position data all taken to be 3 mm.

Figure 14 shows the results for the trials on the glass sheet. The best-fit parameters indicate a small constant resistance, as expected, and a more substantial quadratic component. Assuming the drag is dominated by air resistance, we calculate the equivalent drag coefficient for the fit C_2 values as

$$(1+\alpha)m\ddot{x} = (1+\alpha)\pi R^2\rho_c C_2\dot{x}^2 = -C_d\rho_a R\dot{x}^2 \tag{39}$$

$$\implies C_d = -(1+\alpha)\frac{\rho_c}{\rho_a}\pi R C_2 \tag{40}$$

We see that the best-fit parameters are all consistent with an order-one drag coefficient, in agreement with the assumption that air resistance was dominant in the trials on the glass sheet. Using the weighted average of the measurements for each cylinder, we estimate the drag coefficient of this geometry (a cylinder rolling on a nearly flat surface) to be $C_d = 1.3 \pm 0.1$. This tests serves to confirm that the standard quadratic drag law, with an order-one drag coefficient, is sufficient to describe the effects of air drag in our experiments.

Figure 15 and Figure 16 show the fitting results for the trials on the aquarium sand and ballotini, respectively.

If we assume that the cylinder is in vertical equilibrium ($F_n = mg$), the cohesionless plastic model predicts a constant horizontal acceleration given by

$$C_{0,\text{theory}} = -\frac{g}{3(1+\alpha)}\left(\frac{\rho_c}{\rho_s}\frac{2\pi}{(1-\mu^2)p_f}\right)^{1/2} \tag{41}$$

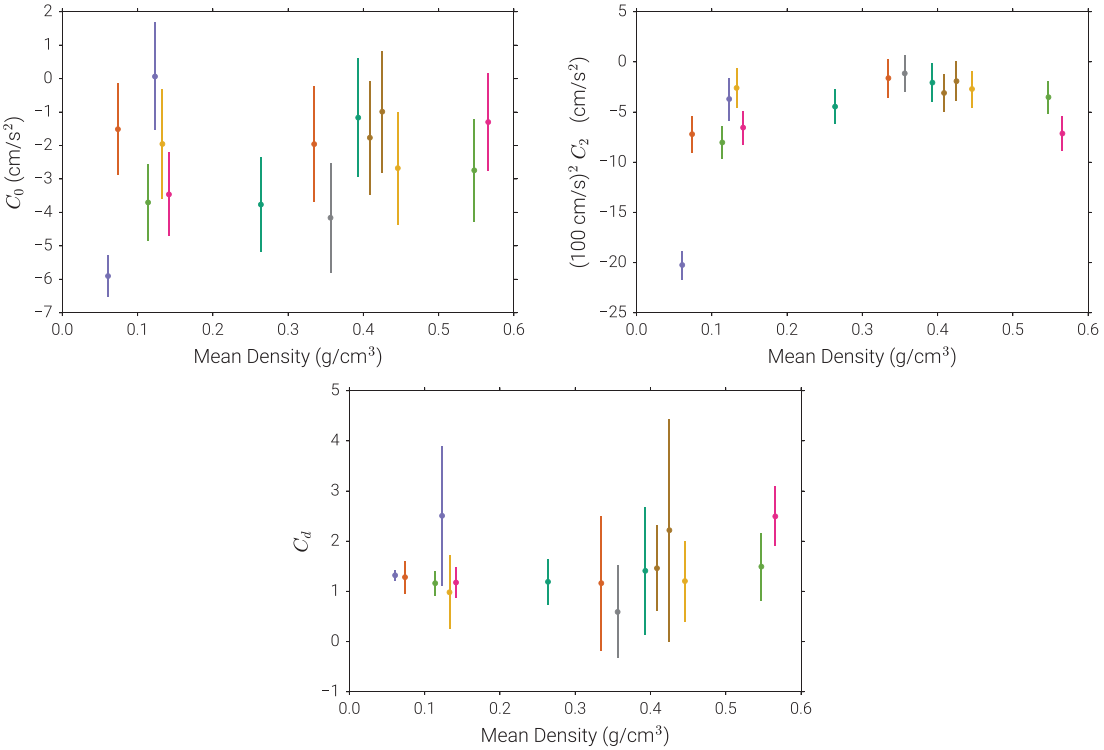

Figure 14: Best fitting force-law coefficients for cylinders rolling on the glass sheet. Top left: constant term fit values. Top right: quadratic term fit values. Bottom: equivalent drag coefficients for the fitted quadratic term coefficients.

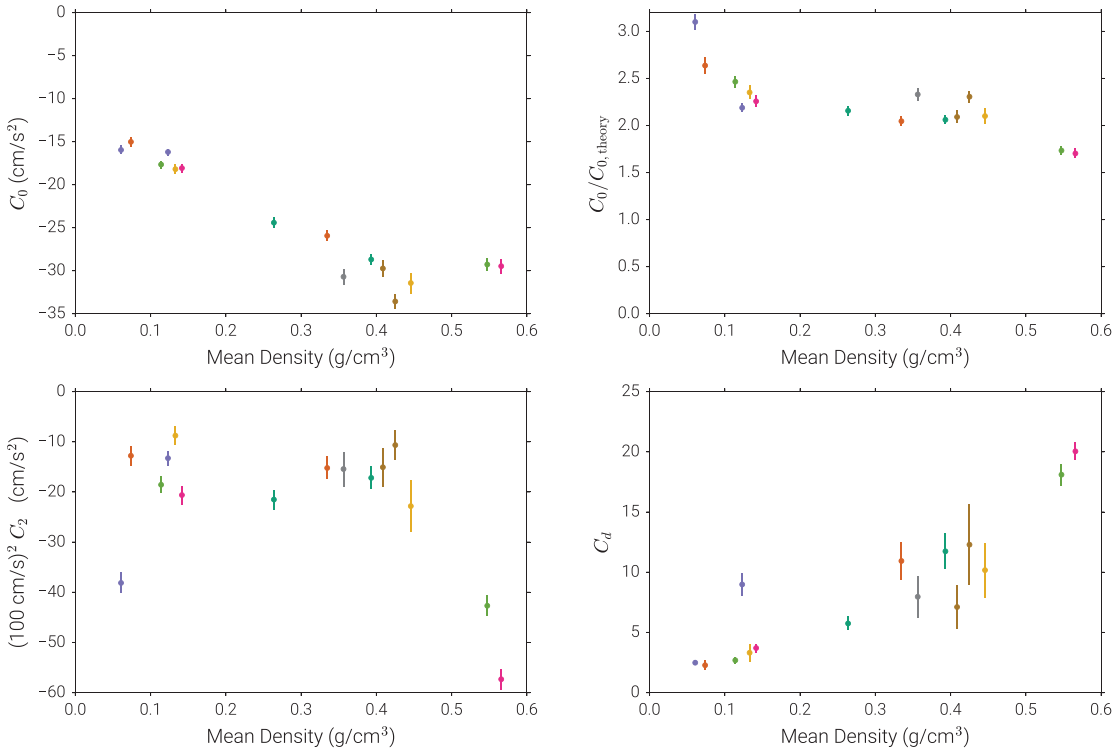

Figure 15: Best fitting force-law coefficients for cylinders rolling on aquarium sand. Top left: constant term fit values. Top right: comparison of constant term fit values to theoretical expectation from cohesionless plastic model. Bottom left: quadratic term fit values. Bottom right: equivalent drag coefficients for the fitted quadratic term coefficients.

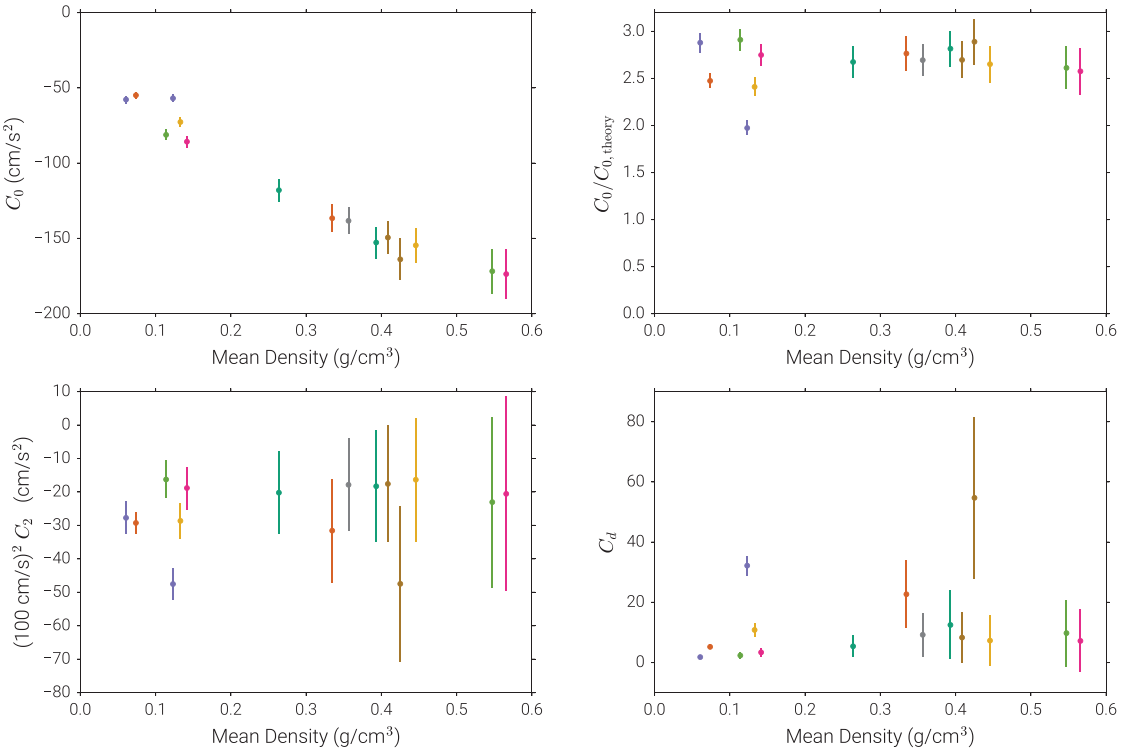

Figure 16: Best fitting force-law coefficients for cylinders rolling on ballotini. Top left: constant term fit values. Top right: comparison of constant term fit values to theoretical expectation from cohesionless plastic model. Bottom left: quadratic term fit values. Bottom right: equivalent drag coefficients for the fitted quadratic term coefficients.

The fitted values for C_0 on both the aquarium sand and ballotini are approximately 2 to 3 times larger than the values this model predicts, as can be seen in the upper right panels of Figure 15 and Figure 16. This ratio holds across the roughly $10x$ range of mean cylinder densities, and $2x$ and $4x$ ranges in the fitted C_0 values for the aquarium sand and ballotini, respectively. This simple model therefore seems to correctly capture the rough magnitude of the rolling resistance and its scaling with the cylinder's mean density.

For most cylinders on both the ballotini and the aquarium sand, the fitted values of C_0 and C_2 indicate that the velocity-dependent component of the acceleration is likely subdominant to the velocity-independent portion. To check if air resistance is important in these trials, we converted the fitted C_2 values to the equivalent drag coefficients as described for the runs on the glass sheet. For the aquarium sand, these equivalent drag coefficients are $\mathcal{O}(10)$ and increase roughly linearly with the mean density. For the ballotini, these equivalent drag coefficients are also $\mathcal{O}(10)$, but do not clearly display a systematic dependence on the mean density. In both bases, this indicates that the fitted C_2 values are not consistent with air drag, and that instead there may be a velocity-dependent portion of the rolling resistance.

Our data and the form of our trajectory model preclude us from more precisely characterizing the velocity dependence of the resistance. For instance, Figure 17 shows the covariance matrix for the fit for cylinder 20 on aquarium sand. This fit, as is typical for the runs on aquarium sand, shows strong covariances between C_2 and the initial velocities of the faster trials, which limits our confidence in the inferred values of these parameters. In addition, our trajectory model does not allow for a non-quadratic velocity dependence, which if present could influence both the C_0 and C_2 measurements. Furthermore, for some cylinders, the measured acceleration at a given velocity seems to vary with the initial velocity of the trial, with faster runs having a larger deceleration at a given velocity than slower runs, as can be seen in Figure 5 around 80 cm/s. This indicates that taking a force law that is purely a function of velocity may be too strong of a simplification of the dynamics, and a higher-dimensional model may be necessary to more accurately describe the observations.

5 Conclusion

We experimentally investigated the rolling resistance experienced by light cylinders on dry granular media. We constructed a 2.5 m granular bed, and recorded the trajectories of cylinders rolled from a ramp onto the bed. A range of cylinders, primarily sections of PVC pipe, and two granular materials (aquarium sand and ballotini) were used. We selected cylinders with low mean densities compared to the granular material, allowing us to model their interaction with the bed using the asymptotic limit of small deflections to the granular surface. In this limit, we derived the expected contact area and rolling resistance for a cylinder on a cohesionless Mohr-Coulomb plastic, which may serve as a simplified model of dry granular materials as they begin to yield. The predicted rolling resistance in this model is independent of the cylinder's velocity, and scales with the square-root of the cylinder's mean density. Fits to the observed trajectories demonstrate velocity-independent resistances with the same scaling in cylinder density, and amplitudes 2-3 times larger than the theoretical prediction. Trials on the aquarium sand demonstrate an additional velocity-dependent resistance that appears to be inconsistent with the effects of air drag.

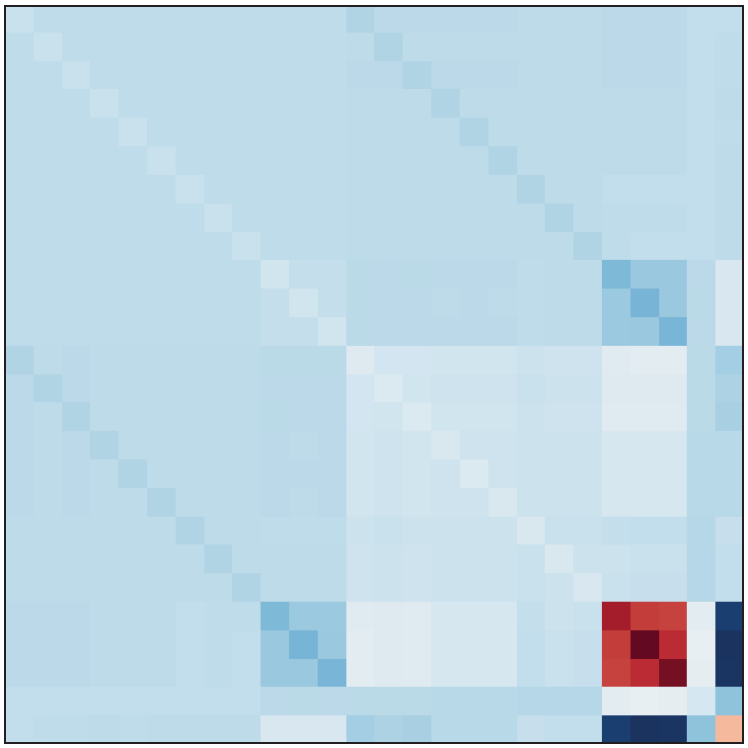

$\mathrm{Cov}(x_i(0), \ldots, V_i(0), \ldots, C_0, C_2)$

Figure 17: Covariance matrix for the fit to 12 aquarium sand trials with cylinder 20. The parameter vector consists of the initial positions of the trials $\underline{x}_i(0)$, the initial velocities of the trials $\underline{v}_i(0)$, the constant acceleration coefficient C_0, and the quadratic acceleration coefficient C_2. The fit shows strong covariances between C_2 and the initial velocities of the last three (fast) trials.

Several extensions to both the experiments and models may allow a better determination of rolling resistance on granular media. An experimental setup with a more precise launching mechanism, a wider bed, and a faster way to resurface the sand would likely help reduce the history dependence and lateral motion of the trials. However, these effects are both interesting in their own right, and may be important to any practical applications of rolling over granular media. A longer bed would make it possible to record the entirety of trajectories with larger initial velocities, which would provide much more power in constraining the velocity dependence of the cylinders' accelerations. While our image analysis procedure can very precisely determine the image trajectories of the cylinders, the inference of the real-world trajectories is limited by the systematic errors in the scene calibration, which could be improved. Finally, a number of extensions to the trajectory modeling are possible. Instead of assuming a vertically and materially equilibrated state, we could include ODEs for the cylinder's vertical motion and the size of the material pile ahead of the cylinder. The model geometry could also be modified with an additional degree of freedom to separate the rolling resistance and torque on the cylinder, to allow for dynamics consistent with rolling without slipping. Ultimately, a model considering a more advanced rheology is likely necessary to predict the velocity dependence of the resistance.

6 Acknowledgements

I would like to thank Neil Balmforth and Ian Hewitt for proposing and guiding this project. Neil and Ian contributed an unbelievable amount of time helping to construct, run, and clean up the experiments in the lab, and to discussing trajectories and slip-lines at the cottage. I would also like to thank Anders Jensen for his assistance with our apparatus. The directors Colm Caulfield and Neil, the lecturers Mike Shelley and Peko Hosoi, and all of the staff and visitors deserve thanks for making every day of the summer informative and engaging. Finally, I'd like to thank the other fellows for all of the great times on the softball field, at the cottage, and around the dinner table.

References

[1] G. Bradski, *Open source computer vision library*, Dr. Dobb's Journal of Software Tools, (2000).

[2] K. J. Burns, G. M. Vasil, J. S. Oishi, D. Lecoanet, B. P. Brown, and E. Quataert, *Dedalus: A flexible framework for spectrally solving differential equations*, In preparation, (2017).

[3] I. F. Collins, *A simplified analysis of the rolling of a cylinder on a rigid/perfectly plastic half-space*, International Journal of Mechanical Sciences, (1972).

[4] F. V. De Blasio and M.-B. Saeter, *Rolling friction on a granular medium*, Physical Review E, 79 (2009), p. 022301.

[5] E. A. Marshall, *Rolling contact with plastic deformation*, Journal of the Mechanics and Physics of Solids, 16 (1968), pp. 243–254.

[6] H. Petryk, *A slip-line field analysis of the rolling contact problem at high loads*, International Journal of Mechanical Sciences, (1983).

[7] A. Sauret, N. J. Balmforth, C. P. Caulfield, and J. N. McElwaine, *Bulldozing of granular material*, Journal of Fluid Mechanics, 748 (2014), pp. 143–174.

[8] A. Tordesillas and J. Shi, *The frictionless rolling contact of a rigid circular cylinder on a semi-infinite granular material*, Journal of Engineering Mathematics, (2000).

Splash and Spray of a Partially Submerged Rotating Disk

Anna Skipper

(advised by Megan Davies-Wykes and Shreyas Mandre)

December 3, 2016

1 Introduction

All vehicles - trucks, car, and bicycles - cause splash and spray when the tires rolls over sufficiently wetted surfaces. Splash (the fluid which is thrown off by the wheels) and spray (fluid droplets atomized by wind and other aerodynamic effects) [8] can be a cause of accidents due to hydroplaning and reduced visibility. In the case of bicycles in particular, splash and spray also cause problems for the unfortunate cyclist who is biking too close to another cyclist in wet or muddy conditions, resulting in the dirtying of a perfectly good outfit.

Despite the commonplace nature of this particular fluid mechanics problem, there are relatively few studies that have been conducted that seek to fundamentally understand such a flow - the splash and spray caused by rotating wheels. Most studies to date are qualitative or completely empirical in nature [8, 3]. Other studies have sought to quantify the effects of splash and spray caused by automotive vehicles, such as visibility reduction. Other studies are extremely specific, addressing a particular issue such as tire treads [11], mudguard performance [8], or visibility loss [12]. All of the studies cited above have been done in the context of automobiles rather than bicycles, which have a significantly different geometry (thinner relative to the radius). Moreover, basic physical understanding of the fluid mechanics can only aid in future designs of mudguards and tire treads that seek to mitigate the risks associated with splash and spray.

A good place to start, then, is to look at problems that have been solved with similar geometry. The fluid mechanics of rotating disks is well studied, e.g. [6]. The setup of these problems is that the flow is oriented normal to the disk surface, and the analysis is commonly done in terms of lubrication theory to find the height of the fluid layer on the disk. Fully submerged rotating disks, where the disk face is parallel to the tank floor with fluid above and below the disk face, have been studied in relation to turbine performance [9]. Similar studies of coating flows have been done investigating the film thickness around rotating cylinders [7, 10]. They are similar to this problem in the existence of an inner rigid surface and an outer free surface; however, these solutions assume that viscous forces are sufficiently large, which is a good assumption for paper pulp and honey, but certainly not for a bicycle wheel. Experiments and numerical analysis were done to investigate the problem of a rotating cylinder with the fluid injected tangentially to the disk face as a downward jet, like a cutting tool coated with cutting fluid [5]. The authors found, without cutting, that fluid is atomized by a spin-off mechanism: a film forms, which begins to pinch off into ligaments, which further pinch off to form droplets, leaving a thinner coating layer

on the cylinder. When cutting, the bulk of the aerosols are products of the splash as the fluid hits the cylinder edge.

These studies are useful for understanding the effects of geometry, the relevant forces to consider, and spin-off mechanisms. However, the problem of the rotating wheel has a unique configuration, with the disk oriented perpendicular to the water surface, where water is pulled upwards and is opposed by gravity. The true problem of car tires on wet pavement is quite complicated: the wheel is translating as well as rotating; the tire interacts with the road surface; and the tire treads and surface characteristics of the tire will undoubtedly influence the flow, as shown by [11]. In the case of automotive tires, the thickness of the tire is comparable to the radius of the tire, unlike the bicycle tire which is quite thin.

Here, we will investigate a simplified model of such a flow: a thin, rotating disk, partially submerged in an unlimited reservoir of water. The disk will rotate in place, without translating, and there will be no surface interaction at the bottom edge of the disk. The speed of the disk, as well as the submergence depth, will be varied. The extent of the resulting spray will be measured. Finally, the fluid will be changed to a shear-thinning, yield-stress fluid (water-bentonite dispersion), and qualitative differences between the two fluids will be noted.

2 Methods

2.1 Experimental Setup

A disk of radius 19.1 cm and thickness 2 cm was constructed of extruded polystyrene (XPS) foam board. The disk was mounted to a shaft which was controlled by a compressed air motor. This setup was mounted to a piece of plywood which sat in a 2 m circular tank. The distance between the bottom of the disk and the bottom of the tank was 10 cm. The tank was filled with water (20 $°C$), dyed with blue food coloring for visualization purposes, up to a specified submergence height on the wheel, h. The experimental setup is shown in Figure 1 below.

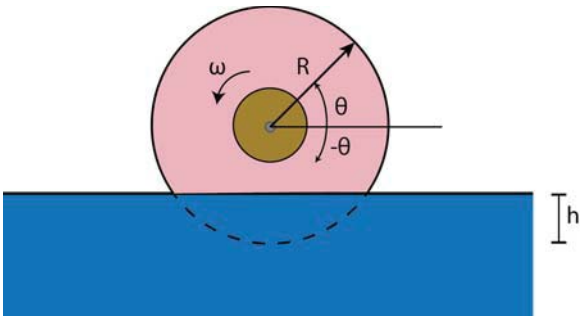

Figure 1: Experimental setup, $R = 19.1\ cm$, $\omega = [80, 220]$

The setup was illuminated by two 20-W LEDs (Ryobi 18-V Work Lights). Images were taken with a high-speed monochrome camera (Photron Fastcam SA3) at 1000 fps (1/3800 s^{-1} exposure). A laser photo tachometer (Extech 461920) was used to estimate the rotation rate of the wheel in order to ensure a sufficient range of speeds were obtained in the

experiments. The rotation rate of the disk was varied between 80 and 220 rpm ($1.6 - 4.4$ m/s), rotating counterclockwise, for all of the experiments. Experiments were conducted at three different submergence depths - $5, 8$, and 15 cm. Each experiment lasted 4.092 s.

2.2 Image Analysis

Images were processed using a suite of custom MATLAB codes. The rotation speed of the disk was measured more precisely by tracking of a piece of reflective tape located on the inner region of the disk. The horizontal extent of the film was taken to be the point at which the edge of the film intersected the reservoir surface. Measurements of this value were obtained for 200 images at equally spaced intervals. The horizontal extent did not vary significantly over the course of each experiment, and so only the mean is reported. The boundaries of the film were obtained by averaging 100 equally spaced images together. This average image was obtained by averaging the pixel value at each pixel location in the images.

3 Results

The typical features of the flow that results from the rotating disk are shown in Figure 2. A large film develops on the right side of the disk, which is rotating counterclockwise. The film is relatively thin, with a thicker outer edge, which acts as a conduit, draining fluid down the edge of the film. The film and the conduit are fairly steady, except near the separation point (labeled in Figure 2). The horizontal distance from the disk edge where it meets the reservoir to the conduit is taken as a characteristic length scale of the film, L. The disk is rotating at 155 rpm and is submerged to a depth of 8 cm.

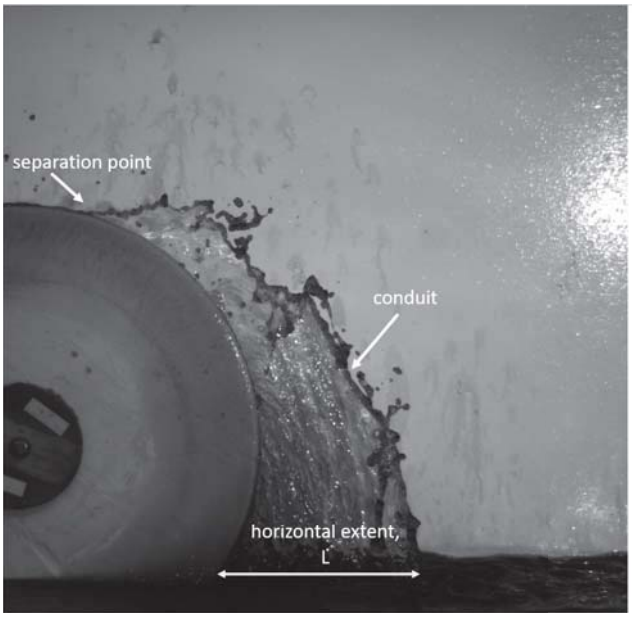

Figure 2: Typical features of the film behind the rotating disk

At lower speeds, the film shrinks and remains stable near the separation point, as shown in Figure 3(a) ($\omega = 115\ rpm$, $h = 8\ cm$). As the speed increases, the film grows radially outward and becomes increasingly more unstable, as shown in Figure 3(b) ($\omega = X\ rpm$, $h = 8\ cm$). In this image, a snapshot of a growing instability in the film is shown, as the film being to tear, likely due to the thinning with increased speeds. The growth of the sheet due to the increased rotation rate is shown for a range of speeds ($80 - 220\ rpm$) in Figure 4. The boundaries from an averaged image (see Section 2.2) are plotted for each speed at the same submergence depth. The x and y axes are centered at the position where the disk meets the reservoir surface (x_0, y_0). The colorbar shows the rotation speed, in $rpms$, of the disk for each boundary.

(a) (b)

Figure 3: Images of the film that develops behind the rotating disk at a lower speed ($\omega = 115$ rpm), left, and higher speed ($\omega = 220\ rpm$), right.

The film also changes as the submergence depth, h, changes, as depicted in Figure 5. As h is lowered, as in Figure 5(a) ($\omega = rpm$, $h = 5\ cm$), the film thins and grows larger. The film has become thin enough to cause the conduit to break up substantially near the separation point. When h is increased, as shown in Figure 5(b) ($\omega = rpm$, $h = 15\ cm$), the film looks quite different - it is much thicker and darker, though the conduit still persists. The film is also smaller and contained much closer to the disk.

3.1 Scaling Analysis

A simple scaling argument is used to show which forces are relevant in governing the size of the film. The forces we will consider are surface tension, gravity, inertia, and viscosity (in the context of a growing viscous boundary layer).

Beginning with surface tension, there are two relevant length scales - the balance between surface tension and inertia (Weber number) and gravity (Capillary number). The lengths scales, L_w and L_c, are given by

$$L_w = \frac{\sigma}{\rho(\omega R)^2} \tag{1}$$

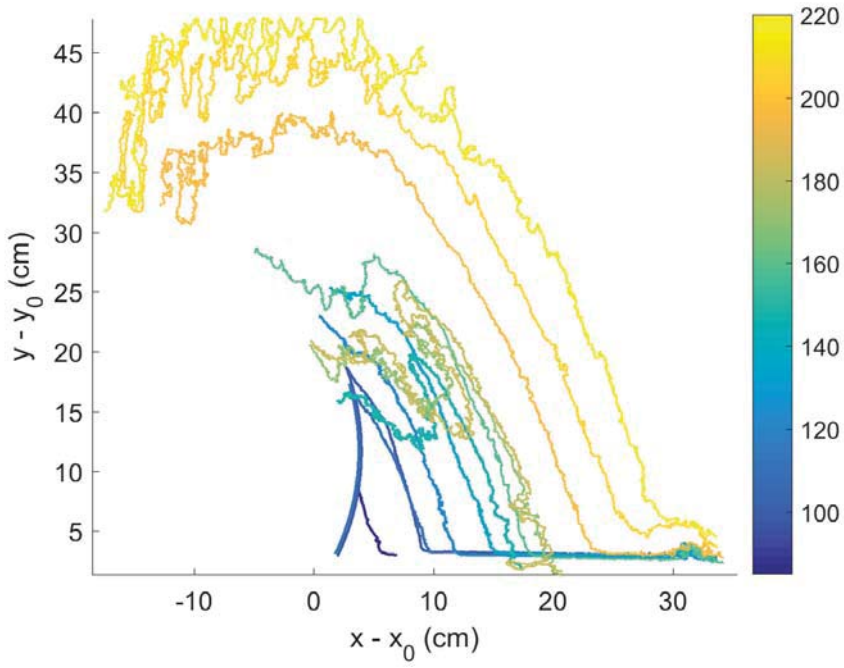

Figure 4: The outline of all the film boundaries for experiments with a submergence depth of $h = 8\ cm$. The colors range from 80 rpm to 220 rpm.

(a) (b)

Figure 5: Images of the film that develops behind the rotating disk at a lower submergence depth ($h = 5\ cm$) , left, and higher submergence depth ($h = 15\ cm$)

$$L_c = \left(\frac{\sigma}{\rho g}\right)^{1/2} \tag{2}$$

Given the surface tension of water in air ($\sigma = 0.1\ N/m$), the density if water ($\rho = 1000\ kg/m^3$), a characteristic rotational velocity ($\omega = 10\ rad/s$), the radius of the disk ($R = 0.1\ m$), and acceleration due to gravity ($g = 10\ m/s^2$), the lengths scales work out to be $x\ mm$ and $x\ mm$ respectively. These values are quite smaller, and therefore we can safely neglect surface tension in our analysis.

The height of a viscous boundary layer, δ, is typically given by

$$\delta = \left(\frac{\nu x}{U}\right)^{1/2} \tag{3}$$

where ν is the kinematic viscosity, x is the distance traveled along the surface of the object, and U is the freestream velocity. In our case, the distance traveled along the disk will be some fraction of the circumference, which is proportional to the radius, R. The "freestream" velocity is analogous to the tangential speed of the wheel, $U = \omega R$. This gives a final estimate of the boundary layer thickness as

$$\delta = \left(\frac{\nu}{\omega}\right)^{1/2} \tag{4}$$

Plugging the kinematic viscosity of water ($\nu = 10^{-6}\ m^2/s$) and the characteristic rotation rate, ω, $\delta = x\ mm$. As in the case of surface tension, this is small enough to be neglected.

Lastly, we expect competition between the inertial force, which pulls the fluid upwards out of the reservoir, and gravity, which is acting in the opposite direction. The length scale is given by the following expression:

$$L_g = \frac{(\omega R)^2}{g} \tag{5}$$

Given the same values of ω, R, and g cited above, $L_g = 10cm$, which is considerably large. It is likely that this balance between inertia and gravity is most responsible for the size of the film.

In Figure 6, the measured horizontal extent of the film, L, is plotted against the Froude length scale, L_g, both normalized by the radius of the disk, R, for a range of speeds. The different colors and markers correspond to different submergence depths, h. For all three values of h, L scales linearly with L_g. The slope changes inversely with h, increasing for smaller h and decreasing for larger h. This figure also indicates that there might be a transition region, which also changes with h, where the slope changes between successive data points. The trend is not consistent among all three experiment sets, however. For the lowest submergence depth, the slope becomes less steep after the transition region, while the other two submergence depth values result in steeper slopes.

4 Modeling

4.1 Projectile Motion

A simple model that involves only inertial and gravitational forces is pure projectile motion. We can think of each fluid particle as an independent particle. These particles move along

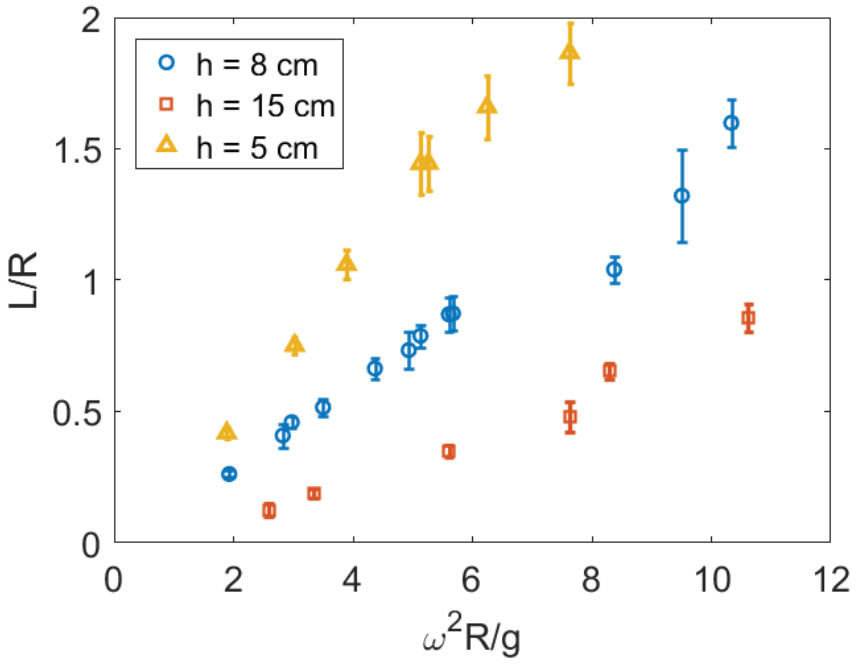

Figure 6: Scaling of the normalized horizontal extent of the film, L/R, against the Froude length scale, $\omega^2 R/g$.

the surface of the disk for some distance and then are ejected, at the local tangent angle and at the tangential velocity of the disk. The aggregate of these fluid particles, assuming the fluid is more or less ejected uniformly along the arclength of the disk, results in the film. The equation describing such motion are given by the simple expressions below.

$$x = x_0 + v_0 \cos(\alpha) t \tag{6}$$

$$y = y_0 + v_0 \sin(\alpha) t - \frac{1}{2} g t^2 \tag{7}$$

In such a model, the horizontal extent of the film, L, would correspond to particles thrown off the disk very near the reservoir surface where the tangent angle is at its most shallow. At this location (x_0, y_0), the final position of the fluid particle will be located at $(x, y) = (L + x_0, y_0)$. L, then, can be solved for exactly in terms of v_0 and α as shown below.

$$L = \frac{v_0^2}{g} \sin(2\alpha) \tag{8}$$

However, this very simple model over-predicts L by 400%.

One feature this model will not describe is the persistent conduit that we found in all our experiments. An easy tweak to the model above is to allow for the coalescence of fluid particles as they come closer to each other. A simple toy model was coded (by Shreyas Mandre) in which particles of a given mass are shed from the disk at regular intervals and

follow the parabolic trajectories described by Equations 6 and 7 above. As the particles close close to each other, within some fraction of the diameter, they combine to form a particle of the mass of the sum of the two particles before coalescence and a diameter proportional to that mass. Figure 7 below shows the steady state output of this model, which replicates the conduit features and reduces the estimate of L. The x and y axes, unlabeled, show the distance, normalized by the radius, from the disk center. Once again, however, L is over estimated, this time by 250%.

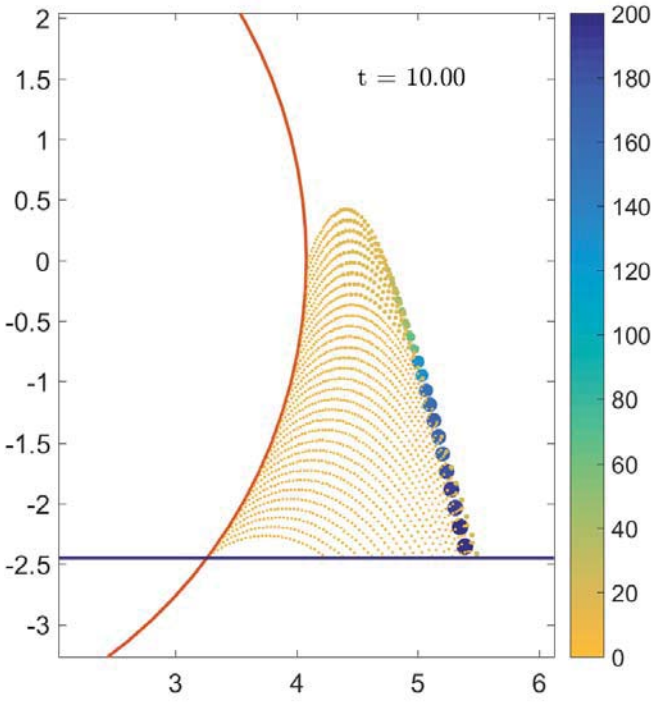

Figure 7: Toy model in which particles are seeded at regular from the disk and coalesce to form larger, heavier particles when two particles come within a short distance of each other. This model replicates the conduit, but still overestimates the horizontal extent of the film.

4.2 Bubble PTV

Estimates of L using Equations 6 - 8 are entirely dependent upon the initial conditions leaving the disk, v_0 and α. In both of the models above, we assumed that the fluid left the disk at the tangential velocity of the disk, ωR, at the local tangent angle. In order to investigate these assumptions, we implemented particle tracking velocimetry (PTV) on the bubbles entrained in the film. First, however, we must ensure that these bubbles will suffice as passive tracers, meaning that the rise velocity of the bubbles does not significantly affect the trajectory of the bubble during the time period that it is tracked. Assuming that the

bubbles in the film have a diameter in the range of 1 mm to 1 cm, there are two equations that describe the terminal rise velocity, u_∞, of the bubble.

For small bubbles, d O(1 mm), u_∞ is given by [13]

$$u_\infty = \frac{gd^2}{18\mu_1}(\rho_1 - \rho_2) \tag{9}$$

where ρ_1 and μ_1 are the density and dynamic viscosity, respectively, of the surrounding fluid, and ρ_2 is the density of fluid within the bubble. Plugging in the values for the surrounding fluid of water ($\rho_1 = 1000\ kg/m^3$, $\mu_1 = 10^{-5}\ Ns/m^2$) and the density of air ($\rho_2 = 1\ kg/m^3$) yields $u_\infty = 0.5\ m/s$.

For larger bubbles, d = O(1 cm), u_∞ is given by [2]

$$u_\infty = 0.707\sqrt{gd} \tag{10}$$

This equation yields $u_\infty = 0.2\ m/s$. Given a typical track length of 70 data points (or 0.07 s), the rise velocity would uncertainty in the y position is confined to the range of $1.4 - 3.5\ cm$.

A total of 100 bubbles were tracked in a single experiment ($\omega = 118\ rpm$, $h = 8\ cm$). The tracks are plotted on top of an image of the film in Figure 8 below.

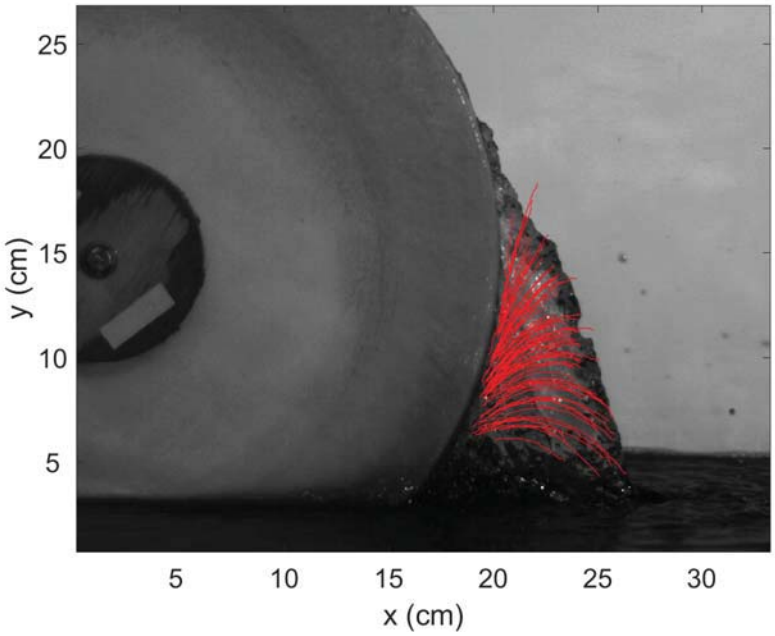

Figure 8: Bubble trajectories.

Each trajectory was fit to a linear curve in x and a quadratic curve in y, both as functions of time. The fitting parameters, assuming the forms of Equations 6 and 7, were used to find v_0 and θ_0. As a sanity check, the fitted acceleration term in y equation was compared to the expected value acceleration due to gravity, plotted against the track length, as shown in

Figure 9. The mean of the fitted acceleration terms is within 2% of the expected value. The data points also converge to the expected value as the tracks get sufficiently long, around 60 data points (0.06 s).

Now more confident in the procedure, the values of v_0 and θ_0 obtained from the fitted parameters were compared to the tangential velocity, v_w, and the local tangent, α, respectively. These parameters are labeled in the schematic in 10 below. The arclength, s set to 0 at the point where the disk meets the reservoir surface (x_0, y_0) and is defined positive upwards along the surface of the disk. The "max" arclength, S, is defined as the distance from $s = 0$ to the point directly horizontal from the center of the disk on the disk edge. S is given by the equation below.

$$S = R(\pi/2 - \alpha_0) \tag{11}$$

where α_0 is the local tangent at $s = 0$.

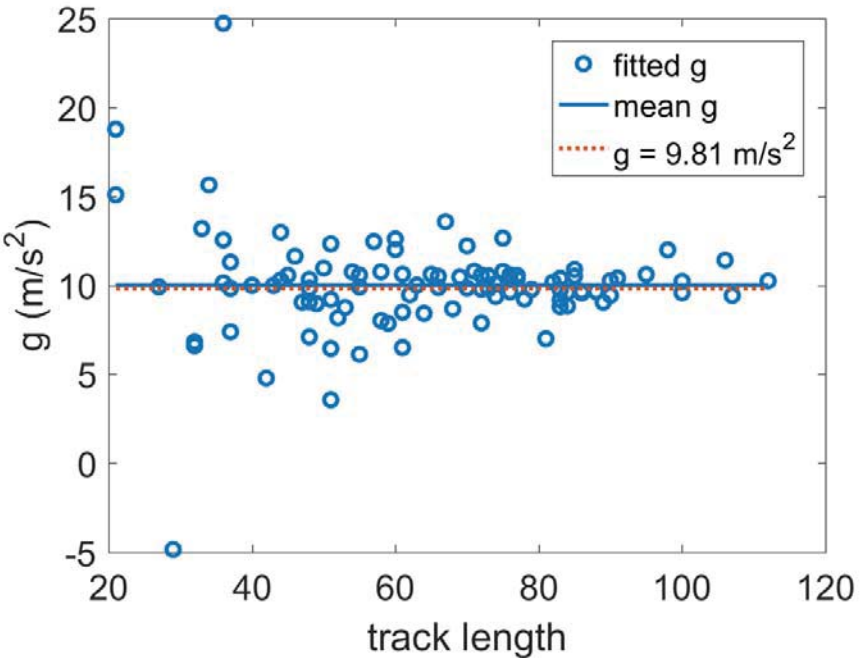

Figure 9: Fitted values of the acceleration due to gravity. The mean of these values is within 2% of the expected value, and the fits converge to the expected value as the track length increases sufficiently.

The results from the bubble PTV are shown in Figures 11 and 12. In Figure 11, the fitted velocity, v_0 is normalized by the tangential disk velocity, v_w, and plotted against the arclength, s which is normalized by the disk circumference, $2\pi R$. The fitted velocity is consistently less than the tangential velocity v_w, ranging from 20% of v_w near the reservoir surface to 60% of v_w further along the disk ($s/(2\pi R) \sim 0.06$). The change in initial velocity with arclength appears linear, albeit with some scatter. In Figure 12, the difference between α and θ_0 is plotted against the normalized arclength. These results are more am-

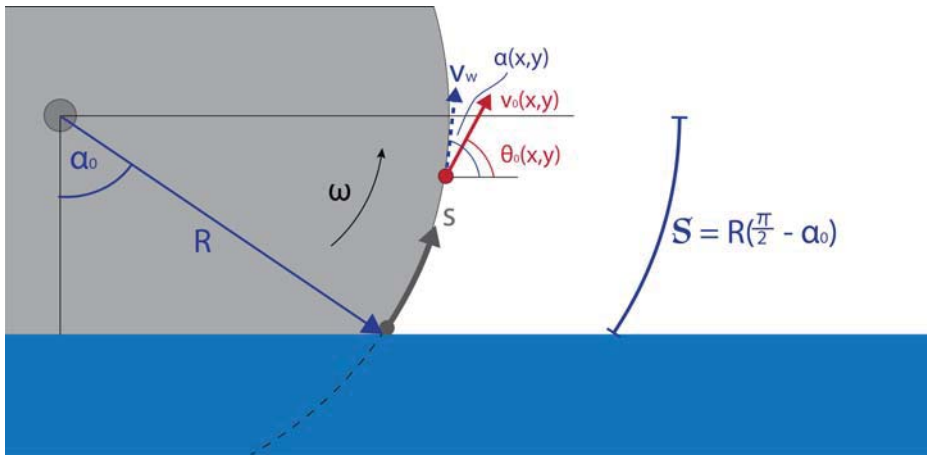

Figure 10: A schematic labelling the important measured and fitted parameters in the bubble tracking analysis.

biguous, but the difference between these two angles is greatest - with a large amount of scatter - near the reservoir and decreases as fluid is ejected further along the disk.

The bubble PTV results demonstrates that our assumptions of initial velocity and initial ejection angle matching that of the disk velocity and geometry is likely wrong. Improving the estimates for these values will result in improved estimates of the size and shape of the film.

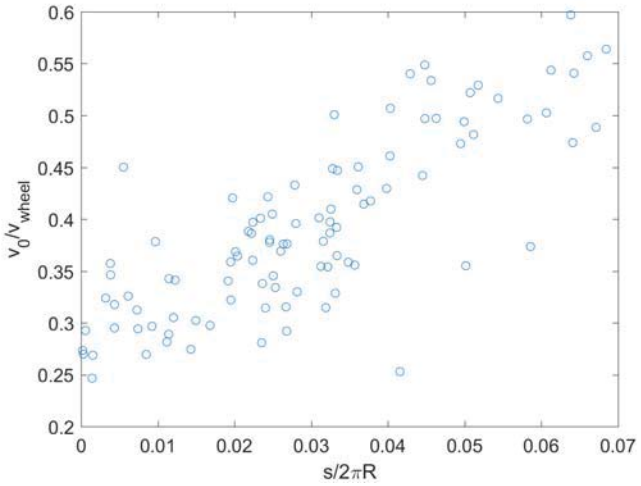

Figure 11: Fitted velocity, normalized by the tangential wheel velocity, plotted against the normalized arclength, where 0 is at the location where the disk meets the reservoir surface.

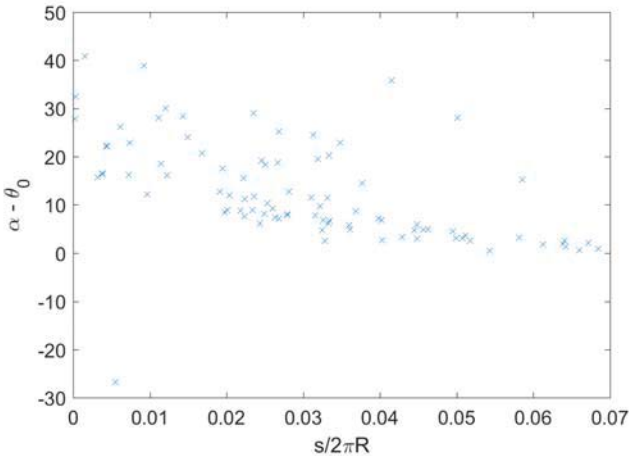

Figure 12: Fitted initial angle, with the local tangent, α, subtracted, plotted against the normalized arclength, where 0 is at the location where the disk meets the reservoir surface.

5 Discussion

5.1 Balance of Inertia and Gravity

The scaling analysis conducted in Section 3.1 indicated that the dominant balance of forces in this problem would be between inertia and gravity, and indeed, this is what Figure 6 seems to indicate. This figure hints at a transition region somewhere around $\omega^2 R/g = 7$. The figure also shows that the size of the film depends on the submergence depth, h.

In Section 3, it was reported that the film thins but grows outward as the submergence depth is lowered, while the film shrinks and thickens as the submergence depth is increased. These two behaviors occurring together, again, reinforces the idea of this balance of inertia and gravity which control the shape and extent of the film. I also suspect, but cannot confirm with the current experimental setup, that the mass of fluid in the sheet is also a function of the submergence depth, or, more precisely, proportional to the submerged arclength of the disk. This value, which we'll call s_s, can be found using the radius and the submergence depth of the disk, h, by the following formula.

$$s_s = 2R\cos^{-1}(1 - h/R) \tag{12}$$

The difference scaling for each experiment set, then, is due to the difference in mass. At low speeds, all three submergence depths show a similar size for the sheet width. The gravity force dominates and causes the film to be relatively small. As the disk speeds up, the set of experiments with the lowest submergence depth grows the film much faster, precisely because there is less mass to support in the film. Likewise, for the highest submergence depth, the film grows slowest because there is more mass to support in the film.

If we assume that the mass of fluid to support the film is purely a function of the submergence depth, what, then, does the transition region represent in each experimental set? For the middle and highest submergence depth, the slope of the line steepens, meaning that the film grows more quickly than before.

At lower speeds, the fluid could be torqued by the relatively nearby fluid on the other side of the film that is moving in the opposite direction, inhibiting the growth of the film and causing it to grow more slowly. Once the speed reaches a certain value, however, there is enough inertia to throw the fluid further out, causing greater separation between the oppositely signed fluid velocities in the film. This allows the film to grow more quickly. The lowest submergence depth shows the opposite trend, that of a shallower slope after the transition. This could be due to the fact that, at this low submergence depth, the film becomes so thin that it begins to break up substantially, and therefore simply cannot grow as quickly.

The bubble PTV results (see Section 4.2), conducted for a disk rotating at the relatively low speed of 115 *rpm* "delays" in the ejection angle of the disk at lower position on the disk, as well as significant reductions in speed. Both of these behaviors are consistent with a torque due to relatively nearby regions of fluid that flows against the disk direction. Together, these results also suggest that, while a good start, pure projectile motion is not the correct model. In order to investigate this question further, more detailed measurements of fluid velocities in the film would need to be made, perhaps using particle image velocimetry (PIV).

5.2 Conduit Formation and Maintenance

A feature that was briefly discussed in Section 4.1 is the conduit, the thicker fluid edge of the film. This conduit is present in all of the experiments conducted (even those in Section 6), and, moreover, is present throughout these experiments. How, then, is this conduit maintained in the steady state?

The bubble PTV results show that the trajectories correspond to those consistent with parabolic motion. Fluid that is released higher up on the disk has a steeper ejection angle, which causes the fluid to turn and fall back towards the reservoir without traveling as far in the x-direction as the fluid below. As the fluid falls, it collects fluid down below and coalesces, growing heavier. This fluid collects at the edge of the film, getting heavier and heavier. Subsequent fluid thrown off by the wheel encounters the film and does not have enough momentum to get past the slower moving fluid which is draining down the edge. The conduit is formed and maintained through this top-down process, where successive fluid "parabolas" collapse into each other.

We also found that the conduit was present at early times, when the disk was accelerating to the steady state speed from rest. The thick outer edge which is formed at early times is created by this acceleration profile, however, as faster moving fluid "catches up" to slower moving fluid ejected at a slightly earlier time step. This feature is then maintained in the steady state through the top-down procedure described above.

6 Yield Stress Fluid

Water is not the only fluid that wheels will encounter - mud, for example, is a very common fluid that bicycles and cars alike run into from time to time. Not only does mud have a different density and viscosity from water, but it is also a thixotropic, yield-stress fluid. Thixotropic fluids build up structure over time [1], and therefore exhibit hysteresis in response to stress, as shown in Figure 13(a) below. Yield stress fluids require a certain

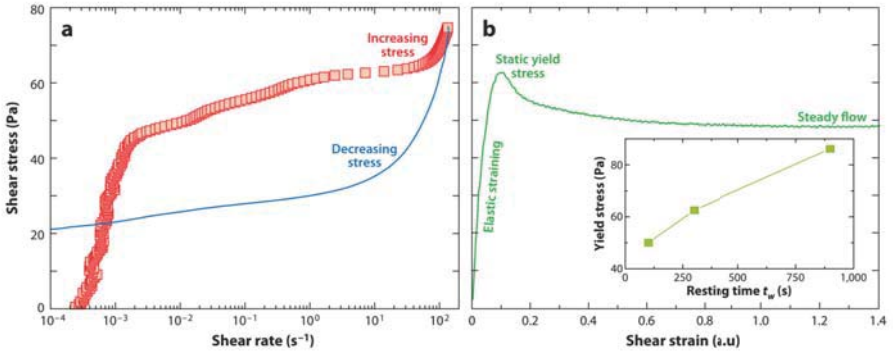

Figure 13: (a)A hysteretic loop with increasing and decreasing stress due to the thixotropic properties of a water-bentonite suspension. (b) The response to strain of a yield stress fluid. The subfigure shows yield stress increasing with resting time, another feature of thixotropic fluids. [1]

shear stress threshold to be reached before they will even begin to behave like fluids. Once the shear stress falls below the critical value, these fluids will simply stop flowing. This behavior is illustrated in Figure 13(b). The subfigure within Figure 13(b) shows the yield stress increasing as the resting time increases, another feature of thixotropic flows.

The data shown in this figure are for a water-bentonite dispersion. Bentonite is better known as drilling mud and is clay that has been weathered from volcanic ash. When suspended in water, creating a water-bentonite dispersion, it exhibits the properties illustrated in Figure 13. In the set of experiments performed here, we did not investigate the effect of thixotropy, only that of yield stress.

6.1 Slump Tests

We first had to determine the yield stress of the fluid. We mixed a water-bentonite dispersion that was 6% bentonite by volume. We then conducted a series of slump tests in order to determine the yield stress.

The procedure of a slump test is simple: fill a container of known volume with fluid, pour the fluid onto a surface, and allow the fluid to flow to rest. The fluid should expand radially as a gravity current. The shape of the resulting deposit gives a measure, then, of the yield stress. The deposit from the slump test conducted for the water-bentonite dispersion is shown in Figure 14. The top figure is a profile view, and the bottom figure is a plan view.

Using thin film asymptotics, an analytical expression can be derived to predict the final shape of the deposit. This expression is provided below.

$$h_s(r) = \sqrt{\frac{2\tau_y(R-r)}{\rho g}} \tag{13}$$

where h_s is the height of the deposit as a function of the radially direction, r, τ_y is the yield stress, R is the maximum measured radius of the deposit, and ρ and g are the density of the fluid and acceleration due to gravity, respectively.

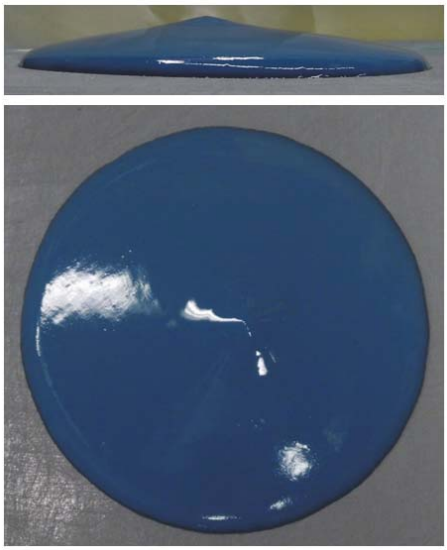

Figure 14: A profile (top) and plan (bottom) view of the slump test deposit of a 6%water-bentonite dispersion.

We used the profile shape obtained and the measured radius of the circle obtained in Figure 14 to fit a least-squares curve corresponding to Equation 13, as shown in Figure 15. The yield stress was the fitted parameter, given R, ρ, and g. We conducted three slump tests and found that the yield stress was approximately $19N/m^2$. This was similar to the value reported for a 6% water-bentonite dispersion using Wyoming bentonite [4].

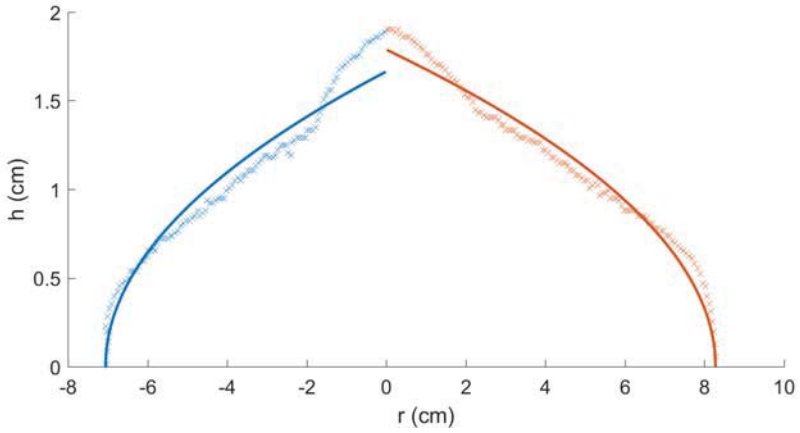

Figure 15: The measured profile of the fluid deposit from the slump test (symbols) and the fitted equation for the right and left sides. The fit resulted in a yield stress of approximately 19 n/m^2

6.2 Results

At low speeds, the two fluids - water and the yield stress fluid of water-bentonite dispersion - are quite similar. The films are both relatively thin with a thicker other edge. The film is somewhat unstable near the separation point of the wheel in both cases. An example of each fluid, rotating at similar speeds ($\sim 130\ rpm$), is shown in Figure 16, with water on the left and the water-bentonite dispersion on the right.

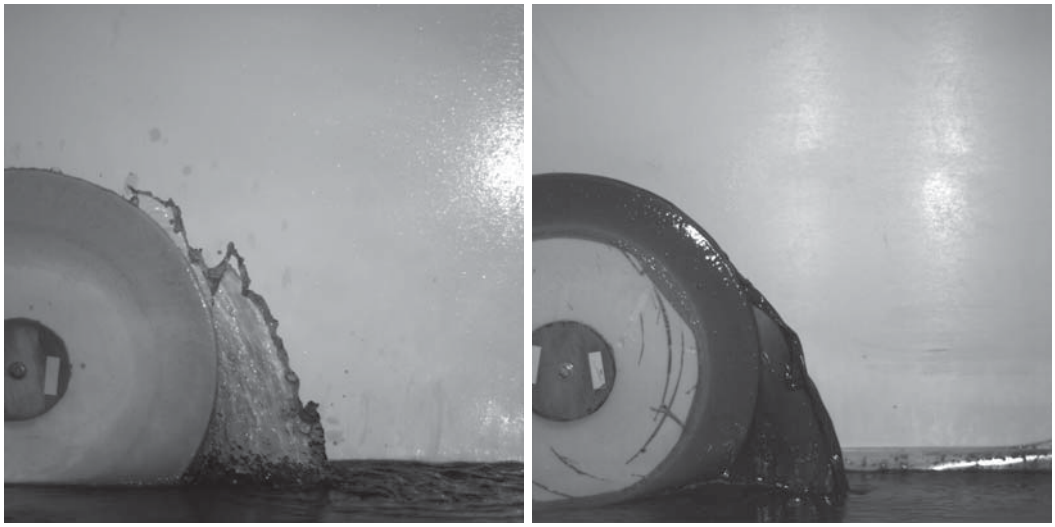

Figure 16: Snapshots of the fluid film created by water (left) and water-bentonite dispersion (right) at relatively low speeds ($\sim 130\ rpm$).

At higher speeds, there are marked differences between the two fluids. Both grow more unstable at high speeds, but the yield stress fluid breaks off from the disk at a smaller arclength location on the disk, where, rather than simply separating, the flow tears off at regular intervals. This is presumably due to the shear stress at that location on the disk falling below the required yield stress of the fluid. This results in a very dramatic shape at the top of the water-bentonite film. The thicker conduit is present in both fluids as well, but for the water-bentonite dispersion, as the fluid begins once again to fall below the yield stress as it slows down on the outside edge, regular tears occur near the bottom and at the edge of the film.

7 Conclusions and Future Work

A partially submerged, rotating disk creates a flow structure of a thin film, with a thick outer edge, of the disk as it emerges from the fluid reservoir. The shape and size of this film is primarily controlled by the forces of inertia and gravity, as well as the submergence depth of the disk. The primary model investigated in this report was that of projectile motion, where each fluid particle is ejected from the disk with an initial velocity and at an initial angle and follows a parabolic trajectory through space. Pure projectile motion, however, does not appear to be quite the right fit: both the conduit, which exerts a top-down control

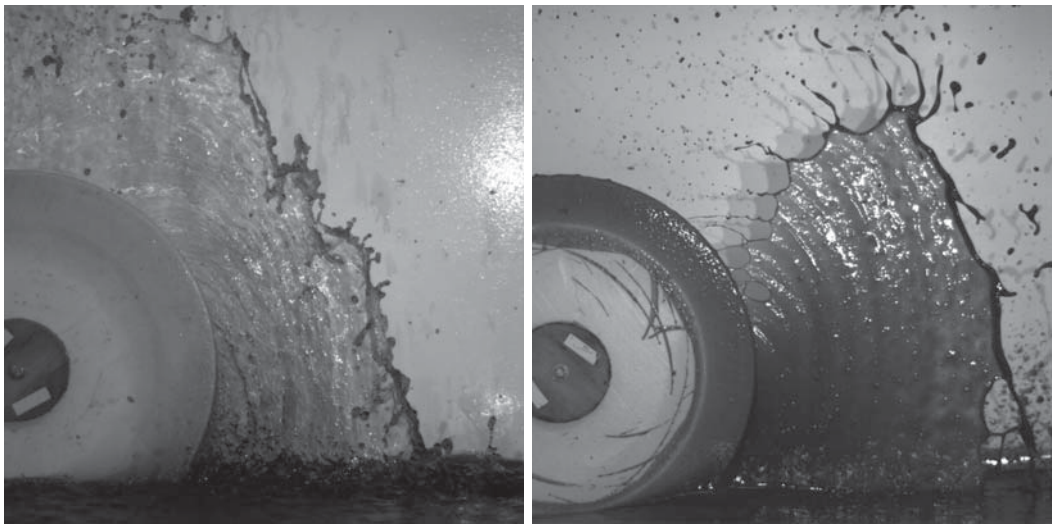

Figure 17: Snapshots of the fluid film created by water (left) and water-bentonite dispersion (right) at relatively high speeds ($\sim 200\ rpm$).

o n the size of the film, as well as interaction with nearby, slower moving particles reduce the extent of the film from that predicted with pure projectile motion.

There are several questions that were not answered in this project, as well as new questions that arose from the results herein. This is an exciting opportunity to do more work and to use new techniques. One obvious issue we did not address in this study is the effect of viscosity on the film shape and size. The study done with the yield stress fluid was preliminary, but showed interesting results that could be studied in greater depth with its own suite of experiments. In particular, the influence of thixotropy and increasing yield stress on the film size and shape could be studied in the future.

New experiments could be conducted to answer questions that arose during the course of these experiments. By backlighting the experiment and carefully calibrating the dye concentration to account for fluid mass, we could better understand how submergence depth affects that mass of fluid within the film. PIV experiments could be conducted to get detailed measurements of the fluid velocity within the film, and particularly near the disk. These measurements could give better estimates for the initial velocity and angle to use on the disk edge in order to use the parabolic equations to estimate the film extent. These estimates, coupled with a continuum model, could then be used to explore a more expansive parameter space and perhaps ask new questions.

8 Acknowledgements

I would like the thank all those who participated in the 2016 WHO GFD summer program - the directors, staff, principal lecturers, and administrators. In particular, I would like to thank Megan Davies-Wykes for proposing the least geophysical project of the summer, which I happily took up, and for the many hours she spent helping me with experiments, watching videos on repeat, scribbling in notebooks, muddling around with yield stress fluids,

and, inevitably, cleaning up a very large mess. I would also like to thank Shreyas Mandre, who also spent time with me scribbling in notebooks and thinking through the physical and modeling aspects of this project. I'd like to thank Claudia Cenedese for her help and her generosity, letting us make a total mess of her laboratory and providing any materials that we needed. Thanks also to Anders Jensen, who built the experiment (several times). Lastly, thanks to all the other fellows, without whom the summer would certainly not have been as fun.

References

[1] N. J. Balmforth, I. A. Frigaard, and G. Ovarlez, *Yielding to stress: Recent developments in viscoplastic fluid mechanics*, Annual Review of Fluid Mechanics, 46 (2014), pp. 121–146.

[2] R. Davies and G. Taylor, *The mechanics of large bubbles rising through liquids in tubes*, Proceedings of the Royal Society, 200 (1950), pp. 375–390.

[3] I. for Road Safety Research SWOV, *Splash and spray by lorries*, (1985).

[4] V. Kelessidis and R. Maglione, *Yield stress of water-bentonite dispersions*, Colloids and Surfaces A: Physiochemical Engineering Aspects, 318 (2008), pp. 217–226.

[5] T. J. Ko, S. H. Park, and H. S. Kim, *Experimental verification of the mist generation mechanism in turning*, International Journal of Machine Tools and Manufacture, 43 (2003), pp. 115–120.

[6] S. Matsumoto and Y. Takashima, *Film thickness of a bingham liquid on a rotating disk*, Industrial and Engineering Chemical Fundamentals, 221 (1982), pp. 198–202.

[7] H. Moffat, *Behaviour of a viscous film on the outer surface of a rotating cylinder*, Journal de Mecanique, 16 (1977).

[8] G. B. Pilkington II, *Splash and Spray*, American Society for Testing and Materials, Philadelphia, 1990, pp. 528–541.

[9] A. Presas, D. Valentin, E. Egusquiza, C. Valero, and U. Seidel, *Experimental analysis of the dynamic behavior of a rotating disk submerged in water*, IOP Conference Series: Earth and Environmental Science, 22 (2014).

[10] L. Preziosi and D. D. Joseph, *The run-off condition for coating and rimming flows*, Journal of Fluid Mechanics, 187 (1988), pp. 99–113.

[11] C. Radovich and D. Plocher, *Experiments on Spray from a Rolling Tire*, Springer Berlin Heidelberg, Berlin, Heidelberg, 2009, pp. 403–417.

[12] P. Rungruangvirojn and K. Kanitpong, *Measurement of visibility loss due to splash and spray: porous, sma, and conventional asphalt pavements*, International Journal of Pavement Engineering, 11 (2010), pp. 499–510.

[13] G. Stokes, *Mathematical and Physical Papers 1*, Cambridge University Press, London, 1880.

Simple Models of Sea Ice Distribution and Mixed-Layer Depths in Fram Strait

Sahil Agarwal

August 20, 2018

1 Introduction

Climate change is at the forefront of the issues being discussed in the world today [21, 7]. The warming of the global oceans as well as of the atmosphere has led to countless numbers of bird and animal species as well as humans to migrate to more favorable conditions. The most affected are the communities living at high latitudes. Whether or not there will be polar ice in the future has geo-political as well as socio-economic consequences.

Arctic sea ice has been a bellwether of climate change [13, 30, 25, 9]. The polar caps act as a storage radiator for the globe, by storing most of the incoming radiation as latent heat in ice. If not for the ice at the poles, the temperature fluctuations would be much larger around the globe. The ice-albedo feedback is another nonlinear mechanism that has been at the center of the ongoing climate change in the polar ice caps. Because ice gets darker as it thins, it absorbs more incoming radiation and in turn thins even more. This nonlinear feedback has been causing the so-called Arctic Amplification which is making the temperature in the Arctic rise twice as fast compared to the rest of the world [28, 29, 39].

Bering Strait, the Canadian Archipelago and Fram Strait are some of the gateways through which the Arctic Ocean interacts with the rest of the world oceans [18, 40, 16, 22]. While all these gateways are important, Fram Strait is the largest of them all [35, 36, 37]. The amount of fresh water exchange, deep water formation and biota cultivation are only some of the few things that influence global ocean circulations [3, 2, 1, 27, 10]. The sea-ice edge in the Fram Strait forms the northern boundary of the Atlantic Meridional Overturning Circulation (AMOC) [19, 14, 15, 23]. AMOC circulates the cold and fresh waters from the Arctic to the Antarctic and back, forming a circulation that regulates the global climate.

We study the interaction of southwards-flowing sea ice with the incoming warm and salty waters of the West Spitsbergen Current from the Northern Atlantic [38, 4] and the flow of sea ice and cold waters of the East Greenland Current. We start by

building a hierarchy of simple thermodynamic models of this interaction in §2. In §2.2 we build a model to examine the formation of a mixed layer through the interaction of ice and warm ocean current. Finally in §2.3 we discuss a fuller model that includes dynamics of the sea-ice distribution and mixed-layer properties in the presence of salt. In §3 we study the time-dependent dynamics of the sea-ice edge in the Fram Strait to look at what are the dominant processes that determine the location of sea-ice edge. We examine how the dominance of first-year ice in the Arctic has led to an asymmetry in the growth vs melt rates of ice by constructing simple column models in §4, and finally conclude in §5 with discussion and comparison with data from satellite observations regarding the variability in sea-ice extent with respect to the sea-ice velocity fields.

2 Model

Simple models are useful to understand the role of individual parameters and particular physical interactions in a highly complex coupled physical system. Norbert Untersteiner [35] studied the interaction of southwards-flowing ice with the northward-bound warm and salty waters of the West Spitsbergen Current. The interaction of these two currents gives rise to an ice wedge, which can be imagined as follows: A rectangular slab of ice starts to melt as it comes in contact with warm water underneath. This melt water in turn is fresh and cold and starts to cool the incoming warm water (see Fig. 1), giving rise to an ice wedge, which we refer to as the *Untersteiner Wedge*. In steady state, the heat energy required to melt the ice is comparable to the heat lost from the warm water current. Untersteiner computed several integral quantities over this wedge, such as the mixed-layer depth, temperature and salinity in steady state, without calculating the length of the wedge itself or its detrended profile. He mentions that, from observations, the ice melt is fully in progress 100km from the sea-ice edge in the Fram Strait, while at 200km there is no ice melt, and hence he takes an approximate length of the wedge as 150km.

Here, we study this phenomenon in more detail. We will look at the sea-ice-thickness distributions and mixed-layer properties along a whole longitude from a central basin in the Arctic to the sea-ice edge. Some of the key questions we ask are: (a)what are the various factors responsible for this ice-wedge formation; (b) can we determine the ice edge based on external parameters, to know the location of this wedge; (c) what is the typical length of the *Untersteiner Wedge* and what controls it; (d) how do these ice-ocean interactions impact the ice-extent dynamics in the Arctic?

Keeping this in mind, we start with a simple model of the ice wedge in absence of salt in the ocean and increase the modeled physics one step at a time.

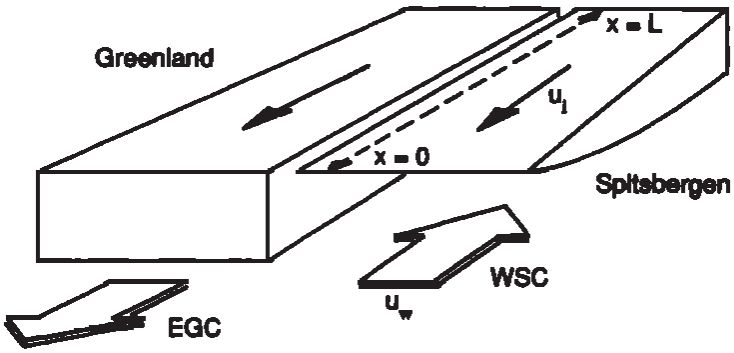

Figure 1: Schematic of an ice wedge from Fig. 3 of [35]. The warm and salty West Spitsbergen Current (WSC) flows northwards which melts the southwards flowing ice creating a wedge like shape, whereas the relatively cold and fresh East Greenland Current (EGC) flows southwards with the ice and therefore does not show this wedge.

2.1 Ice Wedge with No Salt

Consider a slab of ice moving southwards from the north pole with velocity U_i (see Fig. 2). There is an abyssal heat flux from the ocean underneath the ice F_b. The outgoing heat flux from ice to atmosphere is F_a, parameterized using Newton's law of Cooling as

$$F_a = \lambda_a(T_s - T_a). \tag{1}$$

Here, T_s is the surface temperature at the ice surface, T_a is the prescribed atmospheric temperature, which is a simple proxy to explore the role of a latitudinally varying heat flux, and λ_a is the heat-transfer coefficient assumed to be a constant. Taking the *Stefan Number* $= L/c_p\Delta T$ to be large, the temperature profile inside the ice can be approximated as linear. Ignoring, for the moment, the effect of salt in the ocean, the liquidus temperature for ice is maintained at $T_f = 0°C$. Assuming no phase change occurs at the ice surface, the heat flux through the ice will be equal to the outgoing atmospheric heat flux

$$F_a = \lambda_a(T_s - T_a) = k\frac{T_f - T_s}{h}. \tag{2}$$

which gives,

$$T_s = \frac{kT_f + \lambda_a h T_a}{k + \lambda_a h}. \tag{3}$$

where $k = 2.2Wm^{-1}K^{-1}$ is heat conductivity of ice, and h is the ice thickness.

The density of ice is assumed to be the same as the ocean ($\rho_{ice} = \rho_{ocean} = \rho = 1000kg/m^3$). The variation in ice thickness can then be written as the change in the incoming versus the outgoing heat flux, i.e.,

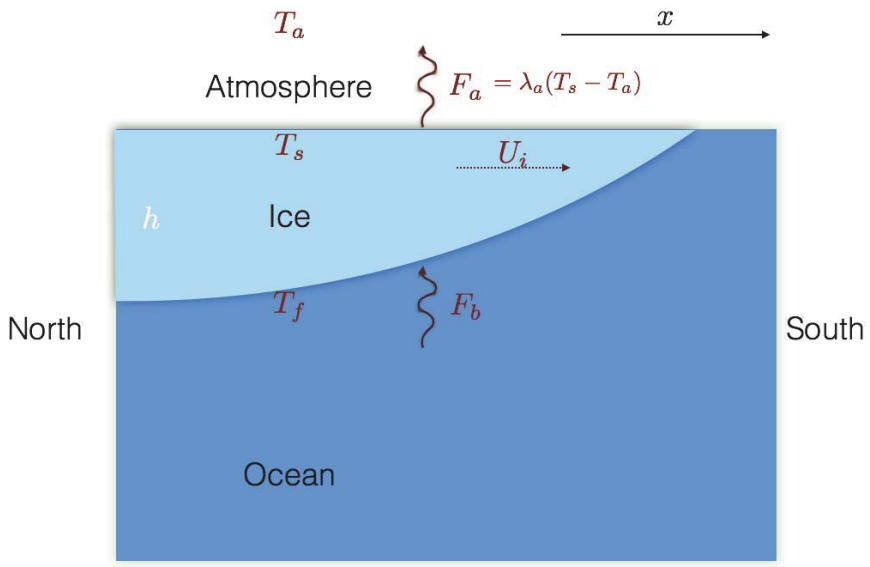

Figure 2: Schematic of the simple model with no mixed layer.

$$F_b - F_a = \frac{D^i}{Dt}\left[-\rho L h\right], \tag{4}$$

where $L = 334kJ/kg$ is the latent heat of fusion of ice, and $\frac{D^i}{Dt}$ is the material derivative with respect to the ice velocity U_i. This comes from conservation of energy, i.e. the change in the heat flux from bottom of ice to its top is the amount of latent heat released from the ice as its thickness h changes in time. In steady state, expanding the material derivative gives

$$F_b - F_a = -\rho L U_i \frac{\partial}{\partial x} h. \tag{5}$$

One can imagine the northern boundary of the system to lie in the central basin of the Arctic. Taking $\frac{\partial}{\partial x} h = 0$ at this northern boundary, we get $F_a = F_b$ which gives

$$h_0 = \frac{k}{\lambda_a}\left(\frac{\lambda_a(T_f - T_{a_o})}{F_b} - 1\right). \tag{6}$$

To examine this model, we prescribe the atmospheric temperature given by Eq. 7, shown in Fig. 3. The abyssal heat flux applied here is $F_b = 40Wm^{-2}$ and the heat-transfer coefficient between ice and atmosphere $\lambda_a = 43.5Wm^{-2}K^{-1}$.

Also, Eq. 6 with T_{a_o} replaced by T_a applies everywhere when there is no ice motion, i.e. $U_i = 0$. This implies that the sea-ice thickness only changes with the latitudinal variation in atmospheric forcing in the absence of ice motion. Fig. 4 shows a solution of Eq. 5 for different ice velocities. The profile with no ice motion is calculated using Eq. 6 over the whole domain, while for non-zero ice velocities Eq. 6

is only needed to determine the sea-ice thickness at the North boundary. The sea-ice profile with no ice velocity only depends on the atmospheric forcing, which is reflected in the linear behaviour near the ice edge. As the ice velocity increases, the ice edge moves further south which reflects the increased flux of sea ice from the north.

$$T_a = -40 \cos\left(\frac{\pi x}{2000}\right) \tag{7}$$

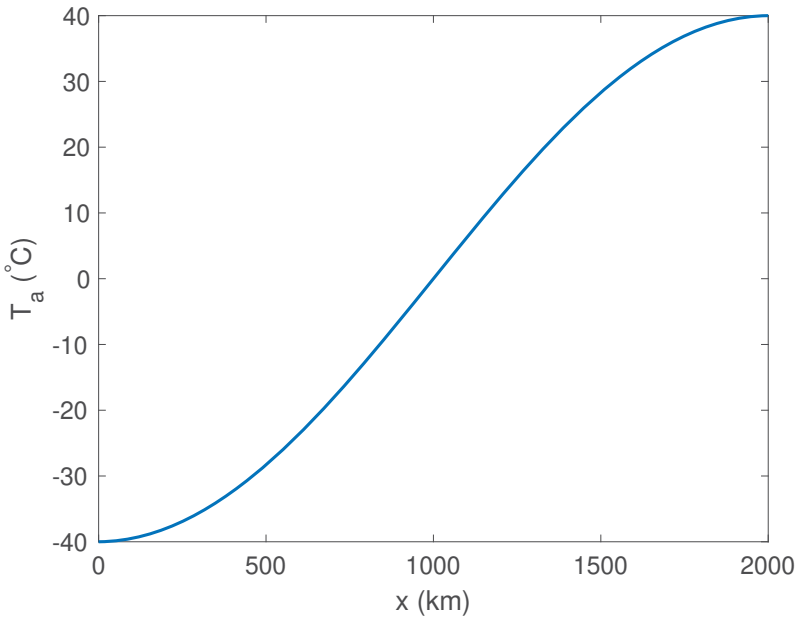

Figure 3: Prescribed atmospheric temperature $T_a(x)$.

Fig. 5 shows the atmospheric heat flux associated with the ice velocities shown in Fig. 4. The atmospheric heat flux F_a at the ice edge changes significantly as U_i and ice-extent vary because the atmospheric forcing varies with latitude. Far from the ice edge, F_a converges to F_b.

Fig. 4 shows that ice motion pushes the ice farther south as compared to when there is no ice motion. As U_i is increased, the ice extent increases.

A couple of questions comes to mind. How do the incoming warm and salty Atlantic waters through the West Spitsbergen Current affect the formation of a mixed layer beneath the ice? How does the mixed layer affect this sea-ice profile?

To understand how each added component affects the system, we first study the formation of mixed layer under *thermal only* forcing condition, while ignoring the effect of salt.

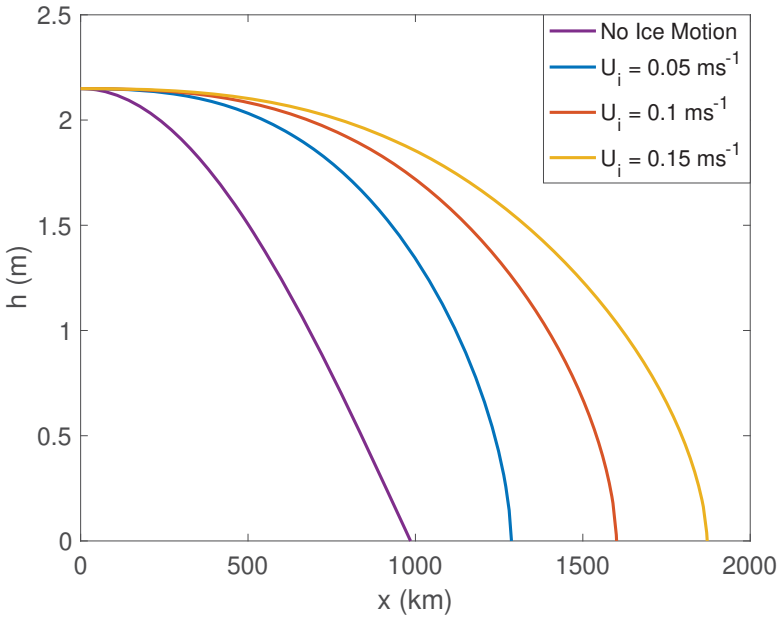

Figure 4: Sea-ice thickness $h(x)$ with no mixed layer underneath the ice for different ice velocities.

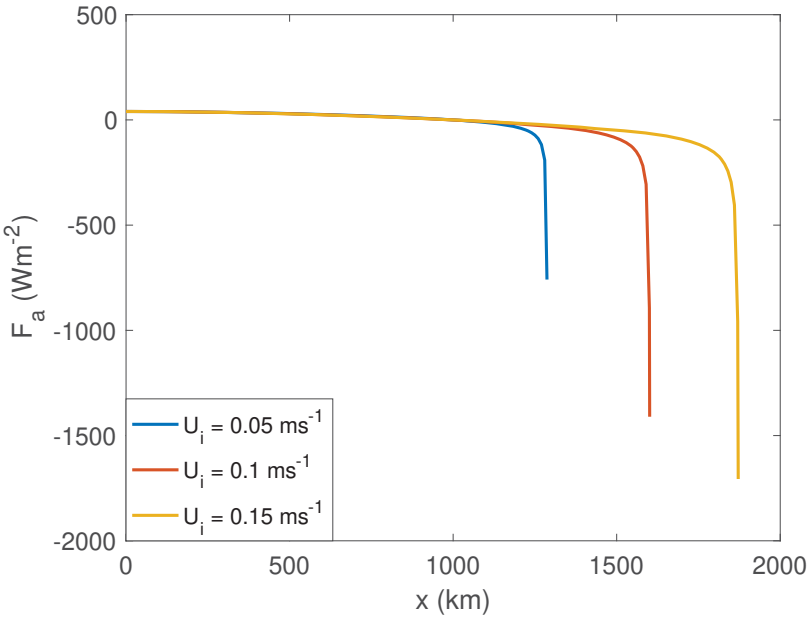

Figure 5: Atmospheric heat flux F_a associated with the ice velocities in Fig. 4.

2.2 Ice/Ocean Motion with Thermal Forcing

As in the previous section, consider ice moving southwards at a velocity U_i, but with *warm* ocean current with temperature T_w moving northwards with velocity U_w,

where we focus on how the thermal forcing influences the sea-ice profile and ignore the effect of salt. The abyssal heat flux is now to the mixed layer and there is an additional component of heat flux from the mixed layer to the ice F_{ml} (see Fig. 6), again parameterized through Newton's cooling law as

$$F_{ml} = \lambda_{ml}(T_{ml} - T_f). \tag{8}$$

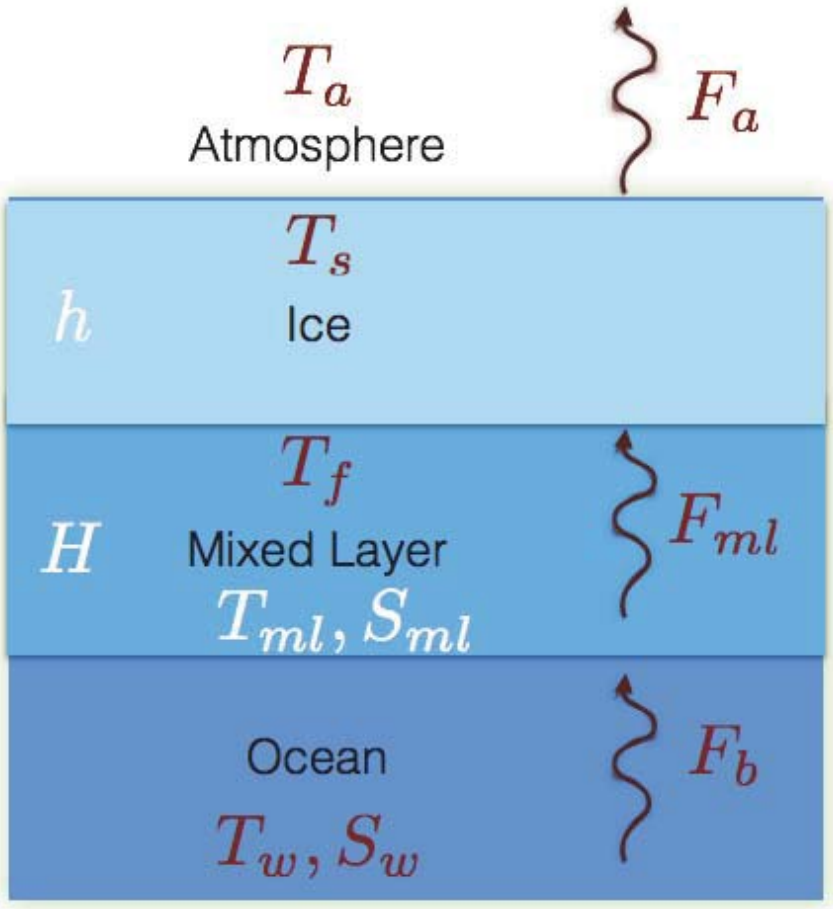

Figure 6: Schematic of the simple model with a mixed layer beneath the ice but no salt.

Here, T_{ml} is the temperature of the mixed layer, $\lambda_{ml} = \rho c_p St|\mathbf{U_i} - \mathbf{U_w}|$ is the heat transfer coefficient [26, 20], $c_p = 4186\ J/kg/^\circ C$ is the specific heat capacity of water,

$St = 1.7 \times 10^{-4}$ is the Stanton number. Using the enthalpy method, balancing the fluxes across the interfaces, and assuming large *Stefan number* for ice, we get

$$\begin{aligned} F_b - F_a &= -\rho L \frac{D^i}{Dt} h + \rho c_p \frac{D^w}{Dt} H (T_{ml} - T_w) \\ &= -\rho L \frac{D^i}{Dt} h + \rho c_p (T_{ml} - T_w) \frac{D^w}{Dt} H + \rho c_p H \frac{D^w}{Dt} T_{ml} \end{aligned} \tag{9}$$

for the total heat flux balance and

$$F_b - F_{ml} = \rho c_p \frac{D^w}{Dt} H (T_{ml} - T_w). \tag{10}$$

for the balance across the mixed layer. Here, $\frac{D^w}{Dt}$ is the material derivative with respect to the ocean velocity U_w.

In steady state, $\frac{\partial}{\partial t} h = \frac{\partial}{\partial t} H = \frac{\partial}{\partial t} T_{ml} = 0$. By ignoring the effects of salinity changes on the mixed layer and assuming that the mixed-layer depth only changes with change in salinity in the mixed layer, we get $\frac{\partial}{\partial t} H = 0$. This gives

$$F_b - F_a = -\rho L U_i \frac{\partial}{\partial x} h - \rho c_p H U_w \frac{\partial}{\partial x} T_{ml}$$

and

$$F_b - F_{ml} = -\rho c_p H U_w \frac{\partial}{\partial x} T_{ml}. \tag{11}$$

Now, as one goes from the north basin boundary towards the sea-ice edge, the ice thickness h goes to zero and the temperature in the mixed layer T_{ml} would go to the ocean temperature T_w, which gives us the following boundary conditions:

$$h \rightarrow 0 \qquad x \rightarrow x_e \tag{12}$$

$$T_{ml} \rightarrow T_w \qquad x \rightarrow x_e \tag{13}$$

where x_e is the sea-ice edge.

Substituting F_{ml} from Eq. 8 in Eq. 11 and solving for T_{ml}, we get

$$\begin{aligned} \frac{\partial T_{ml}}{T_{ml} - T_f - \frac{F_b}{\lambda_{ml}}} &= k_{ml} \partial x, \qquad k_{ml} = \frac{\lambda_{ml}}{\rho c_p U_w H} \\ \Rightarrow T_{ml}(x) &= T_f + \frac{F_b}{\lambda_{ml}} + \left(T_w - T_f - \frac{F_b}{\lambda_{ml}} \right) e^{-k_{ml}(x_e - x)}, \end{aligned} \tag{14}$$

$\Rightarrow$

$$\frac{\partial}{\partial x} T_{ml}(x) = k_{ml} \left(T_w - T_f - \frac{F_b}{\lambda_{ml}} \right) e^{-k_{ml}(x_e - x)} \tag{15}$$

Substituting this back in Eq. 11, we get

$$\rho L U_i \frac{\partial}{\partial x} h = -F_b + \lambda_a (T_s - T_a) - \lambda_{ml} \left(T_w - T_f - \frac{F_b}{\lambda_{ml}} \right) e^{-k_{ml}(x_e - x)} \tag{16}$$

This illustrates the secular variation of h with variation in atmospheric forcing T_a, modified by the forced heat transfer from the mixed layer decaying exponentially from the ice edge with decay length $k_{ml}^{-1} = (U_w H)/(St|\mathbf{U_i} - \mathbf{U_w}|)$. We plot a solution to Eq. 16 in Fig. 7, with $U_i = 0.1 - 0.2\ ms^{-1}$ and $U_w = 0.25\ ms^{-1}$. All other parameters are same as in the previous section.

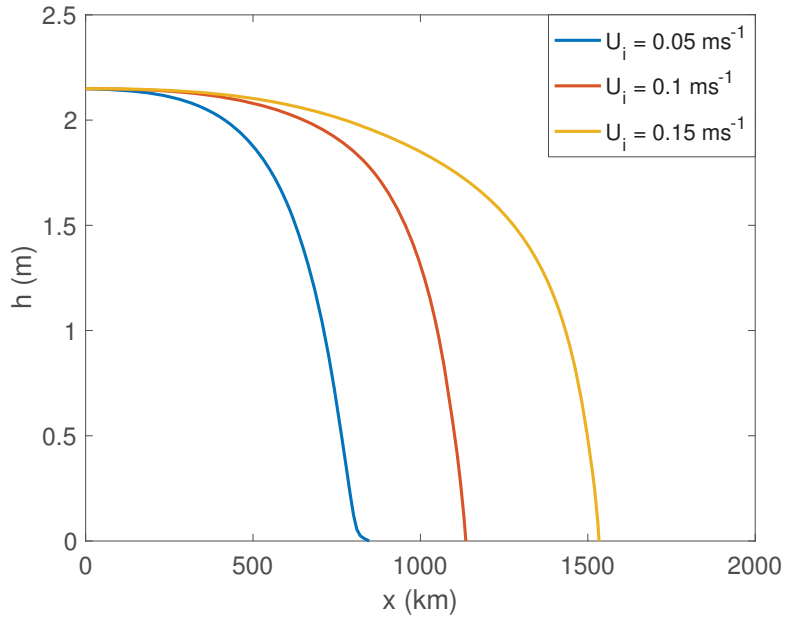

Figure 7: Sea-ice thickness $h(x)$ with both ice and water currents, with velocities $U_i = 0.1 - 0.15\ ms^{-1}$ and $U_w = 0.25\ ms^{-1}$.

A few points to observe are:

- As the mixed-layer depth H increases, the steady mixed-layer temperature T_{ml} also increases, i.e. the mixed layer becomes warmer which reduces the ice extent considerably as compared to when no mixed layer was present (compare Fig. 7 with Fig. 4 and see Fig. 8).

- A length scale for the wedge $1/k_{ml}$ can be seen in the equations and Fig. 9, which for the ice profiles in Fig. 7 varies from 122 - 92 kms as U_i changes from 0.05 - 0.15 m/s.

- Figs. 9 and 10 show the atmospheric flux F_a and the mixed-layer heat flux F_{ml} as a function of x. These values are of the same order of magnitude as of the observations and therefore reasonable given the simplicity of this model.

- Fig. 11 shows the variation in ice extent with the change in velocity of ice current. This has two competing effects: (a) an increase in U_i pushes more ice southward, and (b) increase in U_i increases the heat transfer co-efficient λ_{ml} which increases the heat being transferred from the mixed layer to sea ice and hence pushes the ice edge northwards. Both these effects can be seen in Fig. 11 where at low ice velocity, increase in heat transfer dominates while later the ice extent increases with U_i.

- Fig. 12 shows the variation in ice extent with change in ocean current velocity U_w. As U_w increases, the heat transfer coefficient increases. This increases the amount of heat transferred from the mixed layer to sea ice and hence the ice edge retreats with increase in U_w.

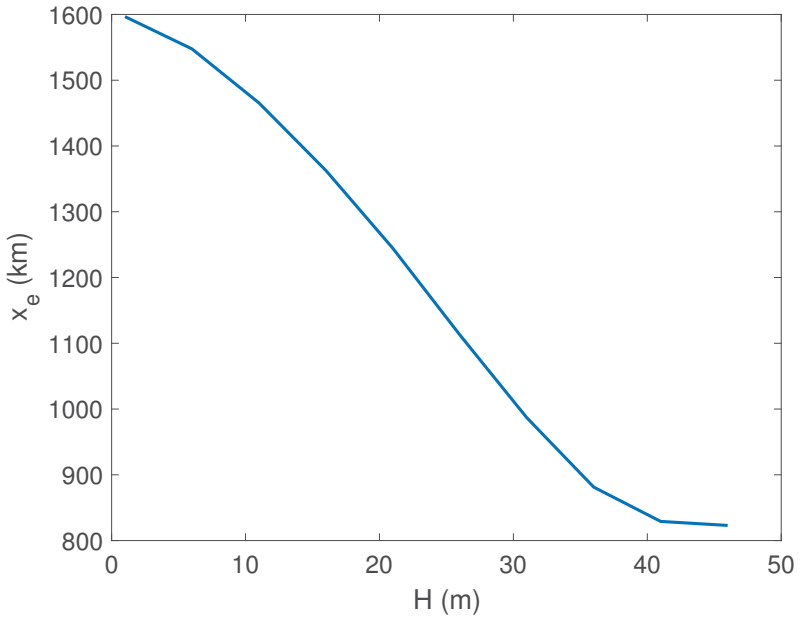

Figure 8: Variation in the location of the ice edge as mixed-layer depth H is varied ($U_i = 0.1\ ms^{-1}$, $U_w = 0.25\ ms^{-1}$).

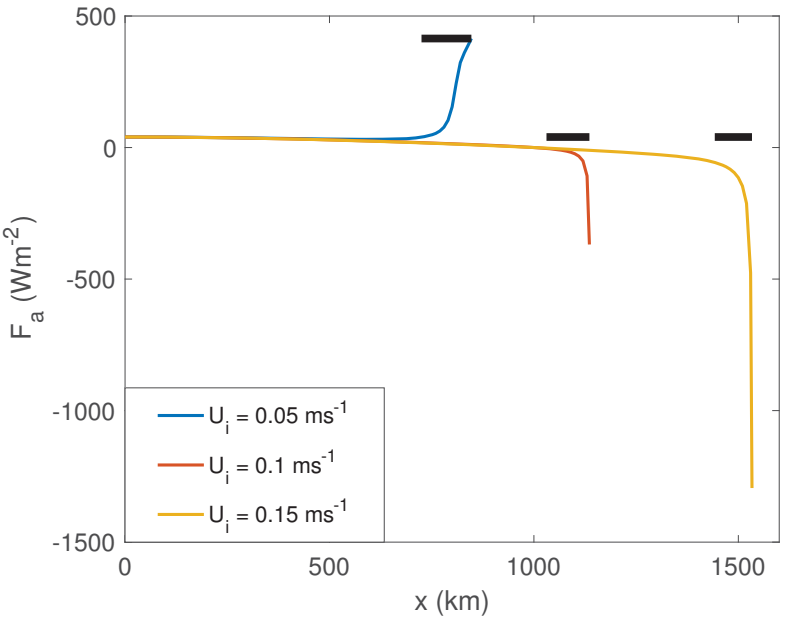

Figure 9: Outgoing atmospheric heat flux F_a with the thick black lines showing the length scale for the wedge k_{ml}, for the ice velocities in Fig. 7.

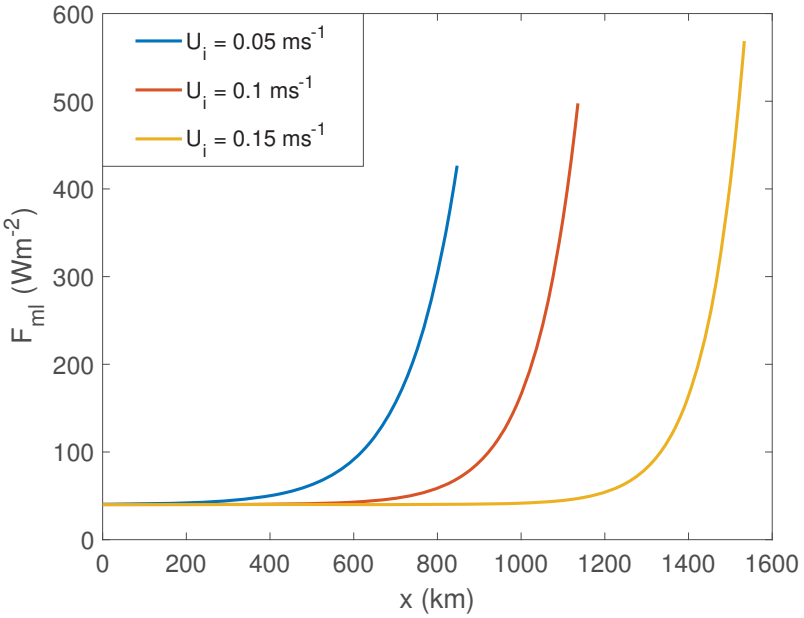

Figure 10: The under ice mixed-layer heat flux F_{ml} for ice velocities in Fig. 7.

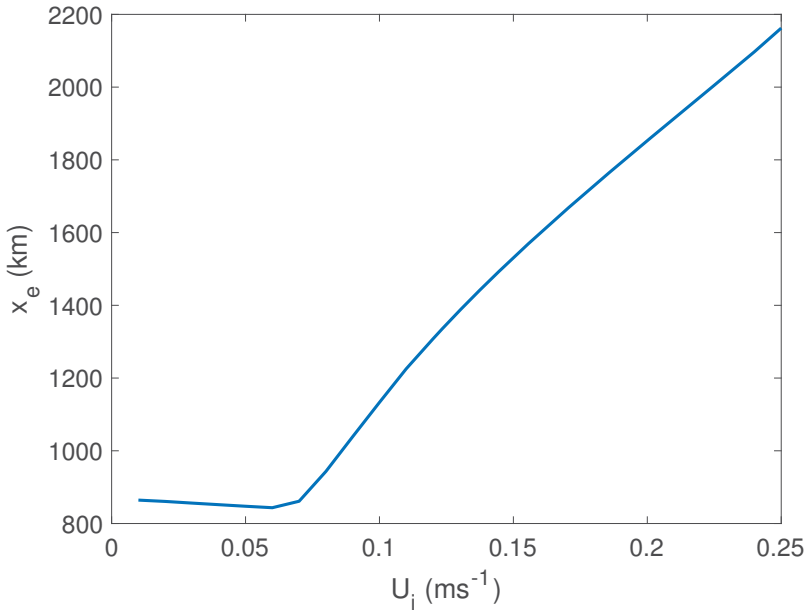

Figure 11: Variation in the location of the ice edge as ice velocity U_i is varied ($U_w = 0.25\ ms^{-1}$, $H = 25\ m$).

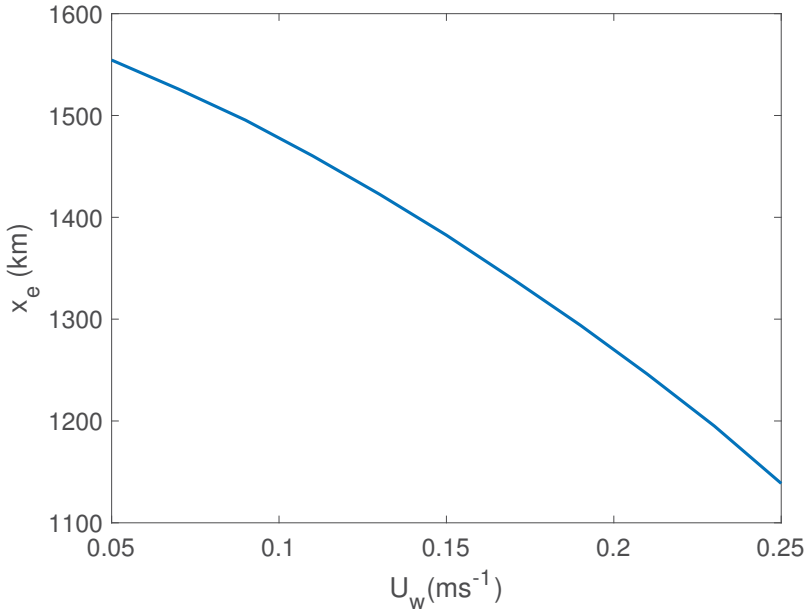

Figure 12: Variation in the location of the ice edge as the ocean current velocity U_w is varied ($U_i = 0.1\ ms^{-1}$, $H = 25\ m$).

2.3 Thermal Forcing with Salt Fluxes

We now take the next step to examine the influence of salt in the ocean to sea-ice and mixed-layer properties. Qualitatively, salt lowers the freezing point of water. It also affects the mixed-layer depth as the mixed layer comprises relatively fresh and cold waters in comparison to the warm and saline ocean below. As the ocean current interacts with ice, it starts to form a mixed layer by melting the ice, which produces a layer of relatively cold and fresh water (see Fig. 13).

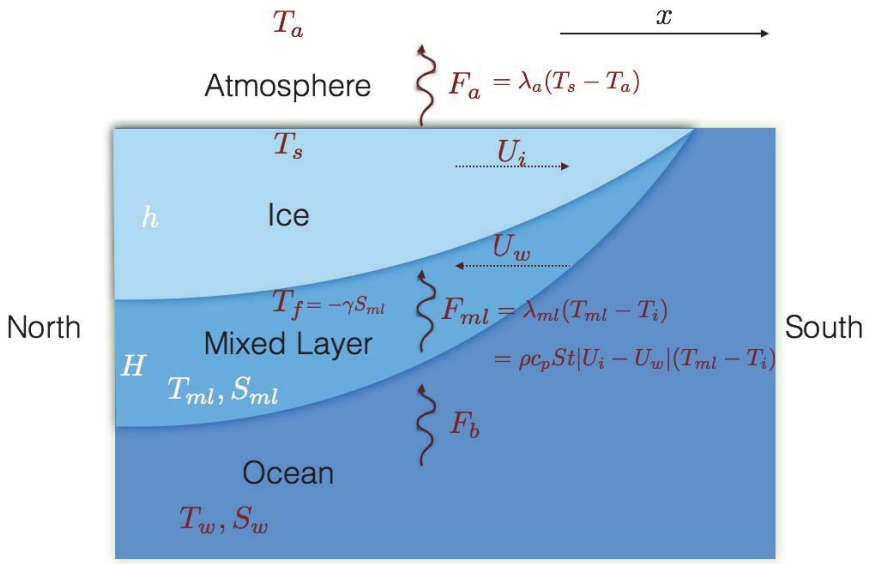

Figure 13: Schematic of the complete model.

The heat-flux balance across the interfaces of ice and mixed layer remain the same as in Eqs. 9 and 10. The fresh water from the ice melt is entrained by the mixed layer, thereby reducing the mixed-layer salinity. In other words, the salt content is conserved in the sea-ice – mixed-layer system. Writing this salt flux balance for the whole system gives

$$\frac{D^i}{Dt}(S_i - S_w)h + \frac{D^w}{Dt}H(S_{ml} - S_w) = 0. \tag{17}$$

Here, S_i is the salinity of ice. We take $S_i = 0$, i.e. consider that the ice is fresh.

The mixed layer is assumed to deepen until it attains neutral buoyancy with respect to the underlying ocean to get a continuous density profile. This gives a constant buoyancy b condition on the mixed layer, which with an assumption of linear equation of state gives

$$\begin{aligned} \frac{D^w}{Dt}b &= \frac{D^w}{Dt}\left[b_0 + (\alpha(T_{ml} - T_w) - \beta(S_{ml} - S_w)\right] = 0. \\ \Rightarrow \alpha\frac{D^w}{Dt}T_{ml} &= \beta\frac{D^w}{Dt}S_{ml}. \end{aligned} \tag{18}$$

In the presence of salt, the liquidus temperature T_f, which is decreased due to the presence of salt (colligative effects), can be approximated as

$$T_f = -\gamma S_{ml}, \qquad \gamma \approx 0.055^{\circ}C/p.s.u. \tag{19}$$

The system of Eqs. 9, 10, 17 and 18 forms the complete system to be solved to determine sea-ice thickness h, mixed-layer depth H, mixed-layer temperature T_{ml} and mixed-layer salinity S_{ml}. In steady state, this coupled system can be written as

$$\begin{aligned} F_b - F_a &= -\rho L U_i\frac{\partial}{\partial x}h - \rho c_p(T_{ml} - T_w)U_w\frac{\partial}{\partial x}H - \rho c_p H U_w\frac{\partial}{\partial x}T_{ml} \\ F_b - F_{ml} &= -\rho c_p(T_{ml} - T_w)U_w\frac{\partial}{\partial x}H - \rho c_p H U_w\frac{\partial}{\partial x}T_{ml} \\ -U_i S_w\frac{\partial}{\partial x}h &= U_w(S_{ml} - S_w)\frac{\partial}{\partial x}H + U_w H\frac{\partial}{\partial x}(S_{ml} - S_w) \\ \alpha\frac{\partial}{\partial x}T_{ml} &= \beta\frac{\partial}{\partial x}S_{ml} \end{aligned} \tag{20}$$

which gives,

$$\begin{aligned} H(B-1)\frac{\partial}{\partial x}T_{ml} &= \frac{\beta S_w(F_a - F_{ml})[\mathcal{F} - B]}{\alpha L\rho U_w} \\ (S_w - S_{ml})(B-1)\frac{\partial}{\partial x}H &= \frac{S_w(F_a - F_{ml})[\mathcal{F} - 1]}{L\rho U_w} \\ \frac{\partial}{\partial x}h &= \frac{F_a - F_{ml}}{L\rho U_i} \\ H(B-1)\frac{\partial}{\partial x}S_{ml} &= \frac{S_w(F_a - F_{ml})[\mathcal{F} - B]}{L\rho U_w} \end{aligned} \tag{21}$$

where, $B = \alpha(T_w - T_{ml})/\beta(S_w - S_{ml})$, and $\mathcal{F} = \alpha L(F_b - F_{ml})/\beta c_p S_w(F_a - F_{ml})$. From Eq. 20 and using *L'Hôpital*'s rule

$$\begin{aligned} \lim_{x\to x_e} B &= \lim_{T_{ml}\to T_w, S_{ml}\to S_w} B \\ &= \lim_{T_{ml}\to T_w, S_{ml}\to S_w} \frac{\alpha(T_w - T_{ml})}{\beta(S_w - S_{ml})} \\ &= \lim_{T_{ml}\to T_w, S_{ml}\to S_w} \frac{\alpha\frac{\partial}{\partial x}T_{ml}}{\beta\frac{\partial}{\partial x}S_{ml}} \\ &= 1 \end{aligned} \tag{22}$$

Now, let $B = f(x)$

$$\begin{aligned}
\Rightarrow -\alpha\frac{\partial}{\partial x}T_{ml} &= -f(x)\alpha\frac{\partial}{\partial x}S_{ml} + f'(x)\beta(S_w - S_{ml}) \\
\Rightarrow -\beta\frac{\partial}{\partial x}S_{ml} &= -f(x)\alpha\frac{\partial}{\partial x}S_{ml} + f'(x)\beta(S_w - S_{ml}) \\
\Rightarrow (f(x)-1)\frac{\partial}{\partial x}S_{ml} &= f'(x)(S_w - S_{ml}) \qquad (23)
\end{aligned}$$

Therefore, S_{ml} has a singularity at the ice edge unless $f(x) \equiv 1$ and $f'(x) \equiv 0$. Therefore,

$$B \equiv 1. \qquad (24)$$

We can estimate the behavior of Eqns. 21 near the ice edge as $H \to 0$ and determine that

$$\begin{aligned}
\lim_{x\to x_e} \alpha L(F_b - F_{ml}) - \beta B c_p S_w(F_a - F_{ml}) = 0 \\
\Rightarrow \lim_{x\to x_e} \mathcal{F} = \lim_{x\to x_e} B = 1. \qquad (25)
\end{aligned}$$

At the ice edge, the system has a singular behavior since $H \to 0$. To overcome this singularity, we rearrange this system to solve for ice thickness h and mixed-layer heat content $H(T_w - T_{ml})$. The coupled system of Equations 21 can be written as:

$$\begin{aligned}
\frac{\partial}{\partial x}H(T_w - T_{ml}) &= \frac{\beta S_w(F_a - F_{ml})}{\alpha L\rho U_w} \\
\frac{\partial}{\partial x}h &= \frac{F_a - F_{ml}}{L\rho U_i} \\
\mathcal{F} = \frac{\alpha L(F_b - F_{ml})}{\beta c_p S_w(F_a - F_{ml})} &= 1 \\
\frac{\alpha(T_w - T_{ml})}{\beta(S_w - S_{ml})} &= 1 \qquad (26)
\end{aligned}$$

Using the conditions that $\mathcal{F} = 1$ and $B = 1$ over the domain, we can obtain T_{ml}, substitute it back in the solution for the first equation above and obtain the mixed-layer depth H. Thus we find

$$\begin{aligned}
\mathcal{F} &= 1 \\
\Rightarrow \frac{K(F_b - F_{ml})}{(F_a - F_{ml})} &= 1, \qquad K = \frac{\alpha L}{\beta c_p S_w} \\
\Rightarrow F_{ml} &= \frac{KF_b - F_a}{K-1} \\
\Rightarrow T_{ml} &= \frac{KF_b - F_a}{\lambda_{ml}(K-1)} - \gamma S_{ml}. \qquad (27)
\end{aligned}$$

Similarly,

$$\begin{aligned} B &= 1 \\ \Rightarrow \frac{\alpha(T_w - T_{ml})}{\beta(S_w - S_{ml})} &= 1 \\ \Rightarrow S_{ml} &= S_w - \frac{\alpha}{\beta}(T_w - T_{ml}) \end{aligned} \tag{28}$$

The mixed-layer temperature T_{ml} can be obtained by substituting Eq. 28 back in Eq. 27.

2.3.1 Analytic Solution for Location of Ice Edge

One of the most important discussions in the recent decade has been the retreat of summertime sea ice. Knowing the location of the ice edge is therefore an important step in determining how the external parameters influence the basin-wide sea-ice properties.

From Eq. 26, using $\mathcal{F}_{edge} = 1$ we can obtain the location of the steady-state ice edge x_e.

$$\begin{aligned} \mathcal{F}_{edge} &= 1 \\ \Rightarrow F_{a_{edge}}(x) &= \frac{\alpha L}{\beta c_p S_w}(F_b - F_{ml_{edge}}) - F_{ml_{edge}} \end{aligned} \tag{29}$$

Also, because we know the boundary condition at the ice edge, we can substitute those back in Eq. 29.

$$\begin{aligned} F_{a_{edge}}(x) &= -\lambda_a(\gamma S_w + T_a(x)) \\ F_{ml_{edge}} &= \lambda_{ml}(T_w + \gamma S_w) \end{aligned} \tag{30}$$

Substituting these back in the Eq. 29, we solve for $T_{a_{edge}}$ at the ice edge. Because $T_a(x)$ is prescribed, the location of the ice edge x_e is the root of the equation

$$T_a(x) - T_{a_{edge}} = 0. \tag{31}$$

2.3.2 Basin Properties

In many cases, one is interested in how the central Arctic basin sea-ice properties are affected by what goes on at the ice edge. One way is to integrate the coupled system of equations and get that information, but that can be a tedious task. From the system of Eq. 26, we can get the basin properties analytically without integrating the complete system as follows.

Using $F_b = F_{ml}$ in the steady basin and from Eq. 26, we get

$$S_{ml} = S_w - \frac{\alpha}{\beta}(T_w - T_{ml}) \qquad \text{and} \tag{32}$$

$$\begin{aligned} F_b &= F_{ml} \\ &= \lambda_{ml}(T_{ml} + \gamma S_{ml}). \end{aligned} \tag{33}$$

Substituting S_{ml} in Eq. 33 we get

$$T_{ml_{Basin}} = \frac{F_b - \gamma\lambda_{ml}\left(S_w - \frac{\alpha}{\beta}T_w\right)}{\lambda_{ml}\left(1 + \gamma\frac{\alpha}{\beta}\right)} \tag{34}$$

Substitution of $T_{ml_{Basin}}$ from Eq. 34 in Eq. 32 gives us $S_{ml_{Basin}}$.
From the linear temperature profile in ice, we have

$$T_s = \frac{-k\gamma S_{ml} + \lambda_a h T_a}{k + \lambda_a h} \tag{35}$$

Using $F_b = F_a$ in the basin, we get

$$T_s = \frac{F_b}{\lambda_a} + T_a \tag{36}$$

Equating Eqs. 35 and 36, we get the sea-ice thickness at the basin.

$$h_{Basin} = \frac{-k\left(\gamma S_{ml} + T_a(0) + \frac{F_b}{\lambda_a}\right)}{F_b} \tag{37}$$

2.3.3 Untersteiner's Sea-ice Wedge

As explained in §2, one can imagine a rectangular block of sea ice moving southwards. As it starts to interact with northward bound warm and salty ocean current, it starts to melt [35]. In steady state, this would take a wedge like shape, with the heat required to melt the ice being comparable to heat released from cooling of the incoming warm waters. A length scale can be ascribed to this wedge related to this transfer of heat. The maximum amount of heat being advected with respect to ice is

$$F_{Advect} = \rho c_p |U_w| H_o (T_{ml} - T_f) \tag{38}$$

where H_o is the mixed layer depth at the basin, calculated numerically.

The amount of heat transferred from the mixed layer to ice that results in the melting of ice is

$$F_{Transfer} = \rho c_p St |U_i - U_w| \eta (T_{ml} - T_f). \tag{39}$$

Here, η is the length of the wedge over which $F_{Advect} = F_{Transfer}$. Equating Eqs. 38 and 39, we get

$$\eta = \frac{|U_w| H_o}{|U_i - U_w| St}. \tag{40}$$

We show this wedge length scale in the solutions plotted in the next section.

2.3.4 Results

Solutions to Eq. 26 are plotted below for various velocity pairs. A few important things to note are as follows:

- The *Untersteiner Wedge* is more apparent in the mixed-layer properties than in the sea-ice profile itself. This wedge forms a boundary layer between the incoming ocean current and the mixed layer generated by the melting of ice.

- The wedge length scale in [35] was approximated as 150 km, by arguing that ice melt is fully apparent at 100 km from the ice edge, whereas at 200 km there is no ice melt, and hence the ice wedge must be approximately 150 km. Using similar velocity profiles and external parameters we calculate this wedge to have a length of approximately105 km (see Fig. 14, $U_i = 10^{-1} m/s, U_w = 2.5 \times 10^{-1} m/s$).

- The mixed-layer temperature T_{ml} in [35] at the end of the wedge was calculated as $-1.74°C$. Given approximately the same parameters, we calculate T_{ml} in this model as $-1.559°C$. The average heat flux from the mixed layer to ice F_{ml} was approximated as 300 Wm^{-2} in [35], while we calculate this quantity as ~ 400 Wm^{-2} (see Fig. 14).

- As the ice velocity is decreased, keeping the ocean current velocity fixed, the ice wedge becomes sharper (see Fig. 15, $U_i = 10^{-3} m/s, U_w = 2.5 \times 10^{-1} m/s$).

- As the ocean velocity is decreased, keeping the ice velocity constant, the wedge becomes long. Since the heat transfer coefficient is decreased, the ice edge moves further south, hence elongating the wedge (see Fig. 16, $U_i = 10^{-1} m/s, U_w = 2.5 \times 10^{-3} m/s$).

- As both ice and ocean currents are slowed down, the ice wedge becomes extremely narrow, behaving more as the rectangular ice slab which flowed south (see Fig. 17, $U_i = 10^{-5} m/s, U_w = 2.5 \times 10^{-2} m/s$).

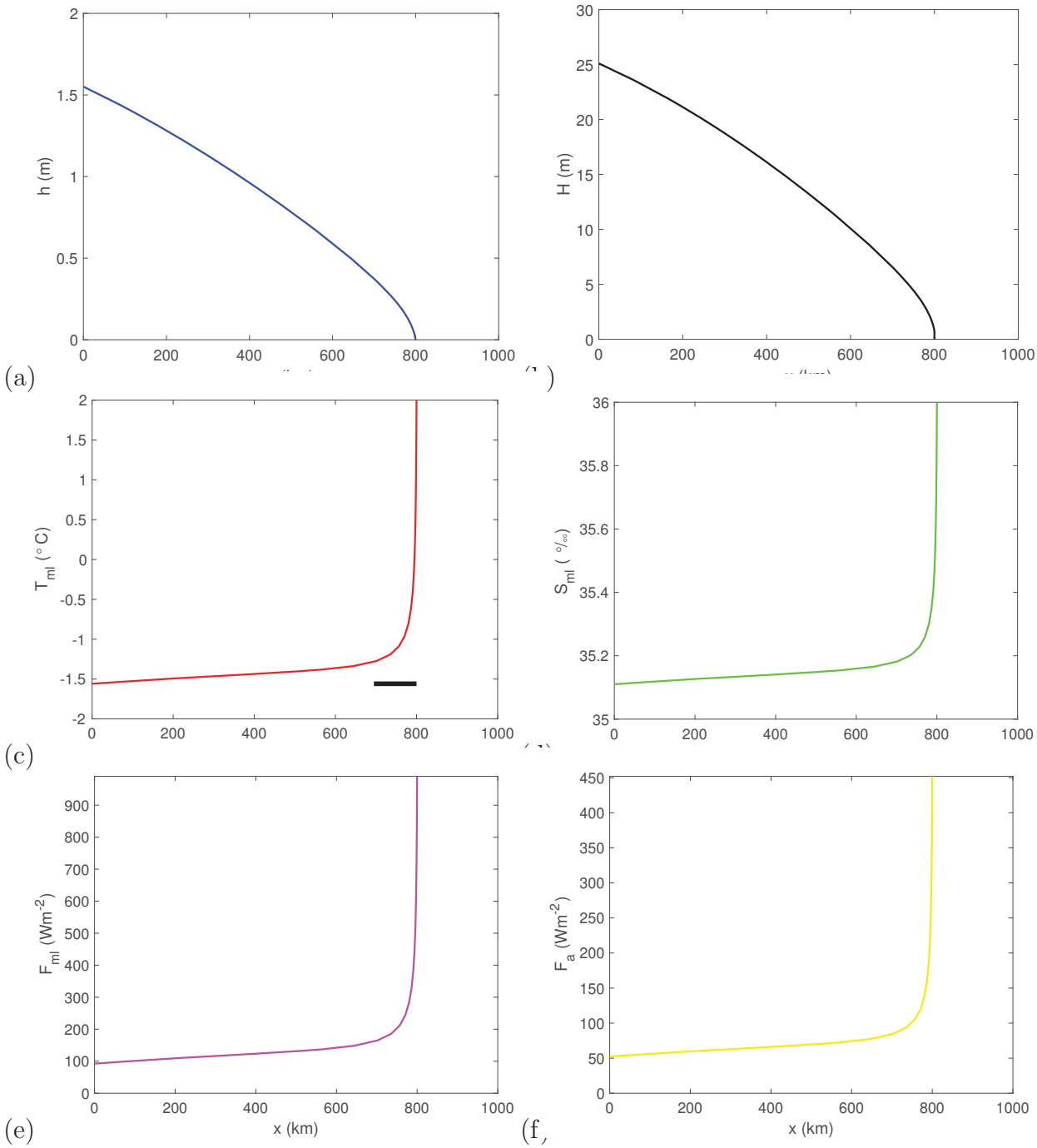

Figure 14: With ice velocity $10^{-1}m/s$ and ocean velocity $2.5 \times 10^{-1}m/s$.(a)Ice thickness, h;(b)mixed-layer (ML) depth, H;(c)ML Temp., T_{ml}, Thick black line is the *Untersteiner's Wedge*, $\eta = 105.5km$;(d)ML Salinity., S_{ml}; (e)mixed-layer heat flux F_{ml}; (f) Atmospheric heat flux F_a

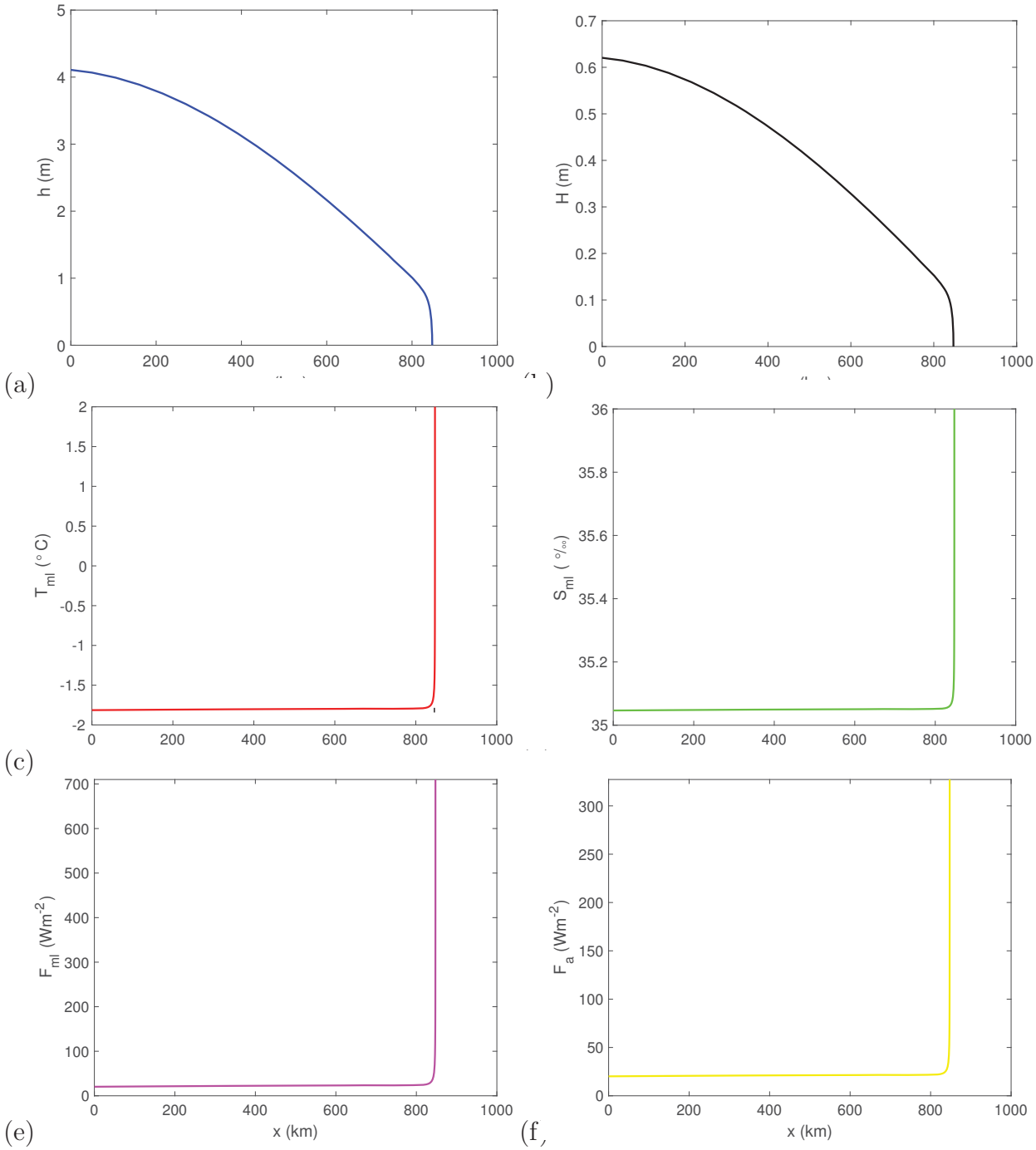

Figure 15: With ice velocity $10^{-3}m/s$ and ocean velocity $2.5 \times 10^{-1}m/s$.(a)Ice thickness, h;(b)mixed-layer (ML) depth, H;(c)ML Temp., T_{ml}, Thick black line is the *Untersteiner's Wedge*, $\eta = 3.6km$;(d)ML Salinity., S_{ml}; (e)mixed-layer heat flux F_{ml}; (f) Atmospheric heat flux F_a

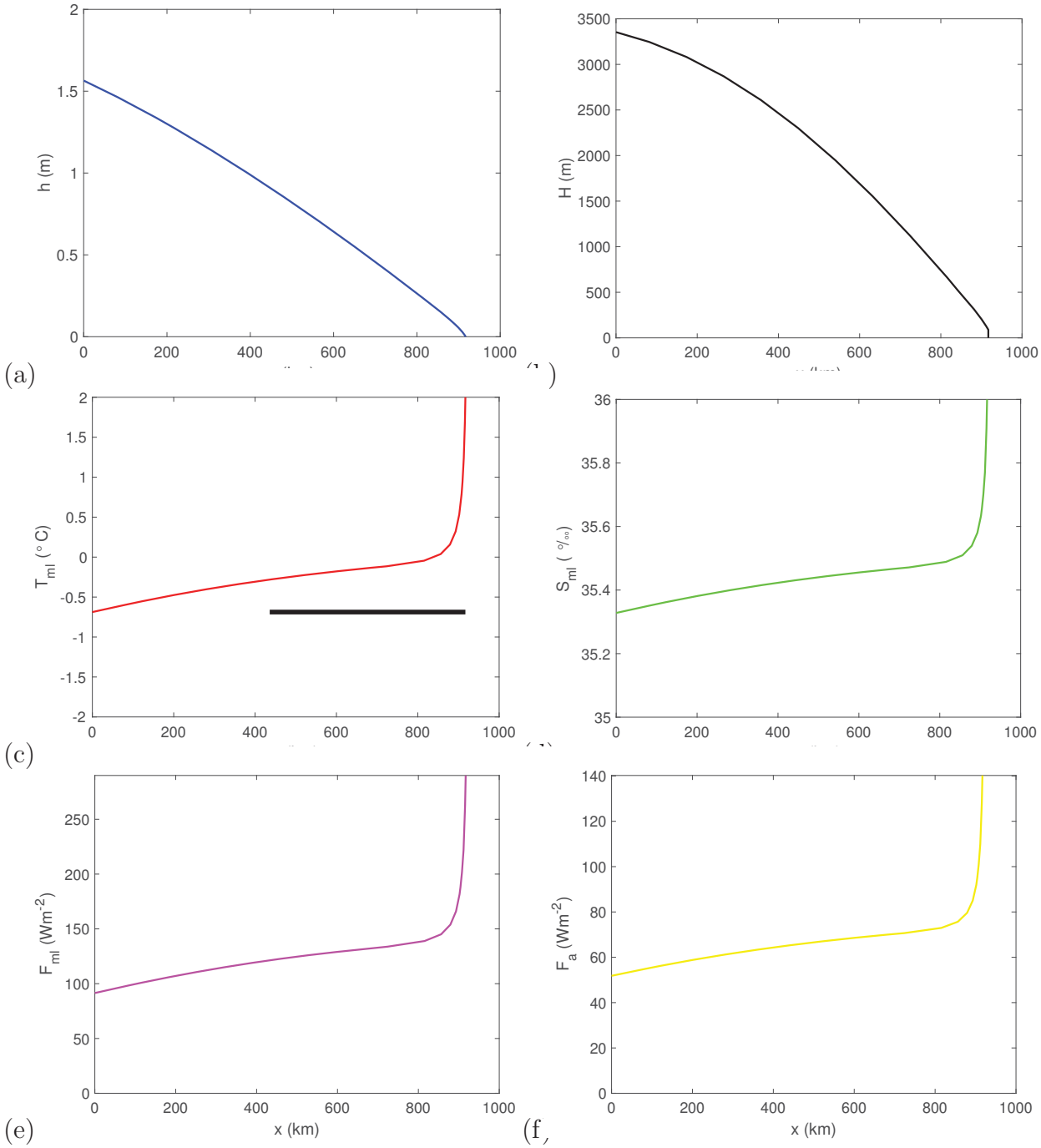

Figure 16: With ice velocity $10^{-1}m/s$ and ocean velocity $2.5 \times 10^{-3}m/s$.(a)Ice thickness, h;(b)mixed-layer (ML) depth, H;(c)ML Temp., T_{ml}, Thick black line is the *Untersteiner's Wedge*, $\eta = 481.2km$;(d)ML Salinity., S_{ml}; (e)mixed-layer heat flux F_{ml}; (f) Atmospheric heat flux F_a

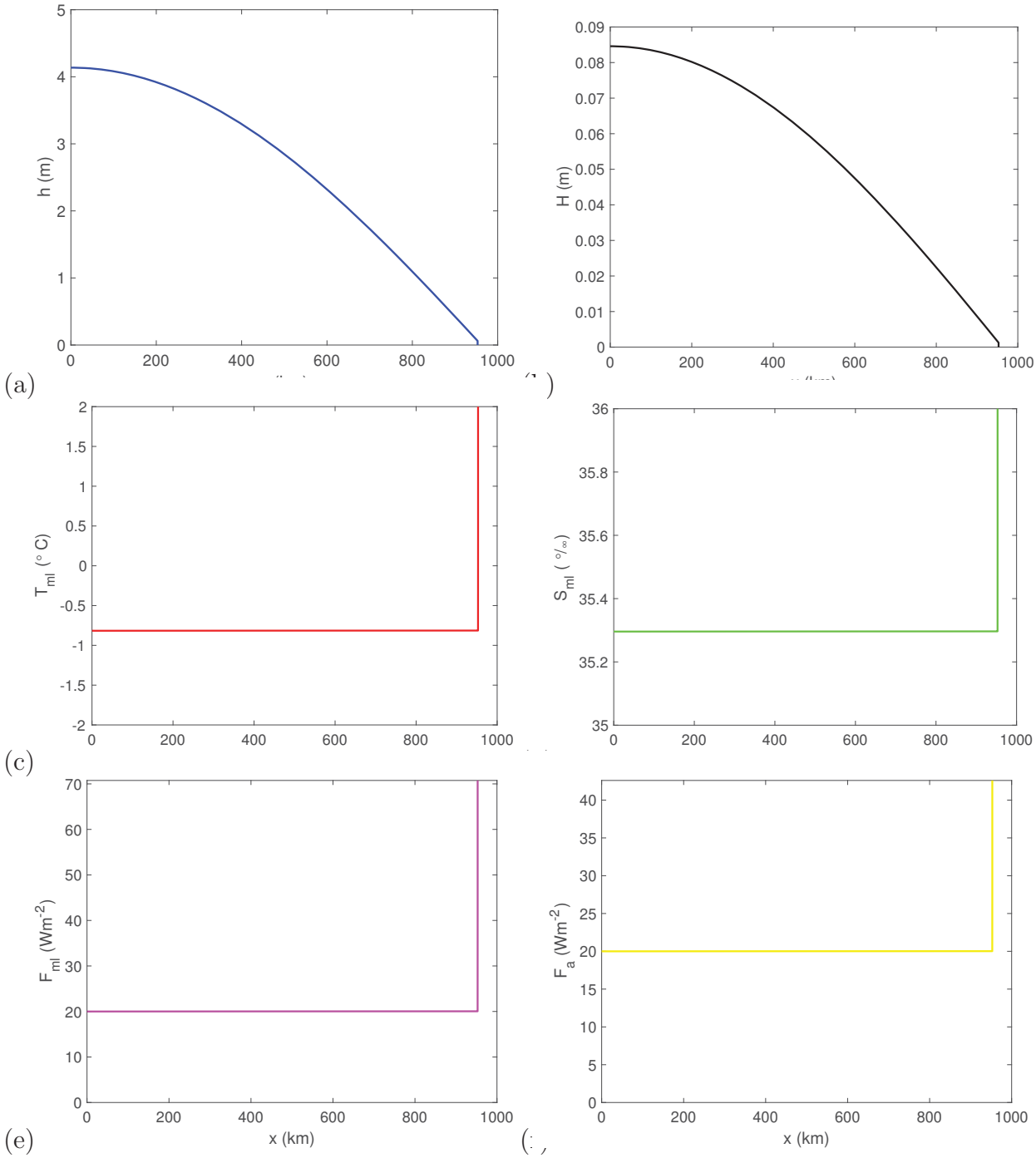

Figure 17: With ice velocity $10^{-5}m/s$ and ocean velocity $2.5 \times 10^{-2}m/s$. The insets show the near edge characteristics. (a)Ice thickness, h;(b)mixed-layer (ML) depth, H;(c)ML Temp., T_{ml}, Thick black line is the *Untersteiner's Wedge*, $\eta = 0.5km$;(d)ML Salinity., S_{ml}; (e)mixed-layer heat flux F_{ml}; (f) Atmospheric heat flux F_a

3 Time Dependent Solutions

Now that we understand the steady state dynamics of interaction between ice and ocean currents, we would like to understand how these dynamics play a role in the sea-ice export in the Fram Strait. How does this interaction manifest itself in pushing sea ice out of the Fram Strait through the East Greenland Current and push the ice edge northward through the West Spitsbergen Current.

The fully coupled time-dependent system of equations can be written as,

$$\begin{aligned}
\left(\frac{\partial}{\partial t} + \mathbf{U_w}\frac{\partial}{\partial x}\right) H(T_w - T_{ml}) &= \frac{\beta S_w (F_a - F_{ml})}{\alpha L \rho} \\
\left(\frac{\partial}{\partial t} + \mathbf{U_i}\frac{\partial}{\partial x}\right) h &= \frac{F_a - F_{ml}}{L\rho} \\
\mathcal{F} = \frac{\alpha L (F_b - F_{ml})}{\beta c_p S_w (F_a - F_{ml})} &= 1 \\
\frac{\alpha (T_w - T_{ml})}{\beta (S_w - S_{ml})} &= 1 \\
sgn(\mathbf{U_w}) &= \left\{ \begin{matrix} -1 : WSC \\ 1 \quad : EGC \end{matrix} \right\}
\end{aligned} \tag{41}$$

The system of Eqs. 41 make up a simple model for mixed-layer properties and sea-ice thickness in the Fram Strait. This hyperbolic system can be solved numerically. At first glance, one can know that this is a moving boundary problem. Since the ice edge will evolve in time and hence we scale this system accordingly.

Define a new variable $\xi = \frac{x}{x_e}$, where $0 < x < x_e$ and x_e is the ice edge at any time t.

$$\begin{aligned}
\xi &= \frac{x}{x_e} \\
\Rightarrow \frac{\partial}{\partial x} &= \frac{\partial}{x_e \partial \xi} \qquad \text{and} \\
\frac{\partial}{\partial t} &= \frac{\partial}{\partial t} - \frac{\dot{x_e}}{x_e}\xi\frac{\partial}{\partial \xi}
\end{aligned} \tag{42}$$

where, $\dot{x_e} = \frac{dx_e}{dt}$

Substituting Eq. 42 back in Eqs. 41, we obtain for the sea-ice thickness h

$$\frac{\partial}{\partial t}h - \frac{\dot{x_e}}{x_e}\xi\frac{\partial}{\partial \xi}h + \frac{U_i}{x_e}\frac{\partial}{\partial \xi}h = \frac{F_a - F_{ml}}{L\rho}. \tag{43}$$

The dynamics of the ice edge x_e is given by

$$\begin{aligned} \dot{x_e} &= U_i, \qquad h_e > 0 \\ \dot{x_e} &= U_i - x_e \frac{\Delta F}{\frac{\partial h}{\partial \xi}}\Big|_{\xi=1}, \qquad h_e = 0. \end{aligned} \tag{44}$$

where $\Delta F = \frac{F_a - F_{ml}}{L\rho}$ and h_e is the ice thickness at the edge.

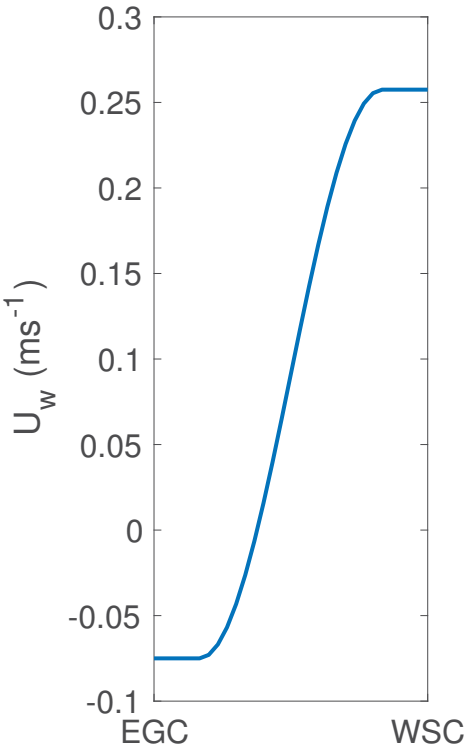

Figure 18: Velocity profile of the mixed layer in the Fram Strait from Eq. 45.

$$U_w = \begin{cases} 0.075 \text{ ms}^{-1} & : 0 \leq n \leq 5 \\ \frac{1}{2}((0.075 - 0.257) + (0.075 + 0.257)(-\cos\left(\frac{\pi(n-6)}{20}\right))) \text{ ms}^{-1} & : 6 \leq n \leq 26 \\ -0.257 \text{ ms}^{-1} & : 27 \leq n \leq 31 \end{cases} \Bigg\}. \tag{45}$$

We solve this coupled system of Eqs. 41, 43 and 44 numerically using the Upwind Scheme. We obtain the ocean velocities from previous analysis [3, 2, 11, 41, 8, 31, 10], keeping ice velocity fixed at $U_i = 0.1\ ms^{-1}$. It has also been shown that the waters in the Fram Strait do not interact significantly longitudinally in comparison to their latitudinal interaction, i.e. the measured east-west velocity is much smaller than the north-south component [6, 41]. This allows us to use the model above to compute individual sea-ice profiles for each (U_i, U_w) velocity pair and stack them together. The

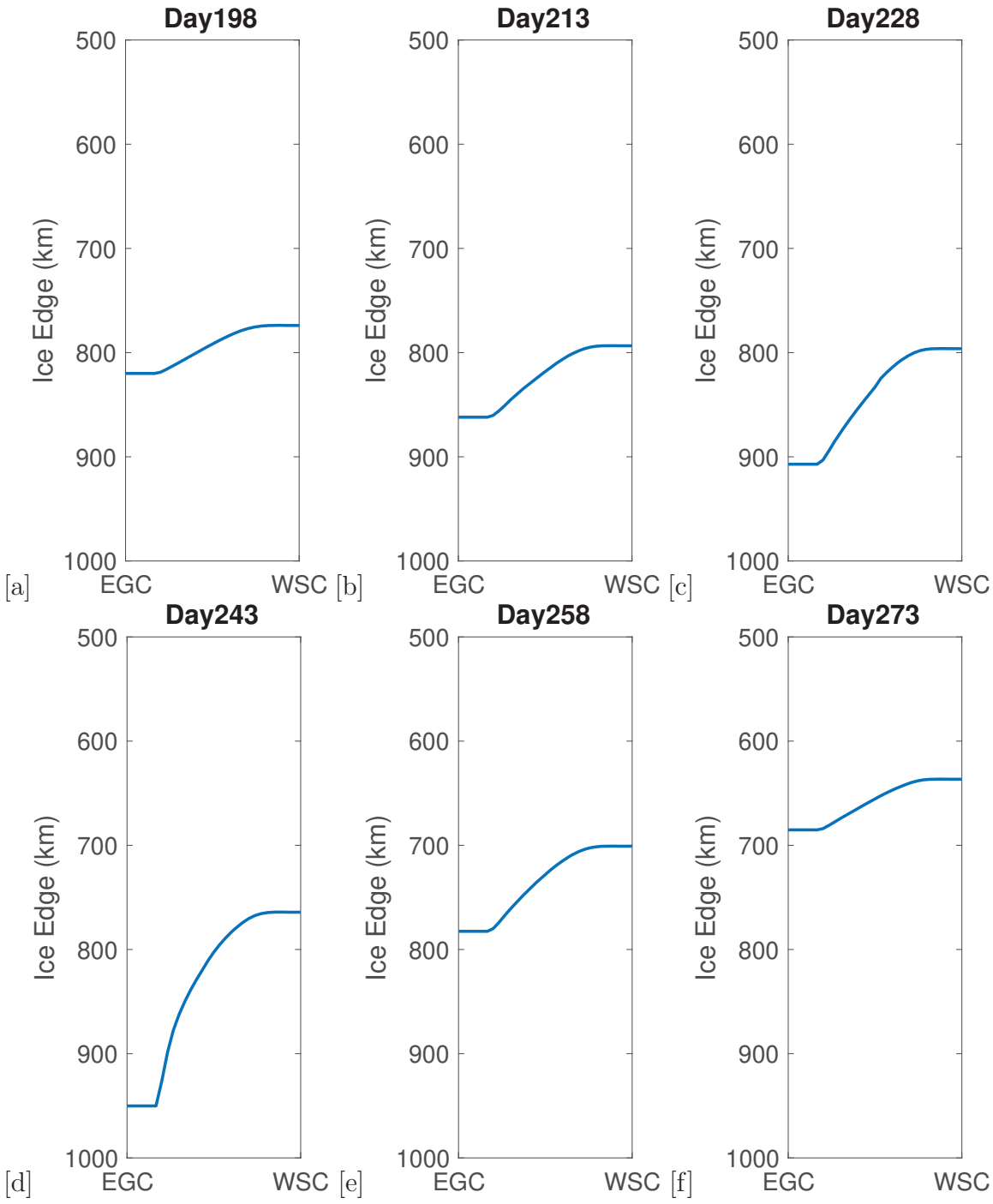

Figure 19: Location of the ice edge in the Fram Strait as a function of time (a)-(f). The ice edge extends for more than 200km in the East Greenland Current compared to the West Spitsbergen Current.

input ocean velocity, approximated from the observed ocean velocities in the Fram Strait is formulated as Eq. 45, also depicted in Fig. 18. In Fig. 19 we plot the location of the ice edge in the Fram Strait as a function of time, where day number denotes the time from start of the simulation. We limit the mixed-layer velocity in the East Greenland Current $U_i \leq 0.075\, ms^{-1}$.

Figs. 19(a)-(f) show the asymmetry in the slow growth rate of ice as it moves southwards vs the fast melt rate as it retreats back. It takes more than 45 days to grow approximately 150km while it only takes less than 30 days to retreat back more than 250km. The variation among the East Greenland Current vs. the West Spitsbergen Current is more than 200km, ascribed only by the variation in the ocean current velocity. Another point to note is the difference in time when the respective longitudes reach the maximum ice-extent. The ice-extent in EGC keeps increasing even when the ice-edge in the WSC has started to retreat. This lag produces a non-linear-like response in an almost linear change in the relative velocity. Agarwal and Wettlaufer [5] showed that sea-ice velocity may be the dominant physical process in explaining the variability in the ice extent dynamics in the Arctic. This independent modeling study shows that only a small change in the relative velocity between ice and ocean currents can cause a huge variation in the sea-ice extent dynamics.

4 Seasonal Asymmetry

As the sea-ice extent is declining in the Arctic, more and more first-year ice is starting to dominate the sea ice present in the region, with most of the melt taking away the multiyear ice pack. The multiyear ice has gone from covering more than two-thirds of the basin 20 years ago to less than one-third presently [17]. Because first-year ice is more transparent than its multiyear counterpart, it appears to be darker over the ocean waters, and the ice-albedo feedback is enhanced. This is leading to prolonged summers and a shift in the growth vs the melt rates of the sea ice.

Observations show that an asymmetry in the melt vs growth rate has emerged in the last decade owing to this shift towards an ice pack dominated by first-year ice. To quantify and understand this emerging asymmetry in more detail, we study another set of simple models. Fig. 20 shows the satellite observations of the annual sea-ice extent for the past 35 years. A key observation is that ice-albedo feedback causes a large spread near the annual minima compared to the maxima. Fig. 21 shows the daily sea-ice extent for the satellite era, with marked annual minima and maxima. The large inter-annual variability in the sea-ice minima reflects the large spread just explained.

In order to quantify the melt and growth rates of the sea ice, we do a linear regression fit of each maximum-minimum and minimum-maximum to compute the respective rate. A measure κ (see Eqn. 46), defined as the ratio of this melt rate to the growth rate tells us about this asymmetry.

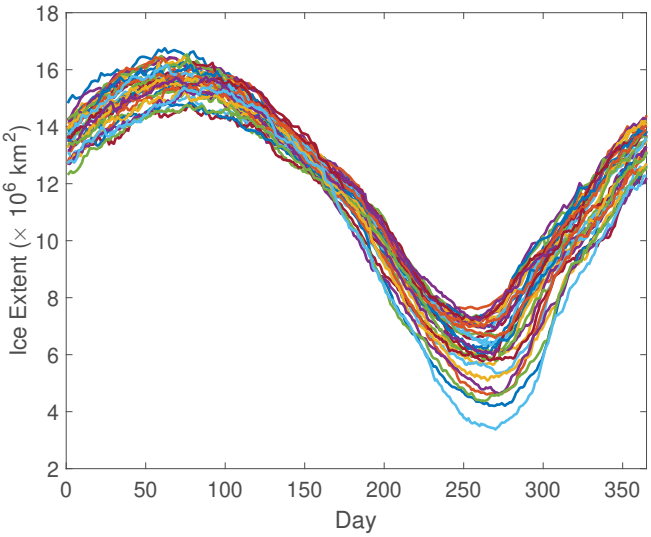

Figure 20: Arctic sea-ice extent for different years from the satellite era (1978-present). The spread near the ice minima is large compared to the spread at the ice maxima due to ice-albedo feedback.

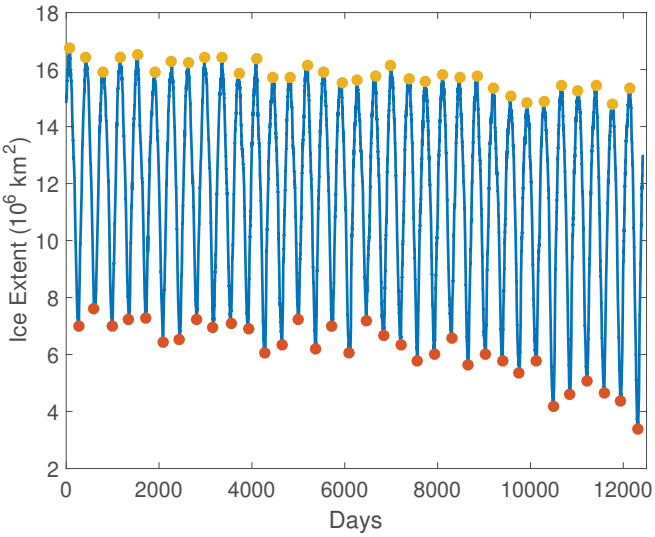

Figure 21: The observations of Arctic sea-ice extent with marked annual maxima/minima.

$$\kappa = \frac{\text{Melt Rate}}{\text{Growth Rate}} \tag{46}$$

Fig. 22 shows the variability in κ during the satellite era with the red/yellow lines showing the trend in κ for the first 17 and next 16 years, respectively. This plot is quite informative in telling us about the state of sea ice. The trend for the initial period is

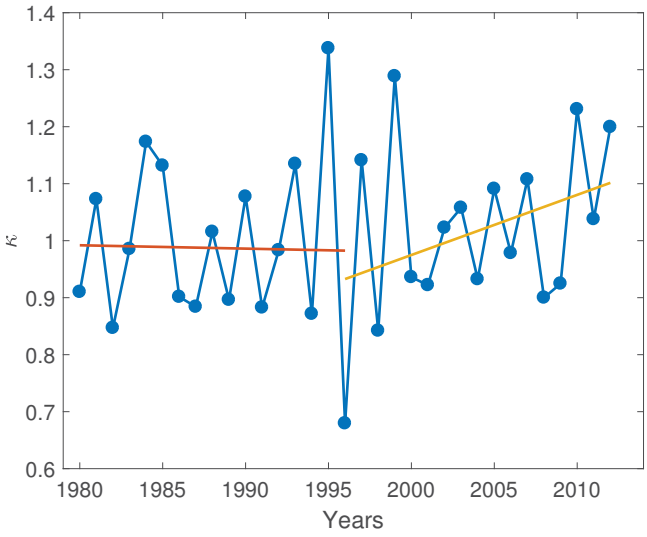

Figure 22: κ as a function of years. Initial 17 years does not show any asymmetry due to dominance of multi-year ice which is less prone to ice-albedo feedback. But as the ice melts away more first-year ice is now present in the basin, leading to asymmetry in growth vs melt rates.

almost flat, i.e. the growth rate was approximately equal to the melt rate during this time. But as the sea-ice extent declined and first-year ice started to dominate the basin, the melt rate enhanced due to the ice-albedo feedback with increase in heat storage in the ocean and thus reducing the growth season as well as the growth rate of sea ice in the Arctic Ocean. To further understand this asymmetry, we construct two simple models.

4.1 One-Category Column Model

Imagine looking at a very small grid cell in the central Arctic basin. This grid cell is assumed to always have ice in it. Fig. 23 shows this grid cell along with the dominant fluxes acting on this cell. The abyssal heat flux from the mixed-layer/ocean F_b beneath the ice is assumed to be constant as the ice-ocean interface always exists at the same temperature. In turn, the atmospheric heat flux F_a can be parametrized using Newton's Law of Cooling as in Eqn. 1. The heat transfer coefficient λ_a will depend on the albedo and hence on the area of the ice in the grid cell. Because this grid cell is assumed to always have ice, λ_a is taken to be constant as well. The ice-ocean boundary is assumed to be at the melting temperature $T_f = 0°C$, i.e. we ignore the effect of salinity of the ocean.

As in §2.1, we ignore the heat capacity of ice and assume no phase change at the surface of ice. Taking the *Stefan Number* to be large, the temperature profile in ice can be approximated as linear. Using the above assumptions, we can write the total

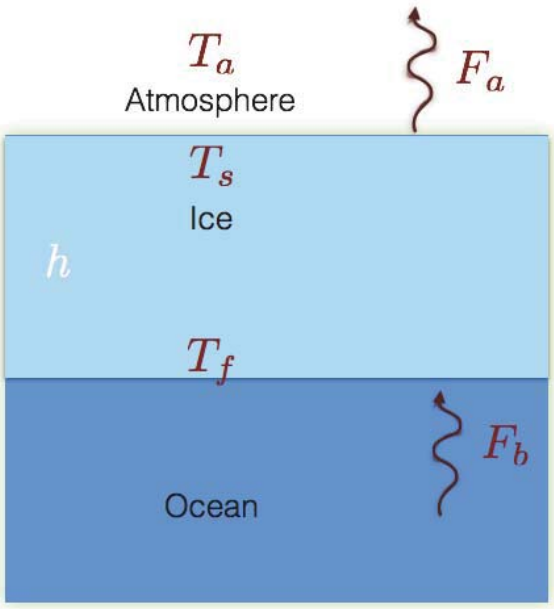

Figure 23: Schematic of a one-category column model, with the dominant fluxes marked.

heat flux balance for the system as

$$\rho L \frac{d}{dt} h = F_a - F_b, \tag{47}$$

where,ρ is ice density, L is the Latent heat and h is the ice thickness at time t.

The outgoing atmospheric heat flux can be written as

$$\begin{aligned} F_a &= \lambda_a (T_s - T_a) \\ &= k \frac{T_f - T_s}{h} l \end{aligned} \tag{48}$$

where T_a is the prescribed atmospheric temperature, and k is the thermal conductivity of ice. Eq. 48 gives us an equation for T_s which on substitution in Eq. 47 gives the complete system to be solved as

$$\rho L \frac{d}{dt} h = \lambda_a k \frac{T_f - T_a}{\lambda_a h + k} - F_b. \tag{49}$$

In this model formulation, ice grows when $h \geq 0$ with $T_s < T_f$ and melts when $h > 0$ with $T_s = T_f$.

Fig. 24a shows a solution of the system for a given set of parameters. To study the asymmetry in the ice extent, we stack 100 such grid cells side-by-side, and vary

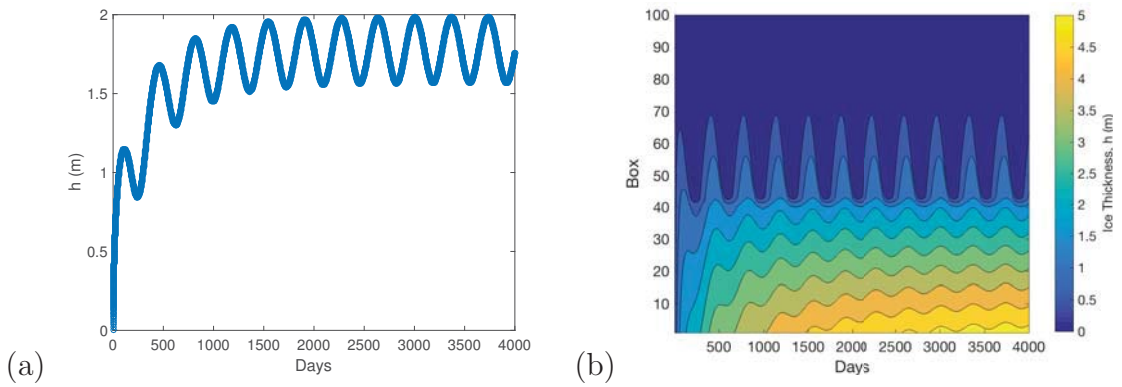

(a) (b)

Figure 24: (a)Solution of the system Eq. 49 for a given set of parameters. (b) Contour plot of ice thickness vs time, when 100 grid boxes are stacked together and T_a is gradually varied. *One Category Model* does not show any asymmetry in the ice edge dynamics.

the atmospheric temperature linearly, with a $0.5°C$ increase per grid cell. Fig. 24b shows the contour plot for the variation of h in space vs. time. The contour line of $h = 0$ can be imagined to be the sea-ice edge. This model does not show any asymmetry in the ice-edge properties. Therefore, we go on to a next step and allow part open ocean in the grid cell to build a *Two Category Model* as described below.

4.2 Two Category Column Model

The *One Category Model* described in §4.1 ignores many physical process such as opening of leads and patchy ice just to name a few which are all the more important given the recent retreat of sea ice at the poles. The presence of open ocean leads to a contrast in the albedo between ice and ocean in a grid cell. This contrast in albedo requires us to include the incoming shortwave radiation to model the different heat fluxes for ice and ocean.

Fig. 25 shows a schematic of this model. Ice of mean thickness h_i occupies an areal fraction A in the grid cell, while the open ocean occupies areal fraction $1 - A$ [12, 24]. The mean ice thickness for the whole cell can then be written as

$$h = Ah_i \tag{50}$$

Applying the chain rule gives

$$\frac{d}{dt}h = h_i\frac{d}{dt}A + A\frac{d}{dt}h_i. \tag{51}$$

As in the *One Category Model*, as long as there is ice in the cell, the ice-ocean interface as well as the ocean-atmosphere are assumed to be at $T_f = 0°C$. As ice goes away completely the ocean can start to warm up, where the heat transfer between the

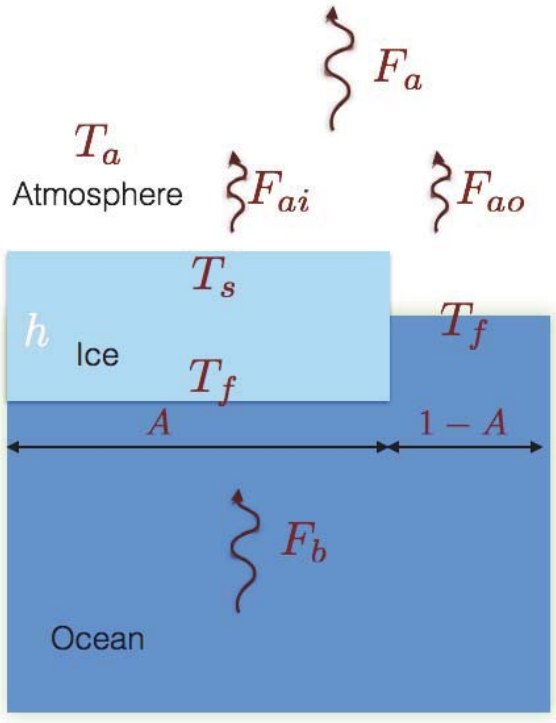

Figure 25: Schematic of a two category column model that includes both ice and open ocean in a single cell, with the dominant fluxes marked.

ocean and atmosphere can be written as $\lambda(T_{s_{ocean}} - T_a)$. We do not solve for $T_{s_{ocean}}$ in the case of no ice here.

Since we have both open ocean and ice in the cell, the net atmospheric heat flux can be written as a weighted sum of the individual components as

$$F_a = AF_{ai} + (1 - A)F_{ao} \tag{52}$$

where, F_{ai} is the heat flux through ice, and F_{ao} is the heat flux through the surface of the open ocean.

$$F_{ai} = -I(1 - \alpha_i) + \lambda_{ai}(T_s - T_a), \qquad F_{ao} = -I(1 - \alpha_o) + \lambda_{ao}(T_f - T_a) \tag{53}$$

where, I is the incoming shortwave radiation flux, α_i is the albedo for ice and α_o is the albedo for open ocean.

The low albedo ($\alpha_o = 0.2$) for open ocean as compared to that for sea ice ($0.6 \leq \alpha_i \leq 0.8$) gives a contrast in the amount of heat energy absorbed in the respective systems. We take the abyssal flux F_b to be constant, as both the ice-ocean and ocean-atmosphere are at the same temperature T_f. Writing the total energy balance for the

whole cell gives

$$\begin{aligned} \rho L \frac{d}{dt} h &= F_a - F_b \\ \Rightarrow \rho L \frac{d}{dt} h &= A(F_{ai} - F_b) + (1 - A)(F_{ao} - F_b) \end{aligned} \tag{54}$$

The first term on the right describes the growth/melt of ice already present in the grid cell, while the second term describes the growth of thin ice from open ocean/lateral melt. Along with the ice thickness, we have to model the growth and melt of the area fraction A as well.

4.2.1 Growth

Ice can grow in two ways: (a) Vertical growth in ice that is already present in the cell and, (b) thin ice freezing from the open ocean. We make the sub-grid scale modeling assumption that during growth, the area fraction A is linearly proportional to the net outgoing heat flux from the open ocean, i.e.

$$\rho L h_o \frac{d}{dt} A = (1 - A)(F_{ao} - F_b) \tag{55}$$

where, h_o, a constant of proportionality can be thought of as an accumulation thickness of thin ice that formed in the open ocean. Using Eqs. 51, 54 and 55, we can examine the evolution of the mean thickness of ice h_i as

$$\rho L \frac{d}{dt} h_i = (F_{ai} - F_b) + \left(1 - \frac{h_i}{h_o}\right) \frac{1 - A}{A} (F_{ao} - F_b). \tag{56}$$

The two terms on the RHS of Eq. 56 describe the two growth scenarios explained above. The first term describes the growth rate of thick ice while the second term describes the growth rate of thin ice in the open ocean. Note that, production of thin ice reduces the mean thickness h_i, given that $h_i \geq h_o$. This system can be solved completely, along with the assumption of linear temperature profile in ice, which gives an equation for T_s as

$$T_s = \frac{k T_f + \lambda_{ai} h T_a + I(1 - \alpha_i)}{\lambda_{ai} h + k}. \tag{57}$$

4.2.2 Melting

During melting, we assume that the aspect ratio of ice remains constant as it melts, i.e. the areal fraction A remains directly proportional to h_i. This is equivalent to the assumption of linear distribution of sea-ice thickness made by Thorndike ([34, 32]).

$$A = a h_i \tag{58}$$

where a is a constant of proportionality. This implies,

$$A\frac{d}{dt}h_i = h_i\frac{d}{dt}A \tag{59}$$

which upon substitution in Eq. 51 gives

$$\frac{d}{dt}A = \frac{A}{2h}\frac{d}{dt}h \tag{60}$$

Assuming a linear temperature profile in the ice, we get

$$2\rho L\frac{d}{dt}h_i = (F_{ai} - F_b) + \frac{1-A}{A}(F_{ao} - F_b) \tag{61}$$

A point to note is that

$$\rho L\frac{d}{dt}h_i \neq (F_{ai} - F_b) \tag{62}$$

which one may have written *a priori*, in accordance with the *One Category Model*.

4.2.3 Solutions

Figs. 26 and 27 show (a) areal fraction A and (b) mean sea-ice thickness h in the grid cell, in two different atmospheric forcing scenarios. Figs. 26a,b represent the multiyear ice pack with mean sea-ice thickness more than 2m. There appears to be an asymmetry in the areal fraction growth and melt rates, but because A is almost 1 all the time, this asymmetry does not show in the sea-ice thickness/volume The plateau in the sea-ice thickness is due to F_a being very close to zero during this time as the outgoing heat flux is almost equal to the incoming heat flux from the shortwave radiation. In turn, a first-year ice pack is represented in Figs. 27a,b. The areal fraction, as well as the sea-ice thickness/volume, goes to zero at the end of the melt season in this scenario. This has a clear asymmetry in the growth vs the melt rate, with the melt rate being much higher than the growth rate.

These solutions, representative of the multiyear ice vs first-year ice are able to reproduce the asymmetry observed in the satellite data which is moving towards a first-year ice pack in recent decade. These solutions embolden the ice-albedo feedback along with lateral melt in the first year ice as the dominant cause of the seasonal asymmetry. As the ice pack is thinning, it is becoming all the more patchy, enhancing the nonlinear interaction of ice-ocean albedo feedback, causing a significantly faster melt and lengthening the melt season.

In the model described for the sea-ice dynamics in the Fram Strait, this lateral growth/melt of first year ice is given by the different relative velocities between ice and ocean currents.

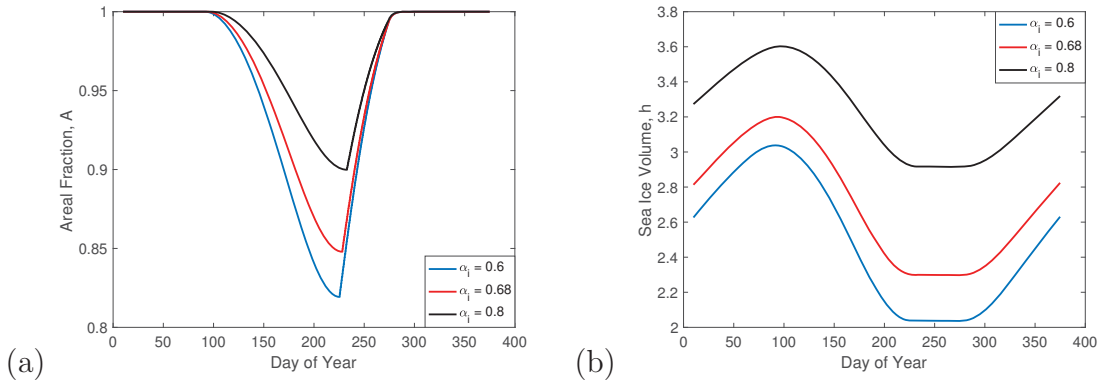

Figure 26: (a)Areal Fraction A and (b) sea-ice thickness/volume h, representative of a multiyear ice pack are shown for three different ice albedo with ocean albedo fixed at $\alpha_o = 0.2$

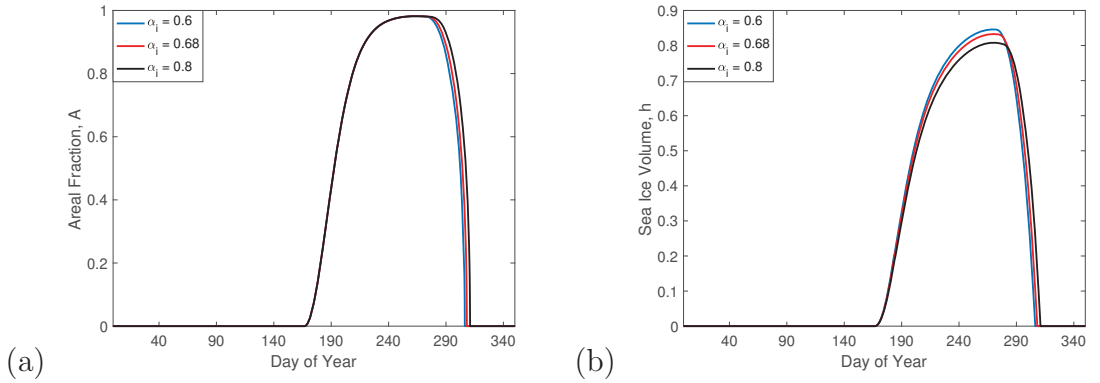

Figure 27: (a)Areal Fraction A and (b) sea-ice thickness/volume h, representative of a first year ice pack are shown for three different ice albedo with ocean albedo fixed at $\alpha_o = 0.2$

5 Conclusion

Fram Strait is the largest gateway in the Arctic through which the polar ocean interacts with the world oceans [35]. Climate change has been a major field of issue in the recent years. The nonlinear ice-albedo feedback has been one of the most important factors in bringing the climate change issue to the Arctic sea-ice melt. Another global issue is the dynamics of the Meridional Overturning Circulation (MOC). Sea-ice edge in the Fram Strait forms the northern boundary for the formation of Deep Water in the North Atlantic that drives the Atlantic MOC. Therefore, the location of the sea-ice edge is a factor in the strength and dynamics of this circulation, which in turn influences the global climate through ocean circulation, with time scales ranging from decadal to centuries.

Thorndike [33] has shown that more than 70% of variability in the sea-ice velocity fields can be explained by the geostrophic winds. Agarwal and Wettlaufer [5] have further shown that this variability in the sea-ice velocity fields explains the dynamics of the observed sea-ice extent on time scales ranging from a few days up to a couple of years. Using a hierarchy of simple models, we have shown how the interaction between sea-ice currents flowing southwards and ocean currents flowing southwards/northwards (East Greenland Current/WestSpitsbergen Current) influences the sea-ice edge and therefore sea-ice extent in the Fram Strait.

We outline the major conclusions below:

- In steady state, the location of the sea-ice edge is determined locally, depending only on the external parameters in the model.
- The steady-state properties (ice thickness h, mixed-layer temperature T_{ml} and salinity S_{ml}) in the Arctic can be determined in terms of external parameters without integrating the complete model.
- The length scale of *Untersteiner's Wedge* is determined by the balance of advected heat flux in the mixed layer to the heat flux transferred to ice.
- The fully coupled time dependent model shows:
  - The time it takes for the transient to reach steady state.
  - Asymmetrical growth and melt of sea ice, consistent with the observations.
  - The export of sea ice in the Fram Strait, *ice tongue* is captured fully, with a variation of nearly than 200 km between the EGC and WSC, by only varying the relative velocity of the ice-ocean currents in the this region.

The numerical solutions only involve the export of first year ice from the Arctic basin, which is then melted as it flows southwards, and hence produces a *shorter* ice tongue as compared to the real observations. There are a lot of other effects/physical mechanisms that have not been included in the simple models above, such as the Coriolis effect on the western boundary current, fresh water runoff from Greenland, eddy dynamics, to name a few.

References

[1] K. Aagaard and E. C. Carmack, *The role of sea ice and other fresh water in the arctic circulation*, Journal of Geophysical Research: Oceans, 94 (1989), pp. 14485–14498

[2] K. Aagaard and L. Coachman, *The East Greenland Current north of Denmark Strait. Part ii*, Arctic, (1968), pp. 267–290

[3] K. Aagaard and L. K. Coachman, *The East Greenland Current north of Denmark Strait. Part i*, Arctic, (1968), pp. 181–200

[4] K. Aagaard, A. Foldvik, and S. Hillman, *The West Spitsbergen Current. Disposition and water mass transformation*, Journal of Geophysical Research: Oceans, 92 (1987), pp. 3778–3784

[5] S. Agarwal and J. S. Wettlaufer, *The statistical properties of sea ice velocity fields*, arXiv preprint arXiv:1608.08340, (2016).

[6] T. J. Boyd and E. A. D'Asaro, *Cooling of the West Spitsbergen Current. Wintertime observations west of Svalbard*, Journal of Geophysical Research: Oceans, 99 (1994), pp. 22597–22618

[7] I. P. O. C. Change, *Climate change 2007: Impacts, adaptation and vulnerability*, Genebra, Suíça, (2001).

[8] E. D. Cokelet, N. Tervalon, and J. G. Bellingham, *Hydrography of the West Spitsbergen Current, Svalbard branch: Autumn 2001*, Journal of Geophysical Research: Oceans, 113 (2008).

[9] J. C. Comiso, C. L. Parkinson, R. Gersten, and L. Stock, *Accelerated decline in the Arctic sea ice cover*, Geophysical research letters, 35 (2008).

[10] L. de Steur, E. Hansen, R. Gerdes, M. Karcher, E. Fahrbach, and J. Holfort, *Freshwater fluxes in the east greenland current: A decade of observations*, Geophysical Research Letters, 36 (2009).

[11] A. Foldvik, K. Aagaard, and T. Tørresen, *On the velocity field of the East Greenland Current,* Deep Sea Research Part A. Oceanographic Research Papers, 35 (1988), pp. 1335–1354

[12] W. D. Hibler, *A dynamic thermodynamic sea ice model*, Journal of Physical Oceanography, 9 (1979), pp. 815–846.

[13] L. D. Hinzman, N. D. Bettez, W. R. Bolton, F. S. Chapin, M. B. Dyurgerov, C. L. Fastie, B. Griffith, R. D. Hollister, A. Hope, and H. P. Huntington, *Evidence and implications of recent climate change in Northern Alaska and other Arctic regions*, Climatic Change, 72 (2005), pp. 251–298 0165–0009.

[14] J. H. Jungclaus, H. Haak, M. Latif, and U. Mikolajewicz, *Arctic-north Atlantic interactions and multidecadal variability of the meridional overturning circulation*, Journal of Climate, 18 (2005), pp. 4013–4031

[15] T. Koenigk, U. Mikolajewicz, H. Haak, and J. Jungclaus, *Variability of Fram Strait sea ice export: causes, impacts and feedbacks in a coupled climate model*, Climate dynamics, 26 (2006), pp. 17–34

[16] R. Kwok, G. Cunningham, and S. Pang, *Fram strait sea ice outflow*, Journal of Geophysical Research: Oceans, 109 (2004).

[17] R. Kwok and N. Untersteiner, *The thinning of arctic sea ice*, Physics Today, 64 (2011), pp. 36–41.

[18] T. Manley, *Branching of Atlantic water within the Greenland-Spitsbergen Passage: An estimate of recirculation*, Journal of Geophysical Research: Oceans, 100 (1995), pp. 20627–20634

[19] C. Mauritzen and S. Häkkinen, *Influence of sea ice on the thermohaline circulation in the Arctic-North Atlantic Ocean*, Geophysical Research Letters, 24 (1997), pp. 3257–3260

[20] M. McPhee, *Air-ice-ocean interaction: Turbulent ocean boundary layer exchange processes*, Springer Science & Business Media, 2008.

[21] G. A. Meehl, T. F. Stocker, W. D. Collins, P. Friedlingstein, A. T. Gaye, J. M. Gregory, A. Kitoh, R. Knutti, J. M. Murphy, and A. Noda, *Global climate projections*, Climate Change, 3495 (2007), pp. 747–845.

[22] M. Meredith, K. Heywood, P. Dennis, L. Goldson, R. White, E. Fahrbach, U. Schauer, and S. Østerhus, *Freshwater fluxes through the western Fram Strait,* Geophysical Research Letters, 28 (2001), pp. 1615–1618 1944–8007.

[23] M. W. Miles, D. V. Divine, T. Furevik, E. Jansen, M. Moros, and A. E. Ogilvie, *A signal of persistent Atlantic multidecadal variability in Arctic sea ice*, Geophysical Research Letters, 41 (2014), pp. 463–469 1944–8007.

[24] W. Moon and J. S. Wettlaufer, *On the nature of the sea ice albedo feedback in simple models*, Journal of Geophysical Research: Oceans, 119 (2014), pp. 5555–5562.

[25] R. E. Moritz, C. M. Bitz, and E. J. Steig, *Dynamics of recent climate change in the Arctic*, Science, 297 (2002), pp. 1497–1502 0036–8075.

[26] A. Omstedt and J. Wettlaufer, *Ice growth and oceanic heat flux: Models and measurements*, Journal of Geophysical Research: Oceans, 97 (1992), pp. 9383–9390

[27] B. Rudels and D. Quadfasel, *Convection and deep water formation in the arctic ocean-greenland sea system*, Journal of Marine Systems, 2 (1991), pp. 435–450

[28] J. A. Screen and I. Simmonds, *The central role of diminishing sea ice in recent arctic temperature amplification*, Nature, 464 (2010), pp. 1334–1337

[29] M. C. Serreze and J. A. Francis, *The arctic amplification debate*, Climatic change, 76 (2006), pp. 241–264

[30] J. Stroeve, M. M. Holland, W. Meier, T. Scambos, and M. Serreze, *Arctic sea ice decline: Faster than forecast*, Geophysical research letters, 34 (2007).

[31] D. A. Sutherland and R. S. Pickart, *The east greenland coastal current: Structure, variability, and forcing*, Progress in Oceanography, 78 (2008), pp. 58–77

[32] A. S. Thorndike, *Estimates of sea ice thickness distribution using observations and theory*, J. Geophys. Res.-Oceans, 97 (1992), pp. 12601–12605.

[33] A. S. Thorndike and R. Colony, *Sea ice motion in response to geostrophic winds*, J. Geophys. Res.-Oceans, 87 (1982), pp. 5845–5852.

[34] A. S. Thorndike, D. A. Rothrock, G. A. Maykut, and R. Colony, *The thickness distribution of sea ice.*, J. Geophys. Res., 80 (1975), pp. 4501–4513.

[35] N. Untersteiner, *On the ice and heat balance in fram strait*, Journal of Geophysical Research: Oceans, 93 (1988), pp. 527–531.

[36] T. Vinje and Ø. Finnekåsa, *The ice transport through the Fram Strait*, 1986.

[37] T. Vinje, N. Nordlund, and Å. Kvambekk, *Monitoring ice thickness in fram strait*, Journal of Geophysical Research: Oceans, 103 (1998), pp. 10437–10449

[38] E. Vowinckel and S. Orvig, *Water balance and heat flow of the arctic ocean*, Arctic, 15 (1962), pp. 205–223

[39] M. Winton, *Amplified arctic climate change: What does surface albedo feedback have to do with it?*, Geophysical Research Letters, 33 (2006).

[40] R. A. Woodgate and K. Aagaard, *Revising the bering strait freshwater flux into the arctic ocean*, Geophysical Research Letters, 32 (2005).

[41] R. A. Woodgate, E. Fahrbach, and G. Rohardt, *Structure and transports of the east greenland current at 75 n from moored current meters*, Journal of Geophysical Research: Oceans, 104 (1999), pp. 18059–18072 2156–2202.

Erosion in a Uniform Background Flow

Jason Olsthoorn

(advisors Geoff Vasil and Saverio Spagnolie)

September 25, 2016

Abstract

We use an immersed boundary method, implemented with a pseudospectral solver to model the erosion of a two-dimensional cylinder in a uniform background flow. Previous experimental work has investigated this problem at high Reynolds numbers for both an eroding cylinder and eroding sphere which results in a wedge and conical geometry respectively. Recent results in the Stokes limit predict a different shape at low Reynolds numbers. We investigate the role of Reynolds number on the shape dynamics of an eroding body. We find that there exists a critical Reynolds number, corresponding to the wake instability criterion, at which the shape dynamics change between an asymmetric "wedge"-like and a more symmetric lens-like shape.

1 Introduction

The erosion of solid bodies plays an important role in geophysics. Numerical modeling of erosion is complicated due to the moving boundary between the solid body and the fluid flow. In this report, we will use an immersed boundary method to model the erosion of solid body, avoiding the complications of a deformable grid. However, immersed boundary methods present their own complications which will be discussed below.

This report follows the approach taken by Ristroph *et al.* (7) and Moore *et al.* (5) to evaluate the shear induced erosion of an erodible body in a uniform background flow. Ristroph *et al.* (7) initially investigated the erosion of a uniform layer of clay on a glass slide when it was placed streamwise in a uniform background flow. In this geometry, Blasius' boundary layer theory can be used to predict the shear along the plate. Figure 1 plots a diagram of the experimental setup used to measure the recession velocity (q_E) of the erodible bed. From the theory, the boundary layer thickness δ scales as $\sqrt{x}$ where x is the horizontal distance from the front of the slide. Ristroph *et al.*(7) makes the simplest possible model for erosion which states that the speed at which the front of the eroding bed recedes is

$$q_E = C_E|\tau|,$$

where $|\tau|$ is the shear stress along the surface of the body and C_E is a material dependent parameter. Solving for the front position, η, as a function of time, one finds that $\eta \sim t^2$, in agreement with the experimental observations.

Ristroph *et al.*(7) further experimented with both an erodible sphere and cylinder placed into a uniform background flow. They observed that over a finite time, the shape of the eroded bodies tend to be sharp (wedge-like). Importantly, the eroded shape appears to tend

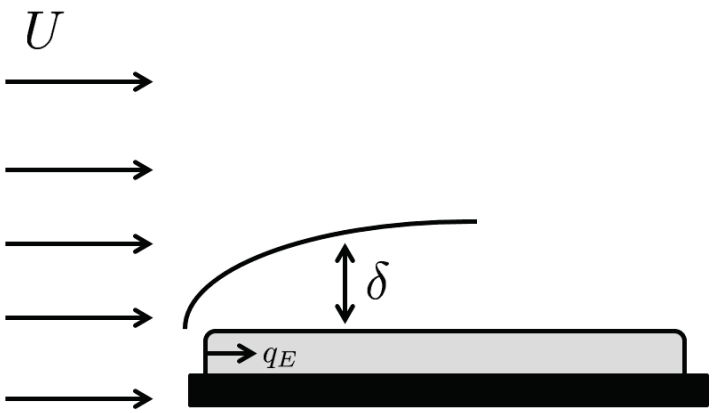

Figure 1: Diagram of the experimental setup presented in (7) in order to measure the recession speed (q_E) of a layer of clay (grey) on a glass slide (black) in a uniform background flow.

to a self-similar form. Using the erosion law above, the rate of mass loss was accurately estimated.

Moore *et al.*(5) continued this work by predicting the opening angle of the wedge produced by eroding a cylinder in a uniform background flow. Again, starting with boundary layer theory, Moore *et al.*(5) used a conformal mapping argument to show that for a wedge with an opening angle greater (less) than 90°, the shear along the wedge will decrease(increase) with distance from the nose. Thus, Moore *et al.*(5) argues that the opening angle of the eroding body must be 90° in order to reach a self-similar form. Numerical simulations of the eroding body agree with this prediction. It is important to note that while Moore *et al.*(5) did numerically simulate the front shape evolution, the simulation procedure did not simulate the full turbulent dynamics of the flow, or the evolution of the posterior eroding body. This report will present simulations of the complete flow field.

Recent investigations of Stokes flow (3) reveal a different conclusion. In the low Reynolds number limit, an eroding body is expected to evolve symmetrically, rather than the asymmetrical shapes found previously (7; 5). Mitchell and Spagnolie(3) predict that an eroding sphere in a Stokes flow does not reach a self-similar form, but, the erosion rate does change significantly once the eroding body reaches an opening angle of 120°. Curiously, this is a better approximation to the experimental opening angles found in (5).

In this report, we will investigate the effect of Reynolds number on the shape dynamics of an eroding cylinder. We begin, in section 2, by describing the equations used in the numerical simulations. Section 3 will investigate two simple one-dimensional problems which highlight the special care required when using immersed boundary methods for modeling erosion. We then present, in section 4, the erosion of a cylinder in a uniform background flow. Finally, we conclude in section 5.

2 Methods

In our implementation of the immersed boundary method, we explicitly model the drag forces, $\underline{F}_D$, acting on the immersed boundary (IB). The IB is delineated through the mask K which is constructed to be continuous in space. The drag force is specified to be linear in the fluid velocity. This is a common approach in immersed boundary methods (4) and is closely related to diffuse interface methods (1). The fluid momentum equations are then modified as,

$$\frac{D}{Dt}\underline{u} = -\frac{1}{\rho_0}\nabla P + \nu\nabla^2\underline{u} - \gamma K\underline{u}. \tag{1}$$

In this notation, vector quantities are underlined. The fluid velocity and pressure are defined as $\underline{u}$ and P. The molecular viscosity of the fluid is given as ν and ρ_0 is the reference density of the fluid.

2.1 Mask Equations

We construct the mask K to be effectively zero in the outer flow, and near one within the object. Thus, for a constant solid density ρ_s, the mass (M) of the IB is defined simply as

$$M = \rho_s \int K dV \tag{2}$$

In the presence of an external flow, the body will erode due to the fluid drag-forces acting on the body. In this problem, we consider a separation of time scales such that the erosion rate is much slower than the corresponding advective time scale. To this end, we do not model the advection of the eroded mass once it has separated from the body. As reported above, we model the deformation speed (q_E) of the solid as linear in the shear stress.

$$\underline{q} = C_E|\tau|\hat{n}.$$

Here, the surface normal is defined as $\hat{n} = \frac{\nabla K}{|\nabla K|}$. However, we note that for flow about a solid cylinder, there exists a forward stagnation point where the shear stress is identically zero, which will result in no erosion. This clearly unphysical result is elsewhere (5) regularized by adding an extra component of erosion where the curvature of K becomes large. Here, we regularize this point by stating that erosion will also occur when a substantial normal stress is applied. That is,

$$\underline{q}_E = C_E\left(|\tau| + \epsilon|\hat{n}\cdot\sigma\cdot\hat{n}|\right)\hat{n}. \tag{3}$$

The stress tensor is denoted σ. In the following discussion, we set $\epsilon = 0.01$. This value was selected to regularize the stagnation points around the IB while retaining the dominance of erosion law determined by (7). Thus, the IB evolves according to,

$$\partial_t K - \underline{q}_E\cdot\nabla K = 0. \tag{4}$$

In this problem, we initialize K to be a circle in the xz-plane with diameter D,

$$K = \frac{1}{2}\left(1 - \tanh\left(\frac{x^2 + z^2 - D^2}{\delta}\right)\right). \tag{5}$$

Due to the smoothness requirements of spectral methods (see below), we require a sufficient number of grid points over the boundary interface. Thus, we prescribe δ to scale linearly with the numerical resolution.

2.2 Nondimensionalization

The problem of uniform flow past a cylinder has characteristic length D and velocity U scales which are determined by the initial cylinder diameter and background velocity, respectively. These two quantities define an advective timescale $T = \frac{L}{U}$. Using these scales, we nondimensionalize the equations of motion as

$$\frac{D}{Dt}\underline{u}' = -\nabla P' + \frac{1}{\mathrm{Re}}\nabla^2 \underline{u}' - \gamma' K \underline{u}', \tag{6}$$

$$\nabla \cdot \underline{u}' = 0, \tag{7}$$

$$\partial_t K = \mathbb{Q}\underline{q}'_E \cdot \nabla K, \tag{8}$$

where primes denote non-dimensional variables. We have defined three non-dimensional parameters. We defined the Reynolds number (Re), the forcing parameter (γ'), and the erosion parameter ($\mathbb{Q}$) as

$$\mathrm{Re} = \frac{UD}{\nu}, \qquad \gamma' = \frac{\gamma D}{U}, \qquad \mathbb{Q} = \frac{C_e}{U}. \tag{9}$$

In this formulation, we construct $\gamma' \gg 1$ such that within the IB, F_D dominates both the viscous and inertial forces. The erosion parameter controls the speed of erosion compared with the fluid advection. In this discussion, we consider the case where $\mathbb{Q}$ is small such that the erosion is slow. We note that the IB parameter γ' has not yet been defined. The functional form of γ' will be discussed below. The primes will be dropped for the remainder of this report for convenience.

2.3 Numerical Implementation

The pseudo-spectral solve,r Dedalus (2) was used to solve the immersed boundary equations. In the work presented in this GFD report, all simulations were run with a grid resolution of 128x128, which is sub-resolving the dynamics at high Re. Future work will run these simulations at a much higher resolution in order to properly resolve the flow. Both a diffusive and spectral filter have been used to remove any Gibbs oscillations in the flow and to keep the mask function K sufficiently smooth.

3 1D Problem

Let us consider a simple, one-dimensional problem that will highlight some of the issues associated with immersed boundary methods.

Consider the one-dimensional problem of a viscous fluid set between two plates located at $z = 0$ and $z = \eta$. The top boundary is no-slip and the bottom boundary is specified

to have a constant horizontal velocity $U = 1$. The steady state equations solving for the horizontal velocity profile are

$$d_{zz}u = 0, \tag{10}$$
$$u(0) = 1, \tag{11}$$
$$u(\eta) = 0. \tag{12}$$

Thus, the steady state solution for the horizontal velocity is linear between the top and bottom boundaries,

$$u = 1 - \frac{z}{\eta}.$$

That is, the shear stress at the top boundary is

$$\frac{|\tau|}{\rho_0 U^2} = \frac{1}{\mathrm{Re}}|\partial_z u| = \frac{1}{\mathrm{Re}\ \eta}.$$

Now, let us instead impose the top boundary condition with an IB method instead of direct Dirichlet (prescribed) condition. The steady state equations must be modified by imposing the IB drag. Here, we will extend the vertical domain infinitely but note that the numerical schemes used in this report, the domain of interest will always be finite. The corresponding IB equations are thus written as

$$\partial_{zz}v = \mathrm{Re}F_D, \tag{13}$$
$$v(0) = 1, \tag{14}$$
$$v \to 0 \text{ as } z \to \infty, \tag{15}$$
$$F_D = \begin{cases} \gamma v, & z \geq \eta \\ 0, & 0 \leq z < \eta \end{cases}. \tag{16}$$

In this case, we find an outer and inner solution. These two solutions are matched to be both continuous and differentiable at $z = \eta$. The matched solution is given,

$$v = \begin{cases} A\exp\left[\sqrt{\gamma\mathrm{Re}}\,(\eta - z)\right], & z \geq \eta \\ 1 - Bz, & 0 \leq z < \eta \end{cases}, \tag{17}$$

$$A = \frac{1}{1 + \sqrt{\gamma\mathrm{Re}}\eta}, \qquad B = \frac{\sqrt{\gamma\mathrm{Re}}}{1 + \sqrt{\gamma\mathrm{Re}}\eta}. \tag{18}$$

There are two key aspects of this solution to note when using an IB method. First, there exists a viscous penetration length scale associated with the IB which is

$$l_{IB} = \sqrt{\frac{1}{\gamma\mathrm{Re}}}.$$

Clearly, in order for the immersed boundary method to be accurate we require that $l_{IB} \ll 1$. Second, the shear stress is computed

$$\frac{|\tau_{IB}|}{\rho_0 U^2} = \frac{1}{\mathrm{Re}}|\partial_z v| = \frac{1}{\mathrm{Re}}\frac{1}{l_{IB} + \eta}.$$

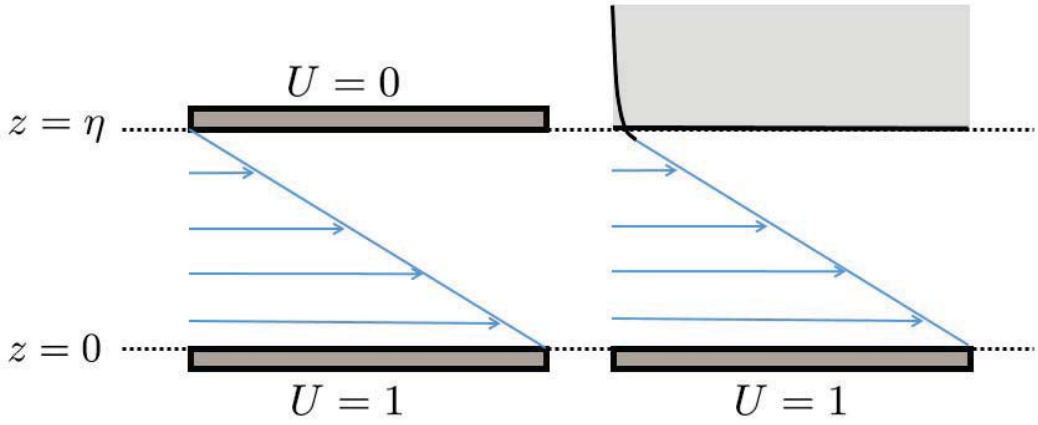

Figure 2: Diagram of the one-dimensional problem setup and steady state solution for an explicit boundary condition (left) and using an IB (right). The difference between steady solutions is highlighted in black.

That is, for all finite l_{IB}, the shear stress at the wall is less than the shear stress for the fixed boundary.

Figure 2 plots a schematic of the solutions for the explicit boundary condition and when using an IB method. Note that the velocity field penetrates into the IB.

3.0.1 Parameterization of γ

Looking at the one-dimensional problem above, the IB penetration length corresponds to the viscous transport of momentum into the IB. In the multi-dimensional case where advection is supported, we also expect to find an advective transport which scales as

$$l_{adv} \sim \frac{1}{\gamma}.$$

As such, as we define γ such that the total momentum penetration length (δ) is constant for all Reynolds numbers. Thus,

$$\delta = l_{visc} + l_{adv} = \frac{\overline{1}}{\gamma \mathrm{Re}} + \frac{1}{\gamma} \implies \gamma = \frac{2\mathrm{Re}\delta + \sqrt{4\mathrm{Re}\delta + 1} + 1}{2\mathrm{Re}\delta^2}. \tag{19}$$

With regards to equation (18), we expect that the IB solution should converge linearly with δ. In this problem, we define δ to scale linearly with the grid resolution N. Figure 3 plots the convergence rate of the simulated long-time solution using the IB method to the prescribed boundary solution with N. We then see that for low Reynolds number, the solution does indeed converge linearly with N, however, this convergence rate is improved for higher Reynolds numbers. This is a consequence of the smoothly delineated K in the numerical simulations.

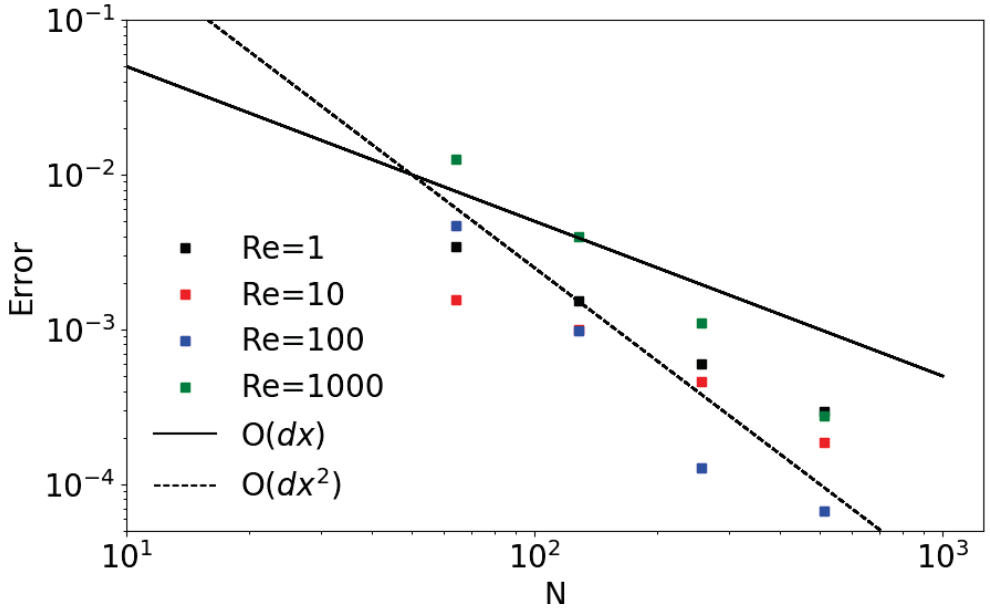

Figure 3: Convergence of the one-dimensional IB solution to the prescribed wall solution for increasing resolution. Convergence appears to improve from first and second order with increasing Reynolds number.

3.1 1D Erosion

We have already seen that an IB method will result in a lower shear at the interface than would be determined with a prescribed boundary condition. Keeping this in mind, let us then consider a similar 1D problem to the above, prescribing the top boundary to "erode," that is, move with a speed proportional by the wall shear. Once again, a viscous fluid is confined between two flat plates, where the bottom plate has a fixed horizontal velocity. In this formulation, the problem can be rewritten such that

$$\partial_t u - \partial_{zz} u = 0, \tag{20}$$

$$u\Big|_{z=0} = 1, \qquad u\Big|_{z=\eta(t)} = 0, \tag{21}$$

$$\partial_t \eta = -\mathbb{Q}|\partial_z u|\Big|_{z=\eta}, \qquad \eta(0) = 1. \tag{22}$$

This problem is identical to that of a melting plate. For a more complete description of the melting problem see (8). The exact solution to these equations is

$$u = 1 - \frac{\mathrm{erf}\left[-\alpha z/\eta\right]}{\mathrm{erf}\alpha}, \qquad \eta(t) = \sqrt{4\alpha^2 t + 1}, \tag{23}$$

$$\mathbb{Q} = \sqrt{\pi}\alpha \mathrm{erf}(\alpha)\exp(\alpha^2). \tag{24}$$

This problem presents an interesting test case to compare with a deformable immersed bound-ary method. In the formulation presented here, we modify the evolution equation for u and

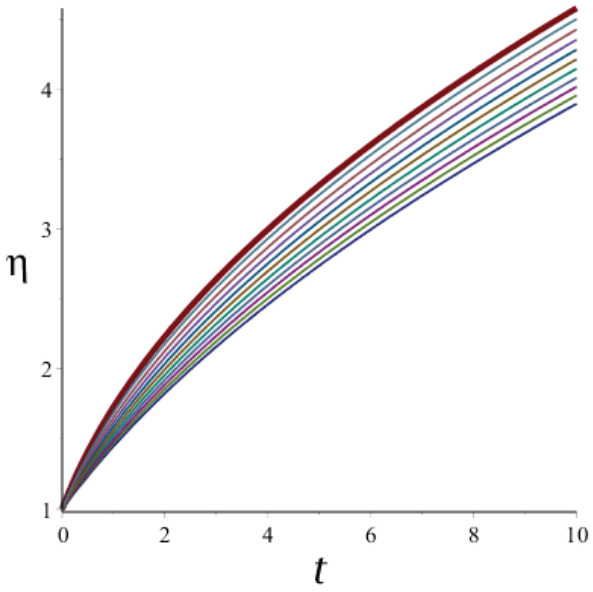

Figure 4: Plot of the interface position as a function of time for different values of $l_{IB} = \{0, 0.1...1\}$. The $l_{IB} = 0$ case has been made bold. Here, time has been scaled by $\mathbb{Q}$.

η such that

$$\partial_t u - \partial_{zz} u = \begin{cases} -\gamma\eta(u-0), & z \geq \eta \\ 0, & 0 \leq z < \eta \end{cases}. \tag{25}$$

$$\partial_t \eta - \mathbb{Q}\partial_z u = 0. \tag{26}$$

There exists a closed from solution to this equation in terms of limits of Kummer functions but this solution is not very enlightening. Instead, consider the case where $\mathbb{Q} \ll 1$, such that the interface evolves much slower than the reaction time of the system. As such, we can consider the system to be in quasi-steady-state. The steady state solution to this problem for a fixed η has been determined previously. As such, we can immediately write down

$$\frac{\tau_{IB}}{\rho_0 U^2} = \mathbb{Q}\frac{1}{l_{IB} + \eta(t)} \approx \frac{\mathbb{Q}}{\eta(t)}\left(1 - \frac{l_{IB}}{\eta(t)} + O\left(\frac{l_{IB}^2}{\eta(t)^2}\right)\right). \tag{27}$$

Figure 4 plots η as a function of time for different values of $l_{IB} = \{0, 0.1...1\}$. The prescribed boundary case, $l_{IB} = 0$, has been made bold for clarity. As expected we see that as l_{IB} decreases, the solution approaches the prescribed boundary case. A finite l_{IB} results in a uniformly slower recession rate but the same qualitative curves are observed. We set $l_{IB} \ll 1$.

Equation (27) highlights that the IB solution will converge linearly with the IB penetration length. However, in the one-dimensional problem presented here, the IB has been delineated by a Heaviside function about the interface. There are two complications when one uses a continuous mask function K to denote the IB. First, the width of the interface complicates the analysis of the interface recession. As we are considering the case of a

smooth mask with a small transition region, to first order the analysis presented above is correct. The second complication is that there is no longer a single "interface" position, rather there exists an interface region. We tackle this issue by asserting that the interface does not move at a single velocity, but rather that each element of the interface moves at a velocity prescribed by its local erosion rate. That is, the erosion rate $\vec{q}_E$ depends on the local shear stress, $|\tau|$ and hence, the mask evolves as:

$$\partial_t K - \underline{q}_E(|\tau|) \cdot \nabla K = 0.$$

In addition, we make an approximation similar to the one originally made in (6). For a perfect IB method (no velocity penetration into the boundary) where the IB drag is given by a series of delta functions, (6) showed that given the stress tensor σ_{ij},

$$[\sigma_{ij}]n_j = -l'F_i.$$

That is, the jump in the wall stress across the boundary can be determined by the IB drag. We do not use delta functions for our forcing function but we will assert that there exists some length scale l, such that

$$[\sigma_{ij}]n_j \approx -lF_D.$$

The precise determination of this length scale $l \approx \delta$ is left for future work. In this study, the length scale l is simply absorbed into the non-dimensionalization of the erosion rate $\mathbb{Q}' = \mathbb{Q}l$. Using this methodology allows us to avoid many numerical issues with computing the boundary gradients directly.

In what follows below, we solve the two-dimensional equations of motion in order to determine the shape dependence of an eroding cylinder as a function of Reynolds number. We reiterate that the IB formulation decreases the wall gradients across the IB interface resulting in a slower erosion rate than for a prescribed boundary condition. As the grid resolution is increased, the difference between solutions will decrease proportionally. Parameter studies have determined that the computed shape dynamics are robust for a large range of IB parameterizations.

4 2D Problem

As described above, we simulate two-dimensional uniform flow past a fixed eroding cylinder. In a domain $L_x \times L_z = 8 \times 8$, we initialize the mask function K as a circle in the xz-plane. Sponge layers were used at the top and bottom of the domain in order to enforce the far-field condition $\underline{u} = \underline{U}$. Due to the IB-imposed no-slip condition on the surface of the cylinder, boundary layer separation and subsequent breakdown will occur at sufficiently high Reynolds number. The transition from a steady wake to unsteady vortex shedding is experimentally observed to occur near Re=49 (9). In order to ensure that the numerical solution is not affected by the downstream sponge layer, the cylinder is located preferentially towards the upstream sponge layer such that the domain is defined $x \times z = [-4, 4] \times [-2, 6]$. The upstream sponge layer is not problematic until there is substantive upstream perturbations due to the presence of the eroding body. Thus, we are constrained in this domain configuration to have Re> 1. Figure 5 plots the vorticity at time $t = 200$ of the

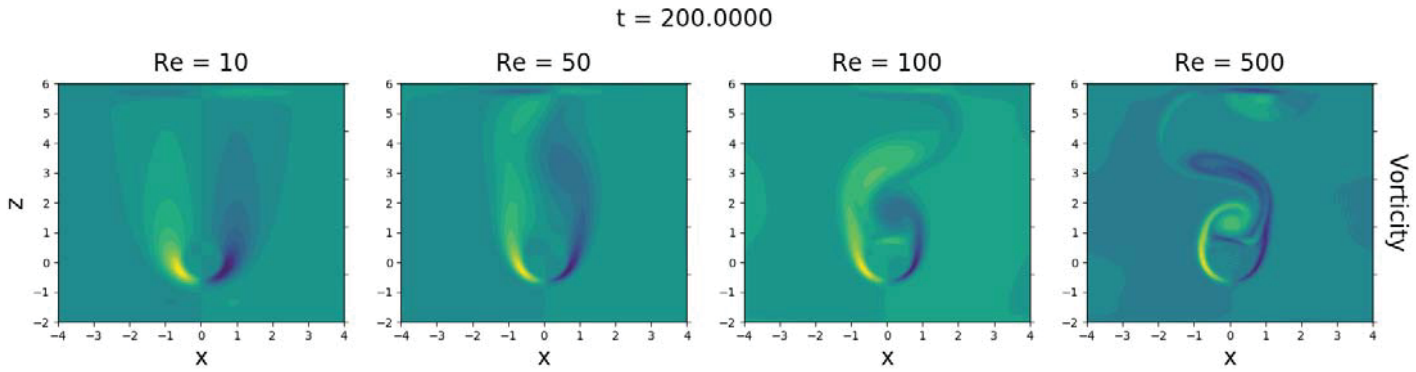

Figure 5: Plot of the vorticity field for a uniform flow past a non-eroding cylinder at time t=200 for four different Reynolds numbers. .

flow past a non-eroding cylinder at various Reynolds numbers. We see that there exists a wake instability behind the IB for high Reynolds numbers. More interestingly, we note that the transition between the laminar wake and the periodic shedding of vortices occurs near Re=50 in agreement with the predicted value.

In order to ensure that the IB condition is accurately predicting the flow field around a cylinder, the cross-stream forces on the IB are computed. For a steady flow, symmetry requires that the total cross-stream forces acting on the body vanish. For unsteady flow, we expect to find a periodic forcing signal due to the periodic shedding of the vortices. Note that an initial random perturbation was added to the velocity field in order to trigger any instabilities in the system, which will result in an initial (transient) force acting on the body. Figure 6 plots the lateral forces acting on the IB normalized by the initial 'kick' as a function of time. The inset provides a detailed view of the forces for Re=$\{10, 50\}$. As before, we observe that the wake instability occurs somewhere between Re=10 and Re=50. In addition, we observe a clear periodic signal to the wake instability. Again, we highlight that the simulations were only run at a resolution of $Nx \times Nz = 128 \times 128$, but we are still capturing the correct fluid dynamical regimes of the flow.

For an eroding cylinder, eight numerical simulations were performed at Re = {2. 10. 25. 50. 100, 500,1000} keeping the erosion parameter fixed ($\mathbb{Q}' = 0.025$). The erosion parameter is selected such that the timescale over which the boundary recedes is much slower than the advective timescale of the system. As with the non-eroding case, we expect to find vortex separation and a subsequent wake instability as a function of Reynolds number. Similarly, we expect to find that for low Reynolds numbers, the shape of the eroded body should maintain its fore-aft symmetry which will be lost at higher Reynolds numbers. Figure 8(a)-(d) plots three isocontours of K ($K = \{0.1, 0.5, 0.9\}$) for a range of Reynolds number at $t = 200$. We observe a clear transition between an asymmetric and symmetric regime associated with the wake instability. Figure 8(e)-(h) plots the corresponding vorticity field. It is interesting to note that due to the decreasing contact area of the eroding cylinder with the background flow, the cylinder which was originally at Re=50, has a near steady wake. This suggests that for an eroding body, the shape dependent Reynolds number will eventually drop below the criterion for the wake instability, resulting in a steady, symmetrical, wake. We do not

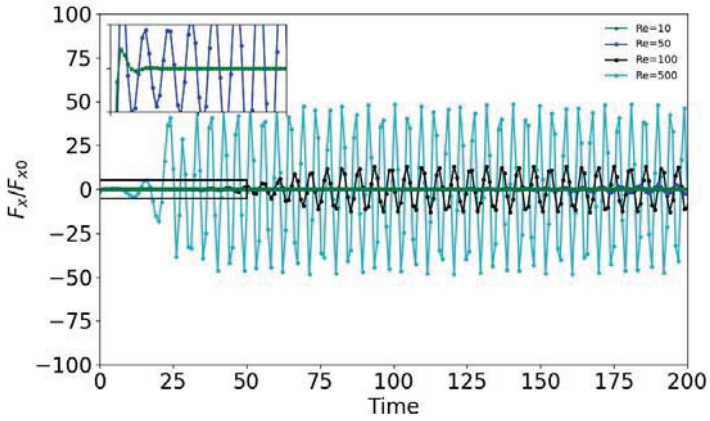

Figure 6: Plot of the horizontal forces acting on the IB normalized by the force experienced at t=0 as a function of time. The inset plots the Re=$\{10, 50\}$ cases within the boxed region drawn on the figure. The inset y-axis has been rescaled for visibility to $y \in [-0.01, 0.01]$.

investigate that further here.

The dynamics of the flow, including the geometry of the IB determine the erosion rate of the object. As the mass of the object is changing as a function of time, we define an erosion rate ratio, $\mathbb{M} = \frac{1}{M}\frac{dM}{dt}$, relating the rate of mass loss to the current mass (M) of the IB. Thus, if the system is evolving in a self-similar manner, we would expect to find that $\mathbb{M}$ is constant. Figure 8 plots $\mathbb{M}$ as a function of time for each different Reynolds number case. It is important to note that as the diameter of the body approaches 2δ, the penetration length scale of the IB becomes significant. For this reason, for a given resolution there exists a finite time at which the simulations diverge from the physical solution. A solution to this issue would be to re-grid and continue the simulation but we do not attempt that here.

We observe two key features of the erosion dynamics through the erosion rate ratio. First, to a good approximation we observe that, after an initialization period, the erosion rate ratio is weakly linear in time, $\mathbb{M} \approx \mathbb{M}_0 + \alpha t$, with $\frac{\alpha}{\mathbb{M}_0} = O\left(10^{-2}\right)$. That is, $\mathbb{M}$ is near constant in time which we expect for $\mathbb{Q} \ll 1$. The second observation is that there exists a regime change observed for Re$>$ 50. As the wake behind the cylinder goes unstable, there is a corresponding regime change in the erosion rate. This is particularly evident in the Re=1000 case. The Re=50 case is just above the wake stability criterion and, as such, there is only weak evidence of this change in erosion regimes. This indicates that a wake instability enhances the erosion rate when compared with a steady solution. Indeed, for Re$<$ 50, the erosion rate is near constant with Reynolds number (due to the constant $\mathbb{Q}'$), but increases drastically with Reynolds number for Re$>$ 50.

This work suggests that the wake instability plays an important role in the erosion dynamics of a solid body. As with the non-eroding cylinder, we analyze how the cross-stream forces acting on the IB change as the body erodes. Figure 9 plots the horizontal forces acting on the IB (F_x), normalized by the force exerted by the initial "kick" (F_{x0}). As before, we observe the vortex shedding produces a periodic lateral forcing on the IB. However, as the object erodes, the amplitude of these oscillations significantly decreases with

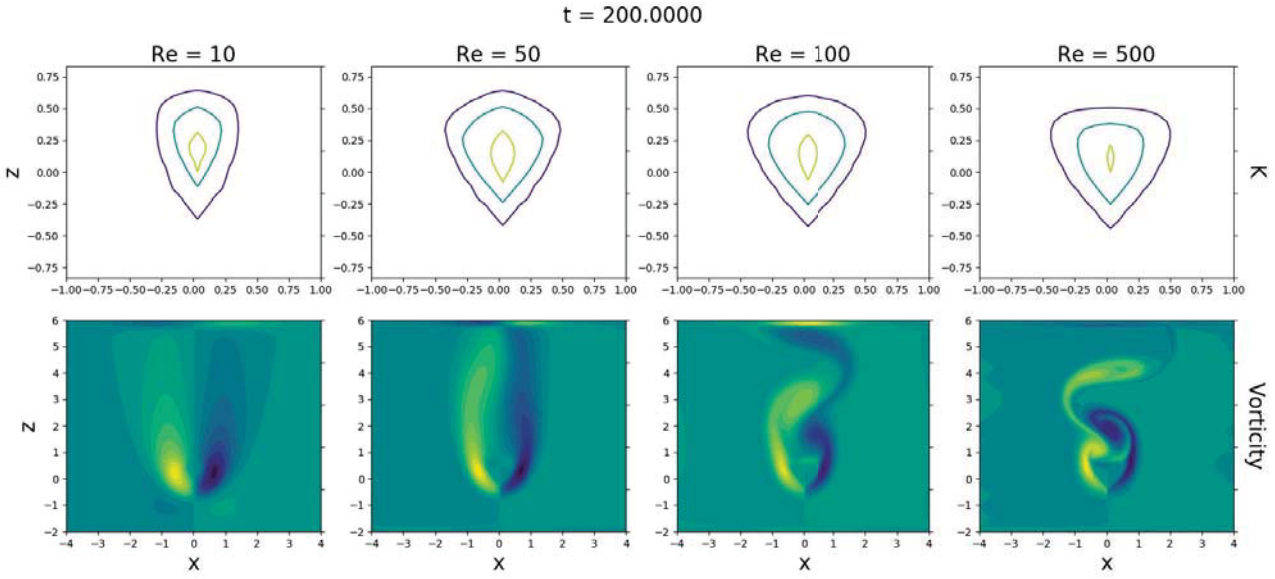

Figure 7: Comparison of the effect of erosion at varying Reynolds number. The top panels plot three isocontours of $K = \{0.1, 0.5, 0.9\}$ at time $t = 200$. The bottom panels plot the vorticity at the corresponding time. Note that the isocontours of K have been windowed for better visualization.

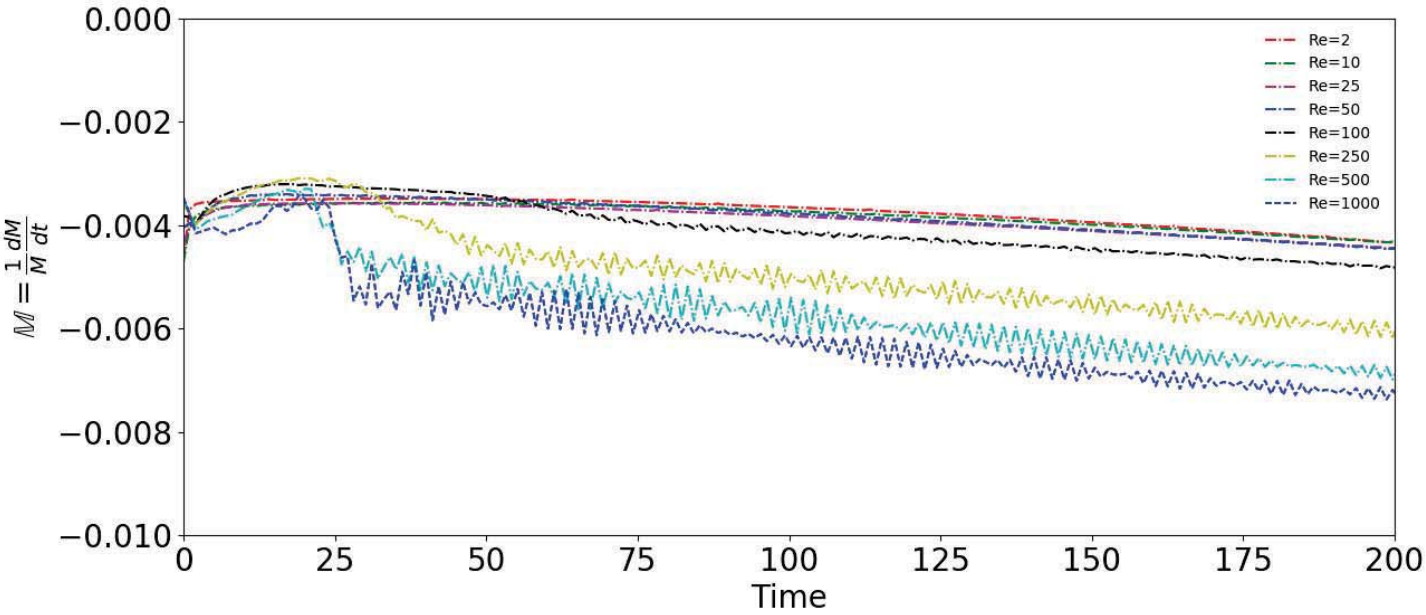

Figure 8: Plot of the erosion rate ratio as a function of time. Note the jump in the mass loss rate with the amplitude of the wake instability.

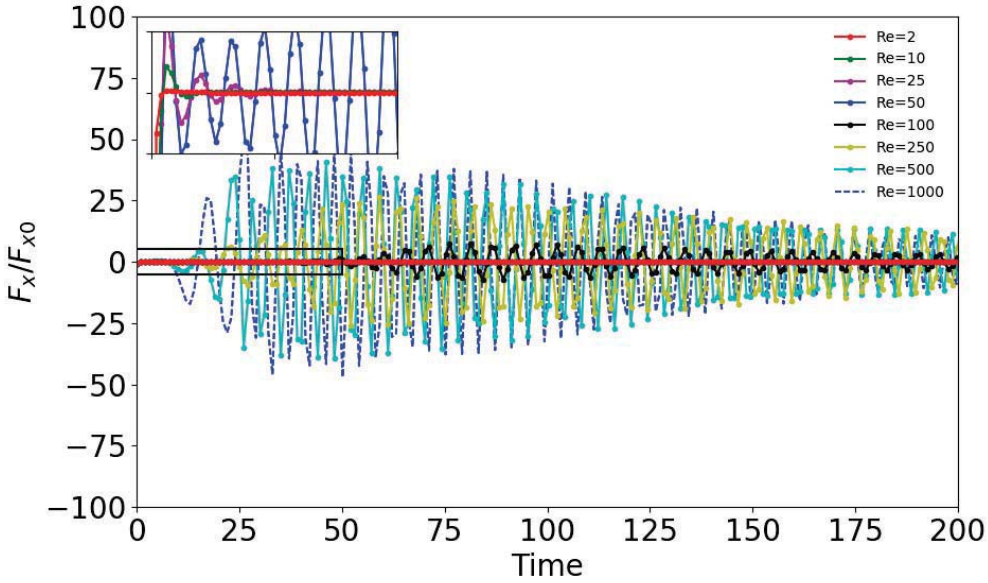

Figure 9: Plot of the horizontal forces acting on the eroding IB normalized by the force experienced at t=0 as a function of time. The insets plot the Re=$\{2, 10, 25, 50\}$ cases within the boxed region drawn on the figure. The inset y-axis has been rescaled for visibility to $y \in [-0.01, 0.01]$.

time. There is a convolution of effects occurring here. First, the size-dependent Reynolds number is decreasing such that the amplitude of the wake instability also decreases. In addition, the change in shape of the IB will change the character of the instability. This indicates that if the IB were allowed to translate cross-stream to the incoming flow, the amplitude of the oscillations observed would be drastically reduced from the non-eroding case. Indeed, simulations of this sort (not shown in this report) confirm this interpretation.

Thus, we have shown that for a range of Reynolds numbers, the eroding body evolves to a shape with a sharp opening angle. We compute the opening angle of the body, for each eroding case, as a function of time. Recall that the theory of (5) predicts an opening angle of 90 degrees though their experimental observations were more consistent with an opening angle of 120 degrees. Figure 10 plots the opening angle of the IB as a function of time. As was done in (5), we determine the opening angle of the body by fitting the contours of the IB to two semi-circles and measuring the angle between the circles along the centerline of the body. Five such contours were fit and averaged to get an estimate for the opening angle (θ) of the IB. By construction, $\theta = \pi$ at t=0. We observe that regardless of the Reynolds number, the opening angle appears to approach an angle near $\theta = \pi/2$. Running the simulations beyond $t = 200$ results in an opening angle below $\theta = \pi/2$ but, as mentioned previously, the penetration depth of the IB approaches the diameter of the eroded object and thus the results become inaccurate.

Many further test cases were performed including allowing the cylinder to translate cross-stream to the incoming flow, allowing the cylinder to rotate as it erodes and allowing

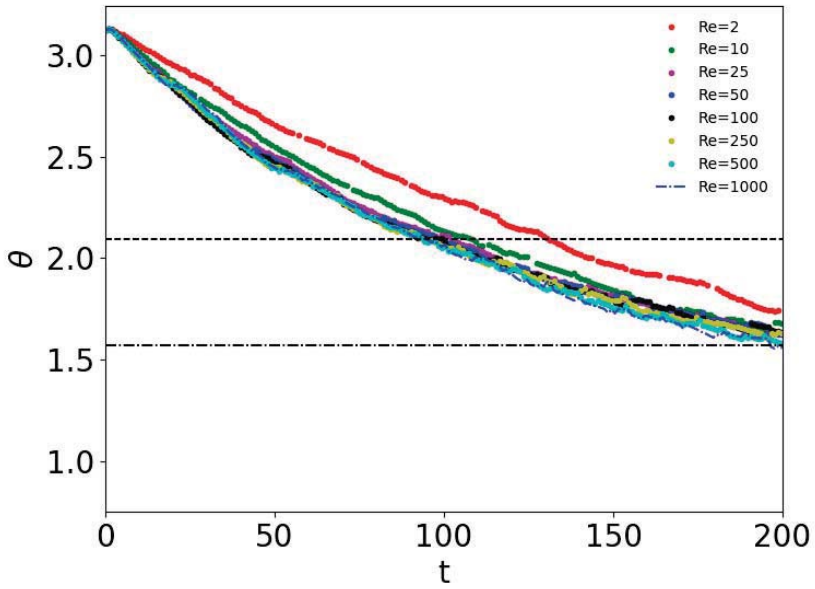

Figure 10: Plot of the opening angle of the IB as a function of time for a range of Reynolds numbers. Two predicted asymptotic limits are highlighted with $\theta = 2\pi/3$ (dashed line) and $\theta = \pi/2$ (dash-dot line).

the cylinder to fall under the influence of gravity. However, in the interest of brevity, we do not present those results here. We simply highlight that as the body erodes, the system becomes increasing dynamically complex due to the change in the shape of the eroding body.

5 Conclusion

This report presents the results of using an immersed boundary method to quantify the shape dynamics of an eroding body in a uniform background flow for a range of Reynolds numbers. We find that as the Reynolds number increases above the criterion for wake instability, there is a transition between a symmetric to an asymmetric eroded shape. This transition point also corresponds to a large increase in the erosion rate of the eroding body. In agreement with the prediction of (5), the opening angle of the eroding body tends towards $\theta \approx \pi/2$. As mentioned previously, the resolution of these simulations is significantly below what is desirable. Future work will run these numerical simulations at resolutions sufficient to resolve the viscous boundary layers at high Reynolds numbers.

There exists many further questions to ask concerning eroding bodies. In particular, comparing the two-dimensional shape dynamics found here with three-dimensional simulations will provide some important insight. The dynamics of a body that is allowed to propagate in space as it erodes is also of interest. We leave these avenues for future research.

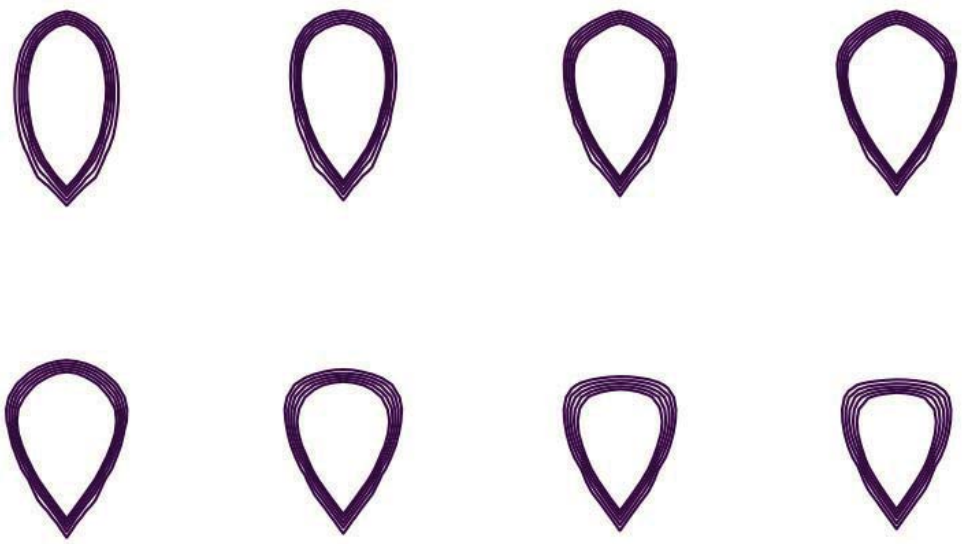

Figure 11: Artistic rendering of the resultant shape of an eroding cylinder at t=200, determined by the numerical simulations, Reynolds numbers. Here, the Reynolds numbers are increasing from low (top-left) to high (bottom-right) Reynolds

Acknowledgments

I would like to thank Geoff Vasil and Saverio Spagnolie for their many hours of help on this project. I would also like to thank the WHOI GFD Summer Program for allowing me to attend this summer program.

References

[1] D. M. Anderson, G. B. McFadden, and A. A. Wheeler, *Diffuse-interface methods in fluid mechanics*, Annual Review of Fluid Mechanics, 30 (1998), pp. 139–165.

[2] K. J. Burns, G. M. Vasil, J. S. Oishi, D. Lecoanet, B. P. Brown, and E. Quataert, *Dedalus: A flexible framework for spectrally solving differential equations*, (In Prep.).

[3] W. H. Mitchell and S. E. Spagnolie, *Viscous erosion with a generalized traction integral equation*, ArXiv e-prints, (2016).

[4] R. Mittal and G. Iaccarino, *Immersed boundary methods*, Annual Review of Fluid Mechanics, 37 (2005), pp. 239–261.

[5] M. N. J. Moore, L. Ristroph, S. Childress, J. Zhang, and M. J. Shelley, *Self-similar evolution of a body eroding in a fluid flow*, Physics of Fluids, 25 (2013).

[6] C. S. Peskin and B. F. Printz, *Improved volume conservation in the computation of flows with immersed elastic boundaries*, Journal of Computational Physics, 105 (1993), pp. 33 – 46.

[7] L. Ristroph, M. N. J. Moore, S. Childress, M. J. Shelley, and J. Zhang, *Sculpting of an erodible body by flowing water*, Proceedings of the National Academy of Sciences, 109 (2012), pp. 19606–19609.

[8] G. M. Vasil and M. R. E. Proctor, *Dynamic bifurcations and pattern formation in melting-boundary convection*, Journal of Fluid Mechanics, 686 (2011), pp. 77–108.

[9] C. H. Williamson, *Vortex dynamics in the cylinder wake*, Annual review of fluid mechanics, 28 (1996), pp. 477–539.

Capillary Sorting: Thin-film Flows of Particles

Michael Gomez

November 23, 2016

1 Introduction

Suspensions of particles flowing in a background fluid are familiar from everyday life: a drying droplet of coffee leaves behind a characteristic ring-like stain [Deegan et al., 1997], while yogurts and smoothies deposit streaking patterns on the side of their containers [Buchanan et al., 2007]. In industry, particles are separated from contaminated liquid during water treatment and other clarification processes [Davis and Acrivos, 1985]. Suspensions also arise frequently in blade coating where the aggregation of particles can cause defects in the final coating [Pranckh and Scriven, 1990]. On much larger scales, suspensions crop up in geophysics in the form of debris flows containing soil or rock particles moving in water [Iverson, 1997].

On a continuum level, the main challenge in modelling suspensions is in writing down the constitutive relation, *i.e.* how the viscosity varies with the particle concentration. At dilute concentrations, a suspension generally behaves as a Newtonian fluid with an effective viscosity that scales linearly with the volume fraction, a result originally due to Einstein [1906]. For dense suspensions, the picture becomes far more complex, as the viscosity is known to diverge as particles reach a maximum packing fraction. Many studies aim to characterize the rheology as this limit is approached, dealing with associated complications such as non-Newtonian effects, the role of normal stresses and shear-induced migration [Leighton and Acrivos, 1987, Bonnoit et al., 2010b, Boyer et al., 2011a,b]. The focus is on particles moving in bulk fluid [Bonnoit et al., 2010a].

In contrast, little attention has been given to situations when the thickness of the fluid region is comparable to the particle size, for example thin films or droplets. Unlike particles moving in bulk fluid, particles deform the fluid interface and capillary effects become important, modifying the transport of particles and the dynamics of the flow. For example, the presence of particles in a pendant drop causes the detachment dynamics to accelerate close to pinch-off, when the neck diameter is on the order of the particle size [Furbank and Morris, 2004, Bonnoit et al., 2012]. When a particle is instead confined by a thin liquid layer on a substrate, capillary forces are able to overcome body forces and deposit the particle onto the substrate [Fiegel et al., 2005].

When multiple particles deform an interface, capillary forces can attract them together to form aggregates [Kralchevsky and Nagayama, 1994]; see figure 1a. This has been demonstrated as a mechanism for pattern formation in suspension coatings [Ghosh et al., 2007, Kao and Hosoi, 2012, Colosqui et al., 2013], gravitational drainage flows [Buchanan et al., 2007], evaporating films [Denkov et al., 1992] and the impact splats formed by droplets

laden with particles [Lubbers et al., 2014] (figure 1b,c). However, the mechanisms controlling the deposition of particles and the clustering dynamics in these systems still remain poorly understood.

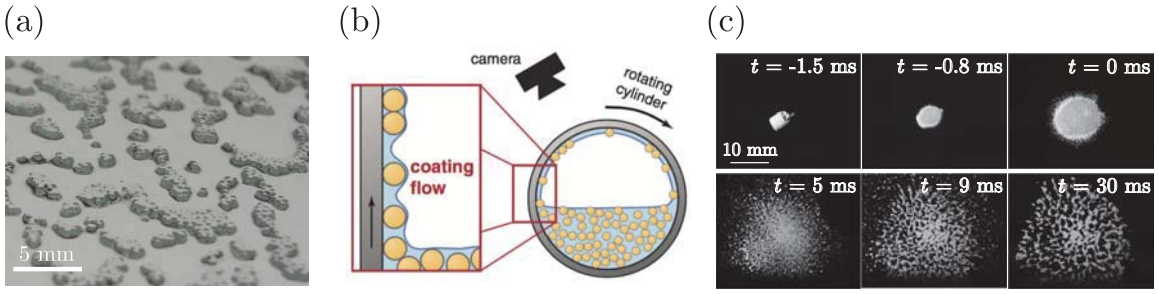

Figure 1: Capillary effects in thin-film flows of particles. (a) Glass particles (radius 250 µm), initially suspended in a thin film of glycerol, are deposited onto a glass pane (held vertically). (b) Analogue of Landau-Levich coating for a suspension. Particles are entrained upwards into the film against gravity as capillary forces drive the formation of aggregates (reprinted from Kao and Hosoi [2012]). (c) The clustering patterns formed by a particle-laden droplet (top view) impacting on a smooth surface (reprinted from Lubbers et al. [2014]).

In this report, we aim to understand how capillary interactions affect the transport and deposition of particles moving in thin liquid films. We focus on gravitational drainage flows, which provide a simple and natural situation in which a fluid layer continually thins below the size of carried particles. In particular, we perform experiments on a model system: a particle-laden gravity current flowing down an inclined plane. Previous work in this system has characterized particle transport in bulk flow, including the role of gravitational settling when particles are heavier than the fluid [Zhou et al., 2005, Ward et al., 2009, Murisic et al., 2011], as well as classifying suspension rheology at high particle concentrations [Bonnoit et al., 2010a] and associated effects of shear-induced migration [Timberlake and Morris, 2005]. Buchanan et al. [2007] have performed experiments on the drainage of dense suspensions containing two sizes of particles, but only the different regimes of pattern formation were investigated qualitatively as the relative proportions of each size were varied. As the film thickness becomes comparable to the particle size, we are interested in where particles are deposited and the effect they have on the suspension drainage. We restrict our attention to neutrally buoyant particles (no density effect) at relatively low concentrations. We begin in §2 by describing the setup used in our experiments, and the techniques we employ to measure the drainage dynamics. In §3 we review the classic drainage of a thin film of Newtonian fluid, which is well approximated by lubrication theory, before presenting results of the drainage of a monodisperse suspension of particles (*i.e.* one particle size). Depending on the concentration of particles, we find that a draining suspension shows behavior that cannot be captured with a Newtonian model, due to the deposition of particles on the substrate. In §4 we explore when an isolated particle is first deposited in terms of the local fluid thickness, demonstrating that this depends sensitively on the particle radius and the inclination angle of the plane. We attempt to rationalize the results based on a static force balance for a deposited particle. We then demonstrate in §5 that our results can be used to design a novel capillary sorting scheme, where

particles of different sizes are naturally deposited at different locations along the substrate. Finally, in §6 we conclude our results and discuss possible f uture work.

2 Experimental setup

The setup we use is shown in figure 2. A finite volume of a suspension, consisting of solid particles in a viscous liquid, is placed on top of a smooth horizontal plane so it spreads to form a thin film. The plane is then inclined at an angle α to the horizontal — held constant throughout each experiment — and the suspension drains under gravity into a tray. The tray itself is placed on an electronic scale (Ohaus NV212 AM Navigator) to measure the mass drained. A digital camera (Nikon D5200) is attached perpendicular to the plane so it views the suspension directly f rom above. We use a macro lens (AF-S VR Micro-Nikkor, 105 mm) to view the transport of particles over a fixed region on the plane. The suspension is back-lit with an LED panel (Porta-Trace LED Light Panel, 8.5 × 11 in) mounted under the plane.

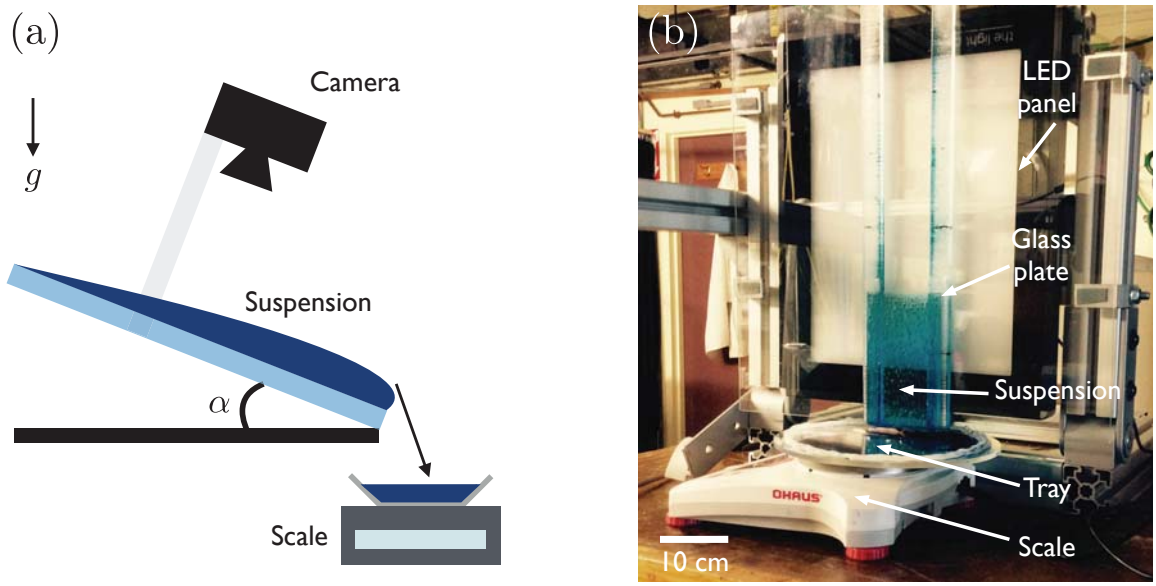

Figure 2: Experimental setup. (a) A particle-laden film of finite volume (dyed blue) is released onto a inclined plane and left to drain under gravity. (b) Photograph of the setup built in the GFD laboratory (here the plane is held at an angle close to vertical).

The Newtonian fluid used is poly(ethylene glycol-ran-propylene glycol) monobutyl ether (PEG, Sigma Aldrich, average molecular weight 3900). The properties of the fluid are its viscosity $\mu_f = 2.15\,\mathrm{Pa\,s}$ and density $\rho_f = 1.056\,\mathrm{g\,cm^{-3}}$. The particles are polystyrene spheres with radii $R = \{40, 70, 125, 250\}\,\mu\mathrm{m}$ and average density $\rho_p = 1.050\,\mathrm{g\,cm^{-3}}$ (Dynoseeds TS80, TS140, TS250, TS500). This precise combination of fluid and particles has been used in previous studies [Boyer et al., 2011a,b], due to the property that the density of the spheres closely matches that of the PEG. The Stokes settling velocity ($= (2/9)(\rho_p - \rho_f)gR^2/\mu_f$) is

less than $0.03\,\mathrm{mm\,min^{-1}}$, so that the particles can be considered neutrally buoyant over the timescale of our experiments. The plane consists of a glass plate of length $L = 30\,\mathrm{cm}$ and width $b = 7.5\,\mathrm{cm}$. We use glass rather than plastic to minimize electrostatic effects, which can become significant for very thin films [Oron et al., 1997].

The lower bound on the size of particles used here ensures that colloidal interactions are negligible along with Brownian effects [Boyer et al., 2011b]. The interfacial tension and equilibrium contact angle between polystyrene and PEG in air was measured using pendant drop tensiometry (see Berry et al. [2015], for example) and found to be $\gamma = 58\,\mathrm{mN\,m^{-1}}$ and $\theta_c = 46 \pm 5^\circ$ respectively; as the PEG is wetting a stable suspension can be obtained. The volume fraction of particles (equal to the volume of particles divided by the total volume of suspension) is denoted ϕ. We restrict attention to relatively dilute mixtures, $\phi = 0$–$20\,\%$, so that we can also neglect effects associated with dense suspensions; for example shear induced migration, jamming, and other bulk non-Newtonian effects.

2.1 Sample preparation

In each experiment, the suspension is prepared by mixing together the particles and PEG at the desired volume fraction ϕ. The mixture is stirred thoroughly to obtain a homogeneous distribution of particles, with care taken to stir slowly to minimize the creation of any air bubbles (these can alter the viscosity of the fluid). The glass plate is always cleaned to obtain repeatable experiments. Starting with the plane horizontal, we pour on a known mass of suspension and wait for the thickness to become roughly uniform (typically 5 minutes). We ensure the suspension initially wets the entire plate so that contact line effects only occur at the boundaries away from the bulk film; in particular, this suppresses the viscous fingering instability associated with a moving contact line [Huppert, 1982]. A similar technique is used by Keeley et al. [1988] in their experiments on the drainage of pure fluid. We then abruptly tilt the plane at time $t = 0$ to the angle α (measured using a digital level) and observe the resulting drainage with the digital camera. To minimize variation of the PEG properties, all experiments were performed in a temperature (and humidity) controlled room (temperature $22 \pm 1\,^\circ\mathrm{C}$) and each mixture is discarded after it drains.

The fluid thickness is denoted h. The initial thickness used is $h_0 \lesssim 2\,\mathrm{mm}$, compared to the length $L = 30\,\mathrm{cm}$ of the glass plate, so the aspect ratio of the film, $\delta = h/L$, remains much smaller than unity. Because the thickness is also small compared to the width b of the plate, the flow field is close to two-dimensional, *i.e.* variations in the cross-stream direction are small. We focus on inclination angles away from zero ($\alpha \gtrsim 5^\circ$) so that the drainage is driven by the component of gravity tangential to the plate rather than horizontal spreading. The reduced Reynolds number for the drainage of pure fluid (the relevant parameter measuring the importance of inertia for a thin film) is $\mathrm{Re} = \delta^2 \rho_f u L/\mu_f = O(10^{-4})$, where u is the typical tangential velocity. As the suspension has a higher viscosity than pure fluid, we deduce that $\mathrm{Re} \ll 1$ throughout our experiments and so inertia is negligible.

2.2 Measuring the film thickness

As well as measuring the mass drained with the electronic scale, we also measure the thickness of the film using a light intensity method, also known as a light-absorption method.

We dye the fluid at a fixed concentration (added at the stirring stage) so that where the thickness of the film is larger, more light emitted by the LED panel is absorbed and the film appears darker. After a suitable calibration, the greyscale intensity recorded by the digital camera can then be mapped to a value of the local thickness. This method has been used by Vernay et al. [2015] to accurately measure the thickness of an expanding liquid sheet down to a few microns. Following Vernay et al. [2015], we use erioglaucine disodium salt (Sigma Aldrich, blue in color) as the dye because of its high molar extinction coefficient; only a minimal amount needs to be added, so any impact on the properties of the suspension is negligible. This is dissolved in distilled water at a concentration $100\,\mathrm{g\,l^{-1}}$, and the water/dye mix is added to the suspension at a concentration $5\,\mathrm{g\,l^{-1}}$.

In performing the calibration, we measure the light intensity for a known fluid thickness, I, and compare this to the intensity without any fluid present, I_0 (the reference). To accurately obtain a known fluid thickness, we place a precise volume of distilled water between two microscope cover slips using a micropipette. The distilled water is dyed at the same overall concentration as the suspensions we use. As the water fully wets the glass, it forms a film whose average thickness is simply the fluid volume divided by the area of the cover slip. This is illustrated in figure 3a. We then measure the average intensity over the entire cover slip. Repeating this process for many volumes allows us to construct a calibration curve, which plots the fluid thickness as a function of the intensity normalized by the reference value, I/I_0 (figure 3b). We used fluid volumes ranging from 10 to 400 µl, corresponding to thicknesses $h \in (30.86, 1235)$µm.

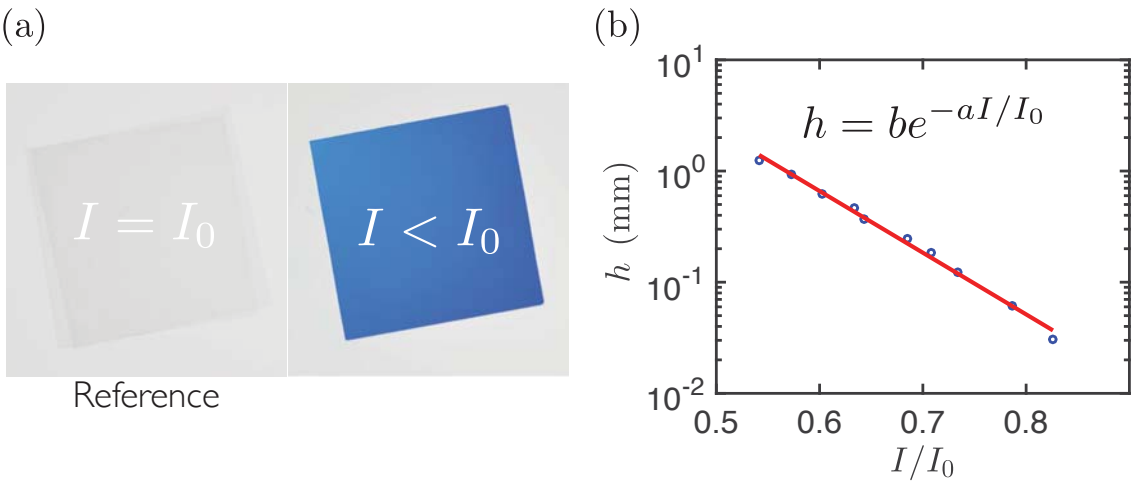

Figure 3: Calibrating the light intensity method. (a) Photographs of two glass cover slips ($18 \times 18\,\mathrm{mm}$) containing no liquid (left) and 150 µl of distilled water and blue dye that forms a film of average thickness 463 µm (right). (b) Calibration curve: plotting the film thickness, h, as a function of the normalized light intensity, I/I_0 (blue points). An exponential fit of the data points (red line, equation) is also shown; the values of the fitting constants are $a \approx 12.77$, $b \approx 1405\,\mathrm{mm}$.

An exponential fit of the data points (red line in figure 3b) allows us to determine the thickness corresponding to a given normalized intensity. We expect an exponential fit

based on a generalization of the Beer-Lambert law to a non-monochromatic light source [Lastakowski et al., 2014, Vernay et al., 2015], as is the case with our LED panel. With this fit, we can then measure the thickness at each pixel inside the fluid region during our drainage experiments, using a photo from the digital camera as input. We perform the image analysis in MATLAB using a custom script. Before each experiment, the glass plate is photographed without any fluid present to determine the reference intensity I_0 at each pixel; as the camera remains fixed relative to the plate, this gives the corresponding reference intensity when fluid is present. We found that variations in I_0 across the LED panel can be significant (up to 20%), so that using a single, averaged value of I_0 does not give accurate results.

The strength of the light intensity method is that it is non-intrusive and yields a very high spatial resolution over a series of photos in time. The drawback is that it relies on conditions being identical to those when the calibration curve is constructed, as these determine the values of the fitting constants. For example, the dye concentration, camera properties and lighting conditions need to be kept constant (the latter is achieved using the LED panel, and keeping the same ambient lighting). The method also relies on the fluid interface being close to flat [Lastakowski et al., 2014]. When particles are present, the method breaks down very close to the particles where the curvature of interface becomes large.

3 Drainage dynamics

We are interested in the impact that the particles have on the dynamics of the draining fluid. As the film drains around the particles, we expect that capillary forces will deposit the particles onto the substrate, leading to a loss of material that is transported downstream. In this section, we first review the classic theory of the drainage of Newtonian fluid, before presenting results of how a suspension of particles shows behavior that differs from this.

3.1 Drainage of Newtonian fluid

When the film thickness is much larger than the particle size, capillary effects are not important. Because we use relatively dilute concentrations of particles, which are neutrally buoyant, the suspension behaves as a Newtonian fluid at early times during the drainage [Bonnoit et al., 2010a]. Moreover, the aspect ratio of the film and the (reduced) Reynolds number (defined in §2.1) are both small, so we can model its evolution using lubrication theory.

3.1.1 Lubrication theory

A schematic of the drainage is shown in figure 4, which also displays the notation we use. We write $\rho = \rho(\phi)$ for the suspension density and $\mu = \mu(\phi)$ for the effective viscosity; this is larger than the viscosity of pure liquid, $\mu_f = \mu(\phi = 0)$. We take Cartesian coordinates so that x measures the distance down the plane from the upstream contact line, and z is the distance normal to the plane; the plane is at $z = 0$, while the free surface of the film is at $z = h(x, t)$, ignoring variations in the y-direction.

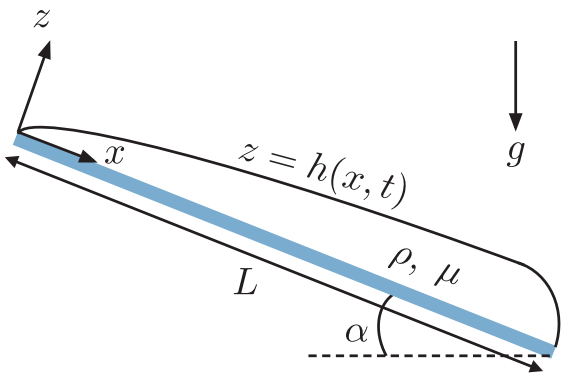

Figure 4: The notation used for a thin film of Newtonian fluid flowing down an inclined plane (shaded).

Under the assumptions of lubrication theory, the momentum equations for the fluid velocity $\mathbf{u} = u(x,z,t)\mathbf{e}_x + w(x,z,t)\mathbf{e}_z$ and pressure $p(x,z,t)$ have the form (see Acheson [1990], for example)

$$0 = -\frac{\partial p}{\partial x} + \mu\frac{\partial^2 u}{\partial z^2} + \rho g \sin\alpha, \tag{1}$$

$$0 = -\frac{\partial p}{\partial z} - \rho g \cos\alpha. \tag{2}$$

The continuity equation (assuming incompressibility) is

$$\frac{\partial u}{\partial x} + \frac{\partial w}{\partial z} = 0. \tag{3}$$

On the plane we have the no-slip and no-flux boundary conditions:

$$u = w = 0 \quad \text{at} \quad z = 0. \tag{4}$$

At the free surface the kinematic boundary condition holds, *i.e.*

$$w = \frac{\partial h}{\partial t} + u\frac{\partial h}{\partial x} \quad \text{at} \quad z = h. \tag{5}$$

We also have the stress balance ($[\cdot]_-^+$ denoting the jump in $\cdot$ across $z = h$)

$$[\sigma\mathbf{n}]_-^+ = \gamma\kappa\mathbf{n}, \tag{6}$$

where σ is the stress tensor, γ is the surface tension, $\mathbf{n}$ is the (outward) unit normal to the free surface and κ is the curvature. In the lubrication limit, the leading-order components of the stress tensor are

$$\sigma_{xx} \sim -p, \quad \sigma_{xz} \sim \mu\frac{\partial u}{\partial z}, \quad \sigma_{zz} \sim -p.$$

Using $\partial h/\partial x \ll 1$, we also approximate

$$\mathbf{n} \sim -\frac{\partial h}{\partial x}\mathbf{e}_x + \mathbf{e}_z, \quad \kappa \sim \frac{\partial^2 h}{\partial x^2}.$$

With these simplifications, the stress balance (6) reduces to

$$p = -\gamma \frac{\partial^2 h}{\partial x^2}, \quad \frac{\partial u}{\partial z} = 0 \quad \text{at} \quad z = h. \tag{7}$$

We would like to obtain a single evolution equation for the free surface $h(x,t)$. We first integrate the z-momentum equation (2) to find the pressure p. Applying the pressure condition in (7) gives

$$p = \rho g (h - z) \cos\alpha - \gamma \frac{\partial^2 h}{\partial x^2}.$$

Inserting into the x-momentum equation (1), we obtain

$$\mu \frac{\partial^2 u}{\partial z^2} = \rho g \left(\frac{\partial h}{\partial x} \cos\alpha - \sin\alpha \right) - \gamma \frac{\partial^3 h}{\partial x^3}.$$

Integrating twice in z gives, after making use of (4) and the second condition in (7),

$$u = \frac{1}{2\mu} z(z - 2h) \left[\rho g \left(\frac{\partial h}{\partial x} \cos\alpha - \sin\alpha \right) - \gamma \frac{\partial^3 h}{\partial x^3} \right]. \tag{8}$$

The velocity profile is therefore a parabola, with the maximum velocity obtained at the free surface. The corresponding fluid flux (per unit length in the y-direction) is

$$q = \int_0^h u \, \mathrm{d}z = \frac{h^3}{3\mu} \left[\rho g \left(\sin\alpha - \frac{\partial h}{\partial x} \cos\alpha \right) + \gamma \frac{\partial^3 h}{\partial x^3} \right]. \tag{9}$$

Finally, we integrate the continuity equation (3) across the depth of the film and apply the kinematic boundary condition (5) to obtain

$$\frac{\partial h}{\partial t} + \frac{\partial}{\partial x} \left\{ \frac{h^3}{3\mu} \left[\rho g \left(\sin\alpha - \frac{\partial h}{\partial x} \cos\alpha \right) + \gamma \frac{\partial^3 h}{\partial x^3} \right] \right\} = 0. \tag{10}$$

Equation (10) represents a balance between the local rate at which the film thins (the $\partial h/\partial t$ term) and the flux due to drainage downstream (the term in braces). Analyzing the expression for the flux, we see that the drainage is driven by either the component of gravity in the x-direction (*i.e.* tangential to the plane), or by the component in the z-direction (normal to the plane), depending on the size of α. The ratio of these terms is

$$\frac{\partial h}{\partial x} \frac{\cos\alpha}{\sin\alpha} \sim \delta \cot\alpha,$$

where $\delta = h/L$ is the aspect ratio of the film. In our experiments, the initial thickness of the film is $h_0 \lesssim 2$ mm and $L = 30$ cm (the length of the glass plate), giving $\delta = O(10^{-3})$. Thus, for inclination angles $\alpha \gtrsim 5^\circ$, we have $\delta \cot\alpha = O(10^{-2})$ and we may neglect the z-component of gravity in our model. The ratio of surface tension to the x-component of gravity is also small:

$$\frac{\gamma \frac{\partial^3 h}{\partial x^3}}{\rho g \sin\alpha} \sim \frac{\gamma \delta}{\rho g L^2 \sin\alpha} \equiv \mathrm{Bo}^{-1}.$$

Typical values of Bo are very large ($\gtrsim 10^5$) owing to the small aspect ratio δ. Hence, while the film thickness is larger than the particle size, we can neglect surface tension effects in the bulk away from any contact line. At leading-order, equation (10) then simplifies to

$$\frac{\partial h}{\partial t} + \frac{\partial}{\partial x}\left[\frac{h^3}{3\mu}\rho g \sin\alpha\right] = 0. \tag{11}$$

Given an initial configuration $h(x,0)$ this equation may be solved using the method of characteristics. A key result (see Huppert [1982], for example) is that for any $h(x,0)$, the solution asymptotically approaches the Jeffreys similarity form

$$h \sim \left(\frac{\mu x}{\rho g t \sin\alpha}\right)^{1/2} \propto \left(\frac{x}{t}\right)^{1/2} \quad \text{for} \quad t \gg \frac{\mu L}{\rho g h_0^2 \sin\alpha}. \tag{12}$$

We can interpret this solution as follows. At each location x, the fluid thickness decays in time like $t^{-1/2}$, with the thickness larger further downstream; or in other words, the shape of the film evolves through a sequence of parabolas that become increasingly flat, with the turning point located on the upstream contact line where the thickness decreases to zero. Note that the viscosity only enters in the combination $\mu/\sin\alpha$, so that changing the inclination angle in our setup has an equal effect to changing the viscosity.

From the expression (9), the fluid flux associated with the Jeffreys similarity solution is at leading-order

$$q \sim \frac{1}{3}\left(\frac{\mu x^3}{\rho g t^3 \sin\alpha}\right)^{1/2}.$$

Evaluating this expression at the end of the plate, $x = L$, gives the flux (per unit width) that leaves the plate and falls into the tray. The mass remaining on the plate, $M(t)$, can be found by integrating in time [Keeley et al., 1988], giving

$$M \sim \frac{2\rho b}{3}\left(\frac{\rho g t \sin\alpha}{\mu L^3}\right)^{-1/2} \propto t^{-1/2} \quad \text{for} \quad t \gg \frac{\mu L}{\rho g h_0^2 \sin\alpha}. \tag{13}$$

For a Newtonian fluid, the mass therefore decays like $t^{-1/2}$ at late times. For later reference, we also compute the leading order velocity components here. From equation (8), and integrating the continuity equation (3) to find w, we have

$$u \sim \frac{\rho g \sin\alpha}{2\mu} z(2h - z), \quad w \sim -\frac{\rho g \sin\alpha}{2\mu} z^2 \frac{\partial h}{\partial x}. \tag{14}$$

This shows that the typical tangential velocity scales as $u \sim \rho g h^2 \sin\alpha/\mu$. Note that w is an order of δ smaller than u due to the $\partial h/\partial x$ factor, so the flow is purely tangential at leading order.

The simplified thin-film equation (11) is valid whenever the film thickness is much larger than the size of the particles. The time when capillary interactions first become important (away from the boundaries of the plate) can be estimated as the time when the film is on the order of the particle diameter $2R$. Setting $x \sim L$ and $h \sim 2R$ in the Jeffreys solution (12), we obtain a time $t \sim \mu L/[4\rho g R^2 \sin\alpha]$. Note that this is independent of the initial thickness

due to the self-similarity of the solution. As the Jeffreys solution itself is asymptotically valid only for times $t \gg \mu L/[\rho g h_0^2 \sin\alpha]$, we expect the limits of its validity are therefore

$$\frac{\mu L}{\rho g h_0^2 \sin\alpha} \ll t \ll \frac{\mu L}{4\rho g R^2 \sin\alpha}.$$

In practice, this bound is not restrictive because the initial thickness $h_0 \gg 2R$. For example, at $\alpha = 90^\circ$ and at low particle concentrations so that the suspension viscosity is close to that of pure fluid, $\mu \approx \mu_f$, we estimate for our experimental system the range of validity is

$$15\,\mathrm{s} \ll t \ll 250\,\mathrm{s}. \tag{15}$$

3.1.2 Experiments

In a first set of experiments, we analyzed the drainage of pure PEG fluid without any particles present, *i.e.* $\phi = 0$. Figure 5a plots the thickness profiles at different times for an inclination angle $\alpha = 90^\circ$. These profiles have been determined by applying the light intensity method described in §2.2 to find the local thickness values. At each time step, we average the thickness in the cross-stream direction y (away from contact lines) to get the profile as a function of the downstream coordinate x only (the variation in y is consistently small). We see that the profiles have roughly parabolic shapes as anticipated from the lubrication model, with the drainage slowing down at later times (the curves become closer together). Re-scaling the x-coordinate according to the Jeffreys similarity solution (with $\rho = \rho_f$ and $\mu = \mu_f$), the profiles collapse well onto each other (figure 5b).

The corresponding evolution of the mass remaining on the plate is shown in figure 5c. This obeys the predicted $t^{-1/2}$ scaling at late times, and agrees well with the pre-factor predicted by equation (13). The disagreement at early times is where the similarity solution is not asymptotically valid, and the evolution depends on the initial shape of the free surface, $h(x, 0)$. The transition between the two regimes occurs at $t \approx 80\,\mathrm{s}$, which is consistent with the lower bound for the validity of the similarity solution calculated in equation (15).

A similar collapse under the similarity scaling is also seen for a variety of inclination angles; see figure 5d, where we have also plotted the Jeffreys similarity solution (12) for comparison (black line). As each parameter appearing in (12) has been measured independently, no fitting parameters are used here. The agreement is good at large x. Near $x = 0$, the upper edge of the glass plate, we expect a significant difference due to the effect of the contact line there (as the thickness decreases to zero). Nevertheless, figure 5 demonstrates that the pure fluid is obeying the scaling laws predicted for a Newtonian fluid. In what follows, any deviation from this behavior can therefore be attributed to the presence of particles.

3.2 Drainage of a suspension

We now consider the drainage of a suspension of particles rather than pure fluid. To isolate the effect of the particles, we fix the particle radius $R = 250\,\mu\mathrm{m}$ and vary the volume fraction ϕ. The mass remaining on the plate as a function of time, $M(t)$, is shown in figure 6. Also shown for comparison is the predicted behavior for a Newtonian fluid with the same density

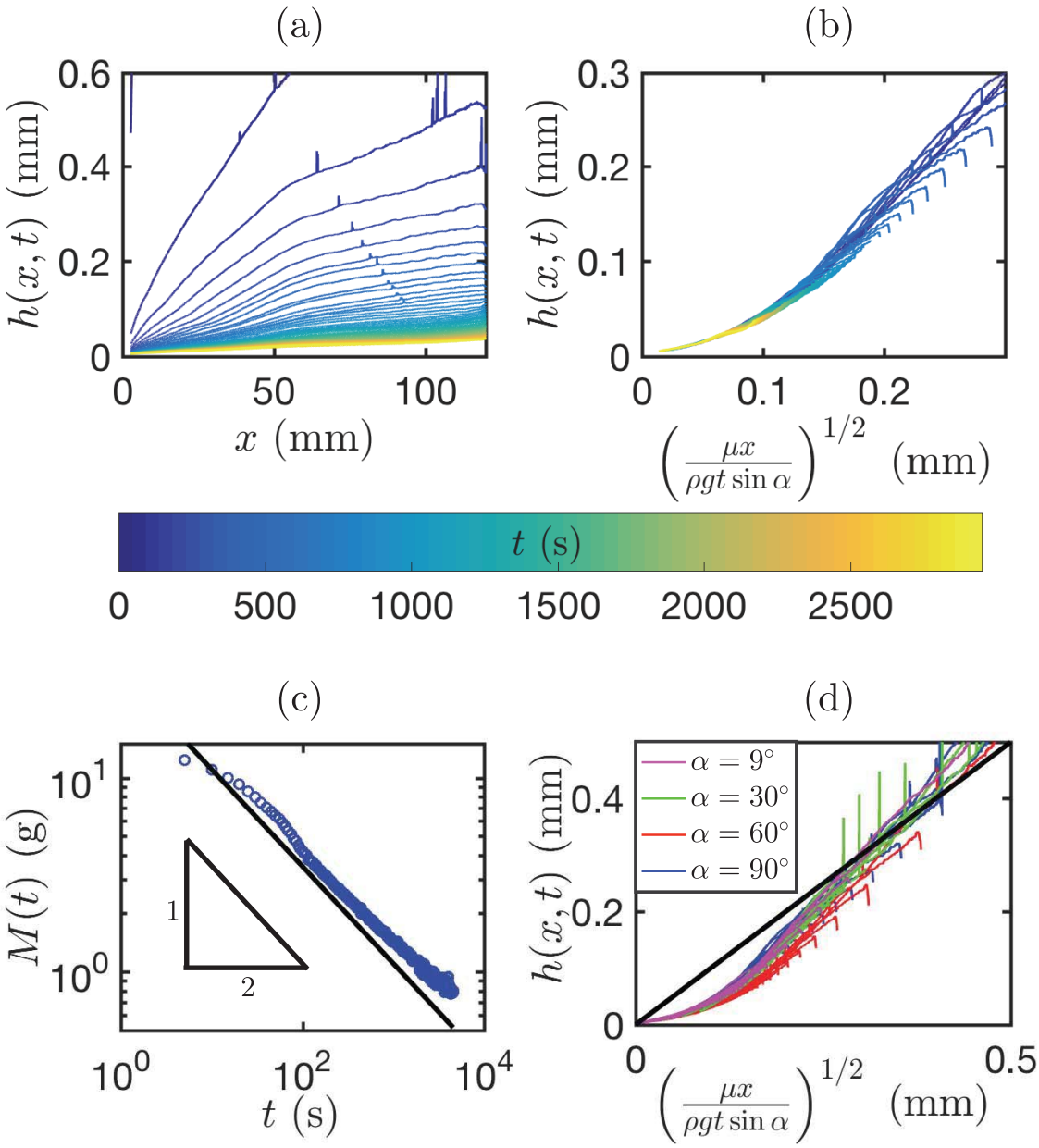

Figure 5: Drainage dynamics of pure PEG. (a) Thickness profiles measured using the light intensity method (inclination angle $\alpha = 90°$) . A total of 59 curves separated by 50 s intervals are shown, with times given by the colorbar (the spikes on the curves are menisci around small air bubbles present in the mixture, which appear as dark rings on photographs). (b) The same data, when re-scaled in terms of the Jeffreys similarity variable, collapse onto a master curve. (c) Corresponding evolution of the mass remaining on the plate (blue circles). The late-time prediction (13) from lubrication theory is also shown (black line). (d) Re-scaled thickness profiles for a variety of inclination angles (coloured curves). Plotted are 40 curves over 100 s intervals for $\alpha = 60°$; 37 curves over 100 s intervals for $\alpha = 30°$; 29 curves over 590 s intervals for $\alpha = 9°$; and the Jeffreys similarity solution (12) predicted by lubrication theory (black line).

and effective viscosity (equation (13)). For each volume fraction, the viscosity is computed using the Einstein relation

$$\mu(\phi) = \mu_f(1 + \frac{5}{2}\phi),$$

which has an error that is $O(\phi^2)$ [Bonnoit et al., 2010a]. Because the particles and fluid are density matched in our system, we simply take $\rho = \rho_f$.

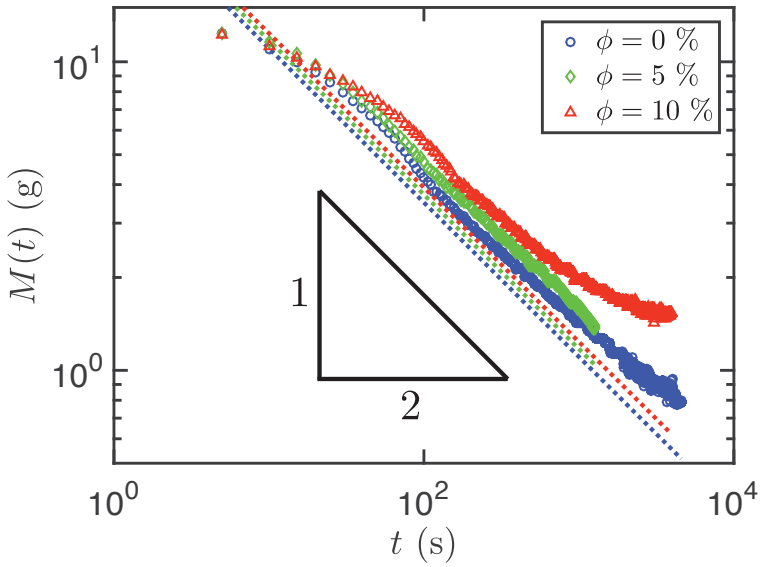

Figure 6: Drainage dynamics of suspensions of polystyrene particles in PEG (radius $R = 250\,\mu\text{m}$, $\alpha = 90°$). Experimental results are shown for increasing particle concentration (symbols), together with the corresponding prediction for a Newtonian fluid with the same effective viscosity (dashed lines). The initial mass of suspension in each case is the same and equal to $M(0) = 12.7 \pm 0.1\,\text{g}$.

At a volume fraction $\phi = 5\,\%$, the suspension still seems to behave as a Newtonian fluid: the drainage obeys a $t^{-1/2}$ power-law for $t \gtrsim 80\,\text{s}$, just as with the case $\phi = 0$. The increase in the pre-factor is consistent with that predicted by the Einstein relation. In particular, the error in the pre-factor is the same order as the corresponding error observed at $\phi = 0\,\%$. (This error is presumably due to variations in the fluid viscosity from the reported value, resulting from changes in temperature and absorption of water into the PEG). Note that while the experiment was stopped after 1275 s, this is after the time when we expect capillary interactions to become important, which from equation (15) is predicted to be at $\approx 250\,\text{s}$ when $\alpha = 90°$. The volume fraction in this case is therefore too low for capillary interactions to cause a noticeable effect, with particles producing only a bulk effect on the suspension viscosity.

At $\phi = 10\,\%$, however, a very different picture is seen: the mass decays as $t^{-1/2}$ only up to around 600 s, after which the drainage rate decelerates. This corresponds to fluid remaining on the plate rather than draining into the tray. We note that the transition time $t \approx 600\,\text{s}$ is consistent with the loss of validity of the Jeffreys solution predicted by

equation (15), so we expect the deviation observed here is due to capillary interactions. We re-emphasize that this behavior cannot be captured using a Newtonian model with any effective viscosity, since this always yields a straight line with slope $-1/2$. By the end of the experiment (time 3920 s), around 12 % of the initial mass remains on the plate compared to 7 % when no particles are present.

3.2.1 Particle dynamics

To gain insight into this phenomenon, we examine the behavior of particles in the film. Figure 7 shows example snapshots of a drainage experiment. Initially, the film thickness is larger than the particle diameter, as indicated by the color at $t = 0$ appearing a dark shade of blue due to the added dye (here the particles appear as light blue circles, with those closer to the free surface appearing brighter). As the film begins to drain ($t = 0$–150 s), indicated by lighter shades of blue, the particles are advected downstream but remain fully immersed in fluid. This is the regime where the suspension acts as a Newtonian fluid.

This regime breaks down when the film thickness reaches the order of the particle size. Figure 7 ($t = 200$–600 s) shows how particles are attracted to each other and form two-dimensional clusters. These aggregates first form at the top of the plate, where the film is thinnest, before appearing downstream. Eventually, the clusters become deposited onto the plate where they remain indefinitely. The key observation here is that a small amount of fluid continues to wet the particles, as seen on the photos by the dark rings that surround each particle or cluster of particles ($t = 1660$ s). This fluid is "trapped" and does not leave the plate: while we stopped recording the drainage at the last photo in figure 7, other experiments left overnight show no visible change in the clustering patterns, with fluid still trapped around the particles.

On the scale of the particles, the importance of inertial forces is measured by the particle Reynolds number $\mathrm{Re}_p = \rho_f u R/\mu_f$, while the particle Bond number $\mathrm{Bo}_p = \rho_p g R^2/\gamma$ measures the ratio of gravity to surface tension forces [Kao and Hosoi, 2012]. Note these differ from the Reynolds number and Bond number described in §3.1.1, which are relevant on the larger scale of bulk fluid drainage. Using the velocity scale $u \sim \rho_f g h^2 \sin\alpha/\mu$ predicted by lubrication theory (see equation (14)), we find that for our experimental system $\mathrm{Re}_p = O(10^{-3})$ and $\mathrm{Bo}_p = O(10^{-2})$. We deduce that capillary forces dominate the behavior of the particles as they deform the free surface of the film. It is these forces which cause clustering and deposition of particles.

The formation of clusters is well-known to occur for particles floating at an air-liquid interface, which is called the "Cheerios effect" [Vella and Mahadevan, 2005] after the tendency of breakfast cereal floating on the surface of milk to aggregate. Its origin is an attractive force that exists between similar floating particles, as the fluid interface deforms to provide a vertical surface tension force that balances the bouyancy force on the particles. In our experiments the particles are not freely floating but are partially immersed in a liquid film. Nevertheless, an analogous attractive force exists in this situation [Kralchevsky and Nagayama, 1994] despite the fact that the particles are supported by a substrate and so buoyancy forces are no longer relevant. The deformation of the interface is instead driven by wetting effects at the particle surface, as with the usual meniscus effect. The attractive force therefore scales much more weakly with the particle radius (more precisely, $\sim R^2$ rather

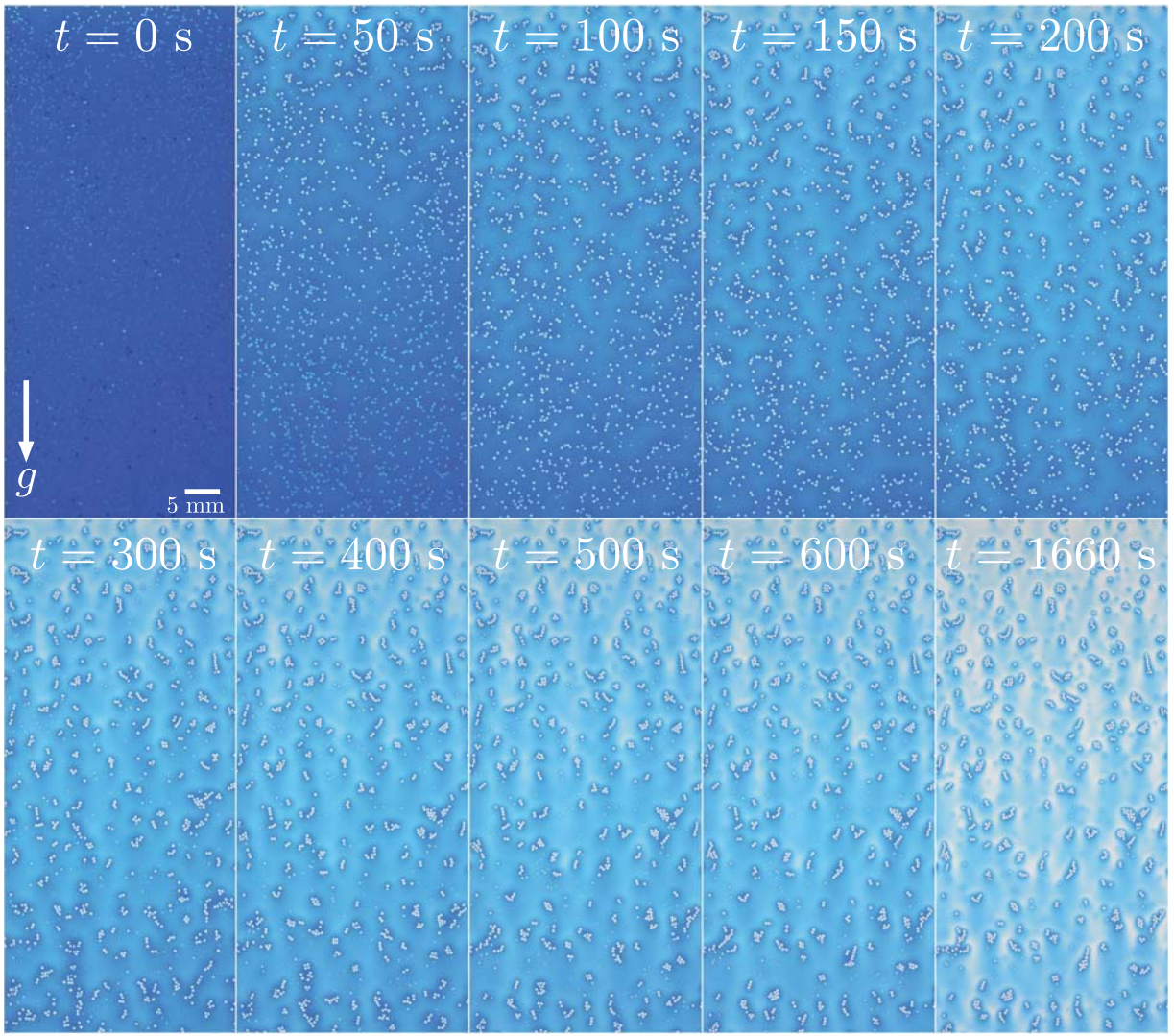

Figure 7: Drainage of a suspension of particles ($R = 250\,\mu$m, $\phi = 5\,\%$, $\alpha = 90°$). The time $t = 0$ corresponds to the point where the plane is first tilted from a horizontal state and drainage begins. Particles can be identified as the white circles in each photo.

than $\sim R^6$ for floating particles) and is several orders of magnitude larger for particles less than a centimeter in size [Denkov et al., 1992]. This attractive force is the mechanism behind the clustering patterns observed here, and also in the studies of Kao and Hosoi [2012] and Buchanan et al. [2007].

We have seen that lateral capillary forces cause particles to form monolayer clusters. The forces also have normal components that act to press particles into contact with the plane, where they become stabilized by friction. This explains why more fluid becomes trapped on the plate at higher volume fractions: as more particles are eventually deposited, more fluid continues to wet the particles rather than draining into the tray. However, it is clear from figure 6 that this effect does not scale linearly with the volume fraction ϕ, as the impact on the drainage at $\phi = 10\,\%$ is much more than double that at $\phi = 5\,\%$. A possible explanation is that a particle traps a different amount of fluid depending on the size of the cluster that the particle is in, or whether it is isolated from other particles. This would mean that the trapping effect depends non-linearly on the distribution of cluster sizes, and hence the volume fraction ϕ. Indeed, at $\phi = 10\,\%$ we observe that more particles are in clusters, and clusters generally consist of more particles compared to $\phi = 5\,\%$.

4 Deposition of particles

The drainage experiments in §3.2 motivate a more careful examination of the amount of fluid trapped by particles as they are deposited on the plane. However, the clustering dynamics of particles represent an extremely complicated physical system. As a first step towards understanding the mechanisms involved, we instead turn to the question: when is a single particle first deposited? Throughout this section, we focus on very small volume fractions ($\phi < 1\,\%$) so that particles rarely interact but behave as isolated hard spheres.

4.1 A single particle

Consider the forces acting on a single particle moving in the flow. At early times, the particle is completely immersed in fluid and is advected downstream as the surrounding fluid drains. The particle experiences only fluid drag forces F_d (and possibly torques) as shown schematically in figure 8a. We note this situation differs to a negatively buoyant sphere rolling in fluid down an inclined plane [Smart et al., 1993]; as the particle here is neutrally buoyant, it experiences only drag forces due to its finite size.

At some later time, the local fluid thickness decreases below the diameter of the particle. Assuming that fluid continues to wet the particle surface, the liquid interface is therefore deformed by the particle (figure 8b). A capillary force F_γ resists this deformation. Because the particle is much smaller than the length of the glass plate L, the length scale over which variations in the fluid thickness occur, the liquid away from the particle can be considered to be uniform and parallel to the plane. As the capillary force acts normal to the undisturbed shape [Colosqui et al., 2013], it must act normal to the plane. We note that there is also a possible gravitational force acting on the particle (not drawn), because only the lower part of the particle is immersed in bulk fluid where it is neutrally buoyant.

At this stage in its motion, the particle has not necessarily made contact with the plane: there is a possible squeeze film underneath the particle. To be deposited on the substrate,

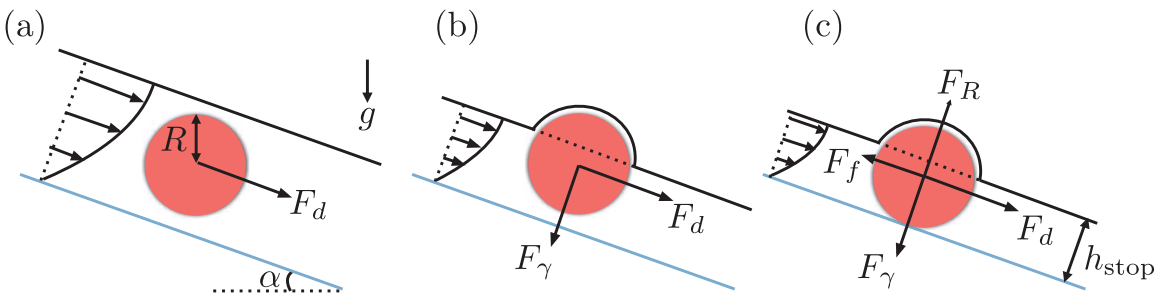

Figure 8: The various forces acting on a single particle as it (a) moves in bulk fluid; (b) is moving but deforms the fluid interface; and (c) is deposited onto the substrate.

the normal capillary force has to overcome the lubrication pressure in this film to establish solid-solid contact (in practice, this requires decreasing the film thickness to the order of surface roughness). This yields a normal reaction force F_R, and a frictional force F_f that acts upstream; see figure 8c. Fluid drag forces continue to act downstream, as fluid is still draining around the particle. The frictional force arising from the capillary force is therefore the *only* possible opposing force which brings the particle to equilibrium.

As the surrounding film drains, the normal capillary force will increase (because the interface becomes more deformed) so the resulting frictional force increases. Meanwhile, the fluid drag force decreases (because the drainage decelerates, and the area of the sphere immersed in bulk fluid decreases). Hence, we expect the particle is first deposited when the local thickness drops below a critical value $h_{\text{stop}} < 2R$. We note that studies usually make assumptions about the size of h_{stop} in drainage flows [Buchanan et al., 2007, Colosqui et al., 2013]. Despite the need to separate particles from a background fluid in many industrial processes [Davis and Acrivos, 1985], we are not aware of any systematic experiments relating h_{stop} to the particle size.

4.1.1 Experiments

Qualitatively speaking, we find that h_{stop} is very sensitive to the angle at which the plane is inclined. At small angles, particles are first deposited when $h_{\text{stop}} \approx 2R$. At larger angles, h_{stop} is generally much smaller and, depending on their initial position in the film, particles are able to undergo much larger displacements. This is evident in figure 9, which compares example trajectories for inclination angles $\alpha = 16.7°$ and $\alpha = 73.9°$.

We can understand this trend using the picture presented in figure 8. The fluid drains faster at larger angles and hence, for a given fluid thickness, the drag force exerted on the particle is larger. There is also a larger downstream component of gravity. It follows that a larger capillary force is needed to bring the particle to rest, which arises from a smaller local fluid thickness, when the liquid interface becomes more deformed as it wets the particle.

To further explore the dependence of h_{stop}, we performed systematic experiments over a variety of inclination angles α and particle radii R. Our procedure is as follows. For each experiment, we zoom in on the motion of a particle (away from any contact lines and other particles) and determine the first instant at which it comes to rest; this "capture" point is labeled for the example trajectories in figure 9. A particle is considered to be at rest if its

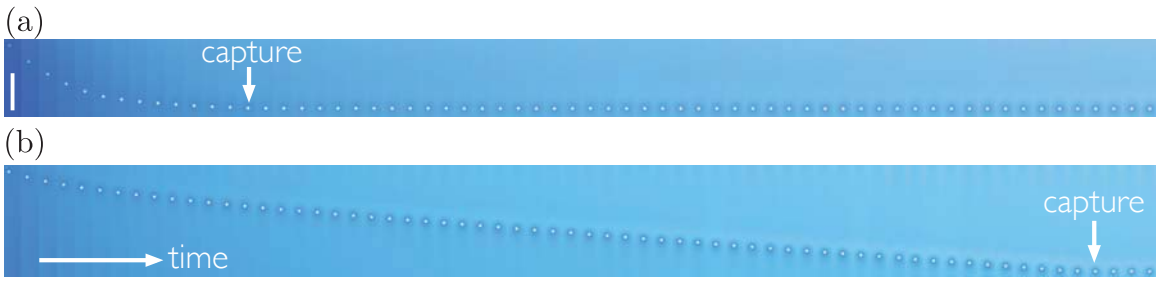

Figure 9: Spatio-temporal plots of individual particles reveals their trajectories in draining films (radius $R = 250\,\mu\text{m}$). In each plot, a total of 64 snapshots separated by 10 s are shown. Scale bar 5 mm. (a) At an inclination angle $\alpha = 16.7°$, a particle (seen as a white circle) is quickly deposited. (b) At a larger angle $\alpha = 73.9°$, the particle is only deposited when the local thickness is much smaller compared to its diameter (indicated by a lighter fluid region), allowing it to travel much further downstream.

displacement from the last photo in the image sequence is less than 1 pixel. We then crop the fluid region around the particle and determine the local film thickness at the moment of capture; an example is shown in figure 10a. We measure the capture thickness by averaging the thickness over an annulus centered on the particle, with inner and outer radii $(2R, 4R)$. By averaging over an annulus, we avoid inaccurate results from the intensity method due to the curvature of the interface very close to the particle. The choice $2R$ ensures the interface in the annulus is always close to flat, and we have checked that our results are not sensitive to the precise choice of annulus used for averaging. By repeating this process for around 10–20 particles, we obtain a particle-averaged value of h_{stop}; see figure 10b.

As anticipated, we find that the capture thickness h_{stop} generally decreases as the inclination angle increases; see figure 11a, which plots h_{stop} as a function of $\sin\alpha$ for different particle radii. However, due to the large variation in the measured values (shown by the error bars), it is difficult to identify a clear trend in the data. In both cases, the relationship appears to be non-monotonic, with possible turning points in h_{stop} located at $\sin\alpha \approx 0.5$ and $\sin\alpha \approx 0.7$. For a smaller particle radius the values of h_{stop} are uniformly lower, with all values found to be below the particle diameter, as expected.

Figure 11a also shows that the capture thickness for the different radii are roughly equal when $\alpha = 90°$; this angle therefore corresponds to where h_{stop} scales weakly with the radius. In fact, the relationship here is very close to linear; see figure 11b, which plots h_{stop} as a function of R for four different particle sizes. A least-squares fit yields $h_{\text{stop}} \approx CR^{0.91}$. However, this scaling law is not obeyed at smaller angles, as it fails to collapse the remaining data points presented in figure 11a, even if the variation is accounted for.

4.1.2 Model

We would like a model that predicts the observed dependence of h_{stop} on α and R. Returning to the picture presented in figure 8, we see the challenge in modeling the dynamics of a single particle. As the particle is captured, there are three relevant timescales in the problem. These are the timescale over which the bulk fluid away from the particle drains

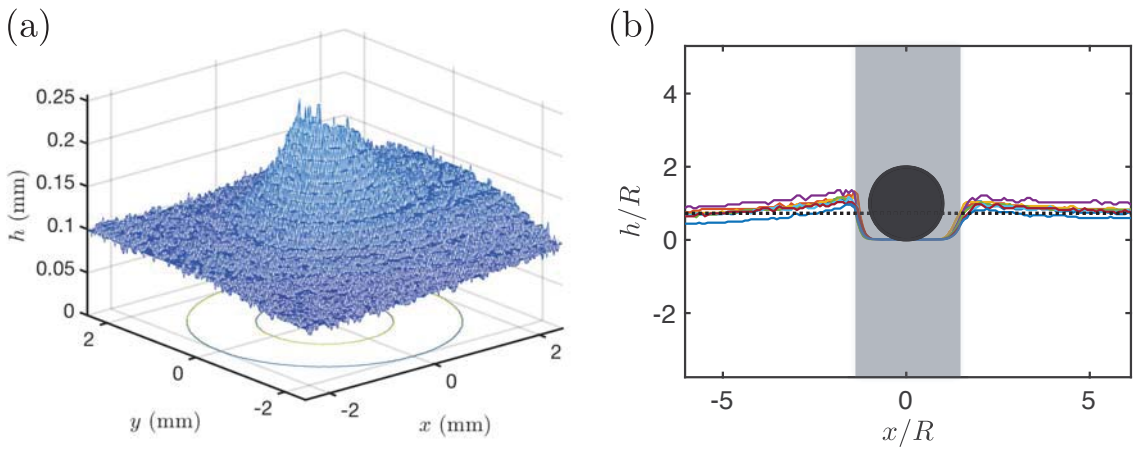

Figure 10: Finding the local fluid thickness upon capture, h_{stop} (radius $R = 250\,\mu\text{m}$, $\alpha = 41.7°$). (a) When a particle becomes captured, the light intensity method yields a surface plot of the local fluid thickness. Here the center of the particle is placed at the origin and the z–axis is exaggerated for clarity. The annulus $(2R, 4R)$ used for averaging is also shown, which gave $h_{\text{stop}} = 0.123\,\text{mm}$ in this case. (b) Profiles of the fluid interface along the line $y = 0$ (colored solid lines), scaled by the particle radius. Data is shown for 8 particles, together with the value $h_{\text{stop}} = 0.182\,\text{mm}$ determined by averaging (black dashed line). The shaded region is where the light intensity method does not give accurate results due to the large interface curvature.

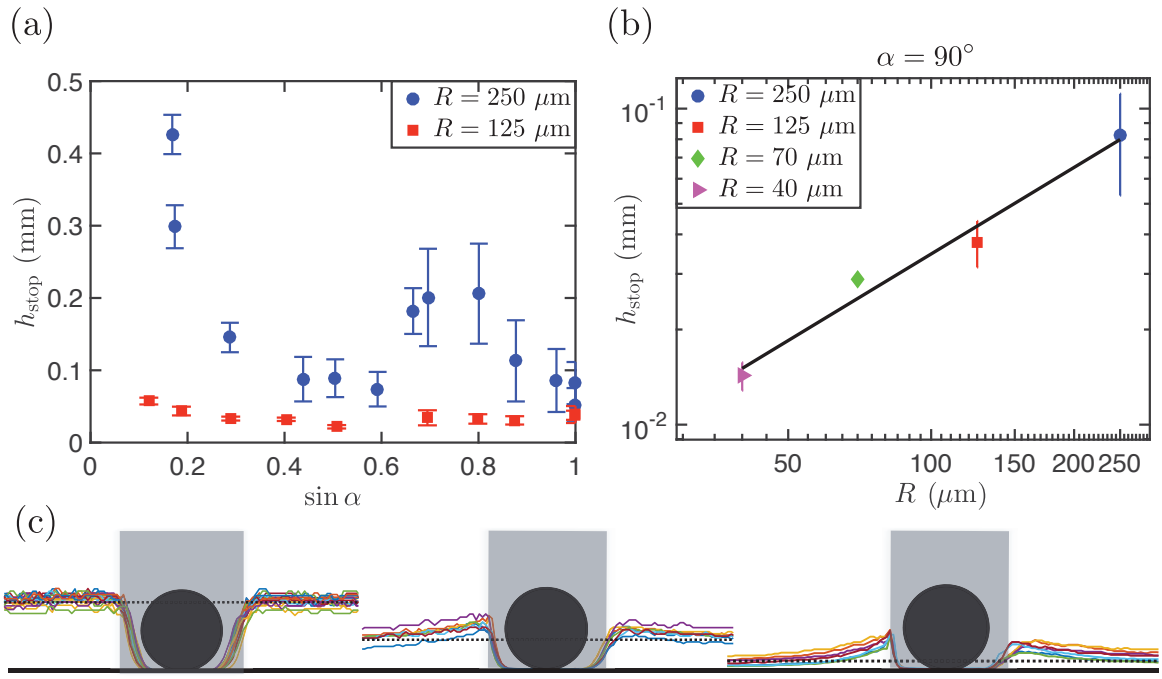

Figure 11: Variation of the particle-averaged capture thickness h_{stop}. (a) Dependence of h_{stop} on the inclination angle α. Vertical error bars correspond to one standard deviation of the measured values for approximately 10 particles. (b) Dependence of h_{stop} on the particle radius R together with the least-squares fit (black line). (c) Profiles of the fluid interface upon capture ($R = 250\,\mu$m) for $\alpha = 9.7°$ (left), $\alpha = 41.7°$ (middle) and $\alpha = 89.6°$ (right). Also shown are the corresponding value of h_{stop} (black dashed lines), equal to $h_{\mathrm{stop}} = 0.426\,$mm ($\alpha = 9.7°$), $h_{\mathrm{stop}} = 0.182\,$mm ($\alpha = 41.7°$) and $h_{\mathrm{stop}} = 0.052\,$mm ($\alpha = 89.6°$). The shaded region is where the light intensity method does not give accurate results due to the large interface curvature.

(described by lubrication theory); the timescale over which fluid that wets the particle reaches an equilibrium state; and the timescale to squeeze out fluid underneath the particle to establish solid-solid contact. The presence of the free surface means that solving for the fluid flow around the particle is difficult and remains an active area of research [Bico et al., 2009]. In light of this, we consider only when the particle has made contact with the plane. We aim to use a static force balance to determine when an equilibrium state is possible in terms of the local fluid thickness.

A key observation is that at small angles, the particle is deposited before a well-defined meniscus is able to form around the particle. This is evident in figure 11c, which compares the fluid profiles around deposited particles for different angles α. Notice how at small angles (*i.e.* $\alpha \lesssim 40^\circ$), the interface is deformed only in a small region around the particle. At larger angles, where h_{stop} is smaller, the interface becomes increasingly curved and more fluid is lifted up as it wets the particle. At small angles, we therefore assume that a thin film coats the entire top surface of the particle, rather than fluid dewetting and forming a contact line along its surface. This enables us to write down a simple model in this regime.

We neglect the gravitational force on the particle: at small angles h_{stop} is close to the diameter $2R$, so most of the sphere remains immersed in bulk fluid where it is neutrally buoyant. The tangential component of the fluid drag must therefore balance the frictional force exerted by the plane (see figure 8c), *i.e.* $F_d = F_f$. A force balance normal to the plane shows that the reaction force, F_R, is equal to the capillary force, F_γ (assuming the normal component of the fluid drag is small). Assuming a Coulomb friction law, we then have $F_f \leq K_f F_\gamma$ where K_f is the coefficient of friction between the particle and the plane. When the particle is first deposited, *i.e.* when the local thickness reaches h_{stop}, we have equality in this relation so that

$$F_d = K_f F_\gamma. \tag{16}$$

We now need to estimate the forces F_d and F_γ.

Assuming the particle remains fully wetted, the capillary force arises from a Laplace pressure in the thin film that coats the particle, which acts to press the particle onto the plane; there is no contact line force. This film coats a spherical cap that deforms the liquid interface (figure 8c). Provided the film is very thin compared to the particle size, the height of the cap is approximately $2R - h_{\text{stop}}$. Moreover, we expect the film to roughly adopt the spherical shape of the cap: the Bond number $\text{Bo}_p = O(10^{-2})$ is small, so gravity is unimportant on the particle scale. This gives a Laplace pressure which scales as $p_c \sim 2\gamma/R$. Integrating the pressure over the area of the spherical cap then gives

$$F_\gamma \sim 4\pi\gamma h_{\text{stop}} \left(1 - \frac{h_{\text{stop}}}{2R}\right).$$

This generalizes the capillary force calculated by Colosqui et al. [2013] in two dimensions for a partially immersed cylinder near a wall. Note that our model predicts that $F_\gamma \to 0$ as $h_{\text{stop}} \to 0$, as contributions of the Laplace pressure on either side of the particle cancel as it approaches a full sphere. This corresponds to the current regime breaking down as the shape of the liquid meniscus needs to be considered.

The expression for the fluid drag F_d is complicated by the presence of the plane, the coating film, and the fact that the sphere is only partially immersed in fluid. Following

Lubbers et al. [2014], we assume that the drag scales as the average shear stress in the fluid multiplied by the reference area A, *i.e.* the projected area of the sphere immersed in bulk fluid. For our system, this reads

$$F_d \sim \frac{\mu_f u_{\mathrm{avg}}}{h_{\mathrm{stop}}} A,$$

where u_{avg} is the average fluid velocity when the local thickness has reached h_{stop}. From the lubrication analysis (see equation (14)), and using $\rho = \rho_f$ and $\mu \approx \mu_f$ for the small volume fractions here, this is given by

$$u_{\mathrm{avg}} \sim \frac{\rho_f g h_{\mathrm{stop}}^2 \sin\alpha}{\mu_f}.$$

The portion of the sphere immersed in bulk fluid is a spherical cap of height h_{stop}. Simple geometry then gives that

$$A = R^2 \left[\cos^{-1}\left(1 - \frac{h_{\mathrm{stop}}}{R}\right) - \left(1 - \frac{h_{\mathrm{stop}}}{R}\right) \sqrt{1 - \left(1 - \frac{h_{\mathrm{stop}}}{R}\right)^2} \right]$$

This expression equals $A = \pi R^2$ when the sphere is completely immersed, $h_{\mathrm{stop}} = 2R$, and decreases for values $h_{\mathrm{stop}} < 2R$. Finally, returning to the force balance (16), we re-arrange to find that

$$f\left(\frac{h_{\mathrm{stop}}}{R}\right) = \frac{\rho_f}{\rho_p} \frac{\mathrm{Bo}_p \sin\alpha}{4\pi K_f}, \tag{17}$$

where $\mathrm{Bo}_p = \rho_p g R^2/\gamma$ is the particle Bond number, and we have introduced the geometric function

$$f\left(\frac{h_{\mathrm{stop}}}{R}\right) = \frac{1 - h_{\mathrm{stop}}/(2R)}{\cos^{-1}\left(1 - h_{\mathrm{stop}}/R\right) - \left(1 - h_{\mathrm{stop}}/R\right)\sqrt{1 - \left(1 - h_{\mathrm{stop}}/R\right)^2}}.$$

To test the prediction (17), we plot $f(h_{\mathrm{stop}}/R)$ as a function of $(\rho_f/\rho_p)\mathrm{Bo}_p \sin\alpha$ using the experimental data reported in figure 11a. This is shown on log–log axes in figure 12. As we do not have data for the friction coefficient K_f, which is a property of contact between polystyrene and glass in PEG, we use K_f as a parameter to fit the data. At $R = 125\,\mu\mathrm{m}$, the points at small angles closely follow the linear relationship predicted by (17), with excellent agreement obtained with the fitted value of K_f over the five smallest angles used (corresponding to $\alpha \leq 30.5°$). However, at the larger size $R = 250\,\mu\mathrm{m}$, the points do not follow a linear trend and do not collapse onto the data for $R = 125\,\mu\mathrm{m}$: the fitted value of K_f in this case is around an order of magnitude larger. A possible explanation is that at a larger radius, gravitational forces mean that the coating film becomes unstable and does not closely follow a spherical cap in shape. In this case, a more detailed model would need to consider the local interface shape. Another possibility is that the coating film is dewetting the surface of the particle. This complication can be addressed in further experiments by using a fully wetting liquid (*i.e.* where the contact angle $\theta_c = 0°$) rather than PEG ($\theta_c = 46 \pm 5°$)

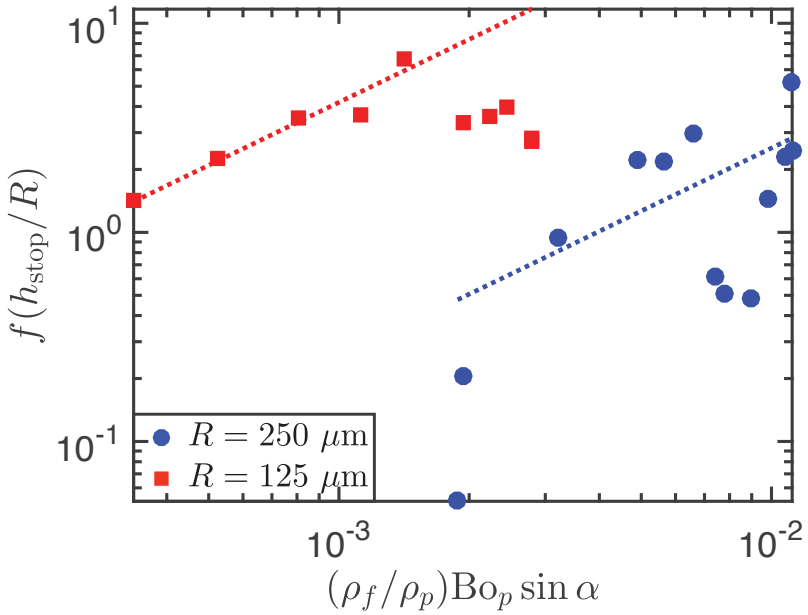

Figure 12: The same experimental data in figure 11a, re-scaled according to predicted relationship (17). Also plotted is the least-squares linear fit over the first 5 points in each case (dashed lines), which correspond to taking $K_f \approx 3.1 \times 10^{-4}$ ($R = 250\,\mu\mathrm{m}$) and $K_f \approx 1.9 \times 10^{-5}$ ($R = 125\,\mu\mathrm{m}$).

5 Multiple particles: capillary sorting

In §4 we have seen that smaller particles are deposited at lower values of the local fluid thickness compared to larger ones. In a draining film, where all particles are advected downstream, this means that smaller particles will naturally come to rest further downstream; in other words, smaller particles can continue to flow in regions where larger particles are already deposited. In this final section, we show how this can be exploited for a novel *capillary sorting scheme*: a passive separation of particles based on their sizes.

5.1 Experiments

We have performed experiments on suspensions containing a mixture of two particle sizes. Just as in the capture experiments discussed in §4.1.1, we focus on the combination $R = 250\,\mu\text{m}$ and $R = 125\,\mu\text{m}$ at very low volume fractions ($\phi \leq 2\,\%$ for each size) to minimize the clustering of particles, so they mostly behave as isolated spheres. Before the plane is tilted, the particles are distributed homogeneously in a thin band of fluid upstream, lying between $x = 0$ and $x = 2\,\text{cm}$. The rest of the glass plate is wetted with pure fluid. As the film drains, the particles move downstream and are deposited at different locations along the substrate, depending on their size and initial position in the film.

An example of a sorting experiment is shown in figure 13, which displays snapshots of the fluid region during drainage. We see that large particles are almost entirely captured in the top third of the plate, while the smaller particles are able to penetrate the entire length of the plate before being captured. The lower part of the plate therefore contains almost exclusively smaller particles. This is confirmed by the distribution of the capture positions; see figure 14a. These positions have been determined once all particles on the plate come to rest, with image analysis performed in MATLAB using the routine `imfindcircles` (part of the Image Processing Toolbox). Note that the distribution in each case is non-uniform because particles are initially at different depths in the film; we know from the lubrication analysis in §3.1.1 that particles closer to free surface move faster, so these are able to undergo larger displacements.

5.1.1 Model

To understand the sorting effect in a quantitative way, we formulate a simple model for the dynamics of the particles. We assume that each particle acts as a passive tracer up to the point of being captured, following the local fluid velocity in the draining film. Particles are considered to be captured when the local value of the fluid thickness decreases below the critical threshold h_{stop}. Once captured, particles remain at their capture position indefinitely. This model neglects all finite-size effects, including hydrodynamic interactions with other particles; fluid drag forces and capillary forces only enter in determining the value of h_{stop}. We aim to model only the bulk separation effect without considering the detailed dynamics of individual particles.

Under these assumptions, the trajectory of a single particle, labeled $\mathbf{x} = x(t)\mathbf{e}_x + z(t)\mathbf{e}_z$ (using the same notation as in §3.1.1), is given by $\mathrm{d}\mathbf{x}/\mathrm{d}t = \mathbf{u}(x(t), z(t), t)$ where $\mathbf{u}(x, z, t)$ is the fluid velocity. The velocity is evaluated using the lubrication model considered in §3.1.1 and given by equation (14), taking $\rho = \rho_f$ and $\mu = \mu_f$ due to the very low volume fractions

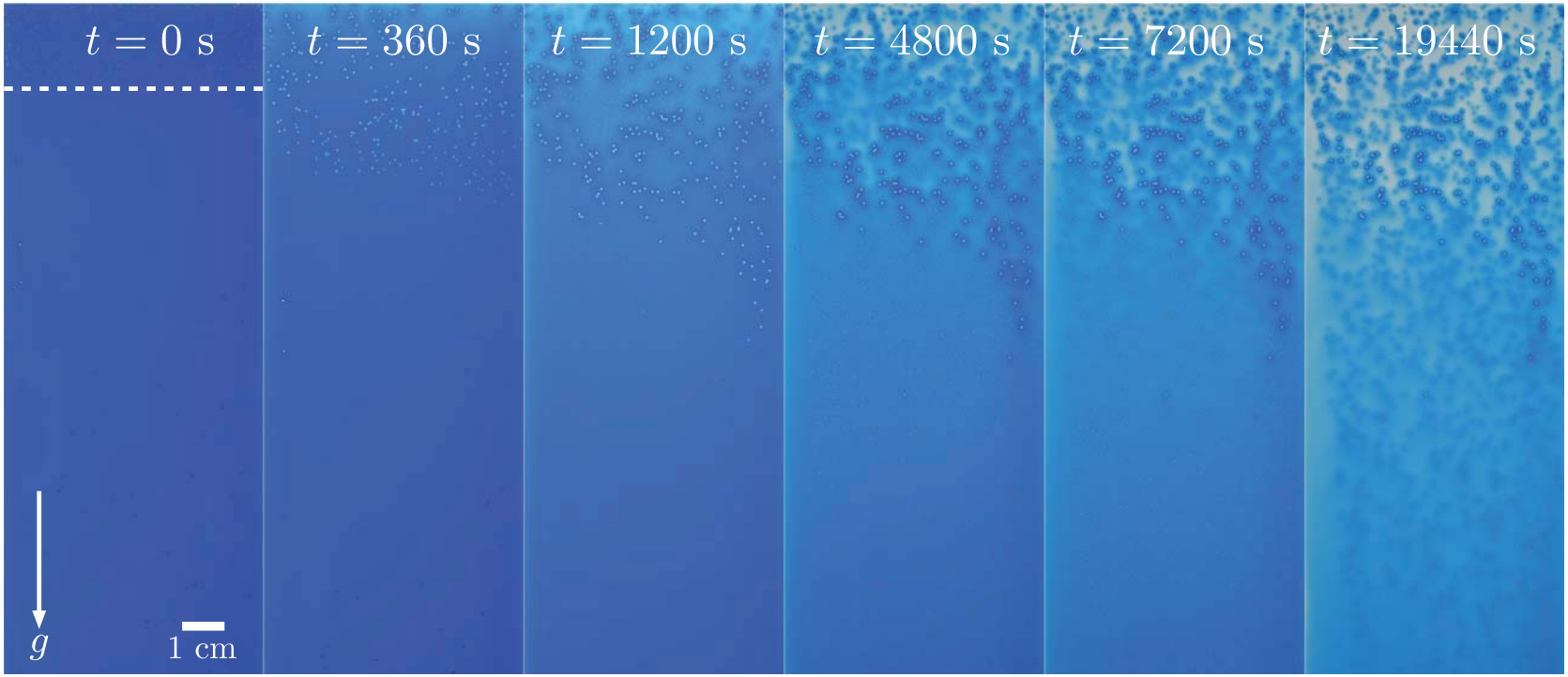

Figure 13: A capillary sorting experiment: particles of two different sizes, initially mixed together in a thin region upstream (above the white dashed line), become separated as they are captured on the plane ($\alpha = 5°$, initial film thickness $h_0 = 1\,\text{mm}$). The particles have radius $R = 250\,\mu\text{m}$ (volume fraction $\phi = 2\,\%$) and radius $R = 125\,\mu\text{m}$ (volume fraction $\phi = 1\,\%$). The time $t = 0$ corresponds to the point where the plane is first tilted from a horizontal state and drainage begins. Particles can be identified as the white circles of differing size in each photo (see also online version).

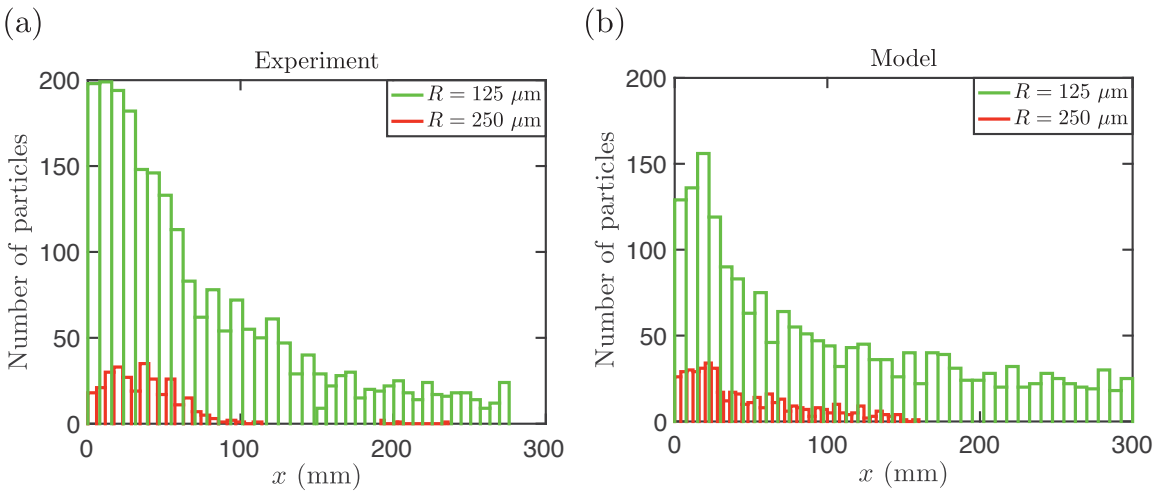

Figure 14: (a) Distribution of the capture positions for the capillary sorting experiment shown in figure 13. (b) Predicted distribution using the passive tracer model with capture condition $h_{\text{stop}} = 2R$.

considered here. In component form, the trajectory therefore obeys for $h > h_{\text{stop}}$

$$\frac{\mathrm{d}x}{\mathrm{d}t} = \frac{\rho_f g \sin\alpha}{2\mu_f} z(2h - z) \tag{18}$$

$$\frac{\mathrm{d}z}{\mathrm{d}t} = -\frac{\rho_f g \sin\alpha}{2\mu_f} z^2 \frac{\partial h}{\partial x}. \tag{19}$$

For $h \le h_{\text{stop}}$, we simply set $\mathrm{d}\mathbf{x}/\mathrm{d}t = \mathbf{0}$.

The free surface height $h(x,t)$ evolves according to the simplified thin-film equation (11). Assuming a uniform initial shape $h(x,0) = h_0 =$ constant, as is approximately the case in our experiments, this equation may be solved exactly using the method of characteristics. The solution is

$$h = \begin{cases} h_0 & \text{for} \quad t \le \frac{\mu x}{\rho g h_0^2 \sin\alpha}, \\ \left(\frac{\mu_f x}{\rho_f g t \sin\alpha}\right)^{1/2} & \text{for} \quad t > \frac{\mu_f x}{\rho_f g h_0^2 \sin\alpha}. \end{cases} \tag{20}$$

Note that the Jeffreys similarity solution is an exact solution at late times in this case.

Equations (18)–(19) represent a coupled set of nonlinear ordinary differential equations in time. For each particle, we integrate the equations numerically in MATLAB using the routine `ode113`, with event location to stop integration once the capture thickness is reached. At each time step, $h(x,t)$ is evaluated using the exact solution given in equation (20). As initial conditions, we assume that particles are distributed randomly in the region $0 < x < 2\,\text{cm}$ and $0 < z < h_0$, as in our experiments. The number of particles used in the model is simply that predicted by the volume fraction used. We integrate up to stage when all particles are deposited on substrate.

To compare the model with the experimental data in 14a, we need to specify a value of the capture thickness h_{stop}. In the absence of a reliable model for the size of h_{stop}, we instead

use the fact that the inclination angle used in the experiment was very small ($\alpha = 5°$). From §4, we know that for small angles h_{stop} is close to the diameter of the particle, so here we take $h_{\text{stop}} = 2R$ in our model. With this condition, we obtain relatively good agreement between experiments and model for the capture positions; see figure 14b. Qualitatively, the model captures the shape of the distribution for each particle size. This includes the peak at $x \approx 50\,\text{mm}$ for $R = 250\,\mu\text{m}$, and the long-tailed distribution for $R = 125\,\mu\text{m}$, which peaks around $x = 0$ and extends across the whole length of the plate. However, there are quantitative differences. For $R = 250\,\mu\text{m}$, the model overestimates the right tail of the distribution, *i.e.* how far the larger particles are able to move downstream. This is also the case for $R = 125\,\mu\text{m}$, meaning the model under predicts the number of smaller particles caught near $x = 0$. We expect this is mainly because the model neglects the drag force of each particle prior to being captured. As a result, it naturally overestimates how far each particle moves.

6 Conclusions

In this report, we have studied a particle-laden thin film flowing down an inclined plane. We focused on the case of non-colloidal, neutrally buoyant spheres at relatively low concentrations, well away from maximum packing, so that effects such as sedimentation and jamming can be ignored. This means that while the particles remain fully immersed in bulk fluid, the suspension acts as a Newtonian fluid with an effective viscosity that scales linearly with the volume fraction (the Einstein relation). In this regime, the drainage evolves according to the well-known Jeffreys similarity solution, with the mass on the plate following the power-law $M(t) \propto t^{-1/2}$.

We have demonstrated experimentally that this classic behavior breaks down when the thickness of the film reaches the order of the particle size. As particles deform the free surface, capillary forces dominate their motion, causing the formation of clusters which become deposited onto the plane. A meniscus of fluid continues to wet each particle, and so these clusters "trap" fluid from flowing downstream. It seems that a critical concentration of particles is needed for an observable effect: at a volume fraction $\phi = 5\,\%$ we found almost no change, while at $\phi = 10\,\%$ the drainage proceeded much slower than $t^{-1/2}$, with over $50\,\%$ more mass remaining on the plate at the end of the experiment compared to when no particles were present. The main difference between these two cases is that at $\phi = 10\,\%$, more particles are in clusters rather than separated from other particles, and the cluster sizes are generally larger. It makes interesting further work to explore in detail how the impact on the drainage scales with ϕ, relating this to the statistics of the cluster sizes.

We then considered when an isolated particle is first deposited, or "captured", under the action of capillary forces. This occurs when the thickness of the film surrounding the particle decreases past a threshold $h_{\text{stop}} < 2R$. We showed that h_{stop} depends sensitively on the angle α at which the plane is inclined, decreasing by up to a factor of 4 as α varies from $9.7°$ up to $90°$. However, our experiments showed large variation in the values of h_{stop}, so that it was not possible to identify a clear scaling law in the data. As far as we are aware, these are the only systematic experiments into the size of h_{stop}, despite the fundamental nature of this problem and its relevance to industrial processes.

By analyzing the profiles of the fluid interface, we found that at small angles the particles

are deposited before a well-defined meniscus is able to form. This enabled us to formulate a simple model for the normal capillary force acting on an individual particle. The model predicts well the dependence of h_{stop} on α for smaller particles ($R = 125\,\mu\text{m}$) at angles $\alpha \lesssim 30°$. The model fails to fit the experimental data at larger angles, and also fails for larger particles ($R = 250\,\mu\text{m}$). One possible explanation is that in these cases, the flow of fluid in the film coating the particle becomes important: an essential assumption in our model is that the coating film adopts the spherical shape of the particle, which may be invalid for large angles and larger particle radii. This would also explain the variation observed in the data, which seems to be largest in the cases where the model does not work well. If the dynamics of the coating film becomes important, then the capillary force acting on a particle would depend on its previous motion in the film, leading to a variation in the values of h_{stop}. Unfortunately, the spherical shape of the particles means a complete model for the fluid flow is extremely difficult. To get a grasp on relative sizes of the many timescales in the problem, it might be helpful to study the simplified case of a cylinder moving in a two-dimensional fluid. Another possibility is that the coating film is dewetting and forming a contact line along the surface of the particle. Further experiments using silicone oil, which is completely wetting, rather than PEG would clarify this issue.

One result which is clear from our capture experiments is that the value of h_{stop} is lower for particles that are smaller is size. We used this fact to design a capillary sorting scheme: when two particles of different sizes are present, they will naturally separate as they are captured on the plane. We were able to recover the sorting effect using a simple model for the particle dynamics, which treats the particles as passive tracers moving in the fluid. As a first step towards a more detailed model, fluid drag forces and capillary forces could be treated in a parametrized way. The capillary sorting demonstrated here has promising potential for future applications, as no active mechanism is needed to separate the particles. While we used a fixed combination of particle sizes and volume fractions, further experiments could explore how the effect depends on these parameters, and also on the initial distribution of particles.

Acknowledgments

My experiments in the GFD laboratory would not have been possible without Anders Jensen, who was extremely helpful in building the setup we used throughout the summer. I am grateful to Ian Hewitt and Howard Stone for many helpful discussions on theoretical aspects. I'd also like to thank the other fellows for picking your brains throughout the summer, cooking me dinner every Tuesday (especially during the presentations week) and generally making it a memorable summer. Finally, Alban Sauret and Emilie Dressaire deserve special thanks: for introducing me to this topic, replying to all my emails, helping with experiments, and all their guidance over the weeks. Without your many trips to NYU to pick up equipment, this project would not have been possible!

References

D. J. Acheson. *Elementary fluid dynamics*. Oxford University Press, 1990.

J. D. Berry, M. J. Neeson, R. R. Dagastine, D. Y. C. Chan, and R. F. Tabor. Measurement of surface and interfacial tension using pendant drop tensiometry. *Journal of Colloid and Interface Science*, 454:226–237, 2015.

J. Bico, J. Ashmore-Chakrabarty, G. H. McKinley, and H. A. Stone. Rolling stones: The motion of a sphere down an inclined plane coated with a thin liquid film. *Physics of Fluids*, 21(8):082103, 2009.

C. Bonnoit, T. Darnige, E. Clement, and A. Lindner. Inclined plane rheometry of a dense granular suspension. *Journal of Rheology*, 54(1):65–79, 2010a.

C. Bonnoit, J. Lanuza, A. Lindner, and E. Clement. Mesoscopic length scale controls the rheology of dense suspensions. *Physical Review Letters*, 105(10):108302, 2010b.

C. Bonnoit, T. Bertrand, E. Clement, and A. Lindner. Accelerated drop detachment in granular suspensions. *Physics of Fluids*, 24(4):043304, 2012.

F. Boyer, É. Guazzelli, and O. Pouliquen. Unifying suspension and granular rheology. *Physical Review Letters*, 107(18):188301, 2011a.

F. Boyer, O. Pouliquen, and É. Guazzelli. Dense suspensions in rotating-rod flows: normal stresses and particle migration. *Journal of Fluid Mechanics*, 686:5–25, 2011b.

M. Buchanan, D. Molenaar, S. de Villiers, and R. M. L. Evans. Pattern formation in draining thin film suspensions. *Langmuir*, 23(7):3732–3736, 2007.

C. E. Colosqui, J. F. Morris, and H. A. Stone. Hydrodynamically driven colloidal assembly in dip coating. *Physical Review Letters*, 110(18):188302, 2013.

R. H. Davis and A. Acrivos. Sedimentation of noncolloidal particles at low Reynolds numbers. *Annual Review of Fluid Mechanics*, 17(1):91–118, 1985.

R. D. Deegan, O. Bakajin, T. F. Dupont, G. Huber, S. R. Nagel, and T. A. Witten. Capillary flow as the cause of ring stains from dried liquid drops. *Nature*, 389(6653):827–829, 1997.

N. Denkov, O. Velev, P. Kralchevski, I. Ivanov, H. Yoshimura, and K. Nagayama. Mechanism of formation of two-dimensional crystals from latex particles on substrates. *Langmuir*, 8(12):3183–3190, 1992.

A. Einstein. Zur theorie der Brownschen bewegung. *Annalen der Physik*, 324(2):371–381, 1906.

J. Fiegel, F. Jin, J. Hanes, and K. Stebe. Wetting of a particle in a thin film. *Journal of Colloid and Interface Science*, 291(2):507–514, 2005.

R. J. Furbank and J. F. Morris. An experimental study of particle effects on drop formation. *Physics of Fluids*, 16(5):1777–1790, 2004.

M. Ghosh, F. Fan, and K. J. Stebe. Spontaneous pattern formation by dip coating of colloidal suspensions on homogeneous surfaces. *Langmuir*, 23(4):2180–2183, 2007.

H. E. Huppert. Flow and instability of a viscous current down a slope. *Nature*, 300(5891): 427–429, 1982.

R. M. Iverson. The physics of debris flows. *Reviews of Geophysics*, 35(3):245–296, 1997.

J. C. Kao and A. E. Hosoi. Spinodal decomposition in particle-laden Landau-Levich flow. *Physics of Fluids*, 24(4):041701, 2012.

A. M. Keeley, G. K. Rennie, and N. D. Waters. Draining thin films — part 1. *Journal of Non-Newtonian Fluid Mechanics*, 28(2):213–226, 1988.

P. A. Kralchevsky and K. Nagayama. Capillary forces between colloidal particles. *Langmuir*, 10(1):23–36, 1994.

H. Lastakowski, F. Boyer, A.-L. Biance, C. Pirat, and C. Ybert. Bridging local to global dynamics of drop impact onto solid substrates. *Journal of Fluid Mechanics*, 747:103–118, 2014.

D. T. Leighton and A. Acrivos. The shear-induced migration of particles in concentrated suspensions. *Journal of Fluid Mechanics*, 181:415–439, 1987.

L. A. Lubbers, Q. Xu, S. Wilken, W. W. Zhang, and H. M Jaeger. Dense suspension splat: Monolayer spreading and hole formation after impact. *Physical Review Letters*, 113(4): 044502, 2014.

N. Murisic, J. Ho, V. Hu, P. Latterman, T. Koch, K. Lin, M. Mata, and A. L. Bertozzi. Particle-laden viscous thin-film flows on an incline: Experiments compared with a theory based on shear-induced migration and particle settling. *Physica D*, 240(20):1661–1673, 2011.

A. Oron, S. H. Davis, and S. G. Bankoff. Long-scale evolution of thin liquid films. *Reviews of Modern Physics*, 69(3):931, 1997.

F. R. Pranckh and L. E. Scriven. Elastohydrodynamics of blade coating. *AIChE Journal*, 36(4):587–597, 1990.

J. R. Smart, S. Beimfohr, and D. T. Leighton. Measurement of the translational and rotational velocities of a noncolloidal sphere rolling down a smooth inclined plane at low Reynolds number. *Physics of Fluids A*, 5(1):13–24, 1993.

B. D. Timberlake and J. F. Morris. Particle migration and free-surface topography in inclined plane flow of a suspension. *Journal of Fluid Mechanics*, 538:309–342, 2005.

D. Vella and L. Mahadevan. The Cheerios effect. *American Journal of Physics*, 73(9): 817–825, 2005.

C. Vernay, L. Ramos, and C. Ligoure. Free radially expanding liquid sheet in air: time- and space-resolved measurement of the thickness field. *Journal of Fluid Mechanics*, 764: 428–444, 2015.

T. Ward, C. Wey, R. Glidden, A. E. Hosoi, and A. L. Bertozzi. Experimental study of gravitation effects in the flow of a particle-laden thin film on an inclined plane. *Physics of Fluids*, 21(8):083305, 2009.

J. Zhou, B. Dupuy, A. L. Bertozzi, and A. E. Hosoi. Theory for shock dynamics in particle-laden thin films. *Physical Review Letters*, 94(11):117803, 2005.

Clusters, Confinement, and Collisions in Active Matter

Chris Miles

(advised by Michael J. Shelley and Saverio E. Spagnolie)

November 10, 2016

Abstract

Building upon the work of active suspensions by Saintillan and Shelley [12], we investigate the dynamics of clusters (localized concentrations of active matter) and the effects of confinement by considering active matter in a droplet. In addition, we show that the physics of binary collisions is absent from the Smoluchowki equation.

1 Introduction

Active matter consists of particles that consume energy to undergo motion or perform mechanical work. Examples of active matter include flocking, bacterial swarms, microtubules and kinesin, fish schools — just to name a few. In this work, we look at suspensions of 'pusher' and 'puller' swimmers (see figure 1) which model bacterial and microtubule-kinesin systems. There are many modeling approaches to self-propelled matter [7, 9, 15, 16], but we will focus on one approach introduced by Saintillan and Shelley [11–13]. We will investigate (1) clusters, localized concentrations of active matter in a droplet, (2) the effects of confinement on active matter, and (3) the assumptions made about binary collisions on the microscopic level to determine its impact on the Smoluchowski equation.

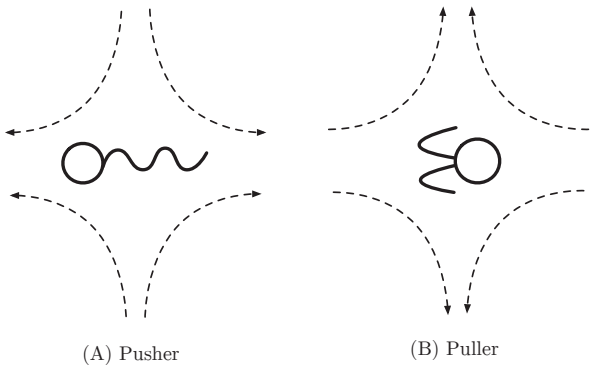

Figure 1: Flow field about (A) pushers and (B) pullers can be approximated as a flow generated by a force dipole.

2 Model

Following Saintillan and Shelley [12], we describe a suspension of N self-propelled rod-like particles within a fluid by the particle distribution function $\Psi(\mathbf{x}, \mathbf{p}, t)$ that evolves in time t through the Smoluchowski equation

$$\Psi_t + \nabla_{\mathbf{x}} \cdot (\dot{\mathbf{x}}\Psi) + \nabla_{\mathbf{p}} \cdot (\dot{\mathbf{p}}\Psi) = 0 \tag{1}$$

where $\mathbf{x}$ is the position, $\mathbf{p}$ is the particle orientation, and $\nabla_{\mathbf{p}} = (\mathbf{I} - \mathbf{pp}) \cdot \partial/\partial\mathbf{p}$. The fluxes $\dot{\mathbf{x}}$ and $\dot{\mathbf{p}}$ are given by

$$\dot{\mathbf{x}} = V_0\mathbf{p} + \mathbf{u}(\mathbf{x}) - d_t\nabla_{\mathbf{x}}(\ln\Psi) \tag{2}$$

$$\dot{\mathbf{p}} = (\mathbf{I} - \mathbf{pp}) \cdot (\mathbf{p} \cdot \nabla\mathbf{u}) - d_r\nabla_{\mathbf{p}}(\ln\Psi) \tag{3}$$

where d_t is the translational diffusion, d_r is the rotational diffusion, V is the swimming speed, and $\mathbf{u}(\mathbf{x}, t)$ is the fluid velocity. Equation (1) conserves the total number N of particles; More precisely, (1) implies

$$\int_\Omega \Psi(\mathbf{x}, \mathbf{p}, t) d\mathbf{p} d\mathbf{x} = N$$

for all time t. The fluid moves as a Stokes flow described by

$$-\nabla q + \mu\nabla^2\mathbf{u} + \nabla \cdot \mathbf{\Sigma}_a = \mathbf{0} \tag{4}$$

$$\nabla \cdot \mathbf{u} = 0 \tag{5}$$

where q is the fluid pressure, μ is the dynamic viscosity, and the active stress $\mathbf{\Sigma}_a$ imparted on the fluid by the suspended particles is given by the following mean-field approximation:

$$\mathbf{\Sigma}_a(\mathbf{x}) = \alpha \int_\Omega \Psi(\mathbf{x}, \mathbf{p}, t) \left(\mathbf{pp} - \frac{1}{3}\mathbf{I}\right) d\mathbf{p} \tag{6}$$

with $\alpha > 0$ for pullers and $\alpha < 0$ for pushers. We used the same scaling as that described by Saintillan and Shelley [12]. The local fluid motion about pullers and pushers are illustrated in figure 1. The flow about a single individual swimmer can be approximated as a flow generated by a force dipole (see figure 1). This approximation is used in the derivation [11] of (6).

3 Numerics

We wish to solve equation (1) in the 2-dimensional case. In terms of phase space, this equation must be solved over 3 dimensions (2 spatial coordinates plus the orientation angle θ). Equation (1) becomes

$$\Psi_t + \nabla_x \cdot (\dot{\mathbf{x}}\Psi) + \partial_\theta(\dot{\theta}\Psi) = 0. \tag{7}$$

The flux conditions become

$$\dot{\mathbf{x}} = V_0\mathbf{p} + \mathbf{u} - d_t\nabla_{\mathbf{x}}\ln\Psi \tag{8}$$

$$\dot{\mathbf{p}} = \dot{\theta}\hat{\theta} = [\hat{\theta} \cdot (\mathbf{p} \cdot \nabla_{\mathbf{x}}\mathbf{u}) - d_r\partial_\theta\ln\Psi]\hat{\theta} \tag{9}$$

where $\mathbf{p} = (\cos\theta, \sin\theta)^T$, $\hat{\theta} = (-\sin\theta, \cos\theta)^T$, and the flow $\mathbf{u}$ is described by equations (4) - (6). Using (5), (8), and (9), note that, in two dimensions, we have

$$\mathbf{p}^\perp \cdot \dot{\mathbf{p}} = \mathbf{p}^\perp \cdot (\mathbf{I} - \mathbf{pp}) \cdot (\mathbf{p} \cdot \nabla \mathbf{u}) \Rightarrow \tag{10}$$

$$\dot{\theta} = -u_x \sin(2\theta) + \frac{v_x}{2}(1 + \cos(2\theta)) - \frac{u_y}{2}(1 - \cos(2\theta)), \tag{11}$$

(using $u_x + v_y = 0$). Then equation (7) becomes (using $\nabla_x \cdot \dot{\mathbf{x}} = 0$ via continuity),

$$\begin{aligned}\Psi_t + (V_0 \cos\theta + u)\Psi_x + (V_0 \sin\theta + v)\Psi_y - d_t(\Psi_{xx} + \Psi_{yy}) \\ + \partial_\theta \left[\left(-u_x \sin(2\theta) + \frac{v_x}{2}(1 + \cos(2\theta)) - \frac{u_y}{2}(1 - \cos(2\theta)) \right) \Psi \right] - d_r \Psi_{\theta\theta} = 0.\end{aligned} \tag{12}$$

The equation (12) will be solved on a periodic domain in each phase space coordinate $x_1 \in [0, \ell_1), x_2 \in [0, \ell_2)$, and $\theta \in [0, 2\pi)$. We will use a pseudospectral method for each phase space coordinate. For time-stepping we will use the following method which solves the linear problem exactly and uses a second-order Adams-Bashforth method of updating the nonlinear terms. Let

$$\Psi(\mathbf{x}, \theta, t) = \sum_{\mathbf{k}} \hat{\Psi}_{\mathbf{k}}(t) e^{2\pi i(k_1 x/\ell_1 + k_2 y/\ell_2) + i k_3 \theta}. \tag{13}$$

Discretizing time uniformly as $t_n = n\Delta t$, for $n \in \{0, 1, 2, ...\}$, and denoting $\hat{\Psi}(t_n)$ by $\hat{\Psi}^n$, we write for each mode $\mathbf{k}$:

$$\hat{\Psi}^{n+2}_{\mathbf{k}} = e^{-\alpha_{\mathbf{k}} \Delta t} \left[\hat{\Psi}^{n+1}_{\mathbf{k}} + \frac{\Delta t}{2} \left(3\hat{\mathcal{N}}_{\mathbf{k}}[\Psi^{n+1}, u^{n+1}] - e^{-\alpha_{\mathbf{k}} \Delta t} \hat{\mathcal{N}}_{\mathbf{k}}[\Psi^n, u^n] \right) \right], \tag{14}$$

where

$$\alpha_{\mathbf{k}} = (d_t([2\pi k_1/\ell_1]^2 + [2\pi k_2/\ell_2]^2) + d_r k_3^2) \tag{15}$$

and

$$\begin{aligned}\mathcal{N}[\Psi^n, u^n] = -(V_0 \cos\theta + u^n)\Psi^n_x - (V_0 \sin\theta + v^n)\Psi^n_y \\ + \partial_\theta \left[\left(u^n_x \sin(2\theta) - \frac{v^n_x}{2}(1 + \cos(2\theta)) + \frac{u^n_y}{2}(1 - \cos(2\theta)) \right) \Psi^n \right].\end{aligned} \tag{16}$$

3.1 Velocity field

The computation of the velocity field is performed as follows in this first approach. Define the velocity and pressure fields (with time dependence suppressed since they are determined instantaneously at any given time), as

$$\mathbf{u}(\mathbf{x}) = \sum_{k_1, k_2} \hat{\mathbf{u}}_{\mathbf{k}} e^{2\pi i(k_1 x/\ell_1 + k_2 y/\ell_2)}, \tag{17}$$

$$p(\mathbf{x}) = \sum_{k_1, k_2} \hat{p}_{\mathbf{k}} e^{2\pi i(k_1 x/\ell_1 + k_2 y/\ell_2)}. \tag{18}$$

Define also the active forcing

$$\mathbf{f}_a = \nabla \cdot \mathbf{\Sigma}_a(\mathbf{x}) = (f_a, g_a). \tag{19}$$

The Stokes equations with continuity yield:

$$-2\pi i(k_1/\ell_1)\hat{p}_{\mathbf{k}} + \mu\left[(2\pi i k_1/\ell_1)^2 + (2\pi i k_2/\ell_2)^2\right]\hat{u}_{\mathbf{k}} + (\hat{f}_a)_{\mathbf{k}} = 0, \tag{20}$$

$$-2\pi i(k_2/\ell_2)\hat{p}_{\mathbf{k}} + \mu\left[(2\pi i k_1/\ell_1)^2 + (2\pi i k_2/\ell_2)^2\right]\hat{v}_{\mathbf{k}} + (\hat{g}_a)_{\mathbf{k}} = 0, \tag{21}$$

$$(2\pi i k_1/\ell_1)\hat{u}_{\mathbf{k}} + (2\pi i k_2/\ell_2)\hat{v}_{\mathbf{k}} = 0. \tag{22}$$

Multiplying the first equation by (k_1/ℓ_1), the second by (k_2/ℓ_2), and adding, and using the third equation, we find that

$$\hat{p}_{\mathbf{k}} = \frac{(k_1/\ell_1)(\hat{f}_a)_{\mathbf{k}} + (k_2/\ell_2)(\hat{g}_a)_{\mathbf{k}}}{2\pi i[(k_1/\ell_1)^2 + (k_2/\ell_2)^2]}, \tag{23}$$

and the velocity field satisfies

$$\hat{u}_{\mathbf{k}} = \frac{(\hat{f}_a)_{\mathbf{k}} - 2\pi i(k_1/\ell_1)\hat{p}_{\mathbf{k}}}{\mu\left[(2\pi k_1/\ell_1)^2 + (2\pi k_2/\ell_2)^2\right]}, \quad \hat{v}_{\mathbf{k}} = \frac{(\hat{g}_a)_{\mathbf{k}} - 2\pi i(k_2/\ell_2)\hat{p}_{\mathbf{k}}}{\mu\left[(2\pi k_1/\ell_1)^2 + (2\pi k_2/\ell_2)^2\right]}. \tag{24}$$

Or, letting $\mathbf{q} = (k_1/\ell_1, k_2/\ell_2)$, we may write this in a more familiar form,

$$\hat{p}_{\mathbf{k}} = \frac{\mathbf{q}\cdot(\hat{\mathbf{f}}_a)_{\mathbf{k}}}{2\pi i|\mathbf{q}|^2}, \quad \hat{\mathbf{u}}_{\mathbf{k}} = \frac{1}{(2\pi)^2\mu}\left(\frac{\mathbf{I} - \mathbf{qq}}{|\mathbf{q}|^2}\right)\cdot(\hat{\mathbf{f}}_a)_{\mathbf{k}}. \tag{25}$$

3.2 Active stress

Inserting the Fourier representation for Ψ, we have:

$$\boldsymbol{\Sigma}_a(\mathbf{x}) = \alpha\int_\Omega \Psi(\mathbf{x},\mathbf{p},t)\left(\mathbf{pp} - \frac{1}{2}\mathbf{I}\right)d\mathbf{p} \tag{26}$$

$$= \frac{\alpha}{N_{xgrid}N_{ygrid}N_{\theta grid}}\sum_{\mathbf{k}}\hat{\Psi}_{\mathbf{k}}(t)\int_\Omega e^{2\pi i(k_1x/\ell_1 + k_2y/\ell_2) + ik_3\theta}\begin{pmatrix}\cos^2\theta - 1/2 & \sin\theta\cos\theta\\ \sin\theta\cos\theta & \sin^2\theta - 1/2\end{pmatrix}d\theta \tag{27}$$

$$= \frac{\alpha}{N_{xgrid}N_{ygrid}N_{\theta grid}}\sum_{k_1,k_2}\begin{pmatrix}\frac{\pi}{2}\left(\hat{\Psi}_{k_1,k_2,2} + \hat{\Psi}_{k_1,k_2,-2}\right) & \frac{i\pi}{2}\left(\hat{\Psi}_{k_1,k_2,2} - \hat{\Psi}_{k_1,k_2,-2}\right)\\ \frac{i\pi}{2}\left(\hat{\Psi}_{k_1,k_2,2} - \hat{\Psi}_{k_1,k_2,-2}\right) & -\frac{\pi}{2}\left(\hat{\Psi}_{k_1,k_2,2} + \hat{\Psi}_{k_1,k_2,-2}\right)\end{pmatrix}e^{2\pi i(k_1x/\ell_1 + k_2y/\ell_2)}. \tag{28}$$

The 2D case is given by

$$\hat{\boldsymbol{\Sigma}}_a = \frac{\alpha}{N_{xgrid}N_{ygrid}N_{\theta grid}}\begin{pmatrix}\frac{\pi}{2}\left(\hat{\Psi}_{k_1,k_2,2} + \hat{\Psi}_{k_1,k_2,-2}\right) & \frac{i\pi}{2}\left(\hat{\Psi}_{k_1,k_2,2} - \hat{\Psi}_{k_1,k_2,-2}\right)\\ \frac{i\pi}{2}\left(\hat{\Psi}_{k_1,k_2,2} - \hat{\Psi}_{k_1,k_2,-2}\right) & -\frac{\pi}{2}\left(\hat{\Psi}_{k_1,k_2,2} + \hat{\Psi}_{k_1,k_2,-2}\right)\end{pmatrix}, \tag{29}$$

and then (omitting the N_xN_y since they are included with $\hat{f}$)

$$(\hat{\mathbf{f}}_a)_{\mathbf{k}} = (\nabla\cdot\hat{\boldsymbol{\Sigma}}_a)_{\mathbf{k}} = \frac{\alpha}{N_{\theta grid}}\begin{pmatrix}\frac{\pi^2 ik_1}{\ell_1}\left(\hat{\Psi}_{k_1,k_2,2} + \hat{\Psi}_{k_1,k_2,-2}\right) - \frac{\pi^2k_2}{\ell_2}\left(\hat{\Psi}_{k_1,k_2,2} - \hat{\Psi}_{k_1,k_2,-2}\right)\\ \frac{-\pi^2k_1}{\ell_1}\left(\hat{\Psi}_{k_1,k_2,2} - \hat{\Psi}_{k_1,k_2,-2}\right) - \frac{i\pi^2k_2}{\ell_2}\left(\hat{\Psi}_{k_1,k_2,2} + \hat{\Psi}_{k_1,k_2,-2}\right)\end{pmatrix}. \tag{30}$$

4 Cluster dynamics

4.1 Single cluster

We consider four simple initial configurations of a single cluster: an isotropic cluster, a polarized cluster of pullers, a polarized cluster of pushers, and an elongated polarized cluster of pushers

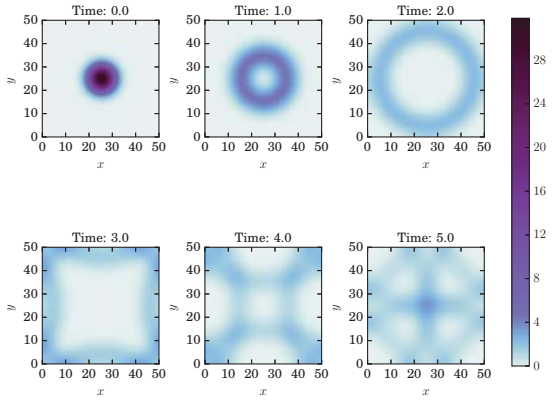

Figure 2: Concentration field during the spreading of an isotropic cluster with a swimming speed of $V = 10\mu m/s$ and $\alpha = -1$. We choose the following other parameters: $l_x = 50$, $l_y = 50$, $l_\theta = 2\pi$, $a = 5$, $d_r = 0.0$, $d_t = 0.0$, $x_0 = l_x/2$, and $y_0 = l_y/2$. (Colormap developed by Thyng *et al* [14])

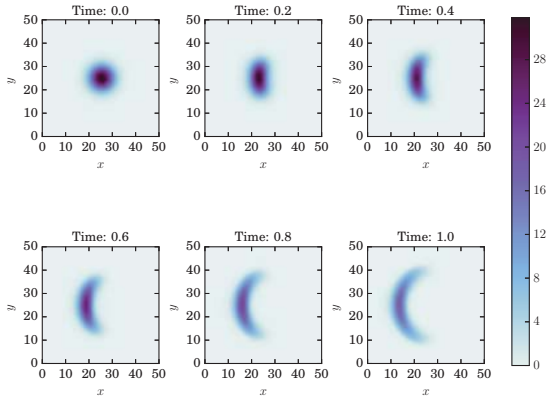

Figure 3: Concentration field during the spreading of a polarized cluster of pullers with a swimming speed of $V = 10\mu m/s$ and $\alpha = 1$. We choose the following other parameters: $l_x = 50$, $l_y = 50$, $l_\theta = 2\pi$, $a = 5$, $b = 0.5$, $d_r = 0.001$, $d_t = 0.001$, $x_0 = l_x/2$, $y_0 = l_y/2$, and $\theta_0 = \pi$.

1. (Isotropic cluster) Consider a cluster of characteristic width a located at the origin with uniformly distributed initial orientation, so that we have

$$\Psi(\mathbf{x}, \theta, t = 0) = Ae^{-((x-x_0)^2+(y-y_0)^2)/a^2} \tag{31}$$

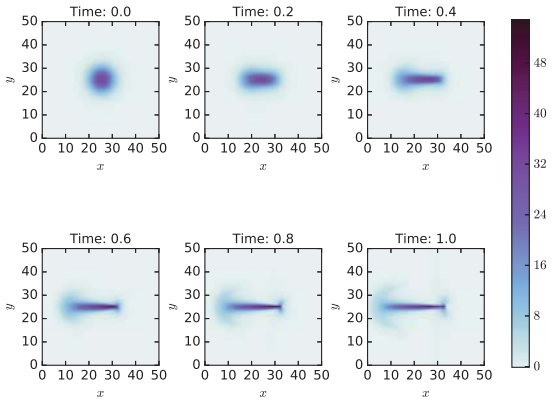

Figure 4: Concentration field during the spreading of a polarized cluster of pushers with a swimming speed of $V = 10\mu m/s$ and $\alpha = -1$. We choose the following other parameters: $l_x = 50$, $l_y = 50$, $l_\theta = 2\pi$, $a = 5$, $b = 0.5$, $d_r = 0.001$, $d_t = 0.001$, $x_0 = l_x/2$, $y_0 = l_y/2$, and $\theta_0 = \pi$.

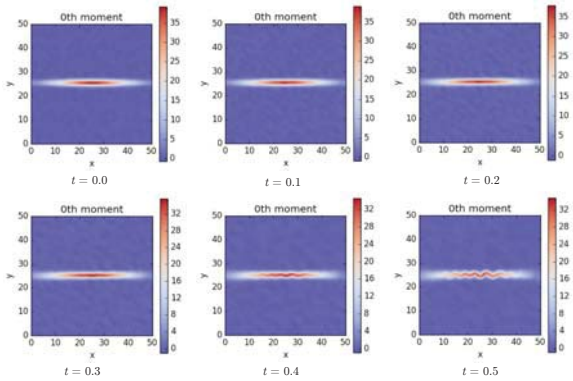

Figure 5: Concentration field of an initially elongated polarized cluster of pushers with a swimming speed of $V_0 = 5\mu m/s$ and $\alpha = -1$ with a small perturbation across Fourier modes. An instability arises which is most visible in the final frame above. We chose the following other parameters: $l_x = 50$, $l_y = 50$, $l_\theta = 2\pi$, $b = 0.5$, $d_r = 0.001$, $d_l = 0.001$, $x_0 = l_x/2$, $y_0 = l_y/2$, $\theta_0 = \pi + \pi/20$, $x_w = l_x/3$, and $y_w = l_y/40$.

with A as a normalization factor to ensure that mean density is $\frac{1}{2\pi}$. We noticed that the dynamics did not depend on α. We think this is due to the symmetry of the problem. We plan to investigate this further in future work.

2. (Polarized cluster of pullers) Consider a cluster at the origin, but now with *polarized* initial orientation to left, so that we have

$$\Psi(\mathbf{x}, \theta, t = 0) = Ae^{-((x-x_0)^2+(y-y_0)^2)/a^2-(\theta-\theta_0)^2/b^2}. \tag{32}$$

Recall that α is negative for pushers; We chose $\alpha = 1$ for the simulation shown in figure 3. We observed splaying of the initial distribution of swimmers and an overall collective radial motion which moved roughly at the individual swimming speed of 10.

3. (Polarized cluster of pushers) Consider a cluster at the origin so that we have

$$\Psi(\mathbf{x}, \theta, t = 0) = Ae^{-((x-x_0)^2+(y-y_0)^2)/a^2-(\theta-\theta_0)^2/b^2}. \tag{33}$$

We have made only one parameter change here relative to the last example — α is now positive for pullers. We observed a 'squeezing' effect lateral to the swimming direction which is consistent with our understanding of the local dynamics surrounding an individual pusher (see figure 1).

4. (Elongated polarized cluster of pushers)

$$\Psi(\mathbf{x}, \theta, t = 0) = Ae^{-(x-x_0)^2/x_w^2-(y-y_0)^2/y_w^2-(\theta-\theta_0)^2/b^2}, \tag{34}$$

We observed an instability in this case (see figure 5). We perturbed the initial condition with small random perturbations across fourier modes with$k_x < 15\frac{2\pi}{l_x}$ or $k_y < 15\frac{2\pi}{l_y}$. As a result, this perturbation excited an instability in this configuration. This suggests that the configuration shown in figure 4 at later times is a singular and unstable situation.

4.2 Dynamics of two colliding point particles

In this section, we will first take a look at a simple two point particle collision to see if it can capture the key features observed in the upcoming section when considering the collision of two patches.

Suppose that the motion of a single point particle at location $\mathbf{x}$ with direction $\mathbf{p}$ is governed by

$$\dot{\mathbf{x}} = V_0\mathbf{p} + \mathbf{u} \tag{35}$$
$$\dot{\mathbf{p}} = (\mathbf{I} - \mathbf{pp}) \cdot \nabla\mathbf{u} \cdot \mathbf{p} \tag{36}$$

where the point particle supplies a point force in a Stokes flow. We consider the collision of two such point particles as shown in figure 6 and investigate their dynamics. The surrounding fluid obeys

$$-\nabla q + \mu\nabla^2\mathbf{u} + \sum_{n=1,2} S(\mathbf{p}_n) \cdot \nabla\delta(\mathbf{x} - \mathbf{x}_n) = \mathbf{0}, \tag{37}$$
$$\nabla \cdot \mathbf{u} = 0 \tag{38}$$

where $S(\mathbf{p}_n) = \sigma\mathbf{p}_n\mathbf{p}_n$. The solution is given by

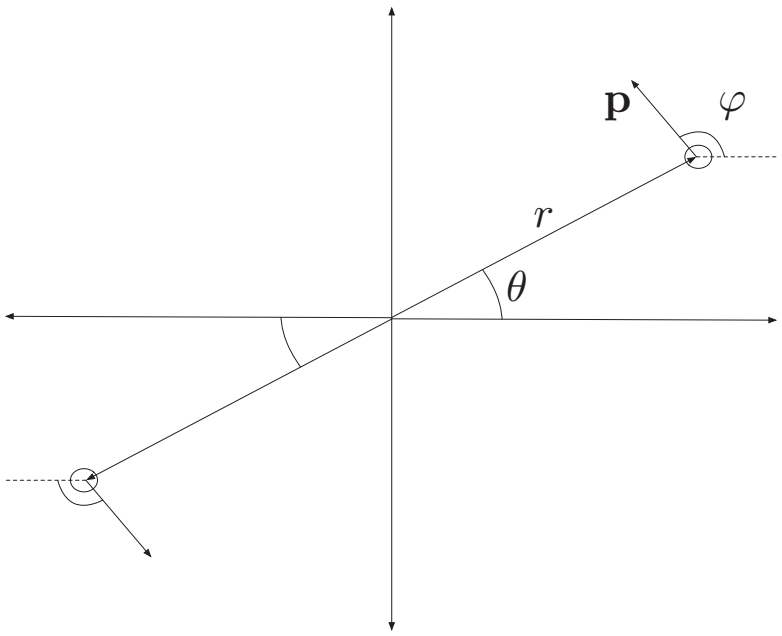

Figure 6: A symmetric collision of two point particles

$$\mathbf{u}(\mathbf{x}) = \sum_{n=1,2} S(\mathbf{p}_n) : \nabla J(\mathbf{x} - \mathbf{x}_n) \tag{39}$$

where $J(\mathbf{r}) = \frac{1}{8\pi\mu}(I - \hat{\mathbf{r}}\hat{\mathbf{r}})\frac{1}{|\mathbf{r}|}$ and $\hat{\mathbf{r}} = \mathbf{r}/|\mathbf{r}|$. Given the symmetry of the collision, the state of the system is completely determined by three dynamic variables r, θ, and φ. We find that

$$\begin{aligned}
\dot{r} &= V_0 \cos(\varphi - \theta) + u^r && (40)\\
r\dot{\theta} &= V_0 \sin(\varphi - \theta) + u^\theta && (41)\\
\dot{\varphi} &= -u_x \sin(2\varphi) + \frac{v_x}{2}(1 + \cos(2\varphi)) - \frac{u_y}{2}(1 - \cos(2\varphi)). && (42)
\end{aligned}$$

or equivalently,

$$\begin{aligned}
\dot{r} &= V_0 \left(\cos(\varphi - \theta) - \frac{\alpha \cos(2(\theta - \varphi))}{8\pi r} \right) && (43)\\
\dot{\theta} &= \frac{V_0}{r} \sin(\varphi - \theta) && (44)\\
\dot{\varphi} &= \alpha V_0 \left(\frac{\sin(4\theta - 4\varphi) - \sin(2\theta - 2\varphi)}{16\pi r^2} \right). && (45)
\end{aligned}$$

Figure 7 shows a series of collision trajectories across a range of the impact parameter y. Interestingly, as you decreased the impact parameter, you eventually surpass a threshold for which the trajectories are trapped in circular orbit at a fixed radius which has a $\sqrt{|\alpha|}$ dependence.

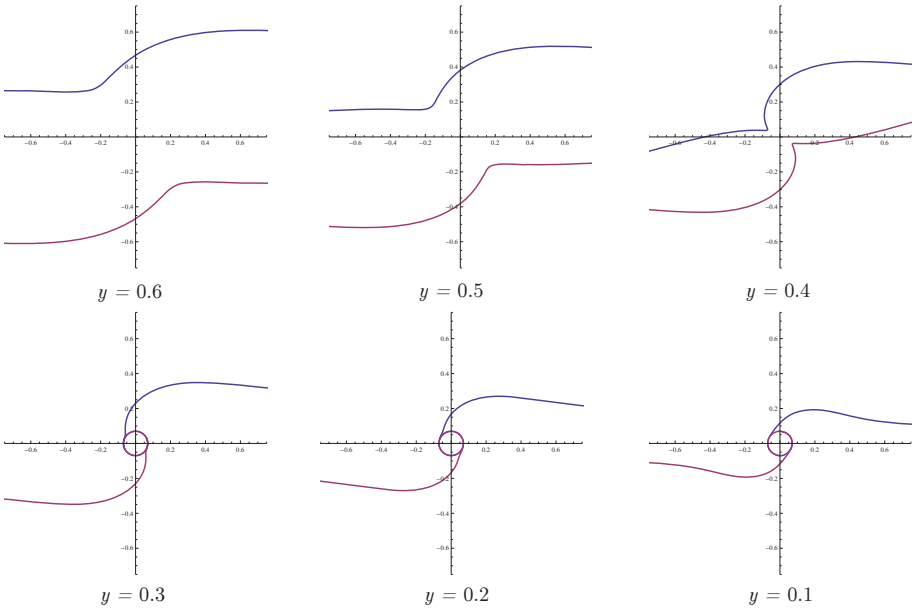

Figure 7: Trajectories of a symmetric collision of two point particles. The horizontal and vertical axes ranges from -0.75 to 0.75. y_0 measures the impact parameter relative to the horizontal axis. We chose the following parameters: $\alpha = -5.0$, $V_0 = 1.0$, and the initial x-coordinate $x_0 = 1.0$.

4.3 Dynamics of cluster collision

$$\Psi(\mathbf{x}, \theta, t = 0) = A\left(e^{-((x-x_0)^2+(y-y_0)^2)/a^2-\theta^2/b^2} + e^{-((x+x_0)^2+(y+y_0)^2)/a^2-(\theta-\pi)^2/b^2}\right), \tag{46}$$

Figure 8 shows how the dynamics change with decreasing impact parameter. Given the point particle analysis of the last section, we expected to see the clusters orbit around each other for small enough impact parameter. This however was not the case. Instead, we saw a 'curling' effect emerge from the interaction of the two clusters. It appears that the collision is exciting the instability discussed earlier when examining the single polarized puller cluster.

5 Droplet Dynamics

Now, we model a droplet with active matter. To do this numerically, we implemented an immersed boundary method [8]. We modeled the boundary by two different methods: a Lagrangian point method and a level-set method.

The Smoluchowski equation (1) remains the same. We add new terms to the flux conditions. The translation flux $\dot{\mathbf{x}}$ now has a new term that is responsible for making the boundary nearly impenetrable; the rotational flux $\dot{\mathbf{p}}$ has a new term that causes the swimmers to turn when encountering the interface. Specifically, the fluxes $\dot{\mathbf{x}}$ and $\dot{\mathbf{p}}$ change to (new terms are in blue)

$$\dot{\mathbf{x}} = V\mathbf{p} + \mathbf{u}(\mathbf{x}) - d_t\nabla_{\mathbf{x}}(\ln\Psi) - V_0\mathbf{p}\cdot\hat{n}\hat{n}\delta_\epsilon(\mathbf{x})1_{\{\mathbf{p}\cdot\hat{n}>0\}} \tag{47}$$

$$\dot{\mathbf{p}} = (\mathbf{I} - \mathbf{pp})\cdot(\mathbf{p}\cdot\nabla\mathbf{u}) - d_r\nabla_{\mathbf{p}}(\ln\Psi) - \beta\mathbf{p}\cdot\hat{n}\mathbf{p}^{\perp}\cdot\hat{n}\hat{n}\delta_\epsilon(\mathbf{x})1_{\{\mathbf{p}\cdot\hat{n}>0\}} \tag{48}$$

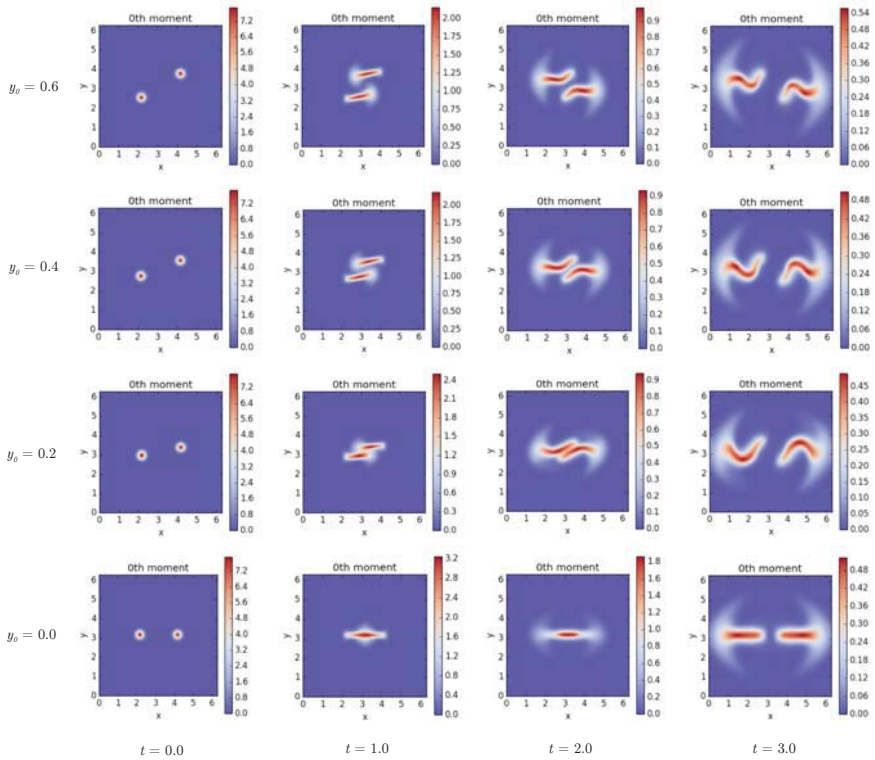

Figure 8: A symmetric collision of two polarized puller ($\alpha = -1$) clusters with varying impact parameter y as function of time t. We chose the parameters: We chose the following other parameters: $l_x = 2\pi$, $l_y = 2\pi$, $l_\theta = 2\pi$, $a = 0.2$, $b = 0.2$, $d_r = 0.01$, $d_l = 0.01$, $x_0 = 1.0$.

where $\hat{n}$ is the surface normal, β is a tunable parameter to set the degree influence the interface has on the rotation of a swimmer, and $\delta_\epsilon(\mathbf{x})$ is a numerical 'delta' function with width ϵ. We add a term for the normal stress due to surface tension in the Stokes equation:

$$-\nabla q + \mu\nabla^2\mathbf{u} + \nabla\cdot\mathbf{\Sigma}_a - \gamma(\nabla\cdot\hat{n})\hat{n}\delta_\epsilon(\mathbf{x}) = \mathbf{0} \tag{49}$$

$$\nabla\cdot\mathbf{u} = 0 \tag{50}$$

where γ is the surface tension. We used two alternative methods for evolving the boundary:

1. (Lagrangian method) We evolved the surface Lagrangian points by $\frac{dx_j}{dt}$ for $j = 1, 2, 3, \ldots, M$ where x_j is the position of the jth Lagrangian point and M is the total number of Lagrangian points.
2. (Level-set method) We evolved a level-set function ϕ according to $\frac{\partial\phi}{\partial t} + \mathbf{u}\cdot\nabla\phi = 0$ where $\phi = 0$ defines the interface, ϕ is positive in the interior, and ϕ is negative in the exterior.

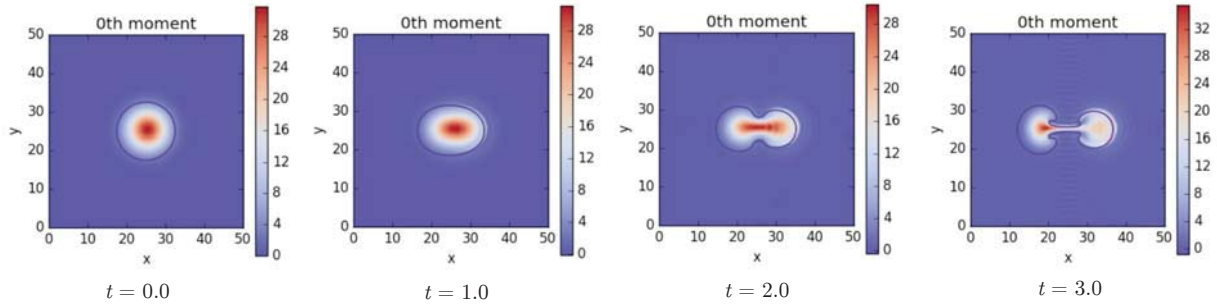

Figure 9: Droplet simulation with $l_x = l_y = 50$, $\alpha = -0.1$, $\beta = 1.0$, $V_0 = 1.0$, $d_t = 0.1$, $d_r = 0.1$ and $\gamma = 50000$. The active matter in the interior is a polarized cluster of pushers oriented to the right.

Figure 9 shows a simulation with $l_x = l_y = 50$, $\alpha = -0.1$, $\beta = 1.0$, $V_0 = 1.0$, and $\gamma = 50000$.

Recall from earlier that we observed an elongation effect for the case without the droplet interface (see figure 4). This effect still seems to be present when the cluster is placed in the interior of the droplet. But now, this elongation process causes the droplet to pinch in the center and creates a small filament between two newly formed daughter droplets (as seen in the last frame of figure 9). We were unable to get the two daughter droplets to completely separate. The problem of separation is two-fold: (1) the simulation used the Lagrangian method which, by construction, does not allow for splitting of the droplet interior domain (this can be solved by using the level-set method) and (2) we believe that we are neglecting physics about phase separation and may consider using a Cahn-Hillard potential for this purpose.

6 Is binary collision physics captured by the Smoluchowski equation?

After observing such rich dynamics in the binary collision of point particles (as seen in section 4.2), we asked the following "Is this physics captured in the Smoluchowski equation?" This may remind some of the Boltzmann equation which accounts for binary collisions of rarefied gases. On the other

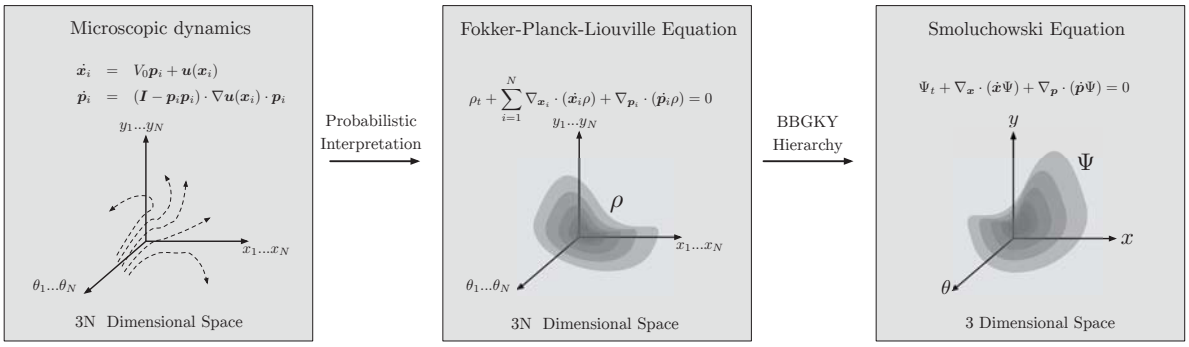

Figure 10: Microscopic description turns from a description in $3N$-dimensional space to a 3-dimensional space through the BBGKY hierarchy.

hand, a related equation, used mostly for describing plasmas, is the Vlasov equation which neglects the effects of binary collisions. So to state our question another way, we ask "Is the Smoluchowski equation Boltzman-like or Vlasov-like?" To answer this question, we will start with a microscopic description for N particles and derive the Smoluchowski equation by using statistical assumptions and the BBGKY hierarchy approach [1–6,17] a. This procedure, illustrated in figure 10, provides a way to reduce the dimension of phase space from $3N$ to 3 coordinates and provides a link between microscopic particle dynamics and the Smolukowski equation.

We begin by considering a periodic box with N particles. The particle motion is governed by (while ignoring random thermal forcing)

$$\begin{aligned}
\dot{\mathbf{x}}_1 &= V_0\mathbf{p}_1 + \mathbf{u}(\mathbf{x}_1) && (51)\\
\dot{\mathbf{p}}_1 &= (\mathbf{I} - \mathbf{p}_1\mathbf{p}_1)\cdot\nabla\mathbf{u}(\mathbf{x}_1)\cdot\mathbf{p}_1 && (52)\\
\dot{\mathbf{x}}_2 &= V_0\mathbf{p}_2 + \mathbf{u}(\mathbf{x}_2) && (53)\\
\dot{\mathbf{p}}_2 &= (\mathbf{I} - \mathbf{p}_2\mathbf{p}_2)\cdot\nabla\mathbf{u}(\mathbf{x}_2)\cdot\mathbf{p}_2 && (54)\\
&\vdots && (55)\\
\dot{\mathbf{x}}_N &= V_0\mathbf{p}_N + \mathbf{u}(\mathbf{x}_N) && (56)\\
\dot{\mathbf{p}}_N &= (\mathbf{I} - \mathbf{p}_N\mathbf{p}_N)\cdot\nabla\mathbf{u}(\mathbf{x}_N)\cdot\mathbf{p}_N && (57)
\end{aligned}$$

where

$$\mathbf{u}(\mathbf{x}_i) = \sum_{j=1, j\neq i}^{N} \mathbf{u}_j(\mathbf{x}_i|\mathbf{x}_j, \mathbf{p}_j) \tag{58}$$

and $\mathbf{u}_j(\mathbf{x})$ is the velocity field generated by the force-dipole particle j satisfying

$$\begin{aligned}
\mu\Delta\mathbf{u}_j - \nabla q + \sigma\mathbf{p}_j\mathbf{p}_j\cdot\nabla\delta(\mathbf{x} - \mathbf{x}_j) = 0 && (59)\\
\nabla\cdot\mathbf{u}_j = 0. && (60)
\end{aligned}$$

The corresponding n-particle Fokker-Planck-Louiville equation associated with equations (51)-(57) is

$$\frac{\partial \rho}{dt} + \sum_{i=1}^{N} \nabla_{\mathbf{x}_i} \cdot \{[V_0 \mathbf{p}_i + \mathbf{u}(\mathbf{x}_i)]\rho\} + \sum_{i=1}^{N} \nabla_{\mathbf{p}_i} \cdot \{[(\mathbf{I} - \mathbf{p}_i\mathbf{p}_i) \cdot \nabla_{\mathbf{x}_i} \mathbf{u}(\mathbf{x}_i) \cdot \mathbf{p}_i]\rho\} = 0 \tag{61}$$

The s-particle probability density is defined as

$$\rho_s(\mathbf{x}_1, \mathbf{p}_1, \ldots, \mathbf{x}_s, \mathbf{p}_s, t) = \int \prod_{i=s+1}^{N} d\mathbf{x}_i d\mathbf{p}_i \rho(\mathbf{x}_1, \mathbf{p}_1, \ldots, \mathbf{x}_N, \mathbf{p}_N, t) \tag{62}$$

where the definition assumes symmetry with respect to permutation of the particles. The time evolution of ρ_s is given by

$$\begin{aligned}
\frac{\partial \rho_s}{\partial t} &= \int \prod_{i=s+1}^{N} d\mathbf{x}_i d\mathbf{p}_i \left(- \sum_{j=1}^{N} \nabla_{\mathbf{x}_j} \cdot \{[V_0 \mathbf{p}_j + \mathbf{u}(\mathbf{x}_j)]\rho\} - \sum_{j=1}^{N} \nabla_{\mathbf{p}_i} \cdot \{[(\mathbf{I} - \mathbf{p}_j\mathbf{p}_j) \cdot \nabla_{\mathbf{x}_j} \mathbf{u}(\mathbf{x}_j) \cdot \mathbf{p}_j]\rho\} \right) \\
&= \int \prod_{i=s+1}^{N} d\mathbf{x}_i d\mathbf{p}_i \left(- \sum_{j=1}^{N} \nabla_{\mathbf{x}_j} \cdot \{[V_0 \mathbf{p}_j + \sum_{k=1, k\neq j}^{N} \mathbf{u}_k(\mathbf{x}_j | \mathbf{x}_k, \mathbf{p}_k)]\rho\} \right) \\
&+ \int \prod_{i=s+1}^{N} d\mathbf{x}_i d\mathbf{p}_i \left(- \sum_{j=1}^{N} \nabla_{\mathbf{p}_j} \cdot \{[(\mathbf{I} - \mathbf{p}_j\mathbf{p}_j) \cdot \nabla_{\mathbf{x}_j} \left(\sum_{k=1, k\neq j}^{N} \mathbf{u}_k(\mathbf{x}_j | \mathbf{x}_k, \mathbf{p}_k) \right) \cdot \mathbf{p}_j]\rho\} \right)
\end{aligned}$$

First, let us break up this expression into the three following parts:

$$\frac{\partial \rho_s}{\partial t} = G_s + G_{N-s} + G' \tag{63}$$

1. a term representing the interaction among a group of s particles

$$\begin{aligned}
G_s &= \int \prod_{i=s+1}^{N} d\mathbf{x}_i d\mathbf{p}_i \left(- \sum_{j=1}^{s} \nabla_{\mathbf{x}_j} \cdot \{[V_0 \mathbf{p}_j + \sum_{k=1, k\neq j}^{s} \mathbf{u}_k(\mathbf{x}_j | \mathbf{x}_k, \mathbf{p}_k)]\rho\} \right) \\
&+ \int \prod_{i=s+1}^{N} d\mathbf{x}_i d\mathbf{p}_i \left(- \sum_{j=1}^{s} \nabla_{\mathbf{p}_j} \cdot \{[(\mathbf{I} - \mathbf{p}_j\mathbf{p}_j) \cdot \nabla_{\mathbf{x}_j} \left(\sum_{k=1, k\neq j}^{s} \mathbf{u}_k(\mathbf{x}_j | \mathbf{x}_k, \mathbf{p}_k) \right) \cdot \mathbf{p}_j]\rho\} \right)
\end{aligned}$$

2. a term representing the interaction among the remaining group of $N - s$ particles

$$\begin{aligned}
G_{N-s} &= \int \prod_{i=s+1}^{N} d\mathbf{x}_i d\mathbf{p}_i \left(- \sum_{j=s+1}^{N} \nabla_{\mathbf{x}_j} \cdot \{[V_0 \mathbf{p}_j + \sum_{k=s+1, k\neq j}^{N} \mathbf{u}_k(\mathbf{x}_j | \mathbf{x}_k, \mathbf{p}_k)]\rho\} \right) \\
&+ \int \prod_{i=s+1}^{N} d\mathbf{x}_i d\mathbf{p}_i \left(- \sum_{j=s+1}^{N} \nabla_{\mathbf{p}_j} \cdot \{[(\mathbf{I} - \mathbf{p}_j\mathbf{p}_j) \cdot \nabla_{\mathbf{x}_j} \left(\sum_{k=s+1, k\neq j}^{N} \mathbf{u}_k(\mathbf{x}_j | \mathbf{x}_k, \mathbf{p}_k) \right) \cdot \mathbf{p}_j]\rho\} \right)
\end{aligned}$$

3. and a term representing the interaction between the s-group and the $(N-s)$-group

$$\begin{aligned}
G' &= \int \prod_{i=s+1}^{N} d\mathbf{x}_i d\mathbf{p}_i \left(-\sum_{j=1}^{s} \nabla_{\mathbf{x}_j} \cdot \{ \sum_{k=s+1, k\neq j}^{N} \mathbf{u}_k(\mathbf{x}_j|\mathbf{x}_k, \mathbf{p}_k)\rho\} \right) \\
&+ \int \prod_{i=s+1}^{N} d\mathbf{x}_i d\mathbf{p}_i \left(-\sum_{j=s+1}^{N} \nabla_{\mathbf{x}_j} \cdot \{ \sum_{k=1, k\neq j}^{s} \mathbf{u}_k(\mathbf{x}_j|\mathbf{x}_k, \mathbf{p}_k)\rho\} \right) \\
&+ \int \prod_{i=s+1}^{N} d\mathbf{x}_i d\mathbf{p}_i \left(-\sum_{j=1}^{s} \nabla_{\mathbf{p}_j} \cdot \{ [(\mathbf{I} - \mathbf{p}_j\mathbf{p}_j) \cdot \nabla_{\mathbf{x}_j} \left(\sum_{k=s+1, k\neq j}^{N} \mathbf{u}_k(\mathbf{x}_j|\mathbf{x}_k, \mathbf{p}_k) \right) \cdot \mathbf{p}_j]\rho\} \right) \\
&+ \int \prod_{i=s+1}^{N} d\mathbf{x}_i d\mathbf{p}_i \left(-\sum_{j=s+1}^{N} \nabla_{\mathbf{p}_j} \cdot \{ [(\mathbf{I} - \mathbf{p}_j\mathbf{p}_j) \cdot \nabla_{\mathbf{x}_j} \left(\sum_{k=1, k\neq j}^{s} \mathbf{u}_k(\mathbf{x}_j|\mathbf{x}_k, \mathbf{p}_k) \right) \cdot \mathbf{p}_j]\rho\} \right)
\end{aligned}$$

Let us evaluate each integral separately.

$$\begin{aligned}
G_s &= -\sum_{j=1}^{s} \nabla_{\mathbf{x}_j} \cdot \left\{ \left[V_0\mathbf{p}_j + \sum_{k=1, k\neq j}^{s} \mathbf{u}_k(\mathbf{x}_j|\mathbf{x}_k, \mathbf{p}_k) \right] \left(\int \prod_{i=s+1}^{N} d\mathbf{x}_i d\mathbf{p}_i \rho \right) \right\} \\
&- \sum_{j=1}^{s} \nabla_{\mathbf{p}_j} \cdot \left\{ \left[(\mathbf{I} - \mathbf{p}_j\mathbf{p}_j) \cdot \nabla_{\mathbf{x}_j} \left(\sum_{k=1, k\neq j}^{s} \mathbf{u}_k(\mathbf{x}_j|\mathbf{x}_k, \mathbf{p}_k) \right) \cdot \mathbf{p}_j \right] \left(\int \prod_{i=s+1}^{N} d\mathbf{x}_i d\mathbf{p}_i \rho \right) \right\} \\
&= -\sum_{j=1}^{s} \nabla_{\mathbf{x}_j} \cdot \left\{ \left[V_0\mathbf{p}_j + \sum_{k=1, k\neq j}^{s} \mathbf{u}_k(\mathbf{x}_j|\mathbf{x}_k, \mathbf{p}_k) \right] \rho_s(\mathbf{x}_1, \ldots, \mathbf{p}_s) \right\} \\
&- \sum_{j=1}^{s} \nabla_{\mathbf{p}_j} \cdot \left\{ \left[(\mathbf{I} - \mathbf{p}_j\mathbf{p}_j) \cdot \nabla_{\mathbf{x}_j} \left(\sum_{k=1, k\neq j}^{s} \mathbf{u}_k(\mathbf{x}_j|\mathbf{x}_k, \mathbf{p}_k) \right) \cdot \mathbf{p}_j \right] \rho_s(\mathbf{x}_1, \ldots, \mathbf{p}_s) \right\}
\end{aligned}$$

G_{N-s} vanishes due to the divergence theorem and periodic boundary conditions.

$$\begin{aligned}
G_{N-s} &= \int \prod_{i=s+1}^{N} d\mathbf{x}_i d\mathbf{p}_i \left(-\sum_{j=s+1}^{N} \nabla_{\mathbf{x}_j} \cdot \{ [V_0\mathbf{p}_j + \sum_{k=s+1, k\neq j}^{N} \mathbf{u}_k(\mathbf{x}_j|\mathbf{x}_k, \mathbf{p}_k)]\rho\} \right) \\
&+ \int \prod_{i=s+1}^{N} d\mathbf{x}_i d\mathbf{p}_i \left(-\sum_{j=s+1}^{N} \nabla_{\mathbf{p}_j} \cdot \{ [(\mathbf{I} - \mathbf{p}_j\mathbf{p}_j) \cdot \nabla_{\mathbf{x}_j} \left(\sum_{k=s+1, k\neq j}^{N} \mathbf{u}_k(\mathbf{x}_j|\mathbf{x}_k, \mathbf{p}_k) \right) \cdot \mathbf{p}_j]\rho\} \right) = 0
\end{aligned}$$

Finally, we simplify G'.

$$\begin{aligned}
G' &= \int \prod_{i=s+1}^{N} d\mathbf{x}_i d\mathbf{p}_i \left(-\sum_{j=1}^{s} \nabla_{\mathbf{x}_j} \cdot \{ \sum_{k=s+1, k\neq j}^{N} \mathbf{u}_k(\mathbf{x}_j|\mathbf{x}_k, \mathbf{p}_k)\rho\} \right) \\
&+ \int \prod_{i=s+1}^{N} d\mathbf{x}_i d\mathbf{p}_i \left(-\sum_{j=1}^{s} \nabla_{\mathbf{p}_j} \cdot \{ [(\mathbf{I} - \mathbf{p}_j\mathbf{p}_j) \cdot \nabla_{\mathbf{x}_j} \left(\sum_{k=s+1, k\neq j}^{N} \mathbf{u}_k(\mathbf{x}_j|\mathbf{x}_k, \mathbf{p}_k) \right) \cdot \mathbf{p}_j]\rho\} \right)
\end{aligned}$$

where we have again used the divergence theorem and periodic boundary conditions to eliminate the 2nd and 4th terms from the original expression.

$$
\begin{aligned}
G' &= -\sum_{j=1}^{s} \nabla_{\mathbf{x}_j} \cdot \left\{ \sum_{k=s+1, k\neq j}^{N} \int \prod_{i=s+1}^{N} d\mathbf{x}_i d\mathbf{p}_i \mathbf{u}_k(\mathbf{x}_j|\mathbf{x}_k, \mathbf{p}_k)\rho \right\} \\
&- \sum_{j=1}^{s} \nabla_{\mathbf{p}_j} \cdot \left\{ (\mathbf{I} - \mathbf{p}_j\mathbf{p}_j) \cdot \left[\sum_{k=s+1, k\neq j}^{N} \int \prod_{i=s+1}^{N} d\mathbf{x}_i d\mathbf{p}_i \nabla_{\mathbf{x}_j} \left(\mathbf{u}_k(\mathbf{x}_j|\mathbf{x}_k, \mathbf{p}_k) \right) \rho \right] \cdot \mathbf{p}_j \right\}
\end{aligned}
$$

Assuming symmetry with respect to particle permutations, we have that

$$
\begin{aligned}
G' &= -\sum_{j=1}^{s} \nabla_{\mathbf{x}_j} \cdot \left\{ (N-s) \int \prod_{i=s+1}^{N} d\mathbf{x}_i d\mathbf{p}_i \mathbf{u}_{s+1}(\mathbf{x}_j|\mathbf{x}_{s+1}, \mathbf{p}_{s+1})\rho \right\} \\
&- \sum_{j=1}^{s} \nabla_{\mathbf{p}_j} \cdot \left\{ (\mathbf{I} - \mathbf{p}_j\mathbf{p}_j) \cdot \left[(N-s) \int \prod_{i=s+1}^{N} d\mathbf{x}_i d\mathbf{p}_i \nabla_{\mathbf{x}_j} \left(\mathbf{u}_{s+1}(\mathbf{x}_j|\mathbf{x}_{s+1}, \mathbf{p}_{s+1}) \right) \rho \right] \cdot \mathbf{p}_j \right\}
\end{aligned}
$$

Then, we have

$$
\begin{aligned}
G' &= -\sum_{j=1}^{s} \nabla_{\mathbf{x}_j} \cdot \left\{ (N-s) \int d\mathbf{x}_{s+1} d\mathbf{p}_{s+1} \left(\mathbf{u}_{s+1}(\mathbf{x}_j|\mathbf{x}_{s+1}, \mathbf{p}_{s+1}) \left[\int \prod_{i=s+2}^{N} d\mathbf{x}_i d\mathbf{p}_i \rho \right] \right) \right\} \\
&- \sum_{j=1}^{s} \nabla_{\mathbf{p}_j} \cdot \left\{ (\mathbf{I} - \mathbf{p}_j\mathbf{p}_j) \cdot \left[(N-s) \int d\mathbf{x}_{s+1} d\mathbf{p}_{s+1} \left\{ \nabla_{\mathbf{x}_j} \left(\mathbf{u}_{s+1}(\mathbf{x}_j|\mathbf{x}_{s+1}, \mathbf{p}_{s+1}) \right) \left[\int \prod_{i=s+2}^{N} d\mathbf{x}_i d\mathbf{p}_i \rho \right] \right\} \right] \cdot \mathbf{p}_j \right\} \\
&= -\sum_{j=1}^{s} \nabla_{\mathbf{x}_j} \cdot \left\{ (N-s) \int d\mathbf{x}_{s+1} d\mathbf{p}_{s+1} \left(\mathbf{u}_{s+1}(\mathbf{x}_j|\mathbf{x}_{s+1}, \mathbf{p}_{s+1}) \rho_{s+1}(\mathbf{x}_1, \ldots, \mathbf{p}_{s+1}) \right) \right\} \\
&- \sum_{j=1}^{s} \nabla_{\mathbf{p}_j} \cdot \left\{ (\mathbf{I} - \mathbf{p}_j\mathbf{p}_j) \cdot \left[(N-s) \int d\mathbf{x}_{s+1} d\mathbf{p}_{s+1} \left\{ \nabla_{\mathbf{x}_j} \left(\mathbf{u}_{s+1}(\mathbf{x}_j|\mathbf{x}_{s+1}, \mathbf{p}_{s+1}) \right) \rho_{s+1}(\mathbf{x}_1, \ldots, \mathbf{p}_{s+1}) \right\} \right] \cdot \mathbf{p}_j \right\}
\end{aligned}
$$

Finally, we have that

$$
\begin{aligned}
&\frac{\partial \rho_s}{\partial t}(\mathbf{x}_1, \ldots, \mathbf{p}_s, t) \\
&= -\sum_{j=1}^{s} \nabla_{\mathbf{x}_j} \cdot \left\{ \left[V_0 \mathbf{p}_j + \sum_{k=1, k\neq j}^{s} \mathbf{u}_k(\mathbf{x}_j|\mathbf{x}_k, \mathbf{p}_k) \right] \rho_s(\mathbf{x}_1, \ldots, \mathbf{p}_s) \right\} \\
&- \sum_{j=1}^{s} \nabla_{\mathbf{p}_j} \cdot \left\{ \left[(\mathbf{I} - \mathbf{p}_j\mathbf{p}_j) \cdot \nabla_{\mathbf{x}_j} \left(\sum_{k=1, k\neq j}^{s} \mathbf{u}_k(\mathbf{x}_j|\mathbf{x}_k, \mathbf{p}_k) \right) \cdot \mathbf{p}_j \right] \rho_s(\mathbf{x}_1, \ldots, \mathbf{p}_s) \right\} \\
&- \sum_{j=1}^{s} \nabla_{\mathbf{x}_j} \cdot \left\{ (N-s) \int d\mathbf{x}_{s+1} d\mathbf{p}_{s+1} \left(\mathbf{u}_{s+1}(\mathbf{x}_j|\mathbf{x}_{s+1}, \mathbf{p}_{s+1}) \rho_{s+1}(\mathbf{x}_1, \ldots, \mathbf{p}_{s+1}) \right) \right\} \\
&- \sum_{j=1}^{s} \nabla_{\mathbf{p}_j} \cdot \left\{ (\mathbf{I} - \mathbf{p}_j\mathbf{p}_j) \cdot \left[(N-s) \int d\mathbf{x}_{s+1} d\mathbf{p}_{s+1} \left\{ \nabla_{\mathbf{x}_j} \left(\mathbf{u}_{s+1}(\mathbf{x}_j|\mathbf{x}_{s+1}, \mathbf{p}_{s+1}) \right) \rho_{s+1}(\mathbf{x}_1, \ldots, \mathbf{p}_{s+1}) \right\} \right] \cdot \mathbf{p}_j \right\}.
\end{aligned}
$$

Note that the evolution of ρ_1 depends on ρ_2 and ρ_2 depends on ρ_3 and so forth. Therefore to make use of the above expression, one must create a closure to truncate the hierarchy. Let us examine the first equation of the hierarchy.

$$\begin{aligned}
&\frac{\partial \rho_1}{\partial t}(\mathbf{x}_1, \mathbf{p}_1, t) + V_0 \mathbf{p}_1 \cdot \nabla_{\mathbf{x}_1} \rho_1(\mathbf{x}_1, \mathbf{p}_1) \\
= \;& -\nabla_{\mathbf{x}_1} \cdot \left\{ (N-1) \int d\mathbf{x}_2 d\mathbf{p}_2 \left(\mathbf{u}_2(\mathbf{x}_1 | \mathbf{x}_2, \mathbf{p}_2) \rho_2(\mathbf{x}_1 \mathbf{p}_1, \mathbf{x}_2, \mathbf{p}_2) \right) \right\} \\
- \;& \nabla_{\mathbf{p}_1} \cdot \left\{ (\mathbf{I} - \mathbf{p}_1 \mathbf{p}_1) \cdot \left[(N-1) \int d\mathbf{x}_2 d\mathbf{p}_2 \left\{ \nabla_{\mathbf{x}_1} \left(\mathbf{u}_2(\mathbf{x}_1 | \mathbf{x}_2, \mathbf{p}_2) \right) \rho_2(\mathbf{x}_1 \mathbf{p}_1, \mathbf{x}_2, \mathbf{p}_2) \right\} \right] \cdot \mathbf{p}_1 \right\}.
\end{aligned}$$

Now we choose the closure $\rho_2(\mathbf{x}_1, \mathbf{p}_1, \mathbf{x}_2, \mathbf{p}_2) = \rho_1(\mathbf{x}_1, \mathbf{p}_1)\rho_1(\mathbf{x}_2, \mathbf{p}_2)$, this physically means that the interaction among the particles is long range rather than short range (only mediated via two particle interactions) as seen in the Boltzmann equation. Furthermore, if we introduce the s-particle density functions,

$$\Psi_s(\mathbf{x}_1, \ldots, \mathbf{p}_s) = \frac{N!}{(N-s)!} \rho_s(\mathbf{x}_1, \ldots, \mathbf{p}_s),$$

then one finds that the 1-particle density function evolves as

$$\begin{aligned}
&\frac{\partial \Psi_1}{\partial t}(\mathbf{x}_1, \mathbf{p}_1, t) + V_0 \mathbf{p}_1 \cdot \nabla_{\mathbf{x}_1} \Psi_1(\mathbf{x}_1, \mathbf{p}_1) \\
= \;& -\nabla_{\mathbf{x}_1} \cdot \left\{ \int d\mathbf{x}_2 d\mathbf{p}_2 \left(\mathbf{u}_2(\mathbf{x}_1 | \mathbf{x}_2, \mathbf{p}_2) \Psi_1(\mathbf{x}_1, \mathbf{p}_1) \Psi_1(\mathbf{x}_2, \mathbf{p}_2) \right) \right\} \\
- \;& \nabla_{\mathbf{p}_1} \cdot \left\{ (\mathbf{I} - \mathbf{p}_1 \mathbf{p}_1) \cdot \left[\int d\mathbf{x}_2 d\mathbf{p}_2 \left\{ \nabla_{\mathbf{x}_1} \left(\mathbf{u}_2(\mathbf{x}_1 | \mathbf{x}_2, \mathbf{p}_2) \right) \Psi_1(\mathbf{x}_1, \mathbf{p}_1) \Psi_1(\mathbf{x}_2, \mathbf{p}_2) \right\} \right] \cdot \mathbf{p}_1 \right\}.
\end{aligned}$$

If we define

$$\mathbf{u}'(\mathbf{x}_1) = \int d\mathbf{x}_2 d\mathbf{p}_2 \mathbf{u}_2(\mathbf{x}_1 | \mathbf{x}_2, \mathbf{p}_2) \Psi_1(\mathbf{x}_2, \mathbf{p}_2), \tag{64}$$

we arrive at the Vlasov-like equation

$$\begin{aligned}
&\frac{\partial \Psi_1}{\partial t}(\mathbf{x}_1, \mathbf{p}_1, t) + V_0 \mathbf{p}_1 \cdot \nabla_{\mathbf{x}_1} \Psi_1(\mathbf{x}_1, \mathbf{p}_1) \\
= \;& -\nabla_{\mathbf{x}_1} \cdot \left\{ \mathbf{u}'(\mathbf{x}_1) \Psi_1(\mathbf{x}_1, \mathbf{p}_1) \right\} \\
- \;& \nabla_{\mathbf{p}_1} \cdot \left\{ (\mathbf{I} - \mathbf{p}_1 \mathbf{p}_1) \cdot \nabla_{\mathbf{x}_1} \mathbf{u}'(\mathbf{x}_1) \cdot \mathbf{p}_1 \Psi_1(\mathbf{x}_1, \mathbf{p}_1) \right\}
\end{aligned}$$

which is exactly the diffusionless Smoluchowski equation used in our model. Therefore, we have arrived at an answer to the question posed — the Smoluchowski equation is Vlasov-like and does *not* include binary-collision physics.

7 Discussion

In this work, we studied the model introduced by Saintillan and Shelley [10]. In particular, we investigated the dynamics of active matter clusters, studied the confinement of active matter within a droplet, and discovered the absence of binary collision physics in the Smoluchowski equation.

The isotropic cluster expanded out in a 'ring' as expected due to the uniform distribution over orientation angle θ. Due to the symmetry of the problem we saw that the dynamics were independent of α. A polarized cluster of pullers showed splaying into a crescent shape with near

radial motion at later times. On the other hand, A polarized cluster of pushers exhibited an elongation along its polarized axis and thinning in the lateral directions. We then considered an initially elongated cluster of pushers with a slight perturbation which excited an instability. Thus, this shows that the final stages of the elongation effect seen in figure 4 may not be stable. We then considered the binary collision of point particles as a reduced model of the collision of two polarized clusters. We found that the dynamics of the polarized clusters did not match this reduced model since the clusters did not retain its coherent structure and quickly deformed. In fact, we observed a 'curling' effect which we suspect to be the result of the instability described earlier.

We then explored the effects of confinement by placing a cluster of active matter in the interior of a droplet. We included new terms to the flux conditions to enforce nearly impenetrable droplet walls. In addition, we endowed the interface with surface tension. We observed that a cluster of pusher particles elongated as seen without the interface. As a consequence, the droplet surface deformed in response to produce a dumbbell-like shape. We surmise that by including further physics of phase separation (by possibly considering the Cahn-Hillard potential), the dumbbell will turn into two separate daughter droplets.

We observed rich dynamics in a single binary collision, this prompted the following question, "Is the physics of binary collisions included in the Smoluchowski equation?" We discovered that the answer is 'No' by performing a derivation of the Smoluchowski equation by using the BBGKY hierarchy approach. Furthermore, we identified the Smoluchowski equation as Vlasov-like rather than Bolzmann-like. If the situation is at all similar to the kinetic theory of rarefied gases, we hypothesize that the inclusion of binary collisions will result in the addition of a new diffusive term, different than the diffusive term already included representing the effect of thermal fluctuations.

References

[1] N. N. Bogoliubov. Kinetic Equations. *Journal of Experimental and Theoretical Physics*, 16(8):691–702, 1946.

[2] N. N. Bogoliubov and K. P. Gurov. Kinetic equations in quantum mechanics. *Journal of Experimental and Theoretical Physics*, 17(7):614–627, 1947.

[3] M. Born and H. S. Green. A General Kinetic Theory of Liquids. I. The Molecular Distribution Functions. *Proceedings of the Royal Society A: Mathematical, Physical and Engineering Sciences*, 188(1012):10–18, dec 1946.

[4] Mehran Kardar. *Statistical physics of particles*. Cambridge University Press, 2007.

[5] John G Kirkwood. The Statistical Mechanical Theory of Transport Processes I. General Theory. *The Journal of Chemical Physics*, 14(3):180–201, 1946.

[6] John G. Kirkwood. The Statistical Mechanical Theory of Transport Processes II. Transport in Gases. *The Journal of Chemical Physics*, 15(1):72, 1947.

[7] M C Marchetti, J.-F. Joanny, S Ramaswamy, T B Liverpool, J Prost, M Rao, and R A Simha. Soft active matter. *arXiv preprint arXiv:1207.2929*, 2012.

[8] Rajat Mittal and Gianluca Iaccarino. Immersed Boundary Methods. *Annual Review of Fluid Mechanics*, 37(1):239–261, 2005.

[9] Sriram Ramaswamy. The mechanics and statistics of active matter. *Annual Review of Condensed Matter Physics*, 1(1):323–345, 2010.

[10] D Saintillan and M J Shelley. Instabilities and pattern formation in active particle suspensions: Kinetic theory and continuum simulations. *Phys. Rev. Lett.*, 100:178103, 2008.

[11] D Saintillan and M J Shelley. Theory of active suspensions. In *Complex Fluids in Biological Systems*, pages 319–351. Springer, 2014.

[12] David Saintillan and Michael J. Shelley. Hydrodynamic fluctuations and instabilities in ordered suspensions of self-propelled particles. *Physics of Fluids*, 20(12):1–16, 2008.

[13] David Saintillan and Michael J. Shelley. Instabilities and pattern formation in active particle suspensions: Kinetic theory and continuum simulations. *Physical Review Letters*, 100(17):1–4, 2008.

[14] Kristen M. Thyng, Chad A. Greene, Robert D. Hetland, Heather M. Zimmerle, and Steven F. DiMarco. True colors of oceanography: Guidelines for effective and accurate colormap selection. *Oceanography*, 2016.

[15] T Vicsek, A Czirok, E Ben-Jacob, I Cohen, and O Shochet. Novel Type of Phase Transition in a System of Self Propelled Particles. *Phys. Rev. Lett.*, 75(8):1226–1229, 1995.

[16] Tamás Vicsek and Anna Zafeiris. Collective motion. *Physics Reports*, 517(3-4):71–140, 2012.

[17] J. Yvon. La théorie statistique des fluides et l'équation d'état. *Actual. Sci. & Indust*, 1935.